Thomas T. C. Hsu *Editor*

Concrete Structures in Earthquake

Springer

Concrete Structures in Earthquake

Thomas T. C. Hsu
Editor

Concrete Structures in Earthquake

Springer

Editor
Thomas T. C. Hsu
Department of Civil and Environmental
Engineering
University of Houston
Houston, TX, USA

ISBN 978-981-13-3277-7 ISBN 978-981-13-3278-4 (eBook)
https://doi.org/10.1007/978-981-13-3278-4

Library of Congress Control Number: 2018961215

This Springer imprint is published by the registered company Springer Nature Singapore Pte Ltd.
The registered company address is: 152 Beach Road, #21-01/04 Gateway East, Singapore 189721, Singapore

Houston International Forum: Concrete Structures in Earthquake

Date: July 1–3, 2018
Venue: University Hilton on Campus
Sponsored by
Department of Civil and Environmental Engineering,
Cullen College of Engineering,
Division of Research and Technology Transfer,
University of Houston

Co-sponsors

American Concrete Institute, USA
National Center for Research on Earthquake Engineering (NCREE), Taiwan

Organizing Committee

Thomas T. C. Hsu, Moores Professor, University of Houston, USA (Chair)
Y. L. Mo, Professor of Civil Engineering
Amr Elnashai, Senior VC/VP for Research and Technology Transfer
Abdeldjelil Belarbi, Cullen Professor of Structural Engineering
Roberto Ballarini, Chair, Department of Civil and Environmental Engineering
Joseph Tedesco, Dean, Cullen College of Engineering
Mina Dawood, Associate Professor and Director of Hsu Structural Research Laboratory

Forum Administrator

Cherish Wallace
Department of Civil and Environmental Engineering
University of Houston
4726 Calhoun Road
Houston, Texas 77204, USA
Tel: 713-743-4295
e-mail: cwallace@uh.edu

Agenda

Sunday, July 1, 2018
Welcome Reception in the Waldorf-Astoria Lobby

6:00 pm–9:00 pm	Reception with refreshments; Registration for speakers

Monday, July 2, 2018
Breakfast in Shamrock Ballroom C

6:30 am–8:00 am	Breakfast Buffet

Morning-Session I: 8:00 am–12:00 pm in Shamrock Ballroom AB
Session Chair: Thomas T. C. Hsu, Moores Professor, Department of Civil and Environmental Engineering

8:00 am–8:05 am	Welcome by Dr. Amr Elnashai University of Houston's Vice Chancellor/Vice President for Research and Technology Transfer
8:05 am–8:10 am	Session Chair: Thomas T. C. Hsu, Moores Professor, Department of Civil and Environmental Engineering
8:10 am–8:35 am	(1) **Title: Periodic Material-Based Three-Dimensional (3D) Seismic Base Isolators for Small Modular Reactors** **Authors:** Y. L. Mo, Professor, Department of Civil and Environmental Engineering, University of Houston, Houston, TX, USA
8:35 am–9:00 am	(2) **Title: Shear Behavior Prediction of Non-ductile Reinforced Concrete Members in Earthquake** **Author**: Shyh-Jiann Hwang, Director General, National Center for Research on Earthquake Engineering (NCREE), and Professor, National Taiwan University
9:00 am–9:25 am	(3) **Title: Experimental Study of Novel RC Frames Considering Earthquake and Progressive Collapse** **Authors:** Xinzheng Lu, Professor, Beijing Engineering Research Center of Steel and Concrete Composite Structures, Tsinghua University, China
9:25 am–9:50 am	(4) **Title: Validation of the PARC_CL 2.0 Crack Model by the Cyclic Tests of 1/13-scale Nuclear Containment Structures** **Authors:** Beatrice Belletti, Associate Professor, Università di Parma, Dipartimento di Ingegneria e Architettura, Parma, Italy
9:50 am–10:10 am	Intermission
10:10 am–10:35 am	(5) **Title: Effect of High Strength Reinforcement for Shear Strength and Shear-Friction Strength of Shear Walls subjected to Cyclic Lateral Loading** **Authors:** Hong-Gun Park, Professor, Department of Architecture and Architectural Engineering, Seoul National University, Seoul, Korea

(continued)

(continued)

10:35 am–11:00 am	(6) **Title: Research on Resilient Reinforced Concrete Building Structural System** **Authors:** Susumu Kono, Professor, Tokyo Institute of Technology, Yokohama, Japan
11:00 am–11:25 am	(Add) **Title: The State of Knowledge and Practice in Concrete Structure Design for Earthquake** **Author:** John S. Ma, Senior Engineer and Charter Member, US Nuclear Regulatory Commission, Washington, DC
11:25 am–11:45 am	Questions and Answers
11:45 am–12:00 pm	Group Pictures

Lunch in Shamrock Ballroom C

12:00 pm–1:00 pm	South of the Border Lunch Buffet

Afternoon-Session II: 1:00 pm–5:00 pm in Shamrock Ballroom AB Session Chair: Shyh-Jiann Hwang, Director General, NCREE, and Professor, National Taiwan University

1:00 pm–1:25 pm	(7) **Title: Development of Large-Diameter Reinforcing Bars for the Seismic Resistance of Reinforced Concrete Bridge Columns** **Authors:** Juan Murcia-Delso, Assistant Professor, Department of Civil, Architectural and Environmental Engineering, University of Texas, Austin, TX, USA P. Benson Shing, Professor, Department of Structural Engineering, University of California, San Diego, CA, USA
1:25 pm–1:50 pm	(8) **Title: Reversed Cyclic Tests of 1/13 Scale Cylindrical Concrete Containment Structures** **Authors:** Chiun-Lin Wu, Research Fellow, National Center for Research on Earthquake Engineering (NCREE), Taipei, Taiwan
1:50 pm–2:15 pm	(9) **Title: Recent Advances on Seismic Retrofit of Reinforced Concrete Shear Walls with FRP** **Authors:** David Lau, Professor, The Department of Civil and Environmental Engineering, Carleton University, Ottawa, Canada
2:15 pm–2:40 pm	(10) **Title: Seismic Response of Shearwall Building Subjected to Long Duration Ground Motion** **Authors:** Carlos E. Ventura, Professor, Civil Engineering, UBC Vancouver, Canada
2:40 pm–3:00 pm	Intermission
3:00 pm–3:25 pm	(11) **Title: Drift Capacity at Onset of Bar Buckling in RC Structural Walls Subjected to Earthquakes** **Author:** Mario E. Rodriguez, National University of Mexico, Mexico City, Mexico

(continued)

(continued)

3:25 pm–3:50 pm	(12) **Title: Numerical Modeling and Experimental Response of Reinforced Concrete Walls with Discontinuities under Cycling Loading** **Authors:** Fabián Rojas, Assistant Professor, Department of Civil Engineering, University of Chile, Chile
3:50 pm–4:15 pm	(13) **Title: Assessment of the Boundary Regions Stability of Special RC Walls** **Authors:** A. G. Haro, Professor, Departamento de Ciencias de la Tierra y la Construcción, Universidad de las Fuerzas Armadas ESPE, Sangolquí, Ecuador
4:15 pm–4:40 pm	(14) **Title: Ductility Demand of a High-Rise RC Flat-Plate Core-Wall Building Structure in a Moderate-Seismicity Region: South Korea** **Authors:** Han Seon Lee, Professor, School of Civil, Environmental, and Architectural Engineering, Korea University, Korea
4:40 pm–5:00 pm	Questions and Answers

Dinner in Shamrock Ballroom C

5:00 pm–6:30 pm	Executive Dinner Buffet

Tuesday, July 3, 2018
Breakfast in Shamrock Ballroom C

6:30 am–8:00 am	Breakfast Buffet

Morning-Session III: 8:00 am–12:00 pm in Shamrock Ballroom AB
Session Chair: Abdeldjelil DJ Belarbi, Hugh Roy and Lillie Cranz Cullen Distinguished Professor, Department of Civil and Environmental Engineering

8:00 am–8:25 am	(15) **Title: Essential Requirements for Reinforced Concrete Structures of Limited Area and Height** **Authors:** Luis E. Garcia, Universidad de los Andes, Bogotá, Colombia
8:25 am–8:50 am	(16) **Title**: **The Seismic Strengthening of Concrete Structures by Ultra-High Performance Concrete** **Authors:** Sung-Gul Hong, Professor, Department of Architecture and Architectural Engineering, Seoul National University, Seoul, Korea
8:50 am–9:15 am	(17) **Title**: **Effect of Strain Penetration on RC Beam-Column Joints Subjected to Seismic Loading** **Authors:** Jung-Yoon Lee, Professor, School of Civil, Architectural Engineering and Landscape Architecture, Sungkyunkwan University, Seoul, Korea

(continued)

(continued)

9:15 am–9:40 am	(18) **Title: Capacity-Based Inelastic Displacement Spectra for Seismic Evaluation and Design of Reinforced Concrete Bridges** **Authors:** Kuo-Chun Chang, Professor, Department of Civil Engineering, National Taiwan University, Taipei, Taiwan Ping-Hsiung Wang, Assistant Research Fellow, National Center for Research on Earthquake Engineering (NCREE), Taipei, Taiwan
9:40 am–10:00 am	Intermission
10:00 am–10:25 am	(19) **Title: Issues Related to the Rapid Seismic Repair of Concrete Bridge Columns** **Authors:** Zachary Krish, Ph.D. Student, North Carolina State University, Raleigh, NC, USA Mervyn Kowalsky, Professor of Structural Engineering, North Carolina State University, Raleigh, NC, USA
10:25 am–10:50 am	(20) **Title: Seismic Analysis of SMA-Retrofitted Concrete Columns Using Material Testing Integrated Simulation** **Authors:** Donghyuk Jung, Graduate Research Assistant, Department of Civil Engineering, University of Illinois at Urbana-Champaign, Urbana, IL, USA Bassem Andrawes, Associate Professor, Department of Civil Engineering, University of Illinois at Urbana-Champaign, Urbana, IL, USA
10:50 am–11:15 am	(21) **Title: Test and Analysis of a Self-Centering Concrete Frame Under Seismic Action** **Authors:** Xilin Lu, Professor, State Key Laboratory of Disaster Reduction in Civil Engineering, Tongji University, Shanghai, China
11:15 am–11:40 am	(22) **Title: Structural Performance of Slender High Strength SFRC Columns (Fc300) Under Axial and Lateral Loadings** **Author:** Yusuke Tanabe, Takenaka Corporation, Japan
11:40 am–12:00 pm	Questions and Answers

Lunch in Shamrock Ballroom C

12:00 pm–2:00 pm	Italian Lunch Buffet (Participants may leave during this time)

Thomas T. C. Hsu Structural Research Laboratory Tour

2:00 pm–4:00 pm	Thomas T. C. Hsu Structural Research Laboratory tour given by Dr. Mina Dawood, Associate Professor and Director of Hsu Structural Research Laboratory, University of Houston

Preface

Since the 1980s, University of Houston (UH) has been in the forefront of researches for concrete structures subjected to earthquake. These researches resulted in the book "Unified Theory of Concrete Structures" published by John Wiley & Sons in 2010. This book by Hsu and Mo provided the basic theory to predict the seismic behavior of wall-type structures. This seismic behavior includes the hysteretic loop, the strength, the ductility, and the energy dissipation.

To foster research in concrete structures under earthquake, UH has hosted two international workshops:

(1) On January 14–16, 1991, an International Workshop entitled "Concrete Shear in Earthquake" was held at UH. This Workshop, sponsored by National Science Foundation, attracted over 100 participants from 14 countries. The presentations in this workshop was collected in a book *Concrete Shear in Earthquake*, edited by Hsu and Mau, and published by Elsevier Science Publishers, Inc., London/New York, 1992, pp. 535.
(2) On December 15–17, 2010, an International Workshop entitled "Infrastructure Systems for Nuclear Energy" was held at NCREE (National Center for Research on Earthquake Engineering), Taipei, Taiwan. This Workshop which was co-sponsored by UH and NCREE, resulted in a book *Infrastructure Systems for Nuclear Energy* edited by Hsu, Wu and Lin, and published by John Wiley & Sons, Ltd., London, January 2014, pp. 584.

In view of the huge, worldwide infrastructure investment in recent years and the rapid advancement of research in this field, it was proposed that an International Forum entitled "Concrete Structures in Earthquake" be held at UH on July 2–3, 2018, immediately following the 11NCEE in Los Angeles. The Proceedings of this Forum is published by Springer Nature in this book.

Houston, TX, USA Thomas T. C. Hsu

Contents

1 Periodic Material-Based Three-Dimensional (3D) Seismic Base Isolators for Small Modular Reactors 1
Y. L. Mo, Witarto Witarto, Kuo-Chun Chang, Shiang-Jung Wang, Yu Tang and Robert P. Kassawara

2 Shear Behavior Prediction of Non-ductile Reinforced Concrete Members in Earthquake 17
Yi-An Li and Shyh-Jiann Hwang

3 Experimental Study of Novel Concrete Frames Considering Earthquake and Progressive Collapse 29
Xinzheng Lu, Kaiqi Lin, Donglian Gu and Yi Li

4 Validation of the PARC_CL 2.0 Crack Model by the Cyclic Tests of 1/13-Scale Nuclear Containment Structures 47
Beatrice Belletti, Alessandro Stocchi and Francesca Vecchi

5 Effect of High-Strength Reinforcement for Shear Strength and Shear-Friction Strength of RC Walls Subjected to Cyclic Lateral Loading 67
Hong-Gun Park, Jang-Woon Baek and Sung-Hyun Kim

6 Research on Resilient Reinforced Concrete Building Structural System 83
Susumu Kono, Ryo Kuwabara, Fuhito Kitamura, Eko Yuniarsyah, Hidekazu Watanabe, Tomohisa Mukai and David Mukai

7 The State of Knowledge and Practice in Concrete Structure Design for Earthquake 95
John S. Ma

8 Development of Large-Diameter Reinforcing Bars for the Seismic Resistance of Reinforced Concrete Bridge Columns 111
Juan Murcia-Delso and P. Benson Shing

9 Reversed Cyclic Tests of 1/13 Scale Cylindrical Concrete Containment Structures 131
Chiun-Lin Wu, Thomas T. C. Hsu, Che-Yu Chang, Hu-Jhong Lu, Hsuan-Chih Yang, Chang-Ching Chang, Yu-Chih Chen and Yuan-Sen Yang

10 Understanding the Seismic Behaviour of FRP Retrofitted RC Shear Walls: Past and Present 151
David T. Lau, Joshua E. Woods, Ahmed Hassan, Jeffrey Erochko, Carlos Cruz-Nuguez and Ibrahim Shaheen

11 Seismic Response and Collapse Risk of Shearwall Buildings Subjected to Long Duration Ground Motion 167
Carlos E. Ventura, Michael Fairhurst, Armin Bebamzadeh and Ilaria Capraro

12 Drift Capacity at Onset of Bar Buckling in RC Members Subjected to Earthquakes 185
Mario E. Rodriguez and Marcelo Iñiguez

13 Experimental and Numerical Response of RC Walls with Discontinuities Under Cycling Loading 201
Leonardo M. Massone, Fabián Rojas, Gonzalo Muñoz, Ignacio Manríquez, Sebastián Díaz and Ricardo Herrera

14 Assessment of the Boundary Region Stability of Special RC Walls 223
Ana G. Haro, Mervyn Kowalsky and Y. H. Chai

15 Ductility Demand of a High-Rise RC Flat-Plate Core-Wall Building Structure in a Moderate-Seismicity Region: South Korea 243
Kyung Ran Hwang and Han Seon Lee

16 Essential Requirements for Reinforced Concrete Structures of Limited Area and Height 265
Luis E. Garcia, Santiago Pujol and Juan Francisco Correal

17 The Seismic Strengthening of Concrete Structures by Ultrahigh-Performance Concrete 283
Sung-Gul Hong, Yousun Yi and Inyoung Gu

18 Effect of Strain Penetration on RC Beam–Column Joints Subjected to Seismic Loading 309
Jung-Yoon Lee and Jongwook Park

19 Capacity-Based Inelastic Displacement Spectra for Seismic Evaluation and Design of Reinforced Concrete Bridges 329
Kuo-Chun Chang, Ping-Hsiung Wang and Yu-Chen Ou

20 Issues Related to the Rapid Seismic Repair of Concrete Bridge Columns 351
Zachary Krish and Mervyn Kowalsky

21 Seismic Performance of Rehabilitated RC Columns Using Material Testing Integrated (MTI) Simulation 369
Donghyuk Jung and Bassem Andrawes

22 Test and Analysis of a Self-centering Concrete Frame Under Seismic Action 385
Chun Jiang, Xilin Lu, Ye Cui and Xu Lu

23 Structural Performance of Slender High-Strength SFRC Columns (Fc300) Under Axial and Lateral Loadings 397
Yusuke Tanabe, Daisuke Honma and Masaro Kojima

Participants from 11 Countries 409

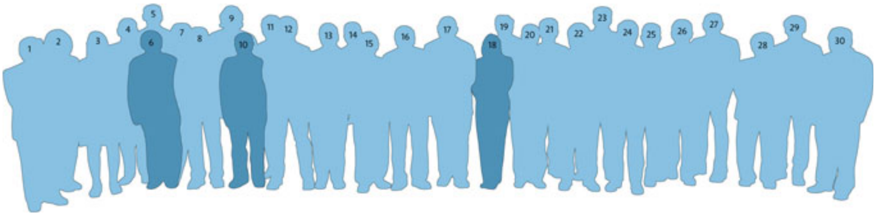
1
2
3
4
5
6
7
8
9
10
11
12
13
14
15
16
17
18
19
20
21
22
23
24
25
26
27
28
29
30

List of Forum Authors in Group Photo

1. Luis E. Garcia, Professor, Universidad de Los Andes, Bogotá, Colombia.
2. Kyung Ran Hwang, Research Assistant Professor, School of Civil, Environmental, and Architectural Engineering, Korea University, Korea.
3. Beatrice Belletti, Associate Professor, Università di Parma, Dipartimento di Ingegneria e Architettura, Parma, Italy.
4. Fabián Rojas, Assistant Professor, Department of Civil Engineering, University of Chile, Chile.
5. Ping-Hsiung Wang, Assistant Research Fellow, National Center for Research on Earthquake Engineering (NCREE), Taipei, Taiwan.
6. Chiun-Lin Wu, Research Fellow, National Center for Research on Earthquake Engineering (NCREE), Taipei, Taiwan.
7. Jung-Yoon Lee, Professor, School of Civil, Architectural Engineering and Landscape Architecture, Sungkyunkwan University, Seoul, Korea.
8. Han Seon Lee, Professor, School of Civil, Environmental, and Architectural Engineering, Korea University, Korea.
9. Zachary Krish, Ph.D. Student, North Carolina State University, Raleigh, NC, USA.
10. Kuo-Chun Chang, Professor, Department of Civil Engineering, National Taiwan University, Taipei, Taiwan.
11. Yusuke Tanabe, Engineer, Takenaka Corporation, Japan.
12. Juan Murcia-Delso, Assistant Professor, Department of Civil, Architectural and Environmental Engineering, University of Texas, Austin, TX, USA.
13. P. Benson Shing, Professor, Department of Structural Engineering, University of California, San Diego, CA, USA.
14. Liang Lu, Associate Professor, Research Institute of Structural Engineering and Disaster Reduction, and Director of State Key Laboratory of Disaster Reduction in Civil Engineering, Tongji University, Shanghai, China.
15. Y. L. Mo, Professor, Department of Civil and Environmental Engineering, University of Houston, Houston, TX, USA.

16. Thomas T. C. Hsu, Moores Professor, Department of Civil and Environmental Engineering, University of Houston, Houston, TX, USA.
17. Carlos E. Ventura, Professor, Civil Engineering, The University of British Columbia, Vancouver, Canada.
18. Ana G. Haro, Professor, Departamento de Ciencias de la Tierra y la Construcción, Universidad de las Fuerzas Armadas ESPE, Sangolquí, Ecuador.
19. Santiago Pujol, Professor, Civil Engineering Department, Purdue University, West Lafayette, Indiana, USA.
20. John S. Ma, Senior Structural Engineer and Founding Members, US Nuclear Regulatory Commission, Washington, DC.
21. Hong-Gun Park, Professor, Department of Architecture and Architectural Engineering, Seoul National University, Seoul, Korea.
22. Sung-Gul Hong, Professor, Department of Architecture and Architectural Engineering, Seoul National University, Seoul, Korea.
23. Mervyn Kowalsky, Professor of Structural Engineering, North Carolina State University, Raleigh, NC, USA.
24. Xilin Lu, Professor, State Key Laboratory of Disaster Reduction in Civil Engineering, Tongji University, Shanghai, China.
25. Susumu Kono, Professor, Tokyo Institute of Technology, Yokohama, Japan.
26. Xinzheng Lu, Professor, Beijing Engineering Research Center of Steel and Concrete Composite Structures, Tsinghua University, China.
27. Bassem Andrawes, Associate Professor, Department of Civil Engineering, University of Illinois at Urbana-Champaign, Urbana, IL, USA.
28. Shyh-Jiann Hwang, Director General, National Center for Research on Earthquake Engineering (NCREE), and Professor, National Taiwan University.
29. David Lau, Professor, Department of Civil and Environmental Engineering, Carleton University, Ottawa, Canada.
30. Mario E. Rodriguez, Professor, National University of Mexico, Mexico City, Mexico.

Chapter 1
Periodic Material-Based Three-Dimensional (3D) Seismic Base Isolators for Small Modular Reactors

Y. L. Mo, Witarto Witarto, Kuo-Chun Chang, Shiang-Jung Wang, Yu Tang and Robert P. Kassawara

The concept of frequency band gaps in periodic materials has inspired the development of a new type of seismic base isolation system known as the periodic foundation. This paper focuses on the experimental validation of the 3D periodic foundation supporting a small modular reactor building. A large-scale 3D periodic foundation with a small modular reactor (SMR) building model was tested on a shake table using various input waves. The frequency band gaps of the test specimen were able to filter out the damaging frequency content of the input seismic waves. The test results motivate the application of periodic foundations for safer nuclear structures in seismic-prone regions.

Y. L. Mo (✉) · W. Witarto
Department of Civil and Environmental Engineering, University of Houston,
4726 Calhoun Road, 77204 Houston, TX, USA
e-mail: yilungmo@egr.uh.edu

W. Witarto
e-mail: wwitarto@uh.edu

K.-C. Chang
Department of Civil Engineering, National Taiwan University, No. 1, Sec. 4,
Roosevelt Road, 106 Taipei, Taiwan
e-mail: ciekuo@ntu.edu.tw

S.-J. Wang
National Taiwan University of Science and Technology, No. 43, Sec. 4,
Keelung Road, 106 Taipei, Taiwan
e-mail: sjwang@mail.ntust.edu.tw

Y. Tang
Argonne National Laboratory, 9700 Cass Avenue, 60439 Lemont, IL, USA
e-mail: yutang@anl.gov

R. P. Kassawara
Electric Power Research Institute, 3420 Hillview Avenue, 94304 Palo Alto, CA, USA
e-mail: rkassawa@epri.com

T. T. C. Hsu (ed.), *Concrete Structures in Earthquake*,
https://doi.org/10.1007/978-981-13-3278-4_1

1.1 Introduction

The concept of seismic base isolation has been developed over decades and has matured into practical applications around the world (Naeim and Kelly 1999). The developed base isolation systems, such as rubber bearings and friction pendulum systems, work by introducing low lateral stiffness devices at the base of a superstructure to lengthen the natural period of the structural system, resulting in a reduction of the acceleration response of the structural system during vibrations. The developed isolation systems had proven to enhance the horizontal seismic performance of many isolated structural systems (Buckle and Mayes 1990). However, vertical earthquakes are still a main issue in the conventional isolation systems. Full-scale shake table tests conducted at the E-Defense facility in Japan show a great amplification in the vertical acceleration response of the isolated buildings when subjected to vertical earthquakes (Furukawa et al. 2013; Ryan et al. 2016). The vertical response amplification causes a wide variety of damages to the non-structural components inside the isolated buildings.

To accommodate the seismic safety of critical structures such as medical facilities and nuclear power plants, researchers have proposed various devices to isolate earthquakes in both the horizontal and vertical directions. Devices such as rolling seal type air spring and hydraulic isolation systems can provide vertical isolation and are proposed to be combined with laminated rubber bearings for horizontal isolation (Inoue et al. 2004; Suhara et al. 2005, 2002). On the other hand, devices such as thick rubber layer bearings (Okamura et al. 2011) and GERB systems (Naeim and Kelly 1999) can simultaneously provide seismic isolation in both the horizontal and vertical directions. All of the proposed devices are based on the same concept as conventional isolation systems, i.e., introducing low lateral and vertical stiffness and subsequently lengthening the natural periods of the isolated structural systems to avoid damaging frequency content of input earthquakes. Researchers (Naeim and Kelly 1999; Takahashi et al. 2008) found these systems are prone to rocking when subjected to horizontal earthquakes. Consequently, rocking suppression devices are needed to control the rocking movement.

This paper presents a novel concept of seismic isolation from the perspective of elastic waves propagation in periodic materials or phononic crystals. Periodic materials, originally developed in the solid-state physics, are artificially made by arranging contrasting materials in the periodic fashion. According to the number of directions where the unit cell is repeated, periodic materials can be classified as one-dimensional (1D), two-dimensional (2D) and three-dimensional (3D) periodic materials, as shown in Fig. 1.1a, b and c, respectively. This metamaterial has the capability to block elastic waves from propagating through if the frequencies of these waves are within certain frequency bands. These frequency bands are termed as frequency band gaps or attenuation zones (Torres and Montero de Espinosa 2004). This concept is depicted in Fig. 1.2a and b. It is shown in Fig. 1.2a that the wave cannot propagate through the periodic material since the frequency of the wave falls within the range of the frequency band gap of the material. The opposite

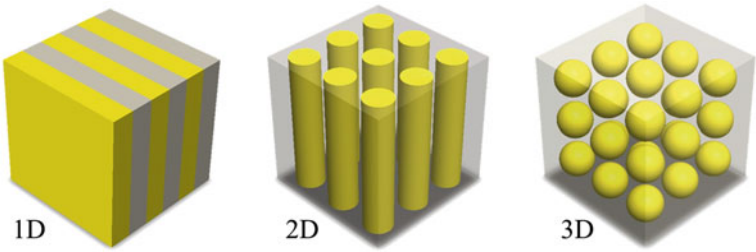

Fig. 1.1 Classification of periodic materials or phononic crystals

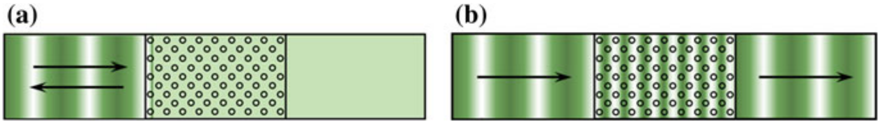

Fig. 1.2 Wave propagation with the wave frequency: **a** inside frequency band gap and **b** outside frequency band gap

case is shown in Fig. 1.2b. The range of the frequency band gap can be engineered by design to cover any frequency of interest.

Guided by the notion of frequency band gaps in periodic materials, researchers have developed periodic material-based seismic isolation systems better known as periodic foundations (Xiang et al. 2012; Yan et al. 2014, 2015). This type of foundation can support the superstructure and isolate the superstructure from the incoming seismic waves since it possesses frequency band gaps. Physical tests of 1D (Xiang et al. 2012), 2D (Yan et al. 2014) and 3D (Yan et al. 2015) periodic foundations were conducted in the feasibility study stage of the periodic foundations. In each of the tests, a simple structure supported by a periodic foundation was tested simultaneously with a non-isolated counterpart. The test results show that the structures isolated with periodic foundations have a much smaller acceleration response than that of the non-isolated structures. Inspired by the success of the feasibility study, we proceed with the application into the real engineering structures. In this study, a 3D periodic foundation is employed to isolate a small modular reactor (SMR) building model. The study reported in this paper begins with the theoretical derivation of the dispersion relation in the 3D periodic materials to design the frequency band gaps on the test specimens. The subsequent section then describes the design of the 3D periodic foundation. Finally, the shake table test results of the 3D periodic foundation structural system are presented and discussed.

1.2 Basic Theory

The frequency band gaps of periodic materials can be obtained from the Eigenvalue analysis of periodic unit cells with the periodic boundary conditions. For a continuum body with isotropic elastic material and assuming small deformation without damping, the governing equation of motion is shown in Eq. (1.1)

$$\rho(\mathbf{r})\frac{\partial^2 \mathbf{u}}{\partial t^2} = \nabla\{[\lambda(\mathbf{r}) + 2\mu(\mathbf{r})](\nabla \cdot \mathbf{u})\} - \nabla \times [\mu(\mathbf{r})\nabla \times \mathbf{u}] \tag{1.1}$$

where $\mathbf{r}$ is the coordinate vector; $\mathbf{u}$ is displacement; $\rho(\mathbf{r})$ is the density; $\lambda(\mathbf{r})$ and $\mu(\mathbf{r})$ are the Lamé constants. The relationship of the Lamé constants with Young's modulus $E(\mathbf{r})$ and Poisson's ratio $v(\mathbf{r})$ are shown in Eq. (1.2). The displacement solution to Eq. (1.1) that satisfies the Bloch theorem (Kushwaha et al. 1994) is shown in Eq. (1.3).

$$\lambda(\mathbf{r}) = \frac{E(\mathbf{r})v(\mathbf{r})}{(1 + v(\mathbf{r}))(1 - 2v(\mathbf{r}))}; \quad \mu(\mathbf{r}) = \frac{E(\mathbf{r})}{2(1 + v(\mathbf{r}))} \tag{1.2}$$

$$\mathbf{u}(\mathbf{r}, t) = \mathrm{e}^{i(\mathbf{k}\cdot\mathbf{r} - \omega t)}\mathbf{u}_{\mathbf{k}}(\mathbf{r}) \tag{1.3}$$

where $\mathbf{k}$ is the wave vector in the reciprocal space; i is the imaginary unit; ω is the angular frequency; and $\mathbf{u}_{\mathbf{k}}(\mathbf{r})$ is the wave amplitude. Based on the periodicity of the periodic structure, $\mathbf{u}_{\mathbf{k}}(\mathbf{r})$ can be written as a periodic function shown in Eq. (1.4). Substituting Eq. (1.4) into Eq. (1.3), the periodic boundary conditions can be obtained, as shown in Eq. (1.5).

$$\mathbf{u}_{\mathbf{k}}(\mathbf{r} + \mathbf{a}) = \mathbf{u}_{\mathbf{k}}(\mathbf{r}) \tag{1.4}$$

$$\mathbf{u}(\mathbf{r} + \mathbf{a}, t) = \mathrm{e}^{i\mathbf{k}\cdot\mathbf{a}}\mathbf{u}(\mathbf{r}, t) \tag{1.5}$$

Applying the periodic boundary conditions to the governing equation, Eq. (1.1), the wave equation can be transferred into the Eigenvalue problem as follows:

$$\left(\mathbf{\Omega}(\mathbf{k}) - \omega^2\mathbf{M}\right).\mathbf{u} = 0 \tag{1.6}$$

where $\mathbf{\Omega}$ is the stiffness matrix and $\mathbf{M}$ is the mass matrix of the unit cell. The Eigenvalue problem in Eq. (1.6) is the so-called dispersion equation. Various methods can be used to solve the Eigenvalue problem. However, it is proposed to use the finite element analysis because it can easily deal with complicated geometry. For each wave vector $\mathbf{k}$, a series of corresponding frequencies ω can be obtained. The relationship between the wave vector and frequency forms the dispersion curve, which provides the information for the frequency band gaps.

Consider periodic material with a simple cubic unit cell as shown in Fig. 1.3a. The unit cell consists of a cubic core (red) wrapped by the coating or matrix (gray).

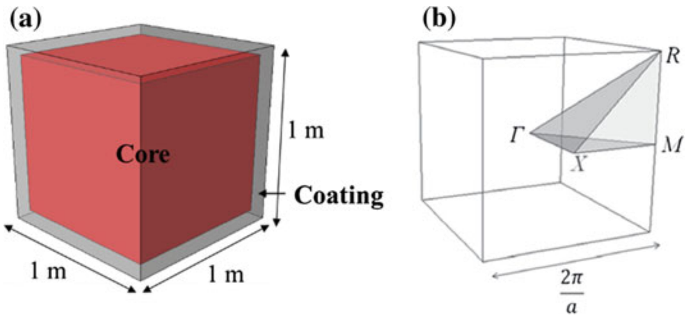

Fig. 1.3 **a** Cubic unit cell **b** First irreducible Brillouin zone

Table 1.1 Material properties of 3D periodic material

Component	Young's modulus (MPa)	Density (kg/m^3)	Poisson's ratio
Concrete	40000	2300	0.2
Rubber	0.1586	1277	0.463

The material for each of the core and coating components is assumed to be concrete and rubber, respectively, with material properties shown in Table 1.1. The frequency band gap of the corresponding periodic material can be obtained by solving the dispersion equation (Eq. 1.6). In the 3D periodic material, the coordinate vector **r** is three dimensional which includes x, y and z directions. Owing to the high symmetry of the periodic structures under consideration, it is sufficient to calculate the Eigenfrequencies for the wave vector varying along the boundary of the first irreducible Brillouin zone (Kittel 2005), the pyramid R-M-Γ-X-M as shown in Fig. 1.3b.

Figure 1.4a shows the dispersion relationship of the corresponding periodic material. An absolute frequency band gap, shown by the yellow shaded area in the figure, is observed in the region between 18.46 and 27.09 Hz, which means elastic waves with frequencies within this region cannot propagate in any direction. However, in this study, the specimen will be tested on a shake table. The wave generated by the shake table will only propagate into the periodic foundation in one direction (vertically). Therefore, it is more meaningful to look into the directional frequency band gap (Γ-X direction) instead. Figure 1.4b shows the yellow shaded area is in the region between 18.46 and 27.36 Hz. The frequency band gap clearly is useful for seismic isolation because it is in a low-frequency range.

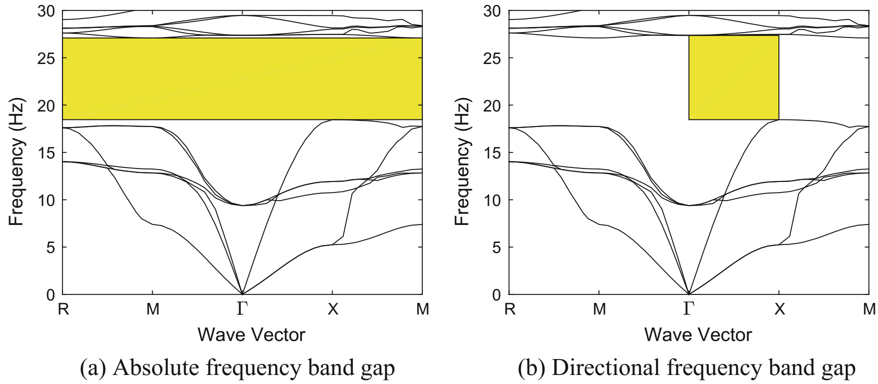

Fig. 1.4 Dispersion curve of periodic material

1.3 Design of Test Specimen

In this study, the prototype used as the superstructure is a representative of an SMR building by NuScale Power. As shown by the symmetric cut of the SMR building in Fig. 1.5a, the SMR building can host up to twelve SMRs inside the water pool. The dimensions and masses of the building structure were estimated from the sketches and the rendering pictures provided by NuScale Power. The length, width and height of the SMR building were selected as 100 m, 40 m and 40 m, respectively. It is assumed that the building structure is made of reinforced concrete (RC) material. Based on the information, a finite element (FE) model was built to study the dynamic characteristic of the prototype building (see Fig. 1.5b). A total of 29.68 million kg of non-structural masses was added to the structure. The non-structural masses represent non-structural elements attached to the building which include water in the reactor pool, all 12 SMRs, crane and utilities. Modal analysis results show that the first expected mode of the superstructure building is a translational mode with a natural frequency of 6.77 Hz.

Due to the limitations of the shake table facility, the validation tests cannot be performed at a full-scale size. Therefore, a scaled-down model was designed for this

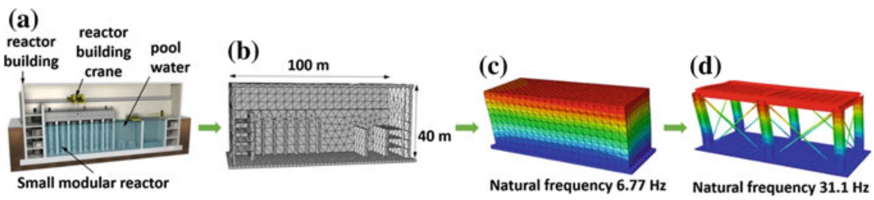

Fig. 1.5 Design process of superstructure model: **a** NuScale SMR building; **b** finite element model of prototype building; **c** modal analysis result of prototype building; **d** modal analysis result of scaled model (Witarto et al. 2018)

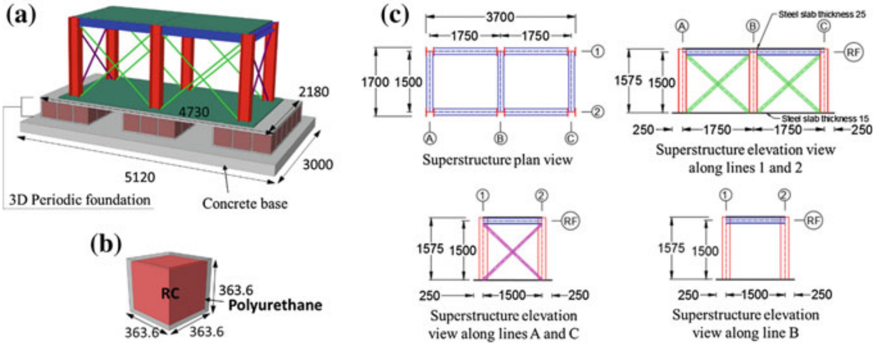

Fig. 1.6 Designed test specimen: **a** 3D periodic foundation structural system; **b** 3D periodic foundation unit cell; **c** superstructure detail (units in mm)

study. The scaling parameters follow the similitude requirements for true ultimate strength (Krawinkler and Moncarz 1982) with a selected length scale (l_r) of 1/22. The goal in this scaling is to obtain a superstructure model that allows its natural frequency to satisfy the frequency scale requirement ($\omega_r = l_r^{-1/2} = \sqrt{22} = 4.69$). Upon satisfying the frequency scale requirement, the displacement demand on the scaled model will be reflected on the prototype structure by the length scale. Note that in this study, the structural systems are assumed to be elastic. For the ease of construction and sensor installation, a steel frame structure was chosen as the SMR building model with the details shown in Fig. 1.6. Wide flange sections of 150 × 150 × 7 × 10 and 200 × 200 × 8 × 12 and angle sections of 65 × 65 × 6 and 50 × 50 × 5 were selected for beams, columns and longitudinal and transverse braces, respectively. Additional masses of 1830 and 8368 kg were provided on the roof and on the floor of the steel frame, respectively. Modal analysis of the FE model shows that the expected natural frequency of the steel frame is 31.1 Hz, which satisfies the frequency scale requirement.

Figure 1.6 shows the detail of the designed test specimen. The designed 3D periodic foundation consists of 54 unit cells that are separated into three blocks; each consists of 18 units with the arrangement of three units by 6 units in the horizontal plane and 1 unit in the vertical direction. The 3D unit cell itself is a cube with the unit cell length of 363.6 mm and cubical core with a length of 325 mm. Each of the core and matrix components was designed with reinforced concrete (RC) and polyurethane materials, respectively, with material properties shown in Table 1.2. On the top of the periodic foundation, a 60-mm-thick RC slab is

Table 1.2 Material properties of test specimen

Component	Young's modulus (MPa)	Density (kg/m^3)	Poisson's ratio
Reinforced concrete	31400	2300	0.2
Polyurethane	0.1586	1100	0.48

provided to connect the periodic foundation and the superstructure. The RC slab also provides a uniform stress distribution on the periodic foundation. The periodic foundation is connected to a 200-mm-thick RC base that will be used to connect the specimen to the shake table. In the real specimen, the interfaces of the RC layers and the polyurethane layers were glued using a polyurethane-based glue. The glue has a tensile strength of 1.5 MPa and a tear strength of 8 MPa.

1.4 Experimental Study

Figure 1.7 shows a test setup of the 3D periodic foundation structural system on a 5 m by 5 m shake table facility in National Center for Research on Earthquake Engineering (NCREE) Taiwan. For aesthetic purposes, the steel frame superstructure was covered using gray polypropylene boards. The polypropylene boards are very light and do not affect the behavior of the structural system. Three types of instrumentation were used to record the response of the structure, namely accelerometers, traditional displacement transducers (temposonics) and vision-aided measurement systems (NDI optotrak optical measurement). The sensors were placed on each corner of the shake table, on the top of the concrete base, the top of the 3D periodic foundation and the roof of the superstructure.

The test specimen was subjected to two types of excitation, i.e., frequency sweeping and seismic tests. In the first type of tests, the specimen was subjected to frequency sweeping tests in each of the horizontal (X) and vertical (Z) directions as well as the torsional mode (Rz). The frequency sweeping tests were conducted to investigate the frequency band gaps on the 3D periodic foundation structural system. In the frequency sweeping tests, the input excitations were a series of simple

Fig. 1.7 Test setup

Table 1.3 Seismograms for seismic tests

Earthquake event	Seismogram station (accelerometer orientation)	Control algorithm	PGA	Input direction
Bishop (Round Valley)	McGee Creek Surface (360)	Acc	0.4 g	Uniaxial (X)
	McGee Creek Surface (UP)			Uniaxial (Z)
	Modified from McGee Creek Surface (360)		25 deg/sec^2	Uniaxial (Rz)
Gilroy	Gilroy Array #3 (58)	Acc	0.4 g	Uniaxial (X)
	Gilroy Array #3 (UP)			Uniaxial (Z)
Ancona, Italy	Ancona-Palombina (0)	Acc	0.4 g	Uniaxial (X)
	Ancona-Palombina (UP)			Uniaxial (Z)
Whittier Narrows	Riverside Airport (180)	Acc	0.4 g	Uniaxial (X)
	Riverside Airport (UP)			Uniaxial (Z)

sine waves. The frequency range starts from 1 Hz to 50 Hz with an increment of 0.5 Hz. The amplitude of the input wave was kept constant throughout excitation. The second type of tests conducted on the specimen was seismic tests. Table 1.3 shows the list of the real seismograms used for the seismic tests and the test protocol. The seismograms were obtained from the PEER database.

1.4.1 Frequency Sweeping Test Results

From the frequency sweeping tests, the accelerations recorded at the top of the 3D periodic foundation and the roof of the superstructure were compared to that at the concrete base (the real input to the specimen). The frequency regions, in which the accelerations recorded on the structural systems are lower than that on the concrete base, correspond to the attenuation zones or frequency band gaps. To obtain the attenuation zones, the acceleration records in the time domain were first transformed into the frequency domain using the Discrete Fourier Transform (Welch 1967). The frequency response function (FRF) curves were then generated from the Fourier spectra. The FRF for each frequency on each response-measured location can be calculated using FRF = $20\log(a_o/a_i)$, where a_o is the acceleration amplitude at the location of interest and a_i is the acceleration amplitude at the shake table.

Figure 1.8 shows the FRF curves for both the top of the 3D periodic foundation and the roof of the superstructure. The negative FRF values indicate response

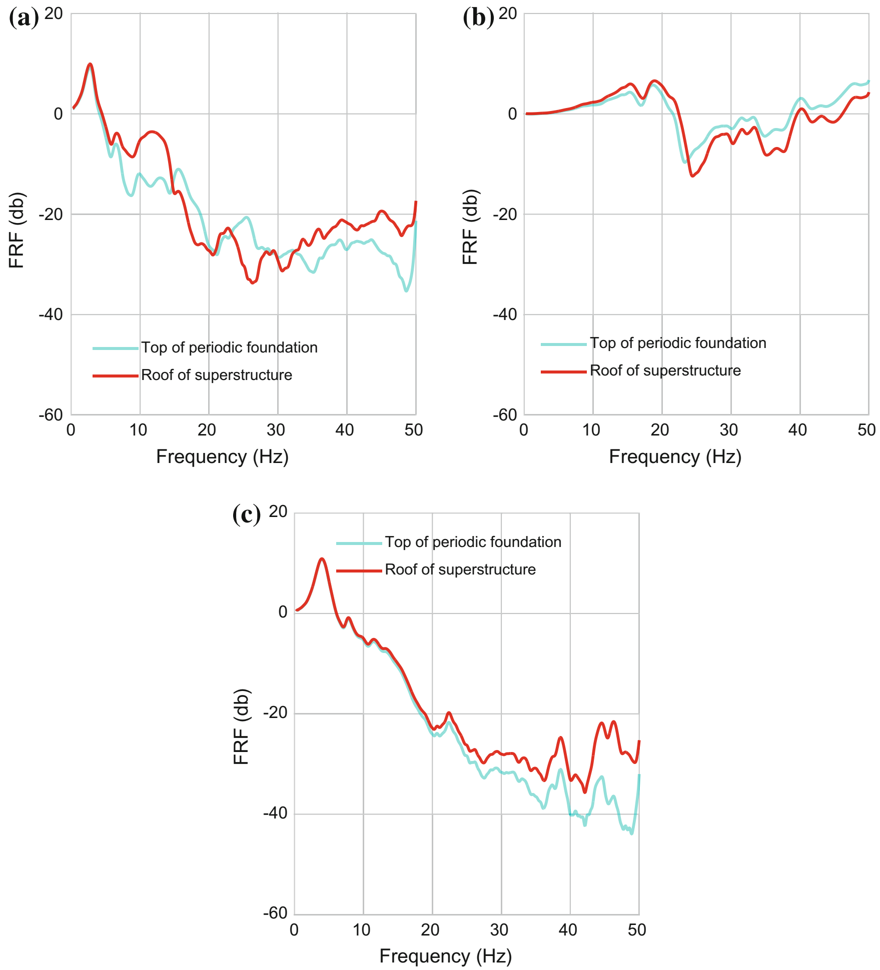

Fig. 1.8 Frequency sweeping test results: **a** in horizontal direction; **b** in vertical direction; **c** in torsional mode

reduction at particular frequencies while the positive values show response amplification. The attenuation zone at the top of the 3D periodic foundation in the horizontal direction is located at 4.1–50 Hz (light blue curve in Fig. 1.8a), while the attenuation zone in the vertical direction is at 21.5–38.75 Hz, as shown by the light blue curve in Fig. 1.8b. The attenuation zone in the torsional mode is located at 6.06–50 Hz (light blue curve in Fig. 1.8c). Large response reduction inside the attenuation zones is observed in all three directions, where FRF of −10 and −20, respectively, correspond to 68.38% and 90% of reduction.

The attenuation zones at the roof of the superstructure response are observed to be close to those at the top of the 3D periodic foundation. In the horizontal direction, the attenuation zone is in the range of 4.5 to 50 Hz (red curve in Fig. 1.8a). In the vertical direction, the attenuation zones are seen from 22.4 to 39.6 Hz and from 40.9 to 46.15 Hz (red curve in Fig. 1.8b). In the torsional mode, the attenuation zone is located from 6.1 to 50 Hz (red curve in Fig. 1.8c).

1.4.2 Seismic Test Results

Figure 1.9 shows the seismic test results in the horizontal direction. It is observed that after passing through the 3D periodic foundation, the maximum accelerations recorded at the top of the 3D periodic foundation and the roof of the superstructure

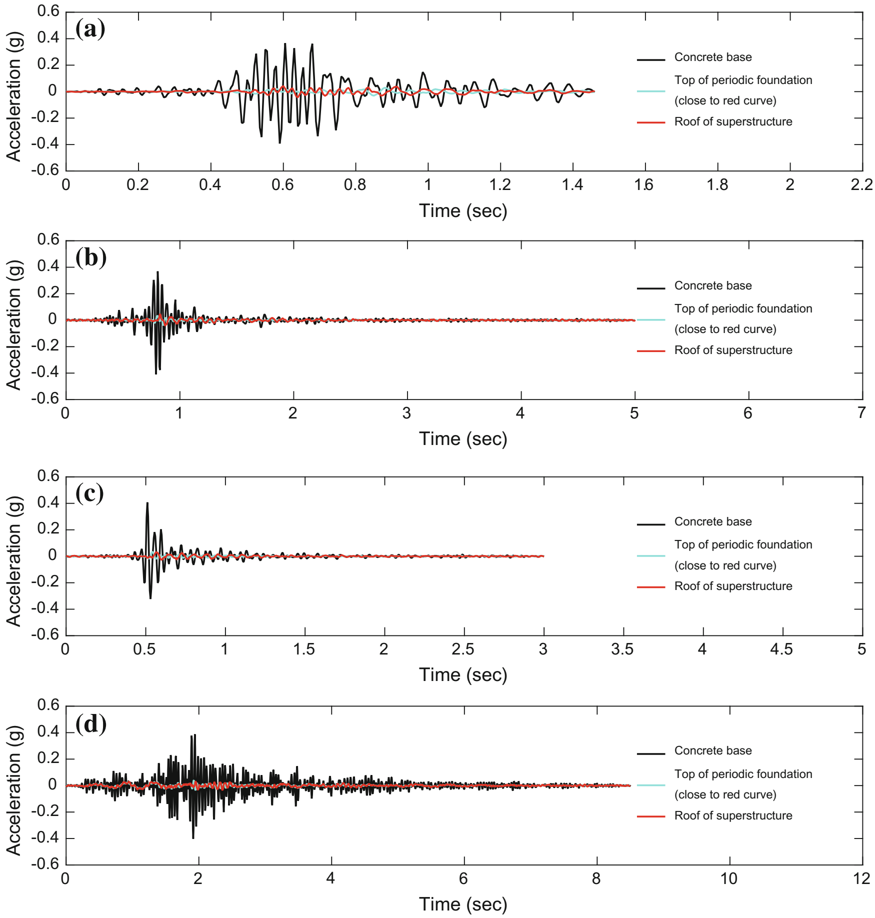

Fig. 1.9 Seismic test results in the horizontal direction: **a** Bishop Earthquake; **b** Gilroy Earthquake; **c** Ancona Earthquake; **d** Whittier Earthquake

Table 1.4 Peak acceleration response and response reduction percentage of 3D periodic foundation structural system in the horizontal direction

Earthquake	Concrete base (g)	Top of 3D periodic foundation		Roof of superstructure	
		Acceleration (g)	Reduction (%)	Acceleration (g)	Reduction (%)
Bishop	0.3925	0.0303	92.28	0.0439	88.82
Gilroy	0.4088	0.0397	90.28	0.0479	88.29
Ancona	0.4075	0.0334	91.80	0.0303	92.57
Whittier	0.4025	0.0400	90.05	0.0352	91.26

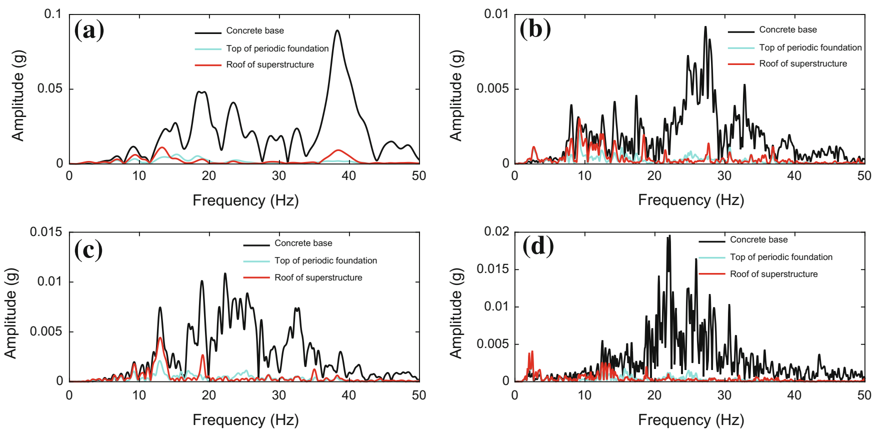

Fig. 1.10 Fourier spectra of the seismic test results in the horizontal direction: **a** Bishop Earthquake; **b** Gilroy Earthquake; **c** Ancona Earthquake; **d** Whittier Earthquake

are reduced significantly when compared to that recorded at the concrete base (input acceleration). The term "maximum acceleration" used in this paper refers to the absolute peak acceleration throughout the time series. The absolute maximum acceleration of each time series and its reduction percentage in comparison to the peak input acceleration is tabulated in Table 1.4. The large response reductions are attributed to the main frequency content of the input seismic waves (depicted by the black curves in Fig. 1.10) that overlap with the attenuation zones (shown in Fig. 1.8a); therefore, effectively filtering out the main frequency content.

The measured maximum rotation at the roof of the superstructure, when subjected to each of Bishop, Gilroy, Ancona and Whittier Earthquakes, was found to be 4.557×10^{-5} rad, 7.28×10^{-5} rad, 8.53×10^{-5} rad and 8.06×10^{-5} rad, respectively. The rotation of the 3D periodic foundation structural system is still smaller than the rotation of a building structure isolated using a combined laminated rubber bearing and air spring systems with oil dampers for rocking suppression, which has a rocking of 2.12×10^{-4} rad (Takahashi et al. 2008).

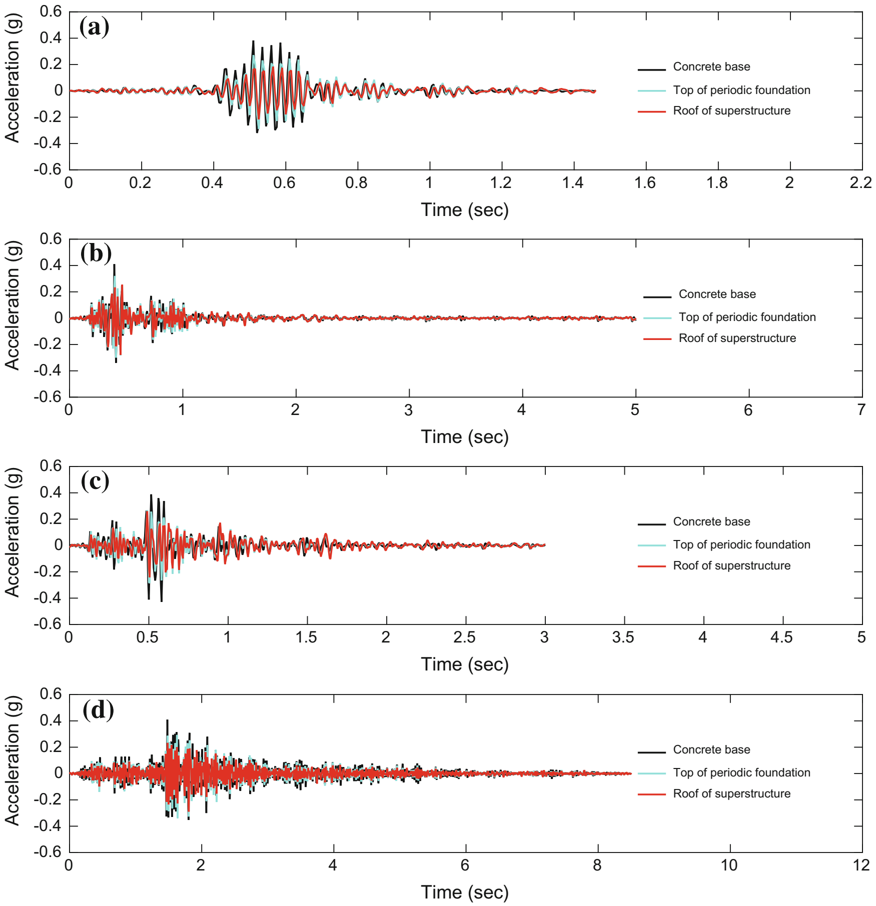

Fig. 1.11 Seismic test results in the vertical direction: **a** Bishop Earthquake; **b** Gilroy Earthquake; **c** Ancona Earthquake; **d** Whittier Earthquake

Table 1.5 Peak acceleration response and response reduction percentage of the 3D periodic foundation structural system in the vertical direction

Earthquake	Concrete base (g)	Top of 3D periodic foundation		Roof of superstructure	
		Acceleration (g)	Reduction (%)	Acceleration (g)	Reduction (%)
Bishop	0.3829	0.2888	24.58	0.2168	43.38
Gilroy	0.4106	0.3209	21.84	0.2789	32.09
Helena	0.4281	0.3005	26.63	0.2646	35.39
Whittier	0.4099	0.3394	17.21	0.2893	29.42

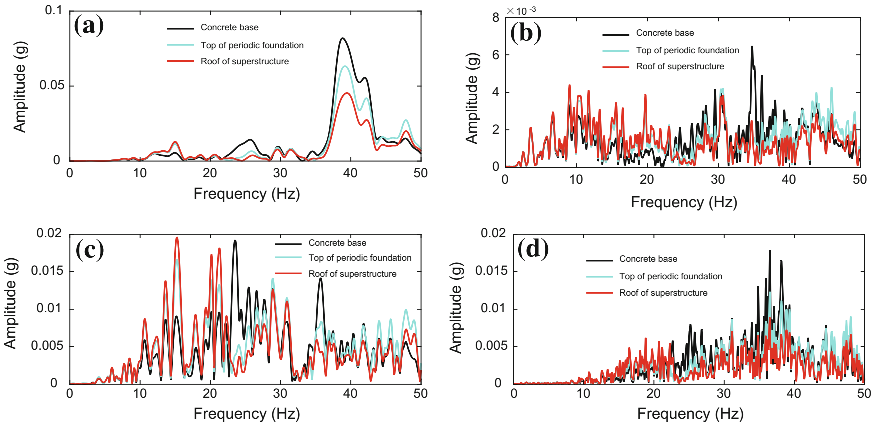

Fig. 1.12 Fourier spectra of the seismic test results in the vertical direction: **a** Bishop Earthquake; **b** Gilroy Earthquake; **c** Ancona Earthquake; **d** Whittier Earthquake

Figure 1.11 presents the seismic test results in the vertical direction. A considerable amount of acceleration reduction to the peak input acceleration is observed when the structural system is subjected to each of the vertical earthquakes. The peak acceleration and the corresponding reduction percentage are tabulated in Table 1.5. Although the attenuation zones in the vertical direction are not as wide as those in the horizontal direction, the 3D periodic foundation still successfully isolates the vertical earthquakes resulting in a 17.2–43.4% response reduction. The attenuation mechanism of the 3D periodic foundation structural system is demonstrated in Fig. 1.12. The main frequency contents of the vertical earthquakes that fall inside the attenuation zones are effectively attenuated.

Figure 1.13 shows the seismic test results in the torsional mode. The acceleration response at the top of the 3D periodic foundation is reduced by 93.7% while that on the roof of the superstructure is reduced by 93.0%. The large response reductions are also due to the main frequency content of the Bishop Earthquake that overlaps with the attenuation zones in the torsional mode. Fourier spectra shown in Fig. 1.14 depict the effective filtering effect in the range of 6.1–50 Hz.

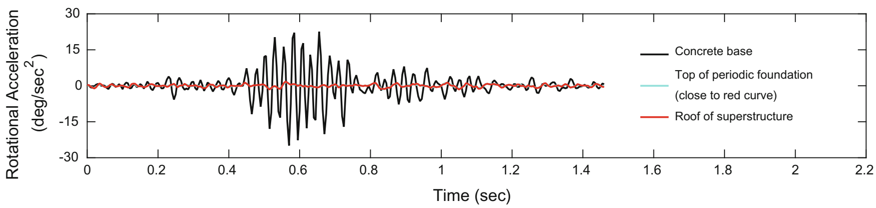

Fig. 1.13 Seismic test results in the torsional mode

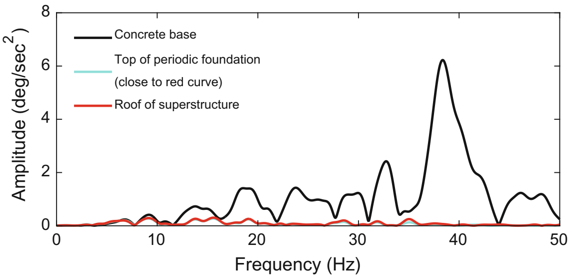

Fig. 1.14 Fourier spectra of seismic test results in torsional mode

1.5 Conclusion

Seismic performance of a 3D periodic foundation supporting a small modular reactor building was examined through shake table tests. The experimental validation has shown that the designed 3D periodic foundation is capable of isolating the superstructure from incoming seismic waves in the horizontal and vertical directions as well as the torsional mode. Different from the conventional seismic isolation systems, periodic foundations utilize the inherent property of frequency band gaps to filter out the damaging frequency content of incoming seismic waves. The configuration and wave blocking mechanism allows the periodic foundations to effectively isolate incoming seismic waves without introducing rocking in the structural system. When the main frequency content of the incoming seismic waves is located inside the frequency band gaps, a significant response reduction as large as 90% can be expected. The research has shown that the technology is certainly beneficial to protect critical facilities, such as a nuclear power plant, in seismic-prone regions.

Acknowledgements The authors acknowledge the support of the US Department of Energy NEUP Program (Proj. No. CFA-14-6446). The opinions and conclusions expressed or implied in the paper are those of the authors. They are not necessarily those of the supporting agency.

References

Buckle, I. G., & Mayes, R. L. (1990). Seismic isolation: History, application, and performance—a world view. *Earthquake spectra, 6*(2), 161–201.

Furukawa, S., Sato, E., Shi, Y., Becker, T., & Nakashima, M. (2013). Full-scale shaking table test of a base-isolated medical facility subjected to vertical motions. *Earthquake Engineering and Structural Dynamics, 42*(13), 1931–1940.

Inoue, K., Fushimi, M., Satoshi Moro, Morishita, M., Kitamura, S., & Fujita, T. (2004). Development of three-dimensional seismic isolation system for next generation nuclear power plant. In *13th World Conference on Earthquake Engineering*, Vancouver, B.C., Canada.

Kittel, C. (2005). *Introduction to solid state physics*. Hoboken: Wiley.

Krawinkler, H., Moncarz, P. D. (1982). Similitude requirements for dynamic models. *ACI Special Publication*, *73*.

Kushwaha, M. S., Halevi, P., Martinez, G., Dobrzynski, L., & Djafari-Rouhani, B. (1994). Theory of acoustic band structure of periodic elastic composites. *Physical Review B, 49*(4), 2313.

Naeim, F., Kelly, J. M. (1999). *Design of seismic isolated structures: From theory to practice*. New York: Wiley.

NuScale power. http://www.nuscalepower.com/smr-benefits/safe/reactor-building-barriers.

Okamura, S., Kamishima, Y., Negishi, K., Sakamoto, Y., Kitamura, S., & Kotake, S. (2011). Seismic isolation design for JSFR. *Journal of Nuclear Science and Technology, 48*(4), 688–692.

PEER ground motion database. (2016). http://ngawest2.berkeley.edu/.

Ryan, K. L., Soroushian, S., Maragakis, E. M., Sato, E., Sasaki, T., & Okazaki, T. (2016). Seismic simulation of an integrated ceiling-partition wall-piping system at e-defense. I: Three-dimensional structural response and base isolation. *Journal of Structural Engineering*, *142*(2), 04015130.

Suhara, J., Matsumoto, R., Oguri, S., Okada, Y., Inoue, K., & Takahashi, K. (2005). Research on 3-D base isolation system applied to new power reactor 3-D seismic isolation device with rolling seal type air spring: Part 2. In *18th International Conference on Structural Mechanics in Reactor Technology (SMiRT 18)* (pp. 3381–3391), Beijing, China: SMiRT18.

Suhara, J., Tamura, T., Okada, Y., & Umeki, K. (2002). Development of three dimensional seismic isolation device with laminated rubber bearing and rolling seal type air spring. In *ASME 2002 Pressure Vessels and Piping Conference* (pp. 43–48), Vancouver, BC, Canada. American Society of Mechanical Engineer.

Takahashi, O., Aida, H., Suhara, J., Matsumoto, R., Tsuyuki, Y., & Fujita, T. (2008). Construction of civil building using three dimensional seismic isolation system: Part 1, design of building using three dimensional seismic isolation system. In *The 14th World Conference on Earthquake Engineering*, Beijing, China.

Torres, M., & Montero de Espinosa, F. R. (2004). Ultrasonic band gaps and negative refraction. *Ultrasonics, 42,* 787–790.

Welch, P. D. (1967). The use of fast Fourier transform for the estimation of power spectra: A method based on time averaging over short, modified periodograms. *IEEE Transactions on Audio and Electroacoustics, 15*(2), 70–73.

Witarto, W., Wang, S. J., Yang, C. Y., Nie, X., Mo, Y. L., Chang, K. C., et al. (2018). Seismic isolation of small modular reactors using metamaterials. *AIP Advances, 8*(4), 045307.

Xiang, H. J., Shi, Z. F., Wang, S. J., & Mo, Y. L. (2012). Periodic materials-based vibration attenuation in layered foundations: Experimental validation. *Smart Materials and Structures, 21,* 1–10.

Yan, Y., Cheng, Z., Menq, F., Mo, Y. L., Tang, Y., & Shi, Z. (2015). Three dimensional periodic foundations for base seismic isolation. *Smart Materials and Structures, 24*(7), 075006.

Yan, Y., Laskar, A., Cheng, Z., Menq, F., Tang, Y., Mo, Y. L., et al. (2014). Seismic isolation of two dimensional periodic foundations. *Journal of Applied Physics, 116*(4), 044908.

Chapter 2
Shear Behavior Prediction of Non-ductile Reinforced Concrete Members in Earthquake

Yi-An Li and Shyh-Jiann Hwang

Based on recent reconnaissance, the plastic hinge zones in D-regions of structural members are vulnerable under earthquake loading. These non-ductile reinforced concrete members are usually dominated by shear behavior due to inadequate reinforcement and low concrete strength. Based on the proposed strut-and-tie models for D-regions, there are two different types of concrete strut: the bottle shape and fan shape. The objective of this study is to propose an analytical model to evaluate the shear behavior of these two force transfer mechanisms in D-regions. With test verifications, this paper provides a rational analytical model to generate the lateral load-displacement curve for the simulation of the shear behavior of structural members under earthquake loading.

2.1 Introduction

Based on recent reconnaissance, the plastic hinge zones in D-regions of structural members are vulnerable under earthquake loading. These non-ductile reinforced concrete members are usually dominated by shear behavior due to inadequate reinforcement and low concrete strength. However, the deformation capacity of the shear-critical members is not too small, as commonly expected according to reconnaissance and test observations. Therefore, a clear understanding of the

Y.-A. Li · S.-J. Hwang (✉)
National Center for Research on Earthquake Engineering, 200, Sec. 3,
Xinhai Rd., Taipei 10668, Taiwan
e-mail: sjhwang@ntu.edu.tw; sjhwang@ncree.narl.org.tw

Y.-A. Li
e-mail: yali@ncree.narl.org.tw

S.-J. Hwang
National Taiwan University, No. 1, Sec. 4, Roosevelt Rd., Taipei 10617, Taiwan

T. T. C. Hsu (ed.), *Concrete Structures in Earthquake*,
https://doi.org/10.1007/978-981-13-3278-4_2

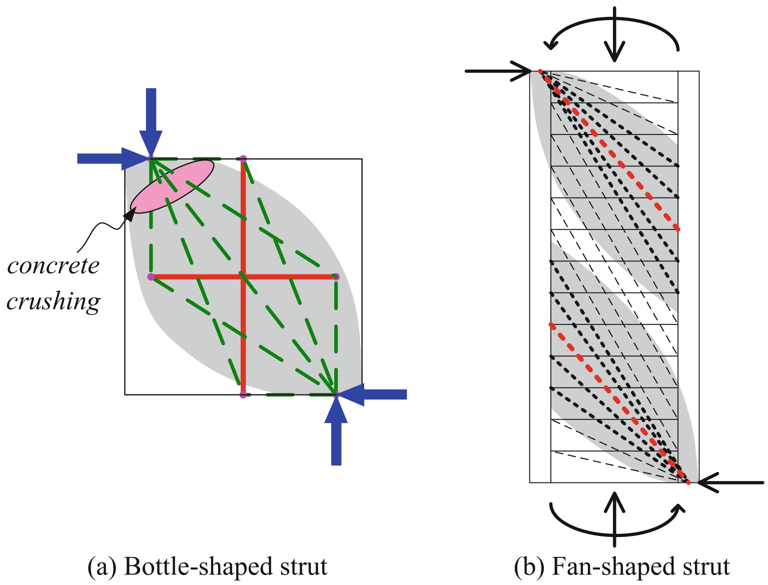

Fig. 2.1 Two force transfer mechanisms in D-regions

seismic behavior of these shear-critical members is essential to the evaluation of the seismic performance of buildings.

The D-region of a reinforced concrete member contains a stress-disturbed area due to geometric discontinuity or concentrated load. The shear strength evaluation for D-region is difficult for engineers because of its complex force transfer mechanism. Based on the proposed D-region macro models, there are two different types of concrete struts (Fig. 2.1). One is the bottle-shaped concrete strut for short and deep structural members, and the second is a fan-shaped concrete strut for longer members. The shear strength predictions in these two concrete strut shapes are different because of the different failure modes. The objective of this study is to propose an analytical model to evaluate the shear behavior of these two force transfer mechanisms in D-regions. Furthermore, a lateral load-displacement curve to simulate the shear behavior of structural members under earthquake loading is also provided.

2.2 Analytical Model for D-Regions

For short and deep members with bottle-shaped struts, the shear strength can be reasonably modeled using the strut-and-tie model. This paper utilizes the softened strut-and-tie model (SST model) proposed by Hwang and Lee (2002) and Hwang et al. (2017) to estimate the shear strength. On the basis of the force transfer mechanism in the SST model, combined with softening behaviors after reinforced concrete cracking, the concrete crushing strength at the ends of diagonal struts is obtained. Figure 2.1a shows the force transfer mechanism in the SST model used to predict the shear strength of bottle-shaped strut.

For intermediate and typical columns, described by the force transfer mechanism in Fig. 2.1b, the concrete struts between the fan-shaped main inclined strut cannot be directly connected from the loading end to the reaction end. As shown in Fig. 2.1b, there are two strengths in the compression fan; the first is the concrete crushing strength ($V_{n,c}$) in the compression zone at the column end of the compression fan and the other is the tensile strength ($V_{n,t}$) induced by the insufficient internal support at the nodes. The concrete crushing strength ($V_{n,c}$) in the compression zone of the column end can be predicted by the softened strut-and-tie model (Hwang and Lee 2002 and Hwang et al. 2017) as shown in Eq. (2.1).

$$V_{n,c} = C_d \cos\theta = K\zeta f_c' A_{str} \cos\theta \tag{2.1}$$

where C_d = compressive strength of the diagonal strut; θ = inclination angle between the diagonal strut and horizontal axis; K = strut-and-tie index; ζ = softening coefficient after reinforced concrete cracking; f_c' = compressive strength of concrete; and A_{str} = effective area at the end of the diagonal strut.

As for the tensile strength ($V_{n,t}$) of the internal support of the compression fan dispersed across the column, it can be predicted by the shear strength of inclined cracking. This paper suggests using the shear strength equation in ASCE/SEI 41-13 (2014) as shown in Eq. (2.2).

$$V_{n,t} = \left[\frac{A_v f_{yt} d}{s} + \left(\frac{0.5\sqrt{f_c'}}{M/Vd}\sqrt{1 + \frac{N}{0.5\sqrt{f_c'}A_g}}\right)0.8A_g\right](\text{MPa}) \tag{2.2}$$

in which A_v = area of transverse reinforcement; f_{yt} = yielding strength of transverse reinforcement; d = effective depth of the column cross-section; s = spacing of transverse reinforcement; N = axial force; A_g = gross cross-sectional area of the column; and M/Vd = maximum ratio of moment to shear times effective depth under loading for the column (which should be between 2 and 4).

Therefore, the shear strength ($V_{n,proposed}$) of a fan-shaped strut can use the following equation:

$$V_{n,proposed} = \text{ smaller of } \left(V_{n,c}\,,\ V_{n,t}\right) \tag{2.3}$$

After the determination of the shear strength of shear-critical members, the proposed lateral load-displacement curve could be established by a tri-linear relationship to simulate the shear behavior of a structural member under earthquake loading as shown in Fig. 2.2. The first segment indicates elastic behavior up to the shear cracking point. The strength at the concrete shear cracking point is V_{cr}, and the corresponding displacement is Δ_{cr} (Li and Hwang 2017). The second segment

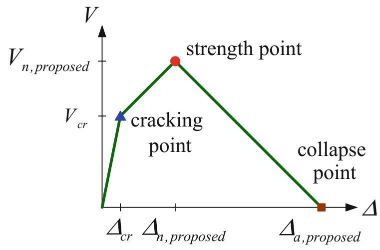

Fig. 2.2 Proposed load-displacement curve for shear-critical structural members

represents the portion from the shear cracking point to the shear strength point. Shear cracking of concrete results in a rapid increase in lateral displacement. The main source of this displacement is shear deformation from cracking. Therefore, the change in the gradient is due to the reduction in column stiffness caused by shear cracking. As cracks propagate, concrete struts are formed in the cracks, and the crushing strength of the struts is subsequently reached. The corresponding shear strength and displacement are $V_{n,proposed}$ and $\Delta_{n,proposed}$, respectively. The shear strength of shear-critical members ($V_{n,proposed}$) was proposed as above, and the prediction of the lateral displacement at the strength point for shear-critical members under double-curvature bending is described by the following equation (Li and Hwang 2017):

$$\Delta_{n,proposed} = \frac{V_{n,proposed} H^3}{12\left(E_c I_{eff}\right)} + 0.006 \sin 2\theta \times H \tag{2.4}$$

where H = net column height; E_c = elastic modulus of concrete; I_{eff} = effective moment of inertia of the column cross-section; and $E_c I_{eff}$ = effective flexural stiffness. Based on ASCE/SEI 41-13 (2014), the effective flexural stiffness is $0.3E_c I_g$ for column with axial load below $0.1A_g f_c'$, in which I_g = moment of inertia of the column gross cross-section. By contrast, the effective flexural stiffness is $0.7E_c I_g$ for column with an axial load larger than $0.5A_g f_c'$. For column with the axial load between $0.1A_g f_c'$ and $0.5A_g f_c'$, the effective flexural stiffness can be calculated by linear interpolation.

The third segment is from post-peak shear strength degradation to axial failure at the loss of vertical load-carrying capacity. This paper refers to the approach in ASCE/SEI 41-13 (2014) to predict the collapse point. Based on the hypothesis that the lateral strength decay of the collapse point is zero, the lateral displacement of the collapse point ($\Delta_{a,proposed}$) can be predicted by

$$\Delta_{a,proposed} = \Delta_{n,proposed} + r \times H \tag{2.5}$$

where r = parameter from Tables 10–8 in ASCE/SEI 41-13 (2014).

2.3 Verification of Bottle-Shaped Strut (Short Columns and Squat Walls)

Experimental data of short columns used in this study is a testing on eight short column specimens (Li et al. 2014), and the material properties of these experiments are listed in Table 2.1. In addition, a paper by Moretti and Tassios (2006) was also included. Moretti and Tassios (2006) reported experimental data on four short column specimens, excluding specimens containing diagonal reinforcements.

Figure 2.3 presents the comparison between experimental envelopes and the proposed lateral load-displacement curve for the test specimens tested by Li et al. (2014) and Moretti and Tassios (2006). It can be seen that prior to reaching shear strength, as concrete cracks in shear, the turning point of stiffness in the proposed curves and experimental envelopes are in good agreement (Li and Hwang 2017). However, ASCE/SEI 41-13 (2014) assumes the shear strength drops rapidly after reaching the peak strength, which is evidently inconsistent with the actual behavior. The assumption of rapid loss of lateral strength will significantly affect the prediction of internal force redistribution within the structure.

Table 2.1 contains the ratio of test results and the calculated values using the proposed curve. In terms of shear strength, the average ratio (AVG) of measured strength to the analytical strength by the proposed model is 1.21 with a coefficient of variation (COV) of 0.15. For the prediction of displacement at strength point by

Table 2.1 Comparison for short columns (Li and Hwang 2017)

Specimens	$\frac{H}{h}$	$\frac{N}{A_g f'_c}$	Hoop ratio, ρ_s	Measured			Analysis for strength point			
				$V_{n,test}$ (kN)	$\Delta_{n,test}$ (mm)	Δ_a (mm)	$\frac{V_{n,test}}{V_{n,proposed}}$	$\frac{\Delta_{n,tesst}}{\Delta_{n,proposed}}$	$\frac{V_{n,test}}{V_{n,ASCE}}$	$\frac{\Delta_{n,test}}{\Delta_{n,ASCE}}$
Li et al. (2014)										
1DL	1	0.09	1.27%	698	6.9	34.1	1.35	2.05	0.75	8.82
1DH		0.29		701	3.5	24.7	0.99	1.00	0.69	4.92
1NL		0.10	0.24%	660	3.5	32.9	1.52	1.06	1.89	11.12
1NH		0.29		757	3.1	14.9	1.21	0.91	1.72	10.02
2DL	2	0.09	1.27%	564	13.3	68.4	1.41	2.24	0.61	3.17
2DH		0.30		589	11.1	50.2	1.17	1.82	0.58	3.53
2NL		0.10	0.24%	402	7.8	57.6	1.44	1.45	1.15	4.78
2NH		0.29		460	6.5	29.5	1.15	1.18	1.04	4.69
Moretti and Tassios (2006)										
1	2	0.3	1.21%	330	5	–	1.06	1.27	0.93	5.23
3				360	4	–	1.07	1.09	0.99	4.23
4			1.88%	360	5	–	1.19	1.35	0.78	3.96
2		0.6	1.21%	410	–	–	0.93	–	0.89	–
AVG							1.21	1.40	1.00	5.86
COV							0.15	0.30	0.39	0.45

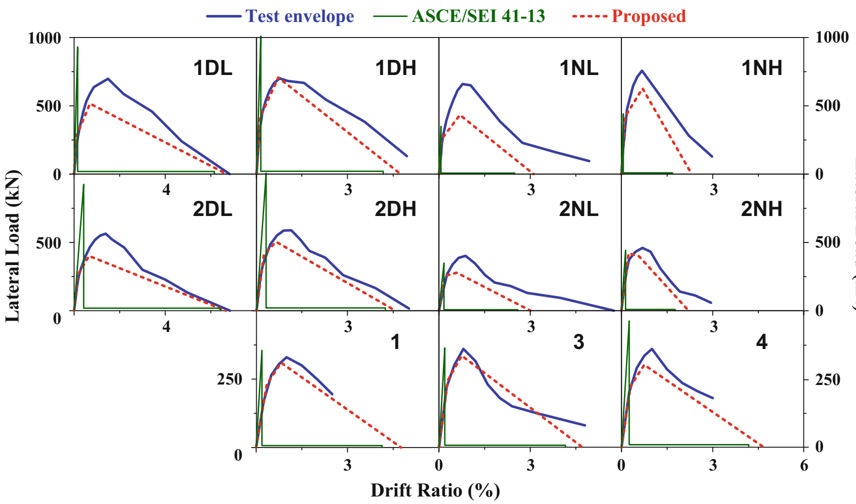

Fig. 2.3 Comparison of the proposed curve and ASCE/SEI 41-13 for short columns (Li and Hwang 2017)

the proposed model (Table 2.1), average test-to-calculation ratio is 1.40 with a coefficient of variation of 0.30. The proposed method utilizes the SST model (Hwang and Lee 2002), which makes it easier to capture characteristics in the mechanical behavior of short columns, leading to more accurate predictions.

According to the test-to-calculation ratio in Table 2.1, for shear strength prediction of ASCE/SEI 41-13 (2014), the average ratio is 1.00 with a coefficient of variation of 0.39. Although the average ratio is 1.00, there is a greater discrepancy among the analytical values. The values in Table 2.1 also indicate that ASCE/SEI 41-13 (2014) significantly underestimates the displacement at the strength point. Its average test-to-calculation ratio is 5.86 with a coefficient of variation of 0.45. This is due to under-estimation of shear deformation.

In this study, eight squat wall specimens of experimental data are used to verify the proposed lateral load-displacement curves. These experiments on double-curvature bending were tested by Lopes (1991). The properties of the database are summarized in Table 2.2 (Weng et al. 2017).

Test envelope curves of specimens and the proposed lateral load-displacement curves are compared in Fig. 2.4 (Weng et al. 2017). At the cracking point, the proposed curves are much closer to the test envelopes in comparison with ASCE/SEI 41-13 (2014) curves. In the comparisons at the strength point shown in Fig. 2.4, both models have similar accuracy in their predictions of shear strength. However, for the displacement prediction at the strength point, the ASCE/SEI 41-13 (2014) model performs more accurately than the proposed model. The test envelopes in Fig. 2.4 indicate that shear failure is attributed to fragile destruction behavior, that is, in a negative linear relationship the lateral strength is suddenly reduced once the shear strength is fully developed. By comparing the aforementioned strength behaviors,

Table 2.2 Comparison for squat walls (Weng et al. 2017)

Specimen		Test parameters					Test results		Calculation			
									Proposed		ASCE 41	
No.	ID.	$\frac{h_w}{\ell_w}$	f'_c (MPa)	ρ_v (%)	ρ_h (%)	$\frac{N}{\ell_w t_w f'_c}$	$V_{n,test}$ (kN)	$\Delta_{n,test}$ (mm)	$\frac{V_{n,test}}{V_{n,proposed}}$	$\frac{\Delta_{n,test}}{\Delta_{n,proposed}}$	$\frac{V_{n,test}}{V_{n,ASCE}}$	$\frac{\Delta_{n,test}}{\Delta_{n,ASCE}}$
1	SW11	1.9	40.1	0.41	0.92	0.04	93	4.7	1.30	0.95	0.97	1.37
2	SW12	1.9	41.2	0.41	0.92	0.04	88	3.1	1.20	0.63	0.92	0.91
3	SW13	1.9	47.8	0.41	0.92	0.03	105	7.0	1.33	1.41	1.08	2.05
4	SW14	1.9	40.4	0.41	0.92	0.04	98	4.2	1.37	0.85	1.03	1.23
5	SW15	1.9	41.3	0.41	0.62	0.04	85	3.2	1.24	0.66	1.20	0.94
6	SW16	1.9	38.7	0	0.92	0.04	80	4.1	1.16	0.83	0.84	1.20
7	SW18	1.9	38.8	0	0.72	0.04	100	3.3	1.45	0.67	1.27	0.96
8	SW17	1.9	39.2	0	0.65	0.04	83	4.1	1.20	0.83	1.14	1.20
Average ratio (AVG)									1.28	0.85	1.06	1.23
Coefficient of variation (COV)									0.08	0.29	0.14	0.30

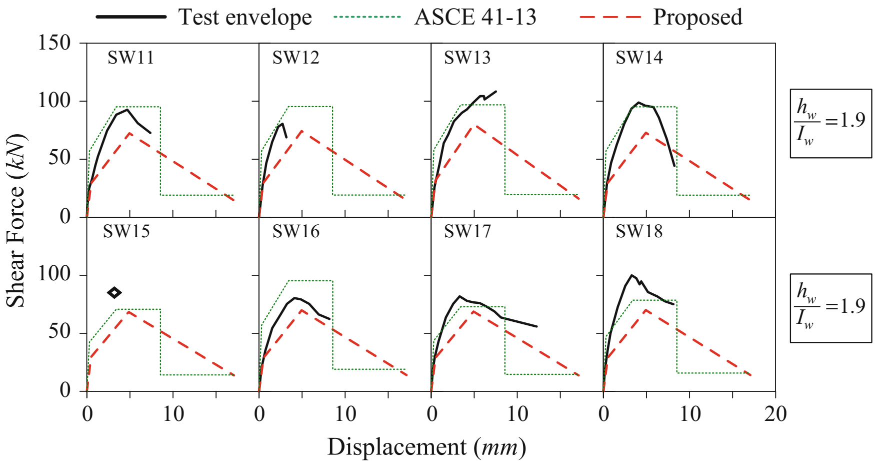

Fig. 2.4 Comparison of the proposed curve and ASCE/SEI 41-13 using specimens from Lopes (1991) [Weng et al. 2017]

the proposed tri-linear model presents curves similar to those of the test envelopes whereas the yield plateau and sudden lateral strength reduction assumed by the ASCE/SEI 41-13 (2014) model do not seem to agree with experimental observations (Fig. 2.4).

The ASCE/SEI 41-13 (2014) standard deems the shear failure to be a type of ductile behavior and indicates that a yield plateau occurs as the shear wall reaches its maximum shear strength. However, this is a different assumption from that in normal practice, which considers shear failure a consequence of brittle destruction. The assumption of a yield plateau leads to the superposition of shear strength from the shear wall and the shear strength of other lateral force resisting structural members, which may cause engineers to misunderstand the internal force distribution in a structure, thus leading to overestimation of the structure's seismic capacity.

2.4 Verification of Fan-Shaped Strut (Intermediate Short Columns)

This paper compares experimental data of intermediate short columns with the existing analytical model, and based on those results, suggests a lateral load-displacement curve for intermediate short columns failed in shear with height-to-depth ratios of between 2 and 4 (Li et al. 2018). The existing analytical model refers to the evaluation method in ASCE/SEI 41-13 (2014), but the experimental database follows the experimental results of this paper, and the material properties of these experiments are listed in Table 2.3.

Figure 2.5 shows the comparison of envelope curves of specimens in the experiment and proposed lateral load-displacement curve, the envelope curves of the experiments in this paper can be seen in Fig. 2.5. Before intermediate short columns reach their shear strength, stiffness softening can occur as the expansion of shear cracks, this indicates the requirement to consider shear deformation induced by shear cracking. After intermediate short columns reaching their shear strength, the lateral strength decreases rapidly, and the straight line of the negative stiffness of the proposed curves matches the results of experiments. The prediction of the proposed curve is rational and conservative.

Table 2.3 shows the prediction of shear strength in the proposed curves and compares it with experimental results. The average value of the test-analytical

Table 2.3 Comparison for intermediate short columns (Li et al. 2018)

Specimens	$\frac{H}{h}$	$\frac{N}{A_g f'_c}$	Hoop ratio, ρ_s	Measured		Analysis for strength point			
				$V_{n,test}$ (kN)	$\Delta_{n,test}$ (mm)	θ	$\frac{V_{n,test}}{V_{n,proposed}}$	$\frac{\Delta_{n,test}}{\Delta_{n,proposed}}$	$\frac{\Delta_{n,test}}{\Delta_{n,ASCE}}$
4DL	4	0.08	0.43%	717	34.5	63.4	0.95	1.65	2.64
4DH		0.22		772	24.4	63.4	0.86	1.32	2.27
4NL		0.08	0.10%	467	16.7	63.4	1.10	1.08	2.25
4NH		0.24		661	14.8	63.4	1.18	1.01	2.21
3DL	3	0.07	0.43%	766	15.4	63.4	0.94	1.23	2.63
3DH		0.22		845	17.6	63.4	0.87	1.50	3.42
3NL		0.07	0.10%	471	7.3	63.4	0.96	0.70	2.06
3NH		0.23		699	6.2	63.4	1.10	0.61	1.83
AVG							0.99	1.14	2.41
COV							0.11	0.30	0.19

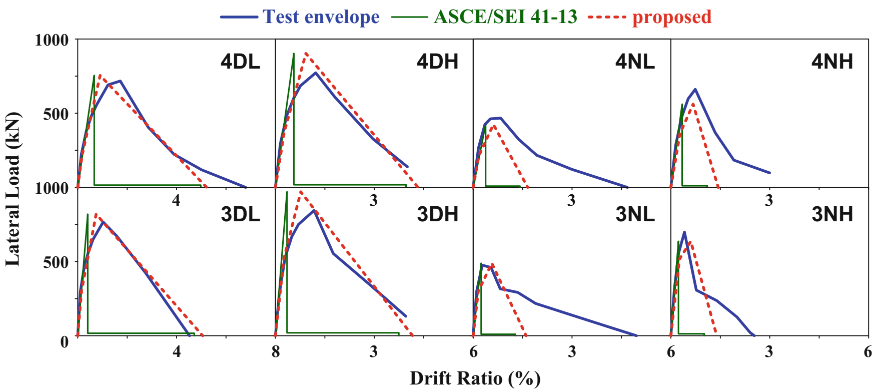

Fig. 2.5 Comparison of the proposed curve and ASCE/SEI 41-13 for intermediate short columns (Li et al. 2018)

strength ratio is 0.99, and the coefficient of variation is 0.11. In terms of the prediction of failure mode in the proposed model, the predictions are all shear tensile failure, so the prediction complies with the results of ASCE/SEI 41-13 (2014).

Table 2.3 also indicates the prediction of lateral displacement at the strength point in the proposed curves and compares it with experimental values, the average value of the test-analytical displacement ratio is 1.14, and the coefficient of variation is 0.30. Since the proposed curve comprehensively takes consideration of shear deformation induced by shear cracks, it can rationally predict the lateral displacement at the strength point for the intermediate short columns failed in shear. Table 2.3 also shows that lateral displacement prediction of intermediate short columns failed in shear by ASCE/SEI 41-13 (2014), the average value of the test-analytical displacement ratio is 2.41, and the coefficient of variation is 0.19. The results show that ASCE/SEI 41-13 (2014) obviously underestimates the lateral displacement of intermediate short columns failed in shear, the reason is when ASCE/SEI 41-13 (2014) evaluates the shear deformation at the strength point, it still regards intermediate short columns as elasticity continuum and does not consider the shear deformation induced by expansion of shear cracks.

Based on the comparison results above, for shear strength prediction in the intermediate short columns failed in shear, the ASCE/SEI 41-13 (2014) formula can be adopted, but more discussion is needed on the physical meaning of formula. However, for lateral displacement prediction at the strength point in the intermediate short columns failed in shear, as abundant shear cracks have already developed, the shear deformation induced by shear cracks should be taken into consideration.

2.5 Conclusions

By the test verification for the bottle-shaped and fan-shaped concrete struts, this paper provided a rational analytical model and a lateral load-displacement curve to simulate the shear behavior of reinforced concrete members under earthquake loading. Comparison with the test envelope and proposed curve confirm that stiffness of concrete members do change before and after shear cracking, and consideration should be given to this phenomenon. Using a strut-and-tie model to predict shear strength can obtain reasonable results. On the prediction of displacement at strength point, shear deformation due to shear cracking should be accounted for, and utilizing the strain field of cracked reinforced concrete proves to be a feasible method.

Comparison shows that, before the intermediate short columns failed in shear reached their shear strength, their stiffness will decline due to the expansion of shear cracks, so the increase rate of lateral displacement of the intermediate short column is improved. This phenomenon indicates that when predicting the lateral displacement at strength points in an intermediate short column, shear deformation induced by the expansion of shear cracks should be taken into consideration. In addition, according to the crack development at the strength point in the intermediate short column experiment, one side of the compression fan can be fixed on the compression zone of column end, and the other side requires force from transverse reinforcement to reach an equilibrium. Therefore, it can be known that transverse reinforcement is critical to shear transfer mechanism in the intermediate short columns failed in shear.

References

American Society of Civil Engineers (ASCE). (2014). *Seismic Evaluation and Retrofit of Existing Buildings (41-13)*, *ASCE/SEI 41-13*, Reston, VA., 518 pp.

Hwang, S. J., & Lee, H. J. (2002). Strength prediction for discontinuity regions by softened strut-and-tie model. *Journal of Structural Engineering, ASCE, 128*(12), 1519–1526.

Hwang, S. J., Tsai, R. J., Lam, W. K., & Moehle, J. P. (2017). Simplification of softened strut-and-tie model for strength prediction of discontinuity regions. *ACI Structural Journal, 114*(5), 1239–1248.

Li, Y. A., Huang, Y. T., & Hwang, S. J. (2014). Seismic response of reinforced concrete short columns failed in shear. *ACI Structural Journal, 111*(4), 945–954.

Li, Y. A., & Hwang, S. J. (2017). Prediction of lateral load displacement curves for reinforced concrete short columns failed in shear. *Journal of Structural Engineering, ASCE, 143*(2), 04016164.

Li, Y. A., Weng, P. W., & Hwang, S. J. (2018). Seismic performance of RC intermediate short columns failed in shear. accepted by *ACI Structural Journal*.

Lopes, M. M. P. S. (1991). Seismic behavior of reinforced concrete walls with low shear ratio, Ph.D. thesis, Department of Civil Engineering, University of London, London.

Moretti, M. L., & Tassios, T. P. (2006). Behavior and ductility of reinforced concrete short columns using global truss model. *ACI Structural Journal, 103*(3), 319–327.

Weng, P. W., Li, Y. A., Tu, Y. S., & Hwang, S. J. (2017). Prediction of the lateral load-displacement curves for reinforced concrete squat walls failing in shear. *Journal of Structural Engineering, ASCE, 143*(10), 04017141.

Chapter 3
Experimental Study of Novel Concrete Frames Considering Earthquake and Progressive Collapse

Xinzheng Lu, Kaiqi Lin, Donglian Gu and Yi Li

Earthquake and progressive collapse are two critical hazards increasing the collapse risks of reinforced concrete (RC) frames. Existing research has revealed that considering the seismic design and progressive collapse design individually for a structure may lead to an undesirable structural performance and unnecessary waste of materials. In this study, two novel concrete frames are proposed to satisfy the demands of both seismic and progressive collapse designs. The experimental results of seismic cyclic and progressive collapse tests indicate that although implementing progressive collapse design can effectively enhance the progressive collapse resistance of RC frame, the beam could be over-strengthened, resulting in a potential unfavorable "strong beam-weak column" failure mode. By contrast, the novel RC frame with a newly proposed structural detailing demonstrates a minor joint region damage with a satisfying progressive collapse resistance. Moreover, the new prefabricated frame exhibits such characteristics as large rotation, low damage, self-centering, and ease of repair.

X. Lu (✉)
Beijing Engineering Research Center of Steel and Concrete Composite Structures,
Tsinghua University, Beijing, China 100084
e-mail: luxz@tsinghua.edu.cn

K. Lin · D. Gu
Key Laboratory of Civil Engineering Safety and Durability of Ministry of Education,
Tsinghua University, Beijing, China 100084
e-mail: linjq13@mails.tsinghua.edu.cn

D. Gu
e-mail: gdl16@mails.tsinghua.edu.cn

Y. Li
Key Laboratory of Urban Security and Disaster Engineering of Ministry of Education,
Beijing University of Technology, Beijing, China 100084
e-mail: yili@bjut.edu.cn

T. T. C. Hsu (ed.), *Concrete Structures in Earthquake*,
https://doi.org/10.1007/978-981-13-3278-4_3

3.1 Introduction

Multiple hazards, such as earthquake, wind, fire and progressive collapse triggered by accidental local failure, impose enormous technical challenges to building structures throughout their service lives. Constructing multi-hazard resistant structures has become one of the most-concerned research focuses worldwide. For commonly constructed multi-story reinforced concrete (RC) frames, a number of existing studies have revealed that earthquake actions and progressive collapse are two critical hazards affecting their structural performance and safety (Sozen et al. 1998; Zhao et al. 2009).

According to the findings of recent literature, a design method targeting for one particular hazard often unfavorably affects the structural performance against other hazards (Li et al. 2011; Fascetti et al. 2015). Lin et al. (2017) discussed the interactions between seismic and progressive collapse designs using a vulnerability-based evaluation method. Their results indicated that using the current progressive collapse design method would result in an unfavorable "strong beam-weak column" failure mode in RC frames, caused by the increased reinforcement ratios in the frame beams. This implies that the structural seismic performance might be weakened after implementing the current progressive collapse design separately. Note that in the current provision of the progressive collapse design guideline (DoD 2010), the re-evaluation and re-design requirement for the seismic performance after performing the progressive collapse design is still absent. As a result, the conventional single-hazard oriented design methods cannot satisfy the performance requirements of the seismic and progressive collapse designs simultaneously. It is therefore urgently needed to propose a comprehensive multi-hazard design solution for RC frames considering both seismic actions and progressive collapse.

In this study, two novel concrete frames, one of which adopts a newly proposed structural detailing, where the layout of the newly added reinforcement of progressive collapse design is changed and the other is made of the self-centering prefabricated frame system, incorporating post-tensioning (PT) tendons, energy dissipating steel angles and shear plates, are proposed to satisfy the demands of both structural seismic and progressive collapse designs. Both cyclic and progressive collapse tests are conducted to evaluate the multi-hazard resistance of the two newly proposed frames. Four design schemes are considered, i.e., a conventional RC frame (RC6), an RC frame after implementing the progressive collapse design (RD1), a novel RC frame with the newly proposed structural detailing (RD2) and a novel multi-hazard resistant prefabricated concrete (MHRPC) frame (PC6). Based on the experimental results, special efforts are paid to: (1) evaluate the influence of the current progressive collapse design on the structural seismic and progressive collapse performances; (2) compare the seismic and progressive collapse resistances between the conventional RC frames and the newly proposed frames.

3.2 Experimental Program

3.2.1 The Proposed RC Frame with a New Structural Detailing

Since the newly added reinforcement for the progressive collapse design enhances the beams and results in a potential unfavorable "strong beam-weak column" failure mode in earthquake, the primary idea is to rearrange the newly added reinforcement in the beams so that it has no contribution to the flexural capacity of the beam. In regards to the effects of different types of longitudinal reinforcement arrangement on the seismic performance or progressive collapse performance, Eom et al. (2015) summarized the results of previous studies on seismic strengthening methods for joint regions, and experimentally evaluated the seismic performance of the U-shaped beams strengthened by two of such methods. Feng et al. (2017) tested the resistance of beams using wave-like reinforcement. In this study, a new structural detailing, whose details are shown in Fig. 3.1, is proposed to resolve the conflict between seismic design and progressive collapse design. The proposed structural detailing changes the layout of the newly added reinforcement. Away from the location of the joint, the newly added reinforcement is arranged at the mid-height of the beam; while in the vicinity of the joint interface, it is bent up to the top and bottom surfaces of the beam and passes through the joint region. The RC frame with the proposed structural detailing can realize "strong column-weak beam" failure mode in earthquake and provide sufficient catenary action against progressive collapse.

3.2.2 The Proposed MHRPC Frame

In this study, in addition to the frame with the newly proposed structural detailing mentioned above, we intend to introduce the MHRPC frame system for improving both seismic and progressive collapse performances of RC frames. A schematic of the proposed MHRPC frame is shown in Fig. 3.2, in which Fig. 3.2b depicts the details of the beam-column joint region. The structure is assembled using precast

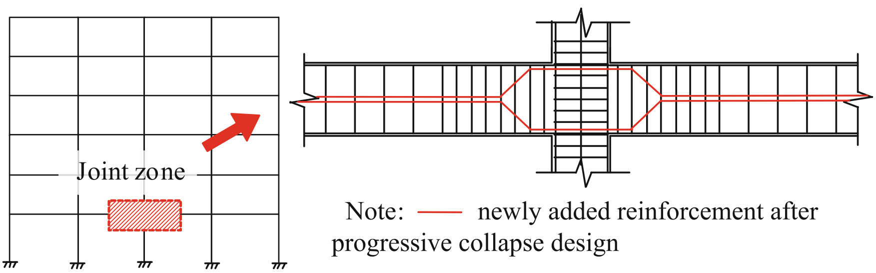

Fig. 3.1 Details of the newly proposed structural detailing

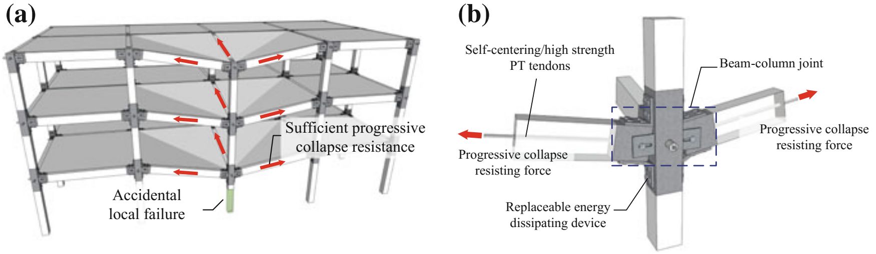

Fig. 3.2 **a** Deformation of MHRPC frame under column removal scenario and **b** details of the beam-column joint of MHRPC frame

RC beams and columns, unbonded PT tendons, energy dissipating steel angles and large rotational shear plates. It should be noted that when the structure is exposed to a specific hazard, one or more of the components may not play a major role. However, these components will become critically important to improve the structural resistance against other hazardous events.

With respect to the seismic action, published experimental studies indicate that the proposed structure has a favorable self-centering capacity, minor post-earthquake damage and is easy to repair after the earthquake (Song et al. 2014; Lu et al. 2015). Under an earthquake scenario, the prestressing tendons, steel angles and shear plates work together to resist the seismic action. More specifically, adequate flexural strengths can be provided by the steel angles and PT tendons while sufficient shear strengths can be provided by the shear plates and PT tendons. In addition, the steel angles also serve as the energy dissipating devices, which are designed to be replaceable after the earthquake. The PT tendons also provide the self-centering capacity to the structure.

When considering the progressive collapse resistance, the structure is expected to deform as shown in Fig. 3.2a. At small deformations, the progressive collapse resistance is provided by the flexural capacities of the beams and the compressive arch action. While at large deformations, both the steel angles and PT tendons are under tension and provide the catenary resistance to redistribute the unbalanced gravity load. The shear plates at the joint region are designed with a slotted hole to accommodate large rotation between the precast columns and beams and help to redistribute the unbalanced load. Hence, the proposed MHRPC system could provide sufficient progressive collapse resistance and alternate load paths, thereby preventing propagation of the initial failure and disproportionate collapse of the entire structural system.

3.2.3 Experimental Design

In order to verify the seismic and progressive collapse performance of the two newly proposed frames, a six-story RC frame with a seismic design intensity of VI (i.e., the design peak ground acceleration (PGA) with a 10% probability of

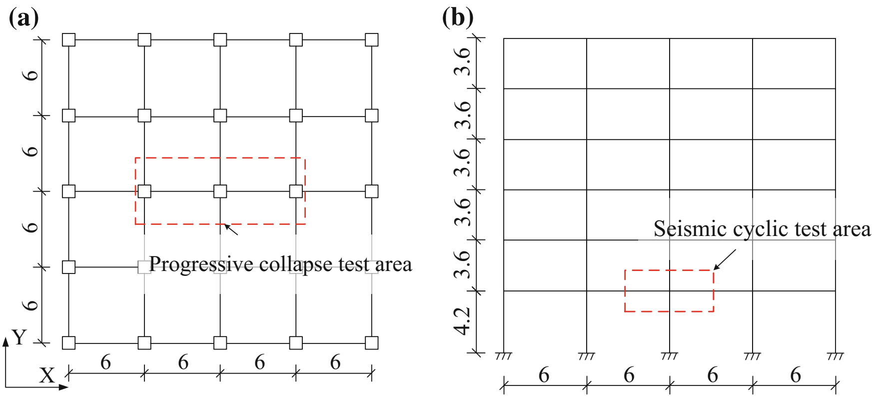

Fig. 3.3 **a** Plane view and **b** elevation of the six-story RC frame (unit: m)

exceedance in 50 years is equal to 0.05 g) is taken as the prototype building. Note that this prototype building has been thoroughly studied experimentally and analytically by Lin et al. (2017) and Ren et al. (2016). Four different frame structures are derived from the design, i.e., a conventional RC frame, an RC frame after implementing the progressive collapse design, an RC frame with the newly proposed structural detailing and the newly proposed MHRPC frame, designated as RC6, RD1, RD2 and PC6, respectively.

Detailed dimensions of the six-story RC frame are shown in Fig. 3.3. The span lengths in both longitudinal and transverse directions are 6.0 m. The structure is considered to be fully fixed to the ground. The dead load considered on each story is 5.0 kN/m^2, whereas the live load is 2.0 kN/m^2. More detailed information about this building have been reported by Lin et al. (2017) and Ren et al. (2016). Initially the structure is designed following the Chinese design codes (MOHURD 2010a, b) to create the conventional RC frame, i.e., RC6.

In the previous work of Lin et al. (2017), nonlinear dynamic analyses of RC6 were conducted to evaluate the structural progressive collapse responses. The numerical results indicated that the prototype building would collapse under gravity load by removing any one of the columns on the first to the fifth story. The outcome of this previous study suggests that RC6 does not satisfy the progressive collapse resistance requirement that is specified in DoD (2010) and should be strengthened to prevent progressive collapse from happening. Hence, RC6 is redesigned according to the tie force method provided in DoD (2010) and the new structure is named as RD1.

In order to avoid the potential "strong beam-weak column" failure mode, the proposed structural detailing in Fig. 3.1 was applied to RD1. The frame with such structural detailing was named as RD2. Furthermore, PC6 is designed by changing the frame beams and columns in RC6 to precast members and keeping the reinforcing details unchanged. These precast beams and columns are then assembled with PT tendons, energy dissipating steel angles and shear plates.

To compare the seismic and progressive collapse performances of the above-mentioned four frames (i.e., RC6, RD1, RD2 and PC6), two substructures enclosed by the red dash lines in Fig. 3.3 are extracted from the building for seismic cyclic and progressive collapse tests. For the seismic cyclic tests, the specimens representing the four frames are designated as S-RC6, S-RD1, S-RD2 and S-PC6, respectively. For the progressive collapse tests, the specimens are named as P-RC6, P-RD1, P-RD2 and P-PC6, respectively. For both the seismic cyclic tests and the progressive collapse tests, a 1/2-scale ratio is adopted for the specimens.

3.2.4 Experimental Setup

The experimental setup for the seismic cyclic test is depicted in Fig. 3.4. The specimens are pinned at both ends of the column. During seismic cyclic tests, a constant vertical force of 486 kN, corresponding to the design axial force ratio of 0.85, is firstly applied to the top of the column to simulate the load transferred from the upper stories. After that, the seismic forces are simulated by gradually increasing the cyclic loads at the beam ends. The loading points on the beams are 1.5 m away from the joint center. Displacement-based loading method is adopted in the tests and each level of displacement after the third cycle is cycled twice to assess the deterioration effect. The loading protocol of the seismic cyclic tests is provided in Fig. 3.4b, which depicts the displacements at the south loading point of the S-series specimens (i.e., S-RC6, S-RD1, S-RD2 and S-PC6).

The relative rotation between the beam and column is calculated by measuring the displacements at the beam ends. The moments (i.e. M) and the joint rotations (i.e. θ) of the specimens are calculated following Eqs. 3.1 and 3.2, respectively:

$$M = F_S \times l_F + F_N \times l_F, \quad (3.1)$$

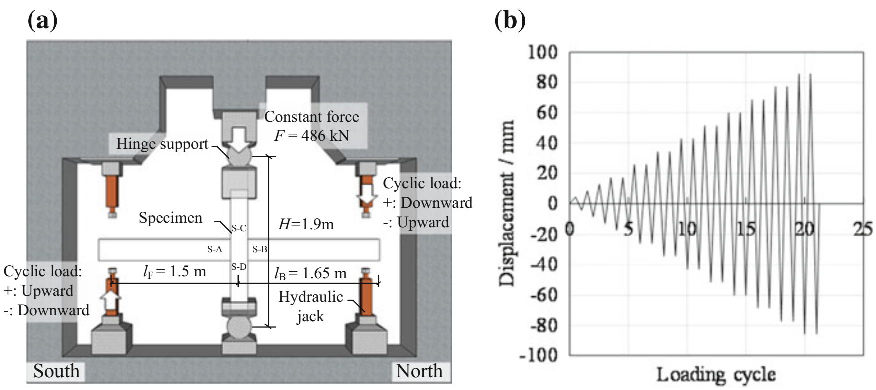

Fig. 3.4 **a** Setup and **b** loading protocol of seismic cyclic test

$$\theta = (\delta_S + \delta_N)/2l_F, \tag{3.2}$$

where F_S and F_N are the forces recorded at the south and north loading points, respectively; δ_S and δ_N are the corresponding displacements; l_F is the distance between the loading point and the joint center as shown in Fig. 3.4a. For the convenience of describing the experimental results, four typical sections (i.e. Sections S-A to S-D) are defined on the joint specimen as shown in Fig. 3.4a.

A middle column removal scenario is considered in the progressive collapse tests and the experimental setup is shown in Fig. 3.5. The tested two-span substructure is fixed to the strong boundary columns. In order to ensure the boundary fixities, H-shaped steel is embedded in the boundary column and two constant forces of 500 kN are applied to the top of the boundary columns. A monotonic concentrated load is then applied to the stub of the removed column to simulate the progressive collapse of the substructure subject to the middle-column removal. The loading process is displacement-controlled. At the same time, rotational restraints are installed in place of the removed column to prevent rotation of the column stub along the X and Z axes as shown in Fig. 3.5. Similar to the seismic cyclic test, six typical sections (Sections P-A to P-F) as shown in Fig. 3.5 are defined on the specimens to better describe the experimental results.

The reinforcing details of the four seismic cyclic test specimens are shown in Fig. 3.6. In addition to the reinforcement of S-RC6 (Fig. 3.6a), two pairs of 8 mm rebars are added to the top and bottom of the frame beams in S-RD1 after performing the progressive collapse design specified in DoD (2010). After that, the four newly added longitudinal bars are rearranged according to the proposed detailing in S-RD2. The typical sectional details of S-RD1 and S-RD2 are given in Fig. 3.6a and b, respectively. Details of the proposed MHRPC frame specimen (i.e., S-PC6) are shown in Fig. 3.6c. The primary design principles of this specimen are: (1) Keeping the reinforcing details of the precast beams and columns identical to those of Specimen S-RC6. (2) The beam-column joint region is covered by

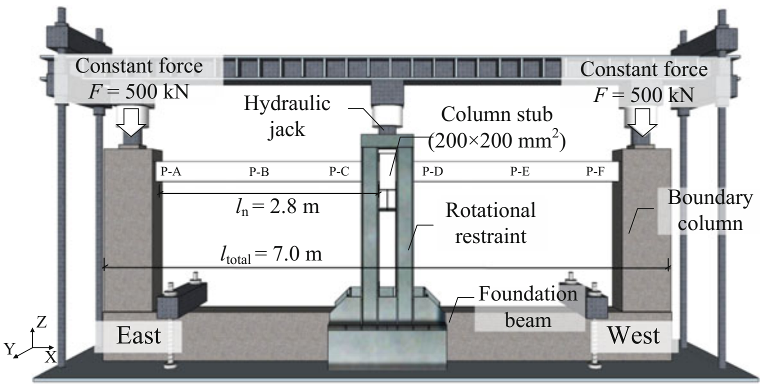

Fig. 3.5 Setup for progressive collapse test

8 mm-thick steel jackets as shown in Fig. 3.6c to prevent local compression failure. (3) According to the Chinese design code (MOHURD 2005), two 12.7 mm PT tendons with a design tensile strength of 1860 MPa are inserted in the specimens as shown in Fig. 3.6c. The minimum prestressing force is determined following ACI 550.3-13 (ACI 2013) to provide a required level of self-centering capacity, which requires the flexural strength provided by the tendons being larger than that provided by the steel angles; (4) Steel angles L100 × 100 × 8 with a thickness of 8 mm are selected as the top and seat angles and bolted to the precast beams and columns with M16 grade 8.8 bolts; (5) The shear plate is 10 mm in thickness. The slotted hole on the shear plate allowing large deformations of the frame beams has a diameter of 18 mm and a length of 53 mm, which meets the deformation demands (i.e., chord rotation is equal to 0.20 rad) in the progressive collapse tests.

The reinforcing details of four progressive collapse test specimens are shown in Fig. 3.7. Note that there is no difference among the details of Section D in all the specimens. And the cross sectional details of the specimens in Fig. 3.7 are the same as those in Fig. 3.6.

3.2.5 Material Properties

The material properties of the specimens are provided in Table 3.1. Specimens S-RC6, S-RD1, S-RD2, P-RC6, P-RD1 and P-RD2 are cast with C30-grade concrete. Note that it is regulated in the Chinese code (MOHURD 2005) that the concrete strength used in the prestressed concrete structures should not be below C40-grade (i.e., the compressive strength determined from the standard cube tests is 40 MPa). Therefore, the C40-grade concrete is used for Specimens S-PC6 and P-PC6 while the reinforcing details of the two specimens remain the same as those of S-RC6 and P-RC6, respectively. Plain round rebars are used for both the longitudinal and stirrup reinforcement in all the specimens. The PT tendons in Specimens S-PC6 and P-PC6 have an equivalent diameter of 12.7 mm and an experimentally measured tensile strength of 1993 MPa. The measured initial stress ratios of the PT tendons (i.e., the ratio between the initial stress and the tensile strength of the PT tendon) in Specimens S-PC6 and P-PC6 are 42% and 34%, respectively. Note that as the residual deformation of Specimen S-PC6 was small and the concrete components were free from damage, this specimen was re-tested after the first cyclic test. In the second test of Specimen S-PC6, the initial stress ratio of the PT tendons was reduced from 42 to 20% and the energy dissipating steel angles were replaced.

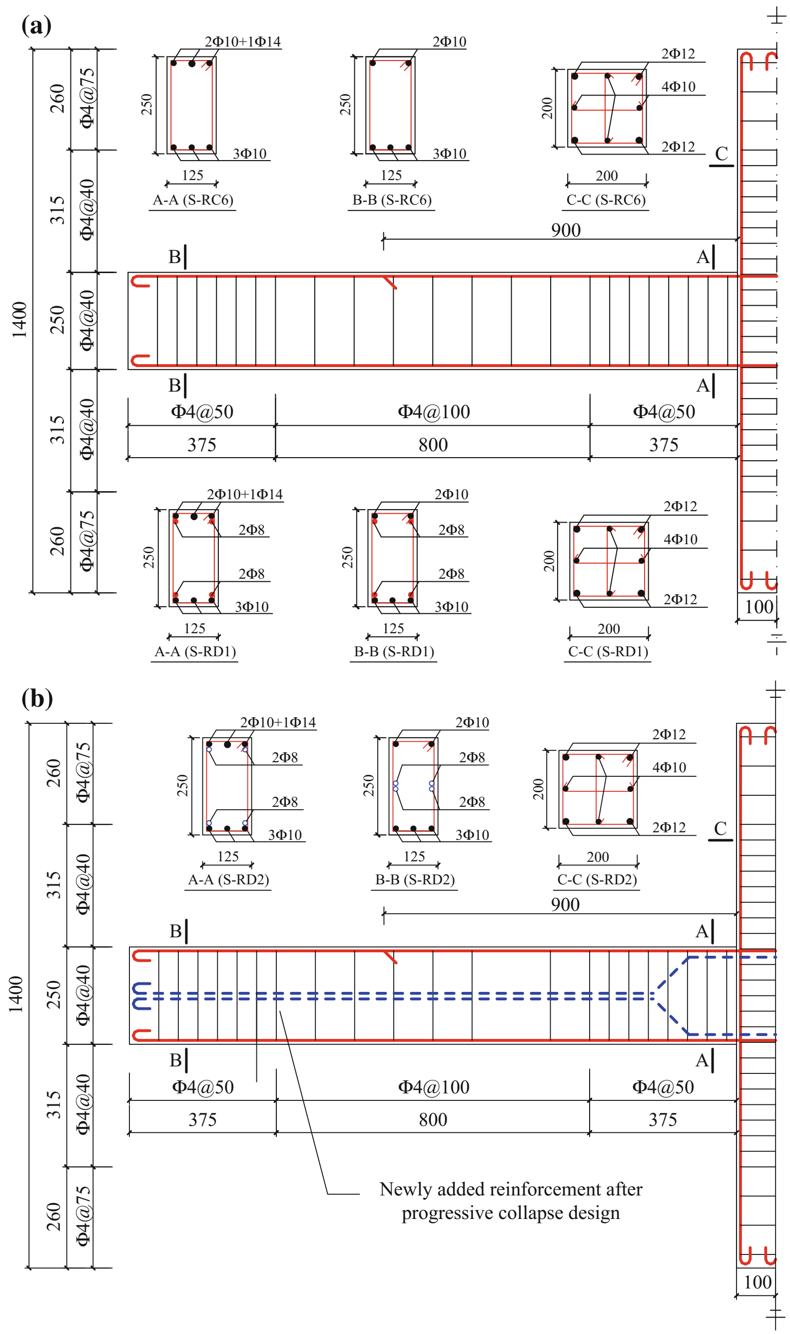

Fig. 3.6 Details of Specimens **a** S-RC6, S-RD1, **b** S-RD2 and **c** S-PC6

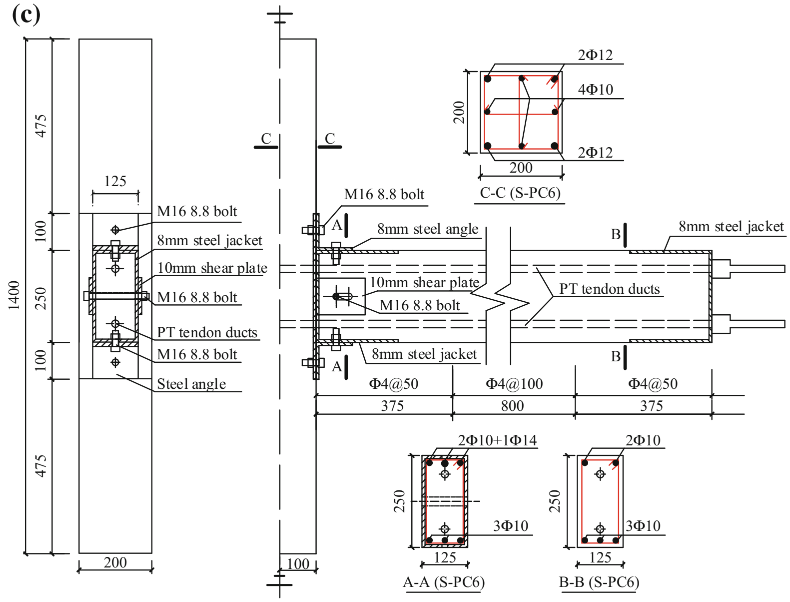

Fig. 3.6 (continued)

3.3 Experimental Results

3.3.1 Seismic Cyclic Test

The moment-rotation relationships of the seismic cyclic test specimens are presented in Fig. 3.8a–d. Correspondingly, their experimental observations are presented in Figs. 3.9 and 3.10, of which, Fig. 3.9 depicts the failure modes of the RC specimens (i.e., S-RC6, S-RD1 and S-RD2) and Fig. 3.10 displays the experimental observations of the PC specimen (i.e., S-PC6).

The final crack distribution of Specimens S-RC6, S-RD1 and S-RD2 are compared in Fig. 3.9. For S-RC6, the damage was concentrated at the ends of the beams while no damage was found in the joint or the column, which indicated that the conventional RC frame meet the requirement of "strong column-weak beam" failure mode under cyclic load. By contrast, it is observed that S-RD1 demonstrated a severe damage at the frame column and joint area due to strengthening of the frame beams after the progressive collapse design was implemented. After applying the newly proposed structural detailing, compared with specimen S-RD1, whose joint surface was covered by dense X-shaped cracks and horizontal cracks, the joint of specimen S-RD2 suffered much slighter damage. Besides, flexural cracks appeared on the column surface of S-RD1 when the joint rotation reached ±2.31%, while no cracks were found on the column surface of S-RD2 during the whole

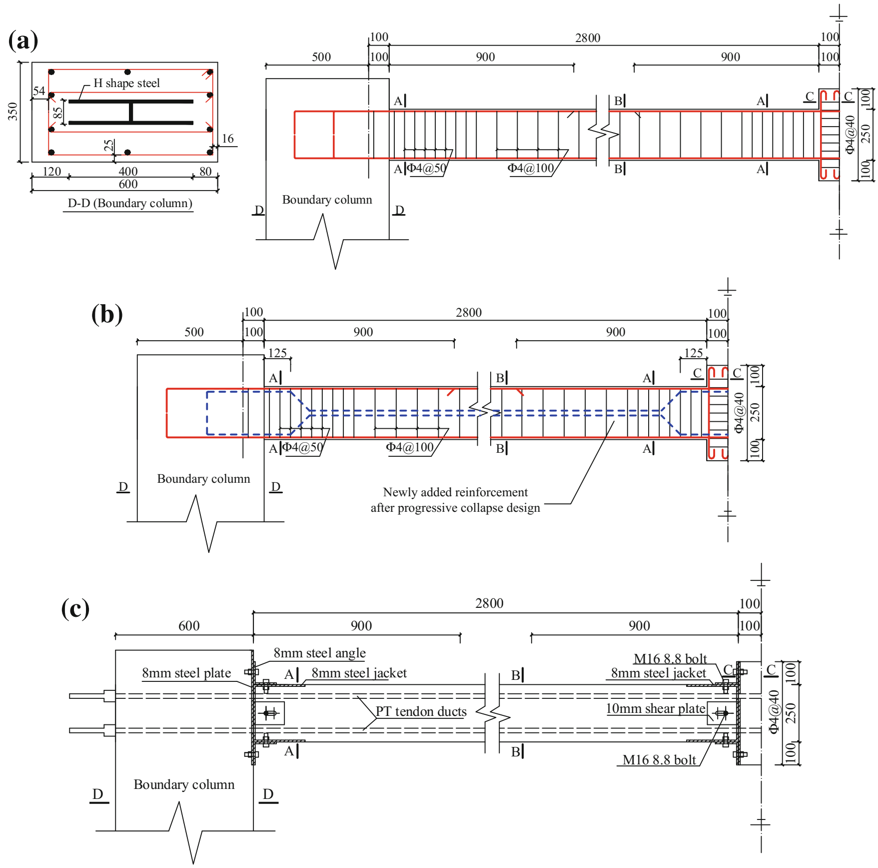

Fig. 3.7 Details of Specimens **a** P-RC6, P-RD1, **b** P-RD2 and **c** P-PC6

seismic cyclic test. Therefore, the proposed structural detailing has a great potential to protect the joint and column of RC frame under cyclic load.

Shown in Fig. 3.10 is the crack distribution of the MHRPC specimen S-PC6. Different from the RC specimens, Specimen S-PC6 deformed elastically in the initial stage of the cyclic loading. When the joint rotation reached ±1.70%, gaps opened at the interface area between the beam and column and some flexural cracks formed near Sections S-A and S-B. However, after unloading at the end of each cycle, the abovementioned flexural cracks and gaps were closed due to the re-centering forces provided by the PT tendons (Fig. 3.10). Note that a larger beam end displacement would result in a wider gap. Upon completion of the cyclic tests, the beams of S-PC6 returned to their original positions. In addition, the cracks on the beams eventually closed and the residual deformation of this specimen was very small, demonstrating an excellent resilient performance. Note that since the joint

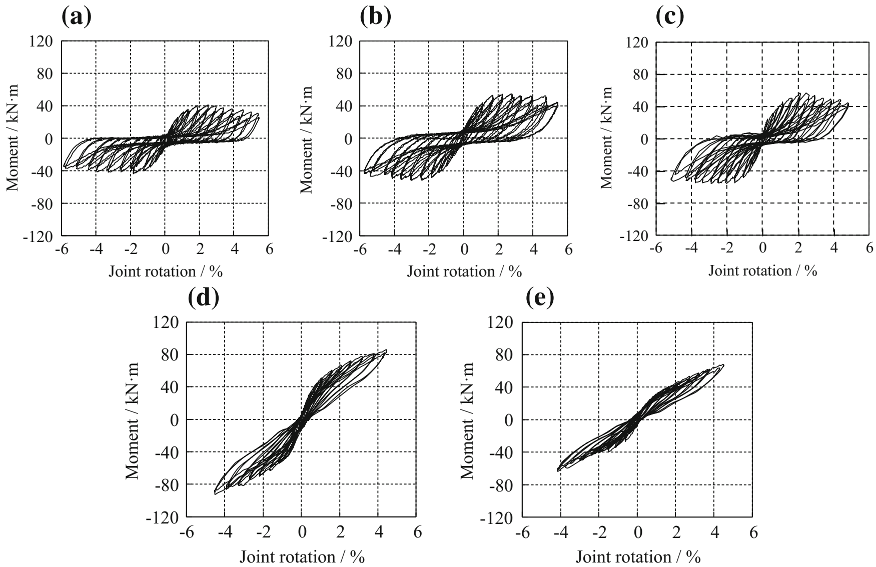

Fig. 3.8 Moment-rotation relationships of Specimens **a** S-RC6, **b** S-RD1, **c** S-RD2, **d** S-PC6 with an initial stress ratio of 42% and **e** S-PC6 with an initial stress ratio of 20%

area of Specimen S-PC6 was protected with 8 mm-thick steel jacket, the joint shear failure, which was found during the test of Specimen S-RD1, was avoided.

By comparing the moment-rotational relationships of the RC and PC specimens, the results indicate that: (1) For the RC specimens, after implementing the progressive collapse design, the flexural capacities of the frame beams in S-RD1 are increased by approximately 30%, compared with that of S-RC6. (2) By adopting the newly proposed structural detailing, the moment-rotation relationship of S-RD2 is very similar to that of S-RD1. Note that the strength of concrete of S-RD2 is slightly larger than that of S-RD1 according to Table 3.1. (3) The MHRPC specimen S-PC6 has a stable post-yielding stiffness and a small residual deformation, which are critical to control the failure modes and resilient performance.

3.3.2 *Progressive Collapse Test*

The load-displacement curves derived from the progressive collapse tests are compared in Fig. 3.11a. The loading process of all the specimens can be divided into two stages, i.e., beam mechanism and catenary mechanism, which are two key resisting mechanisms to balance the applied load under the column removal scenarios. The typical final failure modes of an RC specimen (i.e., P-RC6) and the MHRPC specimen are compared in Fig. 3.11b. Note that the final failure modes of

Table 3.1 Material properties

Reinforcement			
Diameter/mm	Yield strength f_y/MPa	Ultimate strength f_u/MPa	Elongation ratio δ/%
ϕ 4	720	720	4
ϕ 8	300	460	38
ϕ 10	360	535	34
ϕ 12	369	520	39
ϕ 14	370	515	31
Steel components			
Thickness/mm	Yield strength f_y/MPa	Ultimate strength f_u/MPa	Elongation ratio δ/%
8 (Steel jacket)	449	518	39
8 (Steel angle)	305	454	41
10 (Shear plate)	313	537	40
Concrete[a]			
Specimen	Compressive strength $f_{cu,150mm}$/MPa	Specimen	Compressive strength $f_{cu,150mm}$/MPa
S-RC6	28.3	P-RC6	32.5
S-RD1	28.3	P-RD1	32.5
S-RD2	32.5	P-RD2	32.5
S-PC6	51.9	P-PC6	51.9

Note[a]The concrete compressive strength is determined by testing the standard cubes with a size of 150 mm × 150 mm × 150 mm, the mean value of three cubes is taken as the compressive strength

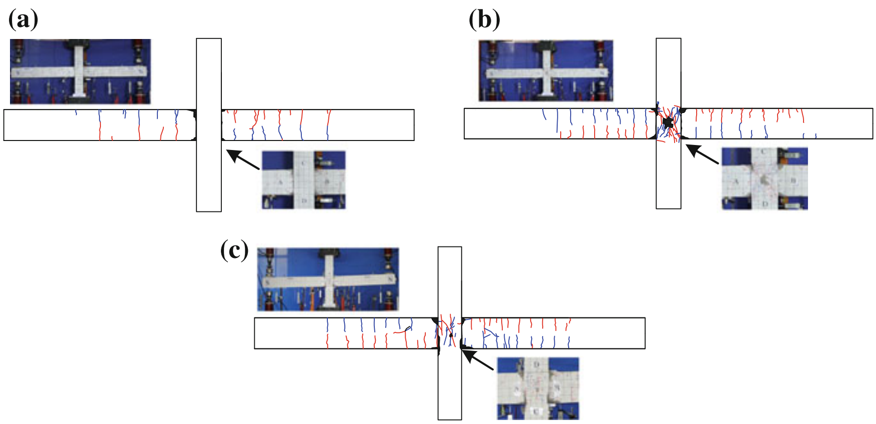

Fig. 3.9 Crack distribution of Specimens **a** S-RC6, **b** S-RD1 and **c** S-RD2

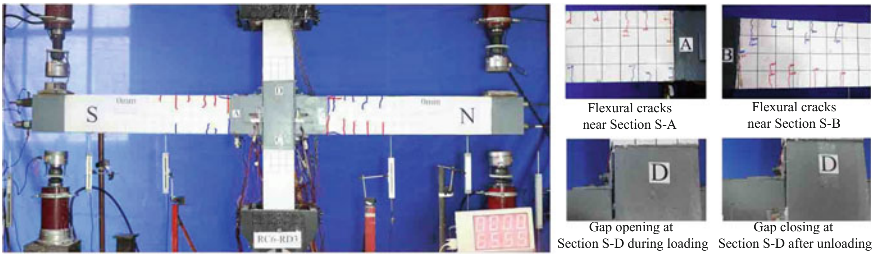

Fig. 3.10 Cyclic test result of Specimen S-PC6 (no residual deformation after the test)

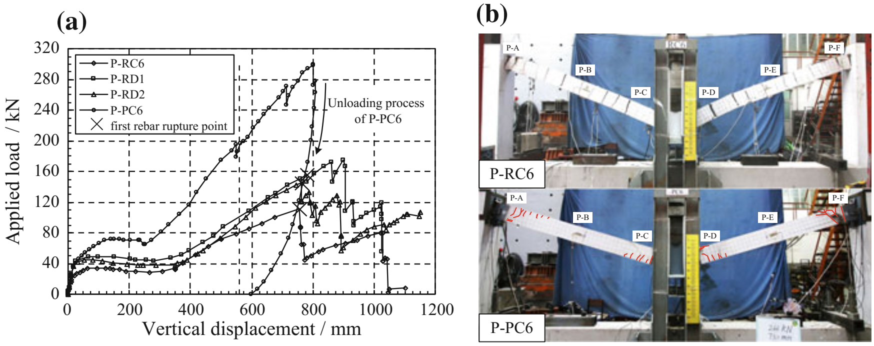

Fig. 3.11 **a** Load-displacement curves of progressive collapse tests and **b** typical failure modes of Specimen P-RC6 and P-PC6

P-RD1 and P-RD2 are both similar to that of P-RC6. Therefore, they are not presented in this paper.

During the progressive collapse test of an RC beam, the unbalanced load is resisted by the beam mechanism at small deformations. At this stage, the flexural strengths of the beams, in conjunction with the compressive arch action in the specimen, provide the resistance to progressive collapse. Moreover, the catenary action at the large deformation stage serves as the last resisting mechanism in progressive collapse scenarios, which utilizes the tensile forces from the rebars to balance the applied load. According to DoD (2010), 0.20 rad of chord rotation is used to define the deformation limit of the specimens. As such, two key points can be identified on the load-displacement curves shown in Fig. 3.11a: (1) the peak point of the beam mechanism (D_b, F_b) and (2) the point corresponding to the chord rotation of 0.20 rad ($D_{0.20}$, $F_{0.20}$), where D and F denote the displacement and force, respectively. Note that the displacement at the 0.20 rad chord rotation (i.e., $D_{0.20}$) is 560 mm. The corresponding values of the two key points are compared in Table 3.2 for all the specimens.

By comparing the load-displacement curves of the progressive collapse test specimens in Fig. 3.11a, it can be found that the characteristic bearing capacities of

Table 3.2 Comparison of progressive collapse resistance of different specimens

Specimen	D_b/mm	F_b/kN	Percentage increase/%	$F_{0.20}$/kN	Percentage increase/%
P-RC6	97	35	/	80	/
P-RD1	98	50	43%	105	31%
P-RD2	80	45	29%	99	24%
P-PC6	145	72	106%	192	140%

P-RD1 (i.e., F_b and $F_{0.20}$) were higher than those of P-RC6: F_b increased by 43% while $F_{0.20}$ increased by 31%. It means for common RC frame, implementing the progressive collapse design can significantly improve the resistances at both beam mechanism and catenary mechanism. Furthermore, by adopting the proposed structural detailing, the flexural capacity (i.e. F_b) of P-RD2 was slightly weakened compared with that of P-RD1. After entering the catenary stage, the behaviors of the two specimens were similar. Therefore, it can be concluded that the proposed structural detailing could meet the requirement of the design guidelines and provide a similar resistance as the conventional progressive collapse design.

In addition, the results also indicate that P-PC6 can provide sufficient progressive collapse resistance under the column removal scenario. The F_b and $F_{0.20}$ of Specimen P-PC6 were 72 kN and 192 kN, respectively. The F_b increased by 106% and $F_{0.20}$ increased by 140% compared with Specimen P-RC6, which were also much greater than those of Specimen P-RD1 and P-RD2. It can be concluded that the MHRPC specimen can provide a stably growing resistance as the displacement increases and meet the code requirement of the chord rotational capacity at the stage of large deformation.

3.4 Conclusions

Building multi-hazard resistant structures has become the future development trend of civil engineering research. In order to improve the multi-hazard resistance of multi-story RC frame structures, two novel concrete frames are proposed in this study. Four different frames, i.e., a conventional RC frame, an RC frame after implementing the progressive collapse design, an RC frame adopting the newly proposed structural detailing and a newly proposed MHRPC frame are tested. Their seismic and progressive collapse performances are compared in some details. Following are the main conclusions of this study:

(1) The influence of progressive collapse design on the seismic performance of RC frames was experimentally studied for the first time. The experimental results of Specimens S-RD1 and P-RD1 show that although implementing the progressive collapse design can effectively enhance the progressive collapse resistance of RC frames, the frame beam could be over-strengthened when designed for

progressive collapse, which may lead to severe damage to the joint area and the frame column, resulting in a potential unfavorable "strong beam-weak column" failure mode.

(2) The seismic cyclic test of Specimen S-RD2 reveals that after applying the proposed structural detailing, the joint damage of S-RD2 under cyclic load can be largely mitigated. In addition, S-RD2 is capable of providing a very similar progressive collapse resistance as the conventional progressive collapse design. Therefore, the proposed structural detailing can meet the requirement of progressive collapse design guidelines.

(3) The seismic cyclic test of the MHRPC specimen S-PC6 indicates that S-PC6 has much smaller residual deformations and less component damage compared with the RC specimens. Moreover, Specimen S-PC6 remains a stable post-yielding stiffness, which is beneficial to the control of structural deformation and energy dissipating mode. Following a simple repair, the MHRPC specimen can recover and maintain a stable seismic performance, which satisfies the demand of resilience.

(4) The progressive collapse test of a MHRPC substructure, which is not found in the existing literature, was successfully conducted. Under the middle column removal scenario, the MHRPC specimen P-PC6 has a much higher progressive collapse resistance than the RC specimens, which demonstrates a superior load redistribution capacity of this newly proposed structural system. In addition, the MHRPC specimen also meets the requirement of the chord rotational capacity as regulated in DoD (2010).

To sum up, the proposed structural detailing balances the confliction between the seismic and progressive collapse designs of RC frame and will have important potential for the multi-hazard prevention of RC frame. Besides, the proposed MHRPC frame system has the characteristics of large rotation, low damage, self-centering and ease of repair, thereby meeting the requirement of multi-hazard resilience of RC frame structures against both earthquake and progressive collapse. The outcome of this study could provide a reference for the future multi-hazard resistant design of building structures.

Acknowledgements The authors are grateful for the financial support from the National Natural Science Foundation of China (No. 51778341).

References

American Concrete Institute (ACI). (2013). *Design specification for unbonded post tensioned precast concrete special moment frames satisfying ACI 374.1 and Commentary*, *ACI 550.3-13*, Farmington Hills, MI.

Department of Defense (DoD). (2010). *Design of structures to resist progressive collapse*, *unified facility criteria*, *UFC 4-023-03*, Washington, DC.

Eom, T. S., Park, H. G., Hwang, H. J., & Kang, S. M. (2015). Plastic hinge relocation methods for emulative PC beam-column connections. *ASCE Journal of Structural Engineering, 142*(2), 04015111.

Fascetti, A., Kunnath, S. K., & Nisticò, N. (2015). Robustness evaluation of RC frame buildings to progressive collapse. *Engineering Structures, 86,* 242–249.

Feng, P., Qiang, H. L., Qin, W. H., & Gao, M. (2017). A novel kinked rebar configuration for simultaneously improving the seismic performance and progressive collapse resistance of RC frame structures. *Engineering Structures, 147,* 752–767.

Li, Y., Ahuja, A., & Padgett, J. E. (2011). Review of methods to assess, design for, and mitigate multiple hazards. *Journal of Performance of Constructed Facilities, 26*(1), 104–117.

Lin, K. Q., Li, Y., Lu, X. Z., & Guan, H. (2017). Effects of seismic and progressive collapse designs on the vulnerability of RC frame structures. *Journal of Performance of Constructed Facilities, 31*(1), 04016079.

Lu, X. L., Cui, Y., Liu, J. J., & Gao, W. J. (2015). Shaking table test and numerical simulation of a 1/2-scale self-centering reinforced concrete frame. *Earthquake Engineering and Structural Dynamics, 44*(12), 1899–1917.

Ministry of Housing and Urban-Rural Development of the People's Republic of China (MOHURD). (2010a). *Code for design of concrete structures*, *GB50010-2010*, Beijing, China (in Chinese).

Ministry of Housing and Urban-Rural Development of the People's Republic of China (MOHURD). (2010b). *Code for seismic design of buildings*, *GB50011-2010*, Beijing, China (in Chinese).

Ministry of Housing and Urban-Rural Development of the People's Republic of China (MOHURD). (2005). *Technical specification for concrete structures prestressed with unbonded tendons*, *JGJ 92-2004*, Beijing, China (in Chinese).

Ren, P. Q., Li, Y., Lu, X. Z., Guan, H., & Zhou, Y. L. (2016). Experimental investigation of progressive collapse resistance of one-way reinforced concrete beam–slab substructures under a middle-column-removal scenario. *Engineering Structures, 118,* 28–40.

Song, L. L., Guo, T., & Chen, C. (2014). Experimental and numerical study of a self-centering prestressed concrete moment resisting frame connection with bolted web friction devices. *Earthquake Engineering and Structural Dynamics, 43*(4), 529–545.

Sozen, M. A., Thornton, C. H., Corley, W. G., & Sr, P. F. M. (1998). The Oklahoma city bombing: structure and mechanisms of the Murrah building. *Journal of Performance of Constructed Facilities, 12*(3), 120–136.

Zhao, B., Taucer, F., & Rossetto, T. (2009). Field investigation on the performance of building structures during the 12 May 2008 Wenchuan earthquake in China. *Engineering Structures, 31*(8), 1707–1723.

Chapter 4
Validation of the PARC_CL 2.0 Crack Model by the Cyclic Tests of 1/13-Scale Nuclear Containment Structures

Beatrice Belletti, Alessandro Stocchi and Francesca Vecchi

The possibility of predicting and evaluating structural performances is a key feature in modern performance-based design. The PARC_CL 2.0 is a physical approach to the modeling of reinforced concrete structures. A multilayer shell approach is applied to the modeling of a 1/13 reinforced concrete vessel subjected to cyclic loading. An assessment of the predictive capacity of the proposed model is analyzed through numerical versus experimental data comparison. Local and global parameters can be assessed with adequate accuracy, although there is room for improvements.

4.1 Introduction

Wall structures are widely adopted as vertical and horizontal load resisting systems in many civil engineering applications. In particular, reinforced concrete (RC) shell and walls are adopted as structural components (e.g., containment vessels, shear walls) in strategic buildings, like nuclear power plants (NPPs). In this case, RC components must ensure adequate resistance to strong load cases (explosion, earthquake, impact) and they must also provide a confinement function for radiation leakage. Therefore, the cyclic and dynamic response of RC walls is of great interest in the nuclear engineering fields and for the seismic assessment of existing

B. Belletti (✉) · A. Stocchi · F. Vecchi
Dipartimento di Ingegneria e Architettura, Università di Parma,
Parco Area Delle Scienze 181/a, 43124 Parma, Italy
e-mail: beatrice.belletti@unipr.it

A. Stocchi
e-mail: ing.stocchi@gmail.com

F. Vecchi
e-mail: vecchi.francesca89@gmail.com

T. T. C. Hsu (ed.), *Concrete Structures in Earthquake*,
https://doi.org/10.1007/978-981-13-3278-4_4

structures. (Hsu 2013; Labbé 2013). Several efforts were made for the comprehension of the behavior of RC wall systems from an experimental point of view. More details might be found in (Riva 2003; Grammatikou 2015; Belletti 2014a). From the numerical point of view, several modeling approaches are available in the engineering practice. However, it was observed that the nonlinear response prediction of RC walls by means of equivalent beam elements with lumped plasticity or fiber element models, is mainly adopted for the verifications of non-critical shear elements, like, for example, slender RC walls (Belletti et al. 2013; Martinelli and Filippou 2009). Furthermore, existing RC wall systems can be subjected to phenomena like steel reinforcement buckling, de-bonding and loss of anchorage, crushing of compressed boundary elements, and out-of-plane global failure (Rosso et al. 2016). Moreover, simplified hypotheses may not be fully suitable in case of the torsional 3D response of the wall structure, like in the case of SMART 2013 international project (Richard 2015). It is then clear the necessity of developing and calibrating reliable numerical tools and material models. The modeling approach should ensure a proper prediction of the in-plane and out-of-plane behavior of wall systems especially for shear-critical members characterized by response dependency on aggregate interlock, dowel action, multiaxial stress states, and multi-direction cracking.

Among different approaches able to catch major nonlinear phenomena, the multilayered shell element approach, based on finite element analysis, is an interesting method. Computational effort is usually less than brick or discrete elements, without a loss of accuracy. In fact, many recent numerical methods based on NLFEA and multilayered shell elements, able to catch failure modes of RC slabs, walls, vessels, and water tanks, can be found in the literature. For example, in Dashti et al. (2014) out-of-plane failure mode of RC walls is evaluated by means of curved shell elements and total strain crack models implemented in DIANA code libraries. A formulation of cyclic softened membrane model for multilayered shell elements, implemented in OpenSees code, is proposed in Luu et al. (2017).

In the presented study, a modeling strategy which relies on multi-layer shell elements and PARC_CL crack model (Belletti et al. 2016, 2017a) implemented in Abaqus Code (Hibbit et al. 2012) is considered. The adopted approach is particularly tailored for shear-critical elements, as proved in previous publications for in-plane (Belletti et al. 2013; Damoni 2014) and out-of-plane (Belletti 2015a; Belletti 2015b) structural response.

It is well known that the hypotheses and assumptions behind adopted strategies can strongly affect NLFEA results (Hendriks et al. 2012; Belletti et al. 2014b). Therefore, the performances of an approach could be checked and calibrated via blind prediction benchmarks. In the presented study the NLFEA is applied to the blind prediction of the seismic performances of a 1/13 scaled cylindrical RCCV subjected to cyclic load. The test has been carried out at the National Center for Research on Earthquake Engineering (NCREE) of Taipei (Taiwan).

The paper presents the prediction results obtained using PARC_CL 1.0 crack model and the post-analyses results obtained using PARC_CL 2.0 model.

Although the good agreement between experimental and NLFEA capacities, in terms of both resistance and ductility, the hysteretic curves were affected by some limits mainly due to the secant unloading approach. In Sect. 4.2 of the study the adopted model is briefly described, with references to more detailed published papers. In Sect. 4.3 the geometry and material parameters of the case study are reported. The adopted modeling strategy is described in detail in Sect. 4.4. In Sect. 4.5, the results of the blind prediction by means of PAR_CL 1.0 are widely discussed and several NLFEA versus experimental results are provided. The paper focuses on results in terms of total base shear versus top displacements, crack opening, strain distribution in steel reinforcement. Section 4.6 is reserved for the description of a preliminary post-analysis where the new PARC_CL 2.0 is applied. Finally, remarks and future perspectives are reported in Sect. 4.7 and the improvements obtained in the post-analysis are discussed. The paper demonstrates that the shell modeling approach represents a useful tool for the evaluation of both local and global damage indicators, which are of great importance in modern performance-based earthquake engineering, as also illustrated in Belletti et al. (2016). Preliminary results of the PARC_CL 2.0 model are also presented for the first time for the case of a cyclic quasi-static analysis.

4.2 PARC_CL Crack Model

As the model is extensively described in (Belletti et al. 2017a, b) only the main characteristics are briefly reported in the paper.

PARC_CL crack model, is a fixed crack model, in which at each integration point two reference systems are defined: the local *x,y* coordinate system, parallel to the global *X,Y* coordinate system, and the *1,2* coordinate system along the principal stress directions.

The angle between the *1*-direction and the *x*-direction is denoted as ψ, whereas $\alpha_i = \theta_i - \psi$ is the angle between the direction of the *i*th order of the bar and the *1*-direction, where θ_i is the angle between the direction of the *i*th order of the bar and the *x*-direction, Fig. 4.1. When the maximum tensile principal stress reaches the concrete tensile strength f_t, cracking starts to develop, and the *1,2* coordinate system is fixed. The concrete behavior is assumed to be orthotropic, both before and after cracking and the reinforcement is modeled through a smeared approach. The model is able to take into account softening in tension and compression, multiaxial state of stress (Vecchio and Collins 1993), the effect of aggregate interlock (Gambarova 1983) and the tension stiffening effect (Giuriani 1981).

PARC_CL 1.0 version is characterized by a cyclic stress–strain relationship for concrete and steel with secant unloading–reloading branch, Fig. 4.2; for this reason, it is suitable especially for the prediction of the monotonic behavior of RC members, while the cyclic behavior cannot be properly model due to the unrealistic modeling of the unloading branch. So to better simulate the cyclic behavior of RC structures, a new release called PARC_CL 2.0 has been developed. In this release a

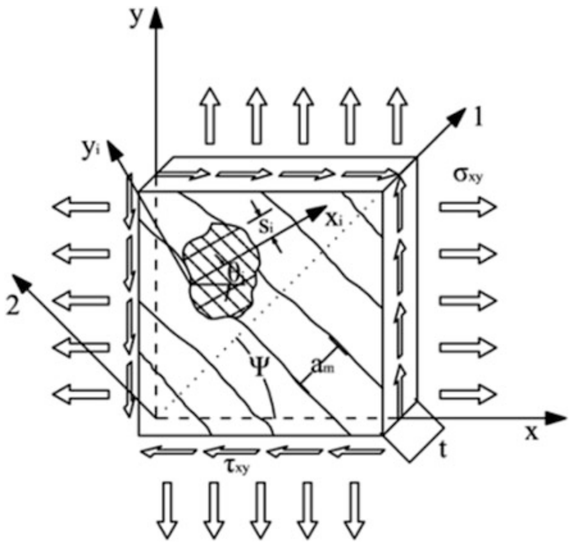

Fig. 4.1 Reinforced concrete member subjected to plane stress state

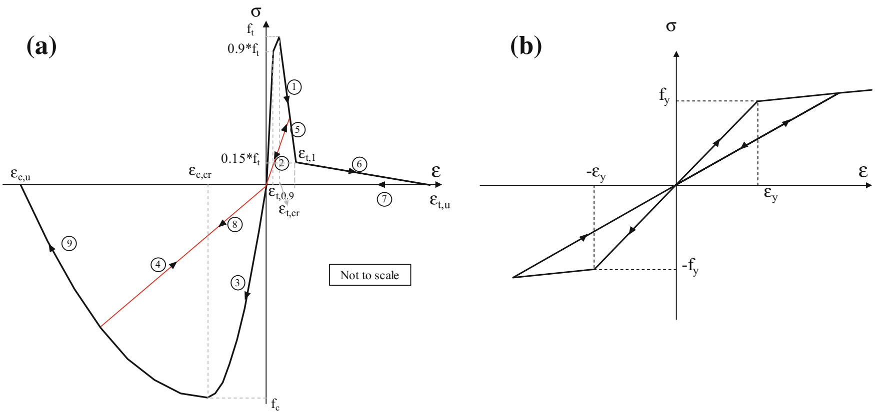

Fig. 4.2 PARC_CL 1.0 cyclic constitutive model: **a** concrete and **b** steel

more refined formulation for concrete, Fig. 4.3a, with plastic and irreversible deformation in the unloading phase, has been added. Moreover, the Menegotto and Pinto formulation has been implemented (Menegotto and Pinto 1973), Fig. 4.3b, and also an extension of the Gambarova's formulation for cyclic loading has been proposed by the authors, Belletti et al. (2017a).

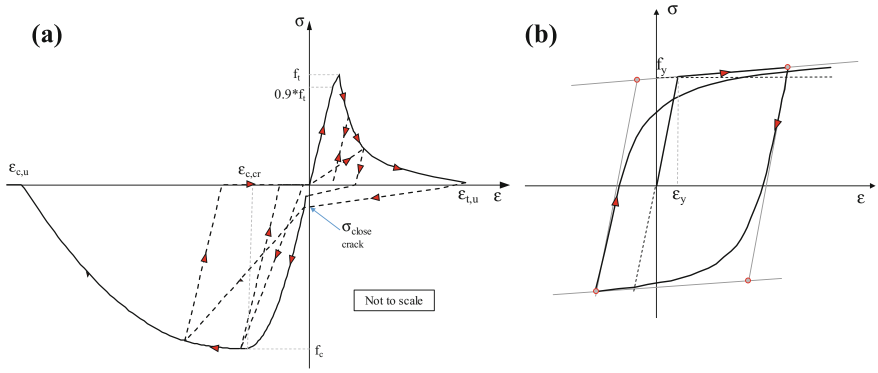

Fig. 4.3 PARC_CL 2.0 cyclic constitutive model: **a** concrete and **b** steel

4.3 1/13 Scaled RCCV Experimental Setup

The experimental campaign is extensively described in (Wu et al. 2018), therefore only essential details are reported here. In Fig. 4.4 it is possible to notice two main reinforcement regions. The top and bottom regions are characterized by vertical reinforcement equal to 4% with a saw-tooth-like geometrical distribution at the interface with the central region; the central region is characterized by vertical reinforcement equal to 2%. The most important material values relevant to the application of the PARC_CL 1.0 and PARC_CL 2.0 are summarized in Table 4.1. Both full experimental loading protocol and numerical blind prediction loading protocol are reported in Fig. 4.5. An additional weight equal to 70 t was applied to the top slab in order to obtain a realistic gravity load.

4.4 Modeling Strategy

The proposed modeling strategy is summarized in Table 4.2 in terms of element types and numbers. It must be noticed that the problem is symmetrical. This allowed to model only half of the structure and the south side, given a set of proper boundary conditions. However, for sake of graphical representation, figures will be mirrored in some cases. The global mesh is reported in Fig. 4.6 where different colors stand for different material parameters. The bottom and top slab have been added to the model to take into account a more realistic geometry and global stiffness. 12520 brick elastic elements with reduced integration (C3D8R) with 8 nodes have been used for the slabs modeling. 2200, two layers, 4 nodes shell nonlinear elements (S4) have been used for the vessel, which is also the main interest of the study. Embedded shell elements are used to consider strain penetration in foundation rebars. Perfect bond has been considered between the slab and

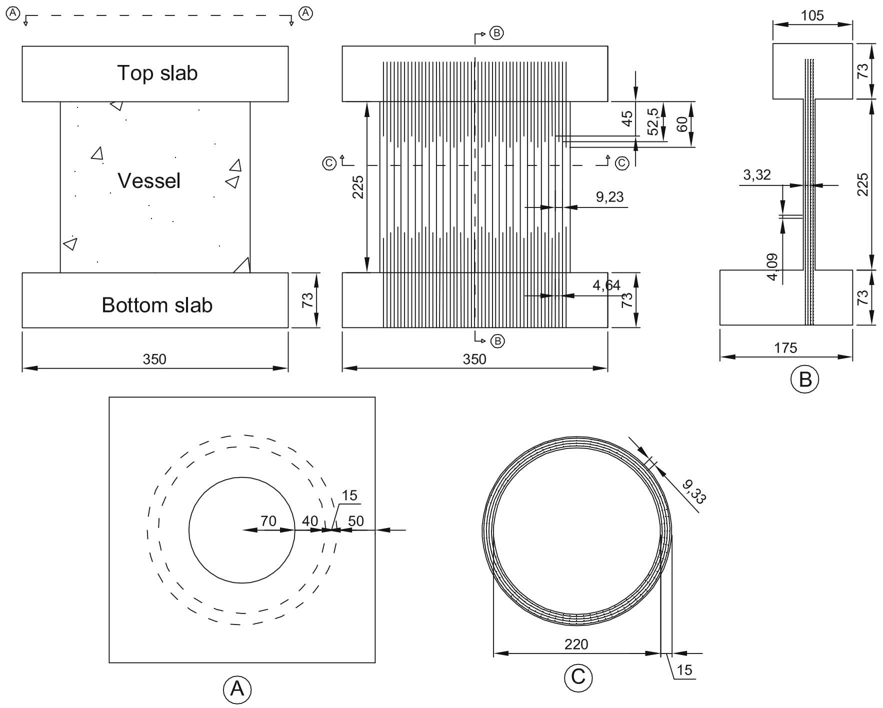

Fig. 4.4 Experimental setup geometry, sections, and reinforcement distribution, 1/80 scale. Measures are expressed in (cm)

Table 4.1 Material parameters

	#3 Rebars (vertical)	#2 Hoops (horizontal)		Concrete
E_s	210000 N/mm^2	210000 N/mm^2	f'_c	−37.76 N/mm^2
f_u	583.6 N/mm^2	576.5 N/mm^2	E_c	32036 N/mm^2
ε_y	0.0017	0.002	f_{cc}	42.2 N/mm^2
ε_u	0.04	0.04	f_{ct}	2.7 N/mm^2
E_{sp1}	5408 N/mm^2	5408 N/mm^2	$\varepsilon_{,c0}$	−0.002
Φ	9.525 mm	6.35 mm		
ρ	2–4%	2%		

such elements. The modeling strategy has been chosen to balance the computational time required and a realistic approach. The load has been applied in displacement control with 0.0125 mm increments applied to a master node of the top section top slab. All the other nodes of the same section were imposed the same displacement of the master node with a kinematic relationship (*EQUATION command of Abaqus code). The standard implicit Abaqus solver was adopted for the resolution of the analysis. The Newton–Raphson method was adopted as convergence

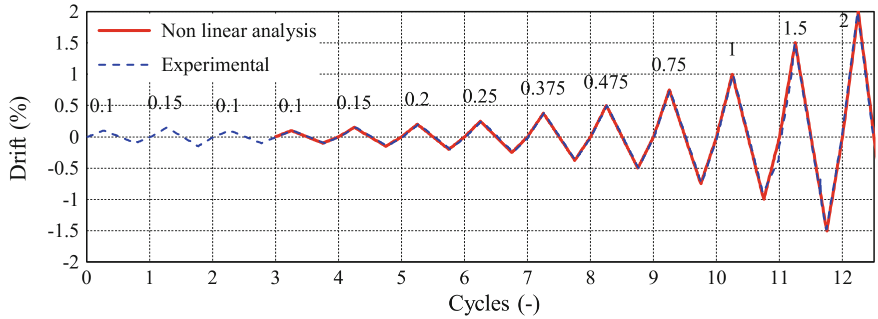

Fig. 4.5 Complete realized experimental loading protocol and numerical loading protocol

Table 4.2 Summary of adopted elements along with their description

Structural part	Element type	Number of elements	Graphical view
Top slab	Elastic 8 nodes	4800	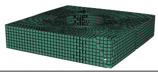
Top embedded reinforcement	4 nodes, 2 layers shells Nonlinear	340	
Top over reinforced vessel	4 nodes, 2 layers shell Nonlinear	300	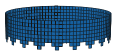
Vessel central body	4 nodes, 2 layers shell Nonlinear	820	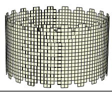
Bottom over reinforced vessel	4 nodes, 2 layers shell Nonlinear	340	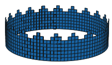
Bottom embedded reinforcement	4 nodes, 2 layers shell Nonlinear	400	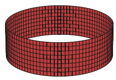
Bottom slab	8 nodes Elastic	7720	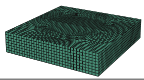

criterium. It is possible to notice that three initial experimental cycles have been neglected at the time of the blind prediction. This is because the first cycles are supposed to remain into the elastic domain and they are mainly run for testing the experimental equipment. Finally, the additional gravity load has been modeled as an equivalent pressure on the top slab.

Boundary conditions are summarized as follows: (1) bottom nodes of the bottom slab are all constrained to vertical displacement, (2) as the bottom slab is connected

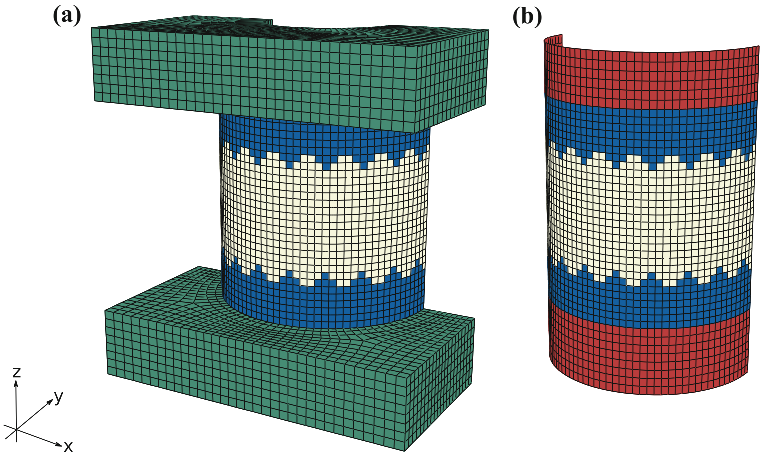

Fig. 4.6 **a** Full global model and **b** vessel model without slab where embedded reinforcement-only elements can be noticed. The global reference system is provided as well

to the ground by means of dowel connections, the slab nodes matching the dowels location are constrained to horizontal displacement (this is as equal to considering dowels with infinite stiffness), (3) top nodes of top slab are subjected to x-direction displacements through the displacement of a master node, and (4) nodes on the axis of symmetry are provided with symmetry constraints.

4.5 NLFEA Blind Prediction Results and Comparison

In the current paragraph, results are presented for the blind prediction. It is remarked that the PARC_CL 1.0 had been applied, while PARC_CL 2.0 preliminary results will be presented in the post-analysis section. Comparisons between experimental and NLFEA results are analyzed in terms of global and local quantities. Results focus on the model response in terms of relevant engineering parameters like maximum base shear, steel strains, crack width, and distribution, failure mode.

4.6 Total Base Shear and Displacements

In Fig. 4.7 the total base shear versus drift plot is reported for the experimental and numerical results. It can be noticed that in terms of peak force the plots are qualitatively in good agreement. The numerical quantitative comparison is provided in Table 4.3. The numerical analyses provided a stronger initial stiffness, probably due to the fact the first cycles were not performed. Indeed, the specimen stiffness had already slightly degraded in the very first cycle. To have a better understanding of the observed phenomena a focus on the first cycle and on the positive quadrant is provided in Fig. 4.8. It is possible to notice in Fig. 4.8a that the initial stiffness is overestimated. However, if cracking phenomena start propagating, the close up of the plot reported in Fig. 4.8b shows that the numerical curve tends to overlay the experimental one. However, the forces up to 0.5% drift are overestimated. The cycle that reaches 0.75% drift catches with better accuracy the damaged stiffness. It is at this point that concrete shear crushing was observed in NLFEA and therefore the following cycle, up to 0.5%, is much lower in terms of stiffness and maximum base shear than the experimental one. Globally, the model could predict the peak force and damaged stiffness up to shear failure. Performances are less reliable beyond 0.75% drift limit. The residual numerical force at 1% drift is approximately one half less than the experimental one. However, in Fig. 4.9, it is possible to

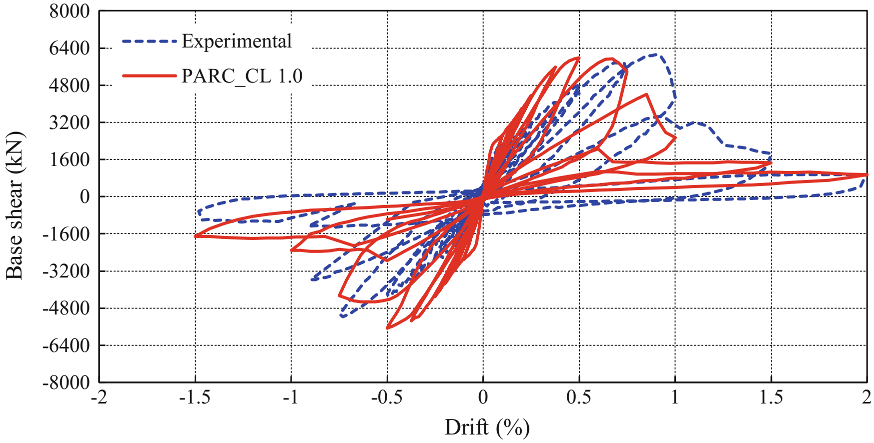

Fig. 4.7 Total base shear versus drift: experimental and numerical results comparison

Table 4.3 Summary of some observed phenomenon in the blind prediction compared to experimental results

	NLFEA drift (%)	NLFEA force (kN)	Exp. drift (%)	Exp. force (kN)	D. error (%)	F. error (%)
Peak force	0.640	5903	0.899	6113	−28.81	−3.44
Hoops Yielding	0.350	5430	0.276	3338	26.81	62.67
Rebars Yielding	0.300	4896	0.430	4426	−30.23	10.62
First crack	0.030	1598	0.073	2095	−58.90	−23.74
1% drift limit	–	2546	–	5668	–	−55.08

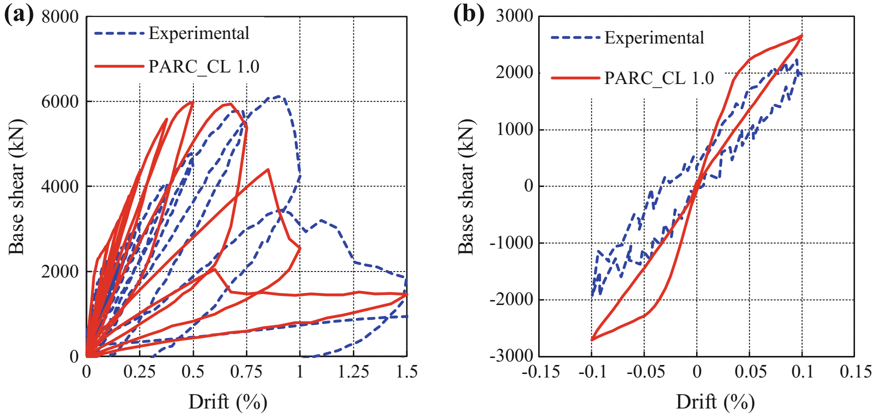

Fig. 4.8 **a** Close up on the first quadrant, and **b** first cycle comparison

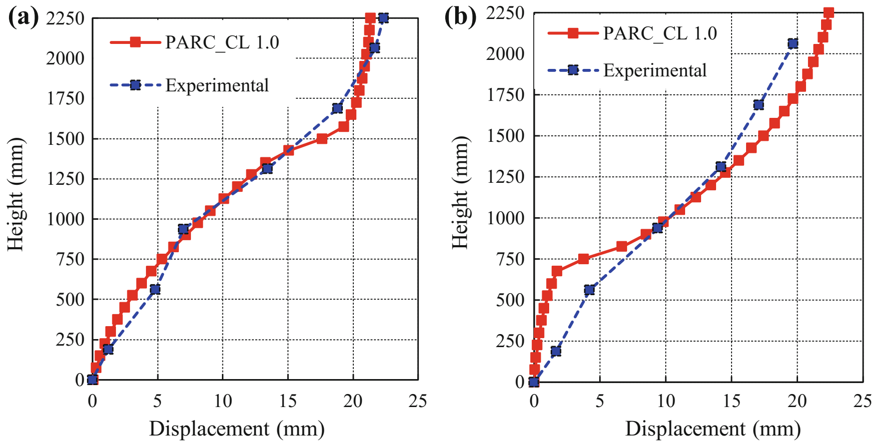

Fig. 4.9 Experimental versus numerical analysis comparison of the **a** east and **b** west side deflections for a drift level equal to 1%

observe that the deflections of the numerical model and of the experimental specimen are in good agreement at 1% drift. It can be noticed that the over reinforced zones at the top and at the bottom of the vessel generate a shear-type-like deformation. Such a deformed shape is less evident in the numerical data. Finally, it is interesting to compare the foundation (which is to say, the bottom slab) extrados displacement, reported in Fig. 4.10. The displacement is measured between the top of the foundation and the ground. The numerical model underestimated such displacement. It must be noticed that the slab is very stiff, as it experienced a maximum displacement of only 0.2 mm. The difference with the numerical model is

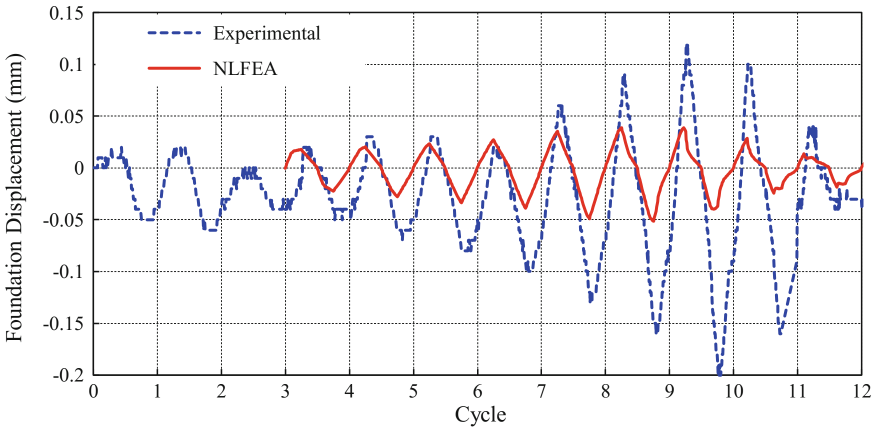

Fig. 4.10 Experimental versus numerical analysis comparison of the bottom slab extrados displacements

because the stiffness of the connection dowels was considered as infinite. Nonetheless, the bottom slab displacement has little consequence on the global behavior.

4.7 Reinforcement Behavior

In this section, the steel reinforcement is analyzed. In particular, strains in vertical rebars (points 1 and 2, Fig. 4.11) and in horizontal hoops (points 3, Fig. 4.11) are presented. It can be noted that the numerical analysis can follow with good accuracy the strain gauges data up to the yielding point (equal to 0.0017), Fig. 4.12. After the yielding point, however, data are less reliable. The vessel model has been "unwarped" in Fig. 4.13 in order to compare numerical and experimental strain

Fig. 4.11 Steel strain: topology of analyzed elements. Points 1 and 2 are mainly subjected to flexural strains while point 3 to shear strains

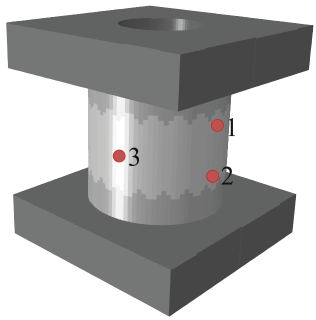

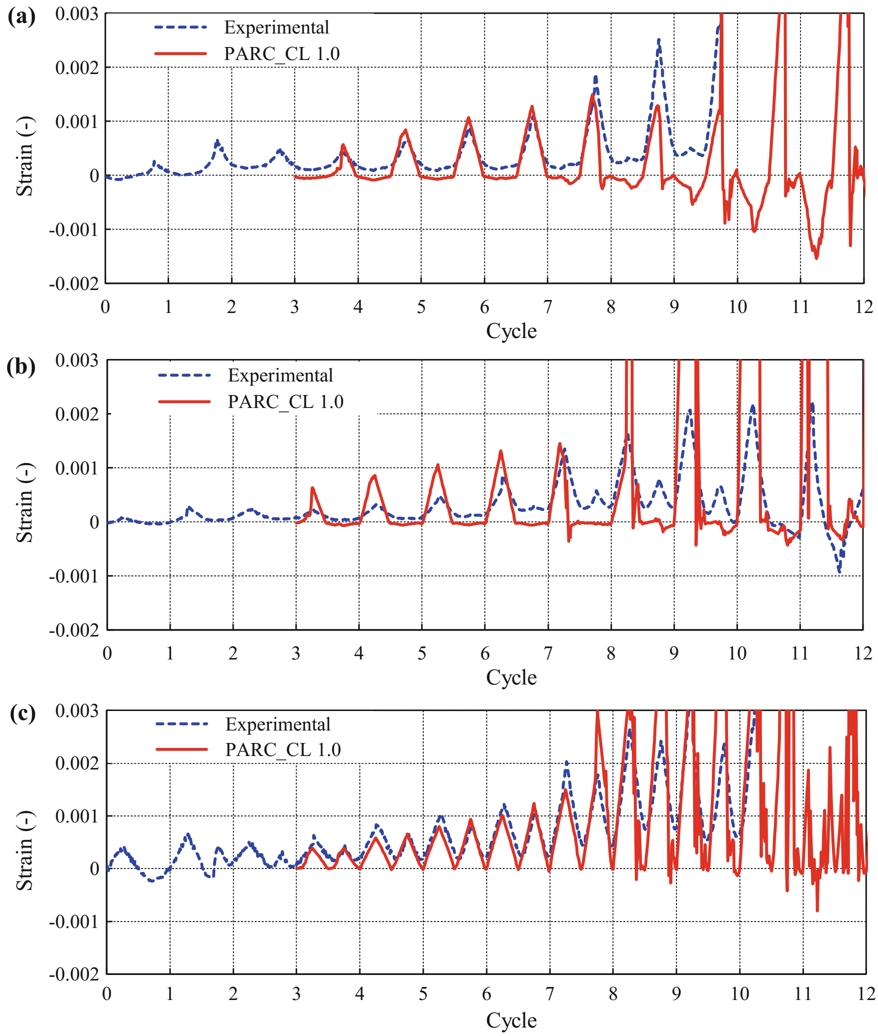

Fig. 4.12 Experimental vs. numerical analysis comparison of reinforcements strain level: **a** rebars, position 1, **b** rebars position 2 and **c** hoops position 3

levels in rebars and hoops. The comparison is taken for a drift equal to 1%, so at an advanced damage state of the specimen. The strain level numerical contour is in good agreement with the experimental one: steel reinforcement yielded essentially in the same zones in both cases. Yet, the strain level in the over reinforced zones shows stronger differences for vertical rebars (Figs. 4.12 and 4.13).

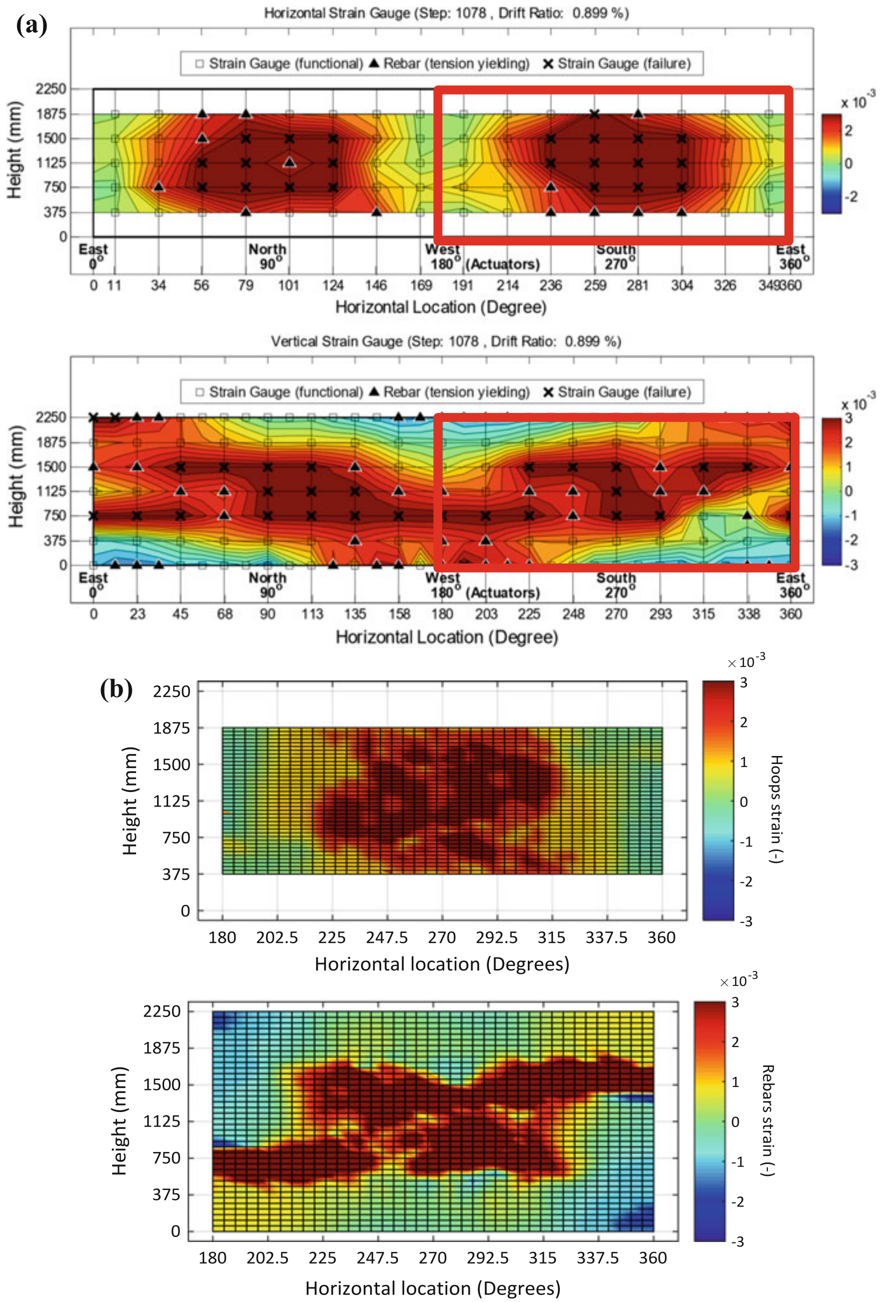

Fig. 4.13 **a** Experimental (Wu et al. 2018) versus **b** numerical analysis comparison of reinforcements strain level at maximum drift equal to 1%. The 270°-south position matches point 3, Fig. 4.11

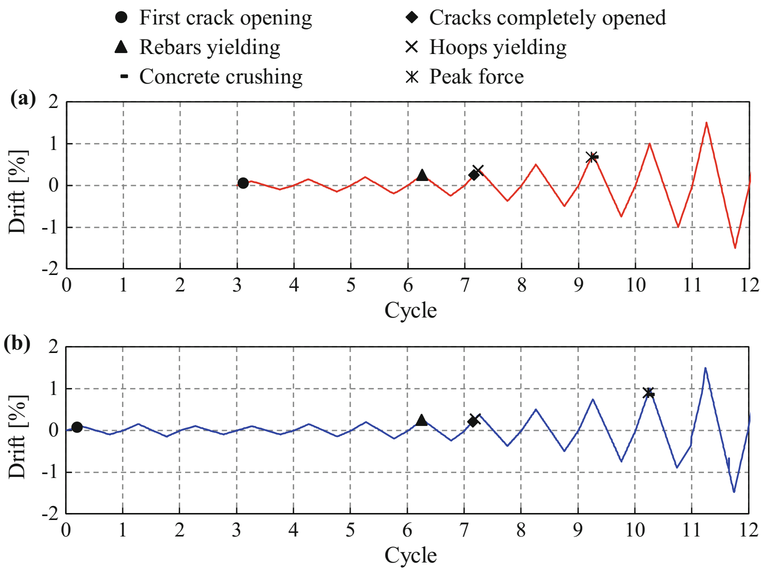

Fig. 4.14 NLFEA structural events: **a** NLFEA sequence and **b** experimental sequence

4.8 Events History

In this section, the results are finally compared in terms of significant engineering events. It is interesting to notice that both curves show early cracking at the first loading cycle (before reaching 0.1% drift), Fig. 4.14. At 0.25% drift, both the numerical and the experimental model show cracks approximately 0.2 mm wide (addressed as "completely opened"). The yielding point of steel reinforcement is achieved during the seventh cycle. Vertical rebars, subjected to flexural behavior, yield slightly before horizontal hoops, which are on the contrary subjected to a shear mechanism. No experimental data are available on the ultimate strain in rebars. The NLFEA reaches the strength peak at 0.75% drift level (concrete web crushing), while the specimen still retains some strength up to a 0.9% drift during the following cycle. Errors on the force level and drift assessment for each event are reported in Table 4.3. Although the whole sequence is accurate, some considerable differences are detected, especially for the force level at hoops yielding point. The peak force and first crack occurrence, on the other hand, are the parameters estimated with the best accuracy. Given that the parameters were blindly predicted, further studies are required to evaluate if the obtained results lie within the limits of fragility assessment for RCCV.

4.9 Crack Openings

A crack pattern has been experimentally observed at a very early stage. This agrees with the numerical analysis, where cracks open at 0.03% drift, which is equal to only 0.675 mm top displacement, Fig. 4.15. In fact, the vessel entered the nonlinear loop during the first numerical cycle. This probably means that the first three elastic cycles already pushed the structure beyond the elastic limit. However, the stereo image system only recorded from the third cycle of the experimental test and the structure probably already showed some microfractures invisible to naked eyes (<0.01 mm). It can be said that results are able to catch the crack direction and the crack width with sufficient accuracy. The model is also able to identify the early cracking phenomenon. The crack distance is a priori equal to 105 mm and it agrees

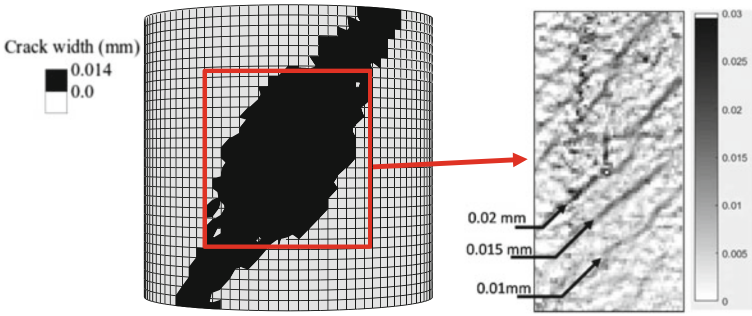

Fig. 4.15 First crack opening at 0.03% drift and comparison with stereo correlation data evaluated at 0.005% drift (Wu et al. 2018)

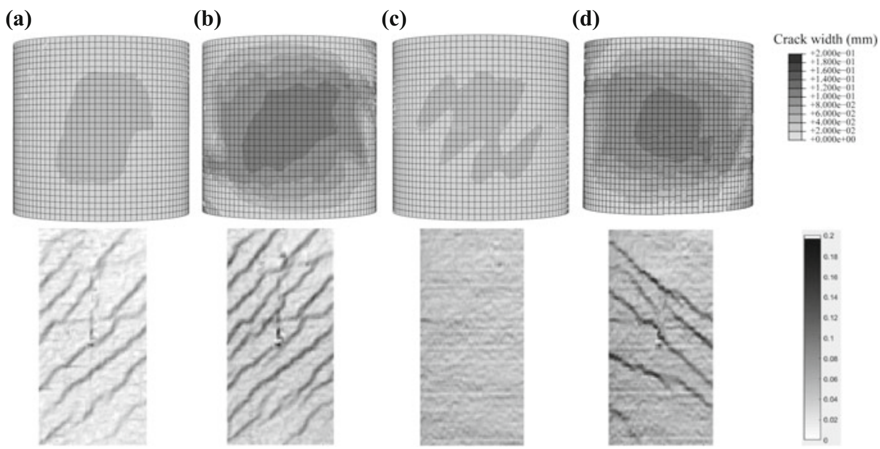

Fig. 4.16 First cycle crack patterns at **a** 0.05%, **b** 0.1%, **c** −0.05%, and **d** −0.1% drift. Numerical versus experimental comparison (Wu et al. 2018)

Table 4.4 Crack opening comparison: experimental versus NLFEA with PARC_CL 1.0

Drift (%)	Exp. crack width (mm)	NLFEA crack width (mm)	Error (%)
0.1	0.1	0.09	−10.0
−0.1	0.15	0.09	−40.0
0.15	0.15	0.14	−6.7
−0.15	0.15	0.14	−6.7
0.2	0.2	0.19	−5.0
−0.2	0.2	0.19	−5.0
0.25	0.25	0.24	−4.0
−0.25	0.25	0.24	−4.0
0.375	0.35	0.36	2.9
−0.375	0.35	0.46	31.4
0.5	0.4	0.58	45.0
−0.5	0.45	0.7	55.6
0.75	0.65	1.8	176.9
−0.75	0.6	3.2	433.3

with the observed crack patterns. Results are compared with available stereo correlation data in Fig. 4.16. In Table 4.4, the crack width detected on the specimen at each cycle peak is compared to the numerical value. Results are in good agreement up to 0.375% drift, so slightly after completely opening of cracks, approximately at 0.2 mm. Results start deteriorating for a drift level of 0.5%. At 0.75% level, crack openings differ extremely as the numerical model is reaching the shear web failure mode with subsequent large cracks propagation. However, the experimental specimen has not yet reached its peak strength at this point. Therefore, it exhibits much less wide cracks.

4.10 Post-analysis

The results provided by the shell modeling with PARC_CL1.0 model stressed the power of the approach as well as its limits. One major limitation of the PARC_CL1.0 was in its poor description of the steel behavior. A second limit was the secant unloading, with consequent unrealistic pinching behavior. The material model was then improved and refined as illustrated in this paper. The analysis was run keeping the same parameters and loading history adopted in the blind prediction.

In Fig. 4.17a, it is possible to observe that PARC_CL 2.0 provides a better estimation of the first cycles in terms of stiffness and maximum base shear. A better estimation of the peak force is also obtained, as highlighted in Fig. 4.17b.

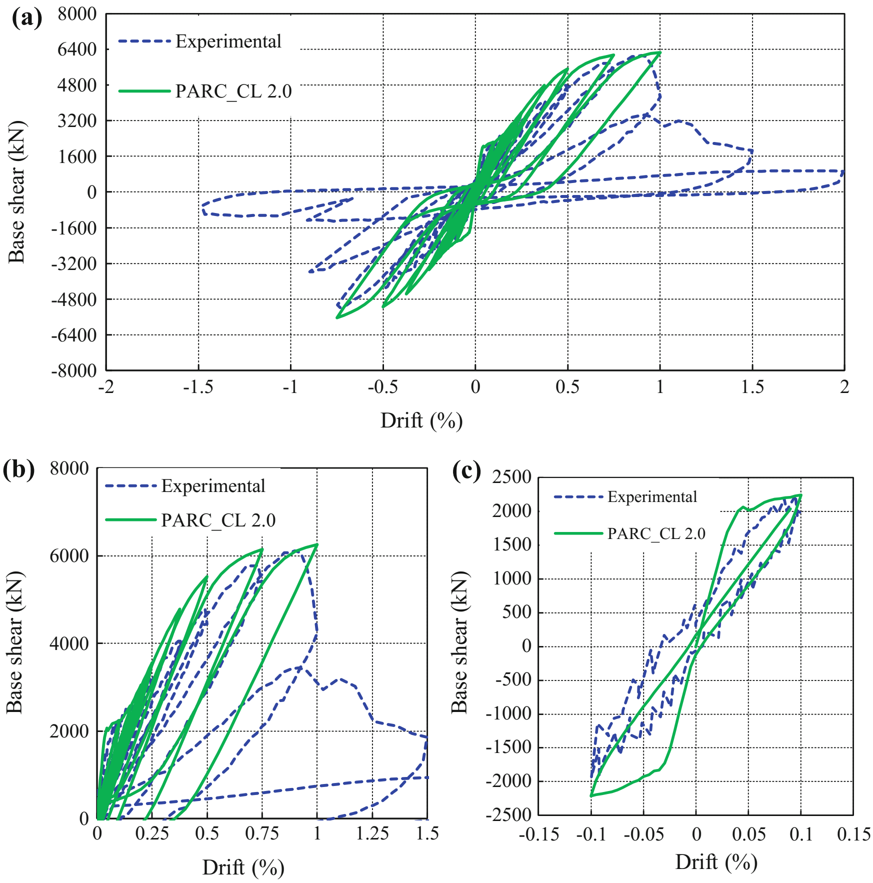

Fig. 4.17 **a** Global numerical versus PARC_CL 2.0 analysis, **b** close up on the first quadrant, and **c** first cycle comparison

The specimen also encountered significant damage and steel yielding with a strong evidence of shear web crushing collapse, although such damage does not lead to a sudden loss in stiffness at 1% drift. However, in Table 4.5 the main engineering events are reported. Results have to be compared with ones provided in Table 4.3. Adopting PARC_CL 2.0 modeling enhanced the performances. A better estimation is provided in terms of both drift and base shear peak value, hoops yielding, first crack opening and 1% drift limit state. The evaluation of the vertical rebars yielding point, on the other hand, does not change significantly. It is stressed also that the force peak is reached during the same cycle in both numerical and experimental case.

Table 4.5 Summary of some observed phenomenon with PARC_CL 2.0 modeling compared to experimental results

	NLFEA drift (%)	NLFEA force (kN)	Exp. drift (%)	Exp. force (kN)	D. error (%)	F. error (%)
Peak force	1.000	6251	0.899	6113	11.23	2.26
Hoops yielding	0.300	4071	0.276	3338	8.70	21.96
Rebars yielding	0.281	3875	0.430	4426	−34.59	−12.45
First crack	0.035	1861	0.073	2095	−52.05	−11.17
1% drift limit	–	6251	–	5668	–	10.29

4.11 Conclusions and Remarks

In this paper, the fixed crack models PARC_CL 1.0 has been adopted for the blind prediction of the behavior of a 1/13 RCCV subjected to cyclic loading. The modeling approach based on multilayered shell elements has been described. PARC_CL 1.0 crack model can, in general, provide good results in terms of failure mode, drift, deflection, steel strain and crack opening, but presents also some cons due to secant unloading. The post-analysis carried out by means of the new PARC_CL 2.0 with plastic strain improved the response prediction, keeping all the parameters, loading history, and mesh unchanged. Preliminary results showed an overall improvement in the results. The study highlighted the capacity of custom models to consider mechanical phenomena which are of great interest also in modern performance-based engineering. Future work will introduce a more refined steel model able to take into account also the dowel effect in rebars. Besides an improvement of the deterministic modeling, applications could be extended in a probabilistic framework for the evaluation of model uncertainties.

Acknowledgements The authors would like to acknowledge Prof. Thomas Hsu (University of Houston) for his remarkable help, and Prof. Chiun-Lin Wu (NCREE), Prof. Shyh-Jiann Hwang (National Taiwan University) and all the NCREE staff for providing experimental data and for their precious collaboration.

References

Belletti, B., Walraven, J. C., Trapani, F. (2015a). Evaluation of compressive membrane action effects on punching shear resistance of reinforced concrete slabs. *Engineering Structures, 95*, 25–39.

Belletti, B., Pimentel, M., Scolari, M., & Walraven, J. C. (2015b). Safety assessment of punching shear failure according to the level of approximation approach. *Structural Concrete, 16*(3), 366–380.

Belletti, B., Scolari, M., & Vecchi, F. (2017a). PARC_CL 2.0 crack model for NLFEA of reinforced concrete structures under cyclic loadings. *Computers & Structures, 191,* 165–179.

Belletti, B., Stocchi, A., Scolari, M., & Vecchi, F. (2017b). Validation of the PARC_CL 2.0 crack model for the assessment of the nonlinear behaviour of RC structures subjected to seismic action: SMART 2013 shaking table test simulation. *Engineering Structures, 150,* 759–773.

Belletti, B., Scolari, M., Almeida, J. P., & Beyer K. (2016) Validation of NLFEA of reinforced concrete walls under bidirectional loading. In *Italian Concrete Days—Giornate AICAP 2016 Congresso CTE*, Roma, Italia, October 27–28. https://infoscience.epfl.ch/record/223004.

Belletti, B., Damoni, C., Scolari, M., Stocchi, A. (2014a). Simulation of RC walls seismic behaviour with shell elements and PARC_CL modelling. In *Second European Conference on Earthquake Engineering and Seismology*, Istanbul (Turkey), August 25–29. www.eaee.org/Media/Default/2ECCES/2ecces_ss/3139.pdf.

Belletti, B., Damoni, C., Hendriks, M. A. N., & De Boer, A. (2014b). Analytical and numerical evaluation of the design shear resistance of reinforced concrete slabs. *Structural Concrete, 15* (3), 317–330. https://doi.org/10.1002/suco.201300069.

Belletti, B., Damoni, C., Gasperi, A. (2013). Modeling approaches suitable for pushover analyses of RC structural wall buildings. *Engineering Structures, 57,* 327–338. https://doi.org/10.1016/j.engstruct.2013.09.023 .

Damoni, C., Belletti, B., Esposito, R. (2014). Numerical prediction of the response of a squat shear wall subjected to monotonic loading. *European Journal of Environmental and Civil Engineering, 18*(7), 754–769

Dashti, F., Dhakal, R. P., Pampanin, S. (2014). Simulation of out-of-plane instability in rectangular RC structural walls. In *Second European Conference on Earthquake Engineering and Seismology*, Istanbul (Turkey), August 25–29. www.eaee.org/Media/Default/2ECEES/2ecces_ss/392.pdf.

Gambarova, P. G. (1983). Sulla trasmissione del taglio in elementi bidimensionali piani di c.a. fessurati. In *Proceedings of Giornate AICAP* (141–156) (in Italian).

Giuriani, E. (1981). On the effective axial stiffness of a bar in cracked concrete. In P. Bartos (ed.) Bond in concrete, Department of Civil Engineering, College of Technology, Paisley, Scotland, (pp. 107–126).

Grammatikou, S., Biskinis, D., & Fardis, M. N. (2015). Strength, deformation capacity and failure modes of RC walls under cyclic loading. *Bulletin of Earthquake Engineering, 13*(11), 3277–3300. https://doi.org/10.1007/s10518-015-9762-x.

Hendriks, M. A. N., Uijl, J. A, De Boer, A., Feenstra, P. H., Belletti, B., Damoni, C. (2012). *Guidelines for non-linear finite element analyses of concrete structures.* Rijkswaterstaat Technisch Document (RTD), Rijkswaterstaat Centre for Infrastructure, RTD:1016:2012.

Hibbit, H. D., Karlsson, B. I., & Sorensen, E. P. (2012) *ABAQUS user manual*, version 6.12. Simulia, Providence, RI.

Hsu, T., Wu, C., & Lin, J. (2013). *Infrastructure systems for nuclear energy*. Chichester: Wiley. https://doi.org/10.1002/9781118536254.ch25.

Labbé, P. (2013). EDF experience on design and construction of nuclear power plants on seismic isolation systems. In *1st Conference on the Technological Innovations in Nuclear Civil Engineering: Construction and Strengthening of Nuclear Buildings*, TINCE 2013 (pp. 29–31), Paris (France), October 28–31.

Luu, C. H., Mo, Y. L., & Hsu, T. T. C. (2017). Development of CSMM-based shell element for reinforced concrete structures. *Engineering Structures, 132,* 778–790. https://doi.org/10.1016/j.engstruct.2016.11.064.

Martinelli, P., & Filippou, F. C. (2009). Simulation of the shaking table test of a seven-story shear wall building. *Earthquake Engineering and Structural Dynamics, 38*(5), 587–607. https://doi.org/10.1002/eqe.897.

Menegotto, M., & Pinto, P. E. (1973). Method of analysis for cyclically loaded RC plane fames including changes in geometry and non-elastic behavior of elements under combined normal force and bending. In *Proceedings of IABSE Symposium on the Resistance and Ultimate*

Deformability of Structures Acted on by Well Defined Repeated Loads (pp. 15–22) Preliminary Rep., Lisbon, Portugal.

Richard, B., Cherubini, S., Voldoire, F., Charbonnel, P. E., Chaudat, T., Abouri, S., et al. (2015). SMART 2013: Experimental and numerical assessment of the dynamic behavior by shaking table tests of an asymmetrical reinforced concrete structure subjected to high intensity ground motions. *Engineering Structures, 109,* 99–116. https://doi.org/10.1016/j.engstruct.2015.11.029.

Riva, P., Meda, A., & Giuriani, E. (2003). Cyclic behaviour of a full scale RC structural wall. *Engineering Structures, 25*(6), 835–845. https://doi.org/10.1016/s0141-0296(03)00020-8.

Rosso, A., Almeida, J. P., & Beyer, K. (2016). Stability of thin reinforced concrete walls under cyclic loads: State-of-the-art and new experimental findings. *Bulletin of Earthquake Engineering, 14*(2), 455–484. https://doi.org/10.1007/s10518-015-9827-x.

Vecchio, F. J., & Collins, M. P. (1993). Compression response of cracked reinforced concrete. *ASCE Journal of Structural Engineering, 119*(12), 3590–3610.

Wu, C.L., et al. (2018) *Reversed cyclic tests of 1/13 scale cylindrical concrete containment structures.* National Center for Earthquake Engineering, *Report No. NCREE-18-001*, Taipei, Taiwan.

Chapter 5
Effect of High-Strength Reinforcement for Shear Strength and Shear-Friction Strength of RC Walls Subjected to Cyclic Lateral Loading

Hong-Gun Park, Jang-Woon Baek and Sung-Hyun Kim

In the shear design of massive walls in nuclear power plants, the use of high-strength reinforcing bars need to be considered to satisfy the high-strength demand and to enhance the constructability and economy. Recently, the use of Grade 550 MPa shear rebars for shear and shear-friction design provisions of RC walls is being reviewed in ACI 349 committee. In the present study, RC walls with Grade 420 MPa, Grade 550 MPa, and higher were tested under cyclic lateral loading to investigate the effect of high-strength reinforcement on the shear strength and shear-friction strength. On the basis of the test results, design recommendations for current shear and shear-friction provisions were proposed.

5.1 Introduction

In the construction of nuclear power plants (NPP), a number of large diameter reinforcing bars are used in massive reinforced concrete (RC) walls, which significantly affects the constructability and economy. After the recent flurry of earthquakes, the structural safety requirements for NPPs have increased, which further increased the number of bars required for RC walls. Such high demand for

H.-G. Park (✉) · S.-H. Kim
Department of Architecture and Architectural Engineering,
Seoul National University, 1, Gwanak-Ro, Gwanak-Gu, Seoul, South Korea
e-mail: parkhg@snu.ac.kr

S.-H. Kim
e-mail: jangson@snu.ac.kr

J.-W. Baek
Department of Civil Engineering and Environmental Sciences,
Korea Military Academy, 574, Hwarang-Ro, Nowon-Gu, Seoul, South Korea
e-mail: baekja1@snu.ac.kr

T. T. C. Hsu (ed.), *Concrete Structures in Earthquake*,
https://doi.org/10.1007/978-981-13-3278-4_5

reinforcement ratio causes bar congestion, concrete segregation, and degradation of constructability and economy. Thus, to enhance the constructability and economy, and to satisfy the increased safety requirement of NPPs, the use of high-strength reinforcing bars needs to be considered.

Currently, the use of Grade 550 MPa rebar is permitted for flexure- axial reinforcement, in both the general and seismic provisions of ACI 349-13 (ACI Committee 349, 2013) [the code requirements for nuclear safety-related concrete structures] and ACI 318-14 (ACI Committee 318, 2014) [the building code requirements for structural concrete]. On the other hand, in the shear design and shear-friction design provisions, the permissible maximum yield strength of shear reinforcement is limited to 420 MPa. Generally, the yield strength of shear reinforcement is limited (1) to ensure yielding of shear reinforcement before shear failure and (2) to control the width of potential diagonal shear cracks. Particularly, in massive low-rise walls of NPPs, the use of high-strength rebars for shear reinforcement is important. This is because in ACI 349 (or ACI 318), the vertical web rebars in such low-rise walls should satisfy the requirements of shear reinforcement as well as flexural reinforcement (in the seismic design provision, for walls with $h_w/l_w \leq 2.0$, the vertical web bar ratio ρ_v should not be less than the horizontal web bar ratio ρ_h [$\rho_v \geq \rho_h$]). For this reason, currently, the yield strength of the vertical web bars, as well as the web horizontal bars, is limited to 420 MPa.

Unlike ACI 349, other design codes permit to use higher strength reinforcement for shear design. In Eurocode 2 (British Standards Institution, 2004) and CSA A23.3-04 (Canadian Standards Association, 2004), the maximum yield strength of shear reinforcement is 600 MPa and 500 MPa, respectively. In JSCE-07 (Japan Society of Civil Engineers, 2010), the use of Grade 800 MPa bars is permitted when the concrete compressive strength f_c' is greater than or equal to 60 MPa.

In case of shear sliding strength (or interface shear strength) in ACI 349 (ACI Committee 349, 2013) [or ACI 318 (ACI Committee 318, 2014)], the yield strength of shear-friction reinforcement is also limited to 420 MPa due to lack of test data using higher yield strength. In shear wall design, the shear-friction strength is also important, because all construction joints are designed by shear-friction. The shear-friction strength was developed based on experimental and theoretical studies by Birkeland and Birkeland (1966). However, the majority of the specimens were tested using push-off test setup, which differs from the actual loading condition of walls under earthquake loading: (1) flexural moment as well as shear force is applied to walls; and (2) repeated cyclic loading degrades the shear-friction resistance of walls. To address such effects, Eurocode 8 (British Standards Institution, 2003), specifies stricter requirements than those of general design code, Eurocode 2 (British Standards Institution, 2003). On the other hand, in ACI 349 (or ACI 318), no special design requirements are specified for cyclic loading.

In the present study, cyclic lateral loading tests were performed for short shear walls (h_w/l_w = 0.5 and 0.33) with Grade 420 and 550 MPa (or higher) rebars to investigate the effect of Grade 550 MPa rebars on the shear strength and the shear-friction strength. The experimental program comprises of two parts: shear test and shear-friction test. The test results were compared with the predictions from current design codes.

5.2 Test Program

5.2.1 Major Test Parameters

In NPP walls, because of the high safety requirements, the shear reinforcement ratio is very high when compared to ordinary walls in building structures. Thus, in the shear strength test (before or after flexural yielding), the specimens were designed with the permissible maximum shear reinforcement ratio (Park et al., 2015). The major test parameters were the grade of the shear reinforcement, failure modes (shear failure before and after flexural yielding), and the presence of boundary confinement hoops.

In the case of shear-friction test, the major test parameters were various actual conditions: various surface conditions ("flat-treated", "untreated", "roughened", or "groove" surface treatment), and effect of flange wall. In actual design of low-rise walls for NPPs, which is susceptible to shear sliding, additional vertical rebars are used to prevent shear sliding mode. Thus, in shear sliding mode specimens, vertical rebars were designed with high reinforcement ratios (0.6% $\sim$ 2.06%). To prevent early diagonal shear cracking failure of walls, intentionally, the horizontal reinforcement ratio was increased (1.59% $\sim$ 2.38%). Further, to induce shear sliding failure mode before flexural yielding, a low aspect ratio of $h_w/l_w \leq 0.5$ [$M/Vl_w \leq 0.66$] was used (Baek et al., 2018).

5.2.2 Design of Specimens

Seventeen specimens were prepared for cyclic loading tests. Figure 5.1 shows the dimensions and details of the specimens and Table 5.1 presents the design parameters. The dimensions of walls with $h_w/l_w = 0.5$ were 1500 mm (length) × 750 mm (height) × 200 mm (thickness) and those with $h_w/l_w = 0.33$ were 1500 mm (length) × 500 mm (height) × 200 mm (thickness) (Fig. 5.1 and Table 5.1). The first letters, **H** and **N**, refer to higher strength deformed bars (Grade 550 or 600 MPa) and normal strength deformed bars (Grade 400 or 420 MPa), respectively. The number **0.5** or **0.33** refers to the aspect ratio of the specimens. The second letter indicates the vertical bar ratio: **M** and **O** refers to code-permitted maximum reinforcement ratio and the higher reinforcement ratio (over-reinforcement ratio), respectively. In the case of Grade 400 or 420 MPa, the permissible maximum bar ratio ρ_{hmax} is higher due to the lower yield strength. The third letter indicates the surface condition of the construction joint: **U**, **R**, and **G** refers to untreated surface, roughened surface (6 mm roughness), and grooved surface (50 mm socketed to foundation slab), respectively. The last letters following dash (-) indicate additional details: **S** for additionally concentrated vertical rebars at wall ends, **LD** for vertical rebars with large diameter (D22), **F** for flanged cross section, and **AF** for asymmetric flanged cross section. For example, **H0.33OU-LD** indicates a specimen with Grade 600 MPa shear bars, aspect ratio of 0.33, relatively large vertical bar ratio, untreated surface in the wall–foundation interface, and vertical rebars of D22. To clarify the effect of parameters, the name of several specimens reported in a previous study (Baek et al., 2017a) were changed in this paper: **NS0.5 M**, **HS0.5 M**, **NF0.5 M**, **HF0.5 M**, and **HF0.5 M-B** to **N0.5MG-S**, **H0.5MG-S**, **N0.5MG**, **H0.5MG**, and **H0.5MG-B**, respectively.

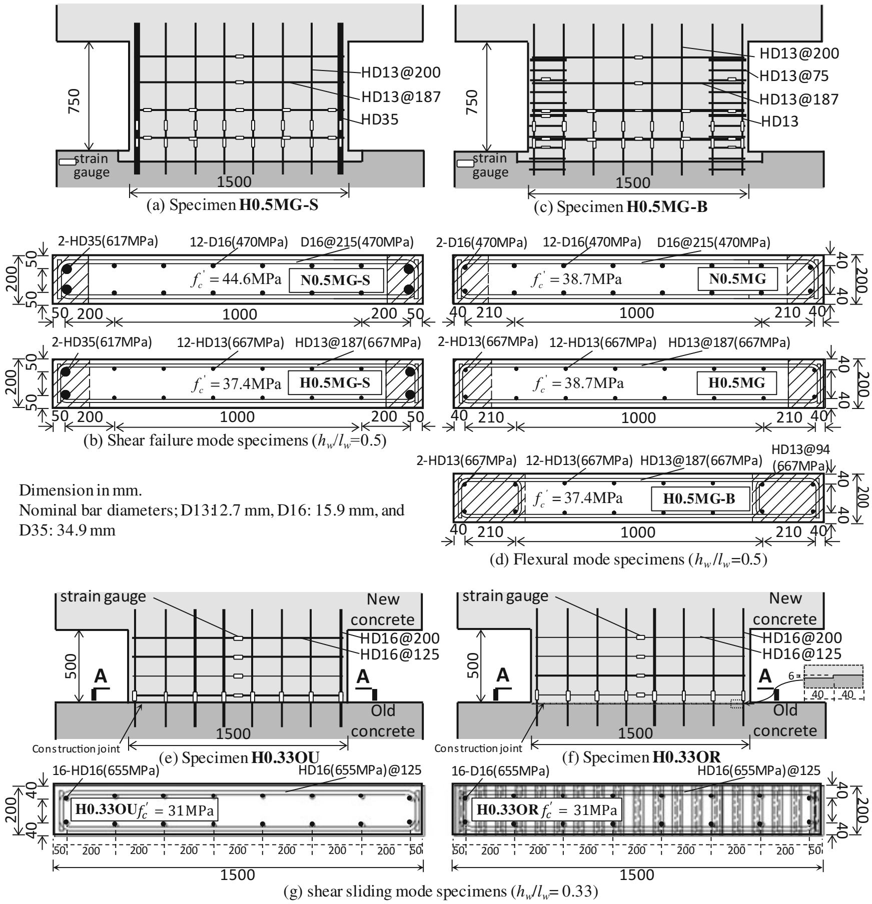

Fig. 5.1 Dimensions and reinforcement details of test specimens

Table 5.1 Design parameters of test specimens

Specimens	Wall aspect ratio h_w/l_w $[M/Vl_w]$	f_c' MPa	Horizontal rebar		Vertical rebar				μ_{aci}	Other details	V_n	V_{nmax}	V_{sf}	V_f
					Web		boundary							
			f_{yh} MPa	ρ_h (%)	f_{yv} MPa	ρ_v (%)	f_{ybe} MPa	ρ_{be} (%)						
N0.5 MG-S	0.5 [0.66]	44.6	470	0.93	470	0.92	617	9.57	1.4		1318	1330	6547	2941
H0.5 MG-S		37.4	667	0.68	667	0.58	617	9.57	1.4		1331	1218	5627	2740
N0.5 MG		38.7	470	0.93	470	0.92	470	1.99	1.4		1299	1239	3120	1432
H0.5 MG		38.7	667	0.68	667	0.58	667	1.27	1.4		1336	1239	2922	1323
HF0.5 MG-B		37.4	667	0.68	667	0.58	667	1.27	1.4	ρ_s = 3.17%	1331	1218	2866	1295
H0.5MU		42.1	667	0.68	667	1.01	–	–	0.6		1346	1292	1217	1319
H0.33MU	0.33 [0.50]	42.1	667	0.71	667	0.76	–	–	0.6		1334	1292	913	1403
N0.33MU		44.5	470	1.01	470	1.06	–	–	0.6		1513	1329	896	1438
H0.33MR		44.0	667	0.71	667	0.76	–	–	1.0		1340	1321	1521	1413
H0.33OU		31.0	655	1.59	655	1.06	–	–	0.6		2725	1109	1249	1754
H0.33MR2		31.0	655	1.59	655	0.66	–	–	1.0		2725	1109	1301	1212
H0.33OR		31.0	655	1.59	655	1.06	–	–	1.0		2725	1109	2081	1754
N0.33MR		31.0	466	1.59	466	1.06	–	–	1.0		2004	1109	1481	1353
H0.33OG		31.0	655	1.59	655	1.06	–	–	1.4		2725	1109	2914	1754
H0.33OU-LD		50.0	655	1.59	670	2.06	–	–	0.6	d_v = D22	2786	1409	2490	3346
H0.33OU-F		50.0	655	1.59	655	1.51	–	–	0.6	Flange Section(s)	2786	1409	2498	4299
H0.33OU-AF		50.0	655	1.59	655	1.13	–	–	0.6		2786	1409	1873	2443

Notes f_c' = compressive strength of concrete, μ = shear-friction coefficient defined in ACI 349, V_n = shear strength prediction, V_{nmax} = maximum permissible shear strength, V_{sf} = shear-friction strength prediction, V_f = flexural strength prediction by ACI 349, ρ_s = bar ratio of hoops in boundary element, d_v = diameter of vertical bar

Figure 5.1 shows the dimensions and details of the specimens with $h_w/l_w = 0.5$ and 0.33. The failure mode was controlled by the flexural rebar ratio in the wall boundary zones and the surface conditions of construction joint at the wall–foundation interface. In the shear failure mode specimens **N0.5MG-S** and **H0.5MG-S** (Fig. 5.1a and b), greater flexural rebar ratios were used to investigate the shear strength before flexural yielding. On the other hand, in the flexural mode specimens **N0.5MG** and **H0.5MG**, smaller flexural rebar ratios were used to investigate the effect of Grade 550 MPa shear rebars on the degradation of shear strength after flexural yielding (Fig. 5.1c and d). In the flexural mode specimens, the flexural design and shear design were performed under an identical magnitude of lateral load. In both shear failure and flexural yielding mode specimens, a groove joint was intentionally used to prevent early shear sliding before shear failure or flexural yielding. In the shear sliding mode specimens, on the other hand, flat-treated or roughened surfaces were used to induce shear sliding mode prior to shear failure or flexural yielding (Fig. 5.1e, f, and g). More details on the specimens can be found in previous literatures (Baek et al., 2017a, b, 2018).

5.2.3 *Test Procedure and Instrumentation*

The lateral loading protocol in Fig. 5.3 was used following ACI 374 (ACI Committee 374, 2013). Figure 5.2 shows the LVDTs for the measurement of lateral displacements, flexural deformations, shear deformations, and sliding at the wall base. Figure 5.1 shows the strain gauges for the reinforcing bars. An axial compressive load and a cyclic lateral load were applied using the test setup in Fig. 5.2a. The axial compressive load of $0.07A_c f_c'$ was applied to the top of the wall. The level of the axial compressive force was maintained during cyclic lateral loading, by manually controlling the vertical displacement. For shear sliding mode specimens, however, axial load are not applied to induce shear sliding mode.

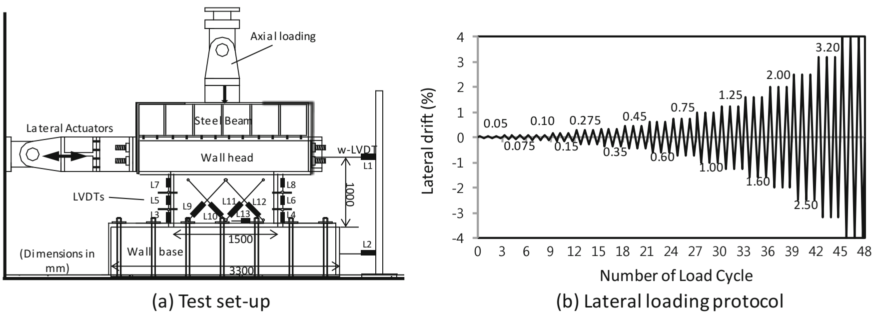

Fig. 5.2 Test setup and lateral loading protocol

5.3 Test Results

5.3.1 Failure Modes

Figure 5.3a, b, and c shows the failure modes of shear failure mode, flexural yielding mode, and shear sliding mode specimens, respectively, at the end of the tests. Table 5.2 presents the failure modes.

Shear failure mode specimens **N0.5MG-S** and **H0.5MG-S** (Fig. 5.3a) failed due to a mixed mode of diagonal tension cracking and diagonal web crushing (**DT** + **WC**), regardless of the bar grade.

Shear sliding mode specimens **H0.33MU** and **N0.33MU** failed due to shear sliding at wall–foundation interface (**SF**), regardless of the bar grade (Fig. 5.3c). The results indicate that the use of higher yield strength rebars (Grade 550 or 600 MPa rebars) did not affect the failure mode.

Flexural mode specimens **N0.5MG** and **H0.5MG** (Fig. 5.3b) with the maximum shear strength $V_{n,\max}$ failed after yielding due to web crushing and compression zone crushing at the lower part of the wall ends (**WC** + **CC**), regardless of the bar grade. Despite the small aspect ratio of the test specimens, sliding failure did not occur due to the groove joint at the wall–foundation interface (Figs. 5.1a and c).

5.3.2 Load–Displacement Relationships

Figures 5.4a, b, and c shows the lateral load–displacement (lateral drift ratio) relationships of the shear failure mode, flexural yielding mode, shear sliding failure

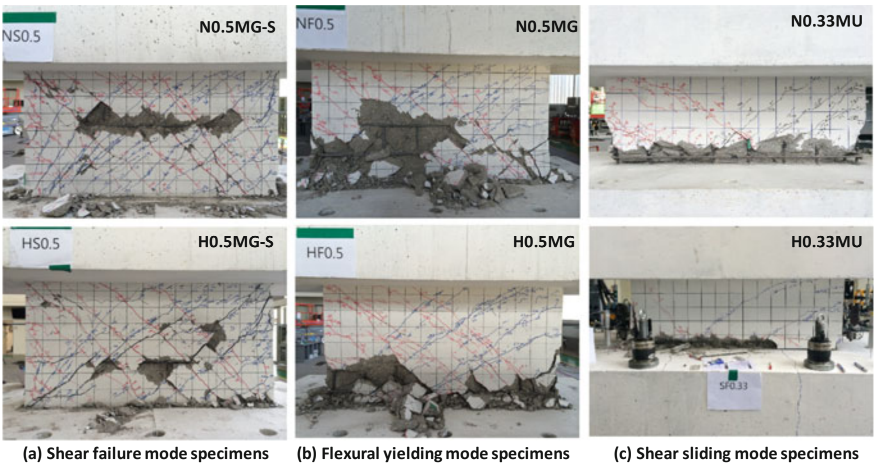

Fig. 5.3 Failure modes of test specimens at the end of tests

Table 5.2 Summary of test results

Specimens	Test results		Ratio of test strengths to predictions			
			Flexure	Diagonal tension	Web crushing	Shear sliding
	$V_{test,s}$ kN	Actual failure mode	$V_{test,s}/V_f$	$V_{test,s}/V_n$	$V_{test,s}/V_{nmax}$	$V_{test,s}/V_{sf}$
N0.5M-S	2492	WC + DT	–	1.89	1.87	–
H0.5M-S	2351	WC + DT	–	1.77	1.93	–
N0.5M	1416	FY	0.99	–	–	–
H0.5M	1368	FY	1.03	–	–	–
H0.5M-B	1382	FY	1.07	–	–	–
H0.5MU	744	SF	–	–	–	0.61
H0.33MU	575	SF	–	–	–	0.63
N0.33MU	969	SF	–	–	–	1.08
H0.33MR	1132	SF	–	–	–	0.74
H0.33OU	1201	SF	–	–	–	0.96
H0.33MR2	1065	SF	–	–	–	0.82
H0.33OR	1487	WC	–	–	1.34	–
N0.33MR	1042	SF	–	–	–	0.70
H0.33OG	1489	WC	–	–	1.34	–
H0.33OU-LD	2078	SF	–	–	–	0.83
H0.33OU-F	2408	DTF + SF	–	–	–	0.96
H0.33OU-AF	1656	DTF + SF	–	–	–	0.88
		Average C.O.V	1.030	1.829	1.622	0.823
			0.031	0.034	0.173	0.177

Notes $V_{test,s}$ = the smaller values of the measured maximum loads in the positive and negative loading directions. WC is the web crushing failure, DT is diagonal tension failure, FY is flexural yielding mode, SF is sliding failure at wall–foundation interface, and DTF is diagonal tension failure at flange wall

mode specimens, respectively. The lateral displacement indicates the net displacement, excluding sliding of the wall base (see L1 and L2 in Fig. 5.2a). For comparison, Fig. 5.4 also shows the shear strength V_n, flexural strength V_f, and shear-friction strength predicted by ACI 349 (or ACI 318) without limitation of f_{yv} ($\leq$420 MPa).

In the shear failure mode specimen **N0.5MG-S** (Fig. 5.4a) with h_w/l_w= 0.5 and Grade 420 MPa (f_{yh} = 470 MPa, ρ_h = 0.93%, ρ_v = 0.92%, and $\rho_h f_{yh}$ = 4.36 MPa), the maximum strength was +2571 and –2492 kN at the drift ratios of 1.35% and –1.2%, respectively. In **H0.5MG-S** (Fig. 5.4b) with Grade 550 MPa rebars (f_{yh}= 667 MPa, ρ_h = 0.68%, ρ_v = 0.58%, and $\rho_h f_{yh}$ = 4.51 MPa), the maximum strength was +2504 and –2350 kN, which are close to the those of **N0.5MG-S**

In flexural mode specimen **N0.5MG** (Fig. 5.4c) with Grade 420 MPa rebars, the peak strengths were V_{test} = + 1415 and –1446 kN, which was close to the predicted

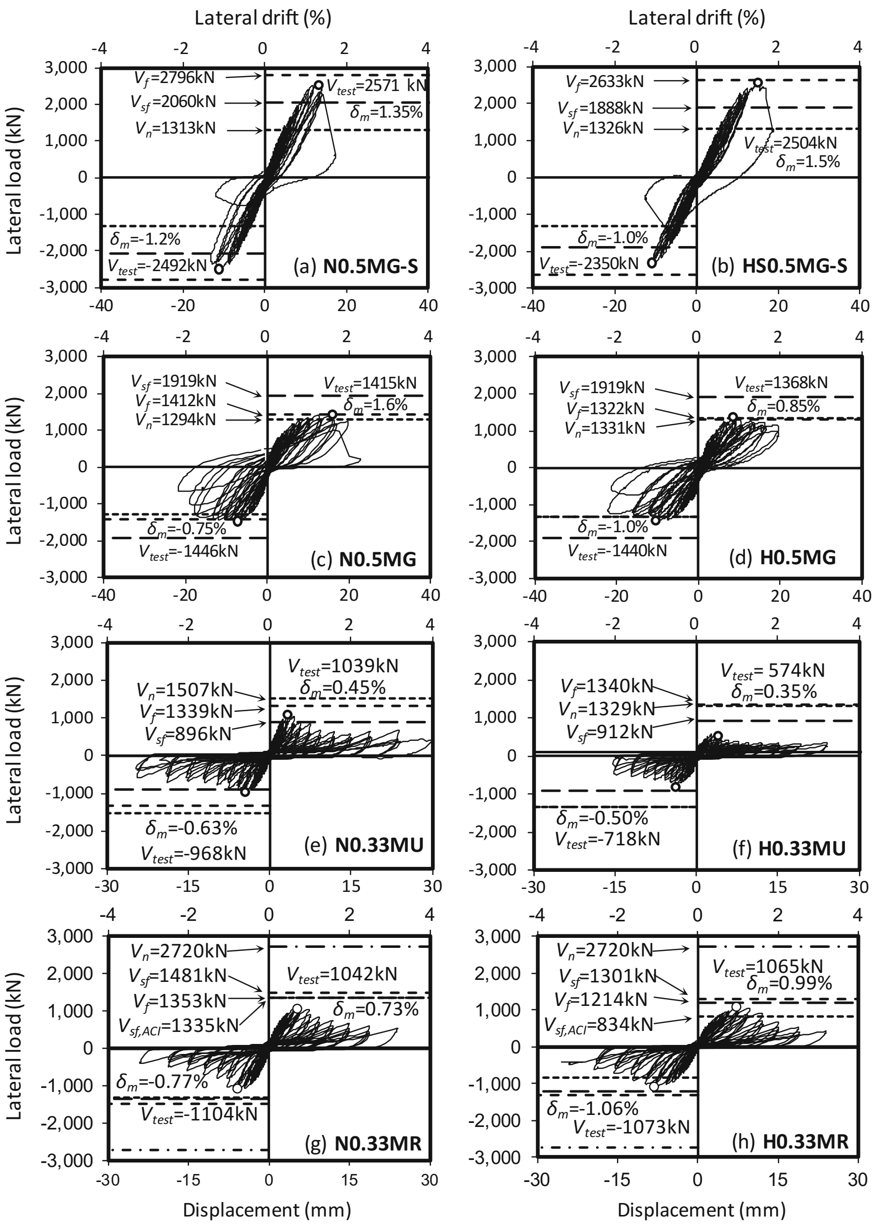

Fig. 5.4 Lateral load–drift relationships of test specimens

flexural strength V_f = 1412 kN. The load–displacement relationship of **H0.5MG** (Fig. 5.4d) with Grade 550 MPa rebars was similar to that of **N0.5MG** with Grade 420 MPa rebars.

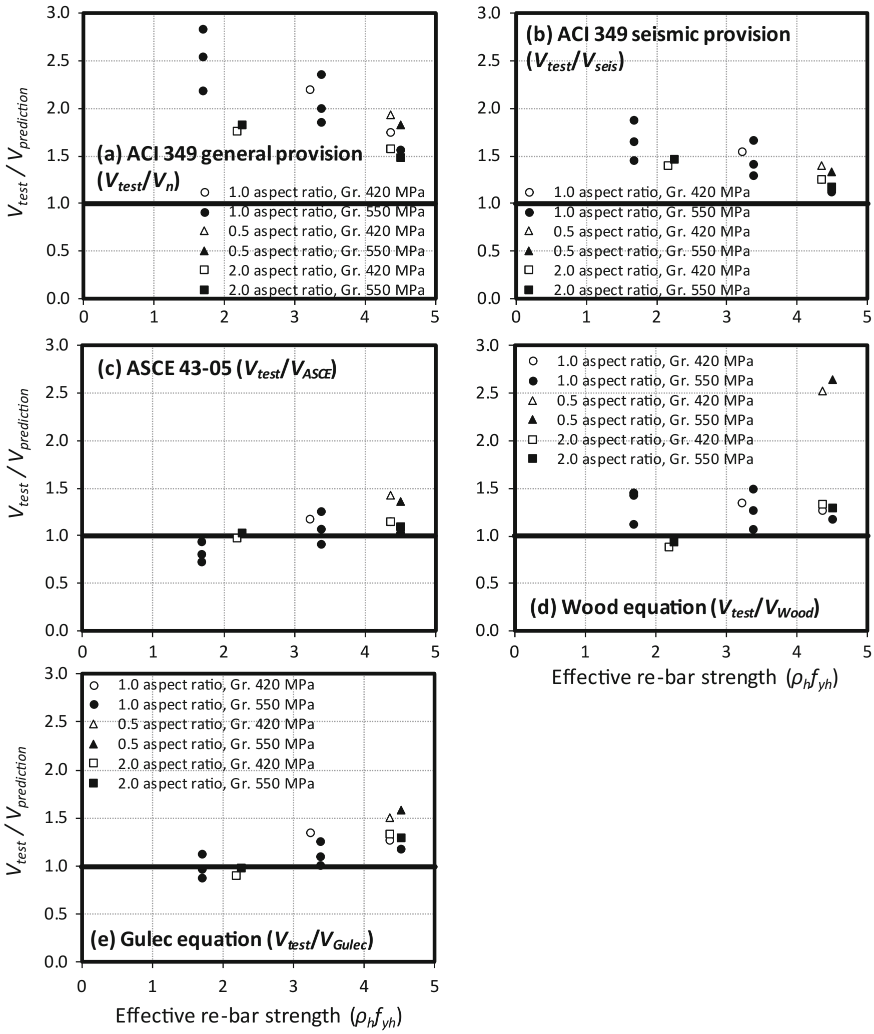

Fig. 5.5 Comparison of test shear strengths and predictions for shear failure mode specimens

In shear sliding mode specimen **N0.33MU** (Fig. 5.4e) with Grade 420 MPa rebars (f_{yh} = 510 MPa, ρ_h = 1.01%, f_{yv} = 470 MPa, ρ_v = 1.06%) and flat-treated surface (μ = 0.6), the maximum tested strength reached the nominal shear-friction strength V_{sf}: +1039 and –968 kN at the drift ratios of +0.45 and –0.60%, respectively. After the peak load, as the lateral drift increased, the load-carrying capacity gradually decreased. In shear sliding mode specimen **H0.5MU** (Fig. 5.4f) with Grade 550 MPa rebars (f_{yh} and f_{yv} = 667 MPa, ρ_h= 0.68%, ρ_v = 1.01%), unlike the walls with Grade 420 MPa rebars, the maximum tested strength V_{test} was +744 and –831 kN in the positive and negative loading directions, respectively, which was only 65% of the nominal shear-friction strength predicted by ACI 349 (or ACI 318) equation: The nominal shear-friction strength significantly overestimated the tested strength when the yield strength of 550 MPa was used in the calculation.

On the other hand, in **N0.33MR** with Grade 400 MPa D16 bars (f_{yh} and f_{yv} = 466 MPa, ρ_h = 1.59%, ρ_v = 1.06%, $\rho_v f_{yv}$ = 4.93 MPa) and roughened surface treatment (Fig. 5.1e), despite the improved roughness, the maximum tested strength did not significantly increase and did not reach the nominal shear-friction strength V_{sf} unlike **N0.33MU** with flat-treated surface: +1042 and –1104 kN; V_{test}/V_{sf} = 0.70-0.75 (Fig. 5.4g). The comparison between the **N0.33MU** and **N0.33MR** indicates that roughening the surface did not significantly increase the shear-friction strength for Grade 420 MPa shear-friction rebars.

Specimens **H0.33MR**, which had a smaller rebar ratio and greater yield strength of vertical rebars (ρ_v = 0.66%, f_{yv} = 655 MPa, $\rho_v f_{yv}$= 4.32 MPa), showed a greater ratio of V_{test}/V_{sf} (= 0.82) when compared to **N0.33MR** (Fig. 5.5e). This result indicates that for roughened surface, high-strength rebars are more effective. However, in both walls with Grade 600 MPa and Grade 400 MPa, the tested maximum strength did not reach V_{sf}, which indicates that for both Grade 400 MPa and 600 MPa shear-friction reinforcement, ACI 349 equation overestimated the shear-friction strength of roughened surface.

In the test results of **H0.33OU-F**, the flange walls significantly contributed to the shear sliding resistance. In particular, the test result of **H0.33OU-AF** showed that the vertical rebars in the tension flange wall provided additional shear sliding capacity more than those in the compression flange wall. Further studies on various flange lengths are required to investigate the effective area of flange section for shear sliding resistance.

5.4 Evaluation of Shear Strength and Shear-Friction Strength

5.4.1 Shear Strength

Figure 5.5 shows the safety margins (i.e., the strength ratio) of the test specimens predicted by the ACI 349 (ACI 318) general and seismic provisions. The test results of the existing walls with h_w/l_w = 1.0 and 2.0, which were reported in the previous study, (Baek et al., 2017a, b; Park et al., 2015) were included in the figure. In the predictions of ACI 349 (ACI 318) [general and seismic provisions], the strength ratio decreased as $\rho_h f_{yh}$ increased (Figs. 5.5a and b). This is because ACI 349 does not include the shear contribution of vertical web rebars in the strength predictions [In the specimens, the ratio of vertical rebars increased with the ratio of horizontal rebars.]. Nevertheless, the strength ratios of the specimens with the maximum shear reinforcement ratio were greater than 1.0, for both Grade 420 and 550 MPa shear rebars. On the other hand, the predictions by ASCE 43-05, and Gulec and

Whittaker (V_{test}/V_{ASCE} and V_{test}/V_{Gulec}) slightly increased as $\rho_h f_{yh}$ increased, and showed better predictions than the other predictions, regardless of h_w/l_w and $\rho_h f_{yh}$. The methods address the shear contribution of vertical rebars varying with wall aspect ratios (Figs. 5.5c and e). In the case of the predictions by the ACI 349 general provision and Wood, the safety margin of the walls with $h_w/l_w = 0.5$ was greater than that of the other methods (Figs. 5.5a and d) because the methods do not address the effect of aspect ratio h_w/l_w.

In the previous study, it was also reported that the contribution of shear deformation to overall lateral deformation was similar regardless of the rebar grade. The shear deformation was affected by the aspect ratio h_w/l_w, effective rebar strength $\rho_h f_{yh}$, and failure mode, rather than the rebar grade f_{yh}. In the case of walls with Grade 420 or 550 MPa rebars, the number of diagonal shear cracks was not directly related to the rebar grade. The average diagonal crack width was related to the effective shear reinforcement strength $\rho_h f_{yh}$ rather than the rebar grade when the spacings of the shear reinforcement were the same. All the evidences indicate that the safety margin of specimens with 550 MPa reinforcement is similar to that of specimens with 420 MPa reinforcement.

5.4.2 Web Crushing Strength

Figure 5.6a shows the tested stress $v_{test,s}$ ($= V_{test,s}/A_c$)–compressive strength of concrete f_c' relationships of the specimens with web crushing failure modes and the permissible maximum strength (i.e., web crushing strength prediction) v_{nmax} ($= V_{nmax}/A_c = 0.66\sqrt{f_c'}$). As f_c' increases, web crushing strength significantly increased and the strength ratio $V_{test,s}/V_{nmax}$ also increased. This result indicates that the web crushing capacity of the squat walls was greater than the permissible maximum strength in the ACI code, particularly for high-strength concrete.

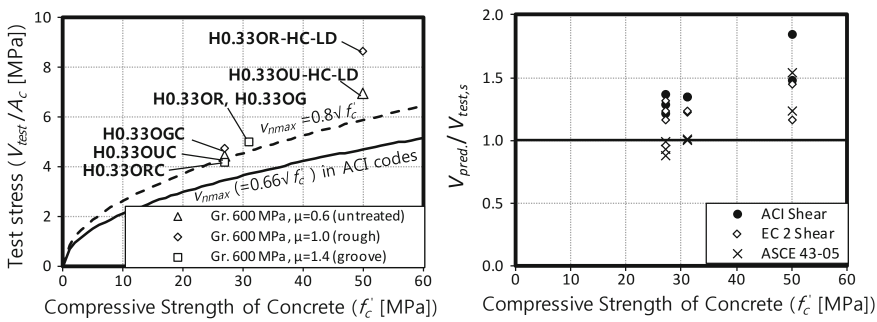

(a) Test stress of specimens with WC (b) Strength ratios of specimens with WC

Fig. 5.6 Comparison of test web crushing strengths and predictions of current design code

Figure 5.6b shows the ratios of the maximum tested strengths to the shear strength predictions of ACI 349 (ACI Committee 349, 2013), Eurocode 2 (British Standards Institution, 2004), and ASCE 43-05 (Nuclear Standards Committee, 2005) with compressive strength of concrete f_c', respectively. In all the predictions, the predicted shear strengths were determined by the permissible maximum shear strength (i.e., web crushing strength) due to the large rebar ratios. Nevertheless, the strength ratios tend to increase as f_c' increases. This result indicates that the web crushing capacity of heavily reinforced squat walls can be further increased by using higher concrete strength: $V_{test,s}/V_{nmax}$ = 1.20 to 1.84. The web crushing strength of squat shear walls can be increased at least 20%: $V_{nmax} = 1.0\sqrt{f_c'}hd$. On the other hand, the strength ratio predicted by ASCE equation (or Barda et al., 1977) was less conservative but more accurate than that of ACI 349 ($V_{test,s}/V_{ASCE}$ = 0.87–1.53).

5.4.3 *Shear-Friction Strength*

Figure 5.7 shows the relationship between the test strengths $V_{test,s}$ and the area of overall vertical bars A_{vall}. The specimens with shear sliding mode, which were reported in the previous study (Baek et al., 2018), were included in the figure. The test strengths $V_{test,s}$ were generally proportional to the reinforcement ratio (or area of overall vertical bars A_{vall}).

The effect of surface treatment varied according to the bar grade. In the specimens with Grade 550 MPa (f_{yv} = 667 MPa, ρ_v = 0.76%), as the roughness increased from flat-treated to roughened surfaces, the test strength $V_{test,s}$ was significantly increased: approximately 85% [= (1132 kN-575 kN)/(575 kN)]. On the other hand, in the specimens with Grade 420 MPa (f_{yv} = 466-470 MPa, ρ_v = 1.06%), the test strength was increased only 7% [= (1042kN-969kN)/(969kN)], even though the roughness increased from flat-treated to roughened.

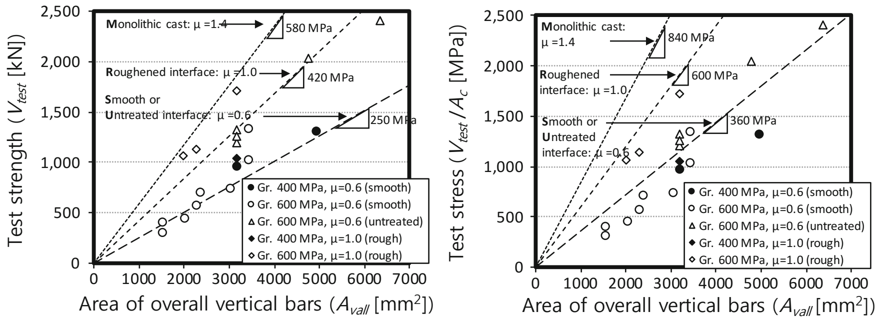

(a) Limitation of f_{yv} = 420MPa (b) Limitation of f_{yv} = 600MPa

Fig. 5.7 Comparison of test shear-friction strength and predictions

The slope lines in Figs. 5.7a and b represent the shear-friction strength predictions by ACI 349 with and without limitation of f_{yv} ($\leq$ 420 MPa), respectively. The three slope lines represent various wall–foundation interface conditions: μ = 0.6, 1.0, and 1.4 for untreated, roughened, and monolithic surfaces, respectively.

In Fig. 5.7a with limitation of f_{yv}, the test strengths of walls with flat-treated surface (● and ○) reached the nominal ACI shear-friction strength, whereas those of untreated surface (△) were underestimated by the prediction. In the case of the specimens with roughened surface, the tested strengths using Grade 400 and Grade 600 MPa (♦ and ◇) were underestimated and overestimated, respectively (Fig. 5.7a). On the other hand, in Fig. 5.7b without the limitation of f_{yv}, the test strengths of walls with untreated surface (△) reached the nominal ACI shear-friction strength, whereas those of flat-treated surface (○) and roughened surface (◇) were less than the predictions.

5.5 Conclusion

To investigate the validity of Grade 550 MPa (or higher) rebars for shear and shear-friction reinforcement of low-rise walls, 17 wall specimens (6 specimens with h_w/l_w = 0.5 and 11 specimens with h_w/l_w = 0.33) were tested under cyclic lateral loading. The test results of the walls with Grade 550 MPa (or 600 MPa) rebars were directly compared with those of walls with Grade 420 MPa (or 400 MPa) rebars.

The major findings of the present study are summarized as follows:

1. The use of Grade 550 MPa rebars in low-rise RC walls did not change the failure modes when compared to that of Grade 420 MPa rebars.
2. In the shear failure mode specimens with Grade 550 MPa rebars, the test shear strengths V_{test} were greater than the predictions of the ACI 349 (ACI 318) general and seismic provisions. The safety margins of the specimens with Grade 550 MPa shear reinforcement were slightly less than those with Grade 420 MPa web rebars.
3. The test results of walls with 550 MPa rebars were comparable to those of walls with 420 MPa rebars in terms of failure mode, safety margin, and average crack width. This test result indicates that Grade 550 MPa shear reinforcement is applicable to shear provision of walls in ACI 349.
4. For heavily reinforced squat wall specimens that failed due to web crushing, the web crushing strength was underestimated by the maximum shear strength in ACI 349: V_{test}/V_{nmax} = 1.20-1.84. Particularly for high compressive strength of concrete, the web crushing capacity was significantly greater than the ACI 349 predictions. This result indicates that for squat walls, the web crushing strength in ACI code can be increased at least 20%: $V_{nmax} = 1.0\sqrt{f_c'}hd$.
5. For the specimens that failed due to shear sliding, the shear-friction strength tends to be increased by using high-strength rebars. However, surface treatment

and other parameters also affected the shear sliding capacity as well as the bar grade. Therefore, at the current stage, it is desirable to limit the bar grade to 420 MPa for the shear-friction design in ACI 349.

6. The use of groove joint significantly increased shear-friction strength, thereby preventing shear sliding.
7. The flange walls significantly contributed to the shear sliding resistance, which is not considered in current design code. In particular, the vertical rebars in tension flange provides shear sliding resistance. When the effect of flange walls is considered, the vertical rebars for shear-friction demand can be significantly reduced in nonplanar walls with flanges.

References

ACI Committee 349. (2013). Code requirements for nuclear safety-related concrete structures (ACI 349-13) and commentary. Farmington Hills, MI: American Concrete Institute, pp. 196.

ACI Committee 374. (2013). *Guide for testing reinforced concrete structural elements under slowly applied simulated seismic loads* (pp. 18). Farmington Hills, MI: American Concrete Institute.

ACI Committee 318. (2014). Building code requirements for structural concrete (ACI 318-14) and commentary. Farmington Hills, MI: American Concrete Institute, pp. 520.

Baek, J.-W., Park, H.-G., Lee, J.-H., & Bang, C.-J. (2017a). Cyclic loading test for walls of aspect ratio 1.0 and 0.5 with grade 550 MPa (80 ksi) shear reinforcing bars. *ACI Structural Journal, 114*(4), 969.

Baek, J. W., Park, H. G., Shin, H. M., & Yim, S. J. (2017b). Cyclic loading test for reinforced concrete walls (Aspect Ratio 2.0) with grade 550 MPa (80 ksi) shear reinforcing bars. *ACI Structural Journal, 114*(3), 673.

Baek, J.-W., Park, H.-G., Lee, B.-S., & Shin, H.-M. (2018). Shear-friction strength of low-rise walls with 550 MPa (80 ksi) reinforcing bars under cyclic loading. *ACI Structural Journal, 115*(1), 65–78.

Barda, F., Hanson, J. M., & Corley, W. G. (1977). Shear strength of low-rise walls with boundary elements. *ACI Journal: Special Publication*, *53*, 149–202.

Birkeland, P. W., & Birkeland, H. W. (1966). *Connections in precast concrete construction.* Paper presented at the ACI Journal Proceedings.

British Standards Institution. (2003). Eurocode 8: Design of structures for earthquake resistance: Part 1: General rules, seismic action and rules for buildings (pp. 229). Bruxelles: CEN: European Committee for Standardization.

British Standards Institution. (2004). Eurocode 2: Design of concrete structures-Part 1-1: General rules and rules for building (pp. 225). Bruxelles, Belgium: European Standard EN-1992-1-1:2004:E, European Committee for Standardization.

Canadian Standards Association. (2004). *Design of concrete structures* (p. 214). Rexdale, Ontario, Canada: Canadian Standards Association.

Japan Society of Civil Engineers. (2010). *Standard specifications for concrete structures-2007: Design* (p. 469). Tokyo, Japan: Japan Society of Civil Engineers.

Nuclear Standards Committee. (2005). *Seismic design criteria for structures, systems, and components in nuclear facilities* (p. 81). Reston, VA: American Society of Civil Engineers.

Park, H. G., Baek, J. W., Lee, J. H., & Shin, H. M. (2015). Cyclic loading tests for shear strength of low-rise reinforced concrete walls with grade 550 MPa bars. *ACI Structural Journal, 112*(3), 299–310.

Chapter 6
Research on Resilient Reinforced Concrete Building Structural System

Susumu Kono, Ryo Kuwabara, Fuhito Kitamura, Eko Yuniarsyah, Hidekazu Watanabe, Tomohisa Mukai and David Mukai

Two real scale five-storey reinforced concrete frame buildings were tested in BRI in order to evaluate damage of reinforced concrete structural members such as beams, columns, and walls for strength-based design buildings. A series of experimental works show that secondary RC walls could have improved seismic performance for damage reduction by changing configuration and rebar arrangement. This strength enhancement with ductile detailing is one of the easiest and most economical solutions to reduce seismic damage. The paper describes current research efforts on resilient reinforced concrete structures in Japan focusing on complete residual flexural crack profile simulation (crack spacing, width, and length). The paper introduces numerical procedures using FEM analysis introduces and compares the computed results to the real scale experimental results. The information will be helpful to evaluate cost of repair after earthquake damage

S. Kono (✉) · R. Kuwabara · F. Kitamura · E. Yuniarsyah
Institute of Innovative Research, Tokyo Institue of Technology, Tokyo, Japan
e-mail: kono.s.ae@m.titech.ac.jp

R. Kuwabara
e-mail: kuwabara.r.aa@m.titech.ac.jp

F. Kitamura
e-mail: kitamura.fht-0917@hotmail.co.jp

E. Yuniarsyah
e-mail: eko.yuniarsyah@gmail.com

H. Watanabe · T. Mukai
Building Research Institute, Tsukuba, Japan
e-mail: wata_h@kenken.go.jp

T. Mukai
e-mail: wata_h@kenken.go.jp; t_mukai@kenken.go.jp

D. Mukai
University of Wyoming, Laramie, WY, USA
e-mail: dmukai@uwyo.edu

T. T. C. Hsu (ed.), *Concrete Structures in Earthquake*,
https://doi.org/10.1007/978-981-13-3278-4_6

This script is a reformatted copy of the paper in the 16th European Conference on Earthquake Engineering, Thessaloniki, Greek, June 18–21, 2018.

6.1 Introduction

Damage to nonstructural (or secondary) members are as important as that to structural members from the viewpoint of continuous post-earthquake functionality. Resilience of building structures specifically means low or no damage of structural and nonstructural (or secondary) members and quick recovery of functions of buildings. In order to achieve resilient building structures, it is important to develop low damage structural systems in a broader sense and propose design procedures to advance the idea.

Engineers in National Institute for Land and Infrastructure Management (NILIM) and Building Research Institute (BRI) designed and tested real scale five-storey reinforced concrete buildings to see the seismic performance of strength-based building system. Three universities and seven companies joined the experimental works at BRI to closely observe damage at different loading stages. The building introduced in this paper was tested in 2014 (Kabeyasawa et al. 2016, 2017). The designed concrete frame building had higher load carrying capacity by adding wing walls to columns, or standing or/and hanging walls to beams. It was supposed to possess load carrying capacity equivalent to C_0= 0.45–0.55 (C_0: base shear coefficient) at mechanism formation with maximum interstory drift as small as 0.4–0.8%. This implies that the building would have an elastic or nearly elastic response even under large-scale earthquakes. Limited deformation would result in dramatic damage reduction in columns, beams, and beam–column connections. This paper discusses features of cracks from a numerical viewpoint and introduces a crack simulation procedure by revising the former strain based concept (Kono et al. 2017).

6.2 Experimental Work

Figure 6.1 shows the configuration of a five-storey RC specimen and typical section size with reinforcement arrangement. It is noted that the building had structural slits (or gaps) between secondary walls as shown by thick blue lines in Fig. 6.1a. Cracks were traced and copied to transparencies and the maximum width for each crack was recorded (Fig. 6.2).

6.3 Simulation of Flexural Cracks

A procedure to evaluate residual cracks is introduced in Fig. 6.3. Based on numerical FEM analysis, it is aimed to obtain complete residual flexural crack profiles (crack spacing, width, and length). The flow has two branches in the midway; flow for

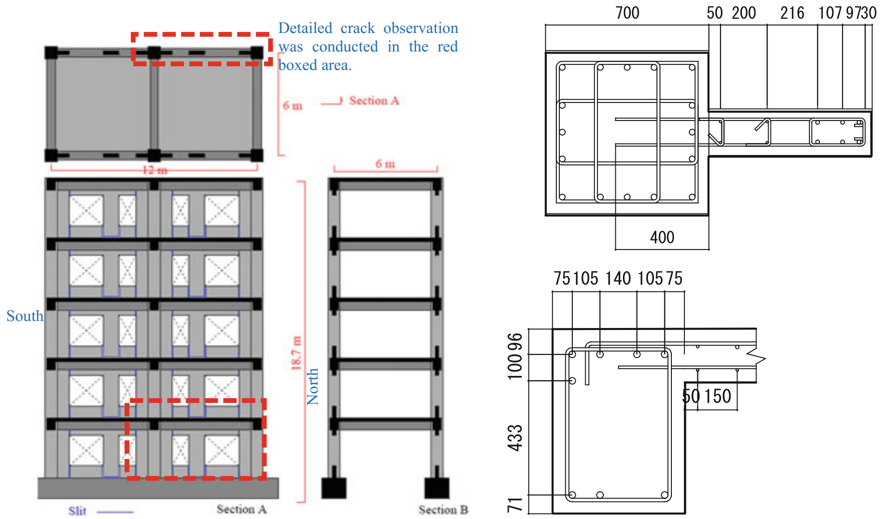

(a) Specimen configuration (b) Column with a wing wall and beam with one side slab

Fig. 6.1 Configuration of 2014 five-storey specimen and typical section size (Fukuyama et al. 2015)

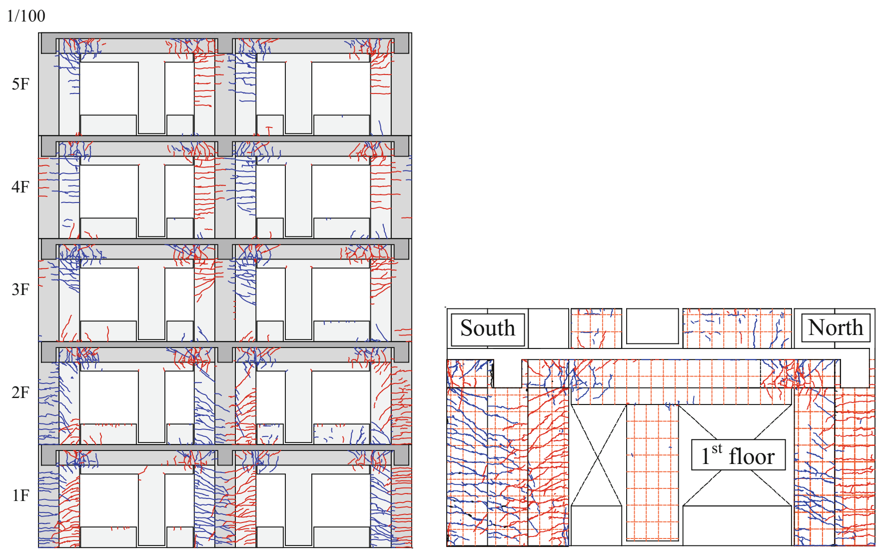

(a) Overall view (Kabeyasawa et al. 2016) (b) Area for detailed observation (Kitamura 2017)

Fig. 6.2 Recorded cracks and spalling at R = 1%

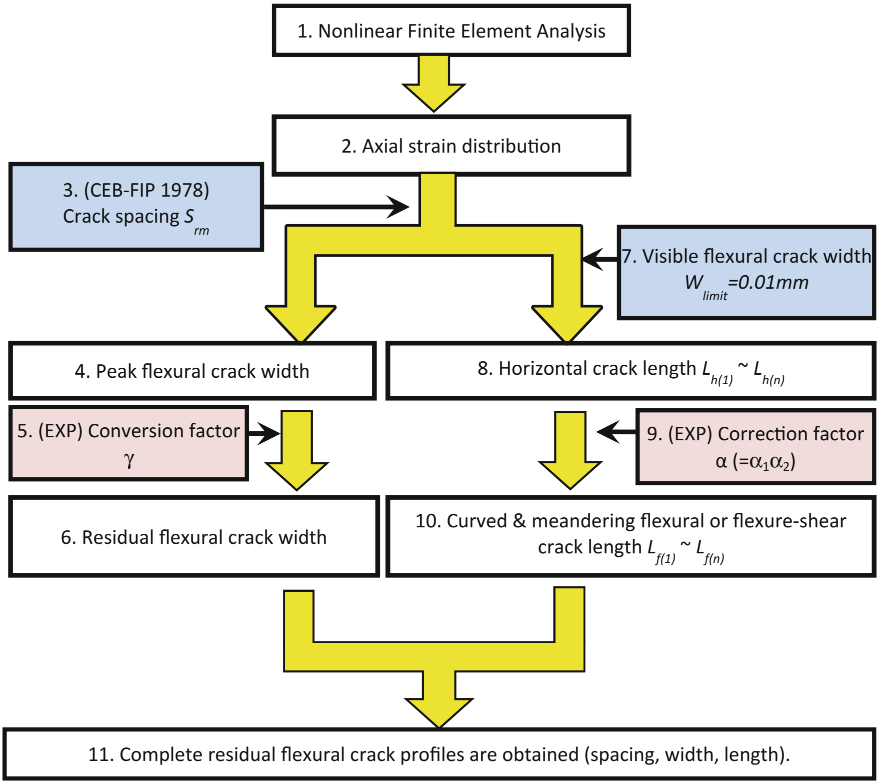

Fig. 6.3 Flow chart how to obtain complete residual flexural crack profiles

residual flexural crack width and flow for crack length. Blue boxes (#3 and #7) are predetermined values and red boxes (#5 and #9) are values obtained from a regression analysis. Crack spacing (#3) is determined based on CEB-FIP Model Code equation (1978) although it is not necessarily for seismic purposes. Residual flexural crack width (#6) is obtained from the peak flexural crack width (#4). Conversion from peak to residual values is conducted by multiplying factor, γ (#5), which is obtained from a regression analysis. Horizontal crack length, L_h, is counted (#8) when crack width is larger than visible flexural crack width $W_{\text{limit}} = 0.01$ mm (#7). Then actual diagonal and meandering crack length (#10), L_f, is obtained by multiplying correction factor (#9), α, which is also obtained from a regression analysis. From #3,#6, and #10, complete residual flexural crack profiles (spacing, width, and length) are obtained.

6.3.1 Numerical Analysis with an Fem Program

Figure 6.4 shows a 2D finite element mesh used in a commercial FEM program "FINAL" (ITOCHU 2016). Concrete was modeled as isoparametric quadrilateral

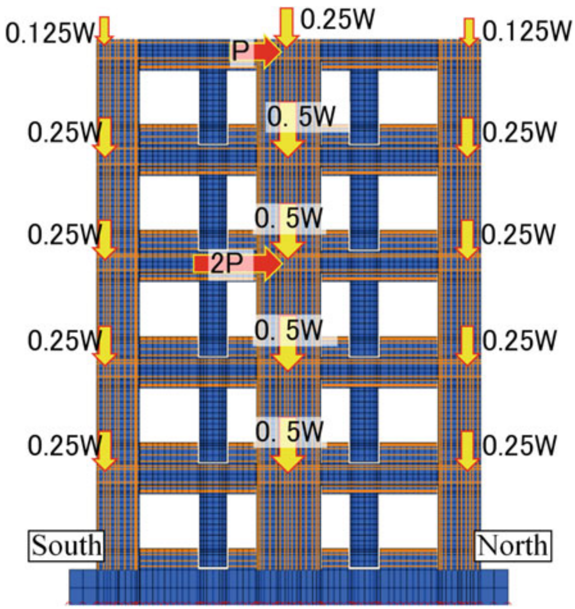

Fig. 6.4 Finite element mesh and loading condition in *2D* finite element analysis (Kitamura 2017)

elements with smeared reinforcement, and longitudinal reinforcement was modeled as beam–column elements. Perfect bond characteristics were assumed for all reinforcement. All degrees of freedom were fixed at nodes on the bottom face of the foundation beams. Self-weight was applied as concentrated load at beam–column connections based on a tributary area. Lateral load was applied at the central beam–column connections of roof and fourth floor by 1:2 ratio to simulate the load conditions in experiment. Load was controlled by the lateral displacement of the roof level and loading protocol followed the measured displacement although the second cycle was skipped to save computational time. The numerical simulation was carried out up to R = 1% since the resisting mechanism of building changed when structural slits (or gaps) closed at R = 1.3% in experiment. The elements employed default material models; modified Ahmad model (Naganuma 1995) and Izumo model (Izumo et al. 1987) were used for concrete and modified Menegotto-Pinto model (Ciampi et al. 1982) was used for reinforcement.

Figure 6.5a shows base shear force–roof level drift relation. The numerical simulation agrees well with the experimental results. Figure 6.5b shows the base shear force–member rotation of the north column (1F). The deformation of each member directly influences the simulation of crack performance. The simulated curve agreed relatively well with the experimental results in the positive side but did not agree very well in the negative side. The results for the beam (2F) and wing wall (1F) had similar trend although their plots are not shown.

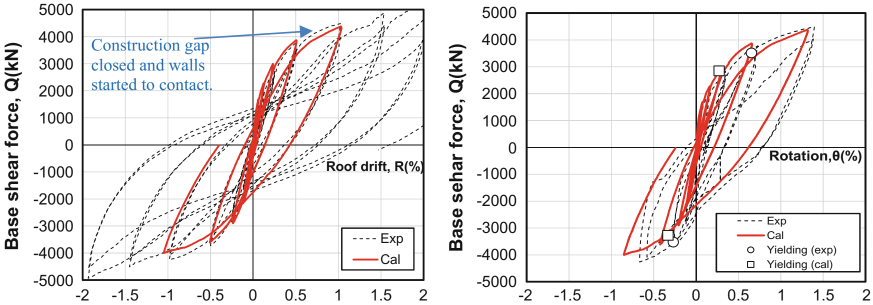

(a) Base shear force – roof leveldrift ratiorelation (b) Base shear – 1F north column rotation angle

Fig. 6.5 Typical results of finite element analysis (Kitamura 2017)

6.3.2 Numerical Simulation of Flexural Cracks

Most cracks were governed by flexure as can be seen in Fig. 6.2 and numerical simulation in this paper treated only flexural cracks. An effect of some flexural-shear cracks was considered with conversion index, α, which is explained later. Treatment of shear cracking is also important but will be discussed elsewhere. The first-floor column is used as an example to explain how to obtain spacing, width, and length of flexural cracks.

First, the left flow (#3, 4, 5, and 6) in Fig. 6.3 is explained step by step. Crack width, W_i, was computed based on Eq. (6.1). It was assumed that concrete does not deform and elongation of a member comes from crack openings. Hence, strain obtained from the finite element analysis represents the effects of smeared cracks. Based on this assumption, the flexural crack width of a member can be obtained by integrating longitudinal tensile strain (ε_{zz}) over a crack spacing (s_{rm}). The crack spacing is based on Eq. (6.2) proposed in CEB-FIP Model Code (CEB-FIP 1978). Equation (6.2) is based on the condition that the number of cracks reached saturated condition. The error of the equation was studied beforehand and turned out to be reasonably small after R = 0.25%.

$$W_i = \int_{h_i - S_{\mathrm{rm}}/2}^{h_i + S_{\mathrm{rm}}/2} \varepsilon_{zz} dz \tag{6.1}$$

$$s_{\mathrm{rm}} = 2\left(c_s + \frac{s_y}{10}\right) + k_1 k_2 \frac{d_{\mathrm{by}}}{p_y} \tag{6.2}$$

where W_i and h_i are crack width and height of the i-th crack, ε_{zz} is tensile strain in vertical (z) direction, s_{rm} is crack spacing. Other notations in Eq. (6.2) should be referred to the original document. Figure 6.6 shows accumulated crack width for the north column (1F) and the wing wall (1F). Crack widths were accumulated from the top to bottom. The accumulated crack width at the bottom is close to the

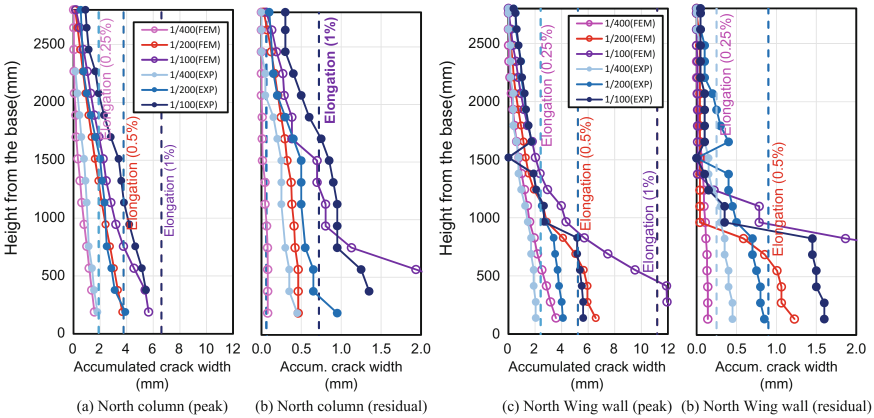

Fig. 6.6 Accumulated crack width distribution

elongation measured by displacement gages, and measured elongation of member is expressed by the vertical break lines in the figure. Figure 6.6a and c shows variations at the peaks and Fig. 6.6b and d shows those at the unloaded conditions. Each figure has comparisons between experimental and analytical results for three drift levels at R = 0.25%, 0.5%, and 1%. Residual crack width was obtained by multiplying reduction factor, γ, which was determined from regression analysis of test results for each type of member. Solid circles on the experimental curves show the location of actual cracks and those for analysis show simulated points with spacing, s_{rm}. Simulated variations for peak load agreed relatively well with experimental results for the column and wing wall. However, the agreement is not very good for residual crack width. If the total elongation of the tension fiber in analysis does not agree with experimental results, the simulation does not agree with the experimental results. Although the AIJ guidelines (AIJ 2004) assumes that residual crack width is half of the peak crack width regardless of axial load mainly to achieve simplicity and conservatism, this concept should be revised based on experimental results.

Second, the right flow (#7, 8, 9, and 10) in Fig. 6.3 is explained. Crack length was computed using analytical results of FEM as well. The crack is assumed visible when the crack width of the i-th crack exceeds the limit crack width, W_{limit}, which is a constant value and defined in Eq. (6.3). The projected crack length, $L_{h(i)}$,was computed based on the neutral axis depth, $x_{n(i)}$, and invisible crack length, $x_{\mathrm{limit}(i)}$, as shown in Eq. (6.4) and Fig. 6.7. In this paper, the crack opening profile is assumed triangular as shown in Fig. 7(d) and the computing process is based on the edge opening, W_i.

$$W_{\mathrm{limit}} = 0.01\ \mathrm{mm} \tag{6.3}$$

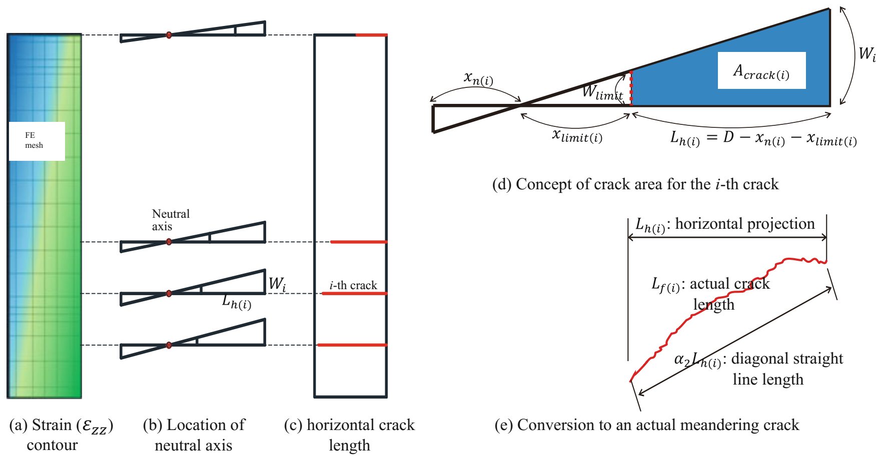

Fig. 6.7 Calculation of crack length in this study

$$L_{h(i)} = D - x_{n(i)} - x_{\text{limit}(i)} \tag{6.4}$$

$$L_{f(i)} = \alpha L_{h(i)} \tag{6.5}$$

$$\alpha = \alpha_1 \cdot \alpha_2 \tag{6.6}$$

$$\alpha_1 = average\left(\frac{L_{f(\text{exp})}}{L_{d(\text{exp})}}\right) \tag{6.7}$$

(from straight length to meandering length)

$$\alpha_2 = average\left(\frac{L_{d(\text{exp})}}{L_{h(\text{exp})}}\right) \tag{6.8}$$

(from horizontal projection to diagonal length)

Conversion index, α, was multiplied to obtain actual diagonal and meandering crack length, $L_{f(i)}$, to take into account the fact that cracks are not smooth nor horizontal. Index, α, was determined from the experimental results and the values were 1.15, 1.28, and 1.51 for the column, wing wall, and beam. Index α_1 and α_2 were computed using regression analysis of experimental data using Eqs. (6.7) and (6.8).

Since complete profiles of residual flexural crack profiles have been obtained (Crack spacing in #3, residual crack width in #6, and crack length in #10 in Fig. 6.3), they are validated with experimental data. Figure 6.8 shows crack area damage ratio, β_A, which is the ratio of all visible crack area summation, $\sum A_{\text{crack}(i)}$,

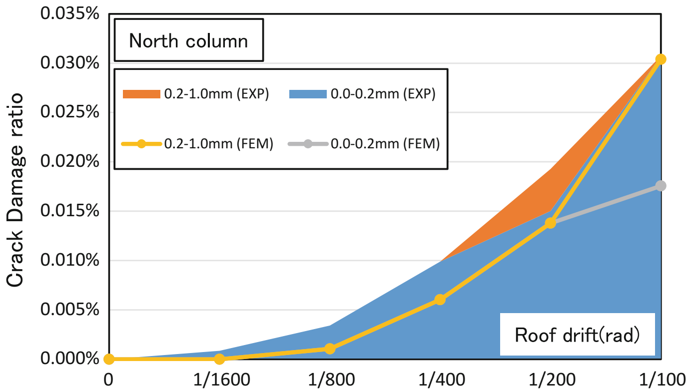

Fig. 6.8 Comparison of experimental and computational variations of crack area damage ratio (North column)

to the concrete surface area, A_{surface}. It is a no-dimensional quantity as expressed by Eq. (6.9). Crack area is defined in Fig. 7(d) as a blue trapezoid shape.

$$\beta_A = \frac{\sum A_{\text{crack}(i)}}{A_{\text{surface}}} = \frac{\sum \left\{0.5 \cdot W_i \cdot \left(D - x_{n(i)}\right) - 0.5 \cdot W_{\text{limit}} \cdot x_{\text{limit}(i)}\right\}}{A_{\text{surface}}} \tag{6.9}$$

where D is the total depth of a member. Based on the reference (JBDPA 2015), crack width is categorized into four classes of crack width ($0 \le w_{cr} \le 0.2$ mm, $0.2\text{ mm} \le w_{cr} \le 1$ mm, $1\text{ mm} \le w_{cr} \le 2$ mm $w_{\text{cr}} \ge 2$ mm), and β_A for each category is expressed as a stack graph in Fig. 6.8. Envelop curve is simulated relatively well for the column. Although it is not shown, the simulation is not very good for wall and beam because the crack width simulation did not work well.

6.4 Design Philosophy for Resiliency

Damage reduction may be achieved by strengthening the whole structure by properly providing reinforced concrete walls. Strength enhancement with ductile detailed walls may be an easy and economical solution. Another way of damage reduction is low damage structural systems such as self-centering rocking walls. Self-centering rocking wall is a ductile system which suffers very little structural damage since deformation of structures concentrates on interfaces between structural components. With these two extreme systems (strong system and ductile system), designers may choose a preferred low damage structural system among strong systems, ductile systems, or system in between to achieve much smaller damage level. All these systems are termed low damage system in a broader sense and play an important role to achieve resiliency. Design philosophy of

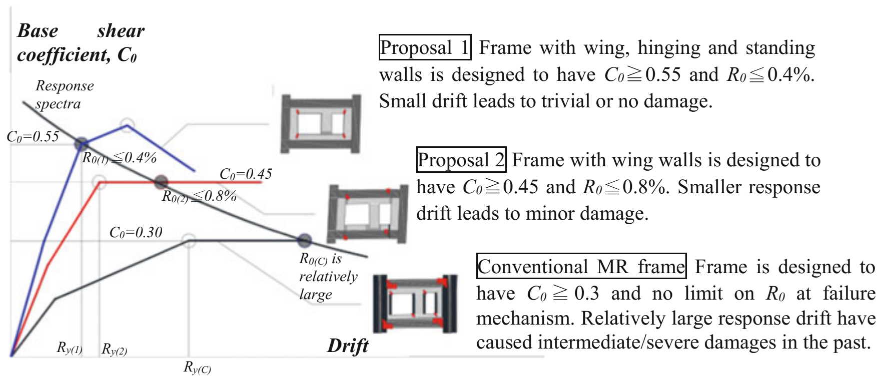

Fig. 6.9 Design philosophy of reinforced concrete buildings for less damage (Fukuyama et al. 2015)

strength-based concept and conventional ductile moment resisting frame concept is shown in Fig. 6.9 (Fukuyama et al. 2015). This paper especially describes the effort of crack evaluation of strength-based reinforced concrete frame since this is one of the unique research efforts on resilient reinforced concrete structures in Japan. Crack simulation under seismic loading has been conducted by several researchers in Japan (Maeda et al. 2004; Sato and Naganuma 2011). Their experimental work dealt with scaled model beams and columns and their simulation model has not been validated with real scale building members.

6.5 Conclusions

In order to assess damage state, complete residual flexural crack profiles (crack spacing, width, and length) were simulated for the real scale five-storey reinforced concrete building specimen tested in 2014.

- Accumulated crack width shows that crack width and spacing were well simulated for peak points of each cycles.
- Crack length can be simulated by making two assumptions; concrete does not deform, and crack is invisible if the crack width is less than the limit crack width.
- Computed crack area damage ratio simulated experimental results relatively well. Computed results should be improved for beams and walls.

The authors hope that simulation of complete crack profiles improves damage evaluation for serviceability and reparability limit states.

Acknowledgements This study was carried out by a joint study of National Technology Development Project of MLIT “Development of function sustaining technologies for buildings used as Disaster Prevention Bases” (2013 ~ 2016) and Priority Research Program of BRI Development on Seismic Design Method for Building with Post Earthquake Functional Use”(2013 ~ 2015). The efforts in measuring concrete cracking by Tokyo Institute of Technology, Tokyo University of Science and Tohoku University and seven participating companies are gratefully acknowledged. A part of this study was conducted as Scientific Research A (PI: Susumu Kono) of JSPS Grant-in-Aid program. Some financial support was also granted by the World Research Hub Initiative of the Institute of Innovative Research and the Collaborative Research Project of Materials and Structures Laboratory at Tokyo Institute of Technology.

References

Architectural Institute of Japan. (2004). Guidelines for Performance Evaluation of Earthquake Resistant Reinforced Concrete Buildings (Draft).

CEB-FIP. (1978). Model code for concrete structures, 15.2.3 Limit states of cracking, pp. 156–160.

Ciampi, V. et al. (1982). *Analytical model for concrete anchorages of reinforcing bars under generalized excitations*. Berkeley: University of California. (Report No. UCB/EERC-82/23).

Fukuyama, H. (2015). *Static loading test on a full scale five story reinforced concrete building utilizing wing walls for damage reduction*. C-2, pp. 361–362. Summaries of technical papers of Annual Meeting Architectural Institute of Japan.

ITOCHU Techno Solutions Corporation. (2016). Science and Engineering Systems Division: Final user’s manual.

Izumo, J., Shima, H., & Okamura, H. (1987). Analytical model for reinforced concrete panel elements subjected to in-plane forces. *Concrete Research and Technology, 25*(9), 107–120.

JBDPA (The Japan Building Disaster Prevention Association). (2015). Seismic Evaluation and Retrofit.

Kabeyasawa, T., Mukai, T., & Fukuyama, H., et al. (2016). A full scale static loading test on five story reinforced concrete building utilizing columns with wing walls. *Journal of Structural and Construction Engineering*, *Transactions of AIJ*, *81*(720), 313–322.

Kabeyasawa, T., Mukai, T., Fukuyama, H., Suwada, H., & Kato, H. (2017). *Full-scale static loading test on a five story reinforced concrete building*. In 16th World Conference on Earthquake Engineering, January 9–13, Paper No. 1242. Santiago: Chile.

Kitamura, F. (2017). *Damage evaluation of five-story building by nonlinear finite element analysis.* Master thesis of Tokyo Institute of Technology.

Kono, S., Kitamura, F., Yuniarsyia, E., Watanabe, H., Mukai, T., & Mukai, D. (2017) Efforts to develop resilient reinforced concrete building structures in Japan. In *Proceedings of the Fourth Conference on Smart Monitoring, Assessment and Rehabilitation of Civil Structures*, September 2017, pp. 13–15, Paper ID #KN30. Zurich, Switzerland.

Maeda, M., Nakano, Y., & Lee, K. (2004). Post-Earthquake Damage evaluation for R/C buildings based on residual seismic capacity. In *Proceedings. of 13 World Conference on Earthquake Engineering*. Paper ID 1179.

Ministry of Land, Infrastructure, Transportation and Tourism (MLIT). (2015). The 2015 guidelines of structural design technology of buildings.

Naganuma, K. (1995). Stress–strain relationship for concrete under triaxial compression. *Journal of Structural and Construction Engineering, Transactions of AIJ, 474,* 163–170.

Sato, Y., & Naganuma, K. (2011). *Crack width analysis using smeared-crack-based fem: Part 8.* C-2, pp. 241–242. Summaries of tech. papers of Annual Meeting Architectural Institute of Japan.

Chapter 7
The State of Knowledge and Practice in Concrete Structure Design for Earthquake

John S. Ma

Abstract The duty of structural engineers is to design and build structures or buildings (1) that are safe, (2) that provide comfort to occupants during strong winds or earthquakes, and (3) that will result in the least construction cost and the most savings to building owners. The state of knowledge is that research has developed nonlinear response history analysis (NRHA) method for predicting the behavior (response) of reinforced concrete structures subjected to winds or earthquake ground motions from reinforcing steel yielding at critical sections to structural member (beam, column, connection, slab, and wall) failures up to partial or the whole structural system collapse. Some of the NRHA methods have been verified by shake table dynamic testing. The state of practice for the design of important structures whose failures could cause significant casualty of people's life has been using NRHA for seismic and wind analyses and to ensure the safety of these buildings and to provide comfort to occupants and savings to building owners. Buildings have been designed and built worldwide using NRHA successively. And local jurisdictions (building departments) in the United States and China and other countries have required NRHA to be performed for high-rise buildings. NRHA is inherently complicated and complex because it involves earthquake ground motions which are random, in conjunction with nonlinear structural analyses due to the decreasing stiffness and increasing damping values of a structure resulting from concrete cracking and steel yielding at each time step of earthquake ground motions. Therefore, knowledge in the NRHA method and understanding of its proper use are essential. The way to gain that knowledge and understanding is

John S. Ma, member of ACI and American Society of Civil Engineers, is a senior structural engineer and charter member of the U.S. Nuclear Regulatory Commission (NRC) and is currently a licensed professional engineer in California, Maryland, and Virginia. He received his Ph.D. degree from the University of Texas at Austin and the Raymond C. Reese structural research award medal from the ACI. Dr. Ma has experience in designing bridges, and industrial, commercial, residential, and nuclear power plant buildings and reviewing nuclear submarine structural design. He provides consulting service to structural design and construction industries and donates his service to charitable/religious organizations.

J. S. Ma (✉)
U.S. Nuclear Regulatory Commission, 11555, Rockville, MD 20852-2738, USA
e-mail: JOHN.MA@NRC.GOV; johnma2000@yahoo.com

T. T. C. Hsu (ed.), *Concrete Structures in Earthquake*,
https://doi.org/10.1007/978-981-13-3278-4_7

timely sowing seeds in a good ground that will reap rich harvest. The proper use of NRHA enables structural engineers to design and build safer and better buildings with less construction cost than buildings without using the NRHA method against environmental hazards, such as earthquakes or winds. The same principle of timely sowing seeds in a good ground is also applicable to building a better and more resilient family structure against environmental hazards, such as drugs or violence, and we must do it timely because time flies.

Keywords ACI codes · Nonlinear response history analysis · Buildings Structures · Safety · Comfort · Winds · Earthquakes

7.1 Introduction

Structural engineers are expected to design and build structures or buildings to be safe and provide comfort to occupants during strong winds or earthquakes and savings to building owners. Building codes, such as ACI 318 for conventional buildings, ACI 359 for concrete nuclear containments, and ACI 349 for concrete structures other than containments in nuclear power plants, only provide minimum requirements and provisions for the protection of people's life. Building codes are neither design guides nor methods to predict the behavior (response) of a building subjected to wind or earthquake ground motions. Therefore, for important structures or buildings, such as high-rise buildings, whose collapse could cause significant casualty of people's life are designed, or/and required by local jurisdictions (building departments) to perform nonlinear response history analysis (NRHA) for the intensity of earthquake ground motions that is called maximum considered or credible earthquake (MCE), which is 1.5 times the intensity of design-basis earthquake for the design of ordinary buildings or structures, to ensure these important buildings do not collapse at MCE. For structures or buildings in nuclear power plants whose failure or collapse could cause significant release of radiation into the atmosphere, the Nuclear Regulatory Commission (NRC) requires these buildings or structures to sustain, without failure or collapse, a review level earthquake (RLE) intensity of earthquake ground motions that is 1.67 times the intensity of the safe-shutdown earthquake (SSE) that automatically triggers the shutdown of the plant (SECY 1993).

In addition to building safety, comfort to building occupants in high-rise buildings during strong winds or earthquakes is required. Good design that will result in the least construction cost and the maximum savings to the building owners is desired and expected from structural engineers. Accurate predictions of in-structure-floor-response spectra (ISRS) for piping that runs through several floors and important equipment supports (anchors) in nuclear power plant structures are necessary for the safe design of these important piping and anchor design. Therefore, the use of NRHA is necessary and essential for the design and construction of important buildings, such as high-rise buildings, or important nuclear power plant structures.

The state of knowledge is that research has developed the NRHA method for predicting the behavior (response) of reinforced concrete structures subjected to dynamic loadings, such as winds or earthquake ground motions, from reinforcing steel yielding at critical sections to structural member (beam, column, connection, slab, and wall) failures and up to partial or/and the entire structural system (building) collapses. Some of the NRHA methods or computer programs have been verified by shake table dynamic testing.

The state of practice for the design of high-rise buildings has been using NRHA to analyze and ensure no collapse at MCE. And the NRHA method is also required by local jurisdictions (building departments), such as Los Angeles and San Francisco, California, Seattle, Washington, New York City, New York in the United States, and cities in China and other countries.

The evolution of knowledge and practice in concrete structure design for earthquake is described first, followed by the validation of an NRHA method against shake table test data, followed by the explanation and description of the NRHA method. NRHA is inherently complicated and complex because it involves earthquake ground motions which are random, in conjunction with nonlinear structural analyses due to the decreasing stiffness and increasing damping values of a structure resulting from concrete cracking and steel yielding at each time step of earthquake ground motions. Therefore, knowledge in the NRHA method and understanding of its proper use are essential. The way to gain that knowledge and understanding is timely sowing seeds in a good ground that will reap rich harvest. An example of improper use of the NRHA that led to the wrong conclusion of safety which was found by the NRC staff is provided as a caution for recognizing the adequacy of the NRHA method and its results.

An example of knowledge in prestressed concrete and its proper analysis method that brought peace and smile back to residents, who were terrified by information of imminent building collapse in previous reports resulting from improper investigations, is provided to stress the importance of knowledge in, and understanding of, structural engineering principles and methods of analysis and design.

Anchor failures in nuclear power plants, resulting from design using an incorrect ACI 349 provision of a 45° concrete failure cone shape, created opportunities for research and testing for anchor bolts embedded in concrete. As a result, new anchor design criteria were developed for anchors in ACI 349 and 318 Codes.

A three-hinge arch building was built by volunteers with stability problems and was corrected by a structural engineer to illustrate the power of daring to ask and willing to give.

Finally, applying the same principle and approach of timely sowing seeds in a good ground to enable us to gain knowledge and understanding to build safer and better structures or buildings against environmental hazards, such as winds or earthquakes, also enable us to build a better and more resilient family structure against environmental hazards, such as drugs or violence.

7.2 Evolution in Knowledge and Practice in Concrete Structure Design for Earthquake

7.2.1 Static Analysis for Earthquake Design in 1973

In 1973, I designed a 13-story concrete hotel building in Los Angeles, California for earthquake. The building was designed with a base shear = x% of the building weight specified in the Los Angeles Building Code. I used Hardy Cross "moment distribution method" for 1-D (dimensional) linear frame analysis to obtain storey shears and overturning bending moments with a slide rule for calculations. None of us uses this static analysis method or the slide rule for calculation anymore. The knowledge in, and method for, building design in 1973 were primitive in structural/earthquake engineering and limited by calculation tools. Thus, safety of buildings could not be quantified against the building dynamic behaviors during earthquake ground motions because the analysis method and procedures were static and not dynamic. Earthquake design requirements, methods, and procedures in building codes have been updated and improved significantly since 1973. Non-ductile concrete buildings, including the hotel building that I designed, in Los Angles constructed before 1980 were required for mandatory retrofitting because of their brittleness or insufficient ductility, as a result of the 2014 Los Angles City Ordinance (Catherine and Cardno 2015). I have been telling friends not to stay in this hotel that I designed for their own safety.

7.2.2 Nonlinear Response History Analysis (NRHA) Ensures Building Safety for MCE

Last year, 2017, a 73-story (1,100 feet tall) concrete shear wall building, Wilshire Grand Tower, opened for business in Los Angeles, California (Joseph et al. 2015). The building was designed with the shear capacity of the tower = 1.5 mean MCE shear demand calculated from the average of eleven (11) earthquake ground motions that are applicable to the building site. The design used a 3-D nonlinear response history analysis (NRHA) of the computer program "Perform 3-D" to obtain storey shears and overturning bending moments for the tower. Los Angeles Building Department requires the design of buildings taller than 160 feet (the building height corresponds to high casualty of people's life in the event of building collapse) to be analyzed with a predictable 3-D NRHA when the building is subjected to earthquake ground motions and be verified for no collapse at the MCE ground motions (Naeim 2012)

This year, 2018, a 61-story concrete building (1,070 feet tall), Salesforce tower, opened for business in San Francisco, California (Klemencic 2017). The building was designed with the maximum shear stress and tensile/compressive strains in shear walls from the MCE shaking, with eleven (11) earthquake acceleration time histories, that are 20% less than the corresponding shear strength and tensile/compressive strain in walls. The use of extra 20% safety margin was due to the size of this building that exceeded the building code threshold of 5000 people, triggering the building's consideration under Occupancy (or Risk) Category III—Category III buildings require additional safety for wind and seismic demands. The building design used 3-D NRHA (Perform-3D and LS-DYNA computer programs) for the soil-structure interaction (SSI) and the structure-soil-structure interaction (SSSI) to investigate the interactive performance of the building with surrounding soils and with adjacent buildings during earthquakes.

The 1 km (0.6 mile) tall Jeddah Tower in the Kingdom of Saudi Arabia will be the tallest building in the world when the construction is completed. The tower dynamic behavior and structural member load demands were obtained from several computer programs. SAP 2000 was used to study elastic buckling behavior and confirm global stability. Abacus and ETAB were used to study the nonlinear behavior of the tower. Midas Gen was used to conduct the effect of construction sequencing and the values of nonlinear time-dependent concrete modulus, creep, and shrinkage to the analysis and design of the structure. Three-dimensional (3D) sequential construction analyses, with time-dependent materials and loadings, were performed to fine-tune the design and construction (Sin 2016).

7.2.3 Nonlinear Response History Analysis (NRHA) Provides Comfort to Occupants During Strong Winds or Earthquakes and Savings to Building Owner

The 2,073 foot tall Shanghai Tower in China opened in 2014 had used a 1,100-ton mass damper to reduce accelerations and eliminate any feeling of structural movements through the use of NRHA method (Trevor Haskett and Andy Smit 2017).

The 802-foot tall building, located at 181 Fremont, San Francisco, California, had used 32 Taylor dampers, each rated at 225 tons of force to continuously stroking under minor winds or a major earthquake (Taylor 2018).

The design of the 530 feet tall Poly International Plaza building in Beijing, China, was required by the Chinese government to perform NRHA for three levels of seismic hazard with peak ground accelerations of PGA = 0.07 g, 0.2 g, and 0.4 g to verify conformance with performance goals (Mark Sarkisan et al. 2017).

The 662-foot tall One Seaport Tower, located at 161 Maiden Lane, New York, NY, used 4 tuned liquid dampers to ensure occupancy comfort from dynamic motions and limit building accelerations. Extensive soil-structure NRHA not only yielded the best structural performance but also provided savings of approximately $6 million dollars to the building owner (Jeffrey Smilow et al. 2010).

7.3 Design Implication of Building Codes Methods for Earthquake

ACI 318 Code is for conventional building design, and it uses "strength" method. At the intensity of the design-basis earthquake, steel reinforcement is allowed to be yielded at critical sections of structural members in buildings. The ductility design requirements in the code, such as no brittle failure in sections, members, connections, and seismic resisting systems of a building, the redundancy requirements, such as integrity (continuity) steel reinforcement requirements, and steel detailing requirements, are expected to sustain the building from collapse during the design-basis earthquake or earthquake intensity greater than that of the design-basis earthquake. This expectation is partly based on the nonlinear analytical studies on collapses of ductile buildings subjected to earthquake ground motions, and partly on the low numbers of collapses of buildings that met code's requirements during earthquakes. However, such an expectation approach may be sufficient for smaller buildings but is insufficient and not reliable enough for important structures or buildings, such as high-rise buildings, whose collapse could cause significant casualty of people's life. Therefore, the final design (dimensions of structural members and their connections and the amount of steel reinforcement and its placement locations) of an important building is required to subject it to the intensity of earthquake ground motions at the MCE level and to ensure it does not collapse, as stated and described in Sect. 7.2.

ACI 359 Code is for nuclear power plant concrete containments, and it uses "strain" method to limit concrete crack widths and thus the amount of radiation escaped into the atmosphere. At the intensity of a safe-shutdown earthquake (SSE)—the intensity of the earthquake that will automatically trigger the plant to shutdown, steel reinforcement is at 90% of the yield strength at critical sections in containments.

ACI 349 Code is for buildings or structures other than containments in nuclear power plants, and it uses "strength" method. At the intensity of a SSE, steel reinforcement is allowed to yield at critical sections of structural members.

ACI Codes stipulate only the minimum requirements necessary to protect public health and safety but are not detailed specifications, recommended practices, complete design procedures, or design aids.

None of the Codes' requirements and procedures can predict the behavior (response) of a building at the earthquake intensity higher than the design-basis earthquake or SSE, or at what level of earthquake intensity the building will collapse.

Therefore, for important buildings or structures, a method that can predict the building behavior (response) under the intensity of any earthquake ground motions up to the intensity that will cause the collapse of the building is required and should be performed for building collapse prevention.

7.4 NRHA is the only Method that can Predict Building Behavior (Response) Through MCE or RLE up to Collapse Under Earthquake Ground Motions

Nonlinear response history analysis (NRHA) is a method that analyzes the behavior (response) of a building or structure with a known geometry and dimensions of structural members and their connections and the amount of steel reinforcement and its placement locations by subjecting it to acceleration time history ground motions. NRHA can predict the behavior or response of buildings and structures beyond the design-basis earthquake to MCE for conventional buildings, or SSE to RLE for nuclear power plant structures or buildings, up to building collapse. See the demonstration and validation of an NRHA method below.

7.5 Validation of an NRHA Method for a Shear Wall Against Shake Table Test Data

The following drawings show a shear wall that was dynamically tested on a shake table under seismic ground motions. The predicted responses (both in magnitudes and in phases) of the wall from NRHA (red curves) with the shear reinforcement in the wall started yielding at 0.8 g and the wall was near or at collapse at 1.6 g match well with those of test data in blue curves (Thomas et al. 2010).

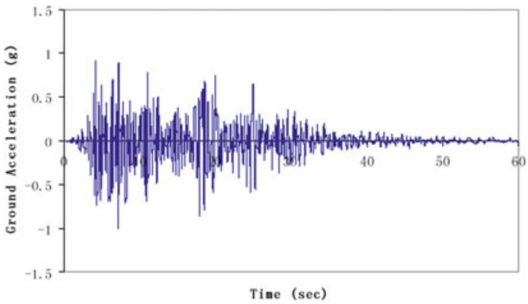

Response history of specimen ST4 at test run of PGA=0.8g

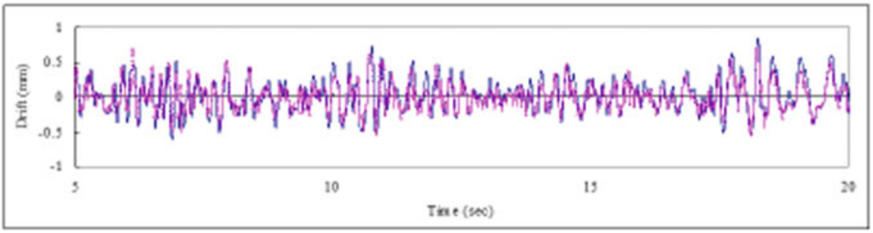

Time history of drift

— Analysis
— Test

Reinforcement starts yielding at PGA = 0.8g

Response history of specimen ST4 at test run of PGA=1.6g

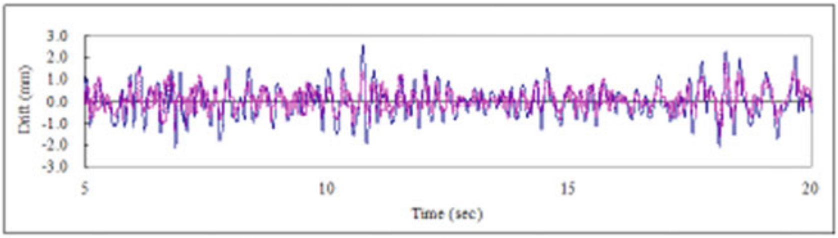

Time history of drift

— Analysis
— Test

Prior to testing, the UH computer code predicted that the wall would fail at 1.6g, and the test indicated that the wall concrete was crushed and failed near 1.6g

7.6 Understand NRHA and Use It Properly

In 1965, I developed a computer program that can calculate bending moments, shears, and axial forces for continuous beams and rigid frames subjected to static vertical and/or lateral loads based on the slope deflection method using matrix solutions (solving linear equations) by meeting the force (including moment) equilibrium criterion between the external forces and internal forces of structural members with an assumption that all members behave linearly (small deflection) elastic (no concrete cracking or steel yielding—constant stiffness). The resulting magnitudes of bending moments, shears, and axial forces are unique and exact and not an approximation.

Linear response history analysis (LRHA) or linear time history analysis calculates moments, shears, and axial forces for members of structures using numerical integration methods by meeting the force equilibrium criterion with an assumption that all members are behaved linearly elastic at each time step of earthquake ground motions. The resulting magnitudes of moments, shears, and axial forces vary depending on the types of numerical integration methods used, but the variations of moments, shears, and axial forces form the different integration methods should be small if done correctly.

NRHA expands LRHA method to calculate moments, shears, and axial forces for members of structures by meeting the force equilibrium criterion and considering the nonlinear and inelastic conditions of structural members caused by concrete cracking and steel yielding at each time step of the earthquake ground motions. The nonlinear analysis procedures use a sequence of linear analysis of a successively changing structure (decreasing stiffness and increasing damping) at a different time interval in accordance with the deformational conditions of the structure at the end of each time interval. The resulting bending moments and forces (shear or axial) may vary greatly depending on the treatment (assumption) used for considering concrete cracking and steel yielding that affects the stiffness and damping of the structure.

If structural members are further divided into elements, such as the finite-element analysis method, then additional variations or approximations are introduced into the analysis, such as types of elements, mesh shapes, and sizes, and thus the results.

Therefore, it is important that (1) an adequate NRHA method (or a verified computer program) is used, (2) analysis is conducted by people who have sufficient knowledge in NRHA, and (3) NRHA results be reviewed for adequacy by experienced structural engineers who understand the behaviors of concrete structures under loads.

That brings the knowledge issue of the structural engineer who performs the NRHA and who reviews the results of the NRHA, and how that knowledge can be effectively and efficiently obtained, and obtained rightfully.

7.7 We Reap What We Sow

Our knowledge in structural engineering principles and understanding of the best analysis and design methods for structures are the result of what we have been learning. Taking time sowing the seed of learning is essential, and making sure that the seed was sowed in good ground is equally important. The good ground is a right place of learning, such as attending good training courses or conferences or reading good technical papers. Learning and understanding the state of current knowledge and best practices and applying them properly, we can design and build safer and better earthquake-resistant structures or buildings, and better protect the public safety, health, and welfare and provide economic savings to the building owners.

An example of improper use of NRHA is provided below as a caution. An example of the proper use of structural analysis method that gave back peace and smile to the residents who were terrified by the imminent building collapse reports that were conducted incorrectly. A miracle structure from heaven—the power of daring to ask and willing to give resulted in a beautiful three-hinge arch building with no cost. An effective and efficient way of gaining proper knowledge and understanding to become a better structural engineer is provided. Finally by applying the same principle and approach of timely sowing the seed in a good ground to become a better informed structural engineer to design and build safer and better structures or buildings against environmental hazard, such as winds or earthquakes, we can build a better and more resilient family structures against environmental hazards, such as drugs or violence. And we must do it timely because time flies.

7.7.1 An Example of Improper Use of NRHA

In the photo below, I was standing in front of a typical tall masonry wall which was physically modified by reducing the unsupported height of the wall by half in a nuclear power plant. I was told that the cost of modifications for walls in the plant had exceeded one million dollars.

Two engineering firms had used NRHA to justify the adequacy of the walls for SSE shaking. The masonry wall was much taller than those I had designed, and I doubted that the NRHA results were adequate. Based on test results of masonry walls from NSF (National Science Foundation) and other sources, I found that stronger cross sections with shorter unsupported heights of masonry walls collapsed at a lower earthquake intensity than the SSE shaking of these walls in the plant. Based on these test results and my knowledge and experience in masonry walls, I rejected the justification from the NRHA performed by the two engineering firms. Additional physical tests for the wall were conducted, and results confirmed that the wall could not sustain SSE shaking. The test results negated the invalid NRHA results and forced physical modifications of most of the walls in the plant. The main problem of these NRHA results was that the assumed ductility value for walls in the analysis was unrealistically high.

Walls Were Improperly Designed, Built, and Justified by NRHA, and Eventually Properly Modified Physically

Tall masonry walls such as this wall were Physically modified by cutting the height of the unsupported wall by half

7.7.2 Reports of "Imminent Collapse" Terrified Residents, but Knowledge in Prestressed Concrete Structures and Understanding of Proper Analysis Methods for Them Brought Back Peace and Smile to the Residents

Reports from two engineering firms gave an impression that imminent collapse of buildings is likely for the about 500 families who lived in the condominium (see buildings in the photo below) without performing structural analysis. The conclusion of the two reports was mainly based on the significant strength loss in the two extracted prestressed tendons with respect to an ASTM specification which was incorrectly cited for the tendons. Residents were terrified of the potential imminent collapse of their buildings and wanted to sell their units with low price and move out, but no one wanted to buy and move in. The condominium association requested me to resolve the problem. I extracted 12 tendons with a total length of 2430 feet and sent them to construction Technology laboratory (CTL), a reputable company, for examination. I found that the previous engineering firms had misidentified the type of tendons used for the building and that type of tendons required higher strength in the ASTM specification than the prestressed tendons existed in the buildings, and thus they concluded "the significant strength loss" of the tested extracted tendons. The two engineering firms did not perform an analysis on whether the structure with the test strengths of the tendons is adequate or not. CTL reported that all test tendons met the yield and breaking strengths requirements of the ASTM A416 specification and that the extent of tendon corrosions was minimal.

By opening up the prestressed tendon anchorage cover plates, I marked the locations and counted the numbers of prestressed tendons in the structure, and with the tendons strengths given by CTL, I performed structural analyses. The analyses results indicated that the structure can sustain loads required by building codes and is safe. Residents got their peace and smile back.

Two 13-Story Buildings Joined at the Podium Level by a Prestressed Slab that Supports Several 3-Story Buildings

7.7.3 Anchor Failures Resulted in Research and Testing and New Anchor Criteria for ACI Codes

In 1988, steel anchor bolts were being pulled out from concrete for piping and equipment supports in nuclear power plants. There were no anchor design criteria in the ACI 318 Code, but ACI 349 Code provided a 45° failure cone criterion. Actual failure cones were far from being 45°. I held a 2-day meeting on anchors at the NRC, which were attended by anchor designers, researchers, bolt manufactures, code committee members, and plant owners to discuss the problems and plans for the resolutions of anchor problems.

Several plant owners formed an owners' group, and hired an engineering firm and an oversight committee to develop anchor verification criteria, based on a probabilistic method, for the qualification of anchors in their plants. I reviewed the criteria, and that criteria would require only about 50% of anchor strength that these failed anchors had originally been designed and installed. I rejected the criteria with a written justification document and proposed directions for developing anchor criteria (Anchor bolts 1989).

Several bolt manufacturers and other plant owners participated in static testing programs for anchor bolts, as proposed in my write-up (Anchor bolts 1989). I initiated a dynamic testing program for anchors embedded in concrete at the

University of Texas at Austin, Austin, Texas under the direction of Professor Richard E. Klingner. I also obtained the European anchor design criteria from Professor Rolf Eligehausen, which was pretty advanced in both testing and theory. Research and test results from the above programs resulted in anchor design criteria—Anchoring to Concrete for both ACI 318 and 349 Codes.

Failures provided opportunities and challenges to find answers. It is important that you must be knowledgeable enough to detect the incorrect answers, such as the one from the owners' group as mentioned above, and looking forward to find and know the correct one.

7.7.4 A Miracle from Heaven

Volunteers built an arch building without a design or review by a structural engineer (see the photo below). The pastor asked me for a favor to take a look at the building, and I said that the three-hinge arch building was beautiful but unstable just like a ladder without a tie between the two legs. There was no money, and the pastor asked me to solve the problem. I then contacted VSL, Inc., on the structural instability and financial problems, and it donated prestressing tendons freely and generously. The pastor was praying next to me while I was connecting and prestressing the tendons between the spread footings for each of the nine (9) arches to counter the outward forces at the spread footing generated by snow, wind, or earthquake. Stability of the arch building was then provided to the three-hinge arch building.

People with volunteering spirit built the beautiful arch building, a structural engineer was contacted and the instability problem identified, the pastor's request for help, the VSL's generous free gift, and the pastor's faith and prayer, completed the building in a condition of no money—a miracle from heaven.

The miracle happened because that the pastor dared to ask for a favor with the courage of not being afraid of rejection. I admired the pastor's faith and courage, and was challenged by him and repeated his action, and that resulted in the VSL's action to give freely and generously. We all have talents and skills to give to, and needs to ask from, others—put them into action and miracles could happen to, or because of, you.

7.7.5 An Effective and Efficient Way to Sow Seeds and Reap Rich Harvests

We only have 24 h a day, and should sow our seeds in a ground that will reap rich dividends in the knowledge of structural/earthquake engineering and understanding of best current practices (analysis, design, and construction methods) available in

Volunteers Built the Arch Building

the industry. The efficient and effective way that I have been learning and using is to (1) select good technical papers or books to read in the field that I am good at and interested in, (2) only attend worthwhile conferences or trainings that are related to my specialties, (3) only accept the interesting and challenging projects, as a consulting engineer, and (4) not overwork or spend too much time to understand subjects what I do not know, (5) be honest with what I do not know and seek advice from those who are true experts in those particular areas that I need to accomplish my jobs, and (6) by applying the above five principles, I can accomplish not only my professional works as a structural engineer effectively and efficiently but also create time for investing and building a better and stronger family structure.

7.7.6 *Applying the Same Principle of Sowing Seed in a Good Ground to Building a Better and More Resilient Family Structure*

We have a limited time to live on this earth. We should find and establish an effective and efficient way to sow seeds in the ground that will reap a great harvest of love and joy with our spouses, children, grandchildren, relatives, and friends. One of the ways that my wife and I have been sowing our seeds with our children and their spouses and our grandchildren is, in addition to our family vacations together, to hold weekly Sunday lunches with them in restaurants that favored by all after church services. The picture below taken by my daughter shows that my grandchildren were intently listening to my teaching on how to develop good characters and behaviors. The eldest kid got it, and said "My dad cursed at, and gave a finger to, the guy who cut him off on the freeway." The other two said "I saw it," with a loud laughter, including me, as if we had caught our common enemy (their dad and my son) and shot him. I was embarrassed, humbled, and benefitted by my 5-year-old granddaughter when she asked “Grandpa, why did you yell at the guy the other day?” at a Sunday lunch table. I notice that we have been sowing our seeds in a good ground and reaping rich harvests because all family members are changing for better characters and behaviors.

Build a Better and More Resilient
Family Structure

7.8 Conclusion

Nonlinear response history analysis (NRHA) is the only method that can predict structural behavior (response) when the structure is subjected to earthquake ground motions or winds. NRHA is also the only method that can take into consideration the effect of time-dependent concrete material changes resulting from construction sequences for the design and construction of a building or structure. Since phenomena of earthquake ground motions, soil-structure interaction, structure-soil-structure interaction, and time-dependent concrete material changes, are complex and complicated, NRHA is inherently complicated and complex to understand, perform, and interpret the results. Therefore, learning the knowledge of NRHA and its proper application are essential.

NRHA is not only the state of knowledge but also the state of practice and it has been used in the design and construction of important buildings worldwide. Structural engineers need to find an efficient and effective way to gain the knowledge of this complicated and complex but necessary NRHA in our limited time so that we can design and build better structures or buildings against environmental hazards, such as earthquakes or winds.

We can and should also apply the same principle and approach of timely sowing seeds in a good ground to design and build better and more resilient family structures against environmental hazards, such as drugs or violence.

What we do matters in the brief moment of our journey in this world. As a structural engineer, we design and built structures to protect the safety, health, and welfare of the public against environmental hazards, such as winds, and earthquakes. As a person, we provide and foster love and joy to our spouses, children, grandchildren, relatives, friends, and protect them from environmental hazards, such as drugs or violence. We must do it timely because time flies.

References

Anchor bolts. (1989). Types of Anchor Bolts, Strength and Safety Factor requirements of Expansion Anchors, New Technical Information–Spacing and Edge Distance effect in Muti-Anchors, and Strength VS. Concrete Crack Width, and Connection Behaviors VS. Anchor Preload," by John S. Ma, January 30, 1989, U.S. Nuclear Regulatory Commission.

SECY-93-087. (1993). Policy, technical, and Licensing Issues Pertaining to Evolutionary and Advanced Light–Water Reactor (ALWR) Design, Nuclear Regulatory Commission, July 21, 1993.

Cardno, C. A. (2015). *Preparing for the big one*. Ph.D., Civil Engineering Magazine, February 2015.

Jeffrey Smilow, P. E., Patrick Chan, P. E., & Llya-Shelevkov, P. E. (2010). One seaport tower. *Structure Magazine*.

Joseph, L. M., Kerem Gulec, C., & Maranian, P. (2015). Performance based design of wilshere grand tower. In *SEAOC Convention Proceedings*.

Klemencic, R. (2017) Saleforce tower. Structure magazine.

Mark Sarkisan P. E., S. E., Nevile Mathias, P. E., S. E., & Rupa Garai, P. E., S. E. (2017). Poly International plaza, Beijing-evolution of an icon. *Structure Magazine*.

Naeim, F., Carpenter, L. D., Ghodsi, T., Hart, G. C., Lew, M., Mehrain, M., et al. J. (2012). An alternative procedure for seismic analysis and design of tall buildings. In *15th World Conference on Earthquake Engineering (15WCEE)*.

Sin, R. C., Peronto, J., & Huizinga, M. (2016). Engineering jeddah tower. *ACI Journal*.

Taylor devices. (2018). Taylor devices-structure solutions. Structure Magazine 58-SS.

Thomas, T., Hsu, C., & Mo, Y. L. (2010). Unified theory of concrete structures. Wiley.

Trevor Haskett, P. E., & Andy Smit, P. E. (2017) Feeling at home in the clouds. Structure Magazine.

Chapter 8
Development of Large-Diameter Reinforcing Bars for the Seismic Resistance of Reinforced Concrete Bridge Columns

Juan Murcia-Delso and P. Benson Shing

This paper presents an investigation on the bond–slip behavior and development of large-diameter bars embedded in well-confined concrete under seismic load conditions. Bond–slip tests and bar pull–push tests were conducted to characterize the bond strength, cyclic bond deterioration, and tension development of large-diameter bars up to No. 18 in size. A bond stress-versus-bar slip model was developed and implemented in a finite element analysis software. The model was validated with test data and used in a Monte Carlo simulation to evaluate the adequacy of the AASHTO requirements for tension bar development. Based on the results of this study, an improved development length formula was proposed. Furthermore, large-scale tests and finite element analyses were conducted to determine the minimum development length required for large-diameter bars connecting a bridge column to an enlarged pile shaft. Design recommendations were proposed based on the experimental and numerical results.

8.1 Introduction

Cast-in-drilled hole (CIDH) shafts are frequently used to support reinforced concrete bridge columns because they have smaller footprints than spread footings. The use of enlarged (Type II) pile shafts has additional advantages in that they provide

J. Murcia-Delso (✉)
Department of Civil, Architectural and Environmental Engineering,
University of Texas at Austin, Austin, TX 78712-0273, USA
e-mail: murcia@utexas.edu

P. Benson Shing
Department of Structural Engineering, University of California, San Diego,
La Jolla, CA 92093-0085, USA
e-mail: pshing@ucsd.edu

T. T. C. Hsu (ed.), *Concrete Structures in Earthquake*,
https://doi.org/10.1007/978-981-13-3278-4_8

more tolerance in pile positioning and also prevent the formation of below-surface plastic hinges in the piles in the event of a severe earthquake. The latter allows easier post-earthquake damage inspection and repair. According to the specifications of the California Department of Transportation (Caltrans 2013), the diameter of a Type II shaft shall be at least 610 mm (2 ft.) larger than the cross-sectional dimension of the column. Hence, the column reinforcement extended into a pile shaft forms a noncontact splice with the shaft reinforcement, as shown in Fig. 8.1. Because of the lack of information on the performance of these splices, the seismic design specifications of Caltrans on the embedment length of column reinforcement terminating in a Type II shaft were very conservative, especially for large-diameter columns. This complicated the construction work and increased construction costs.

This paper presents an experimental and analytical investigation to determine the minimum embedment length required for column longitudinal reinforcement extended into a Type II shaft and the transverse reinforcement required in the bar anchorage regions of these shafts. Experiments were carried out to investigate the bond strength and cyclic bond deterioration of large-diameter bars (No. 11, 14, and

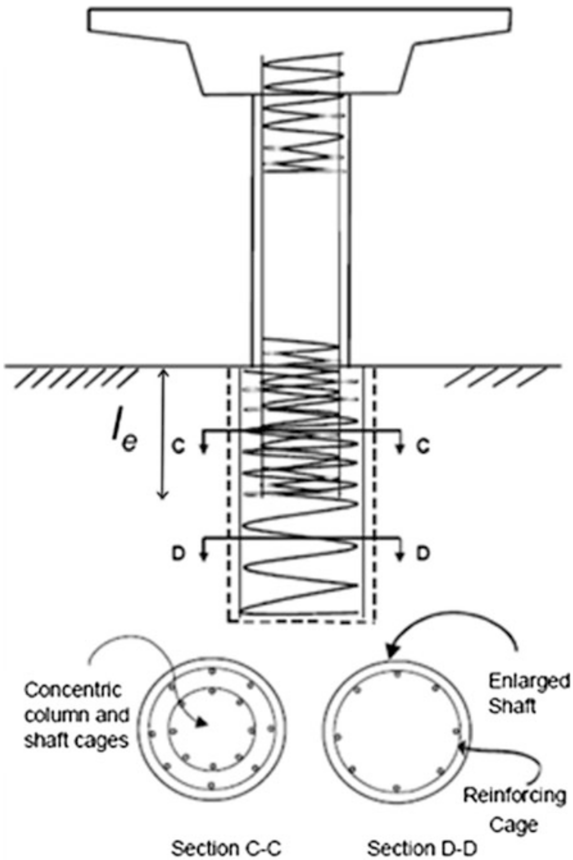

Fig. 8.1 Column supported on enlarged pile shaft (modified from Caltrans 2013)

18 bars), which are frequently used in large-diameter bridge columns and piles, and to evaluate the adequacy of the development length requirements in the AASHTO LRFD Bridge Design Specifications (AASHTO 2012) for these bars when they are subjected to severe cyclic tensile and compressive loads. Such data were not available in the literature and are crucial to acquiring a good understanding of the anchorage performance of large-diameter bridge columns when they are subjected to a severe earthquake event. The experimental results were used to develop, calibrate, and validate a semiempirical bond–slip model for bars embedded in well-confined concrete.

In addition, large-scale tests were conducted on four column–pile shaft assemblies. Based on these tests, additional finite element analyses, and a reliability analysis, new design recommendations on the minimum embedment length for column reinforcement extended into enlarge shafts are proposed. Recommendations on the transverse reinforcement required in the bar anchorage region of a shaft are also provided.

8.2 Bond and Development Tests on Large-Diameter Bars

Bond–slip tests. Four series of tests were conducted to identify the fundamental bond stress-versus-slip behavior of No. 11, 14, and 18 Grade-60 bars embedded in well-confined concrete. In all the tests, bond failure was governed by the pullout of the bars from the concrete rather than concrete splitting.

The test setup is shown in Fig. 8.2a. Each specimen consisted of a reinforcing bar embedded in a 914-mm (3-ft) diameter concrete cylinder. The bar was bonded only in the mid-height region of the specimen over a length of 5 times the bar diameter, d_b. The concrete was confined with No. 4 (13-mm) spiral reinforcement having a pitch of 61 mm (2.4 in.) on center and an outer diameter of 813 mm (32 in.). This resulted in a confinement volumetric ratio of 1%. Series 1 through 3 tests had a concrete with a targeted compressive strength of 34.5 MPa (5 ksi). Series 4 had a concrete with a targeted compressive strength of 55 MPa (8 ksi). All specimens were cast in an upright position.

The local bond stress (τ)–slip (s) relations have been obtained as the average bond stress versus the average of the slips at the two ends of the bonded zone. The bond stress–slip relations obtained from monotonic pullout tests in Series 1 to 3 are plotted in Fig. 8.3a. For comparison, the result obtained by Eligehausen et al. (1983) for a No. 8 (25-mm) bar and 30-MPa (4.35-ksi) concrete is also included in the figure. All the bond stress–slip curves show similar patterns. The slip at the peak strength was around 1.8 mm (0.07 in.) for the No. 8 bar, and around 3.0 mm (0.12 in.) for the No. 11, 14, and 18 bars. With increasing slip, the bond resistance dropped and tended to stabilize at a residual value that was approximately 20–30% of the peak resistance. Eligehausen et al. (1983) pointed out that a practically constant residual resistance was achieved when the value of the slip was approximately equal to the clear rib spacing of the bar, s_R. This can be explained by the

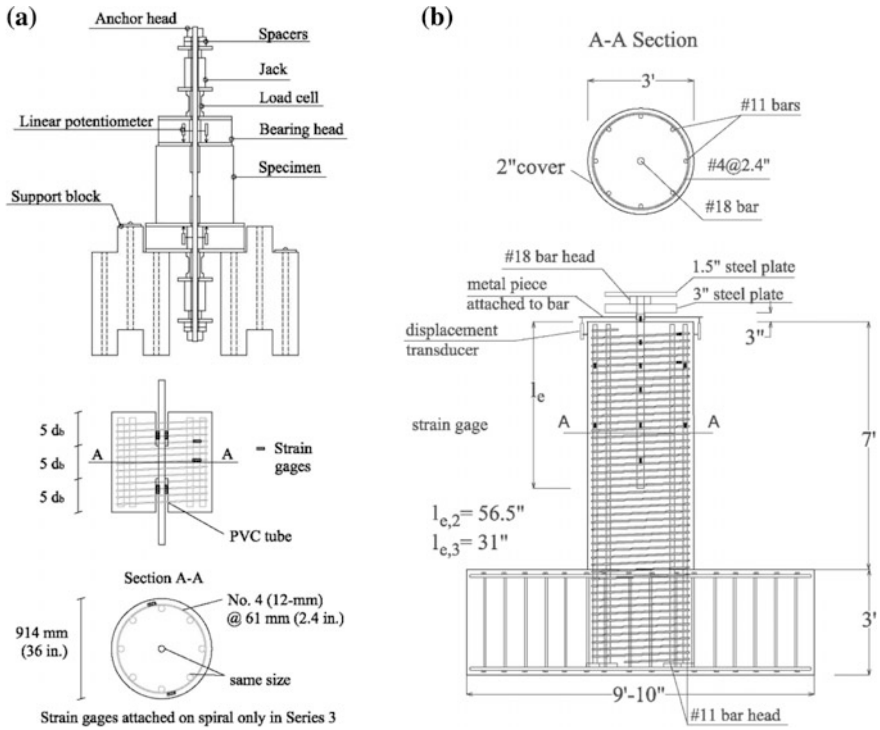

Fig. 8.2 Test setups for: **a** bond–slip tests; **b** development length tests

total damage of the concrete between the ribs. Beyond this point, the resistance to slip was provided solely by friction. This was also observed for the large-diameter bars. However, the transition between the peak and the residual resistance seems to be more gradual for large-diameter bars as compared to No. 8 bars.

Results show that the bond strength, τ_{max}, increases slightly with the increase of the bar diameter. As shown in Fig. 8.3a, the bond strength obtained for a No. 11 bar

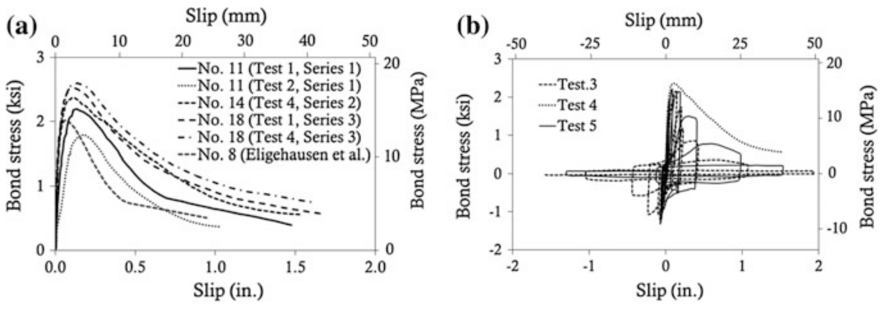

Fig. 8.3 Bond–slip test results: **a** monotonic; **b** cyclic (reprinted from Murcia-Delso et al. 2013)

that was pulled downward (Test 2 in Series 1) was 20% lower than that for a bar that was pulled upward (Test 1 in Series 1). For the bar that was pulled downward, the initial stiffness was also reduced and the peak strength was reached at a slightly higher slip of 4.6 mm (0.18 in.). This observation is consistent with what has been observed in other studies, and it is related to the different qualities of the concrete above and beneath the ribs for bars cast vertically. The concrete right beneath a bar rib can be weaker due to the accumulation of bleed water.

The bond stress–slip relations obtained from two cyclic tests are presented and compared to the monotonic test results in Fig. 8.3b. The hysteresis curves from the tests show a consistent trend. Upon the reversal of the slip direction, a small resistance immediately developed in the other direction. This resistance started to increase when the slip approached the previously attained maximum slip. After this point, the resistance followed a curve similar in shape to the monotonic bond stress–slip curve. However, the stress level attained by this new curve is lower than that by the monotonic bond stress–slip curve due to bond deterioration induced by cyclic slip reversals. In addition, the absolute value of the slip at which the peak stress developed in each cycle increased as the cumulative slip increased. The maximum bond resistance obtained from a cyclic test is between 75% and 95% of that obtained from a monotonic load test. The residual bond resistance diminishes to almost zero after severe cyclic slip reversals. Moreover, the results indicate that full cycles induced a more severe deterioration of the bond resistance than half cycles.

Results from Series 4 tests on No. 14 bars with 55-MPa (8-ksi) concrete have shown a 45% increase of the average bond strength as compared to that obtained from Series 2, which had the same bar size but 34.5-MPa (5-ksi) concrete, implying that the bond strength is more or less proportional to $f_c'^{3/4}$, which is stronger than what has been reported by Eligehausen et al. (1983) and what is assumed in most codes, which suggest that the bond strength is proportional to $f_c'^{1/2}$. This could be due to the fact that the level of confinement in the tests presented here is higher than that used by Eligehausen et al. (1983).

Development Length Tests. Three cyclic pull–push tests were conducted on No. 14 (43-mm) and 18 (57-mm) bars to evaluate whether the tension development requirements stipulated in the AASHTO LRFD Bridge Design Specifications (AASHTO 2012) were adequate to develop the yield and tensile strengths of the bars under severe cyclic loading.

The geometries, reinforcing details, and instrumentation of a typical test specimen are shown in Fig. 8.2b. The same types of reinforcing bars, concrete mix design, and confinement level used in the basic bond–slip tests discussed above were employed. Tests No. 1 and 2 were conducted on a No. 14 bar and a No. 18 bar, respectively, with embedment lengths, l_e, equal to the tension development lengths required by the AASHTO Specifications. Test No. 3 was conducted on a No. 18 bar with an embedment length equal to 60% the development length required by the AASHTO specifications. Specimens 2 and 3 were tested when the compressive strength of the concrete was very close to the target strength of

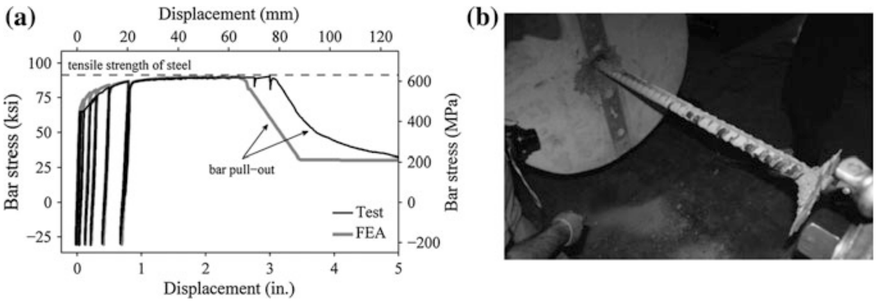

Fig. 8.4 Development-length Test 1: **a** bar stress versus displacement; **b** pullout failure (reprinted from Murcia-Delso et al. 2015)

34.5 MPa (5 ksi). For Specimen 1, the compressive strength of concrete was only 29.3 MPa (4.25 ksi) on the day of the test.

A plot of the bar stress against the displacement of the bar at the top of the anchorage zone for Test No. 1 is presented in Fig. 8.4a. In this test, the No. 14 bar yielded in tension and sustained significant inelastic deformation before it was pulled out from the concrete cylinder. The maximum pull force reached corresponds to 98% of the tensile strength of the bar. After this point, the load dropped with increasing displacement due to the failure of the anchorage. As the bar was being pulled out from the cylinder, pulverized concrete remained attached to the bar between the ribs, as shown in Fig. 8.4b. In Test No. 2, the No. 18 bar yielded and reached its ultimate strength, which was followed by bar necking and fracture. The tensile strength of the bar was reached at a displacement of 60 mm (2.35 in.). After this, the load dropped, which was not caused by the failure of the anchorage, but due to bar necking. The bar fractured at a location right below the surface of the concrete cylinder when the displacement was 93 mm (3.66 in.). Results from these two tests indicate that the AASHTO Specifications are appropriate. The slightly lower bond strength of Specimen 1 was probably due to the lower concrete strength.

Even though the bar in Test No. 3 had an embedment length significantly shorter than the development length required by the AASHTO specifications, it was able to yield and experience a small amount of strain hardening before the bar anchorage failed.

Results obtained from the tests indicate that there was a significant penetration of plastic strain inside the embedment zone. For Test No. 1, plastic strains were measured up to a depth of 18 d_b at a slip of 75 mm (3 in.), prior to the anchorage failure. With the total embedment length of 26 d_b, this means that the lowest 8 d_b of the embedment length was sufficient to develop the yield stress in the bar. In Test No. 2, the maximum plastic strain penetration was at least 11 d_b, or 44% of the total embedment length, which was 25 d_b. In Test No. 3, the maximum plastic strain penetration was at least 3.5 d_b, or 30% of the total embedment length, which was 14 d_b, before the anchorage failed.

The experimental studies on the bond and development length of large-diameter bars are discussed in more detail in Murcia-Delso et al. (2013) and Murcia-Delso et al. (2015).

8.3 Bond–Slip Model

A concrete-to-steel interface model has been developed to simulate the bond–slip behavior of bars based on data obtained from the basic bond–slip tests presented in the previous section. The cyclic bond stress-versus-slip law accounts for the bond deterioration caused by cyclic slip reversals, tension yielding of the bar, and confinement effects. It is based on the model developed by Murcia-Delso et al. (2013) following concepts originally proposed by Eligehausen et al. (1983). The proposed monotonic and cyclic bond-versus-slip curves are shown in Fig. 8.5. This bond–slip model has been extended to account for tension yielding and bar splitting effects. It has been implemented in Abaqus with a user-defined interface element subroutine for finite element analysis, as shown in Fig. 8.6. The main features of the bond–slip model are briefly summarized here.

For monotonic loading, the bond stress (τ) is assumed to be the bond resistance provided by the bearing action of the bar ribs (τ_b) and the friction between steel and concrete (τ_f). Both τ_b and τ_f are functions of the slip (s), and their magnitude is affected by a set of strength reduction factors (ρ_i):

$$\tau(s) = \rho_n\left(\rho_{b,y} \cdot \rho_{b,c} \cdot \tau_b(s) + \rho_{f,y} \cdot \rho_{f,c} \cdot \tau_f(s)\right) \quad (8.1)$$

in which ρ_n is a reduction factor that accounts for the opening of splitting cracks in concrete, $\rho_{b,s}$ and $\rho_{f,s}$ account for the reduction of the bearing and friction resistances, respectively, due to the yielding of the bar in tension, and $\rho_{b,c}$ and $\rho_{f,c}$ account for the deterioration due to cyclic loading. The stress–slip curves for the

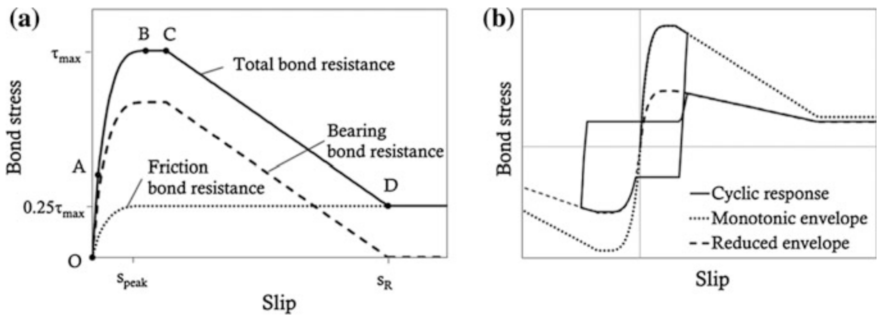

Fig. 8.5 Basic bond stress-versus-slip law: **a** monotonic response; **b** cyclic response (reprinted from Murcia-Delso et al. 2013)

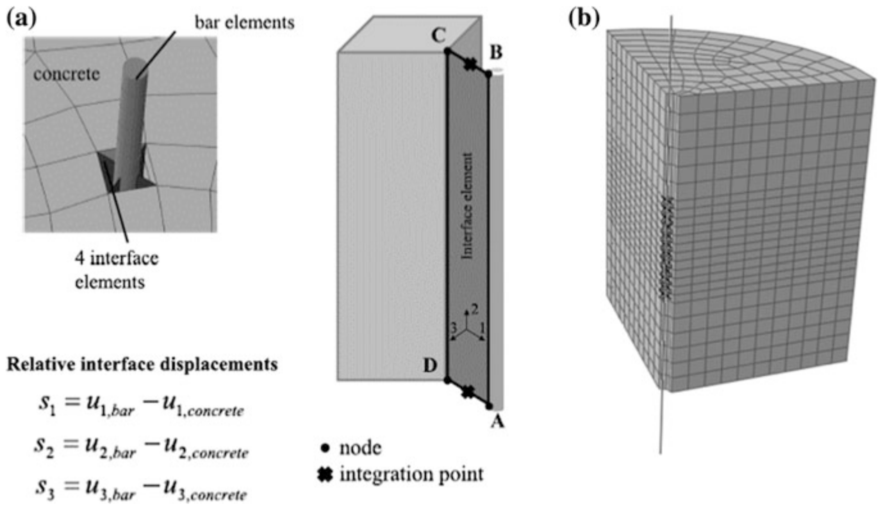

Fig. 8.6 FE modeling of bond–slip behavior: **a** interface element; **b** model of bond–slip test (reprinted from Murcia-Delso and Shing 2015 with permission from ASCE)

bearing, friction, and total bond resistances under monotonic loading are plotted in Fig. 8.5a. These bearing and friction curves are piecewise polynomial functions defined in terms of three governing parameters, namely, the peak bond strength (τ_{max}) of an elastic bar, the slip at which the peak strength is attained (s_{peak}), and the clear spacing between the bar ribs (s_R). These three parameters are easily calibrated based on the compressive strength of the concrete (f_c') and the diameter of the bars (d_b), as described in Murcia-Delso and Shing (2015). Figure 8.5b shows the bond stress-versus-slip relation for cyclic loading. The curve follows Eq. 8.1 for the initial loading and reloading beyond previously attained maximum slip levels. Immediately upon slip reversal, a friction resistance of τ_{rev} is developed in the other direction. Once the maximum slip previously attained in the other direction is reached, the monotonic envelope given by Eq. 8.1 is reengaged. The equations to calculate the bond stress envelopes, deterioration factors, and unloading/reloading for cyclic slip reversals are presented in detail in Murcia-Delso and Shing (2015).

The bond stress-versus-slip relations defined above govern the tangential behavior of the concrete–steel interface along the longitudinal axis of the bar. The interface element shown in Fig. 8.6a has two additional stress and displacement components perpendicular to the bar: one normal and one transverse tangential. The stress–displacement relations in the normal direction are formulated to account for the wedging action of the bar ribs. The normal stress is taken as a fraction of the bond stress by assuming that the resultant bond force has a constant inclination of 60° with respect to the longitudinal axis of the bar. For the transverse tangential direction, a penalty stiffness is introduced to restrain the rotation of the bar about its longitudinal axis.

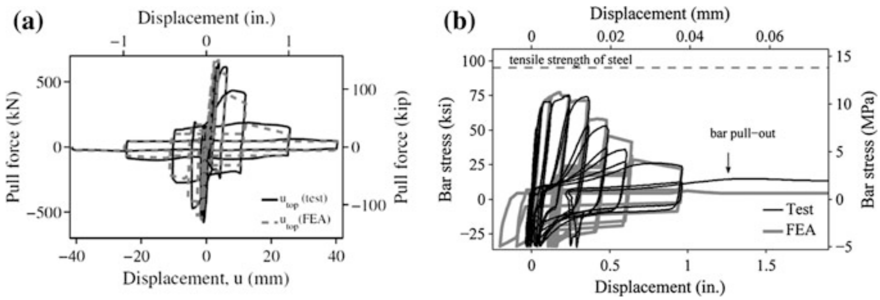

Fig. 8.7 Model validation: **a** bond–slip test (Test 4, Series 4) (reprinted from Murcia-Delso and Shing 2015 with permission from ASCE); **b** development length test (Test 3) (reprinted from Murcia-Delso et al. 2015)

Finite element analyses have been conducted to validate the bond–slip interface model (Murcia-Delso and Shing 2015) with experimental data from bond–slip tests and RC column tests. In the analyses, concrete has been modeled with solid elements and a plastic-damage constitutive law available in Abaqus, and steel reinforcement has been modeled with truss elements and an elastoplastic constitutive law. Figure 8.6b shows the model of a bond–slip test, and Fig. 8.7 compares the numerical and experimental results obtained for bond–slip and development length tests presented in the previous section.

8.4 Numerical Study of the Pullout Capacity of Large-Diameter Bars

Finite element (FE) analyses using the bond–slip model presented in the previous section have been conducted to investigate the pullout capacity of large-diameter bars embedded in well-confined concrete. The model has been first validated with the development (pull–push) test data presented in a previous section. A total of 120 pull–push tests have been simulated to determine how the pullout capacity varies with the embedment length for bars of different sizes and material strengths. The models have the same concrete specimen dimensions and confining reinforcement as the development test specimens, as shown in Fig. 8.2b. The bar sizes considered are No. 11, 14, and 18, and the embedment lengths vary between four and 40 times the bar diameter. Three different compressive strengths of concrete have been used: 24.1, 34.5, and 48.3 MPa (3.5, 5, and 7 ksi).

For each case, the maximum tensile stress, σ_{max}, developed by the bar is recorded. The numerical results show that the yielding of a bar can be achieved with a length as short as eight to 12 times the bar diameter, and the tensile strength of the steel can be developed with a length that is 20 to 32 times the bar diameter, depending on the concrete and steel strengths. To determine the relation between

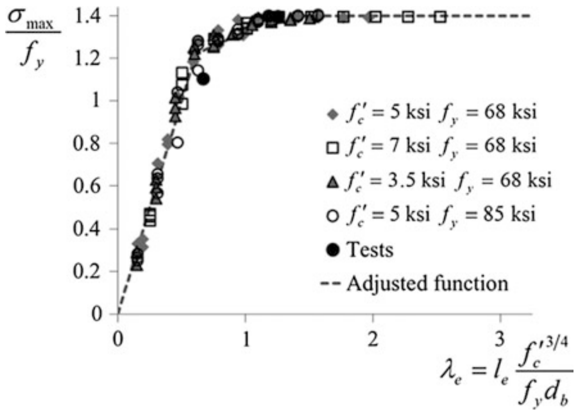

Fig. 8.8 Analytical pullout capacity of large-diameter bars (reprinted from Murcia-Delso et al. 2015)

the maximum tensile stress developed by the bar and the embedment length and concrete and steel strengths, the following development length index is defined:

$$\lambda_e = l_e \frac{f_c'^{0.75}}{f_y d_b} \tag{8.2}$$

Figure 8.8 plots the values of $\sigma_{\max}/f_y$ obtained from FE analyses against λ_e. As shown in the figure, a trilinear function ending with a horizontal line provides a good correlation with the numerical results. The horizontal line corresponds to the ultimate tensile strength of the bars, which has been assumed to be 1.4 times the yield strength of the steel. The trilinear function is expressed as follows:

$$\frac{\sigma_{\max}}{f_y} = \begin{array}{cc} 3.25\lambda_e & if\,\lambda_e \le 0.375 \\ 0.45\lambda_e + 1.05 \le 1.4 & if\,\lambda_e > 0.375 \end{array} \tag{8.3}$$

in which λ_e is calculated with Eq. 8.2 with f_c' and f_y in MPa.

The level of reliability of the AASHTO LRFD Specifications (AASHTO 2012) in developing the yield and ultimate tensile strengths of large-diameter bars in well-confined concrete has been assessed using Eq. 8.3 and the Monte Carlo simulation method. For this purpose, the compressive strength of concrete, the yield strength of steel, the embedment length, and the analytical prediction error have been treated as random variables. The probability distributions of these random variables are provided in Murcia-Delso et al. (2015). The results of the Monte Carlo simulations for different bar sizes and nominal concrete strengths have indicated that the reliability index for the AASHTO LRFD formula in developing the yield strength of a bar is significantly higher than 3.5, which is the minimum reliability index recommended by Darwin et al. (1998). However, with the AASHTO formula, the probability of not developing the full tensile strength of a bar is high, varying from 25 to 50% depending on the bar size and concrete strength. During a strong earthquake, the longitudinal reinforcement of a column may yield and enter the strain-hardening regime; therefore, it is important that the bars can develop their full tensile strength with sufficient reliability. Based on Eq. 8.2 and a target reliability index of 1.75 (probability of failure = 4%), as proposed by Elingwood et al. (1980) for seismic loading, the following embedment length formula is proposed to develop the ultimate tensile strength for well-confined bars:

$$l_{e,min} = 1.15 \frac{f_y d_b}{f_c'^{0.75}} \tag{8.4}$$

in which f_c' and f_y are in MPa. For other confinement situations, in the absence of appropriate data, the development length calculated with Eq. 8.4 should be modified by the relevant factors defined in the AASHTO LRFD specifications.

8.5 Large-Scale Testing and FE Modeling of Column–Shaft Assemblies

An experimental and numerical study has been conducted to determine the minimum embedment length required for the column longitudinal reinforcement extended into enlarged pile shafts. Four full-scale column–pile assemblies were tested under cyclic lateral loading. The test specimens consisted of a column and the upper portion of a pile shaft. One of the specimens and the test setup is shown in Fig. 8.9. The columns had a diameter of 1.22 m (4 ft.) and height-to-diameter ratios

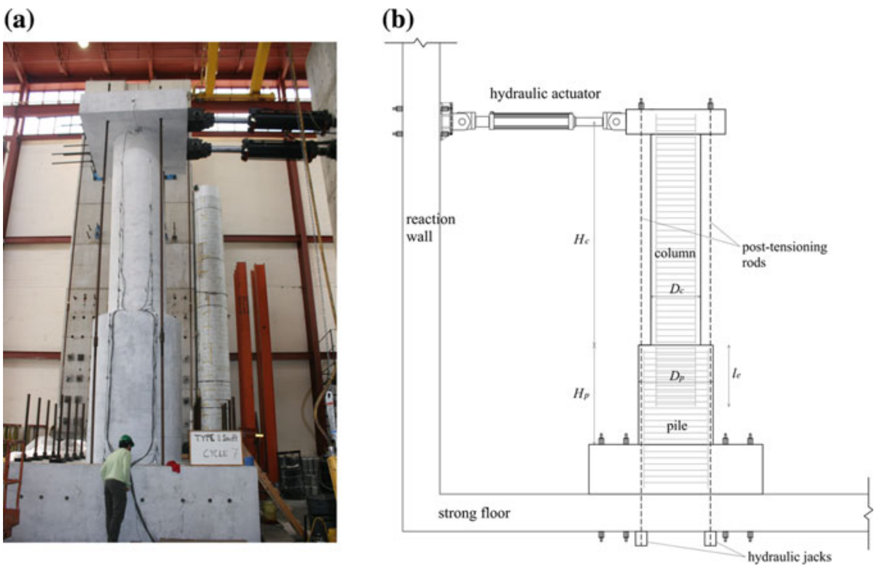

Fig. 8.9 Tests on column-enlarged pile assemblies (modified from Murcia-Delso et al. 2016)

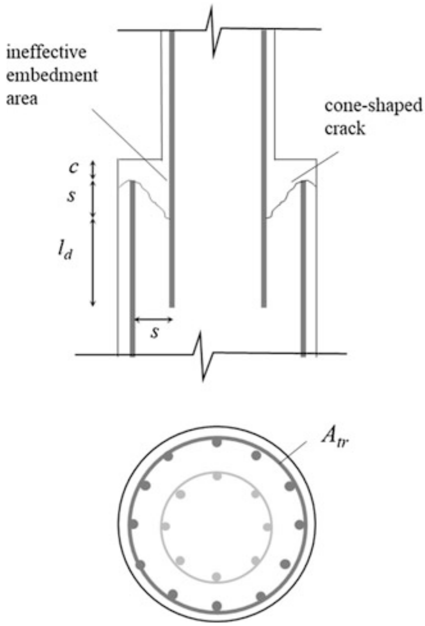

Minimum embedment length of column reinforcement:

$$l_{e,\min} = l_d + s + c$$

Minimum transverse reinforcement to prevent tensile splitting failure:

$$A_{tr} = \frac{1}{2\pi} \frac{N_{col} \tau_u d_{b,col} s_{tr}}{f_{y,tr}}$$

Minimum transverse reinforcement to limit crack opening:

$$A_{tr} = \frac{1}{2\pi} \frac{N_{col} \tau_u d_{b,col} s_{tr}}{f_{y,tr}}$$

where $\alpha = \frac{\varepsilon_{s\max}}{\varepsilon_y} = \frac{u_{cr,\max} N_{sh}}{\pi D_{ext} \varepsilon_y} \leq 1$

Fig. 8.10 Design recommendations for development of column bars in enlarged pile shafts

of 4 or 4.5. The piles had a diameter of 1.83 m (16 ft.), except the pile for one of the specimens, which had a diameter of 1.52 m (5 ft.). The target compressive strength of the concrete in the column and the pile was 34.5 MPa (5 ksi), and ASTM 706 Grade 60 steel was used for the reinforcement. One of the goals of the tests was to assess the adequacy of the minimum embedment length specifications in the Caltrans Seismic Design Criteria (SDC) (2013) and AASHTO LRFD Specifications (2012). The second goal was to validate the new design equations proposed here for the embedment length and transverse reinforcement in the anchorage region of the pile shaft, which are summarized in Fig. 8.10.

The first column–pile assembly tested, Specimen 1, had an embedment length of $D_{c,\max} + l_d$, in which $D_{c,\max}$ is the larger cross-sectional dimension of the column, and l_d is the development length required for a straight bar in tension. The embedment length of Specimen 1 followed the SDC except that the requirement to terminate half of the longitudinal bars at $D_{c,\max} + 2l_d$ was not applied. The size of the column longitudinal bars was No. 11. The transverse reinforcement was determined according to the design requirements for compression members in the AASHTO LRFD Specifications (AASHTO 2012). Specimens 2, 3, and 4 had a reduced embedment length of $l_d + s + c$, in which s is the spacing between the column and the pile longitudinal reinforcement, and c is the thickness of the concrete cover at the top of the pile, as shown in Fig. 8.10. The rationale for the reduced embedment length is the following. According to the development length tests presented in a previous section, l_d was sufficient to develop the full tensile capacity of the bar when no uncertainties are considered. The additional term $s + c$ in this equation was to account for the ineffective force transfer region in the upper part of the noncontact lap splice, as considered in the previous study conducted by McLean and Smith (1997). No.14 bars were used as column longitudinal reinforcement for Specimens 2 and 3. Bundled No. 8 bars were used for Specimen 4. The amount of transverse reinforcement in the anchorage region of Specimen 2 was determined based on a formula proposed by McLean and Smith (1997) to avoid splitting failure in the lap splice region of the pile shaft. Specimen 3 was identical to Specimen 2, except that an additional external steel casing was provided to prohibit splitting failure, and to control the width of the cracks. The thickness of the steel casing was determined with a formula proposed by Murcia-Delso et al. (2016), which is similar to that presented in Fig. 8.10. The transverse reinforcement of Specimen 4 was determined according to the formula presented in Fig. 8.10 to avoid splitting failure. The derivation of these formulas is presented and discussed in Murcia-Delso et al. (2016).

The lateral force-versus-displacement responses of the column–pile specimens are plotted in Fig. 8.11. All the specimens presented a ductile behavior with a plastic hinge forming at the base of the column. The test on Specimen 1 was stopped at a displacement ductility of 5.5, when the lateral load capacity started to drop as a result of buckling and rupture of several column longitudinal bars in the plastic hinge region. No major signs of distress were observed in the anchorage region of the pile, with damage limited to some radial splitting cracks and a circular cone-shaped fracture near the top of the pile. Despite their reduced embedment length, the columns of Specimens 2, 3, and 4 presented a similar behavior to that of Specimen 1.

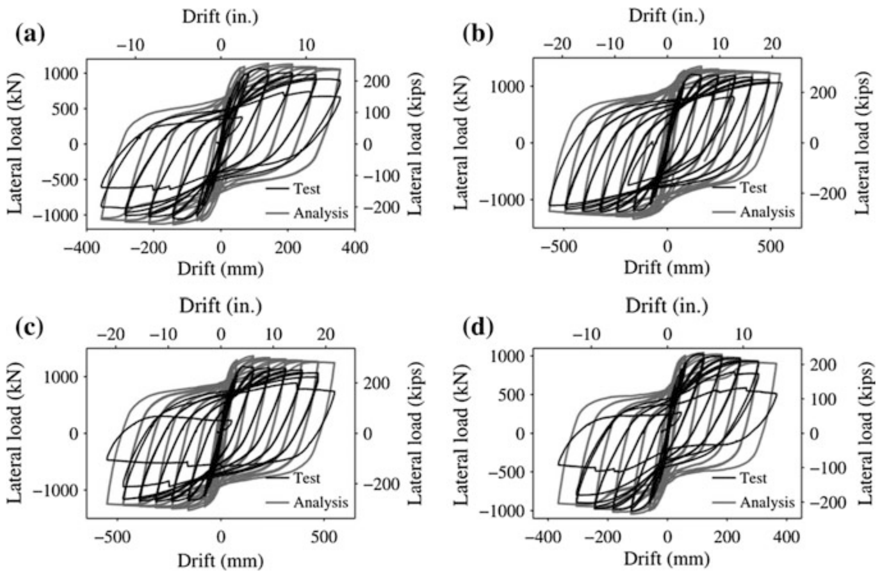

Fig. 8.11 Lateral force versus drift curves: **a** Specimen 1; **b** Specimen 2; **c** Specimen 3; **d** Specimen 4 (reprinted from Murcia-Delso and Shing 2018 with permission from ASCE)

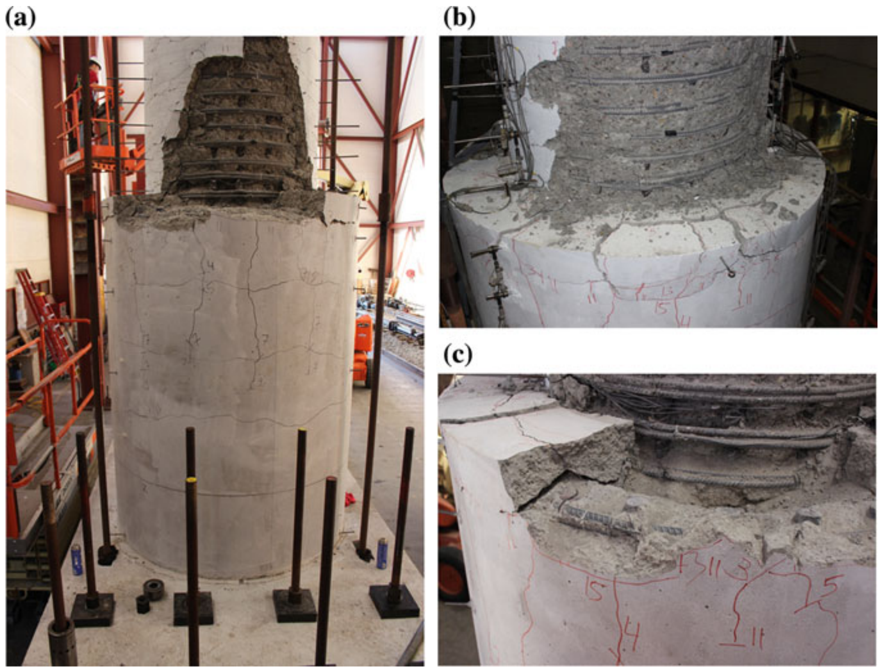

Fig. 8.12 Damage in Specimen 2: **a** column base and pile; **b** cracks atop of the pile; **c** fracture surface atop of the pile (reprinted from Murcia-Delso et al. 2016 with permission from ASCE)

The tests were stopped when one or more column longitudinal bars buckled and ruptured in the plastic hinge region. The maximum displacement ductility achieved by Specimens 2 and 3 prior to the bar failure were 6.9 and 6, respectively. Specimen 2 presented splitting cracks and cone-shaped fracture at the top of the column, as shown in Fig. 8.12. This damage was more severe than in Specimen 1 due to the increased bar slip induced by the shorter embedment length of the bars. The level of damage of the pile in Specimen 4 was similar to that in Specimen 2. As shown in Fig. 8.13, the pile of Specimen 3 showed very minor damage due to the use of the steel casing, which restrained the opening of the splitting cracks.

The experimental data obtained from the large-scale testing has been complemented with results from nonlinear finite element (FE) analyses of the column–pile specimens. Three-dimensional (3D) models comprising the bond–slip model, and concrete and steel material laws described in a previous section have been developed in Abaqus. Only half of the specimen has been modeled considering a symmetry plane in the loading direction, as shown in Fig. 8.14. The results of the FE analyses match the experimental results well in terms of the global lateral load-versus-displacement response of the column–pile specimens, as shown in Fig. 8.11. Figure 8.15 indicates that the FE models also provide good predictions of the strain variations along the embedment length of the column bars, which are influenced by the bond–slip behavior.

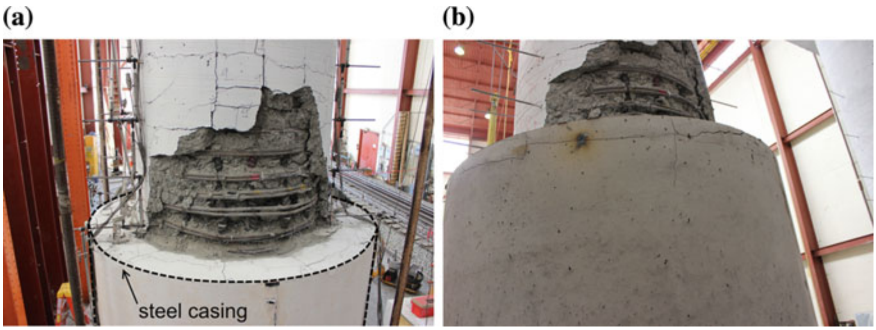

Fig. 8.13 Damage in Specimen 3: **a** column base and top of the pile; **b** pile after removal of the steel casing (reprinted from Murcia-Delso et al. 2016 with permission from ASCE)

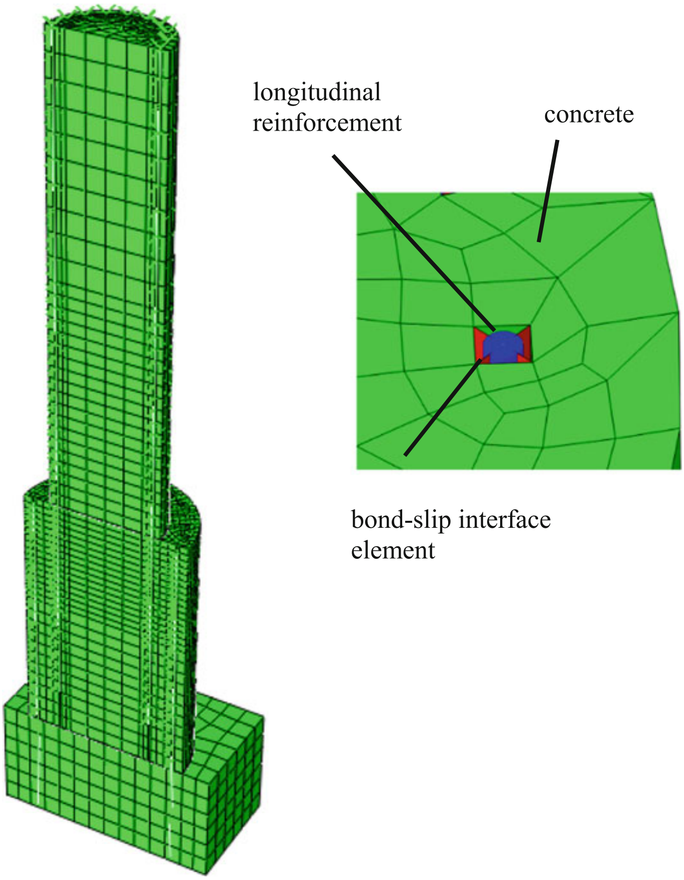

Fig. 8.14 FE model of column–pile assembly

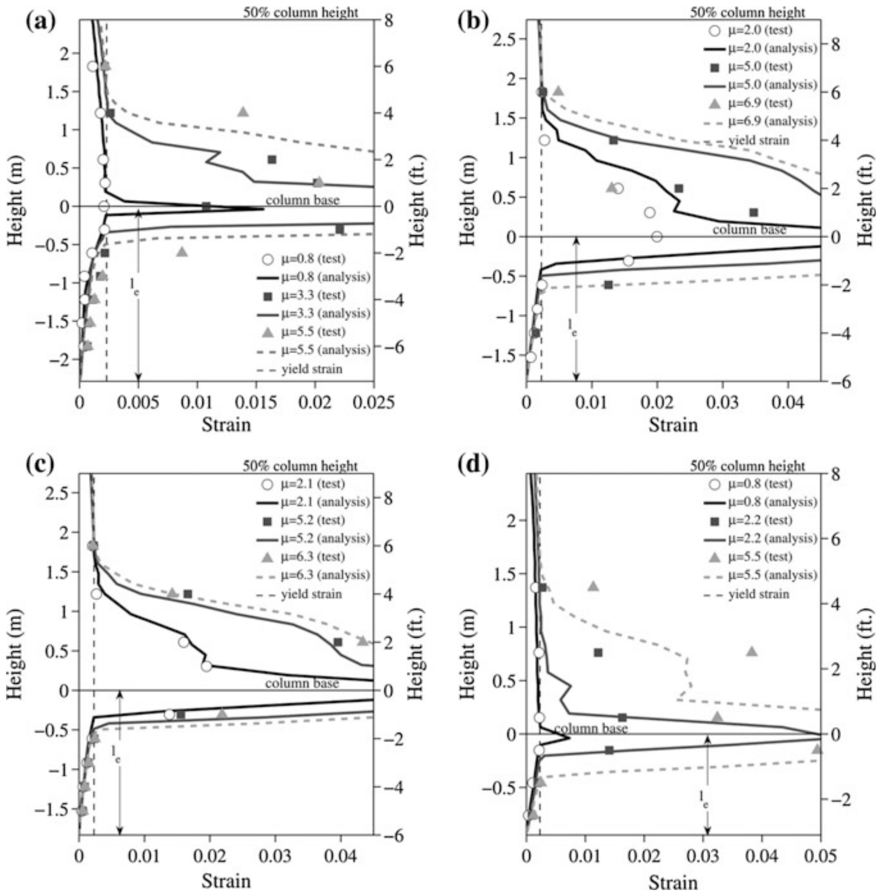

Fig. 8.15 Tensile strains in the column longitudinal bar: **a** Specimen 1; **b** Specimen 2; **c** Specimen 3; **d** Specimen 4 (reprinted from Murcia-Delso and Shing 2018 with permission from ASCE)

The FE models have been used to study the bond stress distributions along the embedment length of the bars. Such data could not be measured in the tests but is crucial for characterizing the bond–slip behavior of bars and for identifying the margin of safety against bar anchorage failure. As shown in Fig. 8.16, the peak bond stress in Specimen 1 occurs near the top of the embedment length in the pile and moves downward as the ductility demand increases due to deterioration caused by bar slip and tensile yielding of the bar. Towards the end of the test, little bond resistance has been activated in the lower half of the embedment length. This indicates that a significant part of the embedment length has not been utilized to develop the full tensile capacity of the bars. Figure 8.16 also shows that the bond stress distribution in Specimen 2 was more uniform along the entire embedment length than for Specimen 1. This indicates that the bond capacities are more fully

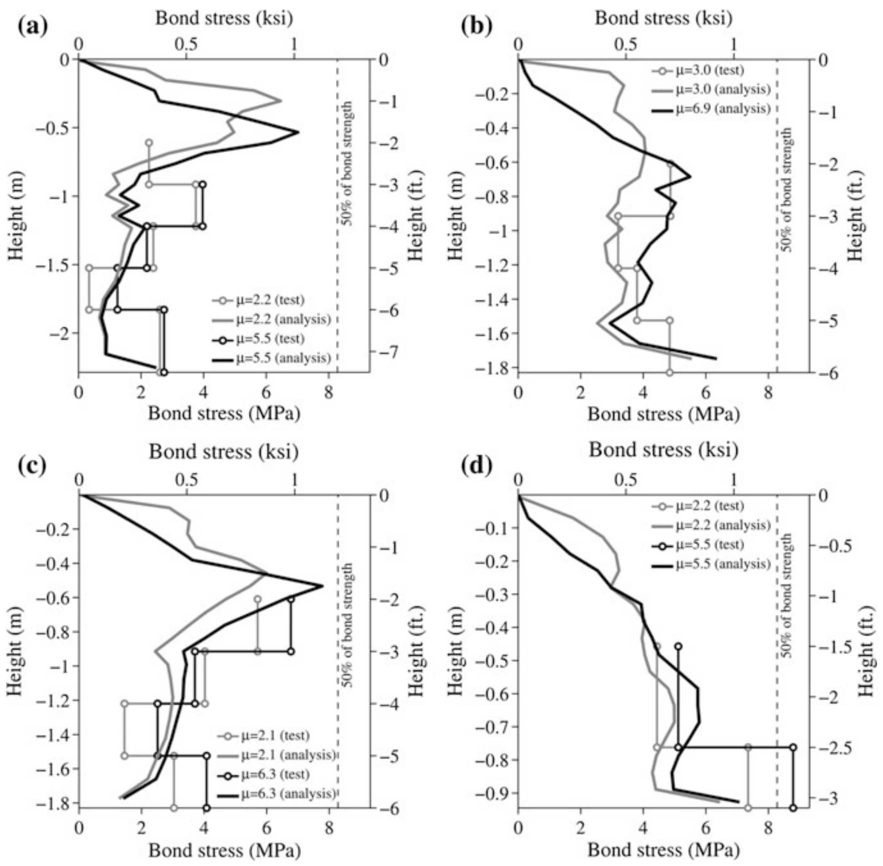

Fig. 8.16 Bond stresses along the anchorage of the column longitudinal bar: **a** Specimen 1; **b** Specimen 2; **c** Specimen 3; **d** Specimen 4 (reprinted from Murcia-Delso and Shing 2018 with permission from ASCE)

mobilized for the reduced embedment length, and that there is little extra anchorage capacity. Specimen 4 shows a similar behavior as Specimen 2. In Specimen 3, the use of the steel casing results in bond stress distribution similar to that of Specimen 1 despite the reduced embedment length. This indicates that the extra confinement provided by the steel casing also improves the bond performance in the anchorage region.

Finally, a parametric FE study has been conducted (Murcia-Delso and Shing 2018). It has shown that $l_d + s + c$ has a sufficient margin of safety against bar pullout failure for different sizes of the column, pile, and longitudinal bars.

8.6 Conclusions

Experimental and numerical studies have been conducted to investigate the bond–slip behavior and development of large-diameter bars subjected to cyclic loading, and to determine the minimum embedment length required for the column reinforcement extended into enlarged pile shafts in seismic-prone regions. The main findings and conclusions of the studies are summarized here:

- The basic bond–slip tests presented in this paper have shown that the monotonic and cyclic bond stress-versus-slip behavior of large-diameter bars, namely, No.11 and larger bars, embedded in well-confined concrete is very similar to that of No. 8 bars that were tested by Eligehausen et al. (1983).
- The interface model proposed in this study is a reliable tool to investigate the effect of bond–slip on the behavior of reinforced concrete members and the anchorage length requirements.
- Development length tests and FE analyses have indicated that the minimum development lengths specified in AASHTO LRFD are not only sufficient to develop the tensile yielding of a bar but also sustain large inelastic deformation up to the ultimate strain of the steel. However, with the consideration of possible uncertainties in material properties and construction quality, a new development length formula has been proposed to provide the desired reliability to develop the ultimate tensile strength of steel.
- Large-scale testing and FE analyses of column–pile assemblies have shown that a reduced embedment length of $l_d + s + c$ is sufficient to develop the tensile capacity of column longitudinal bars extending into oversized pile shafts as long as sufficient transverse reinforcement is provided in the anchorage region of the pile. To provide sufficient safety against bar pullout during a severe earthquake, l_d should be calculated using the development length formula proposed here. Design equations have also been proposed to determine the minimum amount of transverse reinforcement necessary in the anchorage region of a pile shaft to avoid a splitting failure and to control cracking.

References

American Association of State Highway and Transportation Officials (AASHTO). (2012). LRFD bridge design specifications. Washington, DC.

Caltrans, Seismic Design Criteria (Version 1.7). (2013). California Department of Transportation Sacramento.

Darwin, D., Idun, E. K., Zuo, J., & Tholen, M. L. (1998). Reliability-based strength reduction factor for bond. *ACI Structural Journal*, *95*(4), 434–442.

Eligehausen, R., Popov, E. P., & Bertero, V. V. (1983). Local bond stress-slip relationships of deformed bars under generalized excitations, UCB/EERC-83/23, Earthquake Engineering Research Center, University of California, Berkeley, Berkeley, CA.

Ellingwood, B., Galambos, T. V., MacGregor, J. G., & Cornell, C. A. (1980). Development of a probability based load criterion for American National Standard A58. National Bureau of Standards Special Publication 577, Washington, DC.

McLean, D. I., & Smith, C. L. (1997). Noncontact lap splice in bridge column-shaft connections. Report No. WA-RD 417.1, Washington State Transportation Center, Washington State University, Pullman.

Murcia-Delso, J., Stavridis, A., & Shing, P. B. (2013). Bond strength and cyclic bond deterioration of large-diameter bars. *ACI Structural Journal*, *110*(4).

Murcia-Delso, J., & Shing. P. B. (2015). Bond-Slip Model for Detailed Finite Element Analysis of Reinforced Concrete Structures. *Journal of Structural Engineering*, *141*(4).

Murcia-Delso, J., Stavridis, A., & Shing, P. B. (2015). Tension development length of large-diameter bars for severe cyclic loading. *ACI Structural Journal*, *112*(6).

Murcia-Delso, J., Liu, Y., & Shing, P. B. (2016). Development of bridge column longitudinal reinforcement in oversized pile shafts. *Journal of Structural Engineering*, *142*(11).

Murcia-Delso, J., & Shing, P. B. (2018). Numerical study of bond and development of colum longitudinal reinforcement extended into oversized pile shafts. *Journal of Structural Engineering*, *144*(5).

Chapter 9
Reversed Cyclic Tests of 1/13 Scale Cylindrical Concrete Containment Structures

Chiun-Lin Wu, Thomas T. C. Hsu, Che-Yu Chang, Hu-Jhong Lu, Hsuan-Chih Yang, Chang-Ching Chang, Yu-Chih Chen and Yuan-Sen Yang

Nuclear containment structure is one of the most important infrastructure systems ensuring the safety of a nuclear power plant. In this paper, the structural behavior of cylindrical concrete containment structure was investigated using two 1/13-scaled nuclear containment specimens subjected to reversed cyclic loadings. The presentation will first describe the experimental program, including the dimensions, the reinforcement detailing, the test setup, and the loading method. Second, the experimental results of the specimens are discussed including the cracking patterns, the total load versus displacement curves and the failure modes. Third, the test

C.-L. Wu (✉) · C.-Y. Chang · H.-J. Lu · H.-C. Yang · C.-C. Chang
National Center for Research on Earthquake Engineering, Taipei, Taiwan
e-mail: clwu@ncree.narl.org.tw

C.-Y. Chang
e-mail: cheyu@ncree.narl.org.tw

H.-J. Lu
e-mail: paprika8201@hotmail.com

H.-C. Yang
e-mail: hcyang@ncree.narl.org.tw

C.-C. Chang
e-mail: ccchang@ncree.narl.org.tw

T. T. C. Hsu
Department of Civil and Environmental Engineering, University of Houston, Texas, USA
e-mail: thsu@uh.edu

Y.-C. Chen
Sinotech Engineering Consultants Inc, Taipei, Taiwan
e-mail: ycchen@sinotech.org.tw

Y.-S. Yang
Department of Civil Engineering, National Taipei University of Technology, Taipei, Taiwan
e-mail: ysyang@ntut.edu.tw

T. T. C. Hsu (ed.), *Concrete Structures in Earthquake*,
https://doi.org/10.1007/978-981-13-3278-4_9

results were compared to the analytical results predicted at the University of Houston using a 3D finite element program with the CSMM-based shell elements. The predicted results agree very well with the experimental data.

9.1 Introduction

A reinforced concrete containment vessel (RCCV) is considered to be one of the key contributors to a nuclear power plant (NPP) system's Defense in Depth (DID) strategy. The National Center for Research on Earthquake Engineering (NCREE) and the University of Houston, USA, cooperated to design and build two scaled RCCV shell specimens to investigate the mechanical behavior and the failure mechanism of the reinforced concrete cylindrical shells. The advanced boiling water reactor (ABWR) is a Generation III nuclear reactor which is currently offered by GE Hitachi Nuclear Energy and Toshiba. The first four ABWR reactors were built in Japan, while the construction work at Shimane NPP in Japan halted after the 2011 Tohoku earthquake. Shortly thereafter, the construction work of two ABWRs at Lungmen NPP in Taiwan was halted in 2014.

The containment is typically an airtight structure enclosing the reactor normally sealed off from the outside atmosphere. The design and thickness of the containment and the missile shield are governed by the USA federal regulations. The Sandia National Laboratories focus on the integrity research of containments which were constructed in the boiling water reactor and pressurized water reactor power plants. Lots of test projects were designed by using multi-scale, multi-process testing, large-scale validation experiments and phenomenological modeling in chemical, structural, and thermal of containment structures to identify the characteristics of the containment. Three-dimensional finite element dynamic analyses were performed to evaluate the general capabilities of analytical methods for concrete-structures and validate the methods, and interpret the test results (NUREG/CR-6906; NUREG/CR-6639).

A series of studies were focused on the structural behavior of RCCV by using the cyclic tests and shaking table tests in Japan. The scaled RCCV structure was constructed with fully boundary conditions including top slab, tunnel, and fuel-pool girders to confirm that the trial-designed RCCV was safe and reliable at a design-load level. The finite element analysis with 3D solid elements to estimate the deformation, failure load, and nonlinear behavior of RCCV were investigated by Saito et al. (1991, 1993). The ultimate strength and seismic margin by an excitation that led to the model's collapse were determined and verified. The seismic characteristics of RCCV and structural behavior were also studied by Hirama et al. (2005).

From a structural point of view, a nuclear containment can be visualized as assemblies of many elements. This concept facilitates the analysis of the complex structure when the finite element analysis is used, accompanied by the rational constitutive laws of materials. The key to a rational analysis of the structure is to understand fully the behavior of one element isolated from the structure. Once a rational model is developed to predict the behavior of one element, this rational model can be incorporated into a finite element analysis program, such as OpenSees (2013), to predict the behavior of the whole structure under different kinds of loading.

A finite element analysis program was developed at the University of Houston (UH) based on OpenSees as a framework. The UH method utilized wall elements based on the Cyclic Softened Membrane Model (CSMM) (Mansour and Hsu 2005; Hsu and Mo 2010). The constitutive laws of CSMM were developed at UH using the Universal Panel Tester (Hsu et al. 1995). This finite element method was recently extended to include CSMM-based shell elements (Hsu et al. 2012; Luu 2016; Hsu et al. 2017). This FE Program, which is called Program SCS-3D, is capable of predicting the reversed cyclic behavior of cylindrical reinforced concrete containment structures.

9.2 Experimental Program

9.2.1 Design of 1/13-Scaled Specimens

The dimensions and reinforcement detailing for the RCCV specimens of this study are shown in Fig. 9.1 with an exterior diameter of 33 m, an interior diameter of 29 m, and a height of 29.5 m. Considering the available laboratory space, equipments, manpower, resources, etc., scaled test specimens are constructed to investigate the structural behavior of the cylindrical vessels. According to the sliding shear strength calculation (Paulay et al. 1982) and the finite element simulations, two test specimens are designed to be 1/13-scaled given a loading limitation of 5880 kN. Both of the 1/13-scaled specimens have an exterior diameter of 2.5 m, an interior diameter of 2.2 m, and a height of 2.25 m as shown in Fig. 9.2. Specimen 1 has a steel ratio of 2% with the reinforcement extending into the top and bottom blocks. In light of the sliding shear failure occurred on the top portion of Specimen 1, additional dowel rebars were added so that the vertical steel ratio became 4% at the top and bottom quarter of Specimen 2, as shown in Fig. 9.3. Figure 9.4 shows the photos taken during the experiments of Specimen 2.

9.2.2 Material Properties of the Specimens

Two steel plate boxes are provided for the top and bottom blocks and are filled with concrete and large amount of steel reinforcement. Besides constructing two very rigid blocks, the in-filled concrete in the top and bottom blocks are confined to avoid cracking by means of post-tensioning tie rods. For the cylindrical shell,

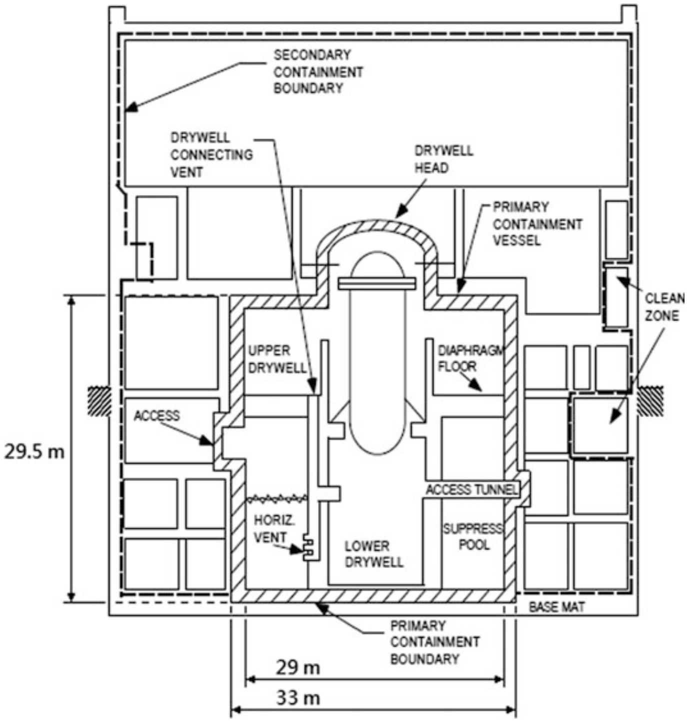

Fig. 9.1 Architectural and structural drawing of an ABWR containment building (slight modification from General Electric (GE) Nuclear Energy 1997)

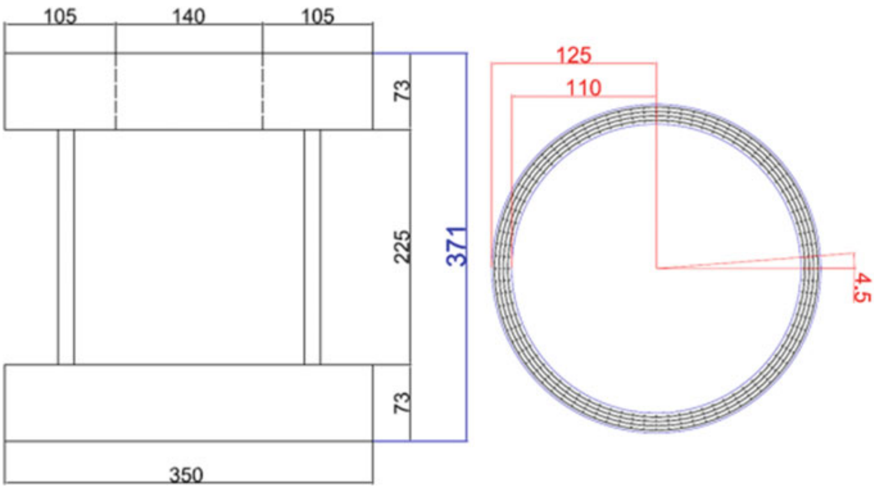

Fig. 9.2 Dimensions of 1/13 scale containment models

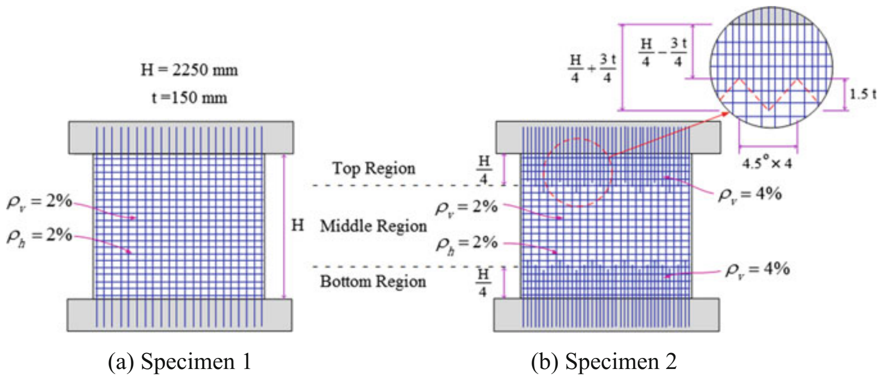

Fig. 9.3 Reinforcement detail of the test specimens

Fig. 9.4 Photographical view of experimental setup

self-compacting concrete mixes were used to accommodate the small reinforcement spacings of the scaled specimens so as to reach the desired strengths and workable conditions. The maximum aggregate size used was 8 mm with a slump of 68 cm. Table 9.1 summarizes major properties of concrete and steel obtained from material tests, including concrete compressive strength (f_c'), Young's modulus of concrete (E_c), steel yield strength (f_y), steel yield strain (ε_y), steel ultimate tensile strength (f_u), Young's modulus of steel (E_s), and coefficient of variation (COV) for material properties.

Table 9.1 Properties of concrete and steel bars from material tests

Concrete		Specimen 1			Specimen 2			
		f_c'		E_c	f_c'		E_c	
		Mean (MPa)	COV (%)	Mean (MPa)	Mean (MPa)	COV (%)	Mean (MPa)	
		37.0	4.2	20984	43.4	2.6	27764	
Steel		Specimens No. 1 & No. 2						
Bar code	Diameter (mm)	E_s		f_y		ε_y	f_u	
		Mean (MPa)	COV (%)	Mean (MPa)	COV (%)		Mean (MPa)	COV (%)
#2	6.0	189529	9.95	376	0.52	0.00198	565	0.4
#3	9.5	204949	2.45	379	0.29	0.00185	572	0.1

9.2.3 Test Setup and Loading Protocols

Eight actuators were used for each of both specimens to apply the horizontal cyclic loading, while four vertical actuators were utilized for the specimens to maintain the up-right position, avoid tilting, and ensure the double curvature structural behavior. Figures 9.5 and 9.6 show that the layout of the horizontal and vertical actuators for Specimen 2. A similar setup was used on Specimen 1. Furthermore, L-frames were utilized as the force transmission beams to allow the resultant force of the horizontal cyclic loads to pass through the mid-height of the specimen, which is to avoid bending moment acting on the specimens. The loading protocols for Specimens 1 and 2 are shown in Fig. 9.7.

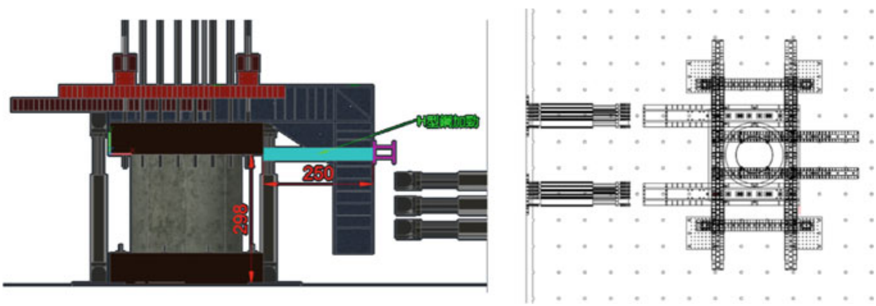

(a) Elevation view (b) Top view

Fig. 9.5 Schematic drawings of experimental setup

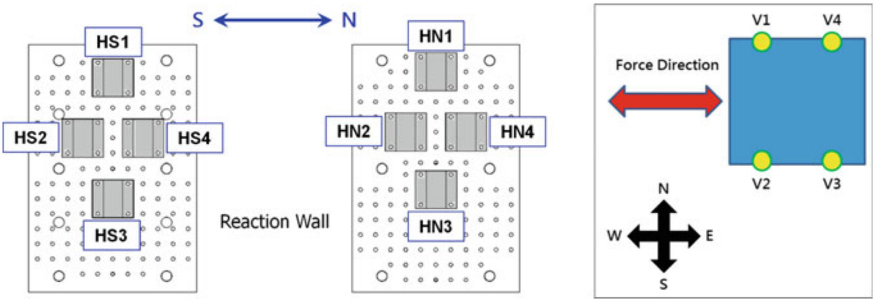

(a) Horizontal actuators (b) Vertical actuators

Fig. 9.6 Layout of vertical and horizontal actuators

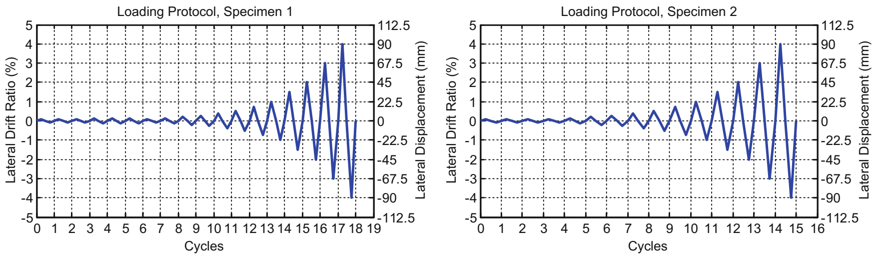

(a) Specimen 1 (b) Specimen 2

Fig. 9.7 Target reversed cyclic loading protocols

9.2.4 Sensor Installations

Six types of measurement systems were installed in the test setup. They are Temposonics displacement sensors, dial gauges, string potentiometers, Optotrak Certus HD optical measurement system, high-resolution digital cameras, and strain gauges. These measuring systems are located on the surface, at the top and bottom blocks, and around the specimens. These measurements provide abundant information on the seismic behavior of the specimens. The installation of each type of measurement systems is separately introduced in the following sections.

9.2.4.1 Temposonics Magnetostrictive Displacement Sensors

The Temposonics displacement sensors are located at the four corners of the top block as shown in Fig. 9.8 (V1t, V2t, V3t, and V4t). The four sensors were placed vertically for measuring the vertical displacements which show the tilting and rotating actions of the specimens should they occur. Another two sensors (HN1t and HS1t in Fig. 9.8) were placed horizontally for measuring the horizontal displacements along the loading direction. These two horizontally placed Temposonics displacement sensors serve as loading indicator for a displacement-controlled experiment in this study.

9.2.4.2 Dial Gauges

The installation of dial gauges (DG) is shown in Fig. 9.9. DG_1, DG_2, DG_3, and DG_4 were installed for Specimen 1 to ensure that the horizontal movements between the bottom block and the strong floor do not take place, while DG_5, DG_6, and DG_7 were installed to ensure that the uplifts of bottom block do not occur. The same applied to Specimen 2.

9.2.4.3 String Potentiometers

String potentiometer (SP) setup is shown in Fig. 9.10. At the four corners of the top block, ten SPs (i.e., SP_1 to SP_10) were installed to measure the specimen's movements in the vertical and the two horizontal directions. Moreover, SPs were also attached to the L-shape loading frame for Specimen 2, shown on the left side in Fig. 9.10. Measurements from SP_11 and SP_12 provided the deformations of the loading arms of the L-shape frames. Small deformation is favorable to ensure a rigid loading frame.

Fig. 9.8 Installation of Temposonics displacement sensors

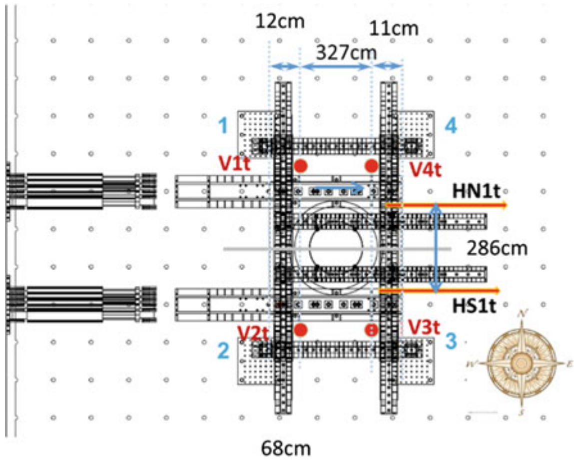

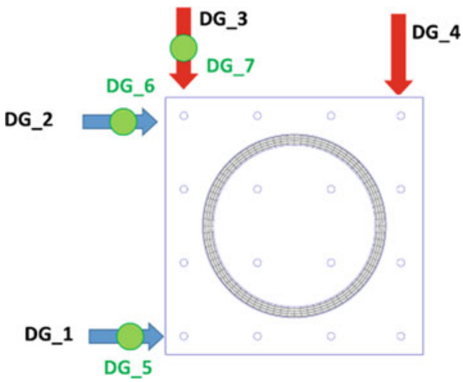

Fig. 9.9 Locations of dial gauges

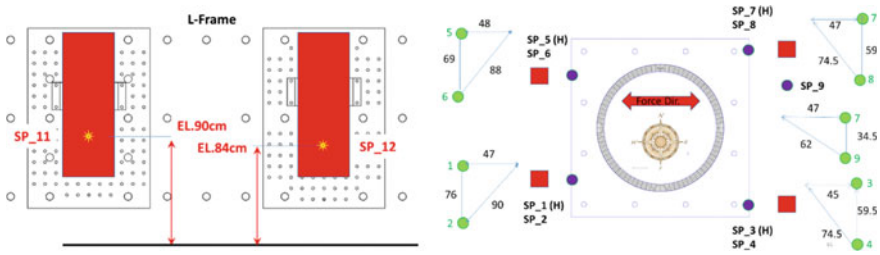

Fig. 9.10 Layout of string potentiometers

9.2.4.4 Optotrak Certus HD Optical Measurement System

The distribution of infrared LED markers (indicated as small dots) for the Optotrak Certus HD optical measurement system is shown in Fig. 9.11. LED markers were attached to embedded tie rods that were installed during the construction stage and ran through the entire thickness of the cylindrical shell. LED markers on the cylindrical surface come with constant intervals for comprehensive observation of the shell deformation and behavior. LED markers were also placed on the top and bottom blocks near the boundary of the cylindrical shell. Measurements from these LED markers gave an insight into the displacements field of the specimen.

9.2.4.5 Full-Frame High-Resolution Digital Cameras

Multiple high-resolution digital cameras were located around the specimens as shown in Fig. 9.12. These cameras simultaneously take photos at each loading step during the experiments. These photos provided a full history of the cracking patterns and their developments.

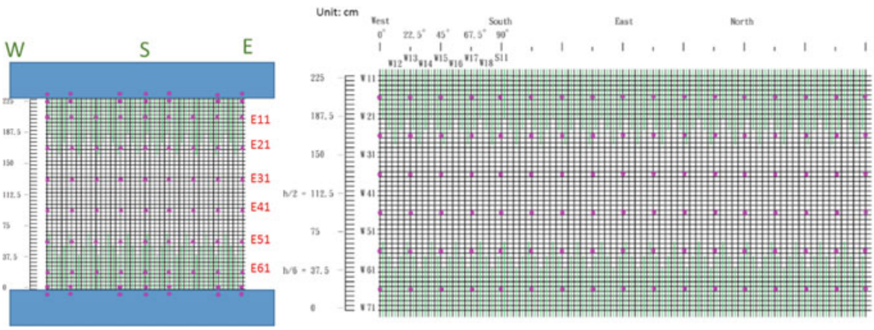

Fig. 9.11 Distribution of infrared LED markers for 3D displacement measurements

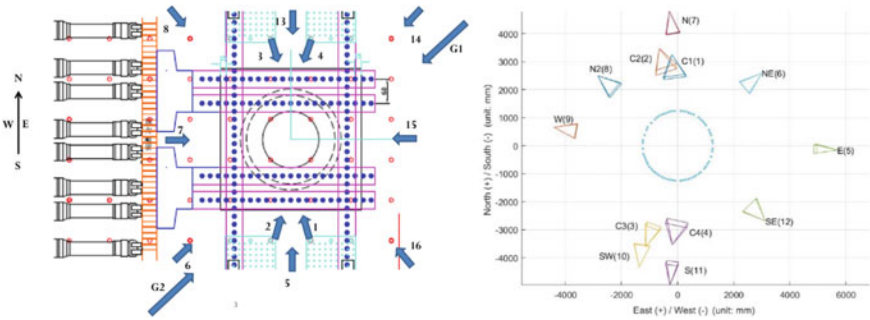

(a) Specimen No. 1 (b) Specimen No. 2

Fig. 9.12 Layout of full-frame high-end digital cameras array

9.2.4.6 Strain Gauges

Strain gauges (SG) were placed on the vertical and horizontal reinforcing bars with constant intervals as shown in Fig. 9.13. These measurements represent the strain fields of the specimen, thus clearly elaborate the structural behavior under the cyclic loading.

9.3 Loading Procedures

As shown in Figs. 9.5 and 9.6, the eight horizontal actuators are marked as HN1 to HN4 on the north side and HS1 to HS4 on the south side. These two groups of actuators applied the cyclic loadings via the north L-frame and the south L-frame, respectively. Since it was a displacement-controlled experiment, the drift ratio served as an indicator for applying cyclic loadings. Measurements of the

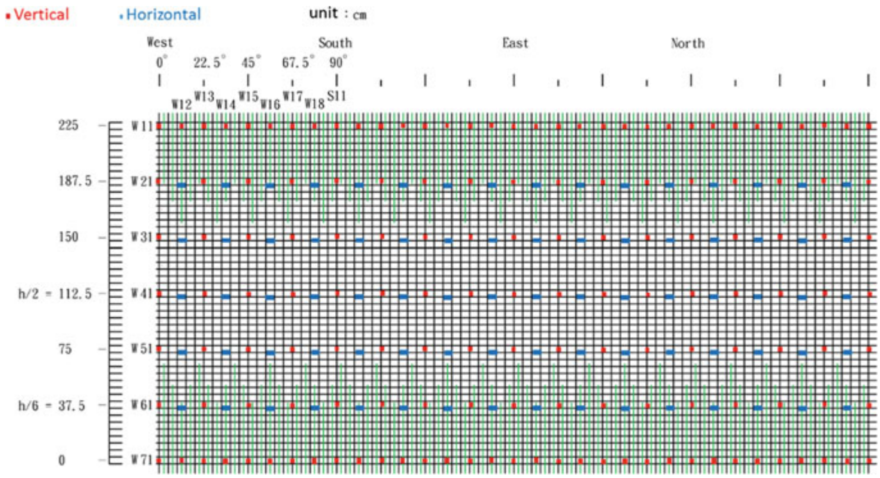

Fig. 9.13 Distribution of strain gauges on vertical and horizontal rebars

Temposonic displacement sensors HN1t and HS1t, shown in Fig. 9.8, provided the displacements needed to compute the drift ratios. Actuators HN1 and HS1 utilized the displacement measurements of the Temposonic sensors HN1t and HS1t, respectively, for determining their loading steps. The three actuators HN2 to HN4 then followed the loading force of HN1 and each applied the same amount of force onto the north L-frame. A similar arrangement is applied to actuators HS2 to HS4 for the south L-frame.

The four vertical actuators were marked as V1 to V4 in Fig. 9.6. The original plan for V2, V3, and V4 were displacement-controlled, given the displacement of actuator V1 as the target movement. However, due to the malfunctioning of the built-in displacement transducer in actuator V3, the actions of actuator V3 was changed to force-controlled. The actions of actuator V1 became dependent on the force required, which was 160 kN (the desired gravity load) minus the forces in V2, V3, and V4.

The achieved loading histories for Specimens 1 and 2 are shown in Fig. 9.14. The total steps of loading are 1045 and 1398 for Specimens 1 and 2, respectively. Figure 9.15 shows the relationships of the horizontal actuator force and the corresponding drift ratio. The predictions conducted by Hsu et al. (2017) from the University of Houston is shown in this figure to compare with the experiment results. The maximum horizontal force applied on Specimen 1 was 5577 kN with a drift ratio of 0.53% and its strength decreased afterward. For specimen 2, the maximum horizontal applied force was 5807 kN with a drift ratio of 0.92% and its strength decreased afterward.

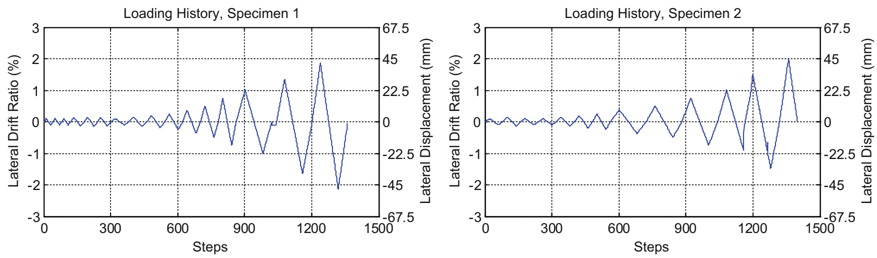

(a) Specimen 1 (b) Specimen 2

Fig. 9.14 Achieved reversed cyclic loading protocols

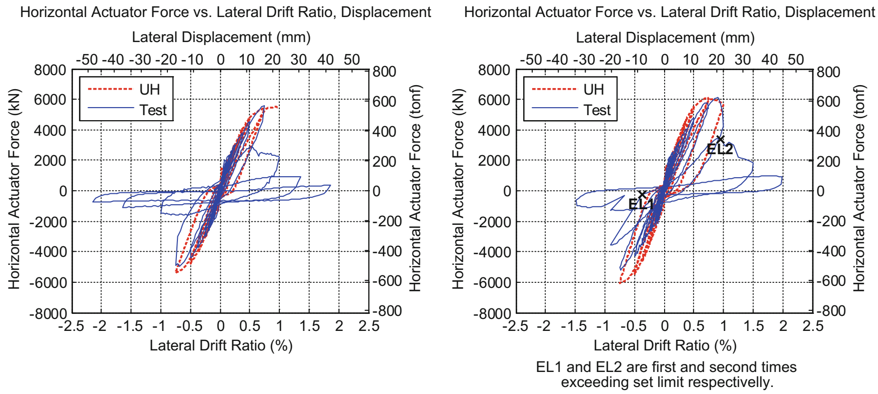

(a) Specimen 1 (b) Specimen 2

Fig. 9.15 Experimental hysteretic loops

9.4 Experimental Results

In order to better understand the seismic behavior, five critical states are selected as follows: (1) first crack of concrete; (2) the maximum horizontal force; (3) drift ratio of 1%; (4) first yield of circumferential reinforcing bars; (5) first yield of vertical reinforcing bars. Table 9.1 summarizes the applied horizontal force and the corresponding drift ratio of each of the five critical states mentioned above for the two specimens.

9.4.1 Hysteretic Loops and Critical States of Engineering Importance

Taking a look at the first quadrant of the horizontal force versus drift relationship (i.e., positive force versus positive drift) as shown in Fig. 9.16a, Specimen 1 reaches its peak strength of 5580 kN (point T2) at a corresponding drift ratio of +0.74%, while the prediction made by CSMM-based finite element analysis (Hsu et al. 2017) is 5404 kN (point U2) and the corresponding drift ratio is accurately predicted. At the +1% drift cycle, Specimen 1 sustained a sudden sliding shear failure at its top portion of the cylindrical wall making its strength degrade from 3189 kN to 2224 kN (point T3) along a mild in-cycle descending slope. This sliding shear failure is accurately captured by CSMM-based FEA through monitoring the vertical bar yielding in the previous loading cycle (Paulay et al. 1982). As for Specimen 2 (Fig. 9.16b), the peak strengths observed from the test and prediction made by the CSMM-based FEA are 6113 kN (point T2) and 6120 kN (point U2), respectively, and their corresponding drift ratios are 0.9% (point T2) and 0.75% (point U2). At the +1% drift ratio, the strength drops from its peak suddenly to 4245 kN (point T3) within the same loading cycle because an abrupt large-piece of concrete cover spalled from the cylindrical wall, which cannot be captured by simulation so that the CSMM-based FEA yielded a prediction of 5668 kN (point U3) under a slight in-cycle strength degradation. Both specimens had their peak strengths before reaching +1% drift and demonstrated abrupt and significant strength loss at +1% drift due to the reasons described above. The shear strength of Specimen 1 at +1% drift ratio is only 52% of that for Specimen 2. Table 9.2 summarizes the critical states of engineering importance. The first yield of circumferential rebars of Specimen 1 took place at a negative drift ratio of −0.35%, which is mapped into the first quadrant of the horizontal force versus drift relationship in Fig. 9.16a (i.e., point T4*).

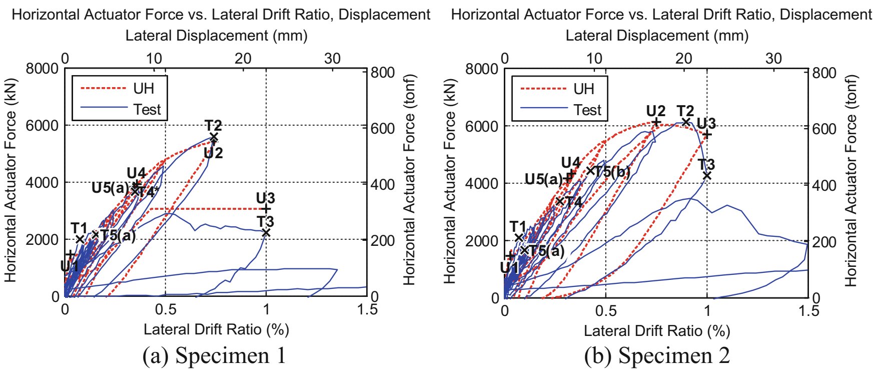

Fig. 9.16 Horizontal load versus drift ratio relations in the first quadrant and their critical states of engineering importance

Table 9.2 Critical states of engineering importance

Critical state	Status	Horizontal force (kN)		Interstorey drift (%)	
		Specimen 1	Specimen 2	Specimen 1	Specimen 2
1	Initial crack of concrete	1993	2095	0.077	0.073
2	Peak strength	5580	6113	0.743	0.899
3	Drift ratio at 1%	2227	4245	1.002	1.000
4	First yield of circumferential rebar	−3634	3338	−0.35	0.276
5(a)	First yield of vertical rebar (Top and Bottom Region)	2144	1660	0.156	0.099
5(b)	First yield of vertical rebar (Middle Region)	–	4426	–	0.427

9.4.2 Concrete Crack Widths

The largest crack widths at the concrete surface of the cylindrical walls were measured as shown in Table 9.3 for Specimen 1 and Table 9.4 for Specimen 2. In the case of Specimen 1, crack widths were measured at the drift ratios of 0.25, 0.375, and 0.5% in both the positive and negative directions. When Specimen 1 was restored back to its initial condition (non-deformed position) after each loading cycle, the largest crack widths were measured again to represent its residual crack widths. As the crack widths of the containment structure taking place during an earthquake may decrease or even close after the earthquake, experimental observations in this regard would help reconnaissance inspectors in the field to gain insight of the possible damage experienced by the structure. A similar procedure was carried out for Specimen 2 at the drift ratios of 0.1, 0.15, 0.2, 0.25, 0.375, 0.5, and 0.75% (see Table 9.4). Due to the safety consideration of personnel, crack width measurements were not performed at the drift ratios greater than 0.5% for Specimen 1, and 0.75% for Specimen 2.

Table 9.3 Crack width development of Specimen 1

Interstorey drift (%)	North face		South face		East face		West face	
	Shear crack width (mm)				Flexural crack width (mm)			
	Max	Residual	Max	Residual	Max	Residual	Max	Residual
+ 0.25	0.15	0	0.25	0.05	0.15	0	0.15	0
−0.25	0.15	0	0.15	0	0.25	0	0.25	0
+0.375	0.15	0	0.3	0.05	0.15	0	0.1	0
−0.375	0.25	0.05	0.3	0.05	0.25	0	0.3	0
+0.5	0.35	0.1	0.35	0	0.45	0.3	0.15	0.1
−0.5	0.3	0	0.3	0.05	0.25	0	0.6	0.2

9.4.3 Failure Modes

The two test specimens were almost identical; however, the failure modes of the two specimens were very different. Specimen 1 failed due to the sliding shear that happened at the top of the specimen, as shown in Fig. 9.17a. The peak load of Specimen 1 might have been higher if the sliding shear had not occurred. The sliding shear cracks started to occur on the top of the specimen at a drift of 0.5% and became larger when the load increased. Before the sliding shear failure, no critical damage of the concrete and reinforcement was observed in the specimen. Learning from the failure of Specimen 1, vertical steel bars(called dowel bars) were doubled in the top and bottom regions of Specimen 2 to prevent the sliding shear failure. The method was successful because no sliding shear failure occurred in Specimen 2 and the sliding shear cracks on the top of the specimen were eliminated. As a result, Specimen 2 failed when the concrete crushed in the mid-height region due to the web shear failure as shown in Fig. 9.17b. Specimen 2 reached a higher peak load and a greater deformation when compared to Specimen 1. In Table 9.1, critical load stage (5b) at the middle region shows measurements of 4426 kN for horizontal force and 0.427% for interstorey drift in the case of Specimen 2, but no measurements in the case of Specimens 1.

Table 9.4 Observations of crack width development of Specimen 2

Interstorey drift (%)	North face		South face		East face		West face	
	Shear crack width (mm)				Flexural crack width (mm)			
	Max	Residual	Max	Residual	Max	Residual	Max	Residual
+0.10	0.1	0.05	0.1	0.05	0.1	0.05	0.05	0
−0.10	0.1	0.05	0.15	0.05	0.1	0.05	0	0
+0.15	0.15	0.05	0.15	0.05	0.15	0.05	0.1	0
−0.15	0.15	0	0.15	0	0.15	0.05	0.05	0
+0.20	0.25	0.05	0.2	0.05	0.2	0.05	0.15	0
−0.20	0.15	0.05	0.2	0.05	0.2	0.05	0.05	0
+0.25	0.25	0.05	0.25	0.05	0.2	0.05	0.2	0
−0.25	0.25	0.05	0.25	0.05	0.25	0.05	0.1	0
+ 0.375	0.3	0.05	0.35	0.05	0.25	0.05	0.25	0
−0.375	0.35	0.05	0.35	0.05	0.25	0.05	0.2	0
+0.50	0.45	0.05	0.4	0.05	0.4	0.05	0.25	0
−0.50	0.6	0.05	0.45	0.05	0.45	0.05	0.2	0.05
+0.75	0.65	0.15	0.65	0.2	0.5	0.1	1.3	0.5
−0.75	0.9	0.55	0.6	0.25	1.4	0.9	0.2	0.45

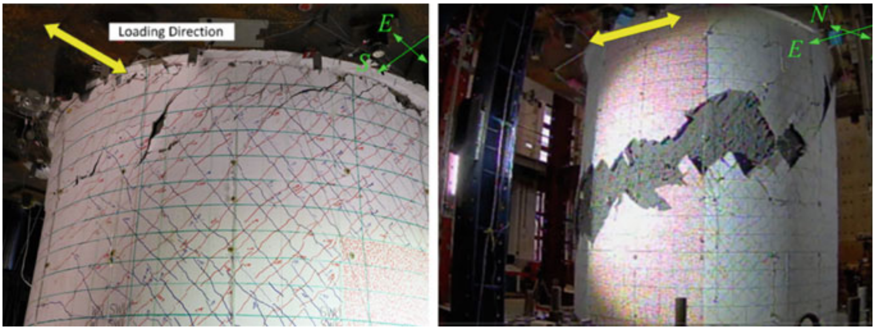

(a) Specimen 1: Sliding shear (b) Specimen 2: Web shear

Fig. 9.17 Photographical view of specimen failure modes at their peak strengths

9.4.4 Strain Contours of Containment Steel Reinforcement

Four layers of #3 vertical reinforcing bars and four layers of #2 circumferential reinforcing bars were installed along the shell thickness. The #3 vertical bars were all continuous along the entire height of the concrete cylindrical walls. The innermost and outermost layers of #2 circumferential bars were lap spliced with point welds to ensure their steel strength could be fully developed, while each of the two intermediate layers of #2 circumferential bars only had about 60 cm of contact lap splices. To observe the overall strain field of steel reinforcement during the cyclic loading process, a dense array of SR4 electrical strain gauges was used on the outer layer of vertical and circumferential reinforcing bars at positions indicated in Fig. 9.13.

Circumferential steel strain contours are plotted in Figs. 9.18 and 9.19 at 1% drift. The symbols of hollow squares represent the positions of strain gauge applications on the outermost layer of circumferential rebars, where digital readings were available; the strain contour is then plotted using linear interpolation scheme connecting digital readings. When a digital reading reaches the tensile yielding strain of steel (i.e., 0.002), the hollow square is then turned into a solid triangle. A solid triangle remains in its position once yielding takes place, but its strain reading will be updated afterward. When a strain gauge fails (i.e., 0.003), the solid triangle is then replaced by a bold “x” cross in the contour and its strain reading at the gauge failure remains unchanged in the contour plot.

The eight horizontal actuators were installed on the west side of the specimen (i.e., 180° from the east) to provide a total of 7,840 kN lateral force maximum. The specimen’s east and west faces sustained flexural cracks, while its north and south faces sustained shear cracks. Figure 9.18 shows several strain gauge failures at the top of the concrete cylindrical walls to echo the sliding shear failure observed in Specimen 1 (Fig. 9.17a). In contrast, Fig. 9.19 shows lots of strain gauge failures at the north and south faces of the concrete cylindrical walls to echo the diagonal shear failure observed in Specimen 2 (Fig. 9.17b).

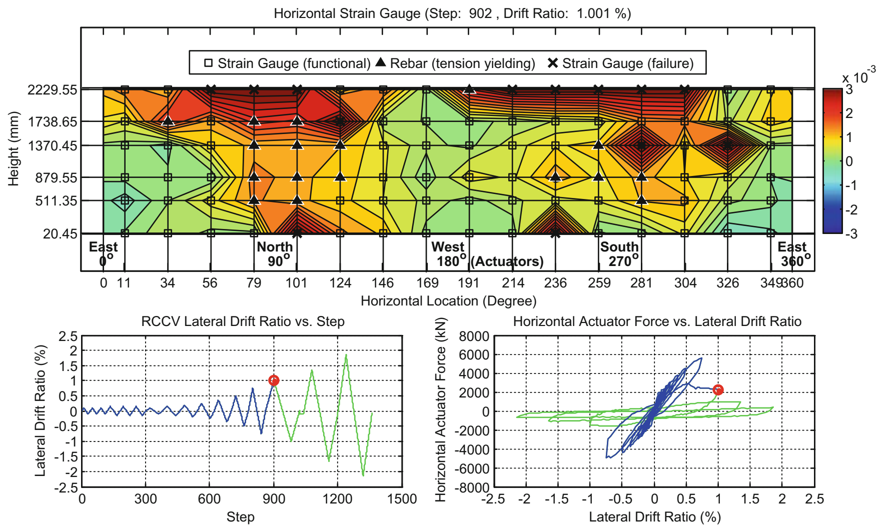

Fig. 9.18 Strain contour of circumferential steel bars of Specimen 1 at 1% drift

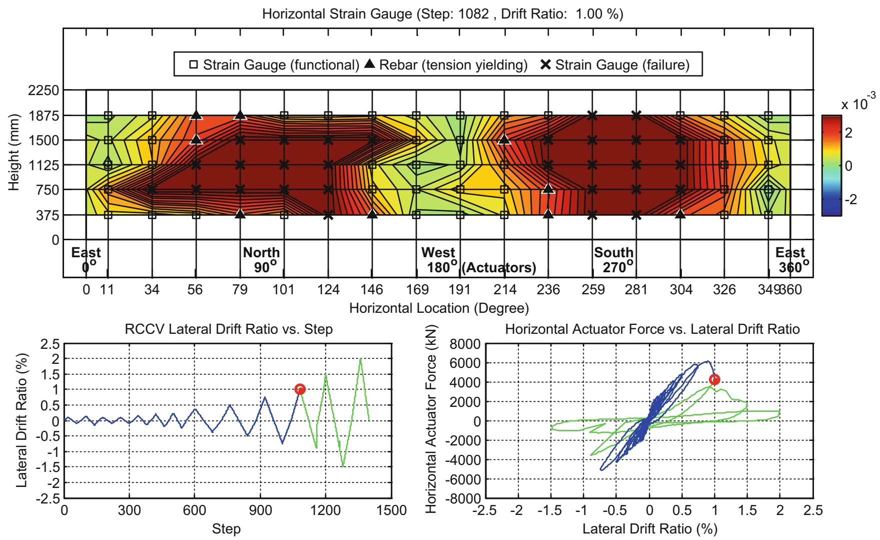

Fig. 9.19 Strain contour of circumferential steel bars of Specimen 2 at 1% drift

9.5 Conclusions

The nuclear containment structure is one of the most important infrastructure systems ensuring the safety of a nuclear power plant. The complex behavior of the RC containment structure has been investigated in an international collaboration project between the National Center for Research on Earthquake Engineering (NCREE) in Taipei, Taiwan and the University of Houston (UH), Houston, Texas. At NCREE two 1/13-scaled cylindrical RC containment specimens were tested under reversed cyclic loads. At UH, a finite element simulation of the two tested specimens was developed using a finite element analysis (FEA) program SCS. This paper summarizes the following findings:

- The two containment specimens sustained two different failure mechanisms, i.e., sliding shear failure and web diagonal shear failure. The sliding shear failure can be successfully predicted by the formula of Paulay et al. (1982).
- The shear strengths of specimens continue to rise after the first yield of rebars to show overstrength, but structural ductility is limited due to lack of clear yielding plateau.
- The flexural cracks appear in the east and west faces of concrete cylindrical walls, which is along the direction of horizontal actuator loading. Shear cracks appear in the north and south faces of concrete cylindrical walls, which is perpendicular to the direction of horizontal actuator loading.
- Crack widths observed at the positive and negative drift peaks of each loading cycle for both specimens get significantly thinner when specimens were restored back to their undeformed position (i.e., initial condition). This is true for both flexure and shear types of cracks. Cracks having widths smaller than 0.3 mm may completely close when specimens were restored back to 0% drift. This observation can serve as useful information in post-earthquake reconnaissance tasks.

Acknowledgements The facilities and technical support from the National Center for Research on Earthquake Engineering are gratefully acknowledged. Special thanks are due to Yi-Lung Mo and Hieu-Cong Luu for comments and suggestions during the preparation of the manuscript, and Kung-Juin Wang for his assistance in conducting the tests. All opinions expressed in this paper are solely those of the authors and do not necessarily represent the views of their affiliated institutions.

References

Hirama, T., Goto, M., Shiba, K., Kobayashi, T., Tanaka, R., Tsurumaki, S., Takiguchi, K., & Akiyama, H. (2005). Seismic proof test of a reinforced concrete containment vessel (RCCV) Part 2: Results of shaking table tests. *Nuclear Engineering and Design, 235,* 1349–1371.

Hsu, T. T. C., Belarbi, A., & Xiaobo, P. (1995). A universal panel tester. *Journal of Testing and Evaluation, 23*(1), 41–49.

Hsu, T. T. C., Luu, C. H., & Mo, Y. L. (2017). Development of CSMM-based shell element for reinforced concrete structures. *Engineering Structures, 132,* 778–790.

Hsu, T. T. C., & Mansour, M. (2005). Behavior of reinforced concrete elements under cyclic shear: Part 1—experiments. *Journal of Structural Engineering, ASCE, 131*(1), 44–53.

Hsu, T. T. C., & Mo, Y. L. (2010). *Unified theory of concrete structures*. John Wiley & Sons.

Hsu, T. T. C., Mo, Y. L., & Xiang, H. J. (2012). *Seismic simulation of RC wall-type structures using sofened shell model in Chinese*. *Journal of Building Structures (建筑结构学报), 3,* Beijing, China.

Luu, C. H. (2016). *Development of CSMM-based shell element for reinforced concrete structures*. University of Houston, PhD Dissertation, Houston, TX.

OpenSees. (2013). Annual workshop on open system for earthquake engineering simulation. In *paper presented at the Pacific Earthquake Engineering Research Center, UC Berkeley, CA*.

Paulay, T., Priestley, M., & Synge, A. (1982). Ductility in earthquake resisting squat shearwalls. *Journal of the American Concrete Institute, 79*(4), 257–269.

Saito, H., Muramatsu, Y., Furukawa, H., Tsurumaki, S., Tanaka, N., & Kei, T. (1991). Experimental study on RCCV of ABWR plant. *Nuclear Engineering and Design, 130,* 179–202.

Saito, H., Muramatsu, Y., Furukawa, H., Hasegawa, T., & Mutoh, A. (1993). Post-test analysis of a 1:10- scale top slab model of ABWR/RCCV subjected to internal pressure. *Nuclear Engineering and Design, 145,* 339–353.

United States Nuclear Regulatory Commission (NRC). (1997). *Issued design certification - advanced boiling-water reactor (ABWR)*. http://www.nrc.gov/reactors/new-reactors/design-cert/abwr.html.

Chapter 10
Understanding the Seismic Behaviour of FRP Retrofitted RC Shear Walls: Past and Present

David T. Lau, Joshua E. Woods, Ahmed Hassan, Jeffrey Erochko, Carlos Cruz-Nuguez and Ibrahim Shaheen

This paper provides an overview of studies on experimental testing and analytical modelling of reinforced concrete (RC) shear walls retrofitted with externally bonded fiber-reinforced polymer sheets (FRP) conducted at Carleton University. The experimental investigations include cyclic lateral load tests on FRP retrofitted RC shear walls in repair and strengthening applications, including those with varying aspect ratios ranging from slender flexural walls to squat walls dominated by brittle shear behaviour. The effectiveness of the FRP retrofit in recovering or enhancing the earthquake resistance of deficient rc structures as well as those that meet modern design standards are investigated. Parallel to the experimental studies, analytical research has also been carried out to develop computer models for predicting the behaviour and performance of FRP retrofitted RC shear walls. These include simplified models suitable for design as well as detailed models that capture the complex interaction and debonding failure mechanisms of the FRP sheets. Ongoing studies combine experience with experimental and analytical modelling and focus

D. T. Lau (✉) · J. E. Woods · A. Hassan · J. Erochko · I. Shaheen
Department of Civil and Environmental Engineering, Carleton University, Ottawa, Canada
e-mail: David.Lau@carleton.ca

J. E. Woods
e-mail: JoshWoods@cmail.carleton.ca

A. Hassan
e-mail: AhmedHassan@cmail.carleton.ca

J. Erochko
e-mail: Jeffrey.Erochko@carleton.ca

I. Shaheen
e-mail: IbrahimShaheen@cmail.carleton.ca

C. Cruz-Nuguez
Department of Civil and Environmental Engineering, University of Alberta, Edmonton, Canada
e-mail: cruznogu@ualberta.ca

T. T. C. Hsu (ed.), *Concrete Structures in Earthquake*,
https://doi.org/10.1007/978-981-13-3278-4_10

on the use of hybrid simulation to accurately capture the system-level earthquake response and performance of FRP retrofitted RC shear walls.

10.1 Introduction

Reinforced concrete (RC) shear walls are an efficient lateral-loading resisting system often used in structures located in seismically active regions. Although performance during recent earthquakes has shown that shear wall buildings that meet current codes of construction have an overall satisfactory seismic behaviour, many older structures are still at risk of suffering severe damage during moderate or large earthquakes because of insufficient in-plane stiffness, flexural, and shear strengths and/or ductility (Lombard et al. 2000). Among the retrofit and repair options available, an attractive, minimally disruptive option for the repair and strengthening of RC shear walls is the use of externally bonded fiber-reinforced polymer (FRP) sheets. The majority of research to date on the seismic retrofit of RC shear walls using FRP sheets has focused on the use of FRP jackets to improve shear strength, energy dissipation capacity, and confinement of the boundary elements in shear wall specimens (Antoniades et al. 2003; Paterson and Mitchell 2003; Khalil and Ghobarah 2005). In comparison, the number of studies that address the use of FRP to increase (in strengthening applications) or restore (in repair applications) the flexural strength of RC shear walls is limited due to concerns over promoting brittle shear failures when additional flexural capacity is provided. However, increasing the flexural strength of structures is often required when retrofitting older buildings to meet current design code requirements. Table 10.1 summarizes the work presented in this paper, which explores experimental and analytical results obtained during nearly 20 years of research at Carleton University on the effectiveness of using externally bonded carbon fiber-reinforced polymer (CFRP) sheets to enhance the flexural and shear strength in RC shear walls. The developed FRP retrofitting system is designed to promote a ductile behaviour in RC shear walls while preventing premature failures in shear. The FRP retrofitting system has been tested on wall specimens with varying geometry, steel reinforcement details, and CFRP configurations. The objectives of the studies are to (1) obtain experimental evidence on the effectiveness of the FRP system in enhancing the flexural/shear strength, stiffness, and ductility of RC shear walls; (2) develop an FRP-concrete anchor system to prevent premature FRP debonding failures; (3) obtain insight on the response behaviour and failure modes of FRP-reinforced shear walls; (4) develop analysis models to capture the nonlinear response of RC walls reinforced with FRP sheets, including concrete-FRP debonding mechanisms; and (5) adapt the use of hybrid simulation to study the global system level and local earthquake response of FRP retrofitted RC shear wall structures.

Table 10.1 Summary of past and present shear wall tests conducted at Carleton University

Phase	Design details	Type of specimens	Aspect ratios	Test type	FRP anchor system
1	Modern	Control/Repaired/ Strengthened	1.20	Reversed cyclic	Angle anchor
2	Modern	Control/Repaired/ Strengthened	1.20	Reversed cyclic	Tube anchor
3	Seismically deficient	Control/Repaired/ Strengthened	0.65 0.85 1.20	Reversed cyclic	Optimized tube anchor
4	Modern	Control/Repaired	1.20	Hybrid	Optimized tube anchor

10.2 Experimental Testing

The effectiveness of using externally bonded CFRP sheets for repair and strengthening of RC structural walls has been investigated through experimental tests conducted on a number of RC shear wall specimens tested under reversed cyclic loading, shown in phases 1 through 3 in Table 10.1. Phases 1 and 2 of the experimental study focused on the feasibility of using FRP sheets as a practical retrofitting solution to enhance the strength and stiffness in flexurally dominated slender walls. After verifying the feasibility of the proposed FRP retrofitting system, phase 3 extended the scope of the research and focused on the ability of the retrofitting system to improve the flexural/shear strength and ductility of nine seismically deficient walls, designed according to older design standards (ACI 318 1968; CSA A23.3 1977). The structural deficiencies in the wall specimens included insufficient shear reinforcement, poor confinement at the boundary elements, and lap splices in the plastic hinge region. Phase 3 included slender and squat wall specimens with three different aspect ratios (1.20, 0.85 and 0.65). Phase 4, which is currently ongoing, is focused on the use of hybrid simulation to capture both the local and global seismic response of a multi-story RC shear wall structure. The use of hybrid simulation allows for the inclusions of dynamic effects, including mass and damping, in the experimental testing of a RC shear wall. Using a substructuring approach, the local failure mechanisms that cannot be easily captured in a finite element model are accounted for in the experimental substructure, while the analytical substructure captures the global response of the rest of the structure.

10.2.1 Flexurally Dominated Walls

The test specimens in phases 1 and 2 comprise seven cantilevered RC shear walls subjected to reversed cyclic in-plane lateral load. All wall specimens were designed according to the Canadian Concrete Design Standard (CSA A23.3 2004), which ensured the wall specimens would exhibit ductile failure before reaching brittle failure modes associated with shear. The wall specimens included two control walls (CW), two repaired walls (RW), and five strengthened walls (SW). The control walls had no FRP reinforcement and no previous damage. They were tested in their original state to serve as a baseline for the evaluation of the repair and strengthening techniques on conventional RC walls that have suffered repairable damage from a moderate to large earthquake. After being subjected to cyclic loading, the control specimens were repaired with one vertical layer of CFRP sheet on each side of the wall and the specimens were tested again to failure. Strengthened wall specimens were retrofitted with CFRP sheets in the vertical direction prior to testing. To avoid brittle shear failure, some of the walls were reinforced with an additional layer of CFRP in the horizontal direction to increase their shear strength. Additional design details and experimental testing configurations are available in Lombard et al. (2000), Hiotakis (2004), and Cruz-Noguez (2014). Figure 10.1 shows the force-deformation response of each shear wall specimen from phases 1 and 2 of the experimental program. These results show the efficiency of the CFRP retrofitting system in increasing the load carrying capacity and ductility of the shear wall specimens in both repair and strengthening applications. Experimental results show that the initial stiffness of the strengthened wall specimens was significantly increased when vertically oriented CFRP layers were provided, whereas in the case of repaired wall specimens the CFRP system was only able to recover the initial stiffness of the control wall specimen.

Phases 1 and 2 experimental results also showed that FRP-concrete debonding mechanisms play a major role in the response of FRP-reinforced RC shear walls, limiting the forces carried by the debonded FRP material. Concrete-FRP debonding starts when flexural cracks form in areas next to the wall edges at the base. In the repaired specimens, debonding of the CFRP material is first observed at locations of previous cracks, which reopen during reloading. In both repaired and strengthened wall specimens, debonding propagates rapidly within a few loading cycles spreading upwards and towards the center of the wall. This type of FRP-concrete debonding that occurs in areas with flexural cracks is known as intermediate crack (IC) debonding (Cruz-Noguez et al. 2014) and effects the transfer of interfacial stresses between concrete and FRP materials.

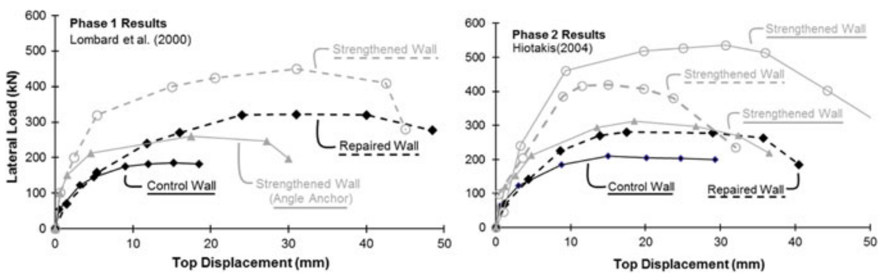

Fig. 10.1 Load-deformation response of the phase 1 and 2 flexurally dominated slender walls

In addition to the influence of debonding on the response of the RC shear wall specimens, phases 1 and 2 also demonstrated the importance of providing an adequate anchor system for the transfer of loads between the FRP sheets and the adjacent structural element to fully realize the benefit of the FRP materials. Observations by Lombard et al. (2000) during phase 1 tests found that the steel angle anchor system used to transfer the load carried by the vertical CFRP layers to the foundation of the shear wall specimen performed poorly because it promoted debonding of the FRP material from the concrete wall prior to the FRP material reaching its ultimate capacity. As illustrated in Fig. 10.2, failure of the steel angle anchor system occurred because of the eccentricity between the tensile force within the FRP sheet and the tie-down reactions of the anchoring bolts. The eccentricity between these two forces caused a moment that ultimately leads to the rotation of the steel angle, also referred to as "prying" action, which was detrimental to the anchors performance. Motivated by the observed behaviour of the steel angle anchor system, an innovative anchor system consisting of a steel tube section was developed. The FRP sheet is wrapped around the steel tube and epoxy bonded to adjacent structural elements. The design of the anchor is based on the pulley principle: as the FRP sheet is loaded in tension, the vertical force in the FRP sheet is equated by the tension in the horizontal portion of the FRP sheet. By wrapping the CFRP sheet around the tube and placing the anchor bolts in the direction of the resultant load the eccentricity between the force in the FRP sheets and anchor bolts was eliminated. Phase 2 results demonstrated excellent performance of the tube anchor system and served as a proof-of-concept. Results showed that the tube anchor system allowed the FRP to carry additional load even after the FRP material deboned from the concrete substrate, ultimately leading to FRP rupture in tension at its ultimate strength. However, results suggested that further optimization of the tube anchor could improve its design efficiency for future tests, which was a primary goal of phase 3 testing.

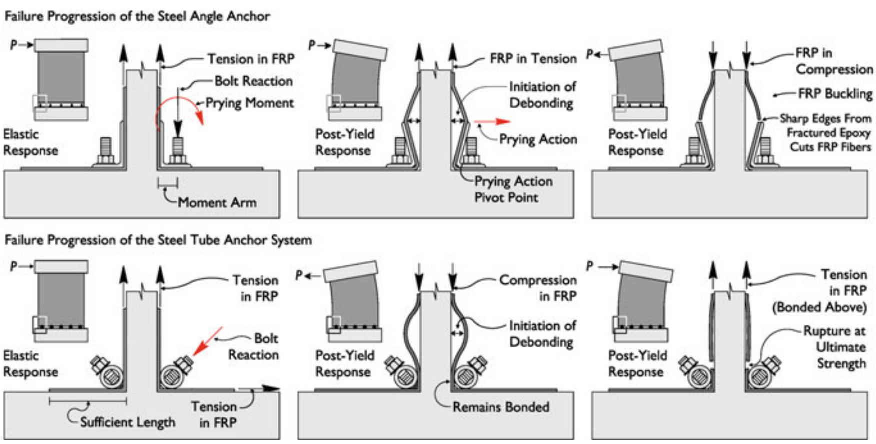

Fig. 10.2 Performance comparison of the steel angle and tube anchor systems

10.2.2 Seismically Deficient Walls

Phase 3 of the shear wall experimental program focused on nine deficient RC shear wall specimens. The structural deficiencies in the walls were intended to represent design details typically found in older construction (ACI 318 1968; CSA A23.3 1977). These deficiencies include insufficient shear reinforcement, poor confinement in the boundary elements, and low concrete compressive strength. The test specimens included two wall specimens with aspect ratios (h_w/l_w) of 1.20, three walls with h_w/l_w = 0.85, and four walls with h_w/l_w= 0.65. Two of the four walls with h_w/l_w= 0.65 had lap splices at the plastic hinge region. Additional design details for these shear walls tests are available in Woods et al. (2016, 2017).

The wall specimens include a control wall for each aspect ratio, which is cyclically tested to failure and then repaired. The repaired specimens provide insight on the ability of the retrofitting system to improve the seismic performance of shear walls that may have experienced some damage during an earthquake and require retrofitting to return the structure to service and meet the current code requirements. The remaining specimens were strengthened with CFRP prior to testing with no previous damage. In the wall specimens with aspect ratios of 1.2 and 0.85, the externally bonded CFRP sheets are applied in the vertical and horizontal directions. The retrofitting scheme aims to facilitate a ductile flexural behaviour in the wall specimens while improving their in-plane flexural strength and preventing any premature shear failure from occurring. Vertically oriented CFRP layers are not provided in the wall specimens with aspect ratios of 0.65 because of the high shear stresses that must be transferred in low aspect ratio squat shear walls and only horizontal CFRP layers are provided. In phase 3, following the observed satisfactory performance of the steel tube anchor in phase 2, the design of the tube anchor system was optimized to improve its cost-efficiency while maintaining its effectiveness. In addition, a detailed design procedure for the steel tube anchor system was been developed. Detailed design and optimization of the tube anchor system are discussed in more detail by Lau and Woods (2017).

Figure 10.3 shows the force-deformation response of the wall specimens tested in phase 3 of the study. The results confirm that walls designed according to older design standards, particularly those detailed with insufficient shear reinforcement and poor confinement of the boundary elements are susceptible to sudden and brittle diagonal tension shear failure with little to no ductility or energy dissipation capacity. Overall, the phase 3 results show that by applying externally bonded CFRP sheets in combination with an effective anchor system the retrofitting system is capable of preventing premature shear failure and enhances the seismic response of deficient shear wall specimens. The results show the influence of aspect ratio on the performance of the retrofitting system. In slender, flexurally dominant wall specimens, the application of FRP sheets significantly improve the strength an ductility in deficient shear wall specimens in repair and strengthening applications. However, as the aspect ratio increases, the effectiveness of the retrofitting system decreases because of their inherent shear dominant behaviour of squat RC shear walls. Nonetheless, the FRP retrofitting system restores the initial stiffness in repair applications and improve the strength of low aspect ratio squat wall specimens. In squat walls with lap splices in the plastic hinge region, the FRP retrofitting system was found to be able to restore the damaged walls to their original state when sufficient lap splice length was provided, however, the retrofitting system was less effective in wall specimens with insufficient lap splice length, which requires more intrusive retrofitting measures to restore their strength and stiffness.

Results from the phase 3 also showed that the optimized steel tube anchor system performs well in transferring the load from the vertical CFRP laminate to the foundation of the shear wall specimen. The optimized tube anchor system was shown to prevent premature debonding of the vertical CFRP sheet and allow the CFRP to reach its ultimate tensile capacity, identified by tearing of the vertical CFRP.

10.3 Analytical Modelling

In addition to experimental testing, analytical modelling of structural walls subjected to in-plane loading has also been conducted parallel to experimental testing over the past 20 years at Carleton University. Finite element analysis models using of 2D membrane elements have been developed using program VecTor2 (Wong and Vecchio 2002) and OpenSees. Program VecTor2 allows for the modelling of

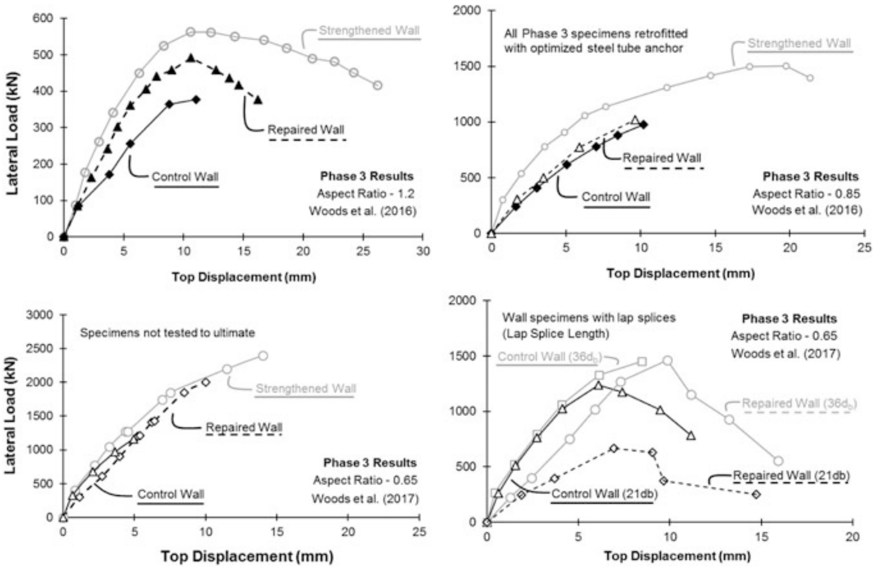

Fig. 10.3 Load-deformation response of the phase 3 shear dominant walls

concrete under normal and shear stresses as an orthotropic material with smeared, rotating cracks. Four-node quadrilateral elements are used to model the concrete. To model the concrete pre-peak and post-peak response behaviour, the Popovics and the modified Park-Kent model for the concrete materials are used, respectively. To model the steel rebars and stirrups, the various reinforcement ratios at different regions of the wall are modelled as uniformly distributed reinforcement. The steel rebar material is modelled as an elastic–plastic material with strain hardening. The CFRP sheets are modelled by a series of discrete truss elements made of a brittle material with zero compressive strength. The connection between the CFRP truss elements and the concrete at the bottom of the wall is represented using the common-node method since mechanical anchorage between FRP and concrete is provided at the base. For the rest of the wall, zero-length link elements are used to connect the FRP trusses and the concrete elements. Additional details on the VecTor2 finite element modelling approach are available in Cruz-Noguez et al. (2014).

To evaluate the ability of the analysis model developed in this study to capture the behaviour of plain RC shear walls, the hysteretic response of two control specimens from phases 1 and 2 of the experimental program are compared with the measured results in Fig. 10.4. These specimens have no FRP reinforcement and are intended to serve as a reference for the behaviour of conventional RC walls subjected to moderate to large earthquakes. It is observed that the experimental response in terms of strength, initial stiffness, and energy dissipation are closely predicted by the analysis model.

The influence of FRP-concrete debonding on an FRP-strengthened or repaired shear wall is illustrated by considering the analytical results for an FRP-strengthened wall specimen from phase 2 in Fig. 10.5. Due to space considerations, only results pertaining to one wall specimen are presented, although results for other walls were found to be similar (Cruz-Noguez et al. 2014). It is shown that neglecting the effects of the FRP-concrete debonding leads to a significant overestimation of the maximum load carrying capacity of the shear wall and an overall poor correlation between the analytical and experimental cyclic

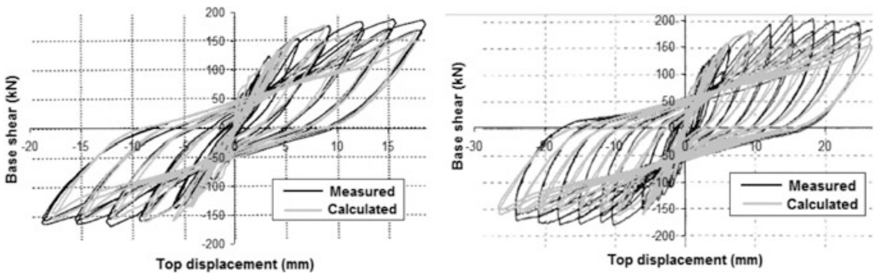

Fig. 10.4 Analytical and experimental hysteretic response comparison for flexurally dominated plain RC walls

behaviour. In contrast, when considering the effects of FRP-concrete debonding, the FRP separates from the concrete as soon as FRP-concrete slip exceeds that associated to the maximum peak stress, which translates into a gradual loss of load carrying capacity because FRP-concrete separation occurs before the FRP trusses fracture. Figure 10.5 shows that analytical results using this modelling approach agree with the experimental observations from phase 1 and 2 tests.

More recently, detailed finite element models have been developed in OpenSees because of its ability to conduct nonlinear time history analysis under the effects of earthquake ground motions as well as its robust set of solution algorithms (McKenna et al. 2000). In OpenSees, the shear wall specimens are modelled using a multi-layered shell element recently developed by Lu et al. (2015). Figure 10.6 shows a typical layered shell element and the distribution of its layers in comparison with a conventionally constructed shear wall specimen. The multi-layer shell element is based on the ShellMITC4 element, which is a four-node shell element that reduces the complex 3D behaviour of a shear wall into a 2D shell by discretizing each layer of a RC shear wall (e.g. cover concrete, horizontal steel reinforcement, vertical steel reinforcement, core concrete, etc.) into several fully bonded layers. In this approach, discrete steel rebars are “smeared” into a thin layer which covers the entire element.

A thickness is assigned to each layer of the RC shear wall until the complete thickness of the RC shear wall is represented. Each layer of the shell element is assigned a uniaxial constitutive relationship which is transformed into a plane stress relationships for concrete and steel. The steel is modelled using a Steel02 material model, which includes isotropic strain hardening and the Bauschinger effect. The concrete model is based on the damage mechanism and smeared crack model. Figure 10.7 shows the nonlinear material models assigned to the concrete and steel reinforcement and compares the finite element modelling results with phase 2 experimental data for a plain RC shear wall specimen without FRP sheets (Hiotakis et al. 2004). Results show that the multi-layered shell element is able to capture the strength, ductility, and energy dissipation capacity of the RC shear wall specimen. Future studies will aim to incorporate the influence of FRP-concrete debonding into the OpenSees finite element modelling approach to capture the behaviour of FRP

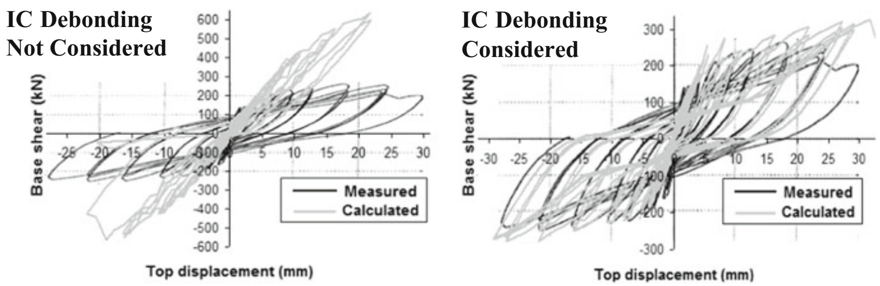

Fig. 10.5 Influence of IC debonding mechanism on the response of specimen SW1-1

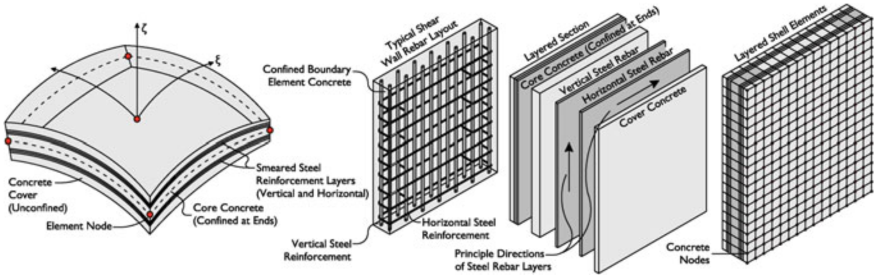

Fig. 10.6 Multi-layered shell element for modelling RC shear wall structures

retrofitted RC shear walls. In the current study, this modelling approach in OpenSees is adapted to a full-scale RC shear wall structure and tested using hybrid simulation, which is discussed in the following section of this paper.

10.4 Hybrid Simulation

Recently, research into experimental testing and analytical modelling of FRP retrofitted RC shear walls have come together and have been applied to hybrid simulation. The use of hybrid simulation provides a cost-effective and accurate method to capture the overall behaviour of full-scale structures. In the hybrid testing technique, the portions of a structure that are expected to experience significant nonlinear behaviour are tested in a laboratory, while the rest of the structure is modelled numerically in a finite element program. The process of splitting the structure into experimental and numerical components is referred to as substructuring. The portion of the structure that is tested in the laboratory is referred to as the experimental or physical substructure, while the remaining portion of the building that is modelled in a finite element software is referred to as the numerical

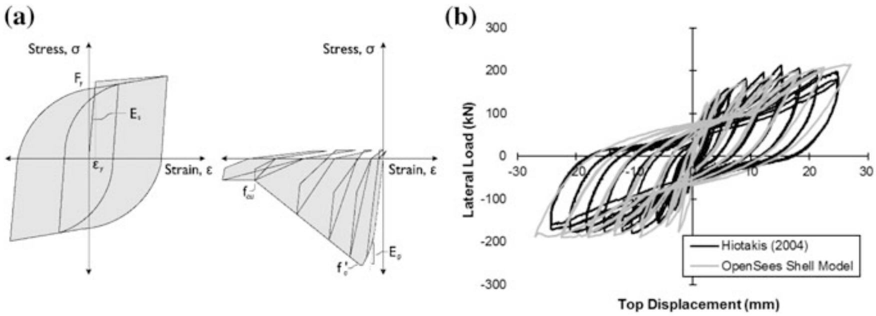

Fig. 10.7 **a** Steel and concrete material models; **b** Hysteretic response comparison with experimental results obtained by Hiotakis (2004)

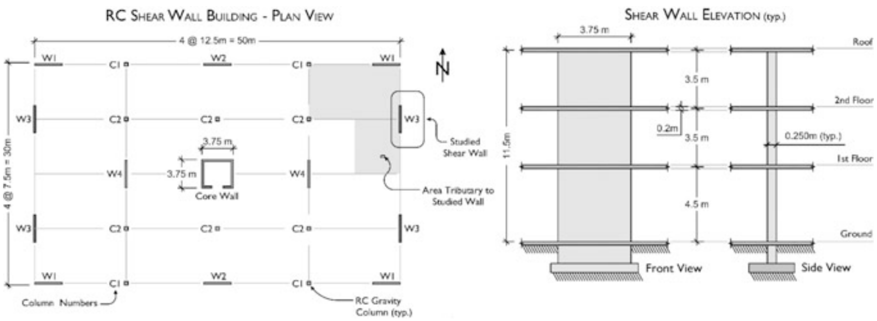

Fig. 10.8 Floorplan and typical shear wall for prototype structure

or analytical substructure. The benefits of hybrid simulation stem from its ability to accurately incorporate the nonlinear behaviour of structural elements that are difficult to model analytically into the response of a full-scale structure by physically testing them in a laboratory, eliminating the need for expensive full-scale tests.

The prototype structures for the hybrid simulation is a three-storey RC shear wall structure. The structure is designed in Victoria, British Columbia, a seismically active region on the west coast of Canada. Figure 10.8 shows a typical floor plan and a single bay of the seismic force resisting system for the prototype structure. The SFRS consists of six moderately ductile RC shear walls and a central core wall in each of the two principle directions (CSA A23.3 2004). The gravity load resisting system is a flat two-way slab and square RC columns.

The goal of the study is to use hybrid simulation to capture the local failure mechanisms of the first-storey shear wall while also capturing the global response of the three-storey structure. However, because concrete shear walls are very stiff structural elements, this presents a challenge on the hydraulic control side of the hybrid simulation; because a small change in displacement can cause a large increment in force. This study will also examine the strategies for overcoming these challenges when using hybrid simulation to test stiff structures.

In the prototype RC structure, the shear walls are designed to survive a major seismic event through the formation of a plastic hinge at their base, dissipating seismic energy and, assuming the shear wall have sufficient ductility, preventing the structure from reaching the collapse state. Due to the highly nonlinear response of the plastic hinge region, it can be difficult to capture its response accurately in a finite element model. Through the use of hybrid simulation, the first-storey shear wall can be selected as the physical substructure, such that its exact nonlinear response can be determined, including local failure mechanisms. The remaining stories of the RC structure are modelled numerically, forming the analytical substructure, assuming that their response will remain at or near elastic. Figure 10.9 shows the physical and analytical substructures for the multi-storey shear wall. Because of the long analysis times associated with modelling the entire RC structure, only a single shear wall is selected for the current hybrid simulation.

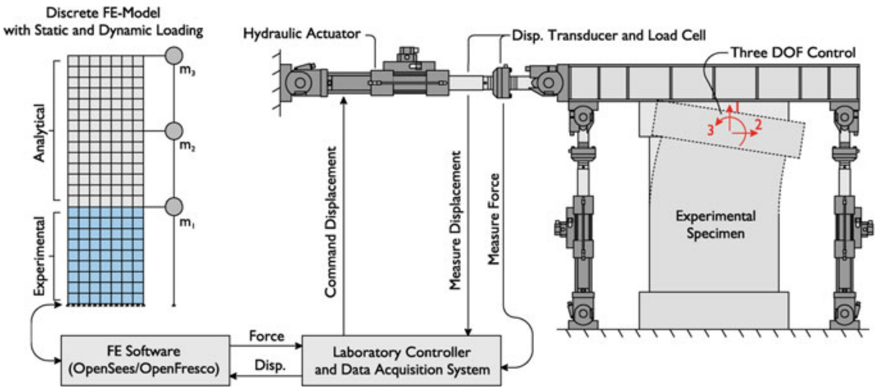

Fig. 10.9 Analytical and physical substructures of the three-storey shear wall structure

Future studies will aim to incorporate the surrounding shear walls into the hybrid simulation. To account for the presence of axial load, shear force and overturning moment, three actuators are required to accurately represent the three degrees-of-freedom force/deformation response at the top of the first-storey shear wall.

To facilitate a hybrid simulation, a communication link between the analytical substructure in the finite element program and the hydraulic control equipment responsible for imposing the target displacements on the physical substructure is required. In this study, the Open Framework for Experimental Setup and Control middleware, commonly referred to as OpenFresco is used to communicate between analytical and experimental substructures (Schellenberg 2009). Figure 10.9 illustrates the three-DOF hybrid testing setup at Carleton University in for a local (one experimental site) hybrid simulation using OpenFresco. In this hybrid test setup, OpenFresco is responsible for sending command displacements to the physical substructure, which are then applied to the wall specimen and load cells/ displacement transducers send the feedback displacement and force back to OpenFresco using MTS Csi communication link from the MTS controller in the laboratory.

Figure 10.10 illustrates the experimental test setup for the RC shear wall hybrid simulation. The shear wall tests are conducted in the horizontal position to accommodate for the length of the hydraulic actuators. A rigid steel loading beam that is connected to a heavily reinforced concrete cap beam is used to transfer the axial, shear and overturning moment applied by the three actuators to the test specimen. A restraint is also fixed to the top of the wall to prevent out of plane displacement/rotation of the shear wall test specimen. At the base of the wall, a heavily reinforced foundation block and a second large supporting block placed adjacent to the shear wall foundation provide sliding/rotational resistance. At this time, the hybrid shear wall tests are ongoing and preliminary test results demonstrate the accuracy and advantage of the hybrid simulation approach.

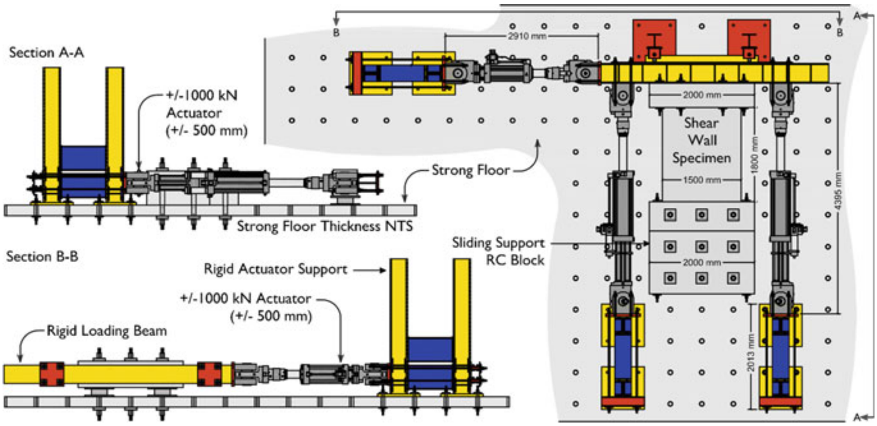

Fig. 10.10 Hybrid testing experimental test setup

10.5 Conclusions

The paper presents an overview of nearly 20 years of research into experimental testing and analytical modelling to better understand and predict the seismic behaviour of RC shear walls repaired and strengthened using externally bonded FRP sheets. Experimental results have validated the feasibility of using a reinforcing system consisting of vertical and horizontal FRP sheets to increase the flexural and shear strengths, enhance ductility, and increase energy dissipation ability of shear walls with varying geometry, steel reinforcement ratios, and steel reinforcement detailing. Experimental results have also demonstrated that the FRP retrofitting system can recover the majority of the initial elastic stiffness and to increase the maximum flexural capacity of seismically damaged RC shear walls. In strengthening applications, the FRP retrofitting system has been shown to significantly increase the stiffness and the ultimate flexural capacity of undamaged walls. The anchoring system has been shown to be a critical component of the FRP retrofitting system. An innovative tube anchor has been developed to prevent premature failure of FRP sheets and a simple design procedure for the design of the tube anchor, suitable for use in practice, has been developed. The application of the FRP system in seismically deficient walls has been analytically investigated by finite element analysis models. Developed models are shown to be able to account for FRP-concrete debonding effects, which are critical components of the model to accurately predict the cyclic response of FRP retrofitted RC shear walls. Ongoing studies are focused on the use of hybrid simulation to capture the earthquake response of a multi-storey shear wall, combining analytical, and experimental substructures.

Acknowledgements The contributions from current and former graduate researchers on the project are acknowledged. The research team includes former graduate students Stelios Hiotakis, Nicolas Londono and Joshua Lombard. Funding for the research program has been provided by the Canadian Foundation for Innovation, Canadian Seismic Research Network, Natural Sciences and Engineering Research Council Canada and Public Works and Government Services Canada. This support and the FRP materials and technical assistance provided by Fyfe Co LLC, Brighton Engineering Taiwan, and Master Builders Technologies are gratefully acknowledged.

References

ACI 318. (1968). *Building code requirements for structural concrete*. American Concrete Institute, Detroit, Michigan, USA.

Antoniades, K., Salonikios, T., & Kappos, A. (2003). Cyclic tests on seismically damaged reinforced concrete walls strengthened using fiber-reinforced polymer reinforcement. *ACI Structural Journal, 100*(4), 510–518.

Cruz-Noguez, C., Lau, D., & Sherwood, E. (2014a). Seismic behaviour of RC shear walls with externally bonded FPR sheets: Analytical studies. *Journal of Composites for Construction, 18*(5), 1–11.

Cruz-Noguez, C., Lau, D., Sherwood, E., Hiotakis, S., Lombard J., Foo, S., & Cheung, M. (2014). Seismic behaviour of RC shear walls strengthened for in-plane bending using externally bonded FRP sheets. *Journal of Composites for Construction,* **19**(1).

CSA. (1977). *Code for the design of concrete structures for buildings*, *CAN3-A23.3-M77.* Canadian Standard Association, Rexdale, Ontario, Canada.

CSA A23.3. (2004). *Design of concrete structures.* Canadian Standards Association, Rexdale, Ontario, Canada.

Hiotakis, S. (2004). *Repair and strengthening of reinforced concrete shear walls for earthquake resistance using externally bonded carbon fibre sheets and a novel anchor system*. Master's thesis, Department of Civil and Environmental Engineering, Carleton University.

Khalil, A., & Ghobarah, A. (2005). Behaviour of rehabilitated structural walls. *Journal of Earthquake Engineering, 9*(3), 371–391.

Lau, D., & Woods, J. (2017). A concentric tube anchor system for fiber-reinforced polymer retrofit of reinforced concrete structural walls under extreme loads. *International Journal of Protective Structures, 9*(1), 1–22.

Lu, X., Xie, L., Guan, H., Huang, Y., & Lu, X. (2015). A shear wall element for nonlinear analysis of super-tall buildings using OpenSees. *Finite Element Analysis and Design, 98*(1), 14–25.

Lombard, J., Lau, D., Humar, J., Foo, S., & Cheung, M. (2000). Seismic strengthening and repair of reinforced concrete shear walls. In *Proceedings of the 12th world conference on earthquake engineering*, paper 2032.

McKenna, F., Fenves, G., Scott, H., & Jeremic, B. (2000). Open system for earthquake engineering simulation (OpenSees). In *Pacific earthquake engineering research center,* University of California at Berkeley. http://opensees.berekeley.edu/.

Paterson, J., & Mitchell, D. (2003). Seismic retrofit of shear walls with headed bars and carbon fiber wrap. *Journal of Structural Engineering, 129*(5), 606–614.

Schellenberg, A., Mahin, S., & Fenves, G. (2009). Software framework for hybrid simulation of large structural systems. *In Proceedings of the ASCE structures congress,* long beach, California. http://openfresco.berkeley.edu.

Wong, P. S., & Vecchio, F. J. (2002). *VecTor2 and FormWorks user's manual (Publication No. 2002–02).* Toronto, ON, Canada: University of Toronto, Department of Civil Engineering.

Woods, J., Lau, D., & Cruz-Noguez, C. (2016). In-plane seismic strengthening of nonductile reinforced concrete shear walls using externally bonded CFRP sheets. *Journal of Composites for Construction,* **20**(6).

Woods, J., Lau, D., Cruz-Noguez, C., & Shaheen, I., Repair of earthquake damaged squat reinforced concrete shear walls using externally bonded CFRP sheets. In *Proceedings of the 16th world conference on earthquake engineering,* paper 1693.

Chapter 11
Seismic Response and Collapse Risk of Shearwall Buildings Subjected to Long Duration Ground Motion

Carlos E. Ventura, Michael Fairhurst, Armin Bebamzadeh and Ilaria Capraro

The damage caused by large subduction earthquakes is due in part to high number of load reversal cycles. Experimental and analytical studies indicate that shaking duration and number of cycles contribute to the damage. Currently, building codes do not include explicit design provisions for shaking duration. This paper investigates how shaking duration affects the response of tall, shearwall buildings in British Columbia, which is located in the Cascadia subduction zone. A suite of concrete shearwall archetype building models are analyzed with suites long and short duration ground motions. A case study of a reinforced concrete frame is presented to illustrate that long duration shaking can also affect significantly their seismic response. The results are useful for the elaboration of design provisions to account for shaking duration.

11.1 Introduction

Currently, the effect of ground motion duration on the damage or collapse probability of structures is not well established. This is in part due to different conclusions reached by researchers studying ground motion duration or number of cycles using

C. E. Ventura (✉) · M. Fairhurst · A. Bebamzadeh · I. Capraro
Department of Civil Engineering, The University of British Columbia, Vancouver, BC, Canada
e-mail: ventura@civil.ubc.ca

M. Fairhurst
e-mail: fairhurstmike@gmail.com

I. Capraro
e-mail: ilaria.capraro@gmail.com

T. T. C. Hsu (ed.), *Concrete Structures in Earthquake*,
https://doi.org/10.1007/978-981-13-3278-4_11

observational evidence, experimental testing, and numerical modeling. Some studies (e.g., Bommer et al. 1997; Iyama and Kuwamura 1999) have observed greater damage caused by the rapid energy release in short duration crustal events, while others suggest that the large number of cycles from subduction interface events cause greater damage (e.g., Tremblay 1998).

Hancock and Bommer (2006) provide a comprehensive state-of-knowledge review on the effect of ground motion duration on structural damage. In their review, they note that most studies using cumulative damage or displacement measures find a correlation between ground motion duration and structural damage. However, studies that use extreme responses (such as maximum interstorey drift or displacement) generally do not find correlations between duration and damage. This, however, may be to a lack of cyclic degradation in the models employed in many of these studies. Additionally, most of the experimental tests reviewed showed a high degree of relevance of ground motion duration and number of cycles on specimen damage.

More recently, a study by Chandramohan et al. (2015) found that the probability of structural collapse increases with increasing ground motion duration when records have equivalent response spectra. A similar study by Raghunandan and Leil (2013) on the collapse risk of structures in the Cascadia Subduction Zone showed that longer duration events can cause collapse at lower intensity levels compared to shorter events. Both of these studies were done using reinforced concrete moment frame numerical models which included cyclic strength and stiffness degradation.

In this paper, the effect of ground motion duration on concrete buildings is investigated. Five prototype Vancouver coupled concrete shearwall buildings from 6 to 30 storeys are considered. A six-storey concrete frame building in Victoria is also considered as part of the study. Cyclic and in-cycle degradation is accounted for in the coupling beam models as well as the material models used in fiber sections of the shearwalls. Two suites of spectrally equivalent records are run at various levels of shaking, from code design level all the way to collapse level. The code-level motions are used to see of ground motion duration effects typical code design, while collapse level motions are used to determine if the collapse risk of the structure is correlated with ground motion duration.

11.2 Prototype Shearwall Building Models

The prototype buildings for this study are a typical reinforced concrete shearwall buildings designed for Vancouver, BC. Buildings with 6, 12, 18, 24, and 30 storeys are considered. The lateral load resisting system of the buildings includes three interior reinforced concrete shearwalls which comprise the elevator and stair core of the buildings. The gravity resisting system of the buildings comprise perimeter and exterior circular columns and 8″ slabs at each level. The prototype building layouts were based on typical designs from a study by Green and Karsh (2012). The structural system and core of the buildings are illustrated in Fig. 11.1.

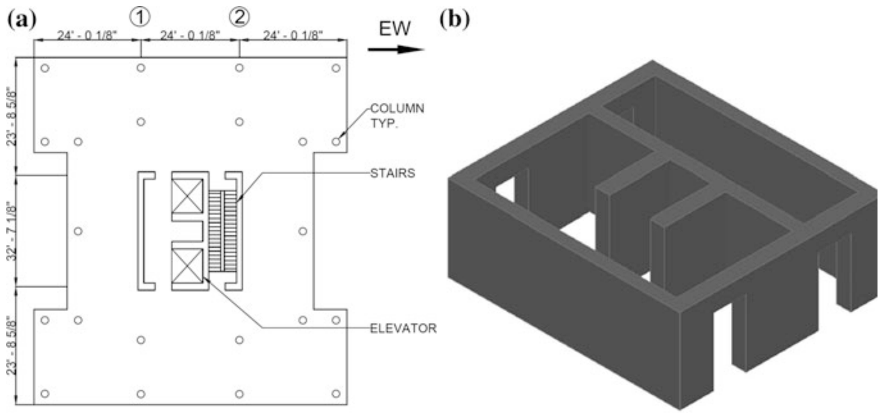

Fig. 11.1 Prototype building: **a** typical floor plan and **b** illustration of core

The floor area is about 5200 ft^2 per storey and the weight is calculated as 0.21 kip/ft^2 (approximately 10 kN/m^2). Three sets of core walls were designed: one for buildings up to 12 storeys, another for buildings up to 20 storeys, and a final design for buildings up to 30 storeys. Reinforcement in the shearwalls for buildings up to 30 storeys is illustrated in Fig. 11.2. The reinforcement in the walls along lines 1 and 2 is the same. The walls are connected by 2′ deep header beams (Fig. 11.3) which are reinforced by transverse 15 M stirrups spaced at 4″.

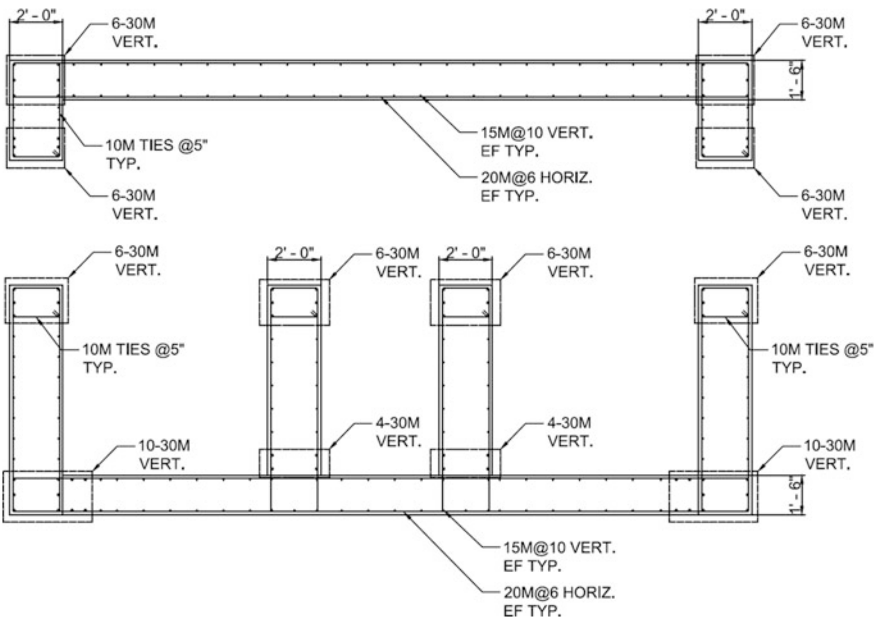

Fig. 11.2 Reinforcement of the interior shearwalls for models up to 30 storeys

The buildings were designed for a base shear calculated in accordance with the National Building Code of Canada (NBCC) 2010 for Vancouver, BC. Only the softer EW direction was considered for analysis.

11.3 Numerical Model

A numerical model of the buildings was developed in OpenSees (McKenna et al. 2000). The three interior shearwalls were modeled using fiber elements with a displacement-based formulation. The header beams were modeled with elastic beam elements with a cracked section modulus ($I_{cracked} = 0.35 I_{gross}$) to account for bending deformations. Between the header beam elements and wall elements, rigid beams were modeled to account for the physical width of the walls. A shear hinge was modeled at the midpoint of each beam to account for the shear yielding and nonlinearity in the elements.

The header beams are 20″ wide by 24″ deep with 15 M stirrups spaced at 4″ as shown in Fig. 11.3. The nonlinear shear hinge properties were calibrated to a reverse-cyclic test on a similar beam performed by Galano and Vignoli (2000). The nonlinear hinges used the Pinching4 material model to capture pinching, in-cycle degradation, and cyclic stiffness and strength degradation (Lowes et al. 2004). The Pinching4 numerical model comparison to the test results is presented in Fig. 11.4.

The concrete was modeled with the Concrete02 material model (Yassin 1994). Confinement was accounted for using the Mander et al. (1988) relationship. Reinforcing steel was modeled using the ReinforcingSteel material model which accounts for cyclic strength degradation according to Brown and Kunnath (2000) and buckling according to Dhakal and Maekawa (2002). Elastic shear hinges were modeled at the midpoint of each wall in each storey to account for shear deformations in the walls. The hinges were modeled with stiffness equal to the cracked shear area multiplied by the shear modulus divided by the storey height. To account

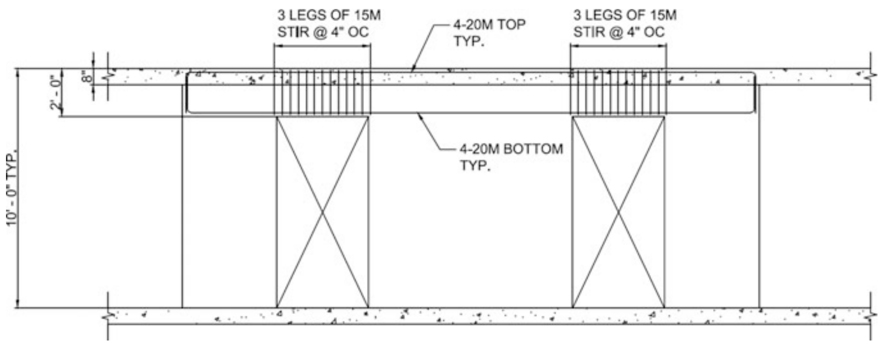

Fig. 11.3 Elevation view of slabs and header beams

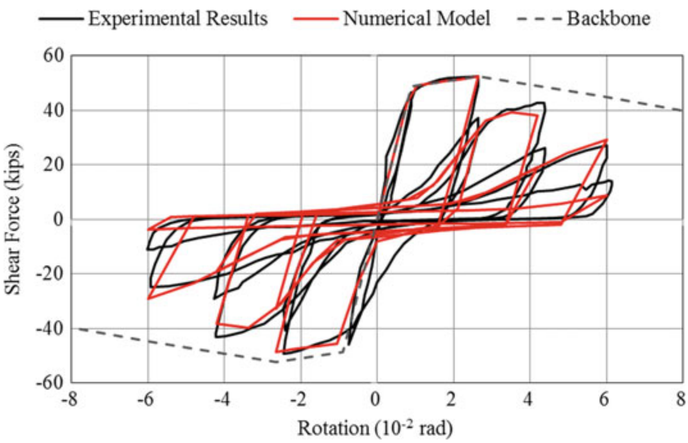

Fig. 11.4 Nonlinear shear hinge model

for the loss of shear area due to cracking, the gross area was multiplied by 0.1 based on the recommendations by Pugh (2012).

The gravity system was not explicitly modeled, but to account for the second order effects of the weight carried by the gravity system a leaning (or PDelta) column was included in the model. The weight of the structure not applied directly on the shearwalls was applied on the leaning column, which was pinned at the base and constrained to the walls at each storey level. Rigid diaphragm constraints were applied at each level. An illustration of the OpenSees model is presented in Fig. 11.5. Damping was taken as 2.5% Rayleigh damping for the first and third modes. The first three periods of the models are summarized in Table 11.1.

11.4 Ground Motion Suites

Two suites of ground motions suites were selected in order to investigate the effect of shaking duration. The records were chosen from the PEER NGA-West1 database (2000) as well as a database comprising several historic subduction interface events obtained from COSMOS (2008) and K-Net (Kinoshita 1998). In order to quantify record duration 5–95% significant duration (D_{5-95}) was adopted. D_{5-95} corresponds to the duration in the ground motion record between 5 and 95% of the total energy accumulation, where energy is expressed as Arias intensity (the time integration of the acceleration squared).

The first suite comprised 30 long duration records selected and linearly scaled to the Vancouver 2015 2% in 50-year spectrum. The events and records selected are summarized in Table 11.2. Most of the events are from subduction interface and large magnitude crustal events.

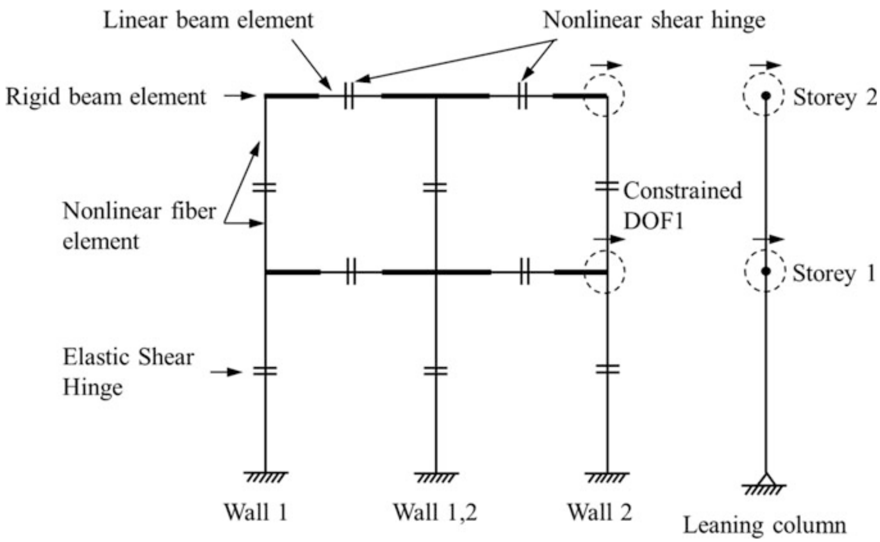

Fig. 11.5 Illustration of OpenSees numerical model

Table 11.1 Periods of the prototype building numerical models

Number of storeys	T1 (s)	T2 (s)	T3 (s)
6	0.44	0.14	0.083
12	1.05	0.32	0.17
18	1.74	0.51	0.26
24	2.56	0.70	0.35
30	3.73	0.85	0.46

For each record in the long duration suite, a spectrally equivalent short duration earthquake record was selected by minimizing the mean squared error between the spectra of the two records. Figure 11.6 illustrates an example of a long record and spectrally equivalent short duration record.

Table 11.3 summarizes the selected short duration record sets. Figure 11.7 presents the spectra of the two suites along with the Vancouver 2015 spectrum. Figure 11.8 compares the significant duration of the two suites.

11.5 Results

The NBCC specifies a ground motion shaking level with a 2% in 50-year probability of exceedance for code-level analysis. Accordingly, the two suites of ground motions were first scaled to the Vancouver NBCC 2015 design spectrum (see Fig. 11.7) and used to analyze the models using nonlinear time history analysis.

Table 11.2 Long duration suite summary

Event	Type	Magnitude (M_w)	Year	Number of stations	Station code(s)
Chi-Chi, Taiwan	Crustal	7.6	1999	7	CHY004, CHY032, CHY055, CHY076, CHY100, CHY116
Hokkaido, Japan	Subduction	8.0	2003	2	HKD125, HKD127
Kobe, Japan	Crustal	6.9	1995	2	ABN, SKI
Kocaeli, Turkey	Crustal	7.6	1999	1	BUR
Landers, Ca.	Crustal	7.3	1992	1	MCF
Michoacan, Mexico	Subduction	8.0	1985	1	VILE
Tohoku, Japan	Subduction	9.0	2011	16	CHB009, CHB010, CHB024, CHB029, FKS022, IBR009, KNG006, KNG201, KNG205, NIG012, SIT009, TKY005, TKY016, TKY017, TKY024, TKY025

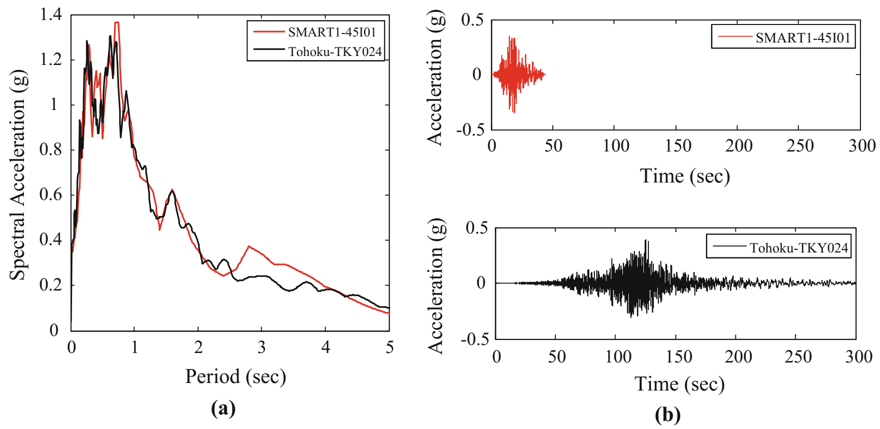

Fig. 11.6 Example spectrally equivalent records **a** spectrum and **b** time histories

The resulting maximum interstorey drifts, storey shear forces and overturning moments for the 30-storey model are shown in Figs. 11.9, 11.10, and 11.11, respectively. The NBCC uses interstorey drifts as a surrogate for structural damage and limits regular buildings to a maximum interstorey drift of 2.5% of the storey height. As seen in Fig. 11.9, on average, neither suite exceeds this drift limit.

The force demands for these two suites of ground motions are similar; however, the drift demands from the long duration suite are slightly higher than the

Table 11.3 Short duration suite summary

Event	Type	Magnitude	Year	Number of stations	Station code(s)
Chi-Chi, Taiwan (3)	Crustal	6.2	1999	1	CHY028
Chi-Chi, Taiwan (4)	Crustal	6.2	1999	1	TCU116
Chi-Chi, Taiwan (6)	Crustal	6.3	1999	2	CHY028, CHY035
Duzce, Turkey	Crustal	7.2	1999	1	DZC
Greece	Crustal	6.2	1999	1	KAL
Imperial Valley, CA	Crustal	6.5	1979	6	E01, E05, E05, E07, ECC, HVP
Kocaeli, Turkey	Crustal	7.6	1999	2	GBZ, IZT
Loma Prieta, CA	Crustal	6.9	1989	6	A01, ADL, CH12, HAD, SLC, SLC
Northridge, CA	Crustal	6.7	1994	5	CCN, LDM, SCE, STM, SYL
San Salvador	Crustal	5.8	1986	1	NGI
Superstition Hills, CA	Crustal	6.5	1987	4	BRA, KRN, POE, PTS

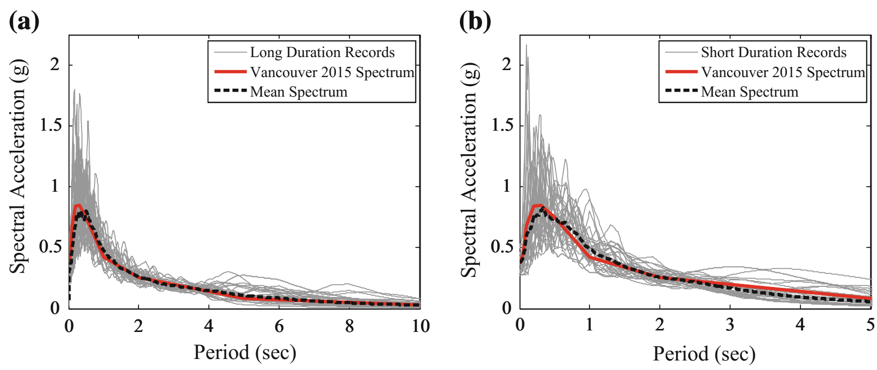

Fig. 11.7 Spectra of **a** long duration suite and **b** short duration suite

equivalent short duration records. This may be because the overall damage (interstorey drift levels) is quite low at this level of shaking. At these lower levels of damage, the amount of degradation in the walls and header beams will be quite low, which will largely nullify the effect of the ground motion duration.

Additionally, the maximum average interstorey drift for each of the other models is summarized in Fig. 11.12. The results are very similar for the two shortest

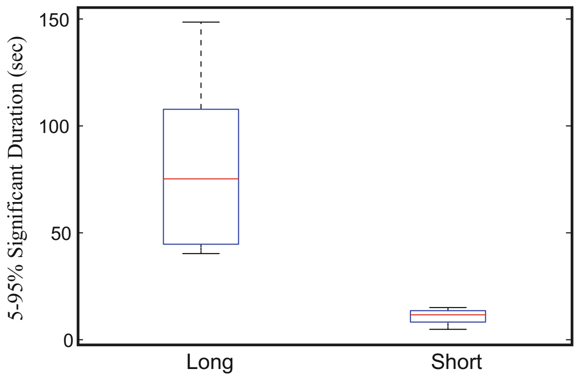

Fig. 11.8 Significant duration (D_{5-95}) statistics comparison

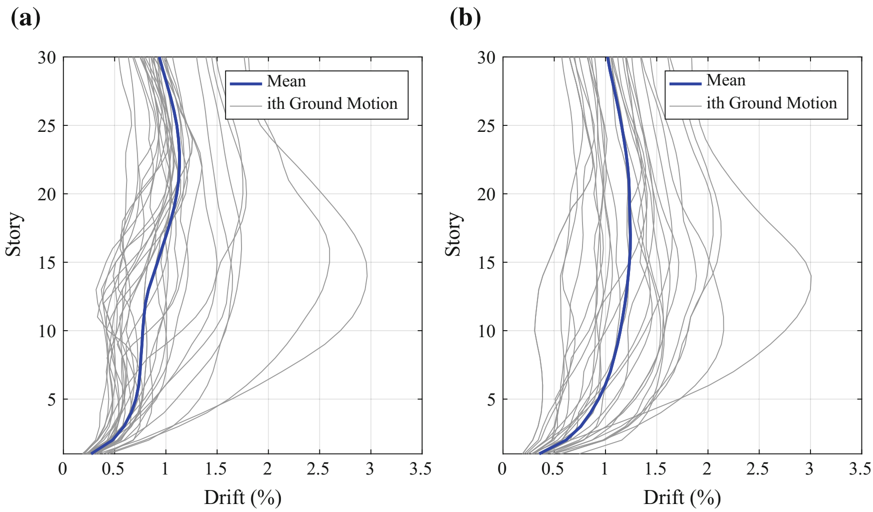

Fig. 11.9 Interstorey drift results for 30-storey model at code shaking level for **a** short duration suite and **b** long duration suite

models (6 and 12 storeys), however, do differ slightly for the three taller models (18, 24, and 30 storeys). This may be due to larger displacements in the taller models which stimulate more damage and degradation.

The energy response of the 30-storey structure was also computed during the time history analysis considering the energy dissipated through both yielding of the walls and header beams. Figure 11.13 compares the energy response calculated in the structure at this level of shaking for the two motion suites. Despite producing comparable peak displacement and force results, the long duration suite has much

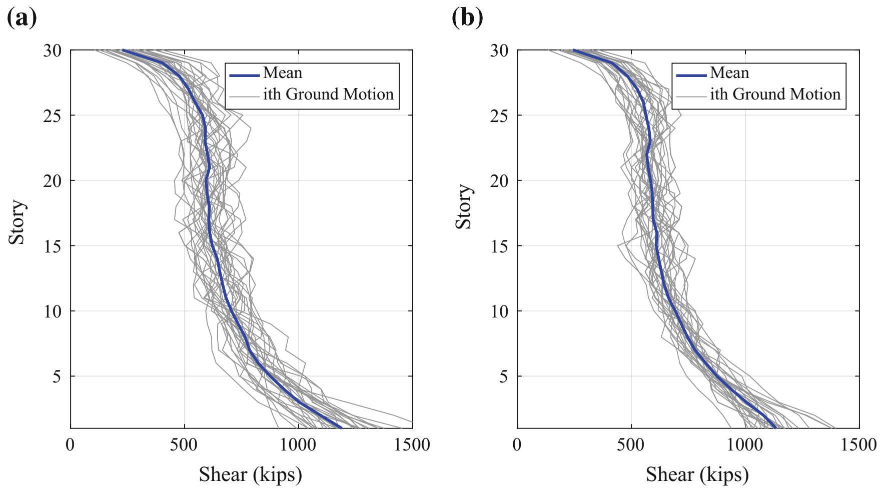

Fig. 11.10 Shear force results for 30-storey model at code shaking level for **a** short duration suite and **b** long duration suite

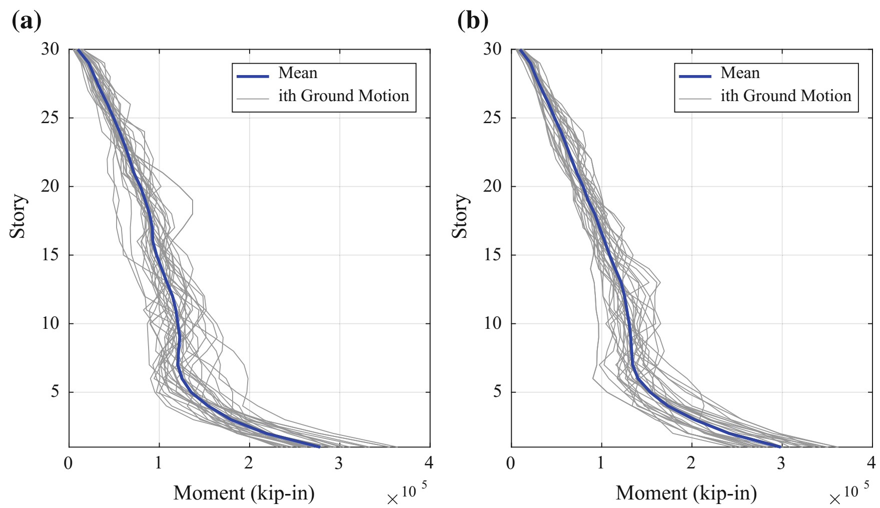

Fig. 11.11 Overturning moment results for 30-storey model at code shaking level for **a** short duration suite and **b** long duration suite

higher energy demands, which may lead to more structural and non-structural damage in the building.

Next, in order to determine if long duration ground motions increase the collapse risk of reinforced concrete shearwall structures at higher shaking levels, the two suites of ground motions were incrementally scaled up until collapse was reached.

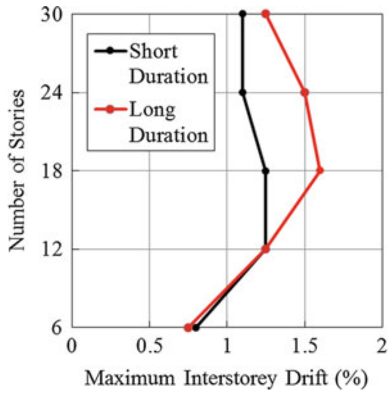

Fig. 11.12 Maximum interstorey drift summary for all model heights at code shaking level

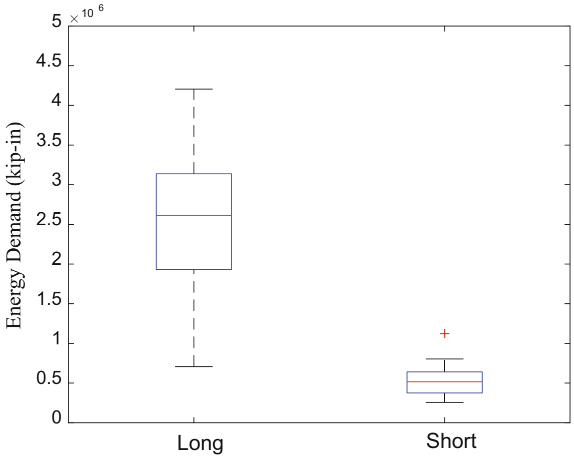

Fig. 11.13 Energy demand statistics comparison for 30-storey model at code shaking level

Collapse is defined as excessive interstorey drifts (>5%) or numerical instability. Figure 11.14 presents the fragility curves derived for the two ground motion suites.

As seen in Fig. 11.14, at lower scaling levels, up to 100% (the design scaling level according to the NBCC 2015 for Vancouver, BC) there is little to no probability of collapse for the short duration suite; however, there is a moderate (~10%) probability of collapse for the long duration suite at the 100% scaling level. The median collapse levels for the short and long suites are approximately 140 and 190% of the design scaling level, respectively.

11.6 Collapse-Level Analysis

The cumulative distribution functions (CDFs) in Fig. 11.14 only consider record-to-record (RTR) uncertainty. According to FEMA P695 (FEMA 2009), there are other sources of uncertainty that should be accounted for including

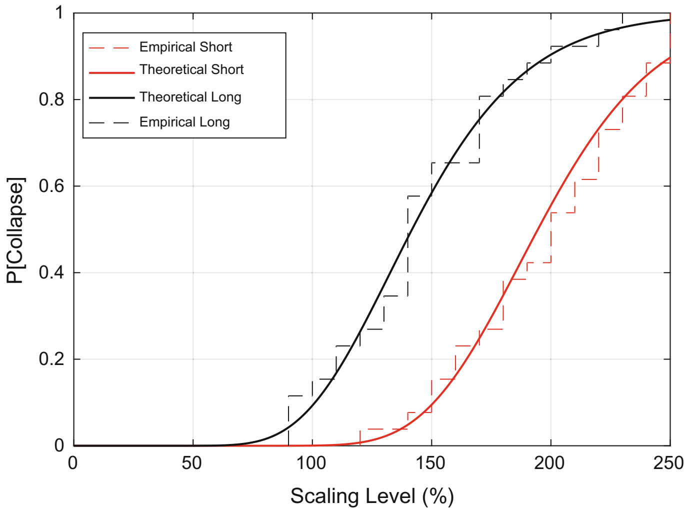

Fig. 11.14 CDF results for long and short duration motion suites for the 30-storey model

design-requirement uncertainty, test-data uncertainty, and modeling related uncertainty. Because the design, testing, and modeling of reinforced concrete shearwalls are well established, it was assumed that each of these uncertainties is very low (the lowest beta values recommended by FEMA P695 of 0.1 were selected for each). In Fig. 11.15, the CDFs were recalculated considering the contributions of these sources of uncertainty. It can be seen that the short duration CDF still shows a probability of collapse well below 10% at the design level (100%). According to FEMA P695, this design would be considered appropriate. However, if the long duration suite CDF was considered, then the design would not meet the 10% probability of collapse requirements and would not be considered appropriate for new construction. This shows the importance of ground motion duration, especially when considering large levels of shaking which is required to assess the safety of new structures.

11.7 Do Concrete Frame Buildings Show a Similar Behavior?

In order to illustrate the effect of long duration shaking on concrete frame buildings, a brief study is presented in this section. The objective is to show that certain types of concrete frame buildings can also exhibit the same sensitivity to duration of ground shaking as shearwall buildings.

For this purpose, two suites of ground motions were selected and scaled to the Victoria, British Columbia, Uniform Hazard Spectrum, UHS, to evaluate the effects

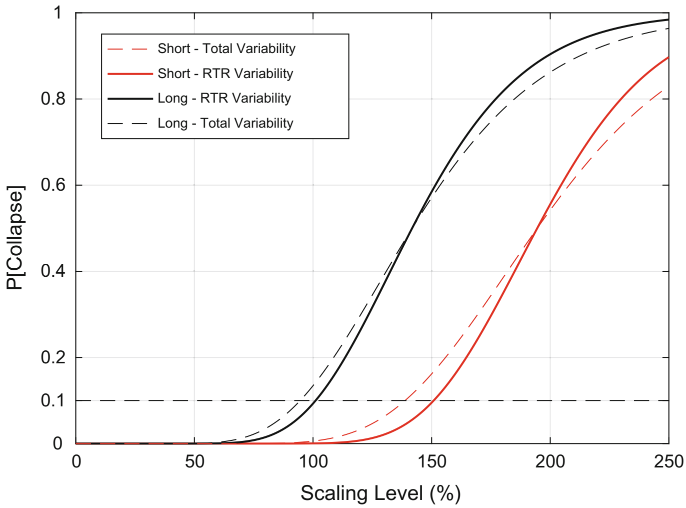

Fig. 11.15 CDF results for long and short duration motion suites for the 30-storey model including all sources of uncertainty

of long duration subduction motions on the probability of drift exceedance of a model of a ductile reinforced concrete frame building. The structural model under consideration is the *Prototype 1* RC frame building developed by the Applied Technology Council and described in the ATC 78 (2011). The general configuration of the Prototype 1 refers to an existing RC frame building originally located in Seattle. For the purpose of this study, the building is assumed to be located in Victoria, BC. According to ATC-78 (2011), the specific properties of Prototype 1 were those recommended by the American Concrete Institute in ACI 328-08 to ensure a ductile performance. This model was implemented in OpenSees and the corresponding fragility curves for probability of collapse were developed in a manner similar to that for the shearwall buildings.

The model configuration is a six-storey, five-bay RC frame building with a square plan area of 112 × 112 ft. The height of the first storey is 13 ft, while the storey height of the other storeys is 11 ft, leading to an overall building height of 68 ft. The building geometry is illustrated in Fig. 11.16, where the perimeter frames are shown in blue and the interior frames in green. The perimeter frames were the Seismic Force Resisting System (SFRS), while the interior frames did not contribute to the lateral resistance. Therefore, the IDA analysis was conducted on the planar 2D perimeter frame. The elevation view of the external perimeter frame is shown in Fig. 11.16. The end bays are 20 ft wide, while the width of each of the central bays is equal to 24 ft. The beams dimensions are illustrated in Fig. 11.17 for the typical end and central bays. The columns dimensions at the first, second and third storey are equal to 28 × 28 in. The columns in the upper storeys are 24 × 24 in. A more detailed description of the elements reinforcement is given in ATC 78-1 (2012).

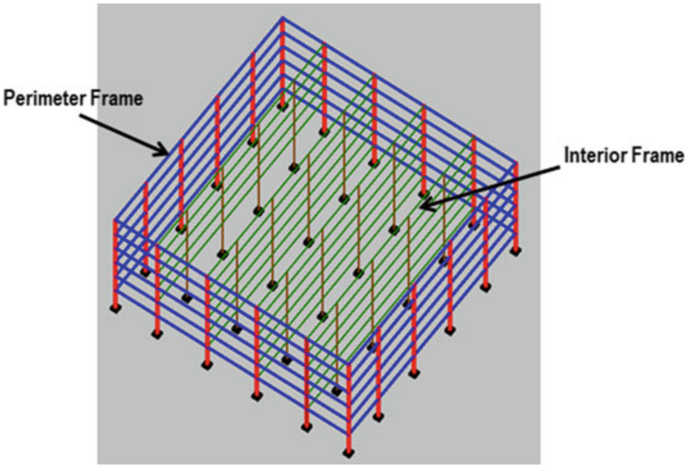

Fig. 11.16 3D view of the prototype building (ATC 78, Applied Technology Council 2011; ATC 78-1 2012)

Beams and columns were modeled by elastic line elements with plastic rotational hinges at each end of the line elements. The elastic flexural stiffness of the line elements was reduced for the analysis to take into account the cracked stiffness as described in ATC 78-1 (2012). The diaphragms were modeled as rigid bodies.

Geometrical nonlinearities caused by the P-Δ effect were modeled connecting a leaning column to the perimeter frame through axially rigid links. An elevation view of the model of the building is shown in Fig. 11.18.

The first three natural periods of the building were determined by modal analysis to be $T_1 = 1.54$ s, $T_2 = 0.54$ s and $T_3 = 0.28$ s.

The rotational springs at each end of beam and column elements were modeled as zero-length elements constraining all degrees of freedom except rotation. Each rotational spring was modeled using the Bilinear hysteretic model developed by Ibarra et al. 2005. The hysteretic model controlling the monotonic and the cyclic behavior of the rotational hinges depends on the parameters M_y, θ_y, θ_p, θ_{pc} and λ. The values of yield moment M_y and yield rotation θ_y are reported in the ATC 78-1 (2012) for each beam and column cross section. The capping rotation capacity θ_p, post-capping rotation capacity θ_{pc} and deterioration parameter λ (in inches), provided by ATC are listed in Table 11.4.

11.8 Fragility Curves

Through an incremental dynamic analysis (IDA) of this model, fragility curves were developed for the short duration (crustal motions) and long duration (subduction motions) ground motions selected for this study. For this study, a drift ratio

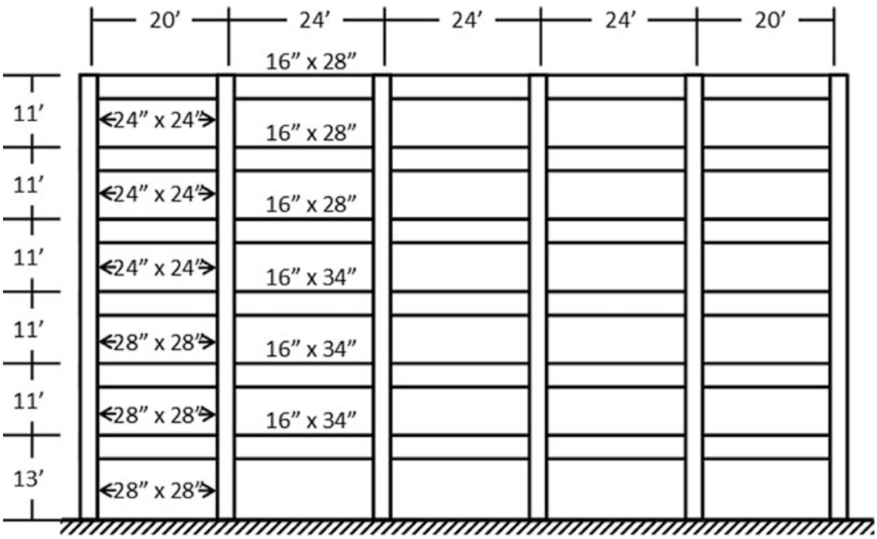

Fig. 11.17 Elevation view of the external perimeter frame of the building (ATC 78-1 2012)

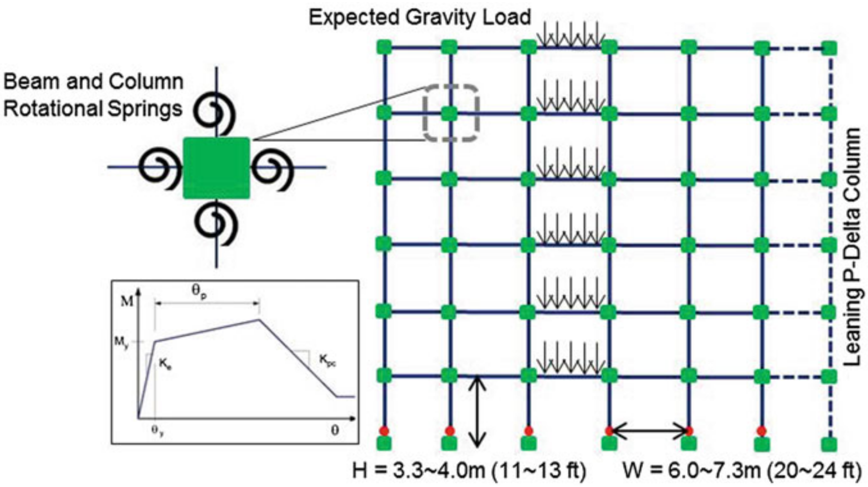

Fig. 11.18 Elevation view and modeling scheme of the RC frame (Chin 2017)

Table 11.4 Backbone curve parameters

Parameter	Columns	Beams
θ_p	0.06	0.05
θ_{pc}	0.1	0.15
λ	110	125

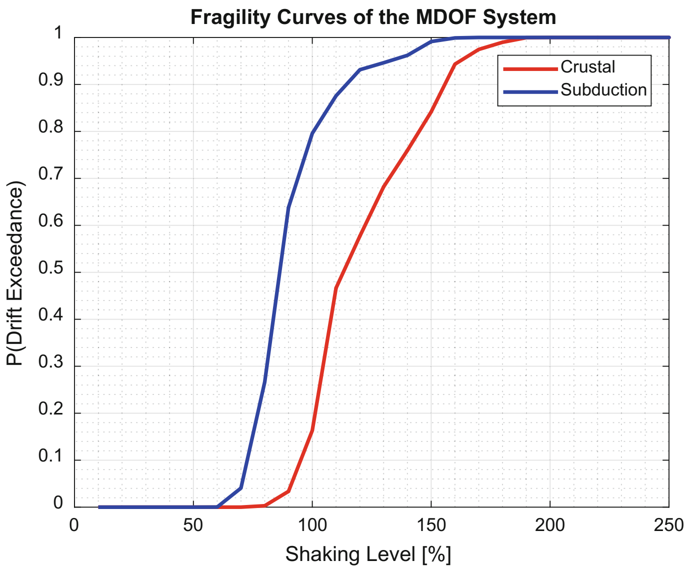

Fig. 11.19 Fragility curves for crustal and subduction motions

of 0.005 was chosen as the drift ratio corresponding to the flattening of the IDA curves, which is assumed to be the onset of the collapse. The fragility curves were calculated as the probability of exceeding this drift ratio. The resulting fragility curves are shown in Fig. 11.19 (the one for crustal motions is shown in red and the one for subduction motions is shown in blue).

At shaking levels between 70 and 180%, the subduction curve lies above the crustal one, leading to higher probabilities of drift ratio exceedance. This is caused directly by the longer duration of motions. For very high levels of shaking (above 190%) and shaking intensities below 60%, the two curves overlap indicating the same probability of drift ratio exceedance for crustal and subduction motions. When the crustal motions are scaled to match the Victoria UHS (100% shaking level), the probability of exceedance of the target drift is about 16%. On the other hand, at the 100% intensity (code design level), the subduction suite of long duration ground motions leads to a probability of drift exceedance of about 80%. This 64% increase in the probability shows very the effect of long duration of subduction ground motions. These observations confirm the findings from the study of the shearwall buildings, which showed the fragility curves for long duration motions lying above the ones for short duration motions.

11.9 Conclusions

In this study, a suite reinforced concrete shearwall buildings were analyzed using two sets of records: a long duration suite, and a spectrally equivalent short duration suite. At a code level of shaking (2% in 50-year probability of exceedance) little damage was observed but the longer motions tended to impose slightly greater interstorey drift demands. The long duration set also imposed much larger energy demands due to the large number of cycles—this effect has been widely recognized in the literature by Hancock and Bommer (2006). Similar behavior was observed for the case study of a reinforced ductile concrete frame.

When an incremental dynamic analysis was performed and the ground motion suites were scaled to very high levels of shaking, the median collapse scaling level was significantly affected by ground motion duration. This implies that ground motion duration may not be an important consideration for shearwall buildings at levels of shaking where little damage is expected (such as the design level), but when using larger levels of shaking, where large levels of damage are expected—e.g., to determine the safety of structures—then duration becomes an essential parameter of the input motions.

Acknowledgements The studies presented in this paper are part of the Ph.D. dissertations of the second and third authors, which were funded by the Natural Sciences and Engineering Research Council of Canada (NSERC) through a research grant awarded to the first author.

References

Applied Technology Council. (2011). *ATC 78: Identification and mitigation of seismically hazardous older concrete buildings*. Interim methodology evaluation, Redwood City.

Applied Technology Council. (2012). *ATC 78-1 Evaluation of the methodology to select and prioritize collapse indicators in older concrete buildins.* Redwood City.

Bommer, J. J., Udías, A., Cepeda, J. M., Hasbun, J. C., Salazar, W. M., Suárez, A., et al. (1997). A new digital accelerograph network for El Salvador. *Seismological Research Letters, 68*(3), 426–437.

Brown, J., & Kunnath, S. K. (2000). Low cycle fatigue behavior of longitudinal reinforcement in reinforced concrete bridge columns. In *NCEER Technical Report 00-0007*, National Center for Earthquake Engineering Research, State University of New York at Buffalo, Buffalo, USA.

Chandramohan, R., Baker, J. W., & Deierlein, G. G. (2015). Quantifying the influence of ground motion duration on structural collapse capacity using spectrally equivalent records. *Earthquake Spectra, 32*(2), 927–950.

Chin, D. H. (2017). *Effects of long duration ground motions on the probability of drift exceedance for reinforced concrete frames near the Cascadia Subduction Zon*e. M.Sc. thesis, The University of British Columbia, Vancouver.

COSMOS Virtual Data Center. (2008). The Consortium of Organizations for Strong-Motion Observation Systems. The Regents of the University of California, CA. http://strongmotioncenter.org/vdc/scripts/default.plx.

Dhakal, R., & Maekawa, K. (2002). Modelling for postyield buckling of reinforcement. *Journal of Structural Engineering, 128*(9), 1139–1147.

FEMA. (2009). *Quantification of Building seismic performance factors*, Federal Emergency Management Agency, Washington, DC.

Galano, L., & Vignoli, A. (2000). Seismic behavior of short coupling beams with different reinforcement layouts. *ACI Structural Journal, 97*(6), 876–885.

Green, M. C., & Karsh, J. E. (2012). *Tall Wood—The Case for Tall Wood Buildings*. BC, Canada: Vancouver.

Hancock, J., & Bommer, J. J. (2006). A state-of-knowledge review of the influence of strong-motion duration on structural damage. *Earthquake Spectra, 22*(3), 827–845.

Ibarra, L. F., Medina, R. A., & Krawinkler, H. (2005). Hysteretic models that incorporate strength and stiffness deterioration. *Earthquake Engineering and Structural Dynamics, 34*(12), 1489–1511.

Iyama, J., & Kuwamura, H. (1999). Application of wavelets to analysis and simulation of earthquake motions. *Earthquake Engineering and Structural Dynamics, 28*(3), 255–272.

Kinoshita, S. (1998). Kyoshin net (K-net). *Seismological Research Letters, 69*(4), 309–332.

Lowes, L. N., Mitra, N., & Altoontash, A. (2004). *A beam-column joint model for simulating the earthquake response of reinforced concrete frames*. Technical Report PEER 2003/10, Pacific Earthquake Engineering Research, Berkeley, USA.

Mander, J. B., Priestley, M. J., & Park, R. (1988). Theoretical stress-strain model for confined concrete. *Journal of Structural Engineering, 114*(8), 1804–1826.

McKenna, F., Fenves, G. L., Scott, M. H., & Jeremic, B. (2000). *Open System for Earthquake Engineering (OpenSees)*, Pacific Earthquake Engineering Research Center, University of California, Berkely, USA.

PEER. (2010). *Technical report for the PEER ground motion database web application*, Pacific Earthquake Engineering Research Center, University of California, Berkeley, CA.

Pugh, J. (2012). *Numerical simulation of walls and seismic design recommendations for walled buildings*. Ph.D. Dissertation, University of Washington, Seattle, USA.

Raghunandan, M., & Liel, A. B. (2013). Effect of ground motion duration on earthquake-induced structural collapse. *Structural Safety, 41,* 119–133.

Tremblay, R. (1998). Development of design spectra for long-duration ground motions from Cascadia subduction earthquakes. *Canadian Journal of Civil Engineering, 25*(6), 1078–1090.

Yassin, M. H. M. (1994). *Nonlinear analysis of prestressed concrete structures under monotonic and cyclic loads*. Ph.D. Dissertation, University of California, Berkeley, USA.

Chapter 12
Drift Capacity at Onset of Bar Buckling in RC Members Subjected to Earthquakes

Mario E. Rodriguez and Marcelo Iñiguez

Performance-based earthquake engineering for RC buildings is necessary to link drift demands with the likelihood of onset of bar buckling. This damage state has been observed in RC buildings that responded to recent earthquakes. This research uses a database of reinforcing bars subjected to reversed cyclic axial loading, as well as a database of RC columns and walls tested by several authors under cyclic reversal lateral loading. In this database, the observed failure mode was related to bar buckling. A procedure is proposed for predicting drift capacity of RC elements considering buckling of longitudinal reinforcement. Results using this procedure are compared with experimental results.

12.1 Introduction

In performance-based earthquake engineering, it is necessary to compare deformation demands in critical sections of structural elements with deformation capacity of concrete and longitudinal reinforcement in those sections, where several modes of failure need to be considered. Past research has addressed most of these modes of failure through proper detailing of transverse and longitudinal reinforcement. However, most research in the area of mode of failure governed by buckling of longitudinal reinforcement has focused on the monotonic behavior of reinforcing bars subjected to compression. There have been some studies on the cyclic behavior of reinforcing bars (Rodriguez et al. 1999; Moyer and Kowalsky 2003; Motter et al.

M. E. Rodriguez (✉)
National University of Mexico, 04510 Mexico City, Mexico
e-mail: mrod@unam.mx

M. Iñiguez
National University of Mexico, Mexico City, Mexico
e-mail: andiiniguez@hotmail.com

T. T. C. Hsu (ed.), *Concrete Structures in Earthquake*,
https://doi.org/10.1007/978-981-13-3278-4_12

2018). Results of these studies show the importance of the ratio of transverse reinforcement spacing to longitudinal bar diameter (s/d_b) and the peak values reached in tensile and compressive strains in the longitudinal bar in a cycle of loading.

The research work presented in this paper uses a database that includes results of cyclic testing of individual reinforcing bars, and results of walls and columns tested quasi-statically with a reversed cyclic loading protocol conducted by several researchers, where peak values of tensile and compressive strains in longitudinal bars at onset of observed bar buckling were recorded. This paper proposes a model for bar buckling based on a modification of the model developed by Rodriguez et al. (1999). Based on this model, a predictive equation for curvature at onset of bar buckling is also proposed. With this curvature, predictions of lateral displacements at onset of bar buckling were obtained for a database of column and wall tests, where bar buckling was observed. Predicted displacements for the database were compared with measured values.

12.2 Model Description

The proposed model that defines the mode of failure initiated with buckling of longitudinal reinforcement is based on the model developed by Rodriguez et al. (1999), with a modification shown later. These authors proposed that onset of buckling in the longitudinal reinforcement occurs when a critical strain is reached in the reinforcement, which is defined below.

Rodriguez et al. (1999) performed tests of reinforcing bars under reversed cyclic axial loading. At onset of observed buckling of these bars, they measured the critical strain defined as

$$\varepsilon_p^* = \varepsilon_o - \varepsilon_{sc} \tag{12.1}$$

where ε_o is defined as the axial strain at zero loading after reversal from tension (Fig. 12.1), and ε_{sc} is the peak compressive strains in the longitudinal bar in a cycle of loading, as shown in Fig. 12.1. In Eq. (12.1), tensile strain and compressive strain are assumed positive and negative, respectively.

Rodriguez et al. (2013) proposed a modification of Eq. (12.1) that could be used in design. In this alternative definition of ε_p^*, strain ε_{st} is used instead of ε_o, which leads to (Fig. 12.1)

$$\varepsilon_p^* = \varepsilon_{st} - \varepsilon_{sc} \tag{12.2}$$

Equation (12.2) is used in this study for defining the curvature of a critical section at onset of bar buckling.

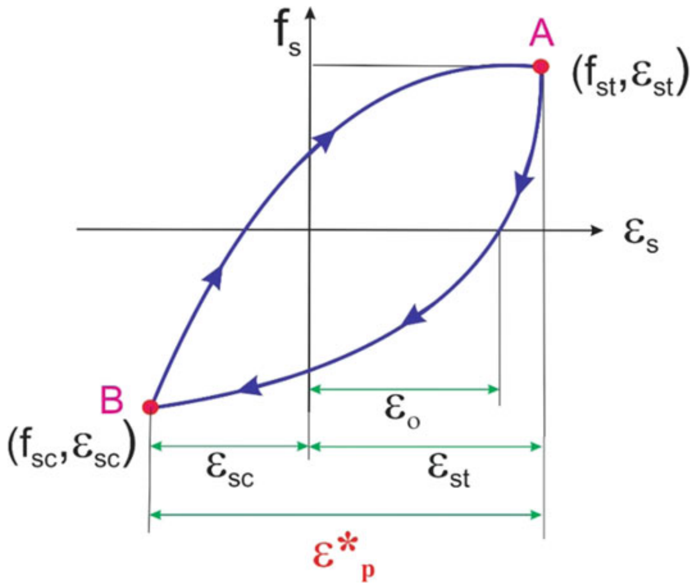

Fig. 12.1 Definition of ε_p^*

12.3 Database Used in this Research

The research presented in this paper used a database that includes results of tests conducted by Rodriguez et al. (1999) on 13 reinforcing bars under reversed cyclic axial loading. The database also includes results of reversed cyclic lateral loading tests of 17 RC circular columns and 8 rectangular RC walls, where the observed mode of failure was buckling of longitudinal reinforcing bars.

12.3.1 Reinforcing Bar Database

Rodriguez et al. (1999) conducted tests on 13 steel coupons under reversed cyclic axial loading. These test units were machined from steel reinforcing bars conforming to most of ASTM A706 specifications, with a specified yield strength of 415 MPa. The test units had s/d_b ratios of 2.5, 4, 6, and 8, and they were tested until they failed. The observed mode of failure for all cases, except the case s/d_b = 2.5, was buckling of the reinforcing bar.

In the research presented in this paper, the critical strain ε_p^* in the cycle of loading corresponding to onset of bar buckling was obtained with Eq. (12.2) through the use of measured values of ε_{st} and ε_{sc} reported by Rodriguez et al. (1999) for the cycle at onset of bar buckling. It must be noted that a different approach for

Table 12.1 Measured critical strain ε_p^* in steel coupons under reversed cyclic axial loading

Symmetrical cycles					Asymmetrical cycles				
Unit	s/d_b	ε_{st}	ε_{sc}	ε^*_p	Unit	s/d_b	ε_{st}	ε_{sc}	ε^*_p
RB1	4	0.0698	−0.0056	0.0754	RB8	4	0.0865	0.0060	0.0925
RB2	4	0.0677	−0.0056	0.0733	RB9	4	0.0841	0.0060	0.0901
RB3	6	0.0424	−0.0051	0.0475	RB10	6	0.0510	0.0063	0.0573
RB4	6	0.0367	−0.0051	0.0418	RB11	6	0.0488	0.0063	0.0551
RB5	6	0.0278	−0.0051	0.0329	RB12	8	0.0203	0.0048	0.0250
RB6	8	0.0129	−0.0044	0.0173	RB13	8	0.0178	0.0048	0.0226
RB7	8	0.0061	−0.0044	0.0106					

the interpretation of bar buckling was used by Rodriguez et al. (1999) since they used Eq. (12.1).

Table 12.1 shows values of s/d_b ratios for the test units and measured values of ε_{st}, ε_{sc} and ε_p^*, where ε_p^* was determined using Eq. (12.2). These results correspond to two cases of cyclic loading. The cyclic tests were conducted using symmetrical and asymmetrical type of cyclic loading, where the ratio $\varepsilon_{st}/|\varepsilon_{sc}|$ was set equal to approximately 1 for the symmetrical case, and 2.3 for the asymmetrical case.

Measured ε_p^* values shown in Table 12.1 are presented in Fig. 12.2 as a function of s/d_b ratios.

Figure 12.2 also shows the results of predicted values of ε_p^* using the modified reduced modulus theory. The compressive stress at onset of bar buckling, f_p, based on the reduced modulus theory is given by

$$f_p = \frac{\pi^2 E_r}{16\left(K\frac{s}{d_b}\right)^2} \tag{12.3}$$

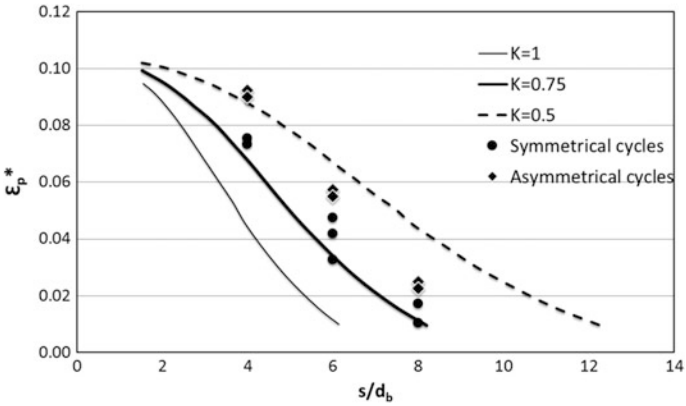

Fig. 12.2 Critical strain ε_p^* that triggers bar buckling as a function of s/d_b

where E_r is the reduced modulus and K is the effective length factor. Predicted values of the critical strain ε_p^* for the cases $K = 0.5$, 0.75 and 1 are shown in Fig. 12.2, and they were obtained substituting the monotonic strain at buckling obtained using Eq. (12.3), ε_p, for ε_p^*. Results shown in Fig. 12.2 for ε_p^* suggest that the modified reduced modulus theory for the case $K = 0.75$ leads approximately to a lower bound of the measured ε_p^* values.

12.3.2 Column Database

Goodnight et al. (2015) tested a set of 17 circular bridge columns subjected to reversed cyclic lateral loading. Table 12.2 shows some relevant properties of these test units, such as diameter of the columns, D; longitudinal and transverse reinforcement diameters, d_b and d_{bt}, respectively; spacing of transverse reinforcement, s; s/d_b ratio; longitudinal reinforcement ratio, ρ_l; and axial load ratio $P/(A_g f'_c)$, where P is the applied axial load, and A_g and f'_c are the gross area of the concrete section and the specified compressive concrete strength, respectively. Table 12.2 also shows values of the aspect ratio L/D, where L is the shear span. An important feature of these tests was the high fidelity strain data in longitudinal reinforcing bars. These data were obtained using an optical 3D position measurement system. Column curvature distributions and fixed-end rotation due to strain penetration in the footing were also measured (Goodnight et al. 2015).

Table 12.2 Relevant properties of circular columns tested by Goodnight et al. (2015)

No	Designation	D (mm)	d_b (mm)	d_{bt} (mm)	s (mm)	ρ_l (%)	s/d_b	$P/(A_g f'_c)$	L/D
1	N-9	609.6	19.1	9.5	50.8	1.56	2.67	0.055	4.0
2	N-13	609.6	19.1	12.7	69.8	1.56	3.66	0.062	4.0
3	N-14	609.6	19.1	9.5	101.6	1.56	5.33	0.057	4.0
4	N-15	609.6	19.1	9.5	70.0	1.56	3.67	0.052	4.0
5	N-16	609.6	19.1	9.5	38.1	1.56	2.00	0.056	4.0
6	N-19	462.6	19.1	9.5	50.8	1.70	2.67	0.100	5.3
7	N-20	462.6	19.1	9.5	50.8	1.70	2.67	0.050	5.3
8	N-21	462.6	19.1	9.5	50.8	1.70	2.67	0.050	7.3
9	N-22	462.6	19.1	9.5	50.8	1.70	2.67	0.100	7.3
12	N-25	609.6	22.2	9.5	50.8	2.13	2.29	0.050	4.0
13	N-26	609.6	22.2	9.5	50.8	2.13	2.29	0.100	4.0
14	N-27	609.6	19.1	9.5	50.8	1.56	2.67	0.100	4.0
15	N-28	457.2	19.1	9.5	50.8	1.74	2.67	0.150	5.3
16	N-29	462.6	19.1	9.5	50.8	1.70	2.67	0.200	5.3
17	N-30	462.6	25.4	9.5	50.8	3.01	2.00	0.150	5.3

Table 12.3 Critical strain ε_p^* that triggers buckling of longitudinal reinforcement of circular columns tested by Goodnight et al. (2015)

No	Designation	ε_{st}	ε_{sc}	ε_{Pm}*	ε_{Pc}*	ε_{Pm}*/ε_{pc}*
1	N-9	0.043	−0.018	0.061	0.056	1.098
2	N-13	0.046	−0.017	0.063	0.049	1.288
3	N-14	0.032	−0.011	0.043	0.038	1.138
4	N-15	0.034	−0.012	0.046	0.049	0.942
5	N-16	0.036	−0.022	0.058	0.060	0.967
6	N-19	0.032	−0.022	0.054	0.056	0.972
7	N-20	0.037	−0.016	0.053	0.056	0.954
8	N-21	0.035	−0.024	0.059	0.056	1.062
9	N-22	0.041	−0.019	0.06	0.056	1.080
10	N-25	0.033	−0.019	0.052	0.058	0.895
11	N-26	0.024	−0.027	0.051	0.058	0.878
12	N-27	0.024	−0.032	0.056	0.056	1.008
13	N-28	0.024	−0.034	0.058	0.056	1.044
14	N-29	0.025	−0.028	0.053	0.056	0.954
15	N-30	0.036	−0.009	0.045	0.060	0.750
					Mean	1.00
					CV	12.6%

The tests conducted by Goodnight et al. (2015) showed that the first significant loss of lateral strength in test units occurred when previously buckled reinforcement fractured. The tests were conducted increasing the lateral displacements in the columns up to failure. Vertical strain profiles of extreme layers of longitudinal reinforcement were measured at each level of increasing ductility using the optical position measurement system. The lateral loading cycle at observed onset of longitudinal bar buckling in each test unit was identified. Using these data, in this study, the measured critical strain ε_{pm}^* in this cycle of loading was obtained with Eq. (12.2) through the use of measured values of ε_{st} and ε_{sc} in this cycle. Measured values of ε_{st}, ε_{sc} and ε_{pm}^* are shown in Table 12.3. These values are compared later with the predicted critical strain ε_{pc}^* which results of a proposed predictive equation for ε_p^*. Table 12.3 does not include results for test units N-23 and N-24 because in these test units, compressive strains in the longitudinal reinforcement at the cycle of onset of bar buckling were not recorded.

12.3.3 Wall Database

The proposed model for bar buckling in RC elements subjected to lateral loads was also calibrated using the observations of bar buckling from a database that included cyclic lateral tests of eight rectangular walls. Relevant properties of these RC walls

Table 12.4 Relevant properties of RC walls in the database

No	Designation	References	f'_c (MPa)	fy (MPa)	h_w (mm)	t_w (mm)	l_w (mm)	ρ_l (%)	d_b (mm)	s/d_b	$P/(f'_c\ A_g)$	h_w/l_w
1	WSH4	Dazio et al. (2009)	40.9	576	4560	150	2000	0.82	12.0	12.5	0.057	2.28
2	WSH2	Dazio et al. (2009)	40.5	583	4560	150	2000	0.54	10.0	7.5	0.057	2.28
3	WSH3	Dazio et al. (2009)	39.2	601	4560	150	2000	0.82	12.0	6.3	0.058	2.28
4	W-MC-N	Villalobos (2014)	32.7	462	3658	203	1524	1.56	25.4	5.0	0.088	2.40
5	RW1	Thomsen and Wallace (1995)	36.5	434	3658	102	1219	1.12	9.5	8.0	0.100	3.00
6	RW2	Thomsen and Wallace (1995)	34.3	434	3658	102	1219	1.12	9.5	5.3	0.070	3.00
7	WSH6	Dazio et al. (2009)	45.6	577	4560	150	2000	0.81	11.0	4.5	0.108	2.28
8	WSH5	Dazio et al. (2009)	38.3	584	4560	150	2000	0.39	8.0	6.3	0.128	2.28

Table 12.5 Critical strain ε_p^* that triggers buckling of longitudinal reinforcement of RC walls

No	Designation	ε_{st}	ε_{sc}	ε_{pm}*	ε_{pc}*	ε_{pm}*/ε_{pc}*
1	WSH4	0.017	−0.003	0.0202	0.0200	1.0100
2	WSH2	0.023	−0.005	0.0280	0.0233	1.2000
3	WSH3	0.026	−0.006	0.0320	0.0317	1.0105
4	W-MC-N	0.034	−0.015	0.0490	0.0400	1.2250
5	RW1	0.022	−0.009	0.0312	0.0200	1.5580
6	RW2	0.030	−0.010	0.0400	0.0377	1.0615
7	WSH6	0.025	−0.014	0.0390	0.0430	0.9063
8	WSH5	0.026	−0.005	0.0310	0.0317	0.9789
					Mean	1.12
					CV	18.6%

are shown in Table 12.4, where h_w, t_w, and l_w are the height, thickness and length of wall, respectively. As seen in Table 12.4, the s/d_b ratio ranged from 4.5 to 12.5. The database has walls with axial load ratio, $P/(A_g f_c')$, varying from 0.06 to 0.13, the longitudinal reinforcement ratio, ρ_l, ranged from 0.39% to 2.4%, and the wall aspect ratio, h_w/l_w ranged from 2.3 to 3.

The measured critical strain ε_{pm}^* in the cycle of loading at the observed onset of longitudinal bar buckling was obtained with Eq. (12.2) through the use of measured values of ε_{st} and ε_{sc} in this cycle. Measured values of ε_{st}, ε_{sc} and ε_{pm}^* are shown in Table 12.5, which also shows predicted values for ε_{pc}^* discussed later.

12.4 Proposed Predictive Equation for ε_p^*

Values of the experimental critical strain ε_p^* presented in Tables 12.1, 12.3, and 12.5, are shown in Fig. 12.3 as a function of the s/d_b ratio. Based on these results, the following expression is proposed to predict ε_p^* :

$$0.02 \leq \ \varepsilon_p^* = \frac{11 - s/d_b}{150} \leq \ 006 \tag{12.4}$$

Results using the predictive Eq. (12.4) are shown in Fig. 12.3. These results indicate that for the case of steel coupons tested by Rodriguez et al. (1999), the measured values of ε_p^* are larger than the measured values of ε_p^* in columns and walls. This can be explained considering that these steel coupons were plain bars, machined from steel reinforcing bars, without the effect of ribs on bar buckling. This effect has been observed in uniaxial bar tests by Restrepo et al. (1993). These authors found that micro-cracks develop at the location of ribs on the compression side of a buckled bar. These cracks reduce the tensile capacity of the rebar,

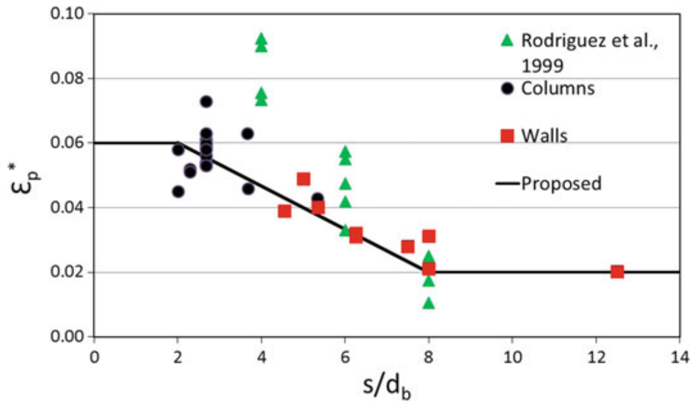

Fig. 12.3 Critical strain ε_p^* that triggers buckling of longitudinal reinforcement in the column and wall database

which can lead to premature bar fracture. Based on these results, in the following, only the database of columns and walls are considered.

Values of the experiment/prediction ratio $\varepsilon_{pm}^*/\varepsilon_{pc}^*$ for columns and walls are shown in Tables 12.3 and 12.5, respectively. Strain ε_{pc}^* represents the predicted value of ε_p^* using Eq. (12.4). According to Table 12.3, the mean and coefficient of variation of the experiment/prediction ratios for columns are 1.00 and 12.6%, respectively. Table 12.5 shows that these statistical values for walls are 1.12 and 18.6%, respectively.

Figure 12.4 shows the experiment/prediction ratios,$\varepsilon_{pm}^*/\varepsilon_{pc}^*$ for columns and walls of the database as a function of s/d_b. For the group of columns and walls of the database, the mean and coefficient of variation of the experiment/prediction ratios are 1.04 and 15.8%, respectively.

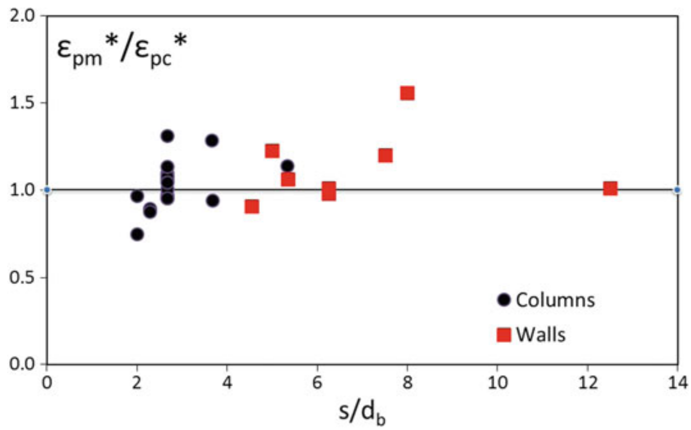

Fig. 12.4 Proposed model for the critical strain ε_p^* compared with experimental results related to s/d_b

12.5 Lateral Displacement Predictions of RC Members with Mode of Failure Governed by Bar Buckling

Predictions of lateral displacements in RC members are necessary in the design of earthquake-resisting structures. For the case of the mode of failure governed by bar buckling, this study proposes a simple procedure to obtain the curvature of critical sections of RC members at onset of bar buckling. With this curvature, lateral displacements at onset of bar buckling are obtained for the column and wall database using the plastic hinge method proposed by Priestley et al. (2007). Experiment/prediction ratios of lateral displacements at onset of bar buckling are also shown in this paper.

12.5.1 Curvature in a Critical Section of an RC Member at Onset of Bar Buckling

Figure 12.5 shows an RC member with a depth h subjected to the lateral force F. In this member, the north and south exterior layers of longitudinal bars are identified as bars N and S, respectively. Figure 12.5 also shows the force versus displacement hysteretic response with peak values at points A and B, where points A and B correspond to the cycles at ductility μ^+ (positive displacement) and μ^- (negative displacement), respectively.

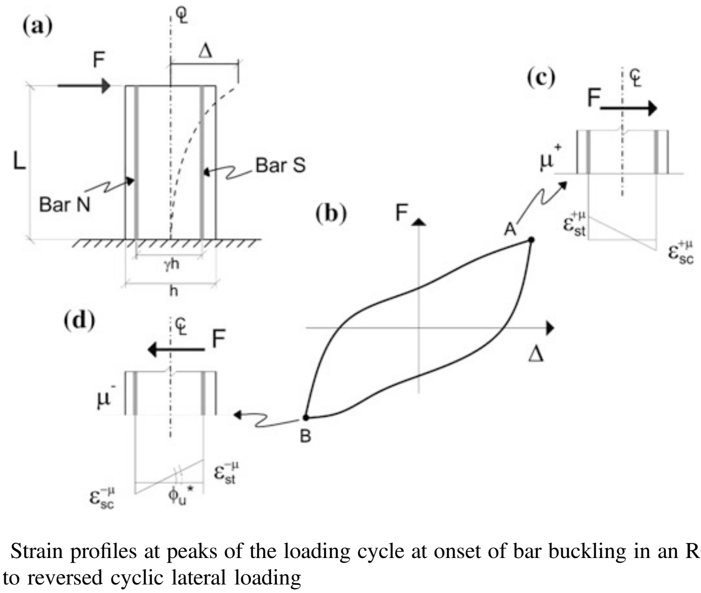

Fig. 12.5 Strain profiles at peaks of the loading cycle at onset of bar buckling in an RC member subjected to reversed cyclic lateral loading

At point A, the peak tensile strain at bar N and the peak compressive strain at bar S are equal to $\varepsilon_{st}^{+\mu}$ and $\varepsilon_{sc}^{+\mu}$, respectively, see Fig. 12.5c. At point B, where the bar N in compression buckles after reversal from μ^+, the peak compressive strain at bar N and the peak tensile strain at bar S are equal to $\varepsilon_{sc}^{-\mu}$ and $\varepsilon_{st}^{-\mu}$, respectively, see Fig. 12.5d.

The curvature at onset of bar buckling, ϕ_u^*, is defined as (see Fig. 12.5d)

$$\phi_u^* = \frac{\varepsilon_{st}^{-\mu} - \varepsilon_{sc}^{-\mu}}{\gamma h} \tag{12.5}$$

where γ is the ratio between the distance between the centroid of the exterior layers of longitudinal bars (bars N and S in Fig. 12.5) to the member depth.

At onset of buckling, after reversal from μ^+, bar N reaches the peak compressive strain $\varepsilon_{sc}^{-\mu}$, and at the previous half cycle μ^+, this bar reached the peak tensile strain $\varepsilon_{st}^{+\mu}$. From the definition of ε_p^* given in Eq. (12.2), we obtain

$$\varepsilon_p^* = \varepsilon_{st}^{+\mu} - \varepsilon_{sc}^{-\mu} \tag{12.6}$$

It is assumed that in a symmetrical cross section, at onset of bar buckling after reversal from μ^+, the peak tensile strain in bar S, $\varepsilon_{st}^{-\mu}$, see Fig. 12.5d, is equal to the peak tensile strain of bar N at the previous half cycle μ^+, $\varepsilon_{st}^{+\mu}$, see Fig. 12.5c, that is

$$\varepsilon_{st}^{+\mu} = \varepsilon_{st}^{-\mu} \tag{12.7}$$

Combining Eqs. (12.6) and (12.7), we obtain

$$\varepsilon_p^* = \varepsilon_{st}^{-\mu} - \varepsilon_{sc}^{-\mu} \tag{12.8}$$

From Eqs. (12.5) and (12.8), we obtain

$$\phi_u^* = \frac{\varepsilon_p^*}{\gamma h} \tag{12.9}$$

12.5.2 Prediction of Member Response

In the following, this study proposes a relationship between the critical strain ε_p^* at onset of bar buckling and lateral displacement in an RC member subjected to reversed cyclic loading. The elastic flexural displacement, Δ_y, is determined based on the use of a triangular yield curvature distribution

$$\Delta_y = \phi_y \frac{(L + L_{sp})^2}{3} \tag{12.10}$$

where ϕ_y and L_{sp} are the yield curvature at the critical section and length of strain penetration, respectively. These parameters are defined as (Priestley et al. 2007)

$$\phi_y = \frac{\alpha\, \varepsilon_y}{h} \tag{12.11}$$

$$L_{sp} = 0.022\, f_y\, d_b \tag{12.12}$$

where for a circular column and a rectangular wall, α is equal to 2.25 and 2.0, respectively.

The plastic displacement in a column, Δ_{pc}, is determined using the plastic hinge method proposed by Priestley et al. (2007) as

$$\Delta_{pc} = \phi_p\, L_p\left(L + L_{sp} - 0.5L_p\right) \tag{12.13}$$

For a wall, Δ_{pc} is determined using Eq. (12.13) replacing L by l_w.

The plastic hinge length in a column, L_p, is found from (Priestley et al. 2007)

$$L_p = kL + L_{sp} \geq 2L_{sp} \tag{12.14}$$

where

$$k = 0.2\left(\frac{f_u}{f_y} - 1\right) \leq 0.08 \tag{12.15}$$

where f_u is the ultimate tensile strength.

The plastic hinge length in a wall is determined as (Priestley et al. 2007)

$$L_p = k\, h_w + 0.1\, l_w + L_{sp} \tag{12.16}$$

The plastic curvature at onset of bar buckling, ϕ_p, is determined using the curvature at onset of bar buckling, ϕ_u^*, as

$$\phi_p = \phi_u^* - \phi_y \tag{12.17}$$

The member lateral displacement at onset of bar buckling, Δ, is found from

$$\Delta = \Delta_y + \Delta_{pc} \tag{12.18}$$

12.5.3 Measured and Predicted Lateral Displacements at Onset of Bar Buckling for the Column and Wall Database

For the column database, Table 12.6 shows computed values of several parameters needed to obtain the predicted lateral displacement at onset of bar buckling,

Table 12.6 Experimental/Predicted lateral displacement ratio and relevant parameters for the column database

No	Designation	γD (mm)	ϕ_u^* (mm^{-1})	L_{sp} (mm)	L_p (mm)	ϕ_y (mm^{-1})	Δ_{yc} (mm)	Δ_{pc} (mm)	Δ_c (mm)	Δ_m (mm)	Δ_m/Δ_c
1	N-9	556	1.10E-04	197	394	8.49E-06	19.6	97	117	171	1.46
2	N-13	552	1.14E-04	197	394	8.49E-06	19.6	101	121	165	1.36
3	N-14	556	7.74E-05	197	394	8.49E-06	19.6	66	86	122	1.42
4	N-15	556	8.28E-05	197	394	8.49E-06	19.6	71	91	127	1.40
5	N-16	556	1.04E-04	197	394	8.49E-06	19.6	92	112	127	1.14
6	N-19	403	1.34E-04	197	394	1.12E-05	25.9	118	144	146	1.01
7	N-20	403	1.31E-04	197	394	1.12E-05	25.9	115	141	151	1.07
8	N-21	403	1.46E-04	197	394	1.12E-05	25.9	130	156	251	1.61
9	N-22	403	1.49E-04	197	394	1.12E-05	25.9	132	158	265	1.68
10	N-25	552	9.41E-05	235	469	8.49E-06	20.2	98	118	130	1.10
11	N-26	552	9.23E-05	235	469	8.49E-06	20.2	96	116	126	1.09
12	N-27	556	1.01E-04	199	397	8.49E-06	19.7	89	109	117	1.07
13	N-28	403	1.44E-04	199	397	1.13E-05	26.2	128	155	170	1.10
14	N-29	403	1.31E-04	199	397	1.12E-05	25.9	116	142	171	1.20
15	N-30	397	1.13E-04	272	543	1.12E-05	27.4	135	163	188	1.15
										Mean	1.26
										CV	17.0%

Table 12.7 Experimental/predicted lateral displacement ratio and relevant parameters for the wall database

No	Designation	γl_w (mm)	ϕ_u* (mm^{-1})	ϕ_y (mm^{-1})	L_{sp} (mm)	L_p (mm)	Δ_y (mm)	Δ_{pc} (mm)	Δ_c (mm)	Δ_m (mm)	Δ_m/Δ_c
1	WSH4	1940	1.04E-05	2.88E-06	152	509	21	17	38	46	1.20
2	WSH2	1950	1.44E-05	2.92E-06	128	585	21	29	51	53	1.04
3	WSH3	1940	1.65E-05	3.01E-06	159	548	22	33	55	77	1.40
4	W-MC-N	1438	3.41E-05	3.03E-06	258	703	15	78	93	88	0.94
5	RW1	1181	2.64E-05	3.56E-06	91	505	17	40	57	69	1.21
6	RW2	1181	3.39E-05	3.56E-06	91	505	17	54	70	86	1.23
7	WSH6	1940	2.01E-05	2.88E-06	140	502	21	38	60	78	1.31
8	WSH5	1940	1.60E-05	2.92E-06	103	507	21	29	50	49	0.97
										Mean	1.16
										CV	13.8%

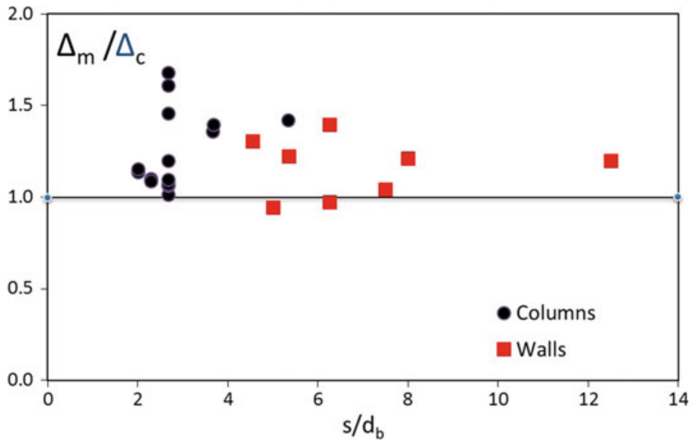

Fig. 12.6 Experimental/Predicted lateral displacement ratio at onset of bar buckling for the column and wall database

Δ_c. This displacement was computed using the definition of ϕ_u^* given in Eq. (12.9), where ε_p^* was determined using Eq. (12.4). Computed values of ϕ_u^* are shown in Table 12.6. Parameter Δ_m in Table 12.6 represents the measured lateral displacement at onset of bar buckling in the column database. As seen in Table 12.6, the mean and coefficient of variation of the experiment/prediction ratio for columns are 1.26 and 17.0%, respectively.

Table 12.7 shows results of predicted lateral displacements at onset of bar buckling for the wall database. This Table also shows values of the measured displacement Δ_m. As seen in Table 12.7, the mean and coefficient of variation of the experiment/prediction ratio for walls are 1.16 and 13.8%, respectively.

In Fig. 12.6, predictions of member lateral displacement at onset of bar buckling, Δ_c, are compared with the experimental database for circular columns and walls. The proposed method provides an acceptable agreement with the data, with a mean displacement ratio of 1.22 and a coefficient of variation of 16.2%. The maximum experiment/prediction ratios for columns and walls are 1.68 and 1.40, respectively.

12.6 Conclusions

A predictive equation of the critical strain ε_p^* at onset of bar buckling of columns and walls subjected to cyclic lateral loading was presented. The predictive equation was compared with measured values of ε_p^* using database of columns and walls. It provided an acceptable simulation of the influence of s/d_b, with a mean value of measured to predicted critical strain at onset of bar buckling of 1.04 and a coefficient of variation of 15.8%.

A predictive equation for curvature at bar buckling at the member critical section, ϕ_u^*, was also presented. This equation uses the predictive equation of the critical strain ε_p^* at onset of bar buckling. Lateral displacement in the member at onset of bar buckling was determined with the plastic hinge method using the proposed predictive equations for ϕ_u^* and ε_p^*. The predicted displacements were compared with results of a database of columns and walls. It provided an acceptable simulation of the influence of s/d_b in drift capacity associated to bar buckling, with a mean value of measured to predicted displacement at onset of bar buckling of 1.22 and a coefficient of variation of 16.2%.

Acknowledgements This research was primarily supported by CONACYT, Project No 167445, and this support is greatly appreciated. Professor Mervyn Kowalsky, from North Caroline State University, timely provided the authors the report on his research on bar buckling in RC columns. The authors are grateful for his generous help.

References

Dazio, A., Beyer, K., & Bachmann, H. (2009). Quasi-static cyclic tests and plastic hinge analysis of RC structural walls. *Engineering Structures*, 1556–1571.

Goodnight, J. C., Feng, Y., Kowalsky, M. J., & Nau, J. (2015). *The effects of Load History and Design Variables on Performance Limit States of Circular Bridge Columns*. Prepared for Alaska Department of Transportation and Public Facilities, Research, Development & Technology Transfer, Volumes 1 and 2.

Motter, C., Abdullah, S., & Wallace, J. (2018). Reinforced concrete structural walls without special boundary elements. *ACI Structural Journal, 115*(3), 723–733.

Moyer, M. J., & Kowalsky, M. J. (2003). Influence of Tension strain on buckling of reinforcement in concrete columns. *ACI Structural Journal, 100*(1), 75–85.

Priestley, M. J. N., Calvi, G. M., & Kowalsky, M. J. (2007). *Displacement-based seismic design of structures*. Pavia, Italy: IUSS Press.

Restrepo, J. I., Park, R., & Buchanan (1993). *Seismic behaviour of connections between precast concrete elements,* Research Report 93–3, Department of Civil Engineering, University of Canterbury, Christchurch, New Zealand.

Rodriguez, M. E.; Botero, J. C., & Villa, J. (1999). Cyclic Stress-strain behavior of reinforcing steel including effect of buckling. *Journal of Structural Engineering, ASCE, V. 125* (6), 605–612. https://doi.org/10.1061/(asce)0733-9445(1999)125:6(605).

Rodríguez, M. E., Torres, M., & Ortiz, A. (2013). Displacement based design of RC walls. In *Proceedings, XIX National Conference on Earthquake Engineering*. In Spanish (*Diseño sísmico de muros de concreto reforzado basado en desplazamientos*), Veracruz, Mexico.

Thomsen, J., & Wallace, J. (1995). *Displacement-based design of reinforced concrete structural walls: an experimental investigation of walls with rectangular and t-shaped cross sections*. Report NSF-BCS-9112962. National Science Foundation.

Villalobos, E. (2014). *Seismic response of structural walls with geometric and reinforcement discontinuities.* PhD Thesis, Purdue University, West Lafayette, Indiana.

Chapter 13
Experimental and Numerical Response of RC Walls with Discontinuities Under Cycling Loading

Leonardo M. Massone, Fabián Rojas, Gonzalo Muñoz, Ignacio Manríquez, Sebastián Díaz and Ricardo Herrera

In this work, the behavior of slender reinforced concrete (rc) walls with different types of discontinuities at the base, under cyclic lateral loading, are experimentally and numerically studied. First, the experimental results of a series of tests of rc walls with setbacks and central openings at the first floor are presented. Second, a robust quadrilateral element with 3 degrees of freedom (dof), 2 displacement and 1 in-plane rotation per node, and a transversal section made of a layered system of fully bonded, nonlinear smeared steel reinforcement and smeared orthotropic concrete material based on a rotating-angle approach, to represent the behavior of rc walls, is reviewed. Finally, the comparison of the experimental results with numerical models of the walls using the robust quadrilateral element is presented. It is observed that the model is able to capture in a good way the global and local response.

L. M. Massone · F. Rojas (✉) · G. Muñoz · I. Manríquez · S. Díaz · R. Herrera
Department of Civil Engineering, University of Chile, Santiago, Chile
e-mail: fabianrojas@uchile.cl

L. M. Massone
e-mail: lmassone@ing.uchile.cl

G. Muñoz
e-mail: gonzmunoza@gmail.com

I. Manríquez
e-mail: ignacio.manriquezr@gmail.com

S. Díaz
e-mail: sebadiazolivares@gmail.com

R. Herrera
e-mail: riherrer@ing.uchile.cl

T. T. C. Hsu (ed.), *Concrete Structures in Earthquake*,
https://doi.org/10.1007/978-981-13-3278-4_13

13.1 Introduction

Reinforced concrete (RC) walls are a fundamental part of lateral resisting force system against earthquake loads for multi-story (tall and mid-rise) buildings. Structural systems with RC walls provide stiffness and strength to limit the story drift and satisfy the demands produced by strong ground motions. Typically, these systems have exhibited a good performance during earthquakes with rare occurrences of complete collapse.

However, after the 2010 Maule earthquake of Mw 8.8, several RC wall buildings presented damage, such as crushing of concrete, buckling, and fracture of steel reinforcement due to lack of confinement, in some walls at the first floors (Fig. 13.1). These levels of damages observed were not expected since these buildings had been designed according to the up-to-date seismic standards in the country, except for a proper boundary detailing. Some common features among the damaged walls were: little or no confinement at the wall ends; narrow thicknesses (below 200 mm); relatively high axial load; and discontinuities in height.

The majority of the issues observed and mentioned before, except for the issue of discontinuities has been addressed by the modifications to the reinforced concrete Chilean code (NCh 430), which have introduced the use of special boundary confinement and limitation of axial load over the walls. However, the discontinuity in walls is still an issue that needs to be addressed by the researchers and seismic codes in Chile and other countries.

The main sources of discontinuities observed in slender RC walls in Chile are commonly due to architectural constraints, which produce mainly two types of

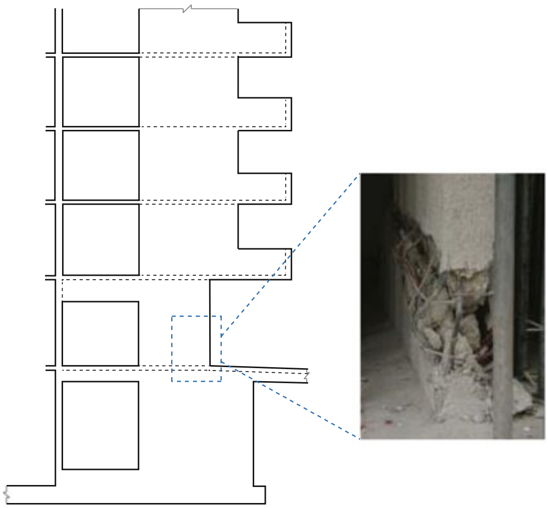

Fig. 13.1 Damage in walls with discontinuities in height after the 2010 earthquake. (Figure after Massone et al. 2017)

walls with discontinuities: walls with central openings and flags walls. The "flag walls" are walls where the length of the walls changes between floors designated for parking use and the upper floors designated for housing or office spaces, which create a setback in the lower levels (see Fig. 13.1). This type of discontinuity has not been investigated experimentally and numerically yet, and therefore it is necessary to study and evaluate its impact on RC walls.

The behavior of RC walls, and in special walls with discontinuities, depends on the interrelation and coupling of a combination of flexural, shear, and axial deformation over their cross sections at different levels, along with other complex mechanisms such as the bond slippage of longitudinal reinforcement at the base, effects of confinement, dowel action in reinforcement, cracking, and tension stiffening, which have been demonstrated by various researchers (Paulay and Priestley 1992; Bertero 1980; Orakcal et al. 2006) and, also on their configurations (wall size, height/length ratio, steel reinforcement, etc.) and loading conditions, producing combined failures such as flexural and compression failure, or combinations of failure ranging between flexural, axial and shear, as has been observed after recent Chilean's earthquakes (Naeim et al. 2011; Rojas et al. 2011; Massone et al. 2012).

These complex behaviors observed in RC walls results in the necessity to have a robust element, which can model and incorporate the majority of the characteristics described before. From the different options to model RC walls, grouped in macro models and micro-models, the micro-model approach, which is based on the finite element method (FEM or FE) and theory of continuum mechanics (Rojas 2016), are the preferred, because these types of elements allow to better represent complex geometries produced by discontinuities, and incorporate naturally the coupling of axial, flexural, and shear inside of these walls.

Between the different micro-models available in the literature (Mansour and Hsu 2005; Palermo and Vechio 2003), the robust quadrilateral layered membrane element with drilling degrees of freedom (DOF) proposed by Rojas et al. (2016) is selected and reviewed in the in this work.

In addition, it is necessary to have experimental data that allows to understand better the behavior and the impact of discontinuities in RC walls systems and also validate the numerical models. Due to this, in this work, two sets of experimental results are also presented and used. The first set of walls, correspond to four slender reinforced concrete walls, one without discontinuity and the other three with different sizes of setbacks ("flag walls"), to study the influence of this type of discontinuity. The second set corresponds to other four slender reinforced concrete walls with different center opening characteristics at the base, in order to determine the influence of this type of discontinuity in the wall behavior. The RC walls with discontinuities were tested under a nominal constant axial load of 0.1 f'_c A_g, and a cyclic lateral load increasing to specific drift levels. Conventional instrumentation and photogrammetry were used to monitor the tests.

13.2 Description of Experimental Program

In this section, the details of the experimental program, which include the instrumentation and characteristics, of two sets of slender reinforced concrete walls with discontinuities (setbacks and central openings) of different sizes at the base, are presented.

In Fig. 13.2, it is presented the test setup used for the study, in which, the specimens were attached to a strong floor by a series of post-tensioning bars placed at the wall foundation beam, and also, a steel frame was used to restrain the out-of-plane movement of the walls. In addition, on the top of the specimen was attached a steel beam to transfer the axial load, which was applied through a system of four bars anchored to the foundation beam tensioned by four hydraulic jacks. The value of the total axial load was selected to be equal to 0.1 f'_cA_g, which is a value representative of the level of axial load on the walls in the first stories of reinforced concrete buildings between 15 and 20 stories high in Chile. However, due to the concrete strength variation, the real value ranges between 0.09 and 0.07 f'_cA_g, for the different specimens.

Finally, the specimens were submitted to lateral load. The load was applied with displacement control using an actuator attached with post-tensioning bars to the strong wall and to the concrete loading beam on top of the wall at a height of 2.8 m. The displacement protocol was based on the recommendation of ACI (2001), and it was applied until reaching failure of the specimens. The displacements selected correspond to the followings drift of the height: 0.1, 0.2, 0.3, 0.4, 0.6, 0.9, 1.35, 2, 3, and 4%. The load was applied first in the negative direction for all tests.

The test specimens are divided in three groups. The first group is a single rectangular wall (W1) without any discontinuity, which is used as the base case,

Fig. 13.2 Experimental setup

with dimensions of 2.65 m height and 15 cm of thickness, and 90 cm of length, and a 40 × 70 cm foundation beam to attach the specimen to the strong floor, and a 30 × 40 cm loading beam on the top to apply the lateral load. The second group corresponds to three RC slender walls (W2, W3, W4) with the same base dimensions as W1, but each wall had overhangs of different sizes (see Fig. 13.3). The openings created by the overhangs are: specimen W2 with 250 mm in length and 300 mm in height, specimen W3 with 500 mm in length and 300 mm in height, and specimen W4 with 250 mm in length and 600 mm in height.

The reinforced used in the specimens are presented in Fig. 13.3. In the figure, it is observed an edge reinforcement of 4-ϕ16 bars on both sides, and a confinement provided by ϕ6 stirrups every 70 mm, over the first meter of the wall height. Similar reinforcement was provided on the hanging part of the wall for specimens W2, W3, and W4, with 4-ϕ16 bars that act as continuation of boundary bars at the wall base on the discontinuous side. The bars on the discontinuous boundary side are in the first one meter over the foundation, resulting in extension of 0.7 m for specimens W2 and W3 within the upper part of the wall, which is sufficient anchorage for such reinforcement. However, in specimen W4, this resulted in an extension of only 0.4 m. Finally, the web of the walls was covered with ϕ8 bars every 200 mm, in both vertical and horizontal directions. Vertical and horizontal reinforcement is doubled at the top of the wall to ensure proper load transfer.

The last group is 4 RC slender walls with central openings of different heights and lengths (see Fig. 13.4). The central openings are: specimen MR1 with 135 mm

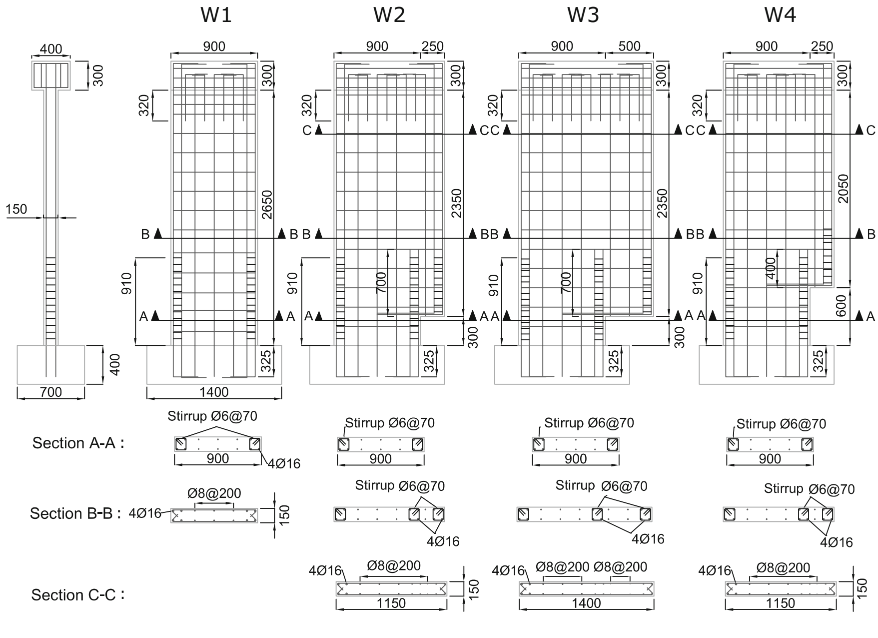

Fig. 13.3 Specimen with setbacks (Flag walls)

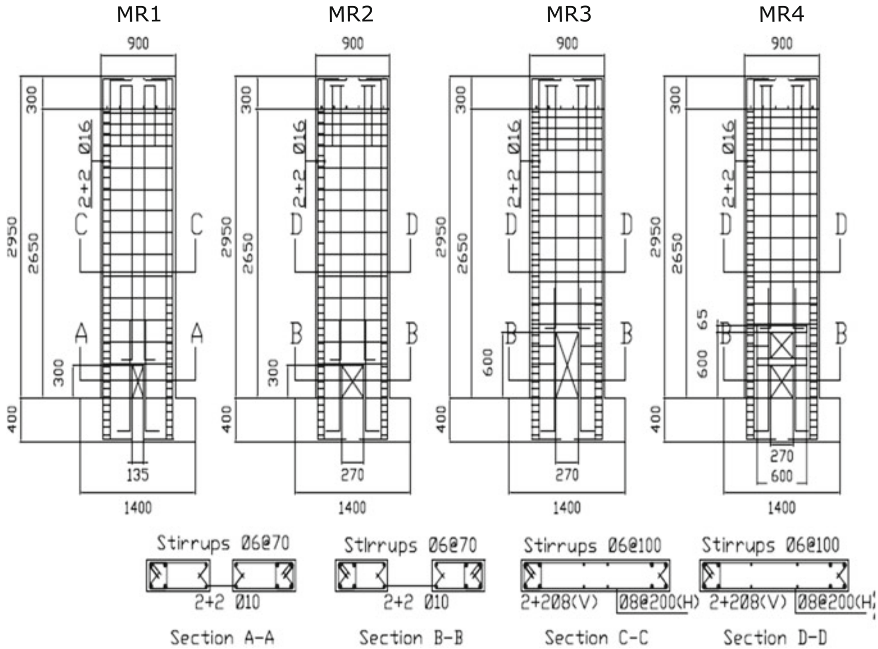

Fig. 13.4 Specimen with central opennings

in length and 300 mm in height, specimen MR2 with 270 mm in length and 300 mm in height, specimen MR3 with 270 mm in length and 600 mm in height and specimen MR4 with the same opening as MR3, but with two slabs of 600 × 900x65 mm centered and located at a height of 300 mm and 600 mm from the base of the wall.

The reinforced used in this second set of specimens, are similar to the first set, with 4 bars ϕ16 as longitudinal reinforcement at each boundary, confined with ϕ6 stirrups spaced every 70 mm over the first 900 mm of the wall; then one side was constructed with no stirrups and the other one with ϕ6 stirrups spaced every 100 mm until the top of the wall. In addition, at each edge of the discontinuity (opening), it was included 2 ϕ10 bars of longitudinal reinforcement. Similar to the other set of specimens, the horizontal reinforcing bar consists of ϕ8 bars spaced at 200 mm in the vertical direction, but the spacing in the opening was decreased to achieve a shear resistance similar to a case without opening. Vertical distributed reinforcement were ϕ8 bars and were spaced such that the bars are spliced with the bars located at the opening edge, simulating a spacing of 200 mm. Vertical and horizontal reinforcement is doubled at the top of the wall to ensure proper load transfer. It is important to mention that the reinforcement quantity and layout, dimensions are similar to W1, which is our base case.

The nominal compressive concrete strength (f′c) was 25 MPa (H30) for all the specimens. However, the value measured from the material samples were compressive strength of 33.0 MPa for W1, a representative value of 38.3 MPa for W2, W3, and W4, an average strength of 39.6 MPa for specimens MR1, MR2 and MR3 (tested at about 130 days of concrete maturity), and 41.2 MPa for specimen MR4 (tested at about 190 days after construction). The steel reinforcement bars were A630-420H, which are similar to grade 60 reinforcement (fy = 420 MPa—nominal). The average measured yield stress for the reinforced bars was 490 MPa. All wall specimens were built with materials properties and steel qualities typical of the construction of buildings in Chile.

In addition, the instrumentation during the testing of the specimen was done with standard devices (strain gages and lvdts) and photogrammetry (see Fig. 13.5). The standard instrumentation was done with 15 strain gages, which were located on the web horizontal bars near the discontinuity, boundary longitudinal bars and longitudinal bars at the side of the discontinuity of each specimen, and in one side of the wall. Around 30 LVDT's were installed, which measured the top lateral wall displacement, internal flexural and shear deformations, besides of sensors located in the pedestal of the specimen to measure any possible sliding or rigid body rotations.

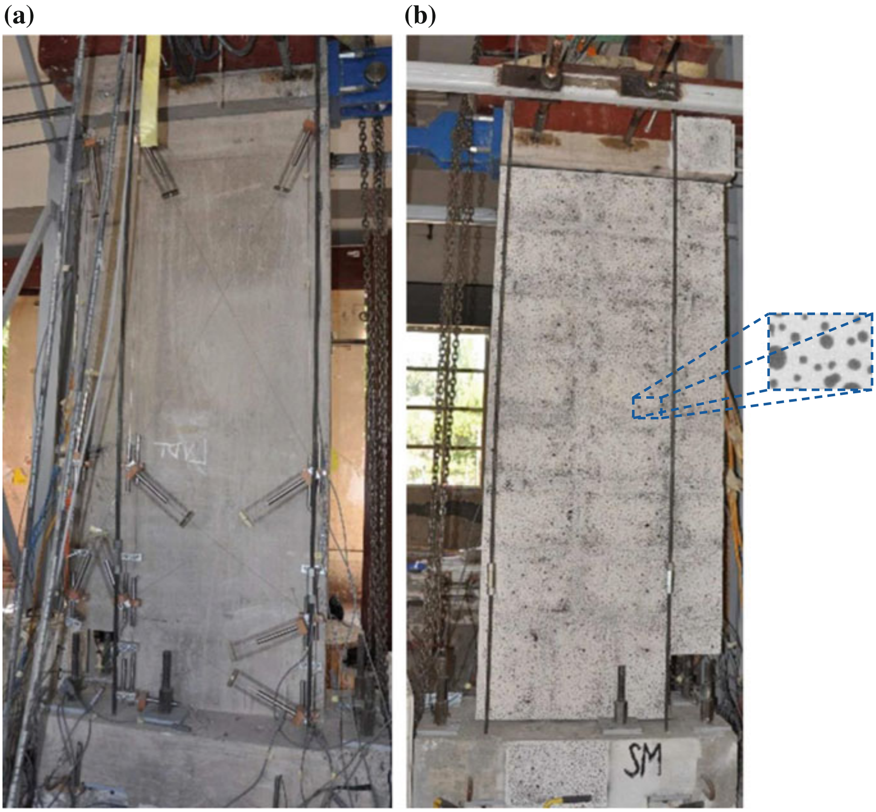

Fig. 13.5 Instrumentation: **a** Standard (LVDT's) **b** Photogrametry

The photogrammetry was done on the other side of the walls, and consists of two cameras, which captured images (globally and locally) of the walls, and irregular dots are drawn over all the height of the wall (see Fig. 13.5). The cameras capture imagines during the entire test process and later these pictures are processed to get displacements and strains over all the wall at different drift levels.

13.3 Experimental Results

In the case of walls with setbacks, since all specimens had similar dimension and longitudinal reinforcement at the base, the global capacity of all four specimens (W1, W2, W3, and W4) was similar (see Fig. 13.6). The lateral displacement was measured at the location of the actuator and corrected due to the pedestal sliding and rotation.

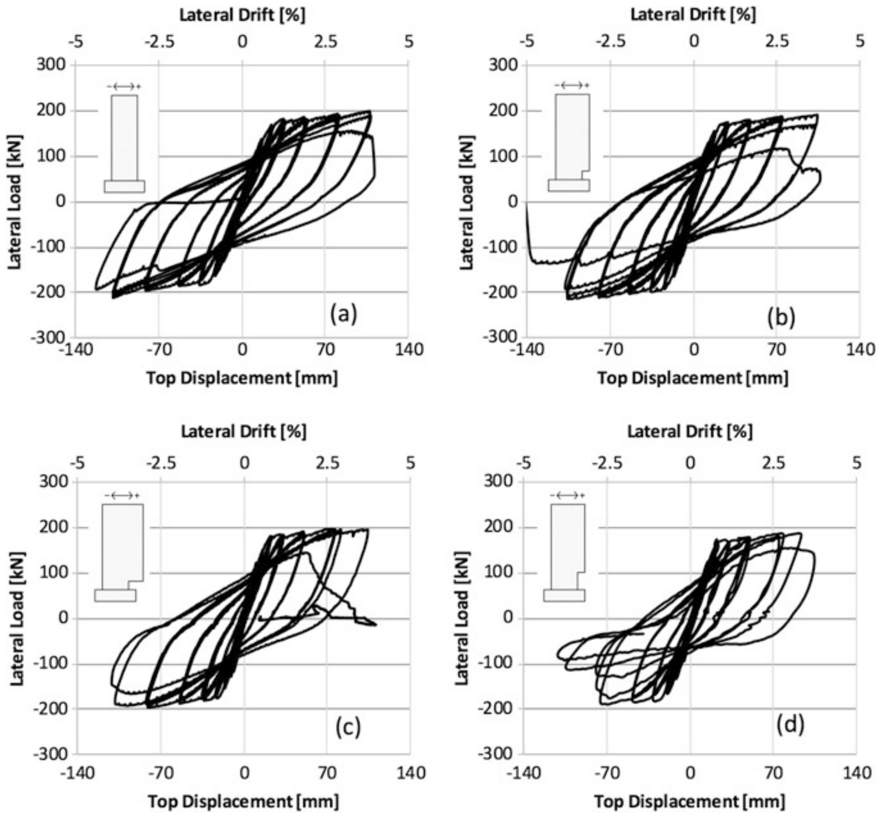

Fig. 13.6 Load versus Top Displacement walls with setbacks (Flag walls)

For wall W1 the strength degradation was observed at the third cycle of 4% drift in the positive direction, because of buckling of the boundary bars and crushing of concrete at the wall edges. W2 began to present spalling of the concrete cover during the first cycle of 3% drift in the negative direction, and degradation was observed during the third cycle at 4% drift in the positive direction, at which point the bars were exposed and presented significant buckling. W3 similar to W2, presented concrete cover loss at the second cycle of 3% in the positive direction and degradation was observed in the second cycle of 4% drift in the positive direction. W4 presented significant diagonal cracks where the longitudinal boundary reinforcement was cut in the discontinuous side at 2% drift, and at the first cycle of 4% spalling of the concrete cover was observed at the same location of the diagonal cracks.

In addition, all specimens with setbacks differed in the location and concentration of damage, but this was only noticeable at large drift levels (4%), as shown in Fig. 13.7. The behavior of all specimens was similar up to about 3% drift. The first distinguishable cracks appeared at the bottom part of the specimens at 0.3% drift in the negative direction, and the number and width of cracks increased with the following cycles. The presence of the discontinuity in specimens W2 and W3 causes an acceleration of the degradation in different cycles of 4% drift level, before specimen W1, which does not present discontinuity.

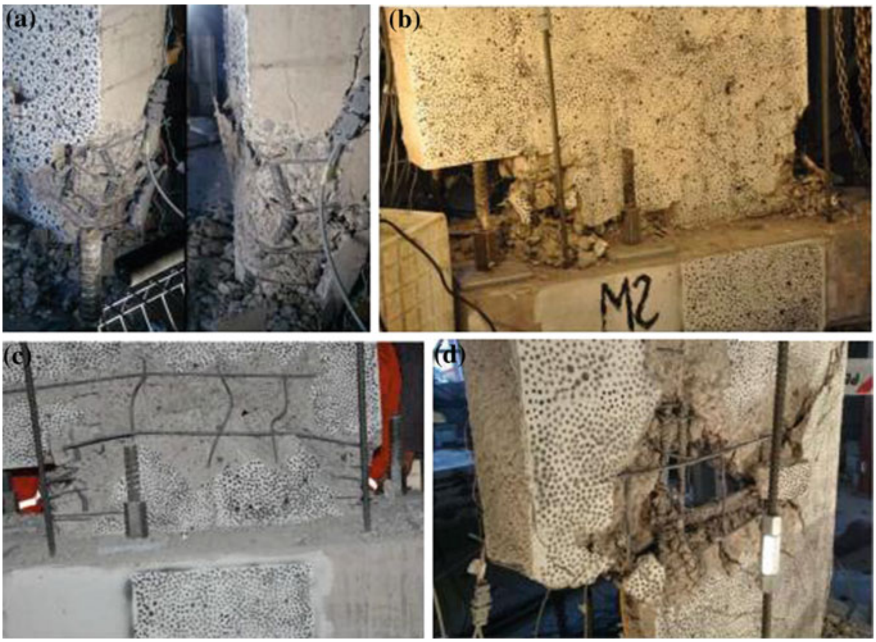

Fig. 13.7 Damage observed at W1 (**a**), W2 (**b**), W3 (**c**) and W4 (**d**) at 4% Drift

For the second set of specimens (walls with central openings), the lateral displacement (corrected also by pedestal sliding and rotation) versus lateral load for all specimens with a central opening is shown in Fig. 13.8. The figure shows with blue line the results for each wall, while the gray line represented the results for W1 (MR0), our base case. Overall global results indicate that all specimens reach almost the same lateral strength because yielding is achieved in flexure, as was expected, since the capacity is largely influenced by the boundary flexural reinforcement. The difference is observed in the displacement capacity reached by the specimens, which is impacted by the central openings.

Results of MR1 are shown in Fig. 13.8a, whose degradation occurs close to 3.7% drift (corrected). The larger (longer) opening in the specimen MR2 reduces considerably the displacement capacity (Fig. 13.8b), and degradation is reached at the 2.6% drift cycle in the positive direction. Figure 13.8c shows the response of specimen MR3, and there is no great difference between MR3 and MR2, and degradation is observed when trying to reach the second cycle of 2.6% drift in the negative direction; although degradation was already observed in the previous cycle. MR4 response is shown in Fig. 13.8d, which is different to MR3, it is

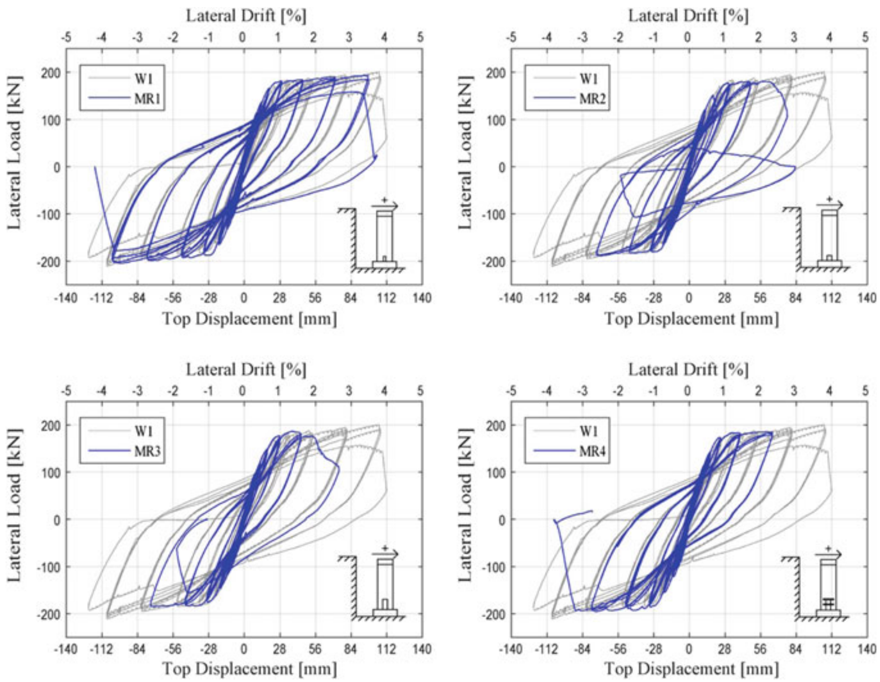

Fig. 13.8 Load versus displacement response of specimen—MR1 (**a**), MR2 (**b**), MR3 (**c**) and MR4 (**d**)

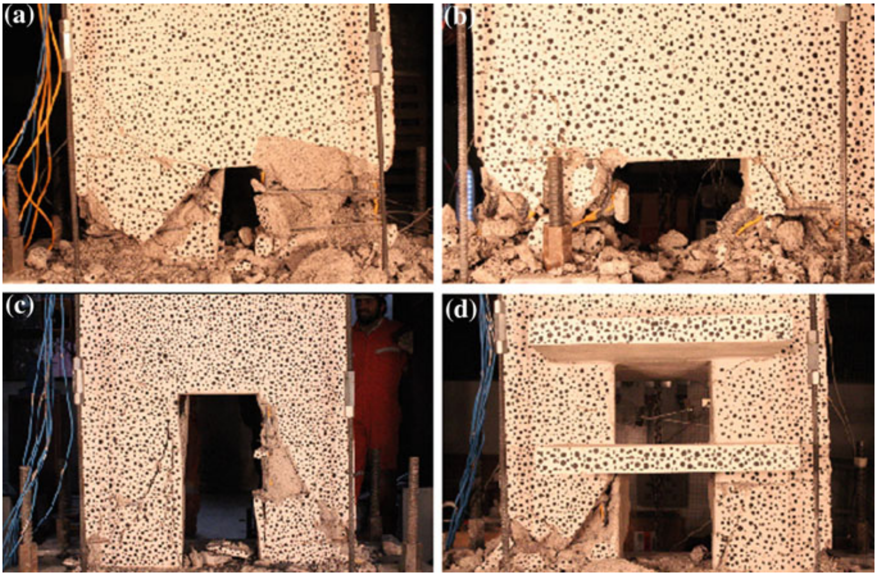

Fig. 13.9 Damage observed at MR1 (**a**), MR2 (**b**), MR3 (**c**) and MR4 (**d**) at 4% Drift

observed an improvement in the deformation capacity, but not as well as specimen MR1. The use of slabs allows finishing all three 2% drift cycles, having the wall a brittle failure trying to reach 3.2% drift. Figure 13.9 shows the final state of the damaged walls with central openings.

In the next sections, the formulation of the micro-model used in this work is reviewed, and the validation of the element using the experimental data is presented.

13.4 Nonlinear Quadrilateral Layered Membrane Element for Rc

In this section, the formulation of the quadrilateral layered membrane element with drilling degrees of freedom (DOF) developed by Rojas et al. (2016) is reviewed (Fig. 13.10a).

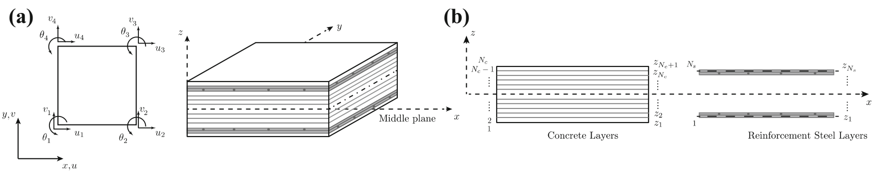

Fig. 13.10 **a** Membrane element DOF, **b** Layers definitions (Figure after) Rojas et al. (2016)

The membrane element is assumed to have only in-plane behavior ($\sigma_z = \tau_{zx} = \tau_{zy} = 0$), and its formulation, using a displacement-based approach, is developed from the concept of virtual work. The element stiffness matrix and resisting force assuming a fully bonded layered section, which is necessary to implement the element in any framework of nonlinear finite element, are presented next.

The tangent stiffness of the layered membrane using a displacement-based approach is defined as

$$K = \int_A [B]^T [D][B] dA, \tag{13.1}$$

where [B] is the kinematic matrix, which relates the deformations and displacements, and it can be defined as

$$[B(x,y)] = \underbrace{\begin{bmatrix} \frac{\partial}{\partial x} & 0 \\ 0 & \frac{\partial}{\partial y} \\ \frac{\partial}{\partial y} & \frac{\partial}{\partial x} \end{bmatrix}}_{[\partial]} [\psi(x,y)] = [\partial][\psi(x,y)] \tag{13.2}$$

and [D] is the material tangent matrix, which includes the concrete and steel layers, Eq. (13.3), and it can be expressed in a discrete form using the approach presented by Zhang et al. (2007)

$$[D] = \int_{-\frac{t}{2}}^{\frac{t}{2}} [D(z)] dz = \sum_{i=1}^{N_c} [D_{c_i}](z_{i+1} - z_i) + \sum_{j=1}^{N_s} [D_{s_j}] t_{s_j}, \tag{13.3}$$

where $[D_{ci}]$ and $[D_{sj}]$ are the plane stress material stiffness tangent of the i^{th} concrete layer and jth steel layer, respectively (see Fig. 13.2b).

Meanwhile, the internal resisting force (R) for the layered membrane assuming zero initial stress, can be obtained using a similar approach as

$$R = \int_A [B]^T \underbrace{\left(\int_{-\frac{t}{2}}^{\frac{t}{2}} \{\sigma\} dz \right)}_{\{\widehat{\sigma}\}} dA = \int_A [B]^T \begin{Bmatrix} n_x \\ n_y \\ n_{xy} \end{Bmatrix} dA, \tag{13.4}$$

where, $\{\widehat{\sigma}\}$ is the average stress at the middle plane, which can be calculated in a discrete manner, as follows:

$$
\begin{aligned}
n_x &= \int_{-\frac{t}{2}}^{\frac{t}{2}} \sigma_x dz = \sum_{i=1}^{N_c} \sigma_{x_i}^c (z_{i+1} - z_i) + \sum_{j=1}^{N_s} \sigma_{x_j}^s t_{s_j} \\
n_y &= \int_{-\frac{t}{2}}^{\frac{t}{2}} \sigma_y dz = \sum_{i=1}^{N_c} \sigma_{y_i}^c (z_{i+1} - z_i) + \sum_{j=1}^{N_s} \sigma_{y_j}^s t_{s_j} \\
n_{xy} &= \int_{-\frac{t}{2}}^{\frac{t}{2}} \tau_{xy} dz = \sum_{i=1}^{N_c} \tau_{xy_i}^c (z_{i+1} - z_i) + \sum_{j=1}^{N_s} \tau_{xy_j}^s t_{s_j},
\end{aligned}
\tag{13.5}
$$

where, $\{\sigma_i^c\}$ is the in-plane stresses at the ith concrete layer, and $\{\sigma_i^s\}$ is the in-plane stresses at the jth steel layer.

Now, the displacement field interpolation for the membrane element is developed by Rojas et al. (2016). This is a blended displacement interpolation that includes rotational DOF, which satisfies the constraint that the rotation at the nodes must be the true rotation derived from the mechanics when the element is rectangular. The blended interpolation is based on the combination of cubic interpolations and linear interpolations to represent the displacement in each direction, which can be represented in a matrix form as

$$
\{u\} = \left\{ \begin{matrix} u \\ v \end{matrix} \right\} = [\psi(x, y)]\{U\}, \tag{13.6}
$$

where $[\Psi(x, y)]$ is the interpolation matrix, and $\{U\}$ is the vector of nodal displacement as seen in Fig. 13.10a.

$$
\{U\} = \{\; u_1 \quad \upsilon_1 \quad \theta_1 \quad u_2 \quad \upsilon_2 \quad \theta_2 \quad u_3 \quad \upsilon_3 \quad \theta_3 \quad u_4 \quad \upsilon_4 \quad \theta_4 \;\}^T \tag{13.7}
$$

The interpolation matrix can be defined as

$$
[\psi(x, y)] = [\mathrm{MN}(x, y)][T_r], \tag{13.8}
$$

where [Tr] is the transformation matrix, that relates the global and local displacement in the element, and can be written as

$$[T_r] = \begin{bmatrix}
1 & 0 & 0 & 0 & 0 & 0 & 0 & 0 & 0 & 0 & 0 & 0 \\
0 & 1 & 0 & 0 & 0 & 0 & 0 & 0 & 0 & 0 & 0 & 0 \\
0 & 0 & \frac{y_4-y_1}{2} & 0 & 0 & 0 & 0 & 0 & 0 & 0 & 0 & 0 \\
0 & 0 & \frac{x_2-x_1}{2} & 0 & 0 & 0 & 0 & 0 & 0 & 0 & 0 & 0 \\
0 & 0 & 0 & 1 & 0 & 0 & 0 & 0 & 0 & 0 & 0 & 0 \\
0 & 0 & 0 & 0 & 1 & 0 & 0 & 0 & 0 & 0 & 0 & 0 \\
0 & 0 & 0 & 0 & 0 & \frac{y_3-y_2}{2} & 0 & 0 & 0 & 0 & 0 & 0 \\
0 & 0 & 0 & 0 & 0 & \frac{x_2-x_1}{2} & 0 & 0 & 0 & 0 & 0 & 0 \\
0 & 0 & 0 & 0 & 0 & 0 & 1 & 0 & 0 & 0 & 0 & 0 \\
0 & 0 & 0 & 0 & 0 & 0 & 0 & 1 & 0 & 0 & 0 & 0 \\
0 & 0 & 0 & 0 & 0 & 0 & 0 & 0 & \frac{y_3-y_2}{2} & 0 & 0 & 0 \\
0 & 0 & 0 & 0 & 0 & 0 & 0 & 0 & \frac{x_3-x_4}{2} & 0 & 0 & 0 \\
0 & 0 & 0 & 0 & 0 & 0 & 0 & 0 & 0 & 1 & 0 & 0 \\
0 & 0 & 0 & 0 & 0 & 0 & 0 & 0 & 0 & 0 & 1 & 0 \\
0 & 0 & 0 & 0 & 0 & 0 & 0 & 0 & 0 & 0 & 0 & \frac{y_4-y_1}{2} \\
0 & 0 & 0 & 0 & 0 & 0 & 0 & 0 & 0 & 0 & 0 & \frac{x_3-x_4}{2}
\end{bmatrix} \tag{13.9}$$

and [MN(x, y)] is the matrix that contains the blended interpolation functions (N_1 and N_2: Linear interpolation; M_1,M_2, M_3, and M_4: the Hermitian interpolations).

$$[MN(x,y)] = \left[\begin{matrix}
M_1(x)N_1(y) & 0 & -M_1(x)N_2(y) & 0 & M_2(x)N_1(y) & 0 \\
0 & M_1(y)N_1(x) & 0 & M_1(x)N_2(y) & 0 & M_1(y)N_3(x)
\end{matrix}\right.$$
$$\begin{matrix}
-M_2(x)N_2(y) & 0 & M_2(x)N_3(y) & 0 & -M_2(x)N_4(y) & 0 \\
0 & M_1(y)N_4(x) & 0 & M_2(y)N_3(x) & 0 & M_2(y)N_4(x)
\end{matrix}$$
$$\left.\begin{matrix}
M_1(x)N_3(y) & 0 & -M_1(x)N_4(y) & 0 \\
0 & M_2(y)N_1(x) & 0 & M_2(y)N_2(x)
\end{matrix}\right] \tag{13.10}$$

In addition, the constitutive models used for each concrete and steel layers are presented with details by Rojas et al. (2016). For the concrete layers, an orthotropic model formulation with rotating angle is used. The concrete formulation assumed the following:

- The main directions of stress and strain coincide.
- The stress–strain relationship can be represented by the average stress–strain relationship.
- The constitutive model of concrete in each of the principal directions of stress can be represented by a uniaxial concrete model.
- The Poisson's ratio is neglected after cracking.

In addition, the model of concrete incorporates features of the models proposed by the group at the University of Houston (CSMM developed by Mansour and Hsu in 2005) and the group at the University of Toronto (cyclic model developed by) Palermo and Vecchio (2003), and incorporate Poisson ratio under biaxial loads in compression developed by Vecchio in 1992, and coefficients biaxial strength and reducing the compressive strength of concrete due to the tensile strain (softening compression).

Meanwhile, the uniaxial constitutive model of the concrete is the model proposed by Massone (2006) with some modification to incorporate the cyclic behavior (Fig. 13.11). In the model, the compression envelope was defined with the curve defined by Thorenfeldt et al. (1987), and later calibrated by Collins and Porasz (1989). The envelope of tension, implemented by Massone (2006) is the proposal by Belarbi and Hsu (1994), which is divided into two sections, pre- and post-cracking. Before cracking, linear behavior is proposed, and after cracking, a descending branch is defined to include tension stiffening (Fig. 13.11). The proposed cyclic behavior uses a linear representation of loading and unloading compression, connected to each other, also with a linear equation with slope equal to the initial stiffness of concrete (Ec), as seen in Fig. 13.11. This constitutive model is used for confined and unconfined concrete, simply by varying the parameters that define the model to be able to incorporate the effects of confinement.

For the steel layer, the constitutive model is based on the following assumption

- Stress–strain relationship can be represented by the average stress–strain relationship of steel bars embedded in concrete, thus, the variation of stresses due to cracking over an area can be modeled using the average stresses and strains.
- Steel is considered homogeneous (smeared) and acts only along the direction of its orientation.
- Concrete and smeared steel are considered fully bonded.

Two different models can be used to represent the uniaxial constitutive model for the average steel. The first, it is the model proposed by Menegotto and Pinto (1973) and later modified by Filippou et al. (1983) (Fig. 13.12a). This model is mainly used to represent the behavior of the longitudinal and transverse bars located in the

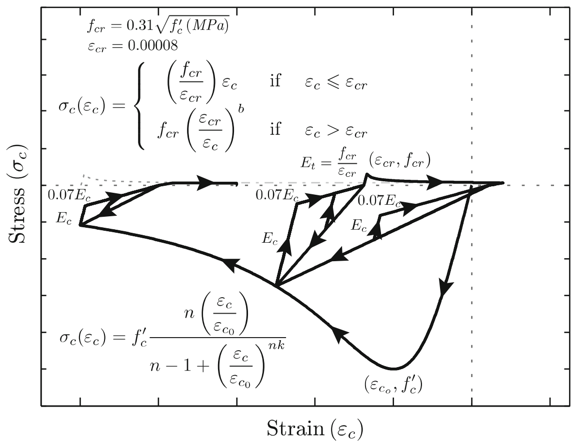

Fig. 13.11 Constitutive model for concrete (Figure after) Rojas et al. (2016)

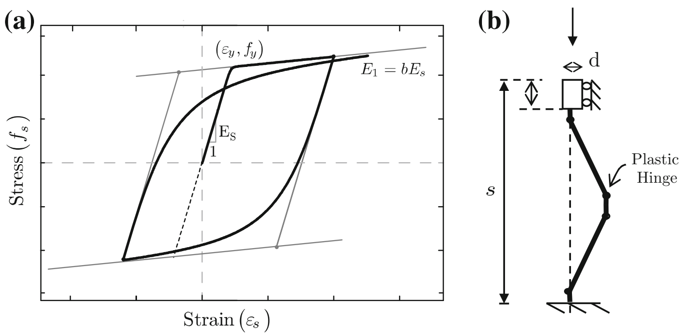

Fig. 13.12 **a** Constitutive Menegotto-Pinto model for steel and **b** Bar buckling model (Figure after) Rojas et al. (2016)

center of walls or the rebars that not suffer buckling during analysis. The second uniaxial constitutive model is the model proposed by Massone and Moroder (2009), which is used to represent the behavior of the longitudinal bars at the edges of walls that are susceptible to buckling. This second model incorporates the buckling of the bars by incorporate an initial imperfection (Fig. 13.12b) and using a sectional analysis that performs equilibrium at four plastic hinges (per bar susceptible to buckling) in the deformed stage.

13.5 Numerical Models

In this section, the comparison of the numerical model and the test results are presented. The models are generated using the nonlinear quadrilateral layered membrane element with drilling DOF presented before, which consider the combination of axial, flexural and shear behavior, and the representation of all the parts of each wall (concrete cover, distributed reinforcement bars, longitudinal reinforcement, stirrups, confined concrete, and unconfined concrete).

For all the models, the measured properties of the materials (as-tested peak strength of concrete and steel bars properties) were used to calibrate the material constitutive models. In addition, the tensile strength of the concrete ($f_{cr)}$ was considered equal to 0.31 f_c' [MPa] (0.118 f_c' [ksi]), and the tension strain ε_{cr} at the maximum tensile strength was equal to 0.00008 [mm/mm], and depending on the level of confinement, a compression strain between −0.003 and −0.0055 [mm/mm] at the maximum compressive strength of the confined concrete for the different specimens, was used. The modification coefficient for damage due to cycling in the material was also included in the model. The discretization distinguishes between confined and unconfined concrete, and the steel reinforcement in the section, using quadrilateral elements between 150 mm by 150 mm in the upper part of the model, and smaller elements of 75 mm high by 50 mm long at the discontinuities and

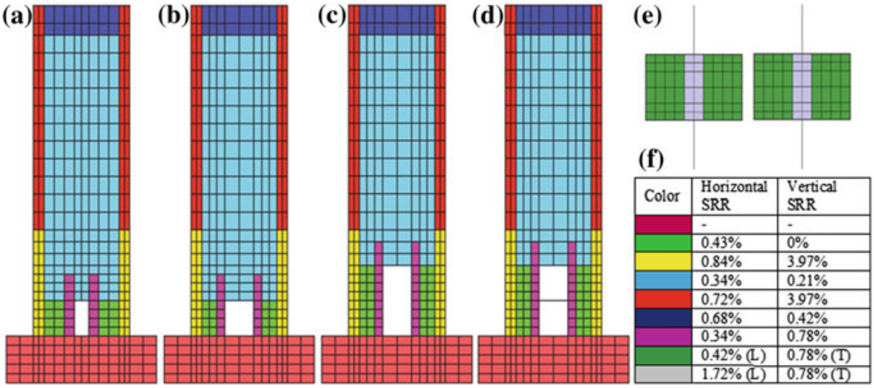

Color	Horizontal SRR	Vertical SRR
	-	-
	0.43%	0%
	0.84%	3.97%
	0.34%	0.21%
	0.72%	3.97%
	0.68%	0.42%
	0.34%	0.78%
	0.42% (L)	0.78% (T)
	1.72% (L)	0.78% (T)

Fig. 13.13 Modeling discretization of walls: **a** MR1, **b** MR2, **c** MR3, **d** MR4, **e** MR4 slabs and **f** steel ratios

boundary elements. As an example, Fig. 13.13 shows the discretization for the model of walls with central openings. The elements of the foundation are generated using an elastic material for simplicity.

Also, the longitudinal reinforcement, which is susceptible to buckling, was model using the uniaxial constitutive material proposed by Massone and Moroder (2009). Meanwhile, the horizontal reinforcement, and the boundary reinforcement (ϕ16) with closed spaced stirrups, in which the buckling is restricted, are modeled using the uniaxial constitutive material modified by Filippou et al. (1983). Moreover, in the steel model, a base value of 1% for the hardening ratio and a value of Es = 200000 [MPa] for Young's modulus of the steel were used. Finally, for the analysis of the models, a 3-by-3 Gauss integration points in each element and the displacement control solution algorithm with pseudo-constant incremental steps, which is a variation of the algorithm developed by Batoz and Dhatt (1979), were used.

Figure 13.14 shows the lateral load versus top lateral displacement response under lateral cyclic loading of the specimens with setbacks (flags walls), where the tested specimens are shown in light gray and the response of the numerical models in black. A good correlation between the model and the experimental results, especially regarding capacity and ductility, is observed. In specimens W2 and W3, it is observed a degradation in earlier cycles at 4% drift, when compared with specimen W1 (no discontinuity) due to the presence of a discontinuity. A slightly higher concentration of strains at the base of flag walls is the cause of concrete crushing, which accelerates the degradation. In addition, the numerical model of specimen W4 also shows a good agreement with the test, and it is able to capture the earlier crushing at the end of the discontinuous longitudinal reinforcement. This was achieved considering a development length with 50% effectiveness.

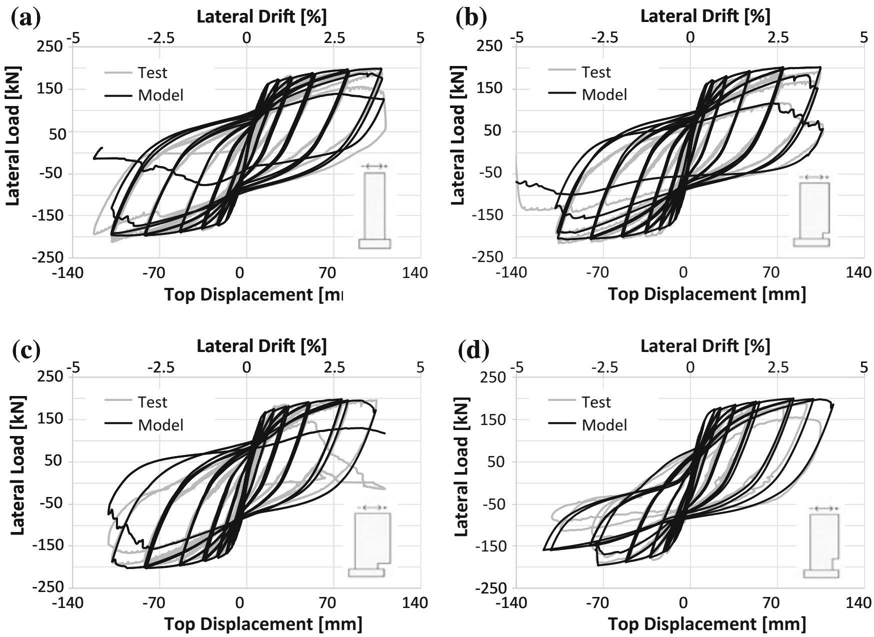

Fig. 13.14 Load displacement response of specimens—**a** W1, **b** W2, **c** W3, and **d** W4

Figure 13.15 shows the lateral load versus top lateral displacement response under lateral cyclic loading of the specimens with a central opening, where the tested is in light gray and the response of the numerical models in red. In addition, it is included in blue color the pure bending model, which is achieved by placing rigid horizontal elements, discontinuous at the opening, at every level of elements that forces the Bernoulli Hypothesis, in order to study the influence of shear in the response of this type of discontinuity. The models are able to accurately reflect the stiffness, strength, and displacement capacity. For the two types of modeling, the hysteresis obtained always shows a greater initial stiffness and a modest over strength ($\sim 10\%$). The initial stiffness difference may be associated with the handling of the test specimens prior to the test. However, the unloading and reloading stiffness are well captured.

Now, if the two type models for each wall with a central opening are compared, it is observed that taking as a reference the first loss of strength in the hysteresis loop, the flexural models are similar to the complete models, but depending on the opening they can produce more or less conservative results. The above occurs because in the walls with small openings (MR1 and MR2) the discontinuity acts as a limiting factor in the propagation of the damage in height, while in the walls with higher openings (MR3 and MR4) this limitation does not control.

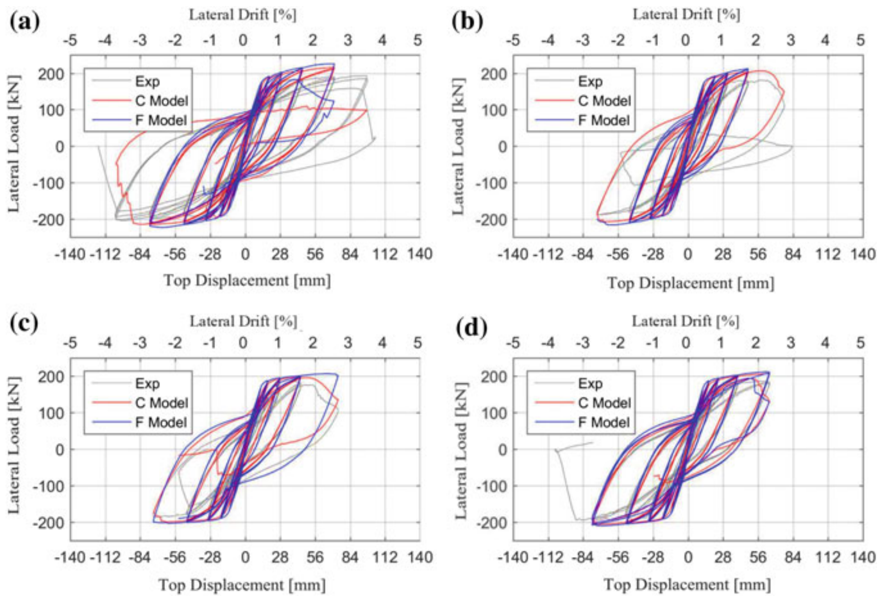

Fig. 13.15 Analytical and experimental load versus displacement response of specimens—**a** MR1, **b** MR2, **c** MR3 and **d** MR4

13.6 Conclusions

In this work, the experimental study of two set of scaled slender RC walls with discontinuities, one with setback (flag walls) and other with a central opening at the base, are summarized. In addition, the quadrilateral layered membrane element with drilling degrees of freedom proposed by Rojas et al. (2016) is validated with the test result to model RC walls with discontinuities.

The specimens are constructed and tested in cantilever with a cyclic lateral point load at the wall top. An axial load was also considered ($\sim 0.07f'_cA_g$). One of the specimens has two centered slabs near the base. The walls with discontinuities were designed to have the same flexural strength as the base case without discontinuity, which is confirmed with the tests. The main global impact or difference between the different types and sizes of discontinuities are the deformation capacity. In the case of the walls with setbacks, initiation of strength degradation indicated that the discontinuity concentrated the damage closer to the base of the wall, forcing the degradation to occur at the same level of displacement of a wall without discontinuity, but at an earlier cycle. Inadequate anchorage of specimen W4 resulted in damage concentration at the bar discontinuity and degradation at an even earlier cycle. In the case of the wall with a central opening, the comparison between MR1 and MR2 and among MR2 and MR3 reveals that width is more influential than height in the displacement capacity degradation. The use of slabs has an impact in the wall response: despite having a taller opening, MR4 has a similar behavior as MR2 (with the same opening width but half the height compared to MR4). Finally, the central opening has a larger impact in the capacity degradation, than the setback. Since the influence of the openings affects the deformation capacity and not strength, proposals for design improvement should be focused on detailing.

In the case of the model validation, the quadrilateral element with layered sections was able to correctly represent the global behavior of all the tested walls, and the failure mode. The complete models and pure bending capture the response of the walls, being slightly more accurate the complete model. Thus, the pure bending model of walls with openings is considered adequate to capture stiffness, strength, and displacement capacity.

References

ACI T1.1-01. (2001). *Acceptance criteria for moment frames base on structural testing*. American Concrete Institute, Farmington Hills, MI, USA.

Batoz, J. L., & Dhatt, G. (1979). Incremental displacement algorithms for non- linear problems. *International Journal for Numerical Methods in Engineering, 14*(8), 1262–1267.

Belarbi, A., & Hsu, T. T. C. (1994). Constitutive laws of concrete in tension and reinforcing bars stiffened by concrete. *ACI Structural Journal, 91*(4), 465–474.

Bertero, V. V. (1980). Seismic behaviors of RC wall structural system. In *7th World Conference on Earthquake Engineering*; vol. 6. Instalbul, Turkey, p. 323–330.

Collins, M. P., Porasz, A. (1989). *Shear strength for high strength concrete; 66 chap. Bulletin D'Information* No. 193—Design Aspects of High Strength Concrete. Paris, France, p. 75–83.

Filippou, F. C., Popov, E. G., & Bertero, V. V. (1983). *Effects of bond deterio- ration on hysteretic behavior of reinforced concrete joints. UCB/EERC83/19; Earthquake Engineering*. Berkeley: Research Center, University of California.

INN, NCh 430Of. (2008). *Reinforced concrete—Design and calculation requirements (in Spanish)*. Instituto Nacional de Normalización, Santiago, Chile.

Mansour, M., & Hsu, T. T. C. (2005a). Behavior of reinforced concrete elements under cyclic shear. i: Experiments. *Journal of Structural Engineering, 131*(1), 44–53.

Mansour, M., & Hsu, T. T. C. (2005b). Behavior of reinforced concrete elements under cyclic shear. ii: Theoretical model. *Journal of Structural Engineering, 131*(1), 54–65.

Massone, L. M. (2006). *RC wall shear—flexure interaction: Analytical and experimental responses*. Ph. D. Dissertation; University of California, Los Angeles, California.

Massone, L. M., & Moroder, D. (2009). Buckling modeling of reinforcing bars with imperfections. *Engineering Structures, 31,* 758–767.

Massone, L. M., Bonelli, P., Lagos, R., Lüders, C., Moehle, J., & Wallace, J. W. (2012). Seismic design and construction practices for RC structural wall buildings. *Earthquake Spectra, 28*(S1), 245–256.

Massone, L., Rojas, F., & Ahumada, M. (2017). Analytical study of the response of reinforced concrete walls with discontinuities of flag-wall type. *Structural Concrete, 18*(6), 962–973.

Menegotto, M., Pinto, P. E. (1973). *Method of analysis of cyclically loaded reinforced concrete plane frames including changes in geometry and non- elastic behavior of elements under combined normal force and bending*. IABSE Symposium on the Resistance and Ultimate Deformability of Structures Acted on by Well-Defined Repeated Loads.

Naeim, F., Lew, M., Carpenter, L. D., Youssef, N. F., Rojas, F., Saragoni, G. R., et al. (2011). Performance of tall buildings in santiago, chile during the 27 February 2010 offshore maule, chile earthquake. *The Structural Design of Tall and Special Buildings, 20*(1), 1–16.

Orakcal, K., Massone, L. M., Wallace, J. W. (2006). *Analytical modeling of reinforced concrete walls for predicting flexural and coupled-shear-flexural responses*. PEER Report 2006/07; UC, Los Angeles.

Palermo, D., & Vecchio, F. J. (2003). Compression field modeling of reinforced concrete subjected to reversed loading: Formulation. *ACI Structural Journal, 100*(5), 616–625.

Paulay, T., Priestley, M. J. N. (1992) *Seismic design of reinforced concrete and masonry buildings*. John Wiley and Sons, Inc.

Rojas, F., Anderson, J. C., & Massone, L. M. (2016). A nonlinear quadrilateral layered membrane element with drilling degrees of freedom for the modeling of reinforced concrete walls. *Engineering Structures, 124,* 521–538.

Rojas, F., Naeim, F., Lew, M., Carpenter, L. D., Youssef, N. F., Saragoni, G. R., et al. (2011). Performance of tall buildings in concepcio´n during the 27 February 2010 moment magnitude 8.8 offshore maule, chile earthquake. *The Structural Design of Tall and Special Buildings, 20*(1), 37–64.

Thorenfeldt, E., Tomaszewicz, A., & Jensen, J. J. (1987). *Mechanical properties of high-strength concrete and application in design*. Stavanger, Norway: Symposium Utilization of High-Strength Concrete.

Zhang, Y. X., Bradford, M. A., & Gilbert, R. I. (2007). A layered cylindrical quadrilateral shell element for nonlinear analysis of RC plate structures. *Advances in Engineering Software, 38*(7), 488–500.

Chapter 14
Assessment of the Boundary Region Stability of Special RC Walls

Ana G. Haro, Mervyn Kowalsky and Y. H. Chai

In the aftermath of the Chile 2010 and New Zealand 2011 earthquakes, the out-of-plane buckling mechanism of reinforced concrete structural walls (RCSW) was reported for the first time in real structures. However, this failure mode had been studied since 1980s through experimental observations that constituted the basis of phenomenological models created to prevent and assess buckling instability of RCSW. Based on these models, a less conservative approach is proposed that was validated through experimental and analytical studies conducted on prisms simulating special boundary regions of planar RCSW. The main parameters considered were the influence of different loading paths acting simultaneously, the longitudinal reinforcement ratio, and the thickness of the wall. The results showed that the onset of out-of-plane buckling instability of planar RCSW is mainly governed by the longitudinal steel content, the in-plane loading demands, and the wall thickness.

A. G. Haro (✉)
Departamento de Ciencias de la Tierra y la Construcción, Universidad de las Fuerzas Armadas ESPE, 171103 Sangolquí, Ecuador
e-mail: agharo@espe.edu.ec

A. G. Haro
North Carolina State University, Raleigh, NC 27695, USA

M. Kowalsky
North Carolina State University, Mann Hall, Stinson Drive, Raleigh, NC 27695, USA
e-mail: kowalsky@ncsu.edu

Y. H. Chai
University of California, 3133 Ghausi Hall, Davis, CA 95616, USA
e-mail: yhchai@ucdavis.edu

T. T. C. Hsu (ed.), *Concrete Structures in Earthquake*,
https://doi.org/10.1007/978-981-13-3278-4_14

14.1 Introduction

The earthquakes in 2010 Chile and 2011 New Zealand revealed the importance of the out-of-plane buckling failure mode in RCSW, which was first studied by Goodsir (1985) during an experimental program conducted on walls to develop a capacity-based seismic design method for RCSW. Figure 14.1 shows an example of wall instability with concentrated damage in the boundary element region of a 300 mm thick L-shaped concrete wall from the Christchurch Earthquake in 2011. Kinematic models have been created to relate tensile strains due to in-plane loading to out-of-plane wall deformations that could cause instability (Paulay and Priestley 1993; Chai and Elayer 1999). The aim of these models is to limit the tensile strains developed in the end regions and, at the same time, to control the crack opening intrinsically associated with the wall out-of-plane buckling mechanism.

Reinforced concrete prisms (RCP) have been tested under cyclic axial loading to simulate the effects of in-plane loading on the boundary ends of walls with two curtains of reinforcement, a worldwide common construction practice. This methodology is convenient to identify the effect of critical parameters on the onset of buckling instability of RCSW (Goodsir 1985; Chai and Elayer 1999; Creagh et al. 2010; Chrysanidis and Tegos 2012; Shea et al. 2013; Flintrop et al. 2013; Welt 2015). The mentioned models provide conservative estimates of the tensile strains that cause instability (Herrick and Kowalsky 2016). A new approach based on these models and the tests results from the study conducted by Haro et al. (2018) is described in this paper. The experimental program consisted of 12 half-scaled RCP representative of well-confined boundary regions, with reinforcement ratios commonly used in RCSW from Chile and

Fig. 14.1 Out-of-plane buckling of the Pacific Brands House's L-Wall during the 2011 Christchurch Earthquake. (Photos courtesy of Sri Sritharan)

New Zealand. An additional variable included in the study was combined axial tension–compression cycles and out-of-plane interstorey drifts to consider the effects of in-plane and out-of-plane demands derived from the horizontal components of earthquakes. The results contribute to the establishment of minimum wall thickness criteria to provide a ductile response of RCSW subjected to important seismic demands.

14.2 Out-of-Plane Buckling Instability of RC Walls

Thin reinforced concrete walls are prone to experience out-of-plane buckling instability as first established by Goodsir (1985). Figure 14.2a shows wide crack openings in the end region of a wall along the potential buckled length L_o, caused by large inelastic tensile strains due to in-plane lateral loading. Upon load reversals two possible scenarios could occur when out-of-plane deformations, δ, develop in the new compressed end region as a result of the eccentricity of the compressive force required to resist the overturning moment. If the out-of-plane deformation is small, as depicted in Fig. 14.2b, the compressive force can be fully developed as cracks gradually close. However, if the out-of-plane deformation is relatively large, as shown in Fig. 14.2c, the wall could become unstable, losing its lateral and vertical load-carrying capacity.

Paulay and Priestley (1993) first proposed a model to consider two key features suggested by the out-of-plane buckling mechanism: (1) a relationship between developed tensile strains due to in-plane loading and out-of-plane deformations exhibited upon reversal of loading, and (2) a limit for the out-of-plane deformation that the wall could sustain before buckling. The model established by Paulay and Priestley, as expressed in Eq. (14.1), prevents inelastic buckling of RCSW by

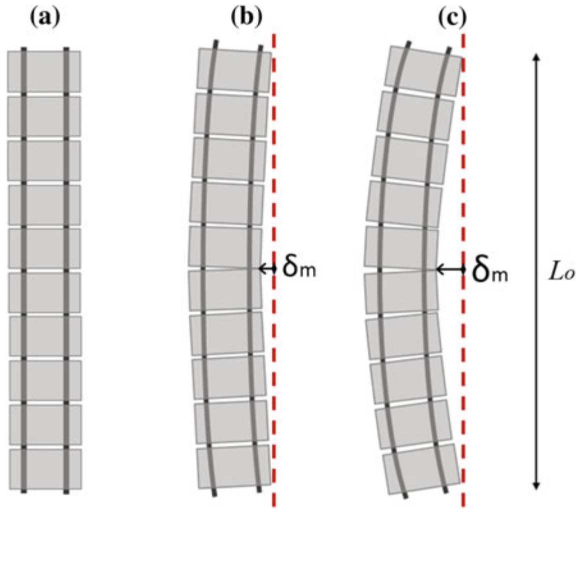

Fig. 14.2 Wall end region buckling mechanism: **a** inelastic tensile incursion, **b** small transverse deformation, and **c** large transverse deformation

limiting the tensile strains imposed on boundary ends. This model contemplates a constant curvature distribution along the potential buckled region as well as a stability criterion, defined by Eq. (14.2), that bounds the out-of-plane deformation, in normalized form ($\xi = \delta_m/b_w$), at mid-height of the buckled region.

$$\varepsilon_{sm} \leq 8\beta\left(\frac{b_w}{L_o}\right)^2 \xi_{cr} \tag{14.1}$$

$$\xi \leq \xi_{cr} = 0.5\left(1 + 2.35m - \sqrt{5.53m^2 + 4.70m}\right) \leq 0.5 \tag{14.2}$$

where b_w is the thickness of the wall, β is the ratio between the distance from the interior side of the wall to the extreme longitudinal reinforcement in the transverse direction and the thickness of the wall ($\beta = d_t/b_w$), ε_{sm} is the maximum tensile strain in the extreme longitudinal steel, and L_o is the height of the buckled region. The mechanical reinforcement ratio is $m = \rho_{lbe}\, f_y/f'_c$, where ρ_{lbe} is the local reinforcement ratio in the end region of the wall, f_y is the longitudinal steel yielding strength, and f'_c is the compressive concrete strength.

Later, Chai and Elayer (1999) executed an experimental program carried out on RCP using an artificial pin-connection at the two ends of the RCP to correspond to the buckled length L_o in their model. These RCP simulated boundary ends of planar walls subjected to axial cyclic loading. The results showed that the hysteretic behavior of the longitudinal reinforcement steel was missing from Eq. (14.1). Subsequently, a modification was proposed considering that the maximum tensile strain consists of three strain components according to Eq. (14.3): $\varepsilon_a{}^*$ is the axial strain at first closure of cracks, ε_e is the strain required to yield the reinforcement in compression, and ε_r accounts for the effect of strains elastically recovered during unloading. The two last components can be expressed as proportions of the yielding strain ε_y (i.e., $\varepsilon_e + \varepsilon_r = 1\varepsilon_y + 2\varepsilon_y$).

$$\varepsilon_{sm} = \varepsilon_a^* + \varepsilon_e + \varepsilon_r \tag{14.3}$$

Chai and Elayer (1999) also considered the stability criterion from Eq. (14.2) and assumed a sinusoidal curvature distribution. The result is expressed by Eq. (14.4), which limits the maximum tensile strains developed in the compression region of RCSW to prevent out-of-plane buckling instability.

$$\varepsilon_{sm} = \frac{\pi^2}{2}\left(\frac{b_w}{L_o}\right)^2 \xi_{cr} + 3\varepsilon_y \tag{14.4}$$

The idealization of wall end regions by RCP subjected to axial cyclic loads suggests a uniform distribution of tensile strains along the height of the critical storey. However, the damage captured in actual walls and previous analytical studies have demonstrated that the end region of a wall exhibits strain gradients not only along the height of the wall but also along the length of the wall (Parra 2015).

In order to account for the effects of a nonuniform distribution of the axial load over the height of a wall, Parra (2015) developed a formula, written as Eq. (14.5), based on the modeling concepts proposed by Paulay and Priestley (1993).

$$\varepsilon_{sm} \leq (5 - 4\alpha)\left(\left(\frac{b_{cr}}{0.7kh_u}\right)^2 + 0.005\right) \tag{14.5}$$

where α is the parameter that represents the axial force profile, considered as 0.2 for practical solutions, b_{cr} is the critical width of the wall, kh_u is the effective length equal to $0.5h_u$ assuming fixed ends, and h_u is the clear interstorey height.

The effects of the longitudinal steel content are omitted from Eq. (14.5) since the stability criterion, Eq. (14.2), was simplified by a coefficient equal to 0.25. However, tests on prisms by, e.g., Chai and Elayer (1999) and Haro et al. (2018), suggest that one of the most influential parameters on the onset of lateral instability is the longitudinal reinforcement ratio. Consequently, this approach would report inappropriate predictions.

The maximum tensile strains predicted by Eq. (14.1) and Eq. (14.4) have been shown to be relatively conservative, especially for steel content greater than 2% (Herrick and Kowalsky 2016; Haro et al. 2018). The tests covered in this paper were part of an experimental and analytical program conducted on RCP with fixed–fixed boundary conditions simulating a more realistic prism length that corresponds to the interstorey height of the wall. The results contributed to develop an improved model for seismic design of RCSW based on the key concepts identified by Paulay and Priestley (1993) and Chai and Elayer (1999).

14.3 Experimental Tests and Results

Twelve half-scaled RCP were experimentally tested in the Constructed Facilities Laboratory (CFL) at NC State University during this study. Three phases were considered during the experimental program. The first phase involved controlled load paths where the specimens were subjected to axial tension/compression cycles combined with lateral loading to mimic the effects of out-of-plane displacements. In the second and third phases, varying longitudinal reinforcement ratios and additional loading protocols were followed. In general, the three phases included reinforcement ratios of typical values used in RC buildings and employed by the Alaska DOT for pier walls.

The 12 RCP were built in accordance with the recommendations of the ACI 318-14, chapter 18. The clear height was 1,524 mm (60in.), corresponding to an aspect ratio (h_w/b_w = *height/thickness*) of about 10, including the missing cover concrete. The reinforcement details associated with the three phases are presented in Fig. 14.3.

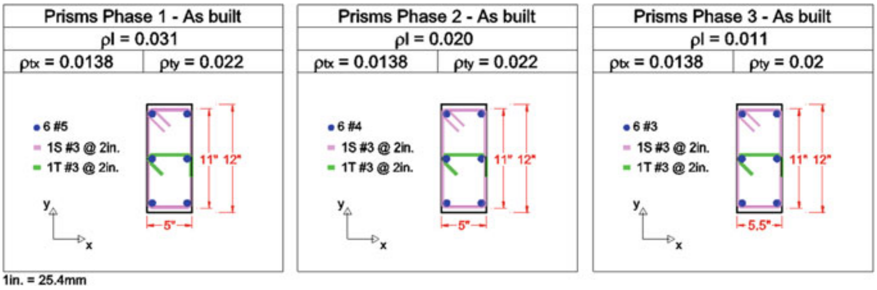

Fig. 14.3 Reinforcement detailing of the RCP

14.3.1 Loading Protocols

Experimental phases 1 and 2 involved controlled load paths where the specimens were subjected to axial tensile and compressive displacements in addition to top out-of-plane drifts estimated as percentages of the clear height of the prisms. The lateral demands contemplated mainly monotonic-type loading; only Prism P5 considered a cyclic-type loading. Phase 3 only involved axial tensile and compressive displacements. Actual material properties were used to calculate tensile demands. An unconfined concrete strength of 35 MPa (5ksi) and a reinforcement yielding strength of 414 MPa (60ksi) were considered as design values to define the experimental load history in compression. Table 14.1 details the experimental test matrix.

Table 14.1 Experimental test matrix

Phase	Prism	Mechanical properties		Load protocol				
				Lateral		Axial		
		f'c (MPa)	ε_y (%)	Drift (%)	Type	Max. Tension	Max. compression	Type
1	P1	53.10	0. 239	17	Monotonic	3%	0.5 in.	[a]Cycle
	P2	52.40		0	–	$12\varepsilon_y$	Po = 358 kips	Cyclic
	P3	51.00		1	Monotonic	$14\varepsilon_y$	$P_{1\%}$ = 319 kips	Cyclic
	P4	49.60		4	Monotonic	$12\varepsilon_y$	$P_{4\%}$ = 241 kips	Cyclic
	P5	49.00		4	Cyclic	$12\varepsilon_y$	$P_{4\%}$ = 241 kips	Cyclic
	P6	53.10		8	Monotonic	$12\varepsilon_y$	$P_{4\%}$ = 182 kips	Cyclic
2	P7	48.30	0. 238	0	–	$14\varepsilon_y$	Po = 322 kips	Cyclic
	P8	52.40		4	Monotonic	$14\varepsilon_y$	$P_{4\%}$ = 222 kips	Cyclic
	P9	51.70		2.5	Monotonic	$16\varepsilon_y$	$P_{2.5\%}$ = 251 kips	EQ-Sylmar Station ('94)
3	P10	44.80	0.217	0	–	$16\varepsilon_y$	P_o = 294 kips	Cyclic
	P11	43.40		0	–	$22\varepsilon_y$	P_o = 294 kips	EQ-Megathrust
	P12	44.80		0	–	$18\varepsilon_y$	P_o = 294 kips	EQ-Sylmar Station ('94)

[a]kip = 4.448 kN; 1in. = 25.4 mm

The experimental program contemplated three different axial loading protocols: cyclic, megathrust-type earthquake, and high pulse-type earthquake. The cyclic-type loading consisted of tensile peak values established as fractions of the yielding strain. Subsequently, three identical cycles at different axial tensile displacement ductility levels continued until buckling was captured upon compressive loading.

The cycles associated with subduction megathrust earthquakes were generated from a loading protocol created according to Bazaez and Dusicka (2016), which requires the calculation of equivalent yielding displacements, δy. For this purpose, moment–curvature analyses of four prototype RCSW were conducted. The effects of near-field records that contain long duration pulses were also considered. The 1994 Northridge earthquake (Sylmar station) was selected for this purpose and consequently, the seismic axial displacement history was determined based on the structural response of a prototype RC wall subjected to in-plane loading.

For all cases, the compressive target loads were established considering P-Δ effects, corresponding to percentages of the maximum axial design compressive load, P_o. P-Δ effects were established through the linear interaction from Eq. (14.6):

$$P_{\%} = P_o - (P_o - P_b)\frac{M_{\%}}{M_b} \tag{14.6}$$

where P_b and M_b are the axial force and bending moment at balanced stage, respectively. The flexural moment at an out-of-plane drift ratio is $M_{\%} = P_{\%}(\%drift*clear\ prism\ height)/2$. Substituting this expression in the previous equation and solving for $P_{\%}$, the compressive load is obtained.

14.3.2 Test Setup and Instrumentation

The test setup consisted of various components as illustrated in Fig. 14.4 The details are further discussed in Haro et al. (2018); however for the completeness of this paper, a brief description is presented in this section. The two vertically inclined actuators had a 2,000 kN (440 kips) capacity and induced the axial loads/ displacements. The third horizontally placed 245 kN (55 kips) capacity actuator applied the out-of-plane displacements in the direction north-south. Loads and strokes in the actuators were measured through integrated LVDTs and loads cells. The vertical actuator located at the north face of the specimen was controlled by rotations captured through an inclinometer attached to the loading beam. The vertical actuator placed at the south face of the specimen was controlled by a combination of forces and displacements depending on the yielding point corresponding to each test. Torsion effects on the loading beam were restrained by two steel frames.

Regarding the instrumentation, relative displacements resulting from the interaction between the specimen and the adjacent components were obtained using four

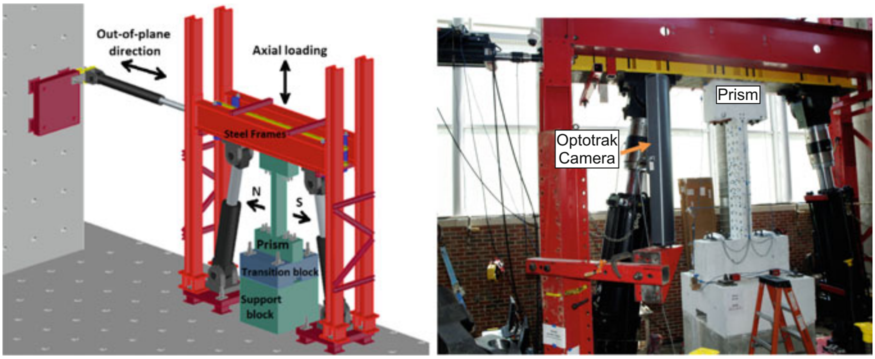

Fig. 14.4 Test setup drawings and constructed facilities laboratory implementation at NC State University

linear potentiometers. Axial deformations of the specimens were registered by four string potentiometers. An additional string potentiometer was also included to verify the lateral out-of-plane displacements induced to the specimens by the horizontal actuator. During the construction of the prisms, voids in the concrete were provided to attach 110 infrared LEDs, from the optical tracking system Optotrak Certus developed by Northern Digital Inc., on the steel reinforcement of each prism. Figure 14.5 shows the method used to provide the voids in the specimens and the distribution of the LEDs in one of the tested prisms.

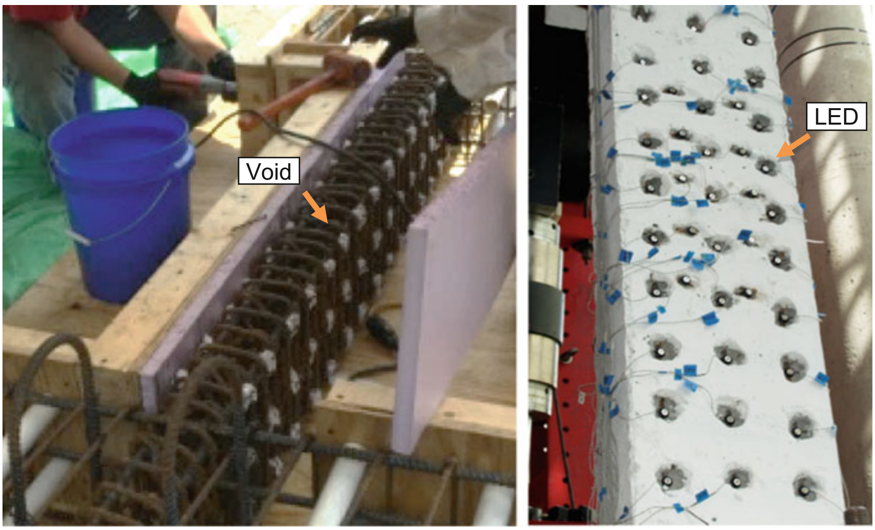

Fig. 14.5 Method for concrete voids and Optotrak infrared LEDs distribution

14.4 Experimental Results

Eleven of the 12 specimens experienced out-of-plane buckling instability. Prism P10 exhibited bar buckling and bar fracture at lower tensile strains than the predicted by Eq. (14.1) and Eq. (14.4), required to cause local wall instability. As an example of the processed data and the key observations from the experimental program, the response of prism P5 is presented in this section. Further details regarding the entire experimental program, can be found in Haro et al. (2017).

14.4.1 PRISM P5

Prism P5 was subjected to cyclic out-of-plane displacements combined with cyclic axial tensile displacements and compressive loads. Table 14.2 includes the principal properties of Prism P5, where ρ_l is the longitudinal reinforcement ratio, d_{bl} is the diameter of the bar, and s_h is the transverse reinforcement spacing.

The axial displacement history started with single elastic cycles, followed by three identical cycles at different drift levels continued until instability developed due to the axial protocol. The targets associated with the out-of-plane displacements were established as ratios of a maximum 4% drift and are shown in Fig. 14.6a. Regarding the axial demands, the peak values in tension were chosen as fractions of the yielding strain referred as: $0.25\varepsilon_y$, $0.50\varepsilon_y$, and $0.75\varepsilon_y$ and $1.0\varepsilon_y$. Subsequently, three identical cycles at different axial tensile displacement ductility levels continued until buckling was captured upon compressive loading. The compressive target loads, $P_{\%}$, were established considering P-Δ effects, representing different percentages of the maximum axial design compressive load, Po = 1,590 kN (358 kips). The compressive loads varied from 1,520 kN (341 kips) to 1,070 kN (241 kips), corresponding to the smallest and the largest out-of-plane displacements applied to the top of the specimen, respectively. Figure 14.6b shows the axial strain history applied to Prism P5.

During the elastic cycles regarding the tensile demands and up to +1.6% drift, cracks propagated along the height of the prism and the joints. Tensile strains close to 0.3% were observed in the bottom north (BN) and top south (TS) regions. Concrete flaking was also detected on the interface between the prism and the moment connections. Upon yielding tensile demands, horizontal cracks became more numerous and wider. During the application of compressive loads, the cracks

Table 14.2 Prism P5: properties

Prism	Dimensions	Longitudinal reinforcement layout	ρ_l	s_h/d_{bl}	ε_y
5	5″×12″×60″ (127 mm × 305 mm × 1,524 mm)	(6) #5 (15.9 mm)	0.031	3.2	0.00239

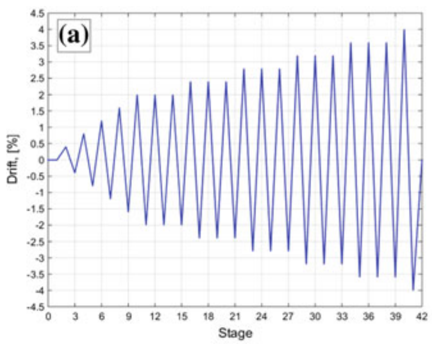

Fig. 14.6 Loading protocol for Prism P5: **a** lateral displacement history, and **b** axial strain history

tended to close mainly in the central region of the prism. The spacing of the transverse reinforcement induced the development of horizontal cracks. Crack widths bigger than 2.0 mm (5/64 in.) were captured at the footing–prism interface during the first cycle at $2\varepsilon_y$ and +2% drift. In the stage when the specimen was subjected to an axial compressive force of 1,280 kN (288 kips) and −2% drift, vertical cracks appeared in the concrete cover at BN and TS regions accompanied by concrete flaking. Through the consecutive two cycles, concrete cover fell down on the south bottom (SB) region, and consequently, transverse reinforcement was exposed on the corners. During the first cycle associated with $4\varepsilon_y$, cracks widths close to 2.4 mm (3/32 in.) were observed close to the moment connections and few new cracks formed in the prism. Concrete flaking and concrete spalling propagated upon 1,240 kN (278 kips) compressive load and a −2.4% drift. This damage was captured along 254.0 mm (10in.) height approximately in the end regions, which extended during the following cycles. Concrete spalling propagated through the cycles related to $6\varepsilon_y$ and +2.8% drift. Upon $8\varepsilon_y$ and +3.2% drift, crack widths greater than 2.0 mm (5/64 in.) were measured in the central region of the prism. Concrete cover continued falling down on the end regions and more stirrups were exposed on the corners. In the interface between the prism and the moment connections, the cracks became visibly wider than previous cycles and close to 6.4 mm (1/4 in.) beyond the $10\varepsilon_y$ cycles.

Through the first cycle related to $10\varepsilon_y$, out-of-plane buckling deformations were visually captured upon compressive loading. The scenario, where these deformations were relatively small, was observed during the three cycles corresponding to $10\varepsilon_y$. After experiencing these out-of-plane deformations, the prism returned to a straight near original position when the cracks closed in the central region, and consequently, the prism was able to resist the compressive forces developed by the overturning moments. Figure 14.7 shows the evolution of out-of-plane deformations when a stable buckling mechanism occurred upon compressive loads during the third cycle associated with $10\varepsilon_y$. During the first cycle related to 12εy and upon compressive loading, a different scenario was captured when instability occurred as

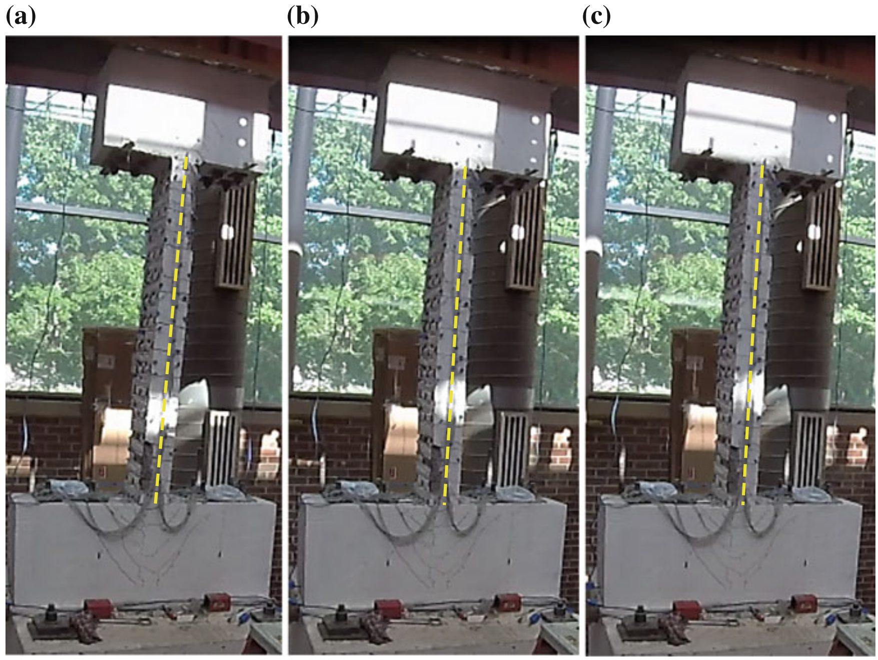

Fig. 14.7 Prism 5: stable out-of-plane buckling mechanism during 10εy(3), third cycle: **a** onset of buckling—cracks opened, **b** stable buckling—cracks partially closed, and **c** end of buckling—cracks closed

presented in Fig. 14.8. Regarding the final state of the stirrups and ties, it was noticed that they almost remained as originally constructed.

Figure 14.9 shows axial strains plotted against axial loads captured where the out-of-plane deformation reached a maximum value at the end of the test. Notice a stable response of the prism at low levels of axial tensile strains. In the last seven cycles, an axial stiffness reduction is evident by the time the compressive load approaches the compressive yielding strength. At this stage, the specimen was still extended. These points were associated with the out-of-plane buckling mechanism. In the last cycle, instability was captured since the prism was not able to recover its strength and straight configuration. The maximum applied compressive load at this stage was 934 kN (210 kips), equivalent to 87% of the axial compressive target load, $P_{4\%}$ = 1,072 kN (241 kips). Figure 14.9 also shows the predictions from the Paulay and Priestley (1993) "P&P" Eq. (14.1), and the Chai and Elayer (1999) "Ch&E" Eq. (14.4) models. In addition, tensile and compressive yielding strengths, *Asfy*, are similarly plotted, where *As* is the total area of the longitudinal reinforcement.

In addition, it was noticed from Fig. 14.9 that out-of-plane deformations increased upon compressive loading during the first cycle associated with $8\varepsilon_y$. Figure 14.10 shows the evolution of out-of-plane deformations at different stages.

Fig. 14.8 Prism 5: instable out-of-plane buckling mechanism during 12εy(1), first cycle

A sudden increment in this deformation took place when the load slightly exceeded the yielding compressive strength. The stability criterion, Eq. (14.2), calculated as out-of-plane deformation and denoted by "Stability Limit", is included in Fig. 14.10, showing that instability could occur beyond this point. During the final cycle, the maximum out-of-plane deformation was δm = 104 mm (4.1in.), which exceeded 50% of b_w.

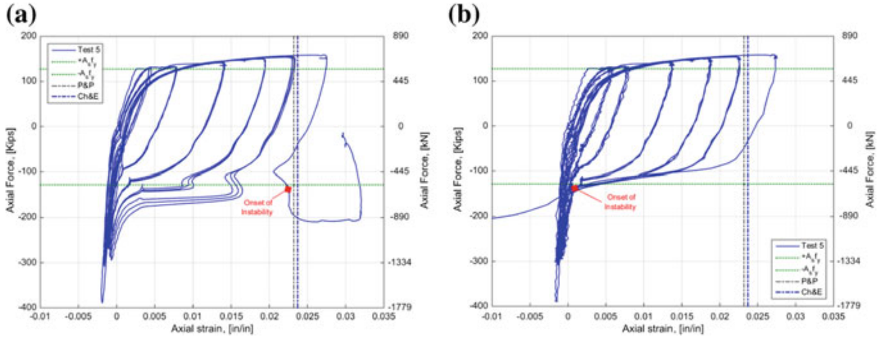

Fig. 14.9 Prism P5: axial strain versus axial force: **a** north face and **b** south face

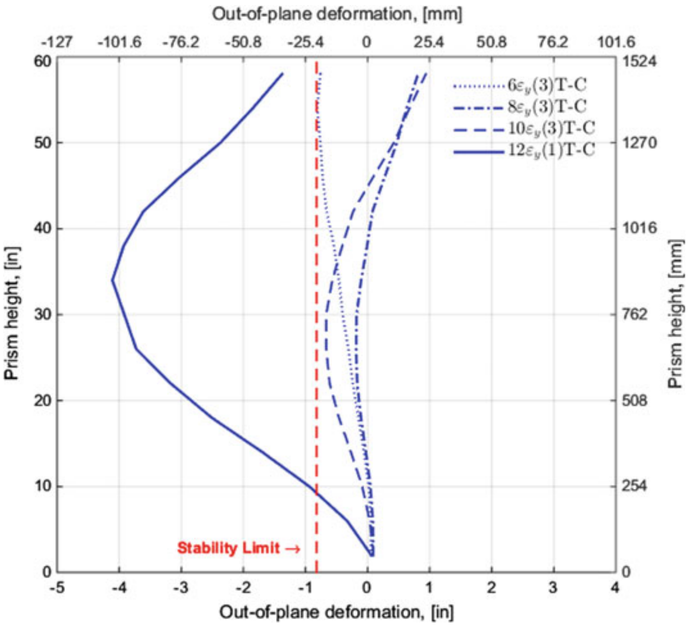

Fig. 14.10 Prism 5: evolution of out-of-plane deformations captured upon compressive loading at different stages

14.4.2 General Results

In general, the prisms from Phase 1 experienced inelastic buckling (IB) upon compressive loading after reaching tensile demands close to 12εy. In accordance with Eq. (14.1) and Eq. (14.4), instability should have occurred at strain levels close to 10εy. Prisms P3 and P6 reported higher maximum tensile strains, close to

14εy, before instability developed. Prism P3 deformed in the same direction that the out-of-plane drift was applied, and consequently, less damage accumulated in the buckled region. In the case of Prism P6, the 8% constant drift applied to the specimen delayed the onset of the buckling mechanism.

The predicted maximum tensile strains from Eqs. (14.1) and (14.4) resulted close to 13εy for Phase 2. However, IB occurred upon compressive loading after reaching tensile demands close to 14εy. Minor damage accumulated in the buckled region when Prism P9 was subjected to axial pulse-type signals scaled to 14εy, target selected according to the responses of P7 and P8. It was until 16εy when buckling instability occurred for P9.

The specimens tested during Phase 3 were only subjected to axial protocols, since out-of-plane demands did not show a trend on the onset of buckling instability in Phase 1 and Phase 2. The estimated maximum tensile strains were close to 20εy for Eq. (14.1) and 18εy for Eq. (14.4). Prism P10 experienced bar buckling (BB) through the 10εy cycle and bar fracture (BF) before the predicted values were reached, leading to the end of the test. Prism P11 exhibited BB during a cycle corresponding to 10εy and IB upon compressive loading after the 22εy cycle. Prism P11 reported higher peak tensile strains before the onset of buckling instability, mainly attributed to the megathrust earthquake-type protocol followed during this test. Prism P12 experienced a combination of IB captured after BB and BF, during the cycle corresponding to a strain level close to 19εy.

In general, the experimental results showed that the onset of instability is mainly affected by axial cyclic strains as suggested also by the predictions from Eq. (14.1) and Eq. (14.4). Regarding the accuracy of Eq. (14.3), it was noticed that the strain components needed further adjustments to contemplate the effect of the steel content. It was also noticed that high longitudinal reinforcement ratios lead to buckling instability at earlier tensile demands. In addition, concrete crushing, established at a compressive strain of 0.004, within the region where the maximum out-of-plane deformation was measured, was consistently associated with the onset of buckling instability.

14.5 Computational Model

This section summarizes the calibration and validation of a fiber-based numerical model considering the experimental outcomes, as the basis of a parametric study to extend the aim of the experimental phase to propose an improved model. Nonlinear static time-history analyses were conducted using SeismoStruct 2016, a fiber-based finite element (FE) package capable of predicting the structural response of space frames elements, accounting for geometric nonlinearities and material inelasticity (Seismosoft Ltd. 2014). A force-based (FB) formulation was implemented, which forms part of the distributed plasticity models that allow the spread of inelasticity along the member length throughout different monitoring sections.

For this study, the Menegotto-Pinto steel model (*stl_mp*) was adopted to characterize the cyclic behavior of reinforcing steel, which is based on the stress–strain relationship developed by Menegotto and Pinto (1973) and the isotropic hardening rules proposed by Filippou et al. (1983). The Mander et al. (1988) nonlinear concrete model (*con_ma*) was adopted over three additional models defined in SeismoStruct. This uniaxial nonlinear constant confinement model follows the constitutive rule proposed by Mander et al. (1988) and the cyclic laws suggested by Martínez-Rueda and Elnashai (1997). SeismoStruct is capable of monitoring different performance limit states (e.g., yielding of steel, fracture of steel, spalling of concrete). The limit state associated with out-of-plane buckling instability is established as cover concrete crushing, in accordance with the analysis described in a previous section.

The numerical models simulating the 12 prisms from the experimental phase included the same corresponding loading protocols. The compressive targets were controlled through displacements equivalent to the effect of the experimental axial compressive loads. A thickness cover equal to 6.4 mm (1/4in.) was assumed for the 12 prisms in accordance with what was observed in the experimental phase. Figure 14.11 shows an acceptable agreement between the experimental response and the computed response of Prism P5, as a sample of what was determined for other specimens.

In general, the maximum experimental tensile strains that caused out-of-plane buckling instability under compressive loading were accurately captured through the numerical model. The limit state associated with cover concrete crushing defined through the performance criteria interface from SeismoStruct detects the onset of out-of-plane buckling instability in the same cycles where this failure mode was detected during the experimental tests. Consequently, the calibrated and validated fiber-based computational model constitutes a powerful tool to develop the parametric study, summarized in the next section, and subsequently, to suggest an improved approach to predict buckling instability in RCSW.

14.6 Parametric Study

The results from the experimental phase and the validation of the numerical model suggested adjustments to Eq. (14.4) to account for the influence of the steel content in the compression region. A parametric study was conducted on 180 RCP to further analyze the most influential variables corresponding to wall geometry and reinforcement ratio. Two common interstorey height-to-wall thickness ratios of hs/bw=16 and hs/bw=10 were selected. Reinforcement ratios ρ_l around 1%, 2%, 3% and 4% were studied. The axial loading protocol consisted of a three-cycle type. Out-of-plane displacements were excluded from this analysis in accordance with

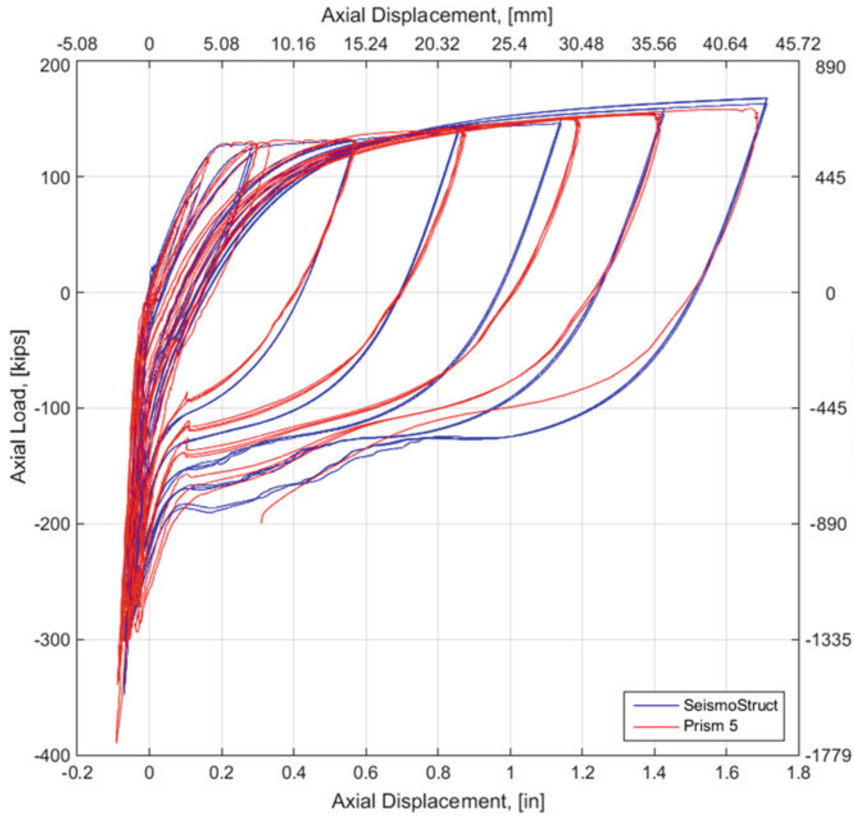

Fig. 14.11 Experimental and numerical hysteretic curves for Prism P5

the experimental results. The concrete and steel reinforcement material properties of the 180 specimens were characterized by typically used values. Figure 14.12 shows the maximum tensile strains reached by the computational RCP, expressed as $\varepsilon_{sm}/\varepsilon_y$, where the influence of ρ_l and the ratio *hs*/*bw* is noted. Phase #1, #2, and #3 were considered in the parametric study associated with interstorey heights of 2.4 m, 2.7 m, and 3.0 m, respectively.

In general, the parametric study revealed that interstorey height-to-wall thickness ratios equal to 10 delay the onset of buckling instability compared with interstorey height-to-thickness ratios equal to 16. This highlighted the importance of considering thicker sections when large in-plane displacements are expected in RCSW. In addition, it was verified that small steel contents lead to greater tensile strains that can be sustained before instability occurs.

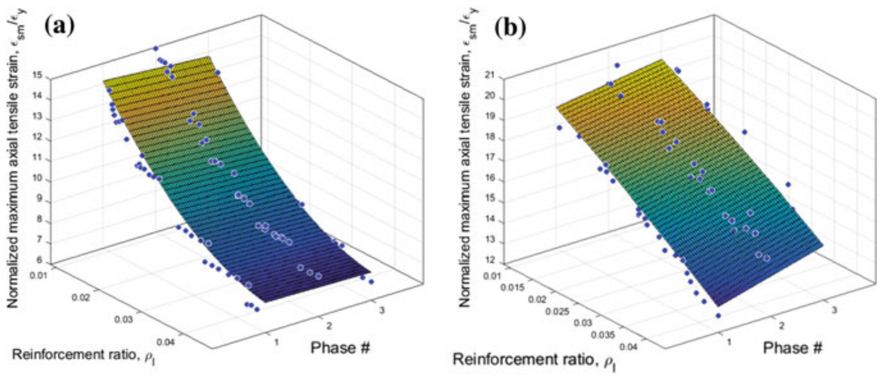

Fig. 14.12 Parametric study: influence of critical variables: **a** *hs/bw* = 16 and **b** *hs/bw* =10

It was also noticed that the interstorey height-to-wall thickness ratio affects the strain components from the hysteretic behavior of the longitudinal reinforcement in the compression region. In this context, the numerical simulation exposed that the ranges of the strain components were similar to the ranges determined in the experimental program. However, the overall results from the parametric study proved that the fundamentals of the existing models covered in this paper are appropriate to be included in an improved approach.

14.7 Preliminary Estimation of the Minimum Structural Wall Thickness

As a result of the experimental and parametric studies currently described, an improved model is proposed expressed as design charts based on a (Direct Displacement Based Design) DDBD procedure that provide the minimum thickness of structural walls that require special boundary elements considering the influence of ductility levels μ, reinforcement ratios ρ, and wall heights, as shown in Fig. 14.13. The mechanical material properties used to develop these charts are f'_c = 30 MPa (4.4ksi) and f_y = 420 MPa (60ksi).

In the charts, *hs* is the interstorey height, *hw* the total height of the wall, *bw* is the thickness of the wall. The charts are created for an axial load ratio equal to 0.15 and a height-to-length ratio equal to 4, selected as a critical combination (Haro et al. 2017). Notice that the minimum thickness of a structural wall tends to be similar for taller walls with similar longitudinal reinforcement ratio. In addition, note the significant effect of the ductility level on the minimum thickness required to prevent out-of-plane buckling instability.

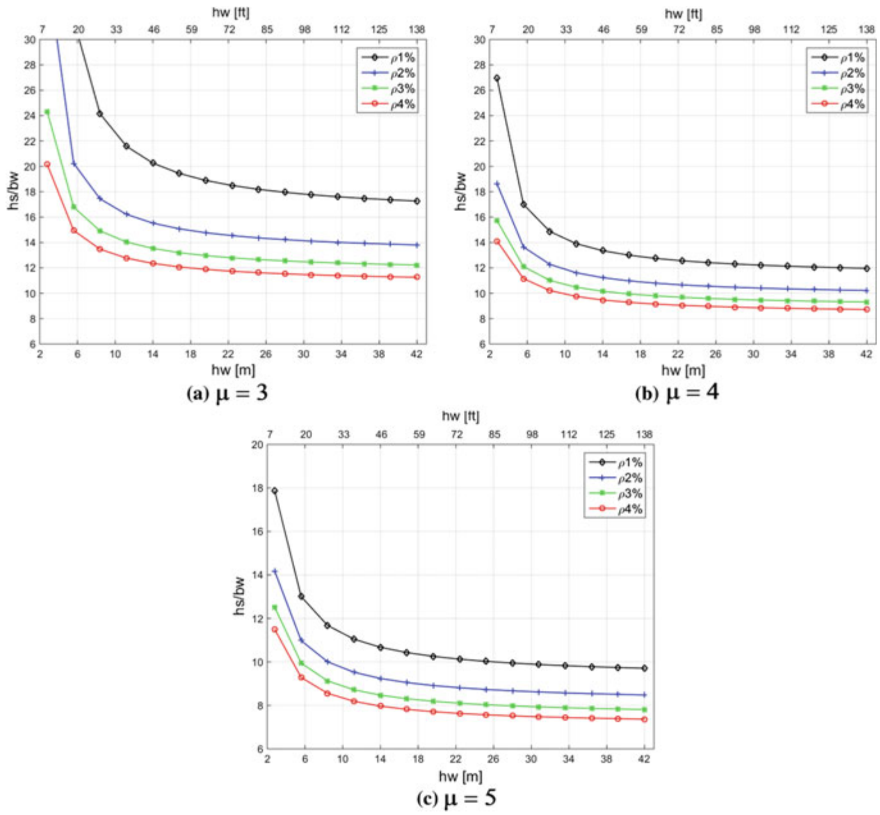

Fig. 14.13 Approximate minimum wall thickness for structural walls

14.8 Conclusions

Results of an experimental program with well-confined boundary elements of special RC planar structural walls designed and built in accordance with the ACI 318-14 are reported in this paper. Different loading patterns were applied combining out-of-plane drifts, established as percentages of clear height of the prisms, and cyclic axial tensile strains and compressive loads and displacements. Critical parameters associated with out-of-plane buckling of RCSW were studied through the experimental and the analytical studies, revealing that applied lateral displacements do not show a trend on the onset of instability. However, the results exhibited how crucial are the reinforcement ratio and the large inelastic tensile strains reached in the boundary ends due to in-plane loading. Finally, since preliminary estimations of specific design parameters are required usually for rapid controls, the proposed charts, based on a DDBD philosophy and an improved version the Chai and Elayer (1999) model, constitute a practical solution for assessment purposes.

Acknowledgements The authors wish to thank the Alaska Department of Transportation and Public Facilities for providing funding for the conduct of this research. In particular, we would like to thank Mr. Elmer Marx for his involvement in the work. We would also like to thank the entire technical staff of the NC State Constructed Facilities Laboratory. Lastly, we wish to thank the NC State Department of Civil Engineering, SENESCYT–IECE from Ecuador, and the Universidad de las Fuerzas Armadas ESPE, for providing additional financial support for former Ph.D. student Ana Gabriela Haro to conduct this work.

References

ACI 318-14. (2014). ACI 318-14 *building code requirements for structural concrete (ACI 318-14) and commentary (ACI 318R-14).*

Bazaez, R., & Dusicka, P. (2016). Cyclic loading for RC bridge columns considering subduction Megathrust Earthquakes. *Journal of Bridge Engineering, 21*(5), 1–13.

Chai, Y. H., & Elayer, D. T. (1999). Lateral stability of reinforced concrete columns under axial reversed cyclic tension and compression. *ACI Structural Journal, 96*(96), 780–789.

Chrysanidis, T. A., & Tegos, I. A. (2012). The influence of tension strain of wall ends to their resistance against lateral instability for low-reinforced concrete walls. In: *15th world conference on earthquake engineering (15WCEE)*, Lisboa, 10.

Creagh, A., et al. (2010). *Seismic performance of concrete special boundary element*. Austin: University of California Berkeley.

Filippou, F. C., Popov, E. P., & Bertero. V. V. (1983). Effects of bond deterioration on hysteretic behaviour of reinforced concrete joints. *Earthquake Engineering Research Center*: 1–212.

Flintrop, A, Wallace, J. W., & Segura, C. (2013). *Testing of reinforced concrete shear wall boundary elements designed according to ACI 318-11*. University of Minnesota.

Goodsir, W. J. (1985). *The design of coupled frame-wall structures for seismic actions*. University of Canterbury.

Haro, A. G., Kowalsky, M. J., & Chai, R. Y. H. (2017). Seismic load paths effects in reinforced concrete bridge columns and pier walls. Vol. 2: Out-of-plane buckling instability of pier walls. *Department of transportation & public facilities, State of Alaska*.

Haro, A. G., Kowalsky, M. J., Chai, R. Y. H., & Lucier, G. (2018). Boundary elements of special reinforced concrete walls tested under different loading paths. *Earthquake Spectra*: 22.

Herrick, C. K., & Kowalsky, M. J. (2016). Out-of-plane buckling of ductile reinforced structural walls due to in-plane loads. *Journal of Structural Engineering, 1,* 1–15.

Mander, J. B., Priestley, M. J. N., & Park, R. (1988). Theoretical stress-strain model for confined concrete. *Journal of Structural Engineering, 114*(8), 1804–1826.

Martínez-Rueda, J. E., & Elnashai, A. S. (1997). Confined concrete model under cyclic load. *Materials and Structures, 30*(3), 139–147.

Menegotto, M., & Pinto, P. E. (1973). Method of analysis for cyclically loaded R. C. plane frames including changes in geometry and non-elastic behavior of elements under combined normal force and bending. In *Symposium on resistance and ultimate deformability of structures acted on by well defined loads*, Zurich, Switzerland: International Association for Bridge and Structural Engineering, 15–22.

Parra, P. (2015). *Stability of reinforced concrete wall boundaries*. Berkeley: University of California.

Paulay, T., & Priestley, M. J. N. (1993). Stability of ductile structural walls. *ACI Structural Journal, 90*(4), 385–392.

Seismosoft Ltd. (2014). *SeismoStruct user manual*. Pavia.

Shea, M., Wallace, J. W., & Segura, C. (2013). *Seismic performance of thin reinforced concrete shear wall boundaries*. University of Massachusetts Amherst.

Welt, T. S. (2015). *Detailing for compression in reinforced concrete wall boundary elements: experiments, simulations, and design recommendations.* University of Illinois at Urbana-Champaign.

Chapter 15
Ductility Demand of a High-Rise RC Flat-Plate Core-Wall Building Structure in a Moderate-Seismicity Region: South Korea

Kyung Ran Hwang and Han Seon Lee

An analytical model, calibrated with the results of shake-table tests on a 1:15 scale 25-storey RC flat-plate core-wall building model, is used to predict the demand of ductility at the critical elements. Under the maximum considered earthquakes in Korea, the maximum chord rotation of coupling beams and slabs reaches 0.01 rad with the maximum roof drift being 0.5%. The maximum curvature of the wall at the base is only 16% of the ultimate curvature, 0.041 rad/m, corresponding to the minimum plastic rotation 0.0064 rad, implemented by ACI 318 for the special-wall boundary. These results indicate that the seismic requirements for ductility in ACI 318 can be greatly alleviated for high-rise buildings in a moderate-seismicity region such as South Korea.

15.1 Introduction

For high-rise residential buildings (higher than 30 stories) in Korea, a combined system of core reinforced concrete (RC) shear walls: a lateral load resistance structural system, and RC flat-plate frames: a gravity load resistance structural system, has been widely used. This structural type is classified as dual frame or building-frame systems in current seismic provisions. For the shear walls in the building-frame system, special shear walls, for which special seismic detailing requirements are imposed, or ordinary shear walls, which have a height restriction, have generally been used. However, in the RC flat-plate structure, seismic detailing

K. R. Hwang · H. S. Lee (✉)
School of Civil, Environmental, and Architectural Engineering,
Korea University, Seoul, Korea
e-mail: hslee@korea.ac.kr

K. R. Hwang
e-mail: dh8149@korea.ac.kr

T. T. C. Hsu (ed.), *Concrete Structures in Earthquake*,
https://doi.org/10.1007/978-981-13-3278-4_15

requirements for the connection with columns are given only as part of intermediate moment frames.

Several guidelines and reports for design of high-rise building structures have been published including not only the prescriptive code design but also the performance-based seismic design (LATBSDC 2017; PEER 2017; PEER/ATC 2010; Moehle et al. 2011). They also contain modeling approaches of the RC high-rise flat-plate core-wall building structural system based on many experimental and analytical studies of the performance of discrete elements: walls, coupling beams, and connections between the columns and the slabs. Several analytical studies have been performed to evaluate the seismic performance of the structural system (Zekioglu et al. 2007; Melek et al. 2012; Munir and Warnitchai 2012), although experimental verification was rarely performed.

The earthquake simulation tests on a 1:15-scale 25-storey RC flat-plate core-wall building model designed per the current seismic codes were conducted by Lee et al. (2015) to evaluate the seismic performance of high-rise RC core-wall flat-plate building structures. The test results showed that cracks occurred near the connections between the slab and column and between the slab and wall under the design earthquake in Korea. While the effect of the higher modes was clearly revealed in the vertical distribution of the storey acceleration, drift, and shear force during the table excitation, the maximum values of the base shear and roof drift with the governing first mode during the free vibration right after the termination of shake-table excitation appeared to be similar to or larger than the values of the maximum responses during the table excitation. No damage was observed in the walls with special boundary elements in the assumed plastic hinge region. The maximum curvature of these walls was only 21% of the ultimate curvature corresponding to an ultimate concrete compressive strain of 0.00638 m/m intended in the displacement-based design approach in ACI 318-05. The limitations of the test model are (1) the effective weight is only 1/3.59 of dead load due to the limited payload capacity of the shake table, and (2) the base of wall portion was not rigid and had nonnegligible deformation.

In this study, the demand of ductility at the critical elements of the same 25-storey RC flat-plate core-wall building model, but subjected to gravity loads of 1.0 dead load, is observed based on an analytical simulation by the nonlinear analysis program, PERFORM-3D V5 (CSI 2011). First, the numerical model is calibrated with the results of the earthquake simulation tests on a 1:15 scale 25-storey distorted model with the gravity loads of 1/3.59 of 100% dead load (Lee et al. 2015). Second, the calibrated model is transformed to the true replica model. Third, the effect of foundation flexibility at the base of walls on the seismic responses is investigated by comparing the results between flexible-base and fixed-base models. Based on these analytical results, addressed are some issues relevant to the building-frame system with special RC shear wall in current seismic design codes such as (1) contribution of the flat-plate frame (gravity system) to the lateral resistance, (2) the demand of ductility at the critical elements, and (3) the requirement of displacement compatibility for a building-frame system.

15.2 Design of Model and Experimental Setup

15.2.1 Design of a Prototype Building

Among the RC flat-plate core-wall building structures constructed in Korea, the most typical type is chosen as a prototype. The prototype is a 25-storey (79.5 m) flat-plate core-wall building as shown in Fig. 15.1a. The first storey is 5.1 m high, and the other stories are 3.1 m high. The prototype building is defined as a building system frame in KBC (2009), and, therefore, the core walls take the most of the resistance to the lateral load, and the peripheral frames are intended to resist the gravity load. The result of the elastic analysis of the prototype building shows that the core walls resist 87% of the lateral load. Although the structure is classified as a building-frame system, no separate design is performed for the walls only under 100% of the earthquake load. The reinforcement details are designed according to KBC (2009), which is similar to IBC (2006) and ACI 318-05, particularly in terms of the requirements of special wall and displacement compatibility for a building-frame system. The design concrete strength (f'_c), 40 MPa, and the reinforcement yield strength, 400 MPa, are applied to the entire building structure. The dead load (DL) of the prototype is 261,000 kN. The effective seismic weight is set as the dead load, with the live loads excluded.

According to the seismic design provision of KBC (2009), which is similar to that of IBC (2006), the design earthquake is defined as the 2/3 of the intensity of the maximum considered earthquake (MCE) that can occur in Korea with a return period of 2,400 years. The design earthquake (DE) load from the equivalent lateral force procedure is V = 6,590 kN as given in Table 15.1. The value of base shear obtained from the response spectrum analysis is $V_{t(x\text{-}dir)}$ = 4,650 kN in the X-direction and $V_{t(y\text{-}dir)}$ = 6,310 kN in the Y-direction; both values are less than the base shear of V = 6,590 kN. Although KBC (2009) specifies the requirement of scaling up or down to 85% of this base shear, the load of V = 6,590 kN is used for design.

The core wall is 600 mm thick along the entire height of the building. The vertical reinforcement of D29@400 mm is uniformly supplied at the walls with a reinforcement ratio of 0.56%, and the horizontal reinforcement of D16@250 mm

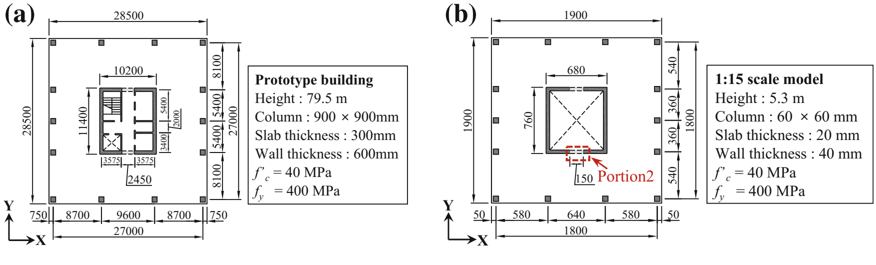

Fig. 15.1 Plan of prototype building (unit: mm): **a** prototype building and **b** a 1:15-scale model

Table 15.1 Design seismic load of the prototype according to KBC (2009) and IBC (2006)

Parameter	Value
Seismic zone factor	S = 0.176 for Seoul
Soil type	S_D
Design spectral accelerations	S_{DS} = 0.425 g (at 0.2 s); and S_{D1} = 0.247 g (at 1.0 s)
Seismic design category	D
Response modification factor	$R = 6$
Displacement amplification factor	$C_d = 5$
Importance factor	$I_E = 1.2$
Fundamental period	T_a = 1.30 s (empirical equation)
Seismic coefficient	$C_s = S_{D1}/(R/I_E \times 1.5\ T) = 0.0253$
Effective seismic weight	W = 261,000 kN
Design base shear	$V = C_s W$ = 6,590 kN
Design roof displacement	$\delta_u = C_d \times \delta_{xe}/I_E = 4.16\ \delta_{xe}$ = 427 mm (X-dir.) and 278 mm (Y-dir.)

with a reinforcement ratio of 0.273% is deployed on the outside of the vertical reinforcement with the exception of D16@125 mm at the first storey. The demands on the walls of the first storey are within the design capacity as presented by the P-M interaction diagram in Fig. 15.2b.

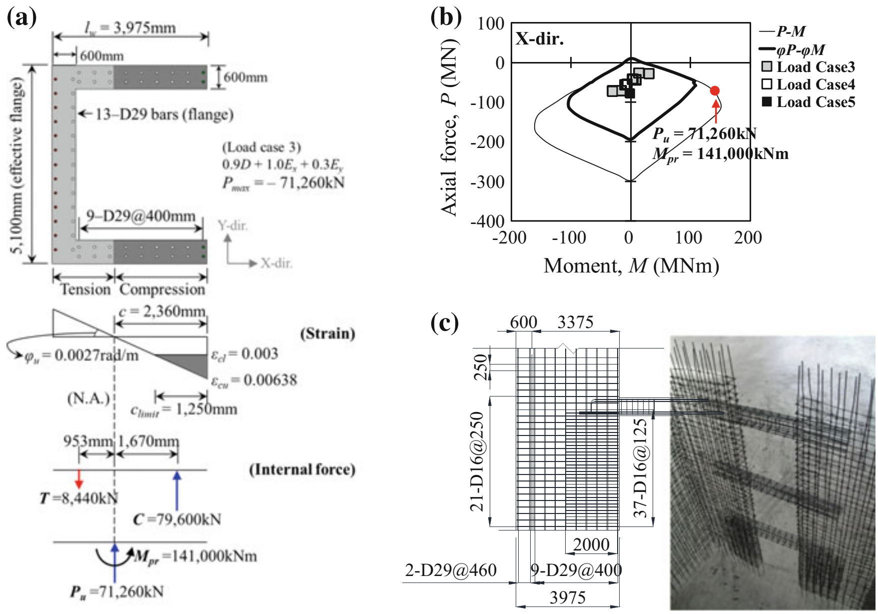

Fig. 15.2 Design and construction of the core wall (unit: mm): **a** wall strain and force distribution in the left X-dir. wall; **b** P-M interaction diagram of the left wall at the first storey; and **c** rebar detail in the 1:15-scale model (Lee et al. 2015)

In accordance with the displacement-based design method given in ACI 318-05, special boundary details are imposed on the X-directional wall in the first storey as shown in Fig. 15.2. The depth of neutral axis, c = 2,360 mm, of the wall is calculated for the factored axial force (P_u = 71,260 kN) and the maximum probable moment (M_{pr} = 141,000 kNm) consistent with δ_u in Fig. 15.2a, b which is greater than the limit value of c_{limit} = 1,230 mm. Detailed information on the design and construction of the specimen is given in the reference Lee et al. (2015).

15.2.2 Experimental Setup for the Earthquake Simulation Tests

The size and payload of a shaking table in the Earthquake Test Center of Pusan National University are 5 m×5 m and 600 kN, respectively, and the model in Fig. 15.1b is scaled down to 1/15, taking availability of model reinforcement and constructability into consideration. Even with a low reduction factor of 1/15, the required self-weight of the model is 1,160 kN, which still exceeds the capacity of the shaking table, 600 kN, if the true replica model is adopted. Therefore, the model's weight should be reduced further, by using a distorted model. Taking into account the length similitude factor, 1/15, and the weight of available steel plates for added artificial mass, the density similitude factor is chosen to be 4.18. Therefore, the acceleration similitude factor is determined as 3.59 to satisfy the similitude law.

Figure 15.3a shows an overview of the model. Displacement transducers and accelerometers are installed at the floors of the 6th, 10th, 14th, 18th, and 22nd stories, and at the roof, to measure the overall behavior of the model as shown in Fig. 15.3b. Displacement transducers are also deployed to measure the local behaviors of the walls and foundations. Since there is no recorded strong-motion accelerogram in Korea, the input accelerogram to the shaking table is derived from the 1952 Taft N21E (X-direction) and Taft S69E (Y-direction) components by compressing the time scale according to the similitude law with the scale factor of, $1/\sqrt{3.59 \times 15}$, and by amplifying the acceleration with the scale factor, 3.59. Detailed information on the experiment is given in the reference Lee et al. (2015).

15.3 Numerical Modeling and Calibration with Experimental Results

15.3.1 Numerical Modeling

The analytical calibration of shake-table responses of the 1:15-scale model (Fig. 15.1b) is carried out using PERFORM-3D version 5 (CSI, 2011). An overview of the analytical model is given in Fig. 15.4a. The portion of the core wall is

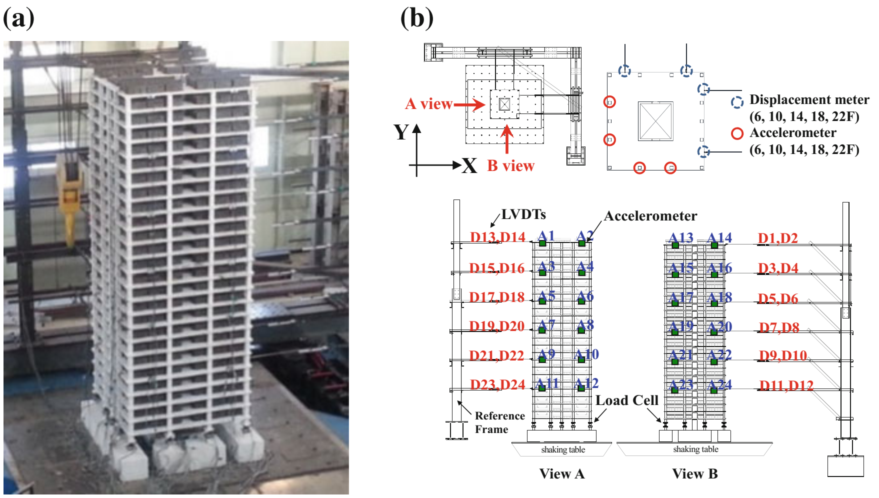

Fig. 15.3 Experimental setup for earthquake simulation tests (Lee et al. 2015): **a** overview of the model and **b** instrumentation of the 1:15-scale model (D: disp., A: accel.)

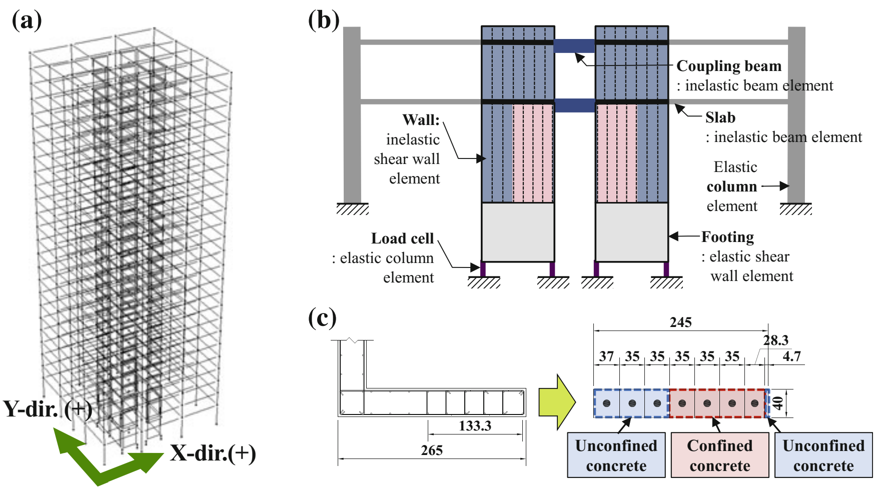

Fig. 15.4 Details of modeling for the 1:15-scale model (unit: mm): **a** analysis model; **b** composition of the element; and **c** fiber section of the core wall

modeled as an inelastic “shear wall” element (Fig. 15.4b), which has four nodes and 24 degrees of freedom. In the longitudinal direction of the element, the axial and in-plane bending behaviors are described using the inelastic vertical fiber sections representing the behaviors of the concrete and reinforcement as shown in Fig. 15.4c. Relationships between the stress and strain for concrete and steel are given in Fig. 15.5a, b, respectively. The elastic modulus and strength of the

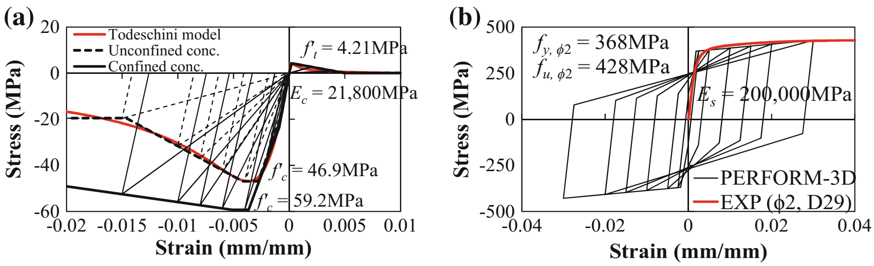

Fig. 15.5 Stress–strain relation of material: **a** concrete and **b** steel

Table 15.2 Values of effective stiffness used for analyses

Element	ASCE 41-13 (2014)			Analytical model in this study		
	Flexural	Shear[b]	Axial	Flexural	Shear[b]	Axial
Core walls	$0.5\ E_cI_g$	GA	E_cA_g	$0.5E_cI_g$	GA	$0.5E_cA_g$
Coupling beams	$0.3E_cI_g$	GA	–	$0.2E_cI_g$	GA	–
Slabs	*see*[a]	GA	–	E_cI_g	GA	–
Columns	$0.7E_cI_g$	GA	E_cA_g	$0.7EI_g$	GA	E_cA_g
Footing	–	–	–	E_cI_g	GA	E_cA_g

[a]In the ASCE 41-13 (2014), approaches for modeling slab–column frame systems differ primarily in how slab stiffness is incorporated in the analytical model
[b]Shear modulus, $G = 0.4\ E_c$

concrete and reinforcement obtained in the material test (Lee et al. 2015) are applied in the analyses. The cyclic degradation of reinforcement is modeled according to Moehle et al. (2011). Based on the damage patterns in the test result (Lee et al. 2015), the shear and the transverse in-plane bending behaviors are assumed to be elastic. The effective stiffnesses of wall elements are given in Table 15.2.

Coupling beams are modeled as elastic beam elements with nonlinear moment–rotation (M-θ) hinges at the ends of the beam. The M-θ hinge behavior in Fig. 15.6a is modeled based on the test results by Naish et al. (2009), for a conventionally reinforced beam with an aspect ratio of, $l_n/h = 3.33$, showing a trilinear moment–rotation relationship with the initial effective stiffness of $EI_{eff} = 0.2E_cI_g$. Although the flat-plate frame is not designed for lateral loads, it is included in the nonlinear numerical model in order to take into account the contribution of the columns and the slabs to the lateral resistance of the building. Columns are defined as elastic column elements with a flexural effective stiffness of $EI_{eff} = 0.7E_cI_g$ as given in ASCE 41-13 (Table 15.2). Slabs are represented by line (beam) elements rigidly interconnected at the slab–column connection, wherein the slab width included in the model is adjusted to account for flexibility of the slab–column connection. The slab elements are composed of the elastic beam elements with inelastic moment–rotation hinges (Fig. 15.6b, Moehle and Diebold 1984) at each end.

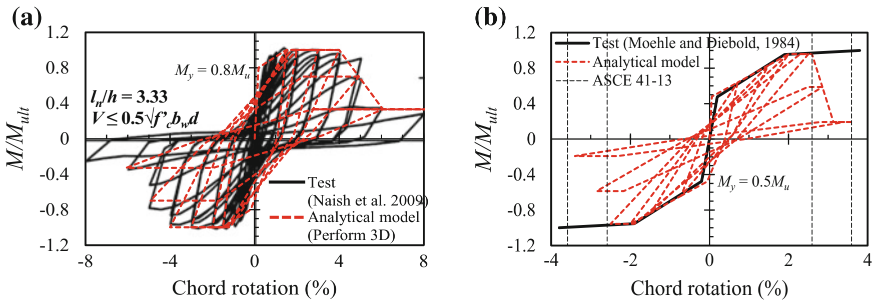

Fig. 15.6 Behavior of moment–rotation hinges of **a** coupling beam and **b** slab

The result of shake-table tests shows that load cells beneath the footing of shear walls as shown in Fig. 15.4b are not rigidly connected to the footing, which led to the minor uplift of the footing. Thus, the load cells are modeled as elastic column elements between the footing and the base, and the parameters of these elements are calibrated by matching deformations of these columns to the test results. In this study, both cases of the flexible foundation accounting for the deformation of load cells beneath the foundation and the fixed foundation that assumes no occurrence of deformation at the load cells are examined and compared. The footings below the core wall are modeled by elastic shear wall elements.

The damping is modeled to increase in the higher modes based on Rayleigh damping in Fig. 15.7. The elastic modal damping ratios of the first six translational modes are set to 1.0% (the first mode), 1.4%, 3.9%, 10%, 14%, and 28% (the sixth mode). The target damping ratio at T_1, ξ_1 = 1.0%, is determined based on the full-scale data on damping of high-rise (more than 50 m and less than 100 m) steel and RC buildings in Japan (Satake et al. 2003).

The seismic mass is lumped at the center of mass of each floor representing the storey mass and the associated rotational moment of inertia. The total seismic weight of the distorted model used for simulating the test results is 323 kN with that of true replica model being 1,160 kN. After the gravity load analysis, the nonlinear

Fig. 15.7 Modeling of modal damping as defined by PERFORM-3D

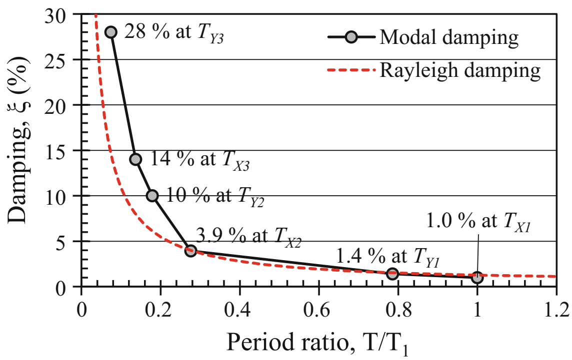

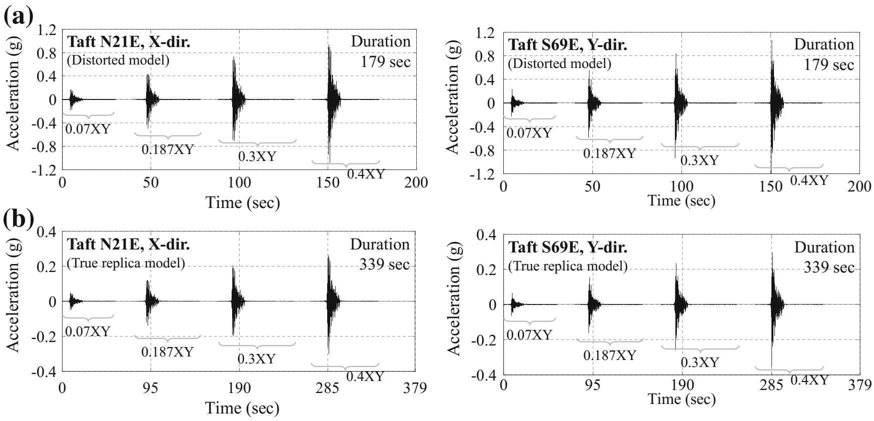

Fig. 15.8 Recorded table excitations used for analysis (see Table 15.2): **a** 1952 Taft EQ. for the distorted model, and **b** 1952 Taft EQ. for the true replica model

time history analysis is conducted with simultaneous application of the Taft N21E (X-dir.) and S69E (Y-dir.) records. The accelerograms recorded at the shake table are used for the distorted model, but those for the true replica model are reformulated by amplifying the time axis with a scale factor of $\sqrt{3.59}$ and by compressing the shake-table accelerograms with a scale factor of 1/3.59, respectively (Fig. 15.8). XY in the designation of each test means that the excitations are implemented in the X- and Y-directions simultaneously. Since the time history analysis is continuously conducted for the whole series of input motions with the intermittent quiescence, the damage caused by the preceding run is taken into account in the subsequent run of shake-table excitations. Time step is 0.0039 s for the distorted model and 0.0074 s for the true replica model. Detailed information on the analytical modeling is given in the reference Hwang (2016).

15.3.2 Calibration of Analytical Model with Experimental Results

The analytical results of the distorted model are calibrated to fit best the shake-table test results by adjusting the parameters of the analytical model given in the preceding sections. The experimental and the best fitted analytical time histories of the base shear coefficient (base shear/building weight, V/W), the roof drift ratio, and the overturning moment in the X- and Y-directions under the MCE in Korea, 0.3XY, are compared in Fig. 15.9.

The time histories can be divided into the duration of table excitation, and that of no excitation right after the table excitation. The maximum response of the base shear and roof displacement during the free vibration (no excitation) reveals a level

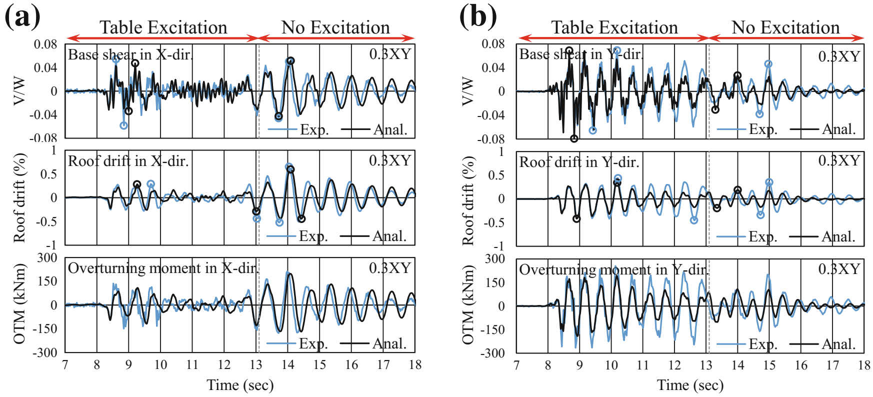

Fig. 15.9 Experimental and analytical time history responses of base shear, roof drift, and overturning moment under 0.3XY (MCE, distorted model): **a** X-dir. and **b** Y-dir

of the maximum response similar to that during the table excitation. The numerical model efficiently simulates the time histories of the experiment not only during the table excitation but also during no excitation, with the exception that the Y-directional time histories of the analysis underestimate those of experimental results after 11 s.

The hysteretic curves between the base shear and the roof drift in the X- and Y-directions under 0.07XY (serviceability level earthquake, SLE, in Korea), 0.187XY (DE in Korea), 0.3XY (MCE in Korea) and 0.4XY are given in Fig. 15.10. The stiffness and strength in the analytical results appear to be similar to those in the experimental results. Elastic behavior is observed under 0.07XY as shown in Fig. 15.10a, with the values of stiffness (unit: kN/mm) in the experiment/analysis of 4.71/4.35 in the X-direction, and 5.26/5.62 in the Y-direction. Under 0.187XY (Fig. 15.10b), a low level of inelastic response is observed in the hysteresis between the base shear and the roof drift in X- and Y-directions.

Significant inelastic behaviors can be observed in the hysteresis under 0.3XY and 0.4XY (Fig. 15.10c, d), and the analytical force–drift relations in the X-direction generally properly simulate those of the experiment. The stiffness significantly degrades with the increase of the severity of shake-table excitation. The stiffness under 0.4XY (unit: kN/mm) in experiment/analysis are 0.97/1.11 in the X-direction, and 1.79/1.86 in the Y-direction, which are about 20.6%/25.5% and 34.0%/33.1% of the stiffness under 0.07XY in the X- and Y-directions, respectively.

In the test results, the uplift behavior of the load cells between the footing of the model and the base of shake table is significant, because the load cells are not rigidly connected to the footing for some unknown reasons. The rotation at this footing due to the uplift, $\theta_{footing}$, is compared with the flexural rotation of the wall in

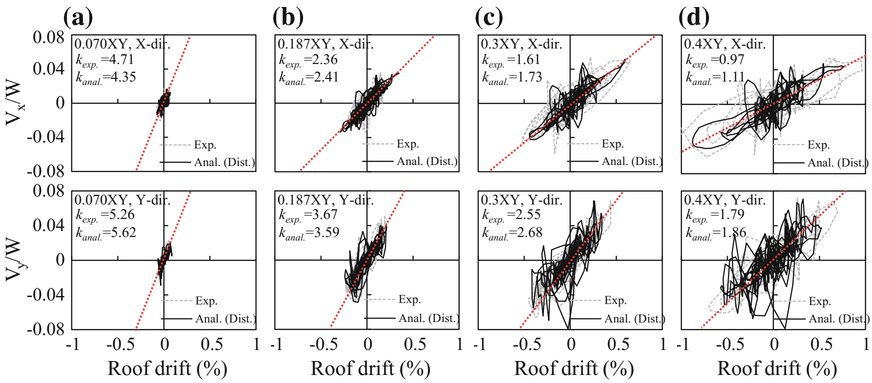

Fig. 15.10 Experimental and analytical relations of hysteretic curves between base shear (V/W) and roof drift: **a** 0.07XY (SLE), **b** 0.187XY (DE), **c** 0.3XY (MCE), and **d** 0.4XY

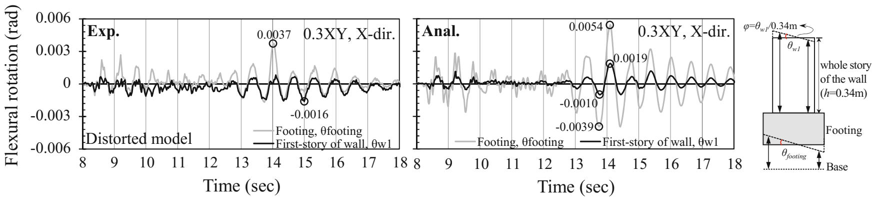

Fig. 15.11 Experimental and analytical relations of time history responses of flexural deformation of the footing and the first storey of wall (the distorted model) under 0.3XY

the first storey only, θ_{w1}, under 0.3XY as shown in Fig. 15.11. The maximum value of $\theta_{footing}$ in the experiment and analysis is 0.0037 rad and 0.0054 rad, respectively, with the maximum value of θ_{w1} in the experiment and analysis being 0.0016 rad and 0.0019 rad, respectively.

15.3.3 Distorted Model Versus True Replica Model

Figure 15.12 compares the hysteretic results of the distorted and true models. In the case of the true replica model (1.0 DL), the Y-directional behaviors are generally similar to those of the distorted model (DL/3.59), but the maximum roof drift and the inelastic energy dissipation in the X-directional behavior under 0.3XY and 0.4XY are less than those in the distorted model. This is because large gravity loads reduce the inelastic behaviors of the core wall and the slab–column connections. The results of the true replica model show also that the higher modes are dominant during the table excitation, whereas the first mode behavior is predominant during the free vibration right after the table excitation leading to the occurrence of the significant roof drift and base shear.

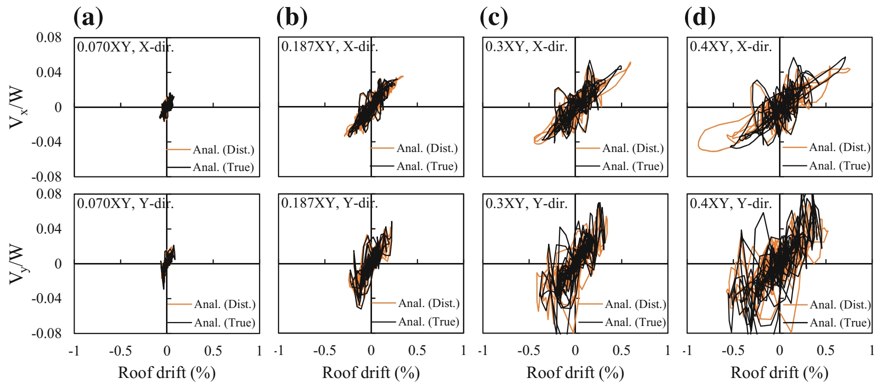

Fig. 15.12 Comparison of hysteretic curves between base shear (V/W) and roof drift: **a** 0.07XY (SLE), **b** 0.187XY (DE), **c** 0.3XY (MCE), and **d** 0.4XY for distorted and true replica models

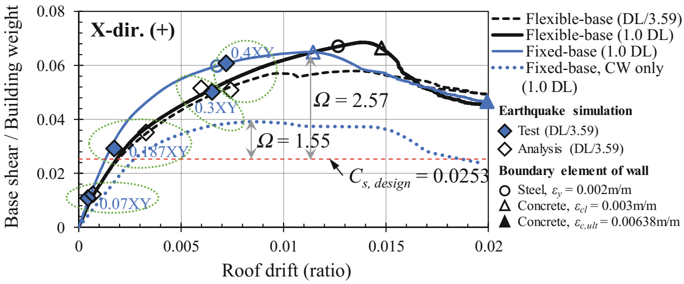

Fig. 15.13 Pushover (capacity) curves of the whole structure in the X-direction

Capacity curves by the static pushover analysis for the whole structure under the lateral force distribution of the first mode are shown in Fig. 15.13. A lateral load distribution based on the first mode is known to be inappropriate for a high-rise building structure by the effect of higher mode responses. However, the results of the earthquake simulation tests and analyses show that the seismic responses during no excitation are governed by the first mode leading to sometimes larger drift than those during the table excitation that are mainly affected by the higher mode. Diamond markers denote the instant of the maximum base shear during no excitation governed by the first mode in the earthquake simulation tests (solid) and in the analyses (hollow) of the distorted model for each level of tests. These diamond markers appear near the capacity curve of the distorted model (black dashed line), except for the maximum experimental response under 0.4XY.

The capacity curves of the distorted and true models having the mass corresponding to DL/3.59 (black dashed line) and 1.0DL (black solid line), respectively, are compared in Fig. 15.13. The true replica model has a higher strength than the distorted model due to a large moment capacity of the wall in the true replica model. *Hereafter, the seismic responses in the X-direction of the true replica model only will be discussed to evaluate the seismic performance of the 25-storey flat-plate core-wall building structures.*

15.4 Evaluation of the Seismic Performance of 25-Story Flat-Plate Core-Wall Building Structures

15.4.1 Effect of Base Flexibility to the Roof Drift and the Base Shear Force

The models with the flexible base and fixed base are used to evaluate the effect of base flexibility on the seismic response of the building model. In Table 15.3, the flexible-base model has generally longer fundamental periods in the X- and Y-directions approximately by 21% and 12%, respectively, than the fixed-base model. The capacity curves with the flexible base and fixed base are compared in Fig. 15.13. Limit states are defined for the strain of steel and concrete at the protruded edge of the core wall in the first storey as follows: steel tensile yielding at ε_y = 0.002 m/m (circle marker), concrete compressive limiting strain at ε_{cl} = 0.003 m/m for unconfined concrete (hollow triangle marker), and concrete ultimate compressive strain at ε_{ult} = 0.00638 m/m for confined concrete (solid triangle marker). In the X-direction, the pushover curve with the flexible base indicates that the initial stiffness 3.96 kN/mm, is 80% of that of the fixed-base model, 4.95 kN/mm. The points reaching the ε_y and ε_{cl} and the maximum base shear of the flexible-base model are significantly delayed compared to those of the fixed-base model.

The X-directional hysteretic curves between the base shear and the roof drift of the fixed-base model show a quite different behavior from those of the flexible-base

Table 15.3 Natural periods (T) and modal participating ratios (M_{ux} and M_{uy} in the X- and Y-directions)

Model			X-direction			Y-direction		
			First	Second	Third	First	Second	Third
Experiment (W/3.59)		T	0.413 s	0.0945 s	0.0486 s	0.341 s	0.0696 s	0.0285 s
Modal analysis	Distorted model (W/3.59)	T	0.436 s	0.121 s	0.0599 s	0.343 s	0.0782 s	0.0325 s
		M_{ux} or M_{uy}	79.0%	12.8%	3.42%	70.2%	17.6%	5.61%
	True replica model (1.0 W)—flexible base	T	0.827 s	0.229 s	0.113 s	0.650 s	0.0148 s	0.0616 s
		M_{ux} or M_{uy}	79.0%	12.8%	3.42%	70.2%	17.6%	5.61%
	True replica model (1.0 W)—fixed base	T	0.686 s	0.20 s	0.10 s	0.581 s	0.130 s	0.0551 s
		M_{ux} or M_{uy}	74.2%	14.2%	4.51%	67.9%	18.2%	6.63%

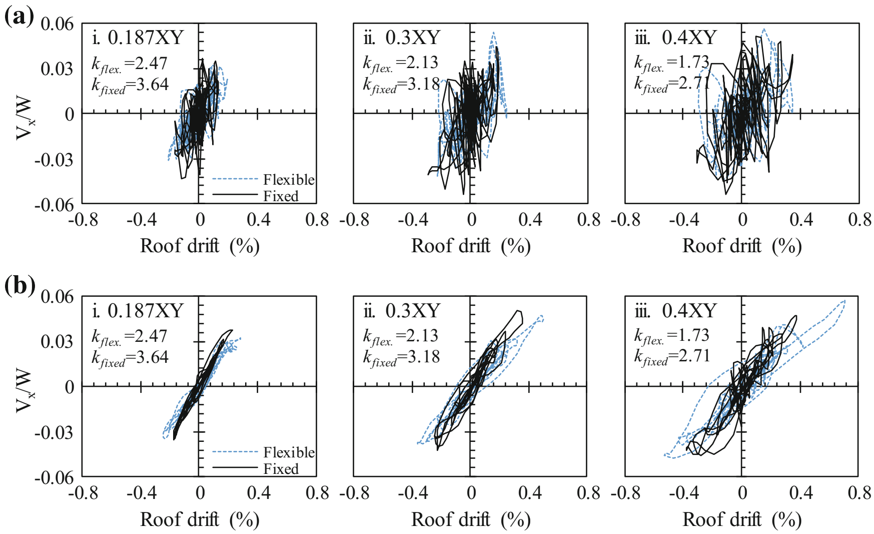

Fig. 15.14 Effect of base flexibility on the hysteretic curves between base shear and roof drift in the X-dir.: **a** table excitation and **b** no excitation right after the termination of shake-table excitation

model in Fig. 15.14. The hysteretic curves of the fixed-base model have relatively sharper peaks and valleys than those in the flexible-base model during the table excitation (Fig. 15.14a). The base flexibility the decreases the lateral stiffness and increases the roof drift, especially during no excitation. The lateral stiffness in the flexible-base model, 2.13 kN/mm under 0.3XY, is 67% of that in the fixed-base model. The maximum roof drift of the flexible-base model, 0.469%, is larger than that of the fixed-base model, 0.344%, under 0.3XY. The corresponding maximum interstorey drift ratios (IDR) in the X-direction under 0.3XY representing MCE in Korea are 0.61% (flexible-base) and 0.50% (fixed-base), which is similar to the estimated design IDR in the X-direction, $\delta_u = C_d \times \delta_{xe}/I_E = 4.16\ \delta_{xe} = 0.56\%$, by applying $C_d = 5$ and $I_E = 1.2$ to the elastic drift (δ_{xe}) of the earthquake load, V, obtained from the response spectrum analysis. This design IDR, 0.56%, is about twice as large as the demand under 0.187XY representing DE in Korea, 0.31% (flexible-base) and 0.27% (fixed-base). (Hwang 2016)

15.4.2 Contribution of the Flat-Plate Frame to Story Shear Force and Overturning Moment

In Fig. 15.13, the capacity curve of the fixed-based model (blue-solid line) for the whole structure is compared to that of the model containing only the core wall with the fixed base (blue-dotted line) to investigate the relative influence of the flat-plate

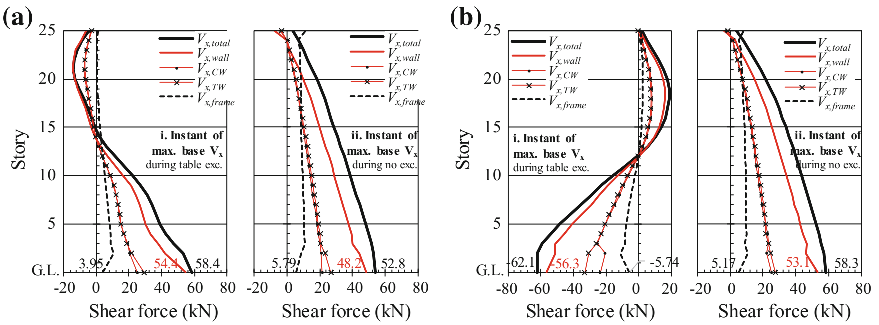

Fig. 15.15 Distribution of storey shear in the X-dir. at instants of the maximum base shear under 0.3XY (MCE): **a** flexible-base model and **b** fixed-base model

frame on the lateral resistance. The value of initial stiffness in the fixed-base model without the flat-plate frame, i.e., having only the wall structure, is 2.07 kN/mm, which is much less than those of the model with the flat-plate frame, 4.95 kN/mm. The value of the maximum strength of the model without the flat-plate frame is 60% of that in the model representing the whole structure. The overstrength factor, Ω, of the whole structure is 2.57, which is similar to that for the building-frame system in KBC (2009), IBC (2006), 2.5.

In Fig. 15.15, the distributions of storey shear force ($V_{x,total}$) at the time instant of the maximum base shear during the table excitation are influenced by the second and third modes in the X-direction, while those at the time instant during no excitation are dominated by the first mode. At the time instants of the maximum response of base shear, the contribution of the flat-plate frame to the base shear is 6.77% (table excitation) and 10.7% (no excitation) of the total base shear in the flexible-base model (Fig. 15.15a), with 9.25% (table excitation) and 8.88% (no excitation) of the total base shear in the fixed-base model (Fig. 15.15b). More than 90% of the total base shear is resisted by the core wall regardless of the base flexibility. The absolute value of the contribution by the flat-plate frame to the storey shear during no excitation is generally constant throughout the height of the structure, whereas the contribution by the wall decreases as the storey becomes higher.

The storey overturning moment (OTM) distributions at the time instant of the maximum OTM (Fig. 15.16) show that approximately 50%/60% of the total base OTM ($M_{x,total} = M_{x,wall} + M_{x,frame}$) is resisted by the core wall of the flexible-base/fixed-base models, respectively. The OTM resistance of the frame, $M_{x,frame}$, due to a large tension and compression forces of the exterior columns is high in contrast to the concept of the building-frame system in which the peripheral frames are intended to resist only the gravity load. The contribution of the flat-plate frame to the storey OTM in the flexible-base model is about 10% higher than that in the fixed-base model. The OTM contributed by the wall, $M_{x,wall}$, can be divided into three parts, which are Tl due to the tension–compression(T/C) forces of the coupled

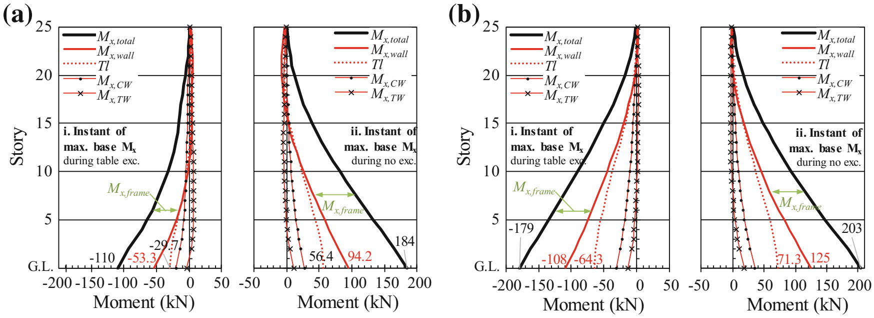

Fig. 15.16 Distribution of storey OTM in the X-dir. at instants of the maximum base OTM under 0.3XY (MCE): **a** flexible-base model and **b** fixed-base model

wall and the bending moments of each side of the coupled walls subjected to the compression and tension forces, $M_{x,CW\ (compression\ wall)}$ and $M_{x,TW\ (tension\ wall)}$. At the instant of the maximum OTM, the contribution ratios of Tl:$M_{x,CW}$:$M_{x,TW}$ to the total are 31%:15%:5.9% and 35%:17%:9.0% in the flexible-base and fixed-base models.

15.4.3 Ductility Demand of Coupling Beam

Although the coupling beam is designed as the conventionally reinforced beam with aspect ratio, l_n/h = 3.5, the coupling behavior of the walls covers approximately 60% of the base overturning moment resisted by the core wall, $M_{x,wall}$. The behaviors of coupling beams at Portion 2 (see Fig. 15.1b) are shown in Fig. 15.17: the distributions of (i) the storey beam shear force, (ii) the storey beam bending moment, (iii) the beam chord rotations, (iv) the dissipated energy, and (v) the representative hysteretic curve between the bending moment and the chord rotation at the plastic hinge (M-θ hinge) in the 4th and 18th stories under 0.3XY. The maximum chord rotation is compared with the performance limits defined in ASCE 41-13 (2014): the numerical acceptance criteria are given at three performance levels with immediate occupancy (IO) = 0.005 rad, life safety (LS) = 0.01 rad, and collapse prevention (CP) = 0.025 rad, if the coupling beams are controlled by flexure.

Under 0.3XY, the maximum bending moment of coupling beams except in the upper five stories exceeded the yield bending moment in the both of the flexible-base and fixed-base models (Fig. 15.17a-ii, b-ii). In Fig. 15.17a-iii, b-iii, the maximum chord rotation reaches the performance limit state, LS = 0.01 rad. In the flexible-base model, the maximum chord rotation (0.0101 rad) occurs in the fourth storey during no excitation, which is larger than that during the table

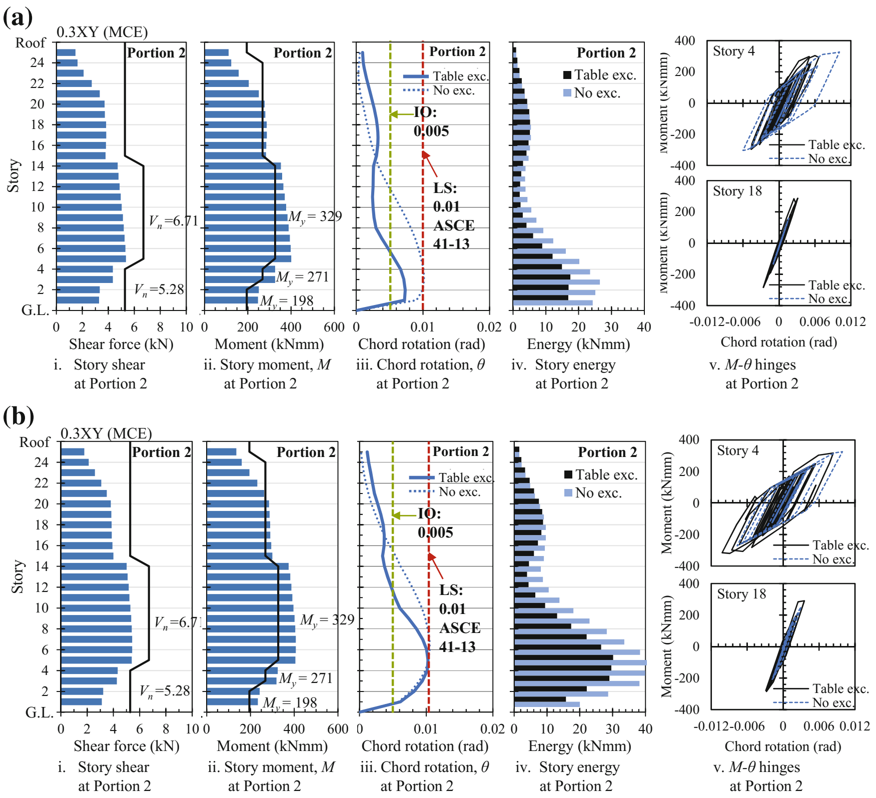

Fig. 15.17 Behavior of coupling beam at Portion 2 (see Fig. 15.1b) under 0.3XY: **a** flexible-base model and **b** fixed-base model

excitation (0.0072 rad), and the relationship of the *M*-*θ* hinge in the fourth storey (Fig. 15.17a-v) also shows that the severe inelastic behavior does not occur during the table excitation but occurs during the free vibration after the table excitation terminated. In the fixed-base model, however, the maximum chord rotation during the table excitation (Fig. 15.17a-iii), 0.01 rad, appears to be similar to the maximum value during no excitation.

The amount of hysteretic dissipated energy of the fixed-base model (Fig. 15.17b-iv) is significantly larger than that of the flexible-base model (Fig. 15.17a-iv), particularly during the table excitation. There is almost no energy dissipation in the coupling beams in the 18th to 25th stories during no excitation. The relationship of the *M*-*θ* hinge in the fourth storey (Fig. 15.17a-v, b-v) shows that the flexible-base model has a lower number of inelastic cycles of energy dissipation than the fixed-base model.

15.4.4 Ductility Demand at the Base of Wall with Special Boundary Element

In accordance with the displacement-based design method in ACI 318-05 (2005), special boundary details are imposed on the web wall in the first storey with the expected plastic rotation of $\theta_p = \delta_u/h_w$ = 427 mm/79,500 mm = 0.00537 rad (Lee et al. 2015). The ultimate curvature corresponding to a strain of 0.00638 m/m is $\varphi_u = \varepsilon_{cu}/c$ = 0.0027 rad/m for the prototype (Fig. 15.2), with φ_u = 0.041 rad/m for the 1:15-scale model, and the value of curvature for the strain of 0.003 is $\varphi_{cl} = \varepsilon_{cl}/c$ = 0.00127 rad/m for the prototype, with φ_{cl} = 0.0191 rad/m for the 1:15-scale model.

Figure 15.18 shows the X-directional bending moment–curvature (M-φ) curves of the left side of the coupled wall in the first storey subjected to the gravity loads of DL/3.59 and 1.0DL under 0.3XY and 0.4XY in comparison with the capacity curves obtained by performing the pushover analysis to the three-storey wall subassemblage isolated from the whole structure. All responses of the curvature under 0.3XY and 0.4XY are within the value of curvature for limiting strain of 0.003, φ_{cl} = 0.0191 rad/m. In the flexible-base model, the distorted model (DL/3.59) has a

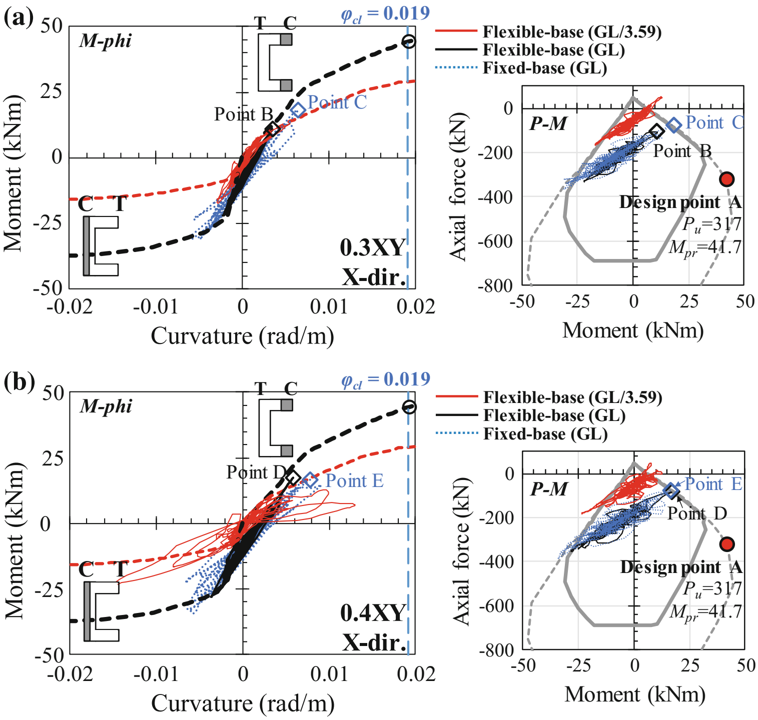

Fig. 15.18 Behavior of left wall at the bottom of the first storey in the X-direction: **a** 0.3XY and **b** 0.4XY

Table 15.4 Maximum responses on the left side of coupled wall in the first storey in the X-direction

Intensity	Model	Moment (kNm)	Curvature (rad/m)	Flexural rotation (rad)	Compressive strain (m/m)
0.3XY (MCE)	Flexible base	+10.9/ −22.1	0.00349	0.00119	0.00116
	Fixed base	+18.2/ −31.1	0.00647	0.00220	0.00144
0.4XY	Flexible base	+17.3/ −28.2	0.00581	0.00198	0.00170
	Fixed base	+16.6/ −34.3	0.00912	0.00310	0.00204

smaller value of moment than the true replica model (1.0DL). In the true replica model, the M-φ relationship of the flexible-base model behaves elastically, whereas that of the fixed-base model reveals a low level of inelastic response. The values of the maximum curvature under 0.3XY are 0.00349 rad/m in the flexible-base model and 0.00647 rad/m in the fixed-base model, which are 8.51% and 15.8% of the ultimate curvature, φ_u = 0.041 rad/m, respectively. The maximum compressive strain at the bottom edge of the web wall having the special boundary details under 0.3XY is 0.00116 m/m versus 0.00144 m/m in the flexible-base versus fixed-base models in Table 15.4, which are significantly smaller than the design value, 0.00638 m/m.

Figure 15.18 also compares the demand in the relations between axial force and bending moment (P-M) of the X-directional wall under 0.3XY and 0.4XY with the capacity, ϕP-ϕM interaction diagram. The demand most of time instants remains within the capacity of ϕP-ϕM interaction surfaces with only minor excursion beyond this surface. The axial force and moment (Point A: $P_u = -317$ kN and M_{pr} = 41.7 kNm) corresponding to the strain distribution assumed for the special detail design as given in Fig. 15.2a does not actually occur, but greatly decreases in the axial compression force shown as Point B (P = −105 kN and M = 10.9 kNm) in the flexible-base model and Point C (P = −74.0 kN and M = 18.2 kNm) in the fixed-base model under 0.3XY in Fig. 15.18a and 15.19a, b. The combinations of P-M under 0.4XY at Point D (P = −83 kN and M = 17.3 kNm) and at Point E (P = −75 kN and M = 16.6 kNm) in Fig. 15.18b and 15.19c, d are also much smaller than that of Point A. It is because the axial force of the wall having the compression strain in the protruded edges is always reduced due to the T/C coupling behaviors in the coupled wall system as shown in Fig. 15.19.

According to ASCE 41-13 (2014), if RC shear walls are controlled by flexure the performance limit on the flexural rotation is determined depending on the level of the axial force, shear force, and the existence of the confined boundary. The acceptable rotation limits for the performance levels are 0.004 rad for IO, 0.01 rad for LS, and 0.015 rad for CP. In Table 15.4, the values of the maximum flexural rotation under 0.4XY are 0.00198 rad/0.00310 rad of the flexible-base/fixed-base models, respectively, less than the limit, 0.004 rad for IO.

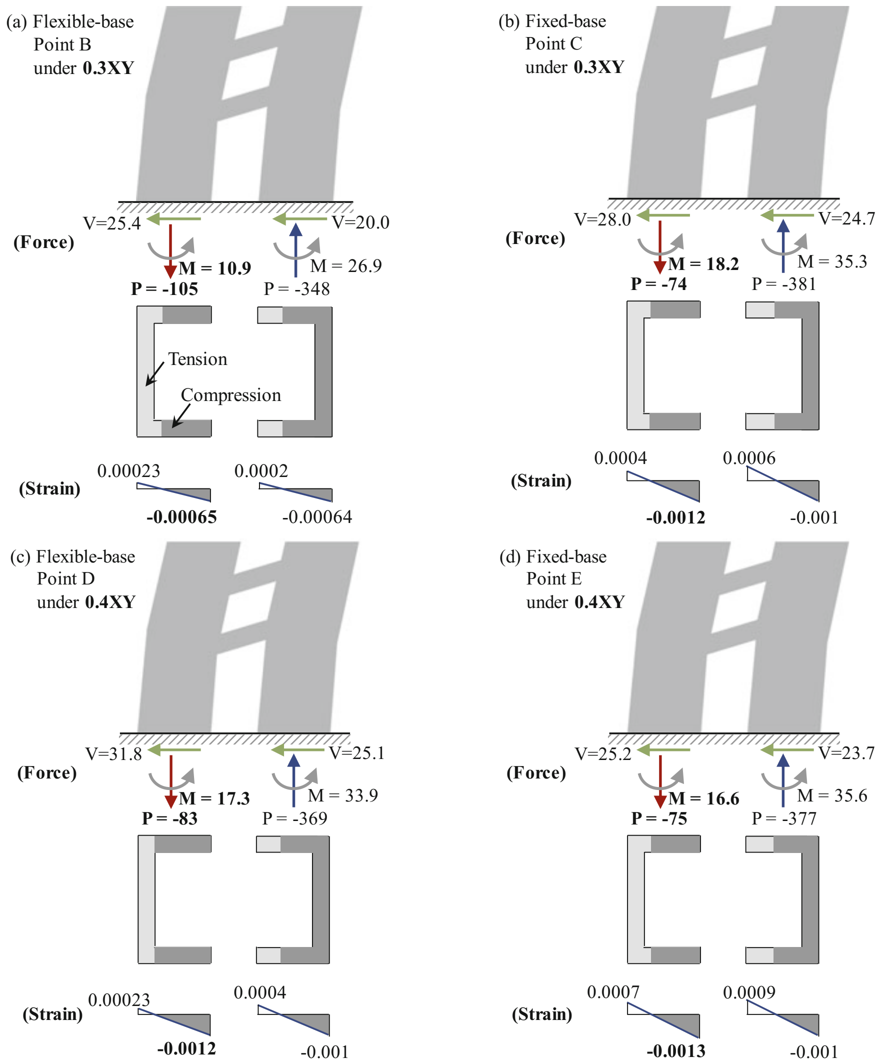

Fig. 15.19 Wall force and strain distribution at the base of core wall when the bending moment of the left wall reaching the maximum (Unit: V = kN, M = kNm, P = kN, and strain = m/m)

15.5 Conclusions

This study investigates seismic responses of an RC high-rise flat-plate core-wall building structure through the analytical simulation of the shake-table responses of a 1:15 scale 25-storey flat-plate core-wall RC residential building model (Lee et al. 2015). The seismic responses in the X-direction of the true replica model are discussed to evaluate the seismic performance of the 25-storey flat-plate core-wall building structures. The following conclusions are drawn from the analytical investigations:

(1) In the test results (Lee et al. 2015), the rocking behavior at the base occurred due to the uplift of the footing beneath the core wall. The numerical models with the flexible base and the fixed base are used to evaluate the effect of base flexibility on the seismic response of the building model. Under MCE in Korea, the base flexibility decreases the overall lateral stiffness by 33% and increases the roof drift by 36%.
(2) The results of the earthquake simulation tests show that the seismic responses during free vibration right after the termination of shake-table excitation are governed by the first mode leading to sometimes larger drift than those during the table excitation that are mainly affected by the higher modes. The numerical model efficiently simulates the time histories of the experiment not only during the table excitation but also during free vibration.
(3) Less than 10% of the base shear is resisted by the flat-plate frame regardless of the base flexibility under MCE in Korea. However, the flat-plate frame has a significant contribution to the overturning moment (OTM) resistance. The contribution ratio of the storey OTM resisted by the core wall to the flat-plate frame is 50%:50% in the flexible-base model and 60%:40% in the fixed-base model. This 10% difference is caused by the higher contribution of *Tl* component in the fixed-base model.
(4) The maximum chord rotation in the coupling beam under MCE in Korea is approximately 0.01 rad, which is the limit state of life safety in ASCE 41-13 (2014) regardless of the base flexibility. The amount of inelastic energy dissipated by the coupling beam in the flexible-base model is approximately one-half of that in the fixed-base model.
(5) According to ACI 318-05 (2005), the special boundary details are imposed on the core wall in the first storey to satisfy the target ductility consistent with δ_u using the design P-M demand, $P_u = -317$ kN and $M_{pr} = 41.7$ kNm. However, it does not actually occur under MCE in Korea, but greatly decreases leading to P = −105 kN with M = 10.9 kNm in the flexible-base model and P = −74.0 kN with M = 18.2 kNm in the fixed-base model, because the axial force of the wall having the compression strain in the protruded edges is always reduced by the T/C behavior in the coupled wall system. The design assumption in ACI 318 is far from reality for the coupled wall system, and, therefore, causes the overdesign regarding the ductility demand.

Acknowledgements The research presented herein was supported by the National Research Foundation of Korea (NRF-2016R1C1B1016653 and NRF-2017R1D1A1B03033488) and the Korea University Grant. The authors are grateful for such support. The authors are grateful for this support.

References

American Concrete Institute (ACI). (2005). Building code requirements for structural concrete and commentary, *ACI 318-05*.

American Society of Civil Engineers (ASCE). (2014). Seismic evaluation and retrofit of existing buildings. *ASCE/SEI 41-13*, Reston, VA.

Architectural Institute of Korea (AIK). (2009). Korean Building Code. *KBC 2009*. Seoul, Korea. (in Korean).

CSI. (2011). *Components and elements for PERFORM-3D and PERFORM-Collapse Ver. 5*. Computers and Structures Inc., Berkeley, CA.

Hwang K. R. (2016). *Seismic Performance of high-rise reinforced concrete wall building structures.* Ph.D. Thesis. Korea University Library.

International Code Council. (2006). *International building code.* Country Club Hills, IL.

LATBSDC. (2017). *An alternative procedure for seismic analysis and design of tall buildings located in the los angeles region.* Los Angeles Tall Buildings Structural Design Council, CA.

Lee, H. S., Hwang, K. R., & Kim, Y. H. (2015). Seismic performance of a 1: 15-scale 25-story RC flat-plate core-wall building model. *Earthquake Engineering and Structural Dynamics, 44*(6), 929–953.

Melek, M., Darama, H., Gogus, A., & Kang, T. (2012). Effects of modeling of RC flat slabs on nonlinear response of high-rise building systems. In *15th world conference in earthquake engineering.*

Moehle, J., Bozorgnia, Y., Jayaram, N., Jones, P., Rahnama, M., Shome, N., Tuna, Z., Wallace, J., Yang, T., & Zareian, F. (2011). Case Studies of the Seismic Performance of Tall Buildings Designed by Alternative Means, Task 12 Report for the Tall Buildings Initiative, Pacific Earthquake Engineering Research Center Report 2011/05, University of California, Berkeley.

Moehle, J. P., & Diebold, J. W. (1984). Experimental study of the seismic response of a two-story flat-plate structure. Report No. UCB/EERC-84/08, Earthquake Engineering Research Center, University of California-Berkeley, Berkeley, CA.

Munir, A., & Warnitchai, P. (2012). The cause of unproportionately large higher mode contributions in the inelastic seismic responses of high-rise core-wall buildings. *Earthquake Engineering and Structural Dynamics, 41*(15), 2195–2214.

Naish, D., Fry, A., Klemencic, R., & Wallace, J. (2009). Experimental evaluation and analytical modeling of ACI 318-05/08 reinforced concrete coupling beams subjected to reversed cyclic loading. UCLASGEL Report 2009/06, 109 pp.

Pacific Earthquake Engineering Research Center. (2017). Guidelines for performance-based seismic design of tall buildings, Report PEER-2017/06, Pacific Earthquake Engineering Research Center, University of California, Berkeley, CA.

PEER/ATC. (2010). Modeling and acceptance criteria for seismic design and analysis of tall buildings. *PEER/ATC 72-1 Report*. Applied Technology Council. Redwood City, C.A.

Satake, N., Suda, K. I., Arakawa, T., Sasaki, A., & Tamura, Y. (2003). Damping evaluation using full-scale data of buildings in Japan. *Journal of Structural Engineering, 129*(4), 470–477.

Zekioglu, A., Willford, M., Jin, L., & Melek, M. (2007). Case study using the Los Angeles tall buildings structural design council guidelines: 40-storey concrete core wall building. *The Structural Design of Tall and Special Buildings, 16*(5), 583–597.

Chapter 16
Essential Requirements for Reinforced Concrete Structures of Limited Area and Height

Luis E. Garcia, Santiago Pujol and Juan Francisco Correal

There is a worldwide criticism that current structural design standards and codes might be too complex for many applications. An international agreement between American Concrete Institute—ACI, and two Colombian institutions was signed and as a result, the document ACI 314 Guide to the simplified design of reinforced concrete buildings was developed. Earthquake-resistant requirements are based on the use of structural concrete walls (shear walls) that limit the lateral deformations of the structure and provide lateral strength. The design can be carried out using solely the document and a hand calculator without the need for a computer. The manuscript will focus on the way the document was developed and how it is organized.

16.1 Introduction

There is no doubt that modern structural engineering has been affected by improvements and developments that took place in the last decades. The use of computers in analysis, design, and drafting, the introduction and widespread use of

L. E. Garcia (✉) · J. F. Correal
Department of Civil and Environmental Engineering,
Universidad de Los Andes, Bogotá, Colombia
e-mail: lugarcia@uniandes.edu.co

J. F. Correal
e-mail: jcorreal@uniandes.edu.co

S. Pujol
Department of Civil Engineering, Purdue University, West Lafayette, IN, USA
e-mail: spujol@purdue.edu

T. T. C. Hsu (ed.), *Concrete Structures in Earthquake*,
https://doi.org/10.1007/978-981-13-3278-4_16

improvements in traditional structural materials aimed at better performance and higher strengths, along with important developments in building and construction procedures, have brought corresponding changes in design procedures and requirements developed initially for a different situation. Complexity in building code requirements is just a consequence of these changes.

From an international perspective, there are many regions and countries of the world that do not have the resources or personnel to develop a local building code. This situation is solved by adopting world-class documents in many cases without any attempt of adaptation to the local situation. The ACI building code has been the model of choice adopted by many countries where the main structural material is reinforced concrete. The reality is that the full use of the code is limited to the larger cities where most well-trained engineers reside with other less developed regions having to use a document far too complex for the type of construction used and where no advanced technology is available and engineering expertise is either not available, nonexistent, or of low quality.

With this in mind, an attempt to bridge the gap was worked as an international agreement between the American Concrete Institute—ACI and two Colombian Institutions: ICONTEC Internacional (Colombian Institute for Technical Standards and Certification—ICONTEC) and the Asociación Colombiana de Ingeniería Sísmica (Colombian Association for Earthquake Engineering—AIS). As a result of this agreement, the document IPS-1 "Essential Requirements for Reinforced Concrete Buildings" (ACI-ICONTEC-AIS 2002) was developed. The document was published in English and Spanish in year 2002. There were SI and US Customary units versions for the English document and a Spanish version in SI units.

Current knowledge on reinforced concrete behavior obtained through experimentation and experience, and its status and dissemination as a structural material used worldwide, made the task of development of a simplified design and construction document, not only feasible but challenging. Given the success of the 2002 IPS-1 document led to the formation on an ACI Committee ACI 314—Simplified Design of Concrete Buildings, whose mission was established as "To develop and report information on the simplified design and economical construction of concrete buildings of limited height." At the end of 2011, Committee ACI 314 presented a new document based on the original IPS-1 publication but also introducing important changes to it in format and content. This new document was ACI 314R-11 (ACI Committee 314 2011) and in 2016 a new version was published as ACI 314R-16 (ACI Committee 314 2016).

16.2 Organization of the ACI 314R-16 Document

ACI 314R-16 presents simplified approaches to assist engineers in designing low-rise buildings within certain limitations, in addition to the following: (a) Information on the order needed in the course of a design; (b) Explanatory material at appropriate places; (c) Computations only requiring a hand calculator; (d) Graphs and graphical explanations; (e) Design information based on simplified strength models; (f) Other limit states accounted for by minimum dimensions; (g) Conservative loads and simplified analysis guidelines; (h) Simplified geotechnical information to help define soil bearing capacity; (i) Shear walls as the seismic-force-resisting system; and (j) Material and construction guidelines based on commonly available steel grades and medium-strength concrete that can even be site mixed.

The document provides a licensed design professional with sufficient information to design structural reinforced concrete members that comprise the structural framing of a low-rise building complying with the limits set in it. Design rules set forth in the document are simplifications that, when used together, comply with the more detailed requirements of ACI 318 (ACI Committee 318 2014), ASCE/SEI 7–10 (ASCE 2010), and the 2015 International Building Code (International Code Council 2015).

Among structural engineers, there is a general concern that current structural design standards are unnecessarily complex for many applications. That criticism might be right on the mark if we take into account that many of the building code requirements for reinforced concrete contained in the ACI 318 Code (ACI Committee 318 2014) are aimed at high-rise buildings, even though there is strong evidence that the bulk of the floor area constructed in the United States, and other countries, corresponds to low-rise buildings (those with one to three storeys) (Kamara and Novak 2011). The building code therefore requires considerations that are not critical for most of the country's concrete construction (Figs. 16.1 and 16.12).

16.3 Scope

The guide is intended for the planning, design, and construction of reinforced concrete structures in new low-rise buildings of restricted occupancy, number of storeys, and area. Although the information presented was developed to produce, when properly used, a reinforced concrete structure with an appropriate margin of safety, the guide is not a replacement for a licensed design professional experience and working knowledge. The guide presents simplified methods and design techniques that, within certain limitations, facilitate and speed the engineering of low-rise buildings. The guide contains design information in an order that follows the typical design process, and with procedures introduced as they will be needed in

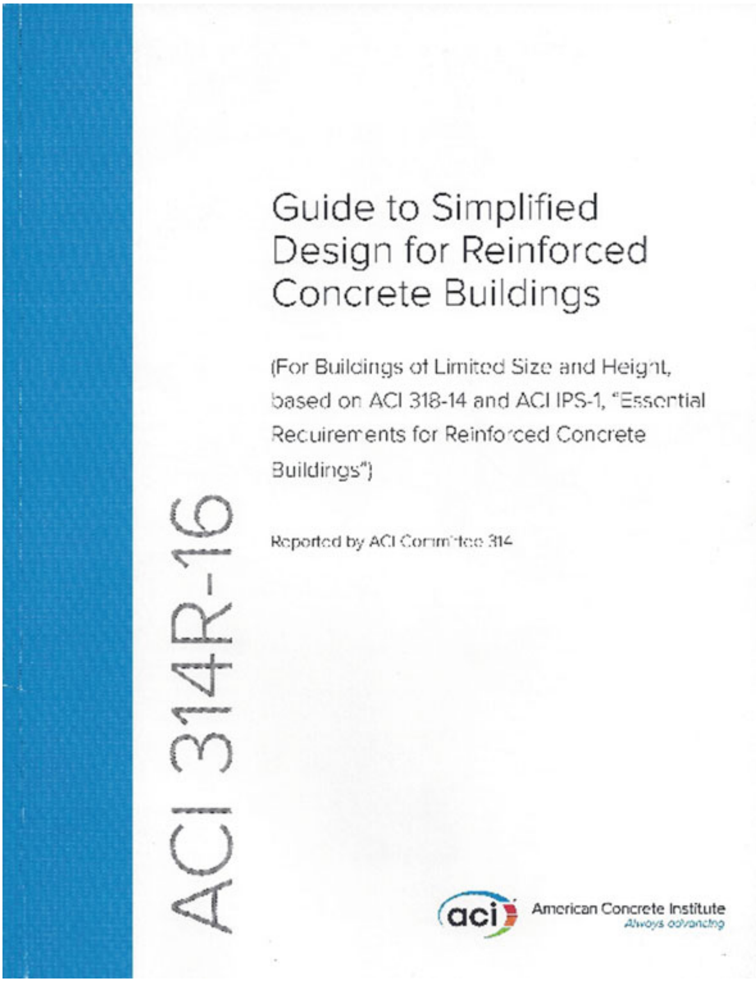

Fig. 16.1 The cover of ACI 314R-16, "Guide to Simplified Design for Reinforced Concrete Buildings"

the course of a building design. Although it is not written in mandatory language, the information in the guide is presented in such a manner that it can be used to design a structure that will comply with the Codes and Standards on which the document was based. For the structure designed by the guide to attain the intended margin of safety, the guide should be used as a whole, and alternative procedures may be used only when explicitly permitted in the guide. The minimum dimensioning prescribed in the guide replace, in most cases, more detailed procedures prescribed in the supporting codes and standards. Table 16.1 lists the chapter distribution of document ACI 314R-16, and Table 16.2 the permitted occupancies.

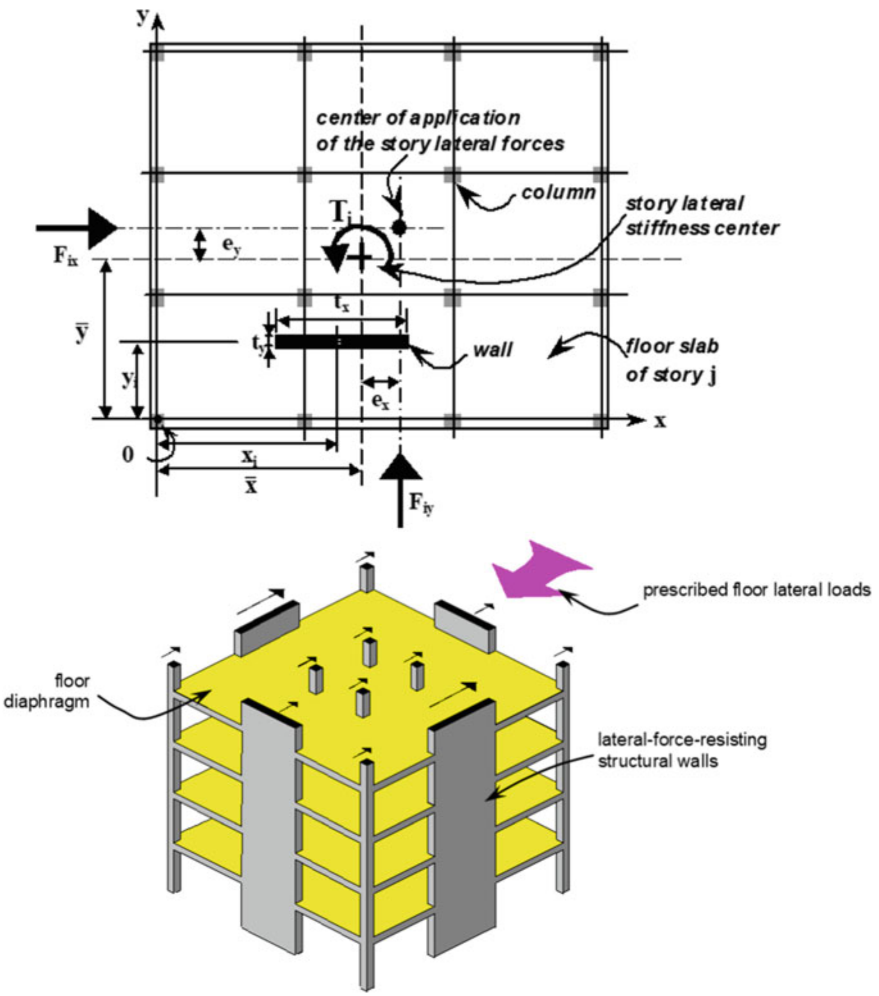

Fig. 16.2 Schematics of lateral force-resisting system based on ACI 314R-16 requirements (Figures reprinted from ACI Committee 314 2016)

16.3.1 Details

As an example of the simplified reinforced concrete design requirements that are presented, Figs. 16.3 and 16.4 illustrate how development length, lap splice length, and standard hook anchorage distance are defined. Relative to the corresponding requirements of ACI 318, the illustrated values are conservative for all deformed bars with diameters of 1 in. (25 mm) or less. The guide ensures that ACI 318 requirements are met by setting a maximum diameter of 1 in. (25 mm) on all

Table 16.1 Chapter titles of ACI 314R-16 (ACI Committee 314 2016)

Chapter number	Chapter title
1	General
2	Notation and definitions
3	Structural system layout
4	Loads
5	General reinforced concrete information
6	Floor system
7	Solid slabs supported on girders, beams, joists, or reinforced concrete walls
8	Girders, beams, and joists
9	Slab–column systems
10	Columns
11	Seismic resistance
12	Reinforced concrete walls
13	Other structural members
14	Foundations
15	Drawings and specifications
16	Construction
17	References
Appendix A	Comparison by topic of ACI 314R-16 to ACI 318-14, IBC 2015, and ASCE 7-10

reinforcing bars employed in designs made using the document. This type of approach is used throughout the document.

Typical reinforcement details are presented for many elements. Figure 16.5 shows the reinforcement layout for girders that are part of a frame. Minimum sectional dimensions are also presented for many elements. Figure 16.6 shows the minimum dimensions for columns required to ensure that the columns will not be considered slender per ACI 318. In other words, meeting these dimensional requirements allows the designer to avoid making the slenderness calculations and checks required by the code. Foundation guidance includes instructions on conducting a limited scope geotechnical investigation, recommendations for foundation types, and defining allowable soil stresses. The document also contains general guidelines for drawings, specifications, and construction, including minimum inspection and quality-control requirements. ACI Committee 314 went to much effort in generating self-explanatory tables, graphics, and design aids to simplify the use of the document and provide clearly defined procedures. Although the guide was developed to be used in the design office rather than in the classroom, it also has great potential to serve as an aid for the teaching of basic reinforced concrete (Fig. 16.7).

Several features of the document make its employment by students useful: (a) The document gives a whole perspective of the design process, from initial planning of the structure layout to the production of construction documents;

Table 16.2 Uses and occupancies permitted by document ACI 314R-16 (ACI Committee 314 2016)

Occupancy group	Occupancy subgroup		Permitted
Group A—Assembly	A-1	Fixed-seating theaters, television, and radio studios	No
	A-2 A-3	Building having an assembly room with capacity less than 100 persons and not having a stage	Yes
	A-4	Arenas, skating rinks, swimming pools, and tennis courts	No
	A-5	Amusement parks, bleachers, grandstands, and stadiums	No
Group B—Business	B	Building for use as offices, or professional services containing eating and drinking establishments with less than 50 occupants	Yes
Group E—Educational	E	Educational purposes with less than 500 students and staff	Yes
Group F—Factory	F-1	Light industries not using heavy machinery	Yes
	F-2	Heavy industries using heavy machinery	No
Group H—Hazardous	H	Manufacturing, processing, generation, or storage of materials that constitute a physical or health hazard	No
Group I—Institutional	I-1	Residential board and care facilities	Yes
	I-2	Hospitals	No
	I-3	Prisons, jails, reformatories, and detention centers	Yes
	I-4	Daycare facilities	Yes
Group M—Mercantile	M	Display and sale of merchandise	Yes
Group R—Residential	R-1	Hotels having an assembly room with capacity less than 100 persons and not having a stage	Yes
	R-2	Apartment buildings and dormitories	Yes
	R-3	Houses	Yes
	R-4	Residential care and assisted-living facilities	Yes
Group S—Storage	S-1	Storage of heavy or hazardous materials	No
	S-2	Storage of light materials	Yes
Group U—Utility and miscellaneous	U	Utilities, water supply systems, and power generating plants	No
	U	Garages for vehicles with carrying capacity up to 4000 lb (1800 kg)	Yes
	U	Garages for trucks of more than 4000 lb (1800 kg) carrying capacity	No

(b) The document describes the different alternatives for structural systems and lists the advantages and disadvantages of each system; (c) Although simplified procedures are employed, they are based on the same requirements of the code; (d) Because the document does not rely on sophisticated analysis tools, the student can more readily and reliably determine the loads and forces acting on the structural elements and more rapidly learn to recognize appropriate dimensions; (e) The

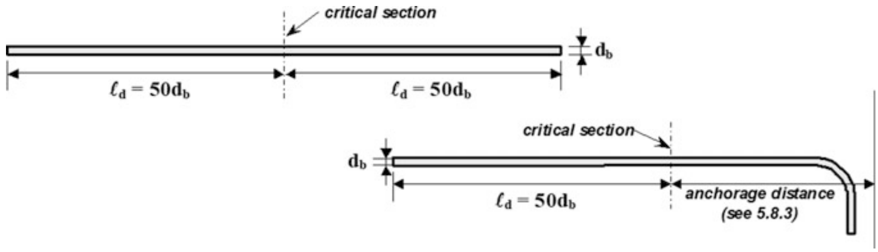

Fig. 16.3 Development length requirements (Figure from ACI Committee 314 2016)

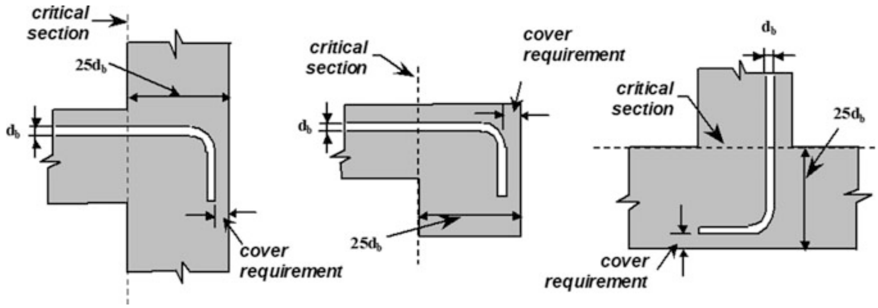

Fig. 16.4 Standard hook anchorage distance requirements (Figure from ACI Committee 314 2016)

document asks for final check of the results, helping to preclude unrealistic designs; and (f) The document integrates related fields, such as foundation engineering and construction supervision, and instructs the student on their importance.

16.3.2 Earthquake Resistance

Resistance to seismic loads should be provided by using a sufficient number of reinforced concrete walls continuous from the foundation to the roof in both principal directions in plan. Reinforced concrete walls produce stiff structures with a short fundamental period of vibration and the seismic loads given in the guide reflect this type of structure. The calculation of seismic loads for more flexible structures is beyond the scope of the guide. The seismic-resistant structural system used in the guide is classified as a dual building frame system, where an essentially complete moment-resistant space frame supports gravity loads, and resistance to lateral loads is provided by reinforced concrete walls, with the moment-resisting space frame providing a minimum collateral lateral-load resistance. Reinforced concrete walls resisting lateral loads are not permitted to carry vertical axial loads greater than the balanced point axial strength. They must have rectangular section,

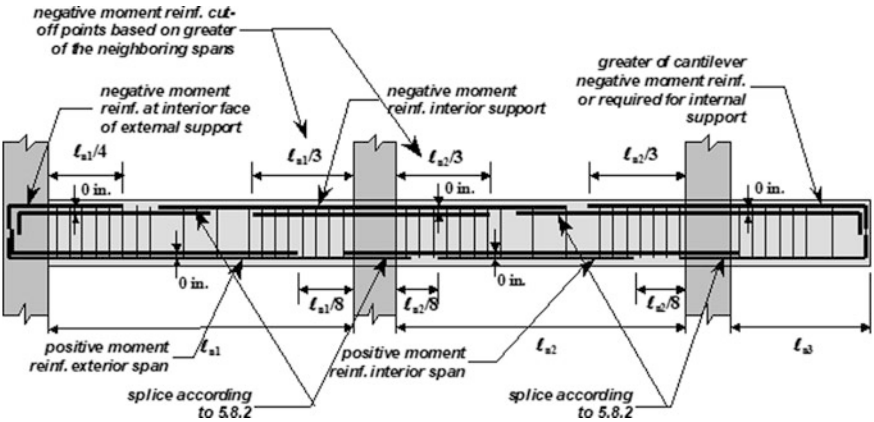

Fig. 16.5 Reinforcement in girders that are part of a moment-resisting frame supported by columns or reinforced concrete walls (Figure reprinted from ACI Committee 314 2016)

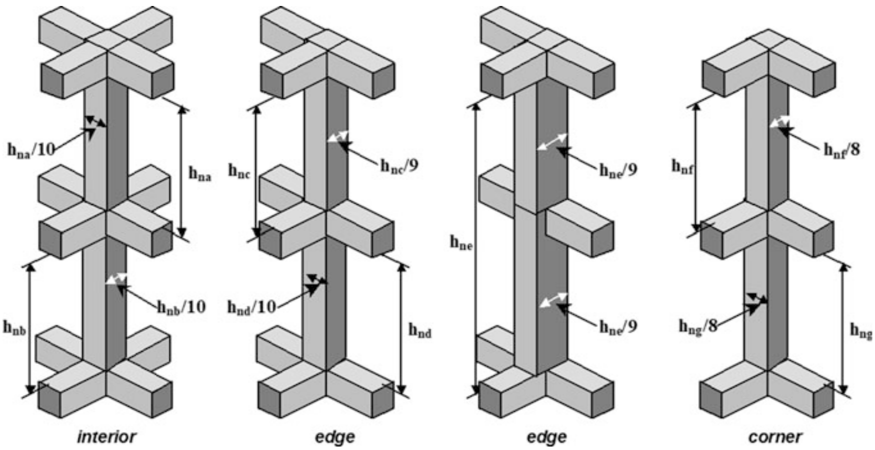

Fig. 16.6 Lateral restraint and minimum section dimension for columns (Figure reprinted from ACI Committee 314 2016)

be vertically continuous from foundation to roof, vertically aligned, have no openings for windows or doors, in each principal direction in plan there must be at least two parallel walls in different planes, and the planes should be as far apart as practicable. The walls should be placed as close to the periphery of the building as possible. At any floor *i*, for the two principal directions in plan, the minimum cross-sectional area $(\ell_w b_w)$ for all reinforced concrete walls acting in the principal direction under consideration should be determined from

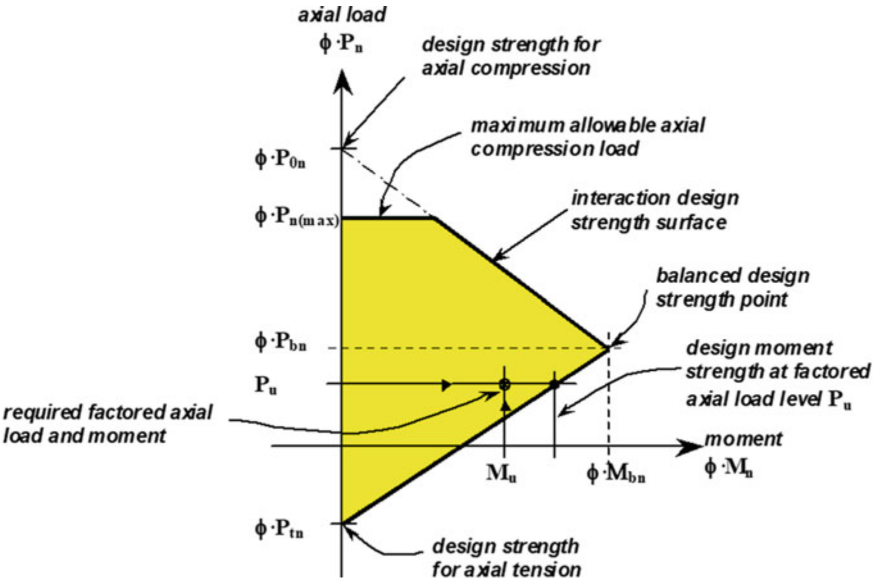

Fig. 16.7 Interaction diagram for columns (Figure reprinted from ACI Committee 314 2016)

$$\sum(\ell_w b_w) \geq \frac{V_{iu}}{2\sqrt{f'_c}} \left[\sum(\ell_w b_w) \geq \frac{6V_{iu}}{\sqrt{f'_c}}\ (SI)\right] \tag{16.1}$$

where V_{iu} is the factored lateral shear of storey i in the plan direction of interest, and the in-plane slenderness ratio, h_w/ℓ_w, for any individual wall should comply with

$$\left(\frac{h_w}{\ell_w}\right) \leq \frac{3+n_s}{2} \tag{16.2}$$

where n_s corresponds to the total number of storeys of the building above the base.

The developers of the IPS-1 document (ACI-ICONTEC-AIS 2002) prescribed the minimum amount of wall area for each principal direction in plan of the building based on having an appropriate shear strength for inhibiting that the walls fail in shear, leading to Eq. (16.1). Because the document does not require an analysis of the structure, it was deemed very important to devise a procedure that would lead to the building meeting an acceptable storey drift in response to the design earthquake prescribed by the general building code. In order to calibrate the proposed requirements, the "Chilean formula" procedure is devised by Mete A. Sozen based on the observation of the behavior of buildings with structural walls during the 1985 Viña del Mar, Chile, earthquake (Sozen Mete 1989), event in which structural concrete walls without special detailing performed exceptionally well. The findings indicated that it is possible to obtain a wall area index, p, in each

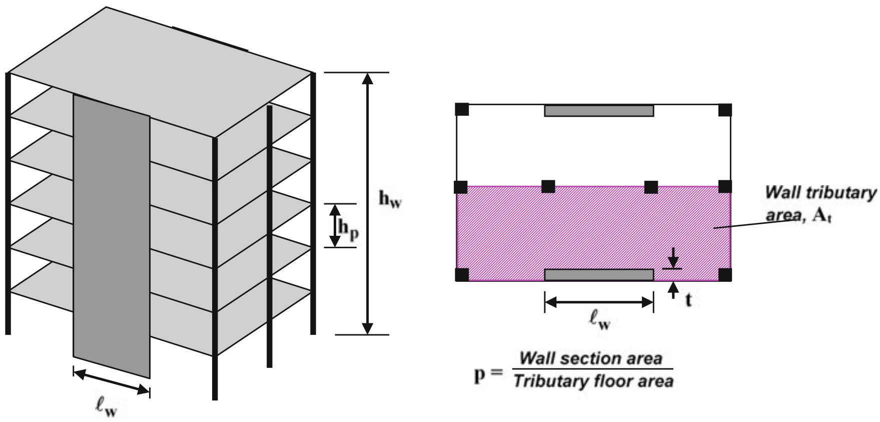

Fig. 16.8 Definition of the wall index parameter (Figure reprinted from Sozen Mete 1989)

principal direction in plan as shown in Fig. 16.8, that would meet a particular mean drift ratio through the use of Eq. (16.3) with the only differences with the original manuscript being the inclusion of the short-period soil amplification F_a factor and a conversion from average roof drift to inter-storey drift, Δ.

$$\Delta = 0.7 A_a F_a \left(\frac{h_w}{\ell_w}\right)\sqrt{\frac{wg}{E_c p h_p}} \tag{16.3}$$

where

Δ = Inter-storey drift.
A_a = Peak ground acceleration as a fraction of g.
F_a = Seismic site coefficient for short periods of vibration.
h_w = Wall height in consistent units.
ℓ_w = Wall horizontal length in consistent units.
w = Building weight per unit area in consistent units.
g = Acceleration of gravity in consistent units.
E_c = Modulus of elasticity of concrete in consistent units.
p = Wall index (non-dimensional).
h_p = Storey height in consistent units.

Figure 16.9 shows the use of Eq. (16.3) with different wall in-plan slenderness ratios, h_w/ℓ_w, building weight per unit area, w, 200 psf, $E_c = 5.2 \times 10^8$ psf, h_p = 10 ft, F_a = 1.0, and A_a = 0.4.

The conclusion derived by Prof. Sozen was based on the premise that energy dissipation would occur only if shear or bond failures are precluded for the wall. The IPS-1 drafting Committee agreed to aim at a slenderness ratio of $(\ell_w/h_w) = 4$ and at a wall area ratio of 1.25% in each principal direction in plan. For the update 2016 of the document ACI 314R-16, these premises were revisited and the result was a change in

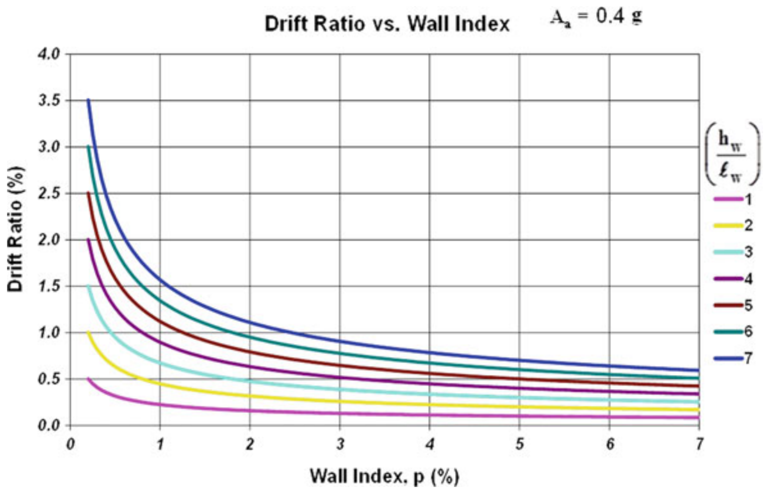

Fig. 16.9 Wall index, p, versus storey drift ratio, Δ

the wall area as required for shear strength to the one shown in Eq. (16.1) before, and a modification in the maximum wall slenderness in-plane ratio to the one shown in Eq. (16.2) that adjust the required value in function of the number of storeys.

Committee ACI 314 conducted a validation of these new requirements using the information available of vulnerability of low-rise buildings using the Hassan and Sozen Index (Hassan and Sozen 1997) in several earthquakes that affected a significant number of buildings of the height and size of those permitted to be designed using ACI 314R-16.

After the publication of the Hassan and Sozen procedure, it has been used in many instances around the World. A manuscript by Professor Sozen published at the time the calibration was being made (Sozen Mete 2014) describes the procedure and gives supporting data for several earthquakes with a sizable inventory of low-rise buildings. The procedure is very simple and works in the following way:

Computation of a wall index, WI, using the following equation:

$$WI = \frac{A_{wt}}{A_{ft}} \times 100 \tag{16.4}$$

where

$A_{wt} = A_{cw} + A_{mw}/10$ = effective cross-sectional area of walls in a given horizontal direction.

A_{cw} = total cross-sectional area of reinforced concrete walls in a given horizontal direction at the base of the building.

A_{mw} = cross-sectional area of nonreinforced masonry filler walls in a given horizontal direction at the base of the building.

A_{ft} = total floor area above the base of the building.

Computation of a column index, CI, using the following equation:

$$CI = \frac{A_{ce}}{A_{ft}} \times 100 \tag{16.5}$$

where

$A_{ce} = A_{col}/2$ = effective cross-sectional area of columns at the base.
A_{col} = total cross-sectional area of columns above the base of the building.

Computation of a priority index, PI, using the following equation:

$$PI = WI + CI \tag{16.6}$$

From the information presented by Sozen (Sozen, Mete 2014), a graph in which the column index, CI, is plotted in the horizontal axis and the wall index, WI, is plotted in the vertical axis, a boundary that contains 95% of the studied buildings that reported severe damage could be drawn as Bound 1 in next figures for the earthquakes listed in Table 16.3.

This means that a reasonable value for the priority index, PI, that would cover buildings that would not report severe damage would be those having a priority index of 0.25%. Or put in other words, the following equation would be a reasonable limit for dimensioning new low-rise buildings combining reinforced concrete walls and a moment-resisting frame that would not sustain severe damage during a strong earthquake:

$$WI + CI \geq 0.025 \tag{16.7}$$

The selection of a lower bound priority index of 0.25% for the case at hand of ACI 314 Guide recommendations is consistent for buildings designed using the guide being new buildings and nonstructural infill walls not being taken into account. If applied to existing buildings, it was decided that it would probably be wiser to use a more conservative value as the one shown as Bound 2 in Fig. 16.10, thus requiring a priority index of the order of 0.50%.

By replacing the defined variables in Eq. (16.7), and disregarding the contribution of nonreinforced masonry filler walls, we can obtain

Table 16.3 Earthquakes whose available information was used to plot Figs. 16.10 and 16.11 (Sozen Mete 2014)

Earthquake	Magnitude M_w	Approx. Distance to Epicenter (km)
Erzincan, 1992	6.7	17
Duzce, 1999	7.2	10
Bingol, 2003	6.4	15
Wenchuan, 2008	7.9	70
Haiti, 2010	7.0	25

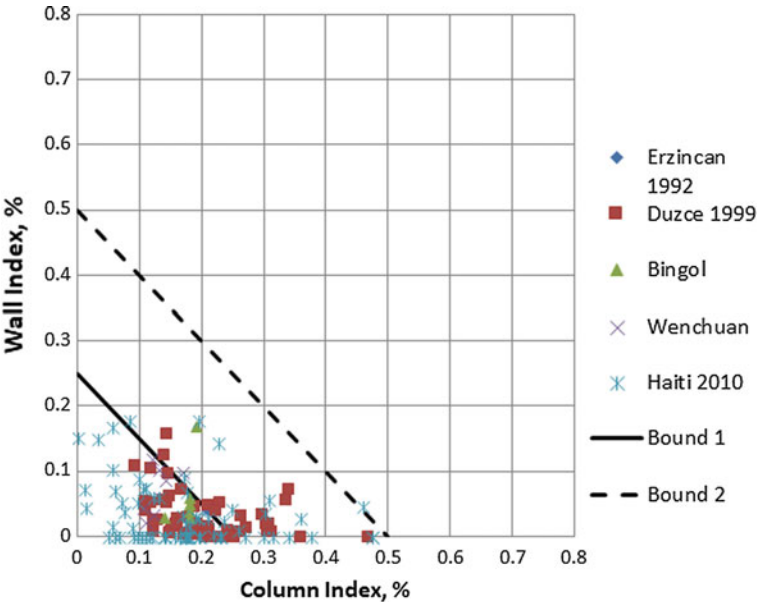

Fig. 16.10 Cases with severe damage during the earthquakes listed in Table 16.3 (Figure reprinted from Sozen Mete 2014)

$$\frac{A_{cw}}{A_{ft}} + \frac{A_{col}}{2A_{ft}} \geq 0.025 \tag{16.8}$$

This last equation can be solved for the minimum required reinforced concrete wall area in each principal direction in plan that would prevent severe damage of new buildings when responding to the design earthquake.

$$A_{cw} \geq 0.025A_{ft} - \frac{A_{col}}{2} \tag{16.9}$$

The variable A_{cw} corresponds to $\sum(\ell_w b_w)$ in ACI 314R-16 document terminology, thus constituting an approach to the minimum wall area at the base of the building in each principal direction that includes the contribution of a moment-resisting frame, based on worldwide documented experience. A_{ft} is the total floor area above the base of the building, corresponding to the total aerial floor slab area including the roof slab. In case a light roof is used, appropriate adjustments of the tone of roof weight expressed as proportional slabs area may be used. The amount of wall area in each principal direction obtained through this equation would inhibit severe damage of the building when subjected to a design earthquake aimed at life preservation, as envisioned in the corresponding supporting ACI 314R-16 documents and constituted the basis of the guide recommendations.

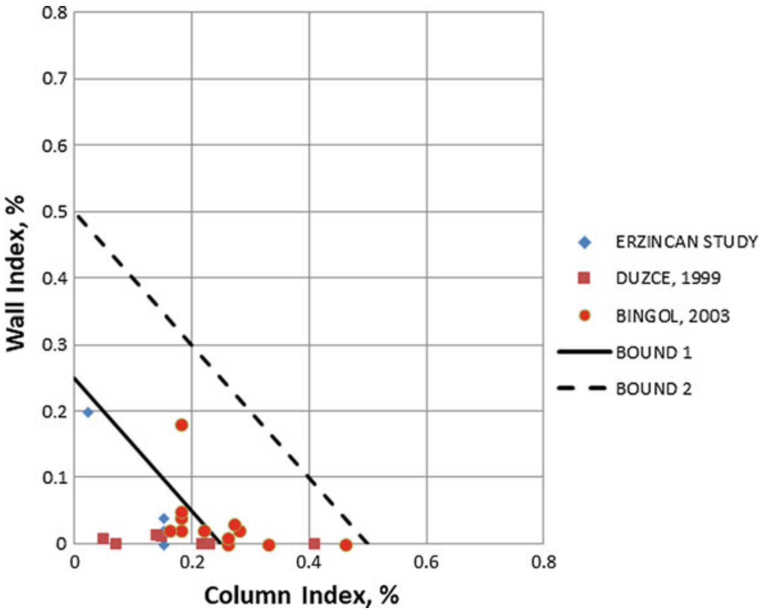

Fig. 16.11 Cases in which collapses were reported during the earthquakes listed in Table 16.3 (Figure reprinted from Sozen Mete 2014)

16.3.3 Detailing for Earthquake Resistance

ACI 314R-16 guide requires that the detailing of the structural members in seismic zones meets the detailing requirements of Chap. 18 of ACI 318-14 code. The procedures to define the proper detailing of the members use simplified instructions that lead to the proper amounts of longitudinal and, especially, transverse reinforcement. In Fig. 16.12, the arrangement of hoops in a column is presented. It must be noted that ACI 314R-16 document simplifies the arrangement and requires

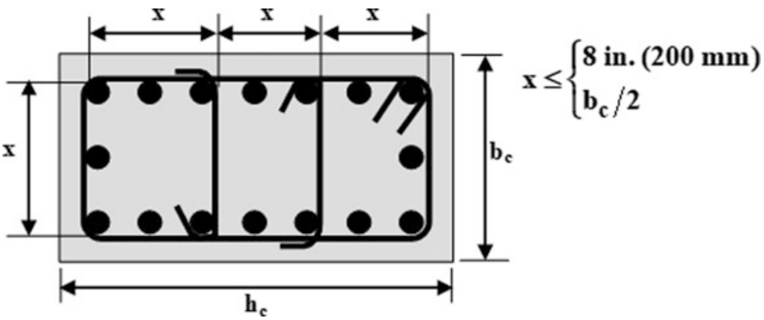

Fig. 16.12 Arrangement of hoop legs and crossties (Figure reprinted ACI Committee 314 2016)

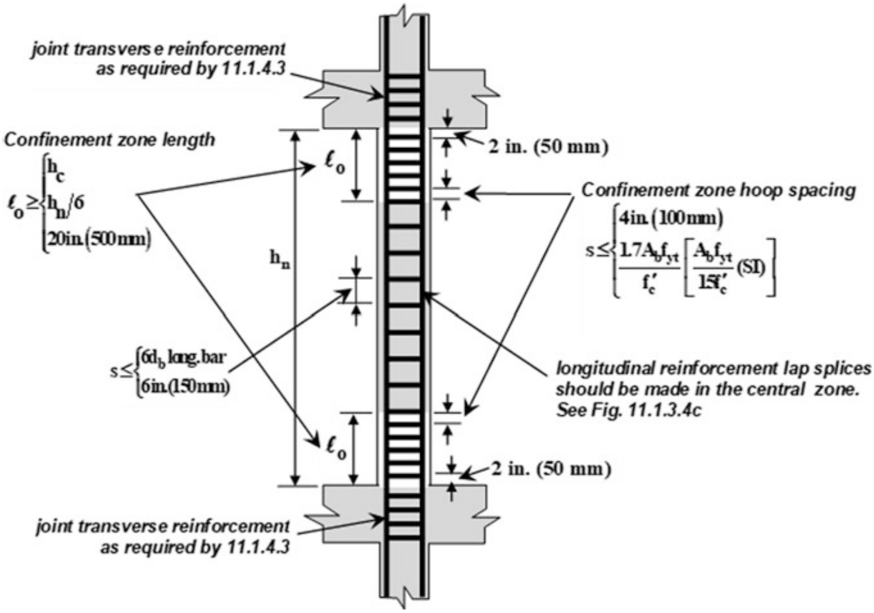

Fig. 16.13 Confinement hoop spacing in columns (Figure reprinted ACI Committee 314 2016)

that the horizontal distance between legs of hoops and crossties is further restricted from what ACI 318-14 requires, thus opening the door to a simpler procedure to designing the vertical hoop spacing at the confinement zones of columns, thus making it easier to meet the same requirements. Figure 16.13 further indicates how the hoops and crossties are arranged, but in the long run meeting the same requirements as explained.

On the last note, the ACI 314R-16 document gives advice on handling issues related to nonstructural elements in seismic situations. There is rarely the situation of an earthquake not reporting short column issues, especially in regions of the world where stiff unreinforced masonry nonstructural elements are still used frequently. The short column's issue is very common in school building where windows are used as shown in Fig. 16.14.

ACI 314R-16 guide suggests two solutions: (a) Separate the infill wall from the column by providing a gap, which gives guidance on the gap allowance and requires that the masonry wall should be anchored to prevent its overturning when subjected to out-of-plane lateral loads, and (b) locate a much shorter window in the central part of the span, thus having the infill masonry wall against the column along its full height. In this alternative, the distance between the column face and the window should be at least twice the vertical dimension of the gap left by the window. Figure 16.15 shows this solution by using a shorter window located in the middle of the span.

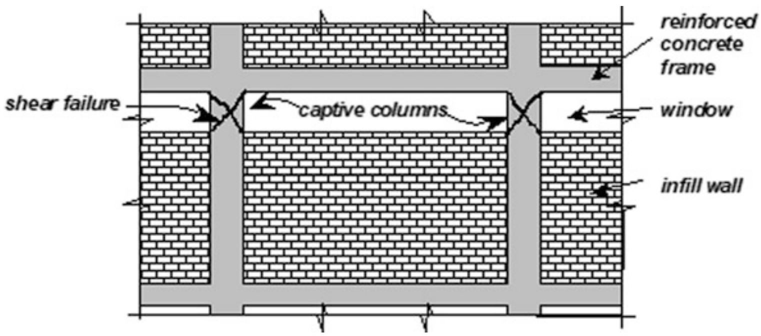

Fig. 16.14 Short column effect (Figure reprinted ACI Committee 314 2016)

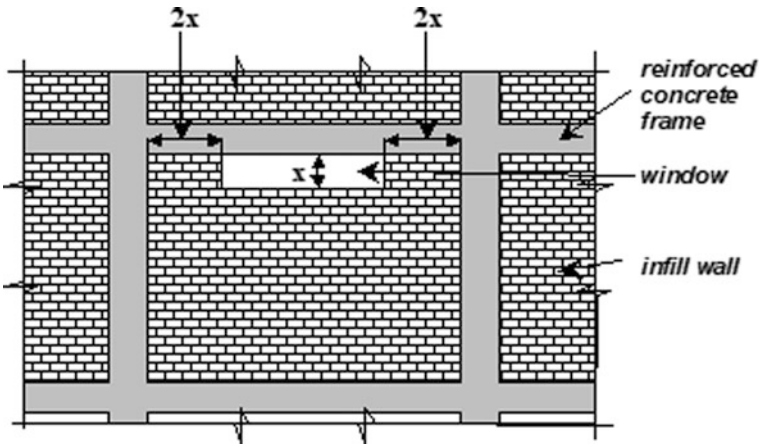

Fig. 16.15 Short column effect solution by using a shorter window located in the middle of the span (Figure reprinted ACI Committee 314 2016)

References

ACI Committee 314. (2011). *Guide to simplified design for reinforced concrete buildings (ACI 314R-11)—for buildings of limited size and height, based on ACI 318-11 and IPS-1, essential requirements for reinforced concrete buildings* (p. 132). Farmington Hills, MI: American Concrete Institute.

ACI Committee 314. (2016). *Guide to simplified design for reinforced concrete buildings (ACI 314R-16)—for buildings of limited size and height, based on ACI 318-14 and IPS-1, Essential requirements for reinforced concrete buildings* (p. 128). Farmington Hills, MI: American Concrete Institute.

ACI Committee 318. (2014). *Building code requirements for structural concrete (ACI 318-14) and commentary* (p. 519). Farmington Hills, MI: American Concrete Institute.

ACI-ICONTEC-AIS. (2002). *Essential requirements for reinforced concrete buildings—for buildings of limited size and height, based on ACI 318-02. In International Publication Series No. 1 (IPS-1)* (p. 248). Farmington Hills, MI: American Concrete Institute.

ASCE. (2010). *Minimum design loads for buildings and other structures ASCE/SEI 7–10* (p. 636). Reston, VA: American Society of Civil Engineers.

Hassan, A., & Sozen, M. A. (1997). Seismic vulnerability assessment of low-rise buildings in regions with infrequent earthquakes. *ACI Structural Journal, 94*(1) 31–39.

International Code Council. (2015). *International building code (IBC-2015)* (736) International Code Council, Washington, DC.

Kamara, M. E., & Novak, L. (2011). *Simplified design of reinforced concrete buildings EB204* (4th ed., p. 330). Skokie, IL: Portland Cement Association.

Sozen Mete A. (1989). Earthquake response of buildings with robust walls. in *Fifth chilean conference on earthquake engineering* (14) Santiago, Chile.

Sozen, Mete A. (2014). Surrealism in facing the earthquake risk, seismic evaluation and rehabilitation of structures, Ilki, Alper and Michael N. Fardis Editors (1–14) Switzerland: Springer International Publishing.

Chapter 17
The Seismic Strengthening of Concrete Structures by Ultrahigh-Performance Concrete

Sung-Gul Hong, Yousun Yi and Inyoung Gu

This paper investigates the behavior of concrete walls and columns strengthened by ultrahigh-performance concrete (UHPC). UHPC has been one of the promising construction materials of high strength and durability with high flow at placing. The jacketing methods using UHPC with/without textile reinforcement to increase sectional area for existing concrete walls and columns are demonstrated seismic strengthening efficiency in strength and ductility by the experimental programs in the paper. To ensure the interface shear strength between UHPC and original concrete, a series of slant shear test programs was performed and analyzed for design strength. This paper also compares with analytical approaches for verification of upgrading. Based on this research, some design equations for seismic jacketing are proposed.

17.1 Introduction

Earthquake hazards in the past had confirmed the deficiencies of concrete building structures yet even built and designed by updated seismic design codes. The damage of RC building after Bingol Earthquake in Turkey by Doabgun (2004),

S.-G. Hong (✉) · I. Gu (✉)
Department of Architecture and Architectural Engineering, Seoul National University, Building 39-429, 1 Gwanakro, Gwanak-Gu, Seoul, South Korea
e-mail: sglhong@snu.ac.kr

I. Gu
e-mail: berksmile@naver.com

Y. Yi (✉)
Seoul National University, Seoul, South Korea
e-mail: shangrian@gmail.com

Y. Yi
Department of Civil Engineering, University of Texas at Austin, Austin, TX, USA

T. T. C. Hsu (ed.), *Concrete Structures in Earthquake*,
https://doi.org/10.1007/978-981-13-3278-4_17

the immediate observation of damage to RC buildings in the Christchurch earthquake with the comparison of buildings built according to old and new seismic design codes by Kam et al. (2011), and the great east Japan earthquake by Maeda et al. (2012) were reported. In order to minimize damage in concrete structure due to earthquake, many engineers and researchers have made efforts to develop seismic design methods, seismic assessment, and strengthening techniques for structures during several decades. Especially, the seismic design of reinforced concrete structures was rationalized by capacity design method by Paulay and Priestley (1992) and the displacement-based seismic assessment proposed by Priestley (1997) in New Zealand. Moreover, many advanced analytical methods and the accumulation of experimental data for seismic capacity of structural concrete members and systems have led to the performance-based design methods and capacity spectrum method for new construction summarized by Moehle (2014) and the retrofit of existing structures.

Concrete walls and columns in building structures mainly transfer the gravity load and lateral loads to foundation. Furthermore, most shear failure of concrete walls and columns under earthquake loading leads to undesirable failure mechanism of concrete structures. Therefore, non-ductile failure of concrete walls and columns should be avoided to prevent the entire collapse of buildings. Most walls and columns of low shear strength definitely need proper retrofitting to enhance its strength, thereby providing tough earthquake resistance with extending the service life.

So far many researches on retrofitting techniques for concrete walls and columns such as sectional enlargement or jacketing, steel plate enforcement, and fiber-reinforced plastics (FRP) have been reported by Sugano (1996), Fukuyama and Sugano (2000), Fukuyama et al. (2000), and FEMA 547 (2006). Many previous studies have focused on fiber-reinforced plate (FRP) reinforcement owing to its convenient fabrication and lightweight property and suggested some design guidelines by ACI (2002). Also, steel plate enforcement familiar with many engineers exhibits a high retrofitting performance. FRP and steel plate reinforcements, however, enhance flexural and shear strengths with ductility only. The improvement of axial strength by confinement effect is also limited. Furthermore, they are vulnerable to fire and chemicals and have weak durability. On the other hand, the RC jacketing using additional concrete can simultaneously achieve the enhancement in axial strength, shear strength, flexural strength, and deformation capacity as Altun (2004), Bousias et al. (2007), and Chalioris et al. (2014) reported. The RC jacketing is applicable to the buildings with critically damaged or undamaged structures to increase strength in globally and locally as discussed by Thermou and Elnashai (2005). However, jacketing methods using concrete require thickness of 70–100 mm, resulting in both significant reduction of service floor areas and increase in the weight of structure itself after retrofit.

In response to the drawbacks of existing retrofitting methods for concrete structures, extensive researches using ultra high-performance concrete (UHPC) have been performed by Hong and Kang (2013), Fehling (2014), Meda et al. (2014), Choi et al. (2016), and EPFL research group under the leadership of Brühwiler

(Habel 2004; Oesterlee 2010; Noshiravani 2012; Bastein-Masse 2015) over longer 10 years focusing on overlay method using UHPC with reinforcing bars, so-called R-UHPC. Recently, the research on the cross-sectional enlargement method, namely, "jacketing" for retrofitting and strengthening the existing reinforced concrete (RC) structures has been widely carried out using the one of advanced concretes such as high-performance concrete (HPC) or UHPC. These methods were proven the superiority of technique through a variety of experimental research.

Jacketing using UHPC, which has higher strength than normal concrete, exhibits superior performance in most seismic capacity as well as reducing jacket thickness of more than 50% owing to its high strength. Furthermore, this method demonstrates high fire resistance and durability, showing long service life, thereby is worth being applied. Additional reinforcement in added sections using UHPC can significantly increase the ductility. Even so, a jacket thickness of at least 50–70 mm is enough to secure the cover thickness and to prevent fibers from agglomeration. Besides, the fabrication of steel reinforcement around existing columns has some disadvantage of constructability, requiring a highly skilled worker. Instead, textile reinforcement (TR) can be an alternative to conventional reinforcing bars in UHPC. Use of textile reinforcement with UHPC is able to reduce the minimum jacket thickness up to 20–30 mm. In addition, the textile reinforcement allows easier fabrication than conventional steel reinforcement. In this paper, the strengthening effects using ultrahigh-performance concrete for walls and columns under seismic loading are investigated with the consideration of shear strength at interface between UHPC and original concrete as well as the effect of the discontinuity of reinforcement in jackets.

17.2 Problem Statement

17.2.1 Interface Between UHPC and Substrate Concrete

For the structural members which are strengthened by jacketing, the interface shear strength between old and new concrete may control the performance of jacketing. Thus, the surface treatment of the surface of substrate original concrete plays a key role to ensure the interface adhesion strength presented in most repair design guidelines. According to recent studies, the use of UHPC for jacketing has the effect on the increase of shear capacity, even if the strengthening thickness is considerably smaller than when the normal strength concrete is used. In addition, the shear resistance increased even though the shear connectors did not installed between the existing concrete and strengthening concrete. However, if shear connectors are not used at the interface between the two concretes, that is, when the interface shear resistance is considerably smaller than shear demand, the sliding failure or delamination may be incurred prior to the member failure. According to ACI

Concrete Repair Guide (2014), the minimum adhesion strength at the interface is allowed as the values of 6.9–12 MPa.

17.2.2 Current Shear Strength Models of Retrofitted Concrete Walls and Columns

RC jacketing is one of the most commonly applied methods for the upgrading of concrete members. Jacketing is considered to be a global intervention if the longitudinal reinforcement placed in the jacket passes through holes drilled in the slab and new concrete is placed in the beam–column joint (Thermou and Elnashai 2005). However, if the longitudinal reinforcement stops at the floor level, then RC jacketing is considered as a member intervention technique.

The previous research on the jacketing methods to increase flexural strength of walls and columns has employed the linear strain distribution assuming the perfect bond between old and new concrete. This assumption confirmed that it is reasonable to determine the flexural retrofitting effect of not only reinforced concrete beams (Altun 2004) but also reinforced concrete columns (Campion et al. 2014) retrofitted with a concrete jacket. When estimating the shear retrofitting effect, however, a more refined analytical model is required because the linear strain distribution assumption cannot explain the shear behavior of the retrofitted members. Based on the previous studies, the strain continuity between both old and new members in analyzing both flexural and shear retrofitting effect may be effective in considering the monolithic behavior of the retrofitted member. Therefore, this study focused on proposing some of the analytical methods for estimating the shear behavior of the web section enlarged RC squat wall using the stain continuity and the limit analysis for retrofitted columns.

To date, apart from qualitative design guidelines in some provisions, no specific design rules exist for dimensioning and detailing of jackets to target performances. The uncertainty regarding bond between the jackets and the original concrete is another disadvantage. The bond and slip at the interface between the outside jacket layers and the original concrete that serves as the core of the upgraded members are overriding considerations.

17.2.3 Use of UHPC and Textile Reinforcement for Jacketing

This study investigates the increase in strength and deformation capacity of column retrofitted by textile reinforcement with UHPC (TR-UHPC) in which the longitudinal reinforcement stops at the floor, thereby to design additional shear reinforcement of column for target performances in stable manner. Textile reinforcement is a combination of fiber-reinforced polymer as a mesh type. The ordinary reinforcement can be replaced by textile reinforcement to improve degradation of durability due to corrosion of steel or steel fiber and constructability; otherwise, fiber in UHPC is not uniformly distributed.

During last decades, some engineering attention on the use of textile reinforcement has been growing around North American and European concrete societies. With those attentions, ACI Committee has published a report pertaining to the textile-reinforced cementitious composites (State-of-the-Art Report on Ferro cement, ACI 549R-97 (1997), Thin Fiber and Textile-Reinforced Cementitious Systems). Up to date, the structural design firms and the precast companies have started to apply textile reinforcement to precast modules and new retrofitting methods for existing structures using textile-reinforced concrete (or mortar) in many countries, eventually reporting systematical design code, while those studies cannot be reported in seismic retrofit techniques with UHPC.

As one of the researches on seismic jacket method, Triantafillou and Papanicolaou (2006) reported the recommendation on textile-reinforced mortar (TRM) jacket contribution to shear resistance V_t. Modeling of the textile-reinforced mortar jacket contribution to the shear resistance of flexural-reinforced concrete members may be based on the well-known truss analogy. The shear strength of TRM jacket has two main drawbacks: (1) axial load is not considered and (2) how to consider the bonding characteristics between textile reinforcement and existing columns. However, UHPC with textile reinforcement overcome the bond between fiber and UHPC and/or existing concrete due to the high strength. The test results for tensile behavior of UHPC with textile reinforcement shows the increase of ductility as the fiber volume ratio of UHPC increases rather than strength as shown in Fig. 17.1.

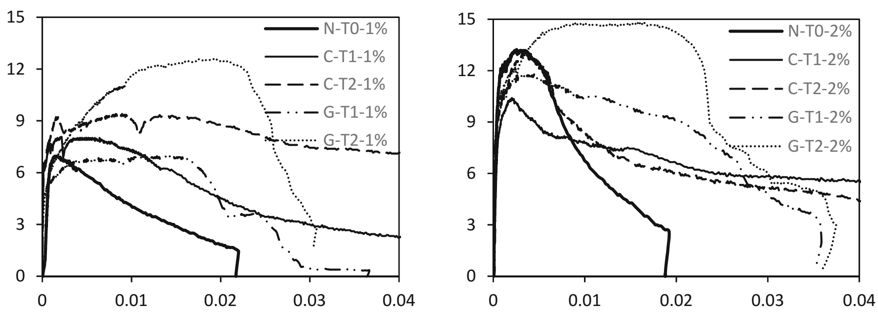

Fig. 17.1 Tensile behavior of UHPC with textile reinforcement dependent on fiber content

17.3 Interface Between UHPC and Substrate Concrete

The shear strength at the interface between old and new concrete is usually obtained using splitting prism tests, direct shear tests, and slant shear tests. Previous studies revealed that the bond strength at the interface highly depends on surface preparation or roughness of the surface. According to Tayeh et al. (2013), the mechanical bond strength between the normal concrete substrate and the UHPC was significantly influenced by the surface. They also demonstrated that sandblasting surface was the most superior mechanical bond capacity. The shear strength of the test specimens with holes on the concrete surface and the specimen with the treated surface using the wire brush were about 31–37.5% of the strength higher than the specimens with smooth surface, respectively. Also, the grooved specimen has the strength enhancement effect of about 64%. On the other hand, the interface shear of the specimen using a sandblasting has shown the strength enhancement effect of about 102.7%. According to previous studies, it appears to be the most effective way as the sandblasted surface. Cheong and MacAlevey (2000) conducted the slant shear tests on 100 × 100 × 500 mm plain and preplaced aggregate concrete prisms to derive a model for the behavior of strengthening RC beams by jacketing. Their interface angles were 60°, 70°, and 75°. The compressive strength of concrete had ranged from 31.3 to 52 MPa for plain concrete and 25.4 to 58.4 for PA concrete. In this study, as a part of the research for the evaluation of structural performance of RC members strengthening with UHPC, the interface shear strength between normal and high strength, and UHPC is evaluated.

17.3.1 Experimental Program

In this study, the slant shear tests were carried out to measure the interface shear strength between normal- and high-strength concrete and UHPC with different slant angles on the interface. The interface angles (α) between the surfaces of UHPC and concrete were 30°, 45°, and 60° with respect to longitudinal axis. The other primary test parameters were fiber volume fraction (V_f) of UHPC, the compressive strength ($f_c{}'$) of normal- and high-strength concrete, and surface roughness. The fiber volume fractions for UHPC were selected as $V_f = 0.5$, 1.0, 1.5, and 2%. The design compressive strength of UHPC was 150 MPa, and normal- and high-strength concretes were 24 MPa and 60 MPa, respectively. The average depths of the surface roughness by sandblasting were 0.3 mm and 0.6 mm. All the slant shear tests were conducted on 100 × 100 × 300 mm prismatic test specimen in accordance with ASTM C882 (1999). Figure 17.2 shows the configurations of the test specimens.

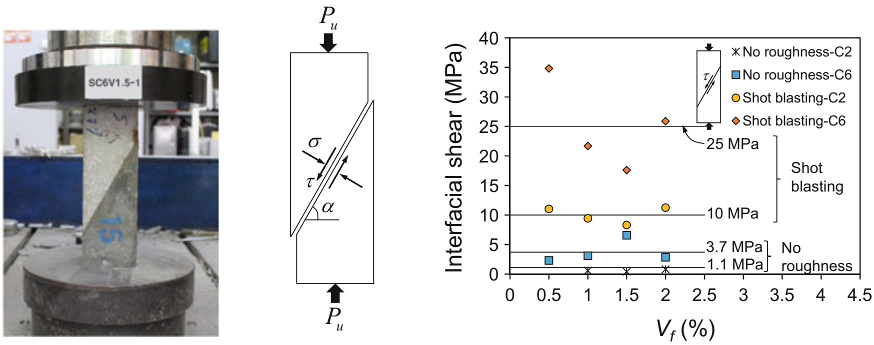

(a) slant test (b) stresses along interface (c) average stresses from test

Fig. 17.2 Slant test for interface shear strength

Slant shear tests can estimate the interface shear strength between old and new concrete through a compression test. The interface shear and normal stresses at the interface between two different types of concrete can be obtained using the uniaxial compressive strength determined by dividing a compressive force with a cross-sectional area of the prism test specimen.

17.3.2 Failure Criteria

As shown in Fig. 17.2b when the load applies to the inclined interface, normal stress (σ_u) and shear stress (τ_u) occur at the same time in a perpendicular direction to the interface and along the interface, respectively. Therefore, the normal (σ_u) and the shear stress (τ_u) at the interface can be obtained or the Mohr's circle:

$$\sigma_u = P_u \cos^2 \beta / A \tag{1}$$

$$\tau_u = P_u \sin \beta \cos \beta / A \tag{2}$$

where P_u is the ultimate load of the prism, α is the angle of the interface to the horizontal, and A is the cross-sectional area of the prism. Theoretically, the slant angle over 45° the failure is controlled by the ordinary concrete of lower compressive strength. Also, the parameters of Coulomb–Mohr, the friction angle, and cohesion vary with the slant angle changed.

Figure 17.2c shows the average interface shear strength of UHPC substrates. Test results showed that shear strength at the interface was highly dependent on the surface treatment and the normal stresses. For the UHPC substrate, as shown in Fig. 17.2c, the interface shear of the specimens with a rough surface was about

6.5–10 times higher than smooth surface. For the specimens with the rough surface, the average interface shear strength of the test specimens which is combined with normal- and high-strength concrete and UHPC is 10 MPa and 25 MPa, respectively. As a result, the shear strength at the interface treated by shotblasting satisfied the ACI concrete repair guidelines. It is noted that the concrete repair manual specifies the minimum allowable bond strength in a range from 6.9 to 12 MPa at 7 days and 13.8 to 20.7 MPa at 28 days for slant shear test in selecting appropriate repair materials (Figs. 17.3, 17.4, 17.5).

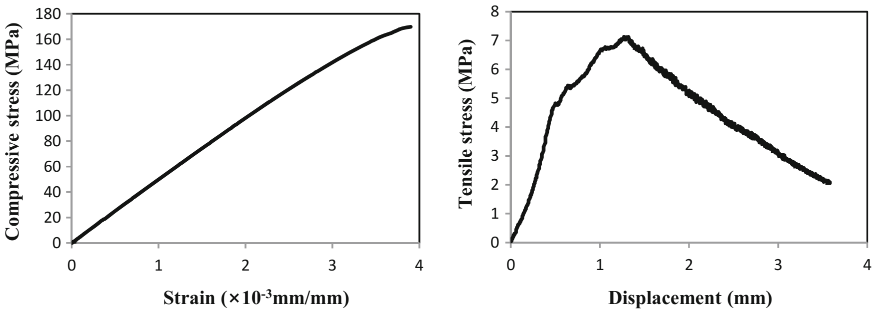

(a) Compressive stress-strain curve (b) tensile behavior

Fig. 17.3 UHPC material test results

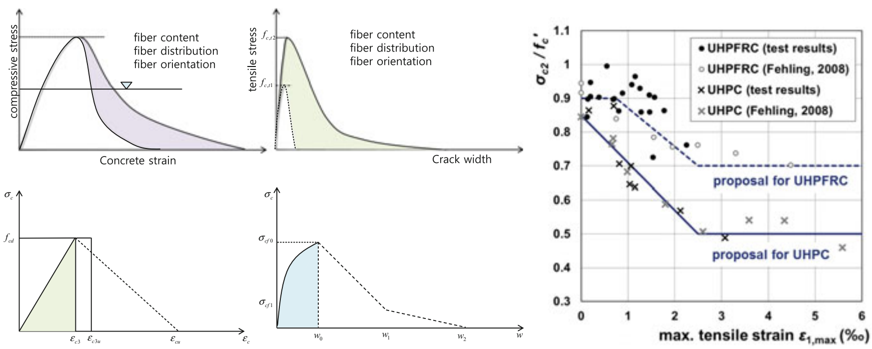

(a) Design strength (b) Strength reduction in biaxial stress state [Lee et al (2017)]

Fig. 17.4 Design strength of UHPC in compression and tension

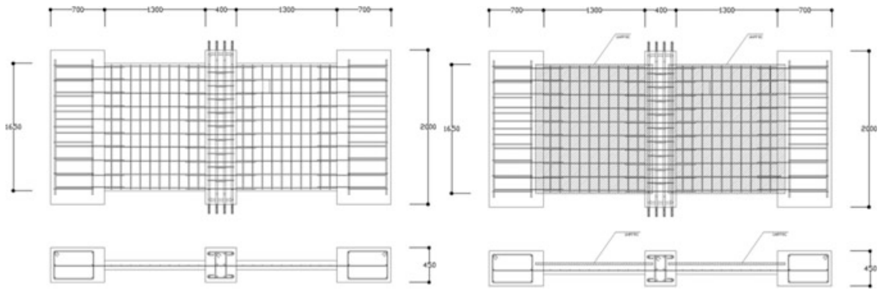

Fig. 17.5 Wall specimens for shear strengthening

17.4 Wall Strengthening

17.4.1 Shear Strengthening

The high-rise residential buildings in Korea have been built using shear wall systems over 40 years. However, the most residential shear wall system buildings before 1990 have been estimated as lower seismic capacity because of non-seismic detailing in critical sections (Table 17.1).

To strengthen the under-capacity of wall structures in Korea, we need to develop efficient retrofit methods. For the experimental program in this study, most typical wall sections in 1980s were reviewed to investigate the shear behaviors of walls strengthened by UHPC jackets. First, the wall of single-layered reinforcement with boundary elements was selected to study the shear strengthening of squat walls by one-side UHPC jacket.

For shear strength retrofit for walls, two deep beams were prepared and simply supported to simulate a squat wall behavior under lateral load (WN: original wall and WR: retrofitted wall). The vertical displacement through the vertical stiff boundary at the center simulated the lateral loads on the walls. The average concrete compressive strength of 21 MPa and the yield strength of steel of 420 MPa were used for the original wall and the substrate wall for retrofit.

The vertical and transverse reinforcement ratios of the specimens 0.33% and 0.47% were placed, respectively, with HD10 reinforcement. The aspect ratio of the wall panels of 1.0 was intended to develop the shear failure in the two wall panels. UHPC for jacketing was applied with the compressive strength of 150 MPa, and direct tensile strength of 7 MPa. The enlargement thickness of UHPC for one-side jacketing is 40 mm. The length of the UHPC jackets into the foundation and loading beam along the center is 200 mm longer than that of web of the original wall to prevent premature failure of the UHPC at the interface between the foundations and the walls.

Table 17.1 The change of detailing in shear walls for residential buildings in Korea

Period	Note	Detail
1980s	No boundary element (Double-layered)	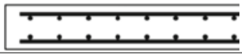
	Single-layered	
1995–2000	Confined with hoop reinforcement	
	Concentrated reinforcements at boundary region	
1995–	Confined with U-shaped reinforcement	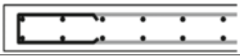

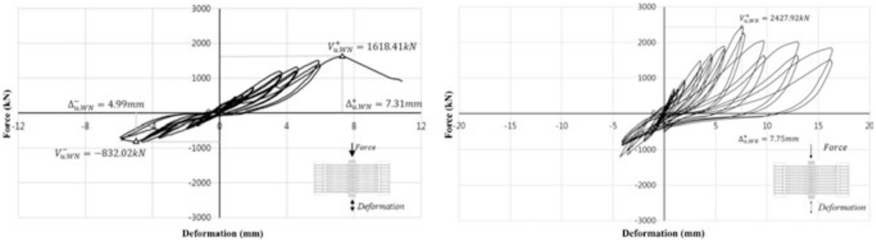

Fig. 17.6 Load–deflection and crack patterns in WN

To evaluate the strengthening capacity, cyclic loading was applied to the specimens at the center. The cyclic responses of WN and WR are shown in Fig. 17.6.

17.4.2 Results

The ultimate state of WN reached when the yielding of the transverse reinforcements in both the wall panels developed. The main failure mode of WN was controlled by the diagonal tension failure in only one wall panel of WN, since the strains in the transverse reinforcement through the cyclic loading showed that both left and right wall panels contributed almost same portion to the resistance of the specimen. Therefore, it is reasonable to consider that the cyclic behavior of the one wall panel is same as the half of the specimen. However, there exists a little difference between the positive directional strength and the negative directional strength of the specimen due to the lack of balance between both the boundary elements and the foundation frame in the opposite direction.

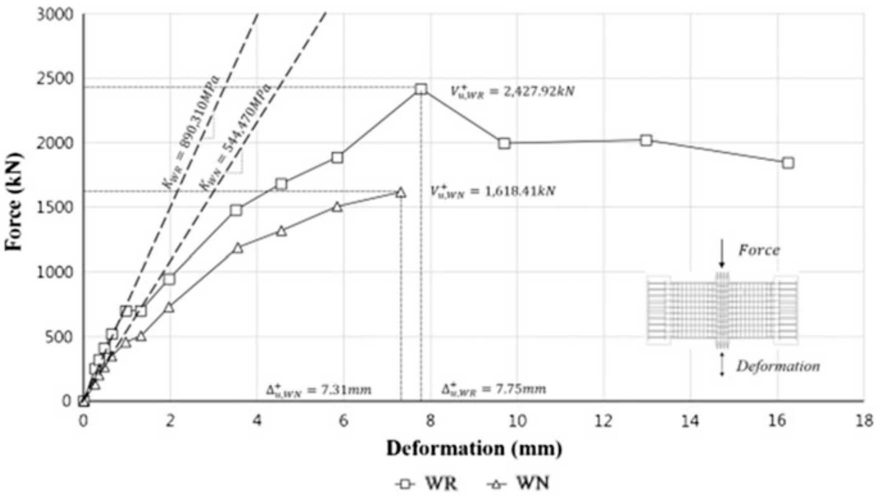

Fig. 17.7 Backbone curves for WN and WR

The total cyclic response of WR terminated by the interface failure is shown in Fig. 17.6. In addition, the cracking of the UHPC panel was observed right after the 12th cycle, meanwhile several diagonal cracks are already developed in the original concrete faces as the crack pattern in WR after the. Based on the cyclic response of upgraded wall, the backbone curves of them can be drawn as shown in Fig. 17.7. The result showed the enhancement of about 60% of initial stiffness and about 50% of ultimate by 40-mm-thickness UHPC web jacketing without reinforcement. Moreover, it was observed that the UHPC panel restraints the strain increment in the transverse reinforcements by comparison of the strain distribution of two specimens at the 10th cycle between WN and WR. The transverse reinforcement in WN yielded while those of WR did not yield at that time. Nevertheless, the dissipated energy of WR is always larger than that of WN at every load cycles. This is due to energy dissipation contribution of the UHPC panel. In conclusion, UHPC jacket delayed the yielding of the transverse reinforcement and increase the dissipation energy capacity.

17.4.3 Arch and Truss Actions

The shear strength of squat wall with UHPC jacket can be derived by the superposition of contribution of the original wall and UHPC layer, respectively. The shear strength of the squat wall by sliding shear failure is not considered here. The shear strength of squat wall web has been explained by the arch action and truss action. The combination of two actions is determined by the mechanical reinforcement ratio. The tensile strength of UHPC is converted to the mechanical reinforcement ratio to apply the existing equation for the arch and truss actions.

$$\frac{\tau}{\nu f_c^{uhpc}} = \frac{1}{2}\left[\sqrt{1+\left(\frac{a}{h}\right)^2} - \frac{a}{h}\right] + \psi\frac{a}{h} \tag{3}$$

where the equivalent mechanical reinforcement ratio is defined as

$$\psi = \frac{f_t^{uhpc}}{f_c^{uhpc}} \tag{4}$$

Substitution of the effective factor of UHPC compressive strength for Eq. (3) as ν = 0.5 and the mechanical reinforcement ratio as ψ = 0.05 into Eq. (4) predicted the increase in shear strength by UHPC in this experimental result.

17.4.4 Plastic Hinge Strengthening

For the plastic hinge, strengthening typical walls of double-layered reinforcement and without boundary elements in 1980s in Korea was selected in this study as shown in Fig. 17.8a.

The continuity of longitudinal reinforcement in jackets for walls and columns provide global invention for seismic upgrading. However, the jacketing with discontinuity of longitudinal reinforcement at floor level can be economical due to the ease of construction as local intervention of member level. No additional lift forces from foundation of upgraded walls allow lower seismic demand for the existing

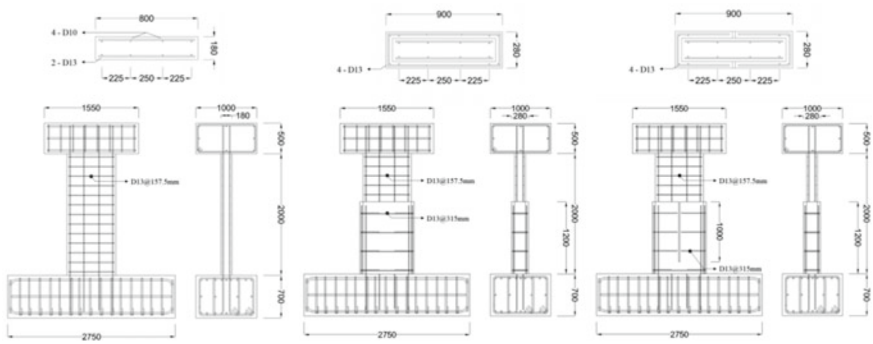

(a) Reference wall (b) Specimen FWR (c) Specimen with vertical slit-FWR-S

Fig. 17.8 Reinforcement details for wall specimens for plastic hinge strengthening foundation to the walls. Three wall specimens including the reference wall of the aspect ratio 2.5 and two strengthened walls by 50-mm-thickness UHPC jacketing in plastic hinge regions of walls were prepared to investigate the strengthening effect of the UHPC jacketing in the plastic hinge regions of walls. The average compressive strength of reference wall was 24 MPa, and the average compressive strength of UHPC was 145 MPa. The jackets include the longitudinal and transverse reinforcement.

The reference wall of Fig. 17.9 showed a stable cyclic behavior and the first cracking at 0.2% drift in 3rd cycle of the negative direction and at 0.3 drift in 4th cycle of the positive direction. After the several flexural cracks, the onset of yielding of the longitudinal reinforcement at 0.3% drift and 0.45% in the negative and positive loading directions was observed. Most flexural cracking was developed in the plastic hinge zone. No concrete spalling was observed until drift ratio reached 1% and 2% in the negative and positive directions, respectively. Cycling at this amplitude resulted in initiation of longitudinal reinforcement buckling near the bottom of wall. The spalling concrete gradually induced the loss of compressive resisting capacity until 3.5% drift ratio at 80% of the maximum strength in the positive direction.

The strengthening of plastic hinge region of walls by jacketing was investigated by the two remaining wall specimens, FWR and FWR-S. Since the discontinuity of longitudinal reinforcement at the bottom of the jacket cannot produce the flexural tension force in the jacket, the additional resistance due to suppression of spalling of cover concrete of the original walls and buckling of longitudinal reinforcement can be developed. Instead of the compression failure due to spalling and buckling, the fracture of tension bars controlled the ultimate capacity of the retrofitted wall at 2.5% drift in the 12th cycle in the negative direction of loading and at 3.0% drift in the positive direction of loading as shown in Fig. 17.10. The remaining specimen for the strengthening of plastic hinge region with the vertical slit of UHPC jacket was intended to lower the uplift force at the bottom as shown in Fig. 17.11. According to the strut-and-tie models for two specimens as shown in Fig. 17.12,

(a) Crack patterns (b) Load-deflection curves

Fig. 17.9 Crack patterns and cyclic behavior of reference wall the increase in shear strength due to the change of force flow was expected. The failure mechanism and global behavior of the specimen were similar to those of FWR. The fracture of longitudinal reinforcement in the original wall led to the ultimate state. In the 12th cycle just before the fracture of the longitudinal reinforcement, the drift ratio was 2.5% (56.25 mm) and the separation between UHPC jacket and the top face of base was observed.

To lower the uplift force at the bottom face after retrofit, the slit along the center in the jacket was made for wall FWR-S. The strut-and-tie model (STM) for FWR and FWR-S explains the difference between two jacketed walls as shown in Fig. 17.12. The increase in the shear strength after retrofit depends on the axial forces in UHPC jacket walls according to STM (Tables 17.2, 17.3, 17.4).

The increase in shear strength may lead to the flexural failure modes in both walls after retrofit. The effect of the vertical UHPC slit on the reduction of tensile stresses in the longitudinal reinforcement of the substrate walls is not significant. However, the vertical full slit rather than the partial vertical slit may be expected to lower the tensile strain (Figs. 17.13, 17.14, 17.15).

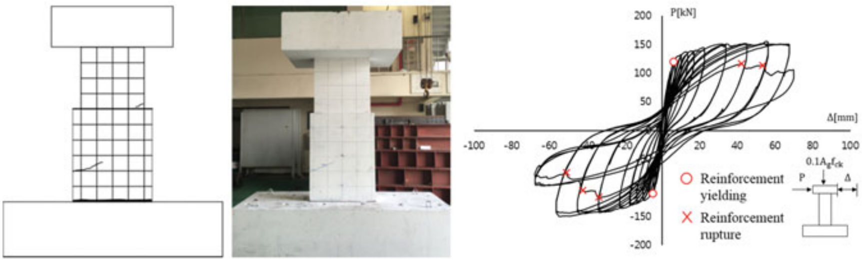

(a) Crack patterns (b) Load-deflection curves

Fig. 17.10 Crack patterns and cyclic behavior of FWR

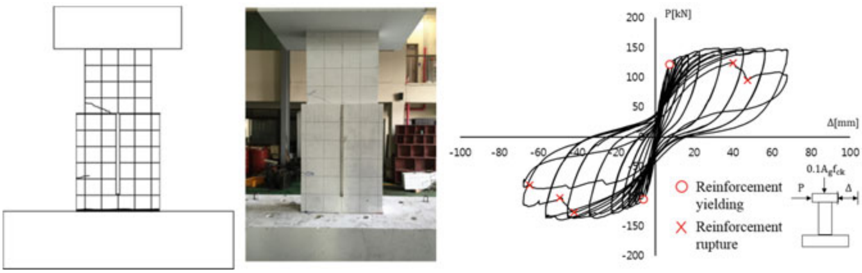

(a) Crack patterns (b) Load-deflection curves

Fig. 17.11 Crack patterns and cyclic behavior of FWR-S

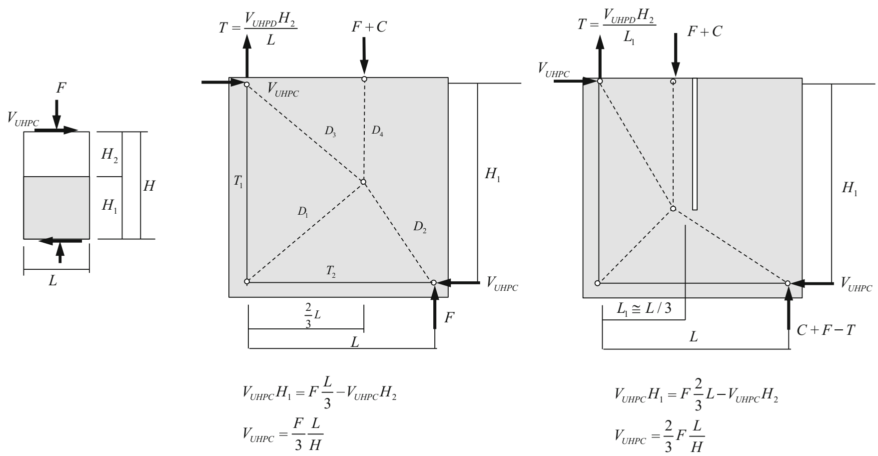

Fig. 17.12 Strut-and-tie models for FWR and FWR-S

Table 17.2 Experimental results of wall FW

Failure mode	Dir	P_{cr}[kN]	P_y[kN]	P_u[kN]	P_{fail}[kN]	K_e [kN/mm]
Flexural (Concrete crushing)	Pos (+)	81.66	95.31	112.86	81.37	10.71
		Δ_{cr}[mm]	Δ_y[mm]	Δ_u[mm]	Δ_{fail} [mm]	
		6.75	10.11	33.75	78.75	
	Dir	P_{cr} [kN]	P_y [kN]	P_u [kN]	P_{fail}[kN]	K_e [kN/mm]
	Neg (-)	69.00	81.93	114.74	86.50	10.48
		Δ_{cr} [mm]	Δ_y [mm]	Δ_u [mm]	Δ_{fail} [mm]	
		4.50	6.76	45.00	67.50	

Table 17.3 Experimental results of wall FWR

Failure mode	Dir.	P_{cr}[kN]	P_y[kN]	P_u[kN]	P_{fail}[kN]	K_e [kN/mm]
Flexural (Reinforcement rupture)	Pos. (+)	N/A	124.46	155.59	150.76	20.66
		Δ_{cr}[mm]	Δ_y[mm]	Δ_u[mm]	Δ_{fail} [mm]	
		N/A	6.75	56.25	67.50	
	Dir.	P_{cr} [kN]	P_y [kN]	P_u [kN]	P_{fail}[kN]	K_e [kN/mm]
	Neg. (-)	N/A	114.38	150.58	150.58	20.91
		Δ_{cr} [mm]	Δ_y [mm]	Δ_u [mm]	Δ_{fail}. [mm]	
		N/A	6.75	56.25	67.50	

Table 17.4 Experimental results of wall FWR-S

Ilure mode	Dir.	P_{cr}[kN]	P_y[kN]	P_u[kN]	P_{fail}[kN]	K_e [kN/mm]
Flexural (Reinforcement rupture)	Pos. (+)	N/A	118.21	149.45	146.33	18.61
		Δ_{cr}[mm]	Δ_y[mm]	Δ_u[mm]	Δ_{fail} [mm]	
		N/A	6.75	45.00	67.50	
	Dir.	P_{cr} [kN]	P_y [kN]	P_u [kN]	P_{fail}[kN]	K_e [kN/mm]
	Negative (-)	N/A	112.81	139.47	115.62	17.52
		Δ_{cr}[mm]	Δ_y[mm]	Δ_u [mm]	Δ_{fail} [mm]	
		N/A	10.13	45.00	67.50	

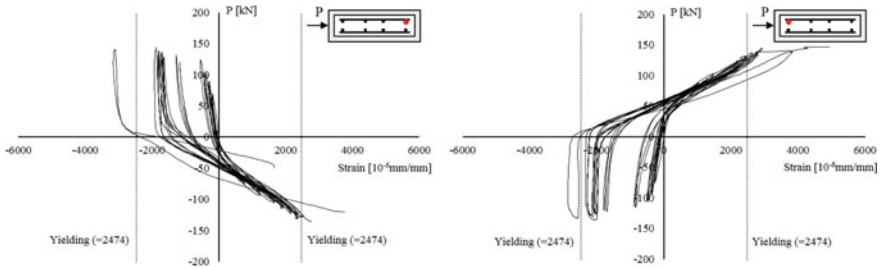

Fig. 17.13 Strain curves in edge longitudinal reinforcement of FWR

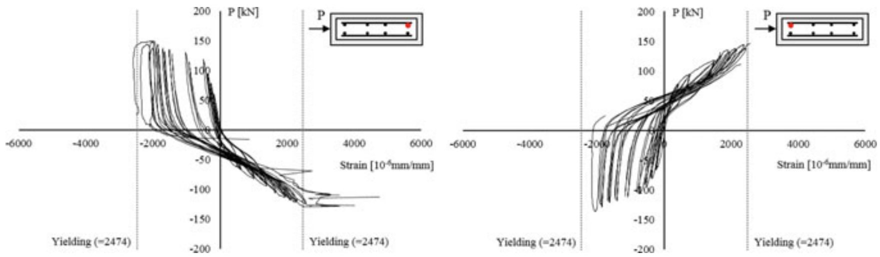

Fig. 17.14 Strain curves in edge longitudinal reinforcement of FWR-S

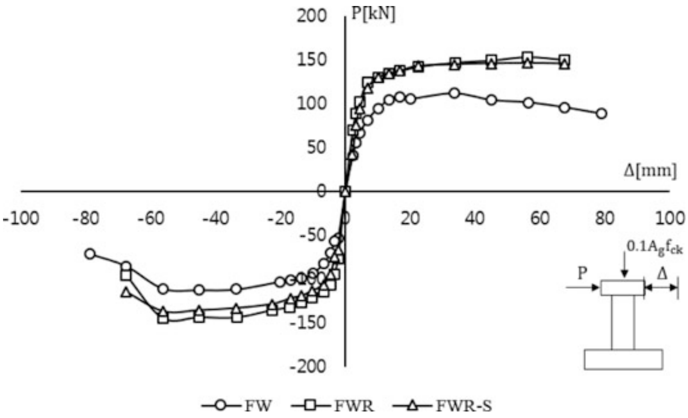

Fig. 17.15 Backbone curve comparison for wall specimens

17.5 Column Strengthening

Columns in reinforced concrete frames exhibit double curvature deformation when lateral loads are applied. This experimental program focused on the shear strengthening performance of textile-reinforced ultrahigh-performance (TR-UHPC) concrete sectional enlargement, so-called jacketing. For this purpose, the loading setup for column specimens was designed in double curvature under lateral load and governed by shear, rather than by flexural capacity. The test specimens include UHPC and/or textile reinforcement with varying the magnitude of axial force. The average compressive strength and direct tensile strength of UHPC were 145 MPa and 7 MPa, respectively. Seven reinforced concrete column specimens of cross section of 300 mm × 300 mm and the height of 1260 mm in 1/2 scale were prepared. The longitudinal reinforcement includes 8-D-19 bars with the reinforcement ratio of 2.5%. The large reinforcement ratio intended to develop shear failure modes both in before retrofit and after section enlargement. The transverse reinforcement uses D-10 with 300 mm spacing. The loading decks at both upper and lower stubs are 1200 mm × 500 mm.

The retrofit scheme according to the capacity design is made to lead to the flexural failure modes after the retrofit of columns. The change of flexural strength of columns after UHPC jacketing also should be controlled for flexural failure. Then, the following equation should be checked for the required additional shear strength of columns:

$$\frac{2(M_{n0} + M_{\text{add}})}{h} - V_{n0} \leq V_{\text{add}} \tag{5}$$

To depict the structural behavior of RC column under seismic load, both axial and lateral loads were applied simultaneously. The seven test programs in

Table 17.5 Specimens for columns strengthening

	R-30	U-30, U-45	UCT-30, UCT-45	UGT-30, UGT-45
	Reference	30 mm UPHC jacket (10% thickness)	30 mm UHPC jacket + Carbon textile reinforcement	30 mm UHPC jacket + AR glass textile reinforcement
Sec.	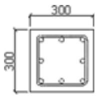	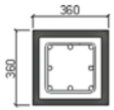	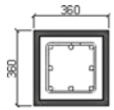	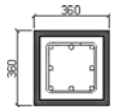
Elev.	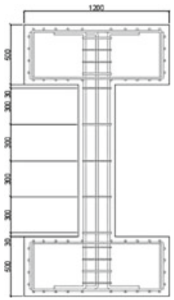	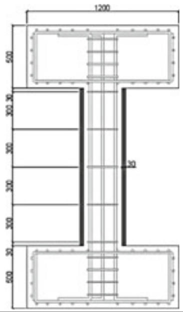	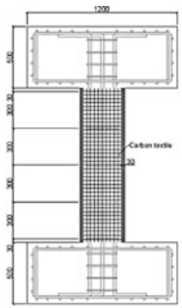	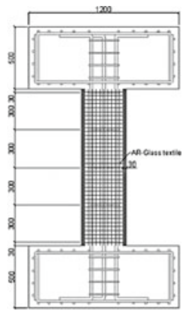

Table 17.5 were conducted in the same setup as presented. Initially, the axial load was applied to column by two 100-ton oil jacks and then, being kept during the lateral loading. In the next stage, a 200-ton actuator was used to simulate the lateral load. Loading was carried out according to ACI 314.2R-13, on which generates the displacement to control the horizontal cyclic load corresponding to lateral loading protocol was based.

For the reference column as an original column, the initial cracks occurred in the bottom and top of the column, which were identified as flexural cracks at 0.5% drift ratio. These cracks spread out in flexural–shear crack patterns until 0.92% drift ratio. However, when the drift ratio reached 1.0%, large diagonal cracks occurred, which were dominant until the next stage. Afterward, the strength had dropped abruptly as shown in Fig. 17.16a. Therefore, it can be seen that the failure mode was identified as shear failure.

The crack patterns of the U-30 specimen reinforced with jacket thickness of 30 mm was different from those of the original column owing to the crack control capability of the steel fiber. Cracks in the column surface were not observed until 0.5% drift ratio, except for horizontal flexural cracks along the top and bottom of the web. It was observed that the magnitude of strength was kept after the occurrence of the cracks. Afterward, the vertical crack occurred at the bottom of web due to the delamination between original column and concrete jacket. A large diagonal crack occurred starting from the top of web at 1.6% drift ratio. As the several micro-cracks were developed around the pullout length of the steel fiber, the contribution of UHPC jacket decreased drastically. It was found that longitudinal reinforcement did not yield and the shear failure was observed due to a diagonal crack in the upper part of column. The maximum strength reached is 419 kN at the maximum displacement 2.63% drift ratio. Figure 17.16b shows the load–displacement curve and extended image of diagonal crack of U-30.

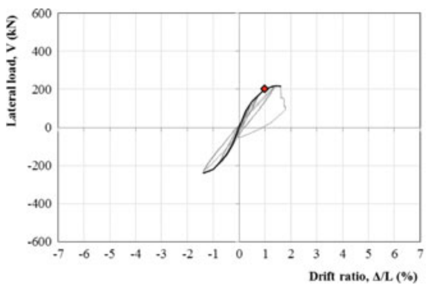

(a) R-30

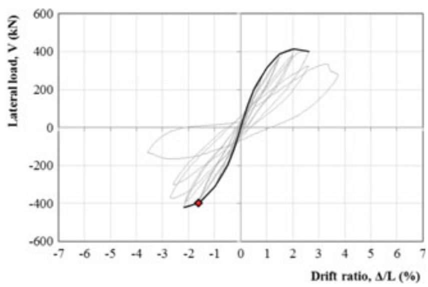

(b) U-30

Fig. 17.16 Load–displacement curves (R-30) and (U-30)

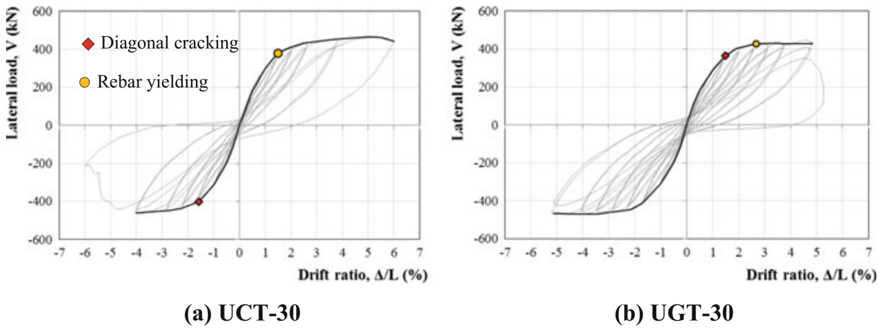

Fig. 17.17 Load–displacement curves for (UCT-30) and (UGT-30)

The specimen UCT-30 jacketed with the thickness of 30 mm and carbon textile reinforcement developed the vertical cracks in the UHPC jacket which were similar to those in ordinary concrete cylinders in compression. The initial cracks occurred in the flexural cracking patterns at 0.5% drift ratio. Then, the vertical cracks started to be developed at 1.5% drift. According to the load–displacement curve shown in Fig. 17.17a, the specimens jacketed with carbon textile reinforcement and UHPC showed superior strength and ductility than the original column. The maximum strength and maximum drift ratio was 466.4 kN at 6% drift ratio. The textile reinforcement fractured at 6% drift ratio in the negative loading direction, and thereafter the capacity dropped by 90% of the maximum load.

The specimen UGT-30 with AR glass in UHPC jacket showed cracking patterns similar to UCT-30. Initial cracks were observed at 1% drift ratio in the flexural crack pattern in the top and bottom of the column. Diagonal cracks developed at the top of the column at 1.5% drift ratio. However, the existence of textile reinforcement suppressed major diagonal crack due to high strength and elasticity of textile reinforcement layer. The maximum load at 460.5 kN was recorded at 5.1% drift ratio in the negative direction and the maximum displacement of 64.26 mm. Meanwhile, the longitudinal bar already yielded at 2.5% drift ratio. Overall crack patterns and the failure of component implied the flexural failure.

Compared with the reference specimen (R-30), the maximum loads of U-30, UCT-30, and UGT-30 were increased by 75.3%, 95.1%, and 92.6%, respectively. The maximum displacement increased by 105%, 233%, and 194%, respectively. The curve of load–drift ratio for the specimens with different retrofitting methods is shown in Fig. 17.17. Furthermore, the initial stiffness of the specimen retrofitted with UHPC was found to be approximately equal to the estimated values.

The specimens jacketed with textile-reinforced UHPC showed a significant increase in ductility compared to the column retrofitted with UHPC only. However, the type of textile reinforcement was less likely to influence the magnitude of ductility. For the positive direction, the ductility performance was the best for the specimens with carbon textile, otherwise, i.e., the negative direction, the specimens with AR glass textile was the best. From the experimental observation, the textile

Table 17.6 Test and theoretical results

Specimens	Failure mode	Test results V_{max} (kN)	Predictions (kN)		Ratio	
			Arch action Shear strength V_{nv} (kN)	Lateral load by Flexural strength V_{nf} (kN)	V_{max}/V_{nv}	V_{max}/V_{nf}
R-30	Shear failure	239	231	330	1.03	0.7
U-30	Shear failure	419	430	409.2	0.97	1.02
UCT-30	Flexural failure	466	520.7	409.2	0.89	1.14
UGT-30	Flexural failure	461	484.7	409.2	0.95	1.13
U-45	Shear failure	490	458	449.2	1.06	1.09
UCT-45	Flexural failure	538	512	449.2	1.05	1.2
UGT-45	Flexural failure	512	548	449.2	0.93	1.14

reinforcement mitigated the opening of large shear cracks after the yielding of steel reinforcement in the substrate columns. UCT-30 and UGT-30 specimens showed a rapid decrease in strength after the failure of textile. Table 17.6 summarizes the strength and stiffness of four specimens. As a result, no significant difference in strengths between the specimens with carbon and with AR glass textile was found.

Along the same experimental program for columns, the higher axial load effects ($P = 0.45A_g f'_c$) were investigated. The specimens included UHPC (U-45) jacketing only, carbon textile reinforcement (UCT-45) in UHPC jacket, and AR glass textile (UGT-45) under either reference axial force ($P = 0.3A_g f_{ck}$) or high axial force. Figure 17.18a shows the load–drift curves for three columns. The curves show the best performance of strength and ductility for the specimens with carbon textile reinforcement. However, the initial stiffness and strength were not changed. The load–drift curve of the column under higher axial force as shown in Fig. 17.18b showed an increase in strength and ductility due to the confinement effect. The use of textile reinforcement suppressed the brittle failure of columns under higher axial force. As further cycle of loading proceeded, the stiffness of CTR-UHPC was the best followed by GTR-UHPC and UHPC (Fig. 17.18).

17.5.1 Strength Model

The shear strength V_{n0} of the original concrete column can be calculated in accordance with ACI 318-11 and some theoretical approach Pujol et al. (2016). The required shear strength by retrofit should be satisfied with Eq. (5) for the flexural failure modes. The jacketing shear strength of columns by UHPC with discontinuity of the longitudinal reinforcement at the top and bottom of the jacket needs to consider compression only at the top and bottom of jacket.

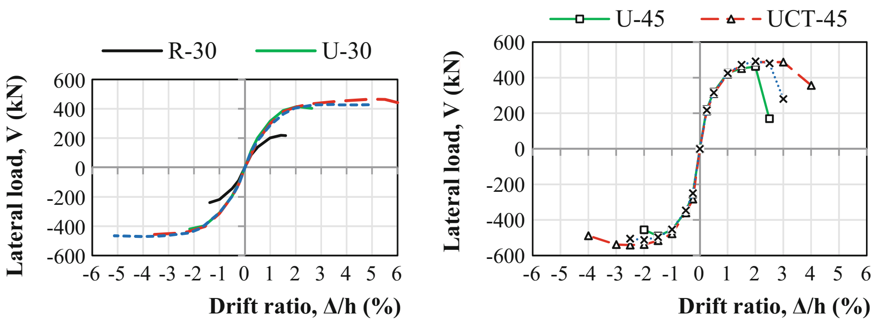

(a) 30% axial force (b) 45% axial force

Fig. 17.18 Effect of axial forces on backbone curves

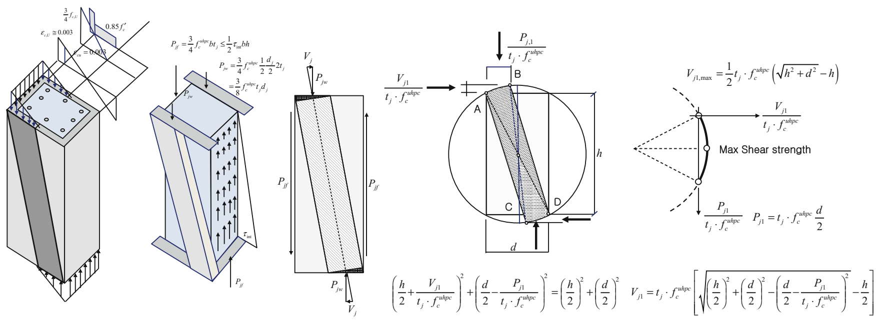

Fig. 17.19 Strength model for shear by arch action and interface shear

$$V_{\text{total}} = V_{n0} + V_{\text{add}} = V_{n0} + V_{j,\text{arch}} + V_{j,\text{truse}} \tag{6}$$

where the shear strength due to the truss action is assumed by 45° truss and tensile strength of UHPC with/without textile reinforcement.

$$V_{j,\text{truss}} = v_t f_t^{uhpc} t_j h \tag{7}$$

where the effective tensile strength of UHPC with textile reinforcement in this study used 12 MPa for glass fiber and 10 MPa for carbon fiber from the test.

The increase in shear strength by UHPC jacket is generated by the axial forces from the equilibrium condition. The axial forces in the UHPC jacket are developed by the lateral displacement and the part of the initial axial loads. The shear strength by arch action is controlled by the diagonal strut strength and by tensile strength of UHPC and textile reinforcement across the failure diagonal crack. However, the contribution of textile reinforcement to the tensile strength was not significant from the tensile strength test for UHPC with textile reinforcement at the material levels as shown in Fig. 17.1. The role of textile reinforcement in UHPC jacket is to increase ductility after the peak load according to the experimental observation. The minimum value for shear strength controls the shear strength of the retrofitted column. In the following, each contribution to the shear strength by jacketing is derived from the free body diagrams (Fig. 17.19).

$$\min.\begin{cases} V_j = \frac{1}{h}\left(P_{jf}d_w + P_{jw}\frac{2}{3}d_w\right) \\ V_j = V_{j,\mathrm{arch}} + V_{j,t} = V_{j,\mathrm{arch}} + f_t^{uhpc}t_w d_w \end{cases} \tag{8}$$

The axial forces in flange and web of UHPC jacket are expressed, respectively.

$$\begin{cases} P_{jf} = \min\left(\frac{3}{4}f_c^{uhpc}b_f t_{fj}, \frac{1}{2}\tau_{\mathrm{int}}bh\right) \\ P_{jw} = \frac{3}{8}f_c^{uhpc}d_w t_{wj} \end{cases} \tag{9}$$

The axial resistance developed in the flange of the jacket in compression is controlled by the interface shear strength between the jacket and the substrate column. It is assumed that the interface shear strength is linearly developed along both interfaces in the flanges of jacket.

The shear strength due to arch action is expressed as

$$V_{j,\mathrm{arch}} = vf_c^{uhpc}t_j\left[\sqrt{\left(\frac{h}{2}\right)^2 + \left(\frac{d_w}{2}\right)^2 - \left(\frac{d_w}{2} - \frac{P_{jw}}{t_j v f_c^{uhpc}}\right)^2} - \frac{h}{2}\right] \tag{10}$$

The flexural strength of column without confinement effect can be calculated by the ultimate strain 0.003 in the extreme fiber of the original concrete columns. Meanwhile, the tensile strength of UHPC jacket is not considered because of the discontinuity of the longitudinal reinforcement at the top and bottom of the jacket. Similarly, due to the absence of anchorage at the end of textile reinforcement, the textile reinforcement does not contribute to the flexural strength.

The failure modes of R-30 and U-30 are expected as shear failure. In the specimen U-45, the shear failure was initially observed in the experiment and in the next loading stage the column was developed in the flexural–shear failure with the yielding of the longitudinal bar. This led to 20% error between the calculated and the experimental result. UCT-30, UGT-30, UCT-45, and UGT-45 columns were controlled by the flexural failure with the yielding of the rebar.

17.6 Conclusion

This study demonstrated the efficiency of UHPC seismic jacketing for concrete walls and columns. The experimental programs for UHPC jacketing method for walls included the upgrading shear strength and flexural strength with discontinuity of longitudinal reinforcement at floor level. In addition, the UHPC jacketing method for non-seismic detailed columns textile reinforcement was investigated for possible application of textile reinforcement. The discontinuity of longitudinal reinforcement at top and bottom levels would be traded-off by the ease of construction. Based on the experimental programs and analytical works on the results, the following conclusions are made:

The seismic upgrading by UHPC jacketing was one of viable options to reduce the jacketing sectional area due to high strength of material. The shear strength of squat wall was increased by compressive and tensile strength of UHPC, while the ultimate deformation was limited by the substrate concrete wall. The plastic hinge strengthening by UHPC jacketing was effective in flexural compression but led to the rupture of longitudinal reinforcement. The vertical slit of UHPC jacketing to lower the tensile force in the edge longitudinal reinforcement was ineffective. The UHPC jacketing increased the confinement effect reducing concrete crushing failure.

Columns jacketing of UHPC with discontinuity of the vertical reinforcement at the bottom and top interfaces of columns increased the strength, stiffness, and ductility. UHPC with textile reinforcement showed the ductility increase with no significant increase in strength. The low strength contribution of textile reinforcement may be understood by the direct tensile behavior of UHPC with textile reinforcement. The axial forces in columns increased the shear strength as the strength equation based on arch actions expected. However, the columns under higher axial loads showed the limited ductility after the peak loads.

References

ACI 440.2R-02. (2002). Guide for the Design and Construction of Externally Bonded FRP Systems for Strengthening Concrete Structures, Reported by ACI Committee 440, American Concrete Institute, Farmington Hills, Michigan.

ACI 546R-14. (2014). Guide to Concrete repair, Reported by ACI Committee 546, American Concrete Institute, Farmington Hills, Michigan.

ACI 549R-97. (1997). State-of-the-Art Report on Ferro cement, Thin Fiber and Textile Reinforced Cementitious Systems, Reported by ACI Committee 549, American Concrete Institute, Farmington Hills, Michigan.

Altun, F. (2004). An experimental study of the jacketed reinforced-concrete beams under bending. *Construction and Building Materials, 18*(8), 611–618.

ASTM C882. (1999). Standard Test Method for Bond Strength of Epoxy-Resin Systems used with Concrete by Slant Shear, ASTM, West Conshohocken.

Bastein-Masse, M. (2015). *Structural behavior of R-UHPFRC-RC composite slabs*, EPFL Ph.D. thesis 6841, p. 145.
Bousias, S., Biskins, D., Fardis, M. N., & Spathis, A.-L. (2007). Strength, stiffness, and cyclic deformation capacity of concrete jacketed members. *ACI Structural Journal, 104*(5), 521–531. Farmington Hills.
Campion, G., Fossetti, M., Giacchino, C., & Minafò, G. (2014). RC columns externally strengthened with RC jackets. *Materials and Structures, 47,* 1715–1728.
Cheong, H. K., & MacAlevey, N. (2000). Experimental behavior of jacketed reinforced concrete beams. *Journal of Structural Engineering, 126*(6), 692–699. ASCE.
Chalioris, C. E., Thermou, G. E., & Pantazopoulou, S. J. (2014). Behavior of rehabilitated RC beams with self-compacting concrete jacketing-analytical model and test results. *Construction and Building Materials, 55,* 257–273.
Choi, J. T., Lim, W. Y., & Hong, S. G. (2016). Strengthening T-shaped RC beams with UHPC. In *4th International Symposium on Ultra-High Performance Concrete and High Performance Construction Materials (HiPerMat 2016), Kassel, Germany.*
Dogabgun, A. (2004). Performance of reinforced concrete buildings during the May 1, 2003 bingol earthquake in Turkey. *Engineering Structures, 26,* 841–856.
Fehling, E., Schmidt, M., Walraven, J., Leutbecher, T., & Fröhlich, S. (2014) *Ultra-high performance concrete UHPC* (p. 188). Wiley.
FEMA 547. (2006). *Techniques for the Seismic Rehabilitation of Existing Buildings.*
Fukuyama, H., & Sugano, S. (2000). Japanese seismic rehabilitation of concrete buildings after the hyogoken-nanbu earthquake. *Cement & Concrete Composite, 22,* 59–79.
Fukuyama, K., Higashibata, Y., & Miyauchi, Y. (2000). Studies on repair and strengthening methods of damaged reinforced concrete columns. *Cement & Concrete Composite, 22,* 81–88.
Habel, K. (2004). *Structural behavior of elements combining ultra-high performance fiber reinforced concrete*, EPFL Ph.D. thesis 3036, p. 195.
Hong, S.-G., & Kang, S.-H. (2013). Formwork development using UHPFRC, UHPFRC 2013. In *RILEM-Fib-AFGC International Symposium, Marseille, France* (pp. 197–206).
Kam, W. Y., Pampanin, S., & Elwood, Ken. (2011). Seismic performance of reinforced concrete buildings in the 22 February Christchurch (Lyttelton) earthquake. *Bulletin of the New Zealand Society for Earthquake Engineering, 44*(4), 239–278.
Lee, J-H, Hong, S-G., Joh, C., Kwahk, I., & Lee, J-W. (2017). Biaxial tension-compression strength behavior of UHPFRC in-plane elements. *Materials and Structures*, *50*(1), 20.
Maeda, M., Al-Washali, H. A., Takahashi, K., & Suzuki, K. (2012). Damage to reinforced concrete school buildings in Miyagi after the 2011 great East Japan earthquake. In *Proceedings of the International Symposium on Engineering Lessons Learned from the 2011 Great East Japan Earthquake, Tokyo, Japan* (pp. 1120–1131).
Meda, A., Mostosi, S., & Riva, P. (2014). Shear strengthening of reinforced concrete beam with high-performance fiber-reinforced cementitious composite jacketing. *ACI Structural Journal, 111*(5), 1059–1067.
Moehle, J. (2014). *Seismic design of reinforced concrete building* (p. 784). McGraw-Hill.
Sugano, S. (1996). State-of the art in techniques for rehabilitation of building, paper No. 2175. In *11th WCEE.*
Noshiravani, T. (2012). *Structural response of R-UHPFRC–RC composite members subjected to combined bending and shear,* EPFL Ph.D. thesis 5246.
Oesterlee, C. (2010) *Structural response of reinforced UHPFRC and RC composite members*, EPFL Ph.D. thesis 4848.
Paulay, T., & Priestley, M. J. N. (1992). *Seismic design of reinforced concrete and masonry buildings*. New York: Wiley.
Priestley, M. J. N. (1997). Displacement-based seismic assessment of reinforced concrete buildings, *Journal of Earthquake Engineering*, *1*(1), 157–192 (Imperial College Press).
Pujol, S., Hanai, N., Ichinose, T., & Sozen, M. A. (2016). Using Mohr-Coulomb criterion to estimate shear strength of reinforced concrete columns. *ACI Structural Journal, 113*(3), 459–468. Farmington Hills.

Tayeh, B. A., Abu Bakar, B. H., & Megat Johari, M. A. (2013). Characterization of the interfacial bond between old concrete substrate and ultra high performance fiber concrete repair composite. *Materials and Structures, 46,* 743–753.

Thermou, G. E., & Elnashai, A. S. (2005). Seismic retrofit scheme for RC structures and local-global consequence. *Earthquake Engineering and Structural Dynamics, 8*(1), 1–15. John Wiley.

Triantafillou, T. C., & Papanicolaou, C. G. (2006). Shear strengthening of reinforced concrete members with textile reinforced mortar (TRM) jackets. *Materials and Structures, 39*(1), 93–103.

Chapter 18
Effect of Strain Penetration on RC Beam–Column Joints Subjected to Seismic Loading

Jung-Yoon Lee and Jongwook Park

Beam–column joints in reinforced concrete structures under seismic loading are crucial elements and should be designed to avoid a brittle failure such as shear failure or bond failure in the joints. Although beam–column joints are designed to exhibit elastic behavior in most design codes, they may show inelastic behavior due to the strain penetration in the plastic hinge region of the beam adjacent to the joint. When the strain of beam penetrates into the joint panel, the deformation of the joint increases and the effective compressive strength of the concrete in the joint panel decreases. As a result, the beam–column joint can fail earlier than the designer expects due to the strength reduction of the joint. In this study, the structural behavior of five reinforced concrete joints under cyclic loading was evaluated. Test results showed that the slippage of the steel reinforcements, concrete strength deterioration, and strain penetration of beam–column assemblages affected the structural response of the RC joints subjected to seismic inelastic loading.

18.1 Introduction

In earthquake regions, reinforced concrete (RC) frame structures are designed to withstand moderate seismic loading within elastic range and absorb the energy of severe seismic loading in plastic range. Performance-based design philosophy ensures that RC structures can maintain their initial strengths and stiffness and show

J.-Y. Lee (✉)
School of Civil, Architectural Engineering and Landscape Architecture, Sungkyunkwan University, Seoul, Republic of Korea
e-mail: jungyoon@skku.edu

J. Park
Lotte Engineering and Construction Lnc, Seoul, Republic of Korea
e-mail: jwp35k@gmail.com

T. T. C. Hsu (ed.), *Concrete Structures in Earthquake*,
https://doi.org/10.1007/978-981-13-3278-4_18

high energy dissipation capacities during high seismic excitations. Under seismic excitation, some structural members such as beams undergo large inelastic deformation, while columns including beam–column joints are in elastic condition.

Beam–column joints are considered critical in the stability of moment resisting RC frames subjected to severe seismic loading. As a consequence of the seismic action on the joints and the fact that high bending moments of opposite signs act on the beams and columns framing the joint, the joint region is subjected to both high magnitude horizontal and vertical shear forces. A fundamental requirement in the design of RC beam–column joints is that for the members of the structure to be able to develop their full strength, premature failure of their joints should be prohibited because joints are the connecting elements of the load carrying columns. Therefore, in the design of the RC beam–column joints under seismic load, it is desirable to limit the joint strength degradation until the connecting beams and columns have reached their full designed capacities.

Since the 1970s, a great deal of research work has been conducted to understand the response of RC joints. In particular, joint research efforts from researchers in three countries (America, Japan, and New Zealand) have made remarkable improvements in RC joint design (ACI SP-123 1991). In spite of the cooperative research efforts, the three countries proposed different approaches on assessing the effect of shear on the response of RC joints. The ACI-ASCE recommendations (2002) and Architectural Institute of Japan (AIJ) guidelines (1999) for the shear strength of RC joints are based on the concrete arch mechanism, while in the New Zealand Standard (NZS) code (1982), joint shear strength is evaluated by both the arch and the truss mechanisms. Furthermore, although the researchers from the three countries showed that the concrete compressive strength and the joint area are the two most important factors to evaluate the joint shear strength, they have different opinions on the effect of reinforcement ratio on joint structural response.

In the ACI recommendations (ACI 352-R02), the joint response is categorized into two types: Type 1 for structures in a non-seismically hazardous region, and Type 2 in a seismically hazardous region (ACI-ASCE Committee 352R-02 2002). Research on the joint shear strength in Type 1 regions (i.e., low seismic region) reached a level which made it possible to develop reliable design methods. However, detailed investigations on the deformation capacities of RC joints in Type 2 regions have been relatively limited and, to a certain degree, controversial. Fujii and Morita (1991) and Park et al. (1998) proposed equations that include the effect of axial forces on joint shear strength in accordance with NZS code for high strength concrete to determine the shear strength and ductility capacity of Type 2 joints. However, the proposed equations did not consider other factors affecting the joint ductile capacity, such as the effect of beam plastic hinges on the joint response and the deterioration of the joint potential shear capacity due to seismic load reversal. Durrani and Wight (1985), Attaalla (2003), and Hwang and Lee (1999, 2000) proposed analytical models for Type 1 and Type 2 joints. However, the main goal of these analytical models was to predict the shear strength of the joints and not the deformability of the joints. Lee et al. (2009, 2010) tried to determine the joint shear strength by taking into account the effect of the flexural deformation of adjacent beams. However, their research did not consider the joint deformation.

In this study, a method is proposed to estimate the deformation of RC beam–column joints that fail in shear after flexural plastic hinges develop at both ends of the beams framing the joint. In order to support the proposed methodology, an experimental study consisting of five joint specimens with varying tensile reinforcement ratios was carried out.

18.2 Research Significance

In order to develop an improved method for predicting the nonlinear response of multistorey RC frames subjected to seismic loading, the displacement contribution to the storey drift of the individual structural components such as beams, columns, and joints should be considered (Filip et al. 1988). The ACI-ASCE Committee 352 (1985) recommends that when assessing the inelastic dynamic response of an RC frame, the displacement of the beam–column joints, including the slip of the reinforcing bars in interior joints, should be considered in the assessment. Figure 18.1 shows the comparison between the observed and calculated base shear versus displacement relationships of RC frames. The displacements were calculated in two ways. The first is the calculation considering the joint deformation due to strain penetration, and the second is assuming that the joint is in elastic condition. As shown in Fig. 18.1, the calculation considers the joint deformation. The analytical result considering the joint deformation predicts the experimental results more accurately than the analysis assuming that the joint is in elastic state. Since RC beam–column joints are crucial elements in the survival of RC frame structures, a brittle failure such as that associated with shear failure or bond failure in the joints must be avoided. RC frame structures, designed according to present building codes, are expected to deform well into the inelastic range and dissipate high energy through stable hysteretic behavior when subjected to seismic loading. Various experimental studies of RC beam–column joints indicated that the slippage of the steel reinforcements, concrete strength deterioration, and strain penetration of beam–column assemblages affect the structural response of the RC joints subjected to seismic inelastic loading. Since the 1970s, a great deal of research has been conducted to predict the strength of RC beam–column joints. However, most of the previously conducted research focused on predicting the strength of the RC joint. Limited research has been carried out to evaluate the deformation capacity of an RC joint. This paper presents the results of an analytical and experimental study with the aim of predicting not only the strength but also the deformation of RC joints failing in shear, after plastic hinge develops at the end of the adjacent beams. The proposed method can be considered useful in understanding the structural response of RC joints and to develop an improved method for predicting the nonlinear response of multistorey RC frames subjected to seismic inelastic loading. In

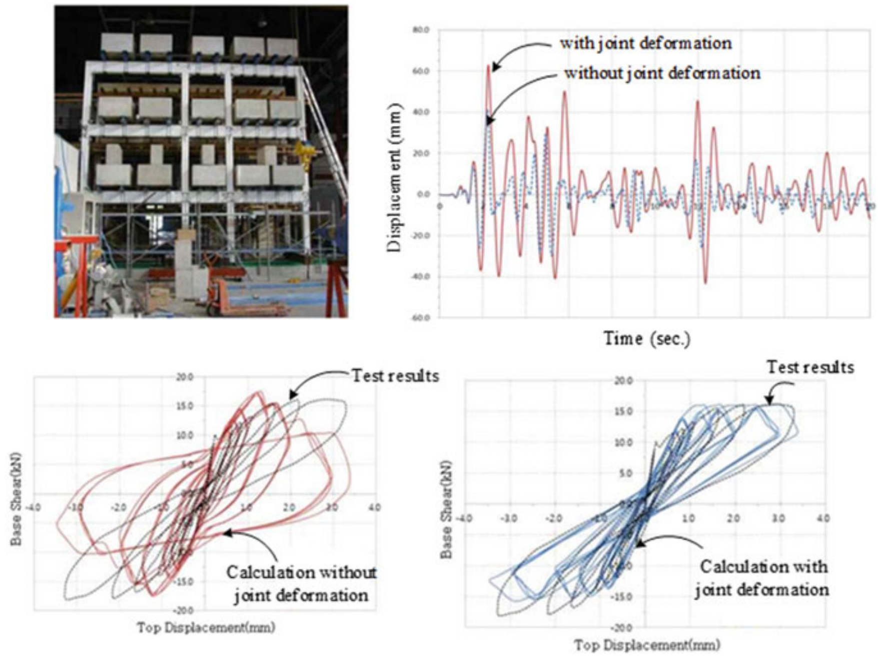

Fig. 18.1 Prediction of RC frame displacement

addition, the deformation of RC frames under seismic load can be more accurately predicted by reflecting the influence of the predicted joint deformation to the frame analysis.

18.3 Yield Penetration of Beam–Column Joints

ACI 352R-02 (2002) categorizes the design and behavior of RC joints into two types: Type 1 for joints of RC members that do not undergo significant inelastic deformation and Type 2 for joints of RC members that undergo significant inelastic deformation. ACI 352-R02 recommendations place a priority on predicting the shear strengths of RC members, while indirectly considering the deformation of the joint by providing some degree of conservatism in the calculation of the joint shear strength (i.e., stress multiplier for longitudinal reinforcement and shear strength factor).

The ACI 352-R02 design philosophy for ductile RC frame buildings allows the beams to form plastic hinges at the beam–column connections. In order to carry out this design philosophy, the ultimate strength of the beam–column joint should be greater than the flexural yielding capacities of the beams connecting to the joint. In addition, the strength of the joint should be large enough to allow the adjacent beams to reach their full ductile capacities. Three joint failure modes are noted in the design and analysis of RC joints: J-failure refers to joint failure before plastic hinges develop at the ends of adjacent beams, BJ-failure refers to joint failure after plastic hinges develop at both ends of adjacent beams, and B-failure refers to beam failure in the plastic hinge regions of the adjacent beams while the joint remains elastic. There are three typical load–displacement curves of joint failures. The current design standards allow only BJ- and B-failure, and not J-failure. When BJ-failure joint is designed, the strength of the joint should be greater than the flexural yielding force of the adjacent beams and the joint strength should not undergo any degradation before the adjacent beams reach their required ductile capacities.

Experimental studies on RC beam–column joints indicated that because of shear strength degradation in the joint due to the formation of plastic hinges at the adjacent beams, the BJ-failure joint may fail before reaching its design capacity. In the plastic hinge region, the longitudinal axial strain at the center of the section (ε_l) abruptly increases after flexural yielding because the neutral axis continues to move toward the extreme compressive fiber and the residual strains of the longitudinal bars continue to increase with additional inelastic loading cycle (Lee and Watanabe 2003a). As the ductility ratio (μ) increases, the joint longitudinal strain increases as much as fifteen times of the reinforcement yielding strain ($\varepsilon_y = 0.002$) due to the tensile strain of the continuous reinforcements from the beam through the joint, as shown in Fig. 18.2 (Lee et al. (2009). In addition, crack width within the diagonal compressive strut becomes wider resulting in a rapid increase in principal tensile strain (ε_{1cj}, normal to the diagonal crack) as depicted in Fig. 18.2. According to the experimental studies on reinforcement concrete specimens by Vecchio and Collins (1986), Belarbi and Hsu

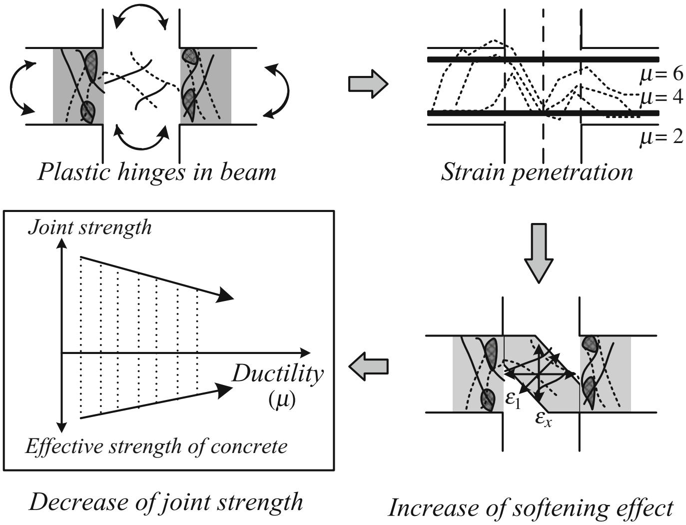

Fig. 18.2 Strength reduction of BJ-failure joints

(1995), Lee and Watanabe (2003b), the effective compressive strength of concrete ($\nu f_c'$, concrete compressive strength after crack develops) is inversely proportioned to ε_{1cj}. Figure 18.2 schematically shows the concrete shear contribution (V_c) and the effective compressive strength of concrete ($\nu f_c'$) as the deflection (Δ) increases. The figure indicates a sharp reduction in $\nu f_c'$ after flexural yielding due to the increase in Δ. Therefore, V_c in joint is correspondingly reduced due to the decrease in $\nu f_c'$. To sum up, in case of BJ-failure, the reduction in joint shear capacity caused by the effect of the ductility of adjacent beams. In this paper, joint ductility capacity (BJ-failure) was proposed considering the effect of plastic hinges in the adjacent beams.

The increase of the longitudinal strain with increasing ductility through an RC joint is referred to as the "strain penetration." Because of the so-called "strain penetration," the crack width within the concrete joint becomes wider, resulting in a rapid increase in principal tensile strain (ε_{1c}, normal to the diagonal crack) and a decrease in the effective concrete strength (refer to Fig. 18.2).

18.4 Deformation of Beam–Column Joints

In order to predict the deformation of a typical Type 2 RC beam–column joint, the deformation of the structural members connected to the joint should be considered (Mansour et al. (2005). As shown in Fig. 18.3, the total drift angle of a typical beam–column assembly consists of three components: the drift angle of the column (noted by R_c), the drift angle of the joint (R_j), and the drift angle of the beam (R_b). The total drift angle of the beam–column assembly can thus be expressed as (Teraoka 1997)

$$R_T = R_c + R_j + R_b \tag{1}$$

where R_c, R_j, and R_b are the column, joint, and beam drift angles, respectively. According to Kurose et al. (1991), the joint contribution increased and the beam and column contributions decreased with an increase in the total drift angle. Test conducted by Cheung et al. (1991) indicated that the components, R_c, R_j, and R_b, made up approximately 0%–5%, 20%–25%, and 70%–90% of R_T, respectively. Test conducted by Sugano et al. (1991) results differed, whereby R_c, R_j, and R_b were approximately 0%–20%, 5%–30%, and 65%–90% of R_T, respectively.

Ductile moment resisting space frames are designed so that yielding starts to develop at the girder ends. Columns of a ductile moment resisting space frame should remain elastic during the earthquake response, except at the base of the building, to avoid the formation of a partial side sway collapse mechanism. Thus, the column deformation (R_c) in Eq. (1) can be calculated from elastic analysis as shown in Fig. 18.4.

Even if it is frequently assumed that the panel within a beam–column joint remains rigid in the linear analysis of RC frames, many test results (Kamimura et al. (2000)

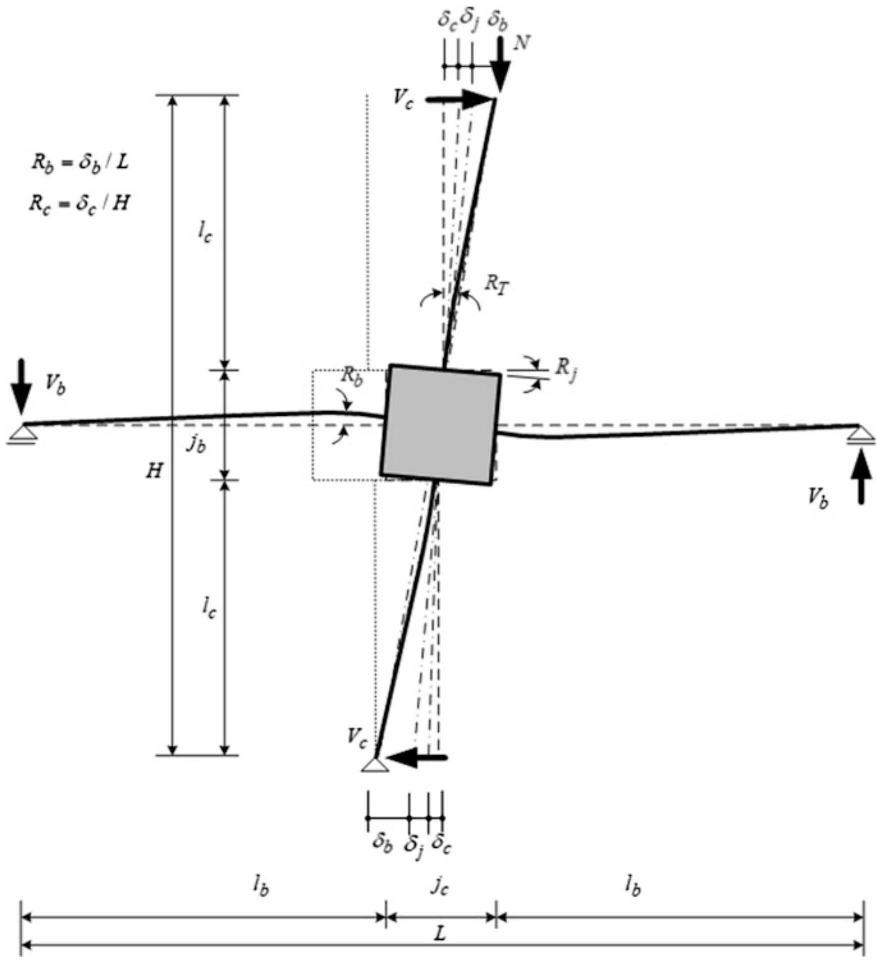

Fig. 18.3 Total drift angle of beam-column assembly

showed that this assumption is not valid in RC structures subjected to large cyclic deformation reversals. Although adequate transverse reinforcement was provided in the joint cores in order for the core to remain mainly in the elastic range, the joint cores were found to be far from rigid as shown in Fig. 18.4. The interior core of the joint bounded by the longitudinal bars in the beams and column is subjected to larger shear stresses. Therefore, the shear strain in the joint panel can be calculated by Eq. (2), and the joint panel deformation (R_j) as defined in Eq. (1) can be calculated by Eq. (3)

$$\gamma_j = \frac{V_j}{A_j G_j} \tag{2}$$

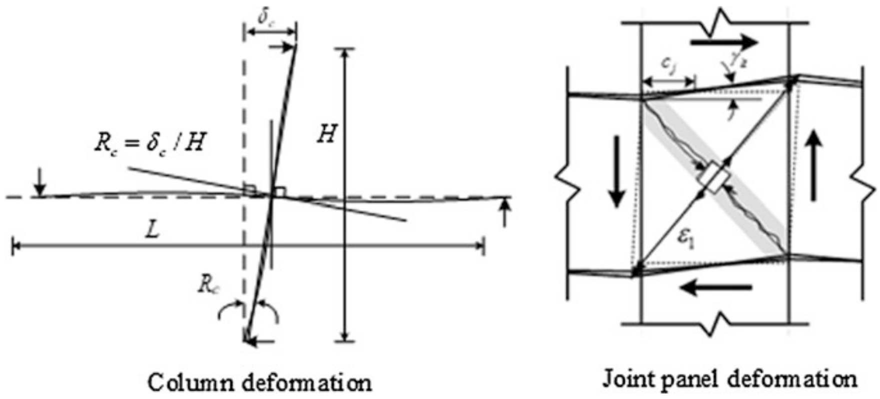

Fig. 18.4 Column and joint panel deformations

$$R_j = \gamma_j \left(1 - \frac{j_c}{L} - \frac{j_b}{H}\right) \tag{3}$$

where γ_j denotes the shear strain of the joint; V_j is the shear force of the joint; G_j refers to the shear modulus of concrete in the joint; A_j is the sectional area of the joint; j_c is the width of the joint; j_b refers to the depth of the joint; L is the length of the beam; and H is the storey height.

In order to calculate the shear strain (γ_j) of Eq. (2), the shear modulus of concrete in the joint (G_j) should be known. After the formation of cracks within the core of the joint, the stresses in the concrete are calculated using the smeared crack approach as given by Eq. (4):

$$\left[f^c_{xy}\right] = [R]\left[f^c_{21}\right][R]^T \tag{4}$$

where $\left[f^c_{xy}\right]$ is the stress tensor acting on the concrete element in the x–y coordinate system; $\left[f^c_{21}\right]$ is the principal stress tensor acting on the concrete in the 1–2 coordinate system; and $[R]$ is a rotation matrix.

Test results indicated that the contribution of the beam deformation was the highest in the total deformation of the Type 2 beam–column assembly. According to the test results, the total beam drift angle consists of four components: angles due to flexural moment, shear force, pullout of beam steel bars in joint panel, and strain shifting. The beam drift angle is thus given below:

$$R_b = R_{bf} + R_{bs} + R_{bp} + R_{bh} \tag{5}$$

where R_{bf}, R_{bs}, R_{bp}, and R_{bh} are the drift angles due to flexural moment, shear force, pullout of beam steel bars in joint panel, and strain shifting, respectively. Among these four components, R_{bs} and R_{bh} can be neglected because the values of both components are much smaller than those of R_{bf} and R_{bp}.

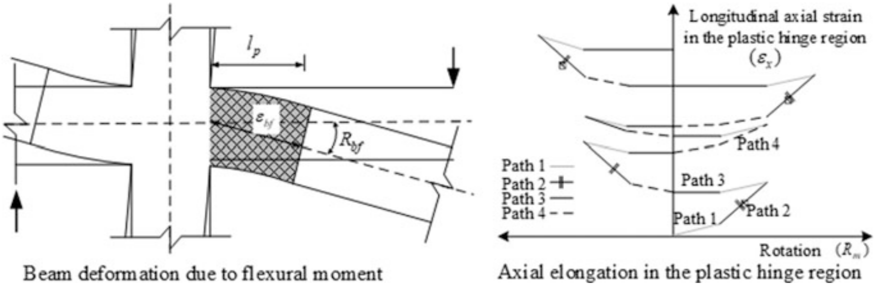

Fig. 18.5 Beam deformation and axial elongation in the plastic hinge region

The flexural drift angle (R_{bf}) depends on the longitudinal axial strain and curvature in the plastic hinge region of RC beams as shown in Fig. 18.5. Fenwick et al. (1996) indicated that when RC members undergo cyclic displacements corresponding to the structural displacement ductility of four to six, the elongation of each hinge is about 2–4% of the beam depth. It also showed that the longitudinal axial strain in the plastic hinge regions of RC beams increases rapidly after flexural yielding. Furthermore, the longitudinal axial strain of RC beams subjected to reverse cyclic loading is larger than the strain of RC beams subjected to monotonic loading due to the cumulative strains in the reinforcement. The longitudinal axial strain, ε_{bf}, at the center of the beam's cross section in the plastic hinge region, is the average value of the strains in the compressive steel bar, ε_{bc}, and the tensile steel bar, ε_{bt}.

$$\varepsilon_{bf} = \frac{\varepsilon_{bc} + \varepsilon_{bt}}{2} \tag{6}$$

The NZS design guidelines ignore the strain of the compressive steel bar, ε_{bc}, in Eq. (6) because the value of ε_{bc} is very small compared to the strain of the tensile steel bar,ε_{xt}. Therefore, the longitudinal axial strain for the beams subjected to reversed cyclic loading can be calculated as

$$\varepsilon_{bf} = \frac{(R_{bfp} + R_{bfn})z}{2l_h} \tag{7}$$

where R_{bfp} and R_{bfn} are the positive and negative rotations, respectively.

Lee and Watanabe (2003a) verified the accuracy of Eq. (7) from 21 RC beam tests subjected to reversed cyclic loading under various loading patterns. Their test results were used to confirm the validity of Eq. (7). Recently, Lee et al. (2018) also investigated the elongation behavior of RC columns by testing five groups of twenty specimens subjected to three different loading patterns. Experimental results showed that longitudinal axial strain of RC columns was quite different from that of RC beams because of the presence of axial force. The longitudinal axial strain of RC columns was reduced with increasing axial force. Axial strain was also function of loading pattern and lateral reinforcement ratio.

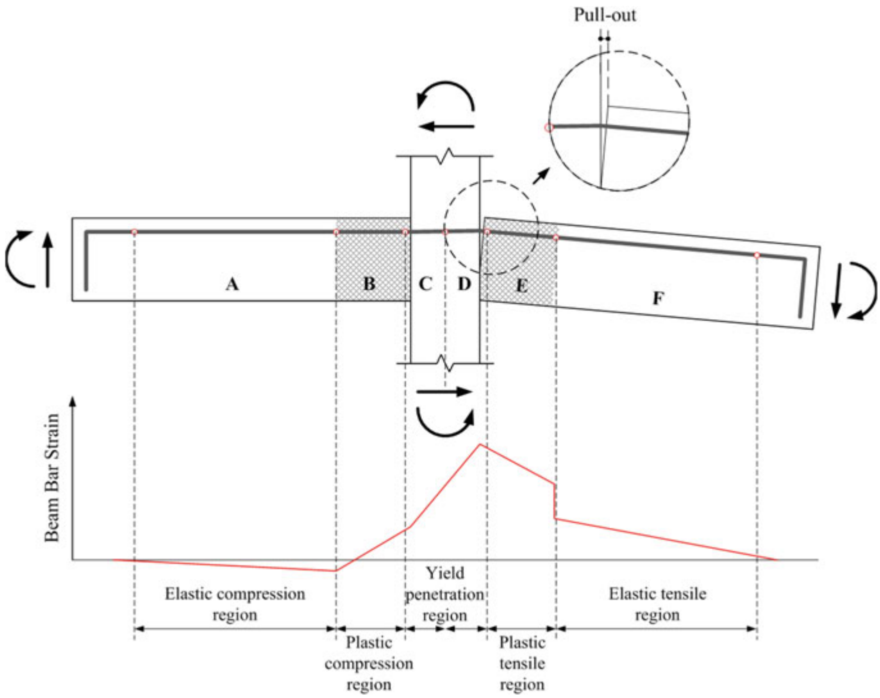

Fig. 18.6 Strain distribution of longitudinal bars

The recommendations of the ACI-ASCE Committee 352 state that when modeling a frame structure under inelastic dynamic analysis, the slip of the reinforcing bars in interior joints should be considered. Figure 18.6 shows the strain distribution of beam reinforcing bars along the member. Before the flexural yielding of the beam, the strain distribution changes almost linearly along the member, while after the flexural yielding, the steel strain in the plastic hinges of the beam abruptly increases because of the "strain accumulation" of the longitudinal steel bars. The analytical results indicated the deformation percentage of anchorage increased with the increase of storey drift. After plastic hinges develop at both ends of the beam, the pullout slip of the beam steel bars in the joint panel can be calculated as

$$S = \int_0^{j_c} (\varepsilon_s - \varepsilon_c)\, dx \tag{8}$$

where ε_s is the strain of steel bars and ε_c is the strain of concrete. Since large inelastic deformations are likely to occur in interior joints, the contribution of the concrete strains to the relative slip is negligible.

18.5 Test Program

Five reinforced concrete interior beam–column joints BJ1 to BJ3 (BJ-failure) and B1 (B-failure) were tested. The beam longitudinal bars were designed to cause the joint failure through the beam sway mechanism with flexural yielding at the beam ends based on the ACI recommendations. The dimensions and details of reinforcements of the specimens are shown in Fig. 18.7, and the other experimental parameters are listed in Table 18.1. The cross section of beam was 200 mm × 300 mm, while that of column was 250 mm^2.

The joint shear strength (V_j) was calculated by Eq. (9) (ACI 352R-02 2002) by multiplying effective joint sectional area. In the equation, the shear strength factor, γ, is 1.660 for Type 1 and 1.245 for Type 2. V_{j1} and V_{j2} in Table 18.1 indicate Type 1 and Type 2 shear strength of joint, respectively. The joint shear strength when beam bar yields (V_{jby}) can be calculated as follows:

$$V_{jby} = \left(\frac{l_c}{z} - 1\right) V_{by} \frac{l_b}{l_c} - \frac{h_c}{z} V_{by}, \tag{9}$$

where l_c is the column height, h_c is the joint height, z is the distance between centroid of upper and lower beam bars, and V_{by} is the beam shear strength when beam bar yields. The beam longitudinal bars of BJ1 to BJ3 and B1 specimens were designed by satisfying $V_{j1}/V_{jby} > 1$ and $V_{j2}/V_{jby} > 1$ to promote BJ-failure and B-failure, respectively.

The specimens were supported in vertical position, and quasi-static cyclic lateral load was applied at the top of the column using a servo-controlled hydraulic

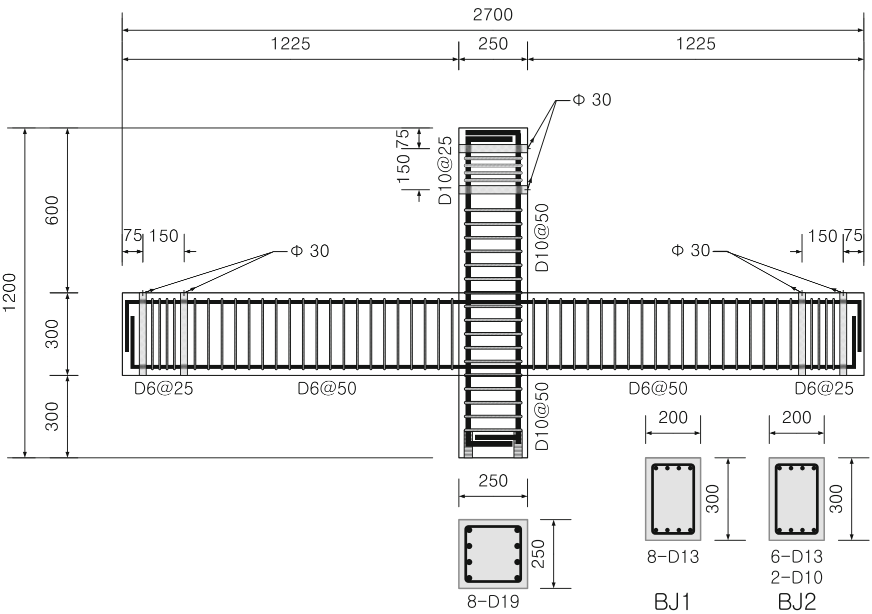

Fig. 18.7 Geometry and reinforcing details of specimens

Table 18.1 Experimental verifications

Specimens	Beam							Column							f_c' (MPa)
	Reinforcing Bar (Upper and Lower each)			Stirrup				Reinforcing Bar			Hoop				
	f_{by} (MPa)	ρ_{bu}, ρ_{bl}	n_b	f_{sy} (MPa)	ρ_s	s_b (mm)	n_s	f_{cy} (MPa)	ρ_c	n_c	f_{hy} (MPa)	ρ_h	s_h (mm)	n_h	
BJ1	530	0.0084	4-D13	385	0.0057	50	D6	530	0.0367	8-D16	529	0.011	50	D10	32
BJ2	530 529	0.0075	3-D13 1-D10	385	0.0057	50	D6	530	0.0367	8-D16	529	0.011	50	D10	32
BJ3	530	0.0063	3-D13	385	0.0040	70	D6	530	0.0367	8-D16	529	0.011	50	D10	32
B1	530 529	0.0054	2-D13 1-D10	385	0.0040	70	D6	530	0.0367	8-D16	529	0.011	50	D10	32
B2	530	0.0042	2-D13	385	0.0040	70	D6	530	0.0367	8-D16	529	0.011	50	D10	32

actuator. The beam ends and the bottom of column were supported by mechanical hinges. In addition, to prevent the displacement in out-of-plane direction, four rollers were placed. Horizontal cyclic load was applied under displacement control by a horizontal actuator with the displacement capacity of ±250 mm. Two cycles of the same amplitude in storey drift were applied with increment of storey drift of Δ_y (deflection at flexural yielding). In order to measure the longitudinal strain in the longitudinal steel bars of the beams, strain gauges were attached on the surface of the steel bars, as shown in Fig. 18.8. Six LVDTs were installed to measure the slippage of the steel bars along the six regions of the beam.

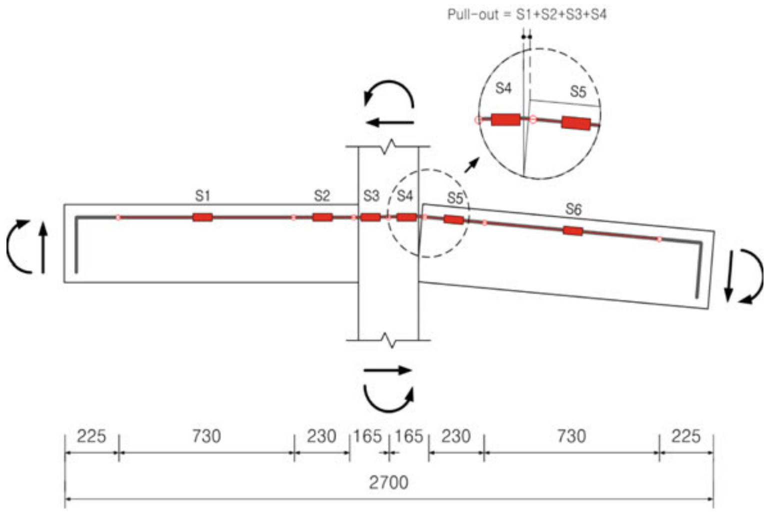

(a) Location of LVDTS on the rebars

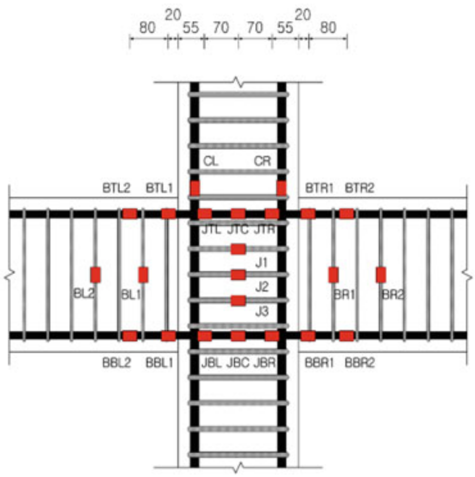

(b) Location of strain gauges

Fig. 18.8 Locations of LVDTs and strain gauges

18.6 Test Results

All test specimens failed in joint–shear after the beam bar yielded. Cracks and concrete spalling were observed in both the joint panel and the plastic hinge regions. Although it was somewhat difficult to distinguish accurately the failure type from the crack patterns of the specimen, the cracks and concrete spalling occurred mostly in the plastic hinge zone of the beam in the case of the BJ-specimen, but occurred both in the plastic hinge and joint panel in the case of the B-specimen. In the specimens subjected to axial force, the cracks and concrete spalling in the joint panel occurred less than in the specimens without axial force. In case of B1 specimen, the failure was caused by concrete crushing in the plastic hinge regions of the adjacent beams and damages in the joint were very limited.

Storey shear–deflection relations for the specimens are compared in Fig. 18.9. The maximum storey shear and the corresponding deflection of the specimens are listed in Table 18.2. As shown in Fig. 18.9 and Table 18.2, an increase in the amount of beam bars leads to an increase in the maximum storey shears and yield storey drift. All specimens showed small energy dissipation because of the pinching effect. The values in Table 18.2 show that the ductility ratio increases due to an increase in the shear strength ratio in Type 2. The shear strength of BJ1 specimen was 113.36 kN and that of B2 specimen was 64.09 kN. The displacement of all specimens except B2 specimen at the flexural yielding of beam was approximately 25 mm. Ductility ratio was calculated by the method of Paully et al., the ratio of the ultimate displacement when the peak load decreased to 85% to the yield displacement at the intersection of the maximum load and the 75% of the maximum load. Test results showed that ductility ratio increased as the amount of beam bars decreased. The calculated ductility ratio is shown in Table 18.2.

Ideally, due to the high shear strength of joint (V_j) compared to the flexural yield strength of beam (V_f), the joint strain should stay constant even after the plastic hinges develop at both ends of adjacent beams. But in fact, the joint strain increases due to tensile strain penetration in the joint core with deterioration of joint strength. Figure 18.10 shows the strain distribution along the beam bar subjected to clockwise bending moment, measured by the strain gauges. The beam bar strain inside of the joint core increases as the beam bar strain in the plastic hinge regions increases. While the beam bar strain in the plastic hinge regions was affected greatly by an increase in the storey drift ratio, the effect on the beam bar strain inside of the joint core was small. The behavior of all the specimens subjected to anticlockwise bending moment was similar.

Repeated loads, such as seismic loads, cause the strain in the plastic hinge region to penetrate into the joint panel, to reduce the bond length of the joint and increase the bond stress. As the bond stress of joint increases, the slip of the longitudinal bars of beam increases and the pullout of the steel bar occurs, affecting the deformation of beam–column joints. In the test, the longitudinal strain in the longitudinal steel bars of the beams was measured by the LVDTs installed on the screw bolts welded to the steel bars, as shown in Fig. 18.8a. Figure 18.11 shows the slip

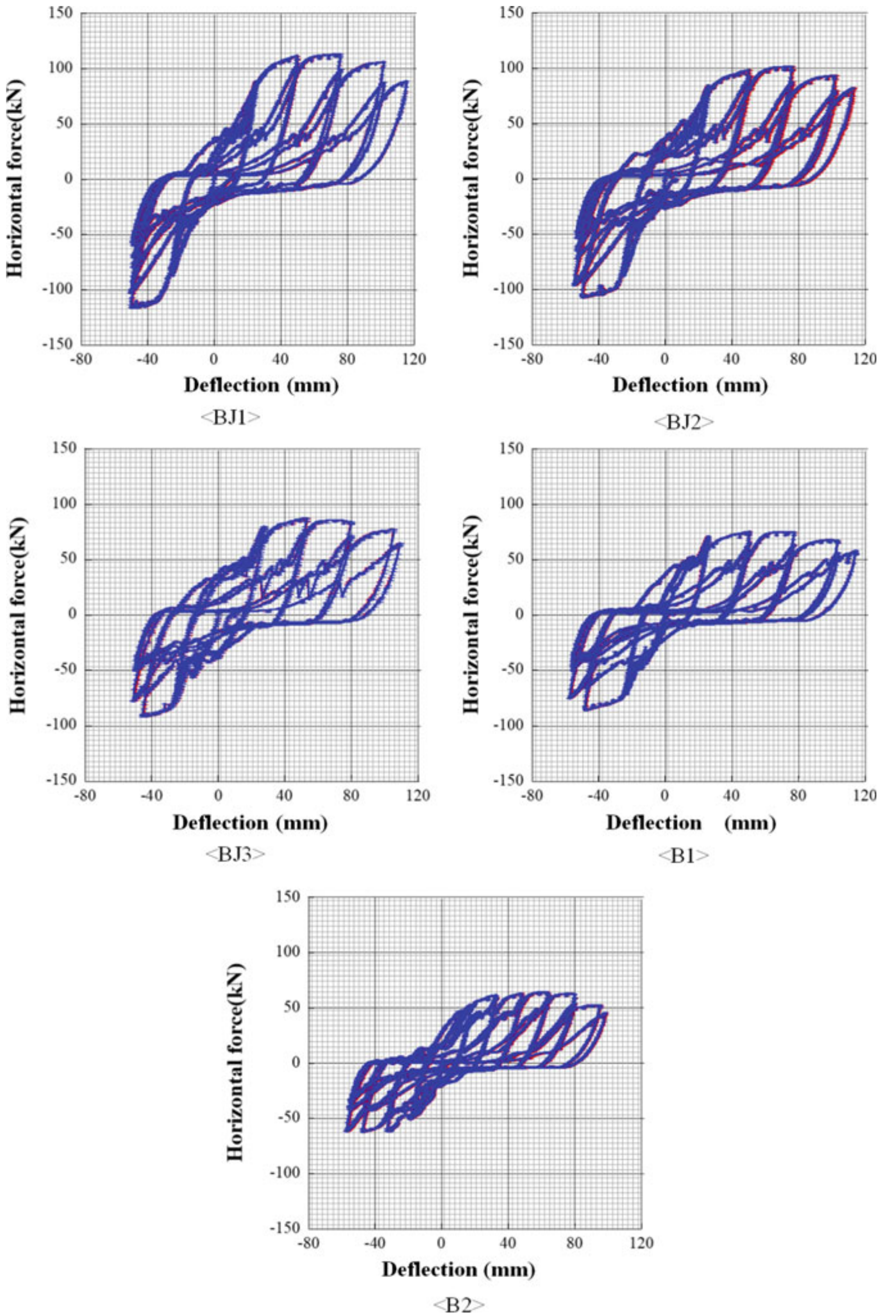

Fig. 18.9 Storey shear force–deflection relations

Table 18.2 Test results

Specimens	BJ1	BJ2	BJ3	B1	B2
Max. storey shear (kN)	+113.36	+101.70	+87.92	+75.44	+64.09
Max. storey drift angle (%)	+6.28	+6.28	+6.33	+6.44	+4.03
Storey drift angle at yielding of beam bars (%)	+2.10	+2.13	+2.09	+2.14	+1.46
Storey drift angle at 85% of max. storey shear (%)	+6.85	+9.07	+8.79	+9.30	+7.84
Ductility ratio (μ_Δ)	3.27	3.51	3.63	3.80	4.75

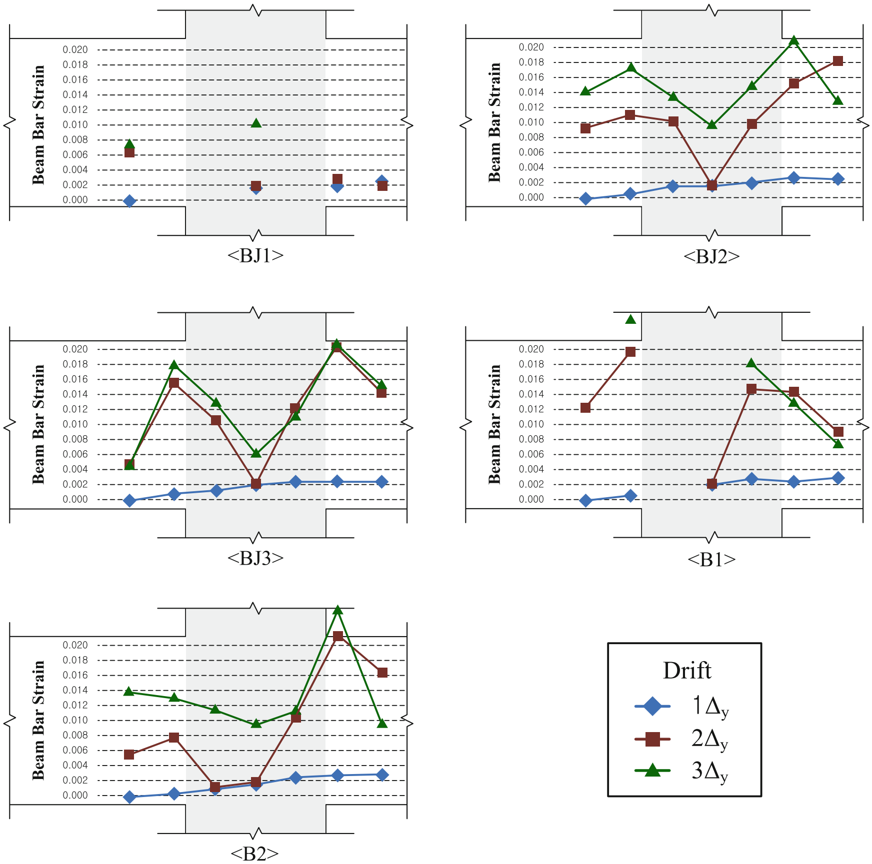

Fig. 18.10 Distribution of beam bar strain

measured in the six regions of specimen. As shown in Fig. 18.11, the slip in the S4 region, boundary between joint and beam, was the largest, while that in the S5 region, plastic hinge region of beam was the second largest. The ship in the S1,

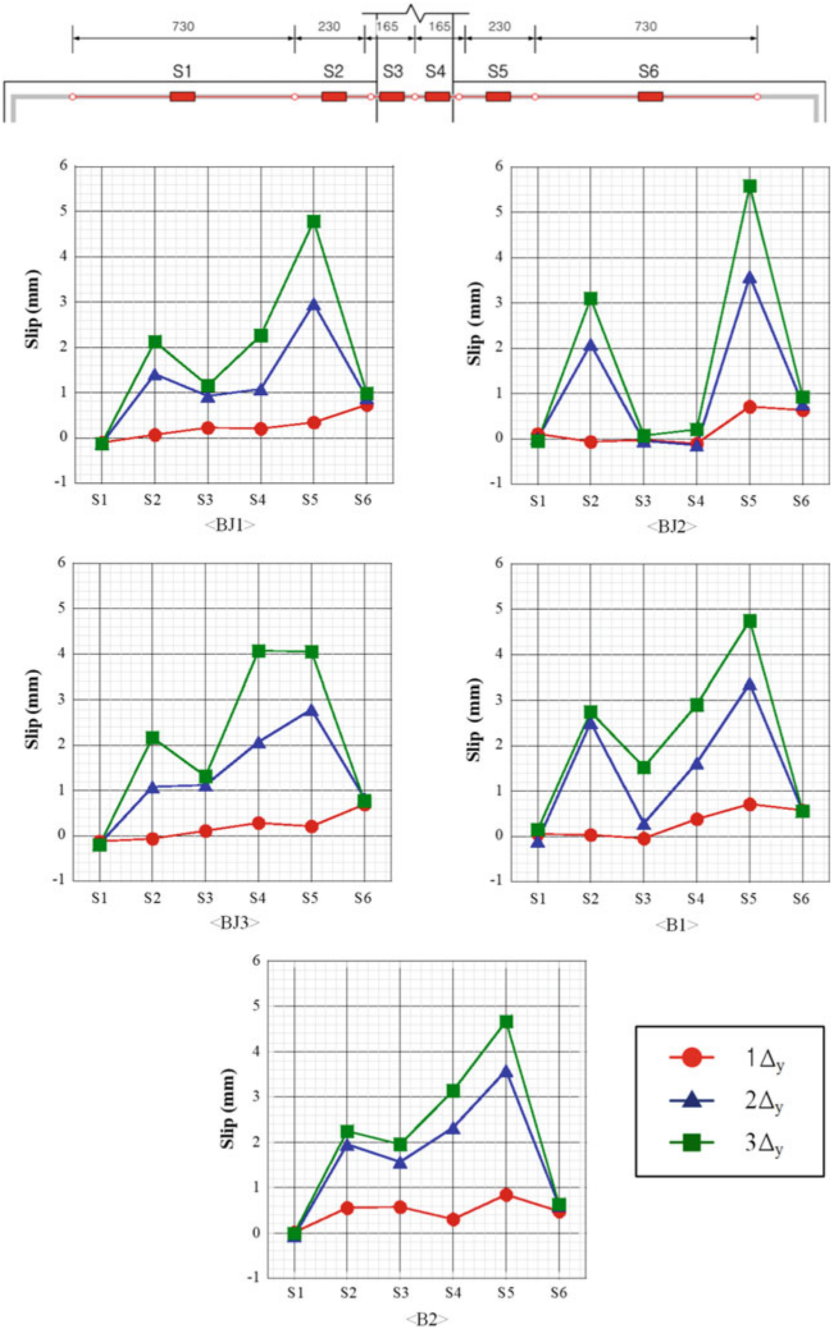

Fig. 18.11 Slip of beam bar strain

elastic region, was the smallest. The slip in the S4 was about two times greater than that in the S1. The joint strain should stay constant even after the plastic hinges develop at both ends of adjacent beams. However, the test results showed that the joint longitudinal strain actually increases due to the tensile “strain penetration” in the joint core.

18.7 Conclusions

Five beam–column joints were tested to investigate the deformation components of RC joints failing in shear after a plastic hinge develops at the end of the adjacent beams in this study. Based on the test results, the following conclusions can be drawn.

(1) Test results of RC beam–column joints indicated that as the amount of the longitudinal beam bars decreased, less damage was noted in the joint core and more damage was noted in the plastic hinge region of the beams. The ductility ratio of joints increased as the increase of shear strength ratio (V_j/V_{jby}).
(2) The slippage of the steel reinforcements, concrete strength deterioration, and strain penetration of beam–column assemblages affected the structural response of the RC joints subjected to seismic inelastic loading. The slip in the S4 region, boundary between joint and beam, was the largest, while that in the S1 was the smallest. The slip in the S4 was about two times greater than that in the S1. The experimental pullout slip was found to decrease as the axial force on the column increases.
(3) As the shear strength ratio (V_j/V_{jby}) increased, the strain penetration was decreased. Joint shear deformation increased and beam and column deformations decreased as drift increased due to tensile strain penetration in the joint core after a plastic hinge develops at the end of the adjacent beams.

Acknowledgements This research was supported by Basic Science Research Program through the National Research Foundation of Korea (NRF) funded by the Ministry of Education (2018R1A2B3001656).

References

ACI-ASCE committee 352. (1985). Design of beam-column joints in monolithic reinforced structures. *ACI Journal*, *82*(3).

ACI-ASCE Committee 352-R2. (2002). *Recommendation for design of beam-column connections in monolithic reinforced concrete structures* (p. 37) American Concrete Institute, Farmington Hills, Michigan.

ACI SP-123. (1991). Design of beam-column joints. In J. O. Jirsa (Ed.), *ACI SP-123* (p. 518).

AIJ. (1999). *Design guidelines for earthquake resistance reinforced concrete buildings based on inelastic displacement concept* (p. 440). AIJ.

Attaalla, S. A. (2003). Deformation characteristics of reinforced concrete beam-column joint cores under earthquake loading. *Advanced in Structural Engineering, 6*(1), 15–21.

Belarbi, A., & Hsu, T. T. C. (1995). Constitutive laws of softened concrete in biaxial tension-compression. *ACI Structural Journal, 92*(5), 562–573.

Cheung, P. C., Paulay, T., & Park, R. (1991). *New Zealand tests on full-scale reinforced concrete beam-column-slab sub assemblages designed for earthquake resistance* (pp. 1–37). ACI SP-123.

Durrani, A. J., & Wight, J. K. (1985). Behavior of interior beam to column connections under earthquake type loading. *ACI Journal Proceeding, 82,* 343–349.

Fenwick, R. C., Davidson, B. J., & McBride, A. (1996). The influence of slabs on elongation in ductile seismic resistant concrete frames. In *The 11th World Conference on Earthquake Engineering*, *Acapulco, Mexico*.

Filip, C., Filippou, F. C., & Issa, A. (1988). *Nonlinear analysis of reinforced concrete frames under cyclic load reversals* (p. 107). Report No. UCB/EERC–88/12, Earthquake Engineering Research Center, College of Engineering, University of California, Berkeley.

Fujii, S., & Morita, S. (1991). *Comparison between interior and exterior RC beam-column joint behavior* (pp. 145–166). ACI SP-123.

Hwang, S. J., & Lee, H. J. (1999). Analytical model for predicting shear strengths of exterior reinforced concrete beam-column joints for seismic resistance. *ACI Structural Journal, 96*(5), 846–857.

Hwang, S. J., & Lee, H. J. (2000). Analytical model for predicting shear strengths of interior reinforced concrete beam-column joints for seismic resistance. *ACI Structural Journal, 97*(1), 35–44.

Kamimura, T., Takeda, S., & Tochio, M. (2000). Influence of joint reinforcement on strength and deformation of interior beam-column sub assemblages. In *12th World Conference on Earthquake Engineering*, *New Zealand* (p. 2267).

Kurose, Y, Guimaraes, G. N., Zuhua, L., Kreger, M. E., & Jirsa, J. O. (1991). *Evaluation of slab-beam-column connections subjected to bidirectional loading* (pp. 39–67). ACI SP-123.

Lee, J.-Y., Kim, J.-Y., & Oh, G.-J. (2009). Strength deterioration of reinforced concrete beam-column joints subjected to cyclic loading. *Engineering Structures, 31,* 2070–2085.

Lee, J.-Y., Kim, S.-W., & Mansour, M. Y. (2010). Nonlinear analysis of shear-critical reinforced concrete beams using fixed angle theory. *Journal of Structural Engineering, ASCE, 137*(10), 1017–1029.

Lee, J.-Y., & Watanabe, F. (2003a). Predicting the longitudinal axial strain in the plastic hinge regions of reinforced concrete beams subjected to reversed cyclic loading. *Engineering Structures, 25,* 927–939.

Lee, J.-Y., & Watanabe, F. (2003b). Shear deterioration of reinforced concrete beams subjected to reversed cyclic loading. *ACI Structural Journal, 100*(4), 480–489.

Lee, J.-Y., Haroon, M., Park, J., & Kim, C. (2018) Longitudinal axial strain in plastic hinge regions of reinforced concrete columns. Magazine of concrete research, accepted paper.

Mansour, M. Y., Lee, J.-Y., & Hindi, R. (2005). Shear behavior and diagonal crack width for reinforced concrete beams with high-strength shear reinforcement. *Engineering Structures, 27* (8), 1138–1150.

NZS. (1982). *The design of concrete structures* (p. 127). NZS.

Park, R., Tanaka, H., & Xin, X. Z. (1998). *High-strength concrete beam-column joints of moment resisting frames* (pp. 357–378). ACI SP-176.

Sugano, S., Nagashima, T., Kimura, H., & Ichikawa, A. (1991). *Behavior of beam-column joints using high-strength materials* (pp. 359–377). ACI SP-123.

Teraoka, M. (1997). *Study on earthquake-resistant design methods for beam-column joints in high-rise moment-resisting frames*, (pp. 90–131). Fusita Corporation.

Vecchio, F. J., & Collins, M. P. (1986). The modified compression-field theory for reinforced concrete elements subjected to shear. *ACI Structural Journal, 83*(2), 219–231.

Chapter 19
Capacity-Based Inelastic Displacement Spectra for Seismic Evaluation and Design of Reinforced Concrete Bridges

Kuo-Chun Chang, Ping-Hsiung Wang and Yu-Chen Ou

Capacity-based inelastic displacement spectra that comprise an inelastic displacement (C_R) spectrum and a corresponding damage state (DI) spectrum are proposed to aid seismic evaluation and design of reinforced concrete bridges. Nonlinear time history analyses of SDOF systems are conducted using a versatile smooth hysteretic model that accounts for the influences of various column design parameters when subjected to far-field and near-fault ground motions. The computed spectra show that the C_R for far-field ground motions approximately conforms to the equal displacement rule for structural period (T_n) larger than around 0.8 s and that for near-fault ground motions departs from the rule in all spectral regions. Moreover, most of the design scenarios investigated in this research cannot survive the near-fault ground motions when relative strength $R = 5.0$. Based on the computed spectra, C_R and DI formulae are presented as a function of T_n, R, and various design parameters for far-field and near-fault ground motions, respectively.

19.1 Introduction

Capacity-based inelastic displacement spectra that comprise an inelastic displacement (C_R) spectrum and a corresponding damage state (DI) spectrum are proposed to aid seismic evaluation and design of reinforced concrete bridges. Nonlinear time

K.-C. Chang (✉) · Y.-C. Ou
Department of Civil Engineering, National Taiwan University,
10617 Taipei, Taiwan
e-mail: ceikuo@ntu.edu.tw

Y.-C. Ou
e-mail: yuchenou@ntu.edu.tw

P.-H. Wang
National Center for Research on Earthquake Engineering, 10668 Taipei, Taiwan
e-mail: phwang@ncree.narl.org.tw

T. T. C. Hsu (ed.), *Concrete Structures in Earthquake*,
https://doi.org/10.1007/978-981-13-3278-4_19

history analyses of SDOF systems are conducted using a versatile smooth hysteretic model that accounts for the influences of various column design parameters when subjected to far-field and near-fault ground motions. The computed spectra show that the C_R for far-field ground motions approximately conforms to the equal displacement rule for structural period (T_n) larger than around 0.8 s and that for near-fault ground motions departs from the rule in all spectral regions. Moreover, most of the design scenarios investigated in this research cannot survive the near-fault ground motions when relative strength $R = 5.0$. Based on the computed spectra, C_R and DI formulae are presented as a function of T_n, R, and various design parameters for far-field and near-fault ground motions, respectively.

To aid seismic evaluation of newly designed or existing bridges, various analysis methods are available according to the seismicity, regularity, complexity, and importance of bridges. The seismic retrofitting manual for highway structures (part 1-bridges) published by FHWA (2006) provided three major evaluation methods for the upper level earthquake. First, for regular bridges that behave as single-degree-of-freedom (SDOF) systems and have rigid in-plane superstructures, it is recommended that a simplified capacity spectrum method (D1 method) be used. In this method, a structural capacity curve is constructed using a bilinear representation with simple calculation rather than conducting pushover analysis and the calculated maximum displacement capacity is reduced by a modification factor R_d to account for the possible underestimation of nonlinear response by the equal displacement rule. Second, for regular and irregular bridges, the structure capacity/demand method (D2 method) is suggested that adopts pushover analysis upon individual piers (or bents) to obtain component capacity and uses the elastic dynamic analysis of the whole bridge to approximate seismic demand. Finally, nonlinear time history analysis (E method) could be used for irregular complex bridges or those of major importance. The AASHTO guide specification for seismic bridge design (2011) suggested similar analysis methods to those of FHWA (2006) except for the D1 method. In addition, the R_d factor in the D1 method was modified as a function of displacement ductility demand instead of relative strength ratio and then used to magnify the elastically analyzed displacement demand in the D2 method. The Caltrans Seismic Design Criteria (SDC 2013) was similar to the AASHTO's methods (2011), but it did not use the R_d factor to estimate seismic demand. Later on, the Caltrans seismic design specifications for steel bridges (2016) retrieved the use of the same R_d factor as AASHTO (2011). On the other hand, the Eurocode 8 (2005) on design of structures for earthquake resistance (part 2: bridges) used the same R_d factor as the D1 method of FHWA (2006) to compute the design seismic displacement of bridges. Accordingly, it can be found that current seismic evaluation of bridges tends toward the well-known displacement coefficient method (FEMA 273 1997).

The key element of the displacement coefficient method is the displacement coefficient (namely, the R_d factor or referred to as inelastic displacement ratio, hereafter) that allows maximum inelastic displacement to be estimated from maximum elastic displacement. Many researchers have focused on this area based on statistical study of nonlinear time history analyses of SDOF systems subjected to a suite of earthquake ground motions (e.g., Veletsos et al. 1965; Shimazaki and Sozen 1984; Miranda 1993; Whittaker et al. 1998; Ruiz-Garcia and Miranda 2003, among others). Instead of the direct method mentioned above, inelastic displacement ratio can also be derived from existing R_μ–μ–T_n relations (Reinhorn 1997; Chopra and Goel 1999; Fajfar 1999), where R_μ is the strength reduction factor due to ductility μ. In particular, Fajfar (1999) utilized the R_μ formula proposed by Vidic et al. (1994) to derive the inelastic displacement ratio, on which the coefficient C_1 in FEMA 273 (1997) and also the R_d factor of FHWA (2006) were based. However, Miranda (2001) revealed that this kind of derivation would cause statistical bias and underestimation of inelastic displacement compared to the direct method, and this was later confirmed by FEMA 440 (2005).

Most, if not all, of the inelastic displacement ratios mentioned above are based on polygonal hysteretic models, such as the elastoplastic (EPP) model, the bilinear model, and stiffness and/or strength degrading models. Nevertheless, real hysteresis behaviors of structures are smooth rather than piecewise linear with abrupt stiffness changes. Furthermore, the severity and characteristics of degradation of hysteresis behaviors depend mainly on the structural system and the design parameters of its components, thus affecting the resulting seismic responses and damage state. But apparently current published formulae for the inelastic displacement ratio lack this kind of link. For bridge application, there should be a better chance to fill this gap since the seismic response of a bridge is primarily dominated by its substructure (i.e., bridge pier or column). The authors recently proposed a versatile smooth hysteretic model (SHM; Wang et al. 2017) that can realistically simulate the seismic behaviors of reinforced concrete (RC) bridge columns with the effects of various design parameters, where the damage index proposed by Park and Ang (1985) was correlated with the strength deterioration and proved to be a good indicator for damage assessment of columns. Therefore, seismic analysis via this model can obtain not only the maximum responses of a column but also its damage state under a given ground motion, providing a better insight into the seismic performance.

The objective of this paper is to statistically compute the inelastic displacement ratio and the corresponding damage state (i.e., the so-called capacity-based inelastic displacement spectrum) of a SDOF system using the proposed smooth hysteretic model that can take into account the effects of various design parameters of RC bridge columns when subjected to both far-field and near-fault ground motions. The computed spectra were then used to evaluate the well-known formulae for inelastic displacement ratio, and new formulae for the capacity-based spectrum as a function of period of vibration, relative strength, and various design parameters of columns were presented for far-field and near-fault ground motions, respectively.

19.2 Smooth Hysteretic Model

The smooth hysteretic model (SHM) used to perform the nonlinear time history analysis of SDOF system is proposed by Wang et al. (2017). The model is based on the Bouc–Wen model (1976) with significant modification to consider hysteretic rules for damage accumulation and path dependence of RC bridge columns. The relationship between the restoring force and displacement of system is described by a differential equation as follows:

$$\dot{z}(t) = h(z)\frac{\left\{A\dot{u} - v\left[\beta|\dot{u}||z|^{n-1}z + \gamma\dot{u}|z|^{n}\right]\right\}}{\eta} \tag{19.1}$$

$$h(z) = 1 - \xi_1 \exp\left\{-\frac{[zsgn(\dot{u}) - qz_u]^2}{\xi_2^2}\right\}\left|\frac{sgn(\dot{u}) + sgn(z)}{2}\right| \tag{19.2}$$

where z and u are the normalized restoring force and displacement of system, respectively; A, β, γ, and n are parameters that determine the basic shape of the z-u relation; v and η are the strength and stiffness degradation parameters, respectively; and $h(z)$ is the pinching function in which ξ_1 controls the severity of pinching, ξ_2 controls the spread of pinching, and q defines the force level z at which pinching reaches its maximum effect.

Equation (19.1) essentially defines the continuous change of stiffness of hysteresis loops with respect to the force level. Figure 19.1a plots in the z–u plane the hysteresis loop of the 4% drift of column COC (Wang et al. 2017), and Fig. 19.1b illustrates in the dz/du–z plane the corresponding measured and simulated stiffness variation for the reloading curve in the negative direction. It can be clearly seen that reloading behavior is a combined effect of stiffness degradation and pinching where each model parameter plays a particular role. For strength deterioration, the model utilizes the damage index (*DI* as defined in Eq. 19.3) proposed by Park and Ang (1985) to initiate strength deterioration until *DI* is accumulated to a threshold value DI_o. More details regarding the model calibration and hysteretic rules for path dependence can be found in Wang et al. (2017).

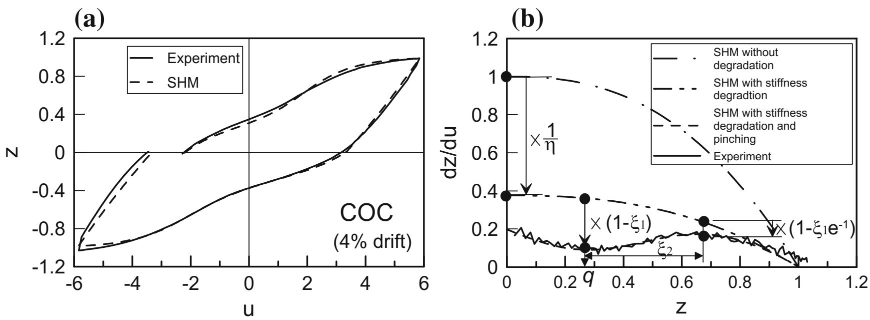

Fig. 19.1 **a** Hysteresis loop of 4% drift ratio of column COC and **b** corresponding dz/du-z relation for reloading in the negative direction (Wang et al. 2017)

$$DI = \frac{\delta_m}{\delta_u} + \lambda \frac{\int dE}{F_y \delta_u} \tag{19.3}$$

where δ_m is the maximum displacement of column; δ_u is the ultimate displacement capacity of column under monotonic loading; $\int dE$ is the accumulated hysteretic energy dissipation; F_y is the yield force; and λ is a parameter to correlate hysteretic energy dissipation to damage, which can be calculated by setting DI equal to one at the ultimate state of column when the strength of column drops to 80% of its peak value.

19.3 Model Identificatoin for RC Bridge Columns with Various Design Parameters

In order to consider the effects of design parameters of RC bridge columns on deteriorated hysteresis behaviors and thus on computed capacity-based inelastic displacement spectrum, model identifications from relevant experimental data were presented first in this section. The design parameters of RC bridge columns considered include the longitudinal and transverse reinforcement ratios, the aspect ratio, and the axial load ratio. Experimental data focusing on these effects are mainly obtained from the structural performance database of Pacific Earthquake Engineering Research Center (PEER 2003). For each of the column specimens, the model parameters capable of representing specific degradation characteristic as illustrated in Fig. 19.1b were identified using the methodology proposed by Wang et al. (2017), allowing the effects of certain design parameter to be quantitatively evaluated. Table 19.1 lists the main design parameters of the tested RC bridge

Table 19.1 Design parameters of columns

Hysteretic model	M1 (EPP)	M2 (SHM)	M3 (SHM)	M4 (SHM)	M5 (SHM)	M6 (SHM)	M7 (SHM)	M8 (SHM)	M9 (SHM)
Specimen name	–	1015	415	407	430	COC/CLC	CTR1	B1	B2
Longitudinal reinforcement ratio (%)	–	1.5	1.5	0.75	3.0	2.1	2.1	2.2	2.2
Transverse reinforcement ratio (%)	–	0.72	0.72	0.72	0.72	1.26	1.79	0.94	0.94
Aspect ratio	–	10	4.0	4.0	4.0	3.2	3.5	3.8	3.8
Axial load ratio ($f_c' A_g$)	–	0.07	0.07	0.07	0.07	0.10	0.10	0.09	0.23

Note 1. Concrete compressive strength f_c' ranges from 28.1 to 47.3 MPa
2. Yield strength of longitudinal reinforcing steel f_{yl} ranges from 448.7 to 606.8 MPa
3. Yield strength of transverse reinforcing steel f_{yt} ranges from 441.5 to 581.2 MPa

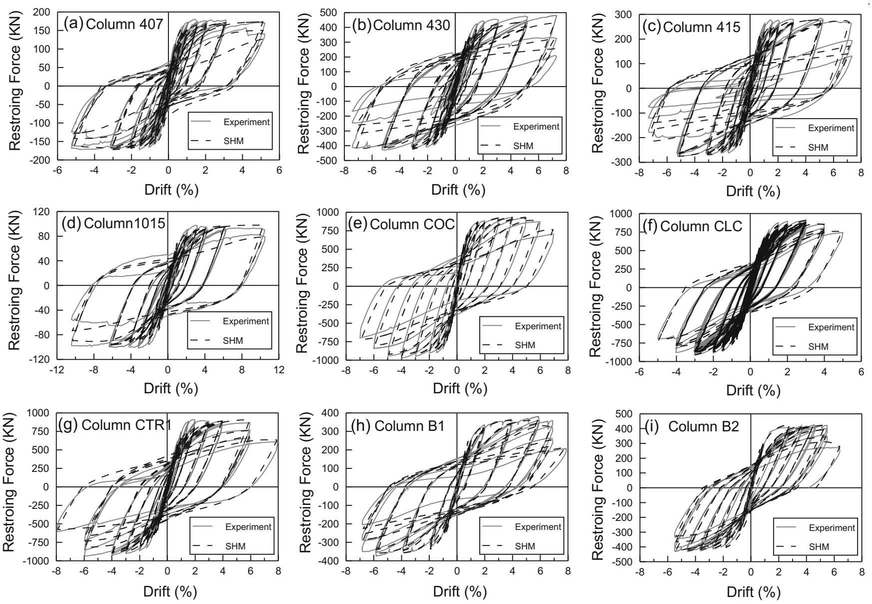

Fig. 19.2 Experimental and simulated hysteresis loops for columns with various design parameters

columns used in this research. Figure 19.2 shows the experimental and simulated hysteresis loops of the tested columns, and Fig. 19.3 shows the identified model parameters with the effects of various column design parameters. More detailed discussions and illustrations regarding the effects of the column design parameters on the deteriorated hysteresis behaviors of RC bridge columns can be found in Wang (2017).

19.4 Capacity-Based Inelastic Displacement Spectrum

The studies on the inelastic displacement ratio mentioned in the introduction are mainly based on seismic responses to far-field ground motions. In contrast, issues regarding the effect of near-fault ground motions, which is characterized by rupture forward directivity toward the site with pronounced velocity pulses, have received increasing attention since the last decade. Baez and Miranda (2000) found that for periods of vibration T_n ranging from 0.1 s to 1.3 s, near-fault ground motions would give rise to a larger inelastic displacement ratio than that computed using far-field ground motions by Miranda (2000). Furthermore, it was concluded that the fault-normal component of near-fault ground motions would result in a larger inelastic displacement ratio than the fault-parallel component. Chopra and

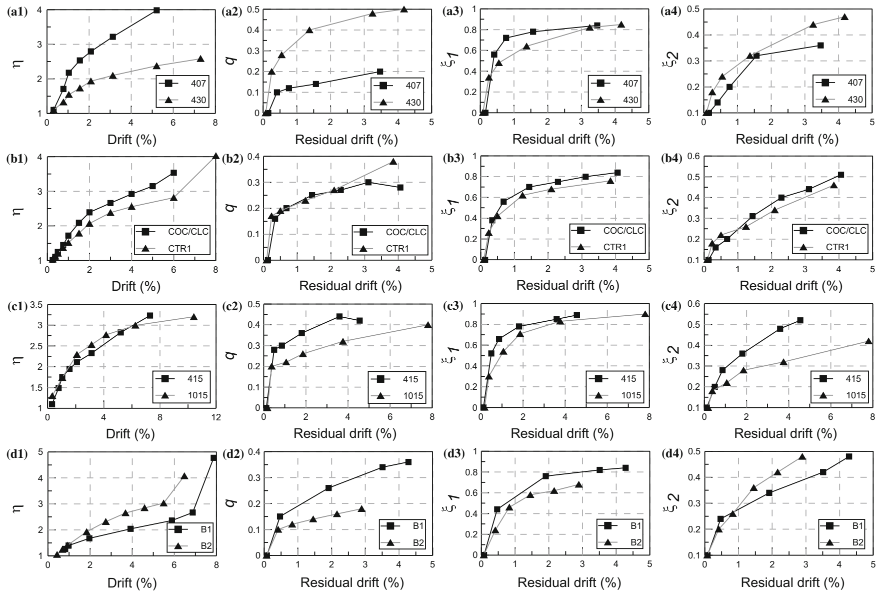

Fig. 19.3 Identified model parameters considering the effects of **a** longitudinal reinforcement ratio; **b** transverse reinforcement ratio; **c** aspect ratio; and **d** axial load ratio

Chintanapakdee (2001) indicated if T_n is normalized relative to the corner period T_c of the ground motion (i.e., the period that separates the acceleration- and velocity-sensitive spectral regions), the calculated mean inelastic displacement ratios for near-fault and far-field ground motions are similar overall spectral regions. Later on, Akkar et al. (2004) computed the median inelastic displacement ratio over 56 pulse-like records versus T_n normalized by the pulse period T_p (i.e., the period associated with the maximum amplitude pulse cycle in the ground velocity time history) and observed that the equal displacement rule can be a satisfactory bound when T_n/T_p is larger than around 0.8. Tothong and Cornell (2007) and Iervolino and Cornell (2008) further grouped an ensemble of pulse-like records into three T_p bins (the average $T_p = 1.0$, 1.9, and 4.0 s) but the computed inelastic displacement ratios with respect to T_n/T_p still showed very different trends between the three T_p bins. More recently, Ruiz-Garcia (2011) proposed to normalize T_n by the predominant period T_g (i.e., the period corresponds to the peak spectral velocity).

As revealed above, it is difficult to well characterize the near-fault directivity effects on seismic responses by a particular featuring period (i.e., T_c, T_p, or T_g). Moreover, from the perspective of seismic design and evaluation, how to determine the featuring period is another challenging issue. Therefore, this study suggests not normalizing T_n by any featuring period but including a wide range of T_p content when selecting the pulse-like near-fault records for statistical analysis. This allows for direct use in estimating the inelastic displacement for near-fault ground motion and direct comparison with that for far-field ground motion. Moreover, the wide range of T_p content in the selected near-fault records is intended to account for as many pulse-like features as possible in response to the uncertainty of future earthquakes.

19.4.1 Spectrum Parameters

The proposed capacity-based inelastic displacement spectrum is comprised of an inelastic displacement ratio spectrum and a corresponding damage index spectrum, forming a twin spectrum to provide estimates not only for the displacement demand but also for the damage state of a system under earthquakes. This study focuses on the constant strength inelastic displacement ratio which is defined as

$$C_R = \frac{\Delta_{inelastic}}{\Delta_{elastic}} \tag{19.4}$$

where $\Delta_{inelastic}$ is the maximum inelastic displacement of an SDOF system with a 5% viscous damping ratio and a lateral yield strength F_y while $\Delta_{elastic}$ is the maximum elastic displacement of the corresponding elastic system having the same T_n and subjected to the same earthquake ground motion.

It should be mentioned that the subscript of C_R is intended to represent that the ratio is based on systems with a constant lateral strength (in contrast to constant ductility C_μ) as suggested by Miranda (2001). The lateral strength of the system is described by a relative strength ratio R (or strength reduction factor), which is defined as

$$R = \frac{mS_a}{F_y} \tag{19.5}$$

where m is the mass of the system, and S_a is the elastic spectral acceleration.

The inelastic displacement ratios (C_R) and the corresponding damage indices (DI) as defined in Eq. (19.3) were computed for SDOF systems having a set of 20 periods of vibration (T_n ranging from 0.05 s to 3.0 s), 9 hysteretic models (M1 to M9) including an EPP model and 8 SHMs as listed in Table 19.1, and five levels of relative strength ratio (R = 1.5, 2, 3, 4, 5) when subjected to 15 far-field (denoted as FF) and 15 pulse-like near-fault (denoted as NF) ground motions.

19.4.2 Ground Motion Records

A total of 30 ground motion records including 15 far-field and 15 near-fault ground motions were selected from the ground motion database of Pacific Earthquake

Engineering Research Center (PEER 2013) to construct the proposed capacity-based inelastic displacement spectrum. As listed in Table 19.2, the 15 far-field records were resulted from 10 different earthquake events with moment magnitude (M_w) ranging from 6.0 to 7.6 and recorded on site classes C and D according to the NEHRP classification (2004). And the 15 near-fault records with the pulse-like characteristic due to forward directivity effects were obtained from 10 different earthquake events with M_w ranging from 6.5 to 7.6, and recorded on site classes B to D. The pulse period T_p of each near-fault record was extracted by Baker (2007) using wavelet analysis. Besides, a wide range of T_p ranging from 1 s to 10 s was considered in the selection of the near-fault records as mentioned above.

19.4.3 Failure Criteria

The smooth hysteretic model used in this research may exhibit severe strength deterioration accompanied with significant inelastic displacement demand under earthquake excitation especially when the system has a low lateral strength (a large *R*) and/or is subjected to pulse-like near-fault ground motions. Therefore, there is a need to define failure criteria both for performing each analysis case and for constructing the capacity-based inelastic displacement spectrum. In the study conducted by Wang (2017), it was proved that the damage index *DI* proposed by Park and Ang (1985) can be a good index to represent the damage state of RC bridge columns in terms of strength deterioration and visual damage conditions under various loading protocols. By definition of the model, the damage index $DI = 1.0$ corresponds to the lateral strength of column dropping to 80% of its peak value. Besides, in accordance with the experimental observation from columns subjected to different types of cyclic loadings and pseudo-dynamic loading, the damage index $DI = 1.0$ also corresponds to damage conditions such as significant crushing of concrete spreading into confined concrete core, distortedly buckling of longitudinal steels, and unhooking of closed hoops and crossties, after which fracture of longitudinal steels associated with abrupt strength drop would occur subsequently. Accordingly, for every analysis case, a column will be deemed failure or collapse if its damage index *DI* accumulated at the end of ground excitation is larger than one (or the analysis cannot be continued due to dynamic instability).

On the other hand, in constructing the capacity-based inelastic displacement spectrum, the mean values of computed inelastic displacement ratios and corresponding damage indices for the 15 (far-field or near-fault) ground motions need to be calculated for each suite of spectrum parameters (i.e., a combination of period of vibration T_n, relative strength ratio *R*, and hysteretic model M). However, as just mentioned one or more than one of the analyzed cases for the 15 (far-field or near-fault) ground motions may show failure at certain spectrum parameters. If we exclude the cases identified as failure from the 15 cases and then take the average

Table 19.2 Far-field (FF) and near-fault (NF) ground motion records used in this study

No	RSN	Earthquake name	Station name	Year	M_w	R_{rup}(km)	PGA(m/s^2)	PGV(cm/s)	T_p(s)	Site class
FF01	57	San Fernando	Castaic—Old Ridge Route	1971	6.6	22.63	2.70	28.63	–	C
FF02	164	Imperial Valley	Cerro Prieto	1979	6.5	15.19	1.54	19.27	–	C
FF03	169	Imperial Valley	Delta	1979	6.5	22.03	3.43	32.98	–	D
FF04	265	Victoria_Mexico	Cerro Prieto	1980	6.3	14.37	6.33	33.57	–	C
FF05	652	Whittier Narrows	Lakewood—Del Amo Blvd	1987	6	26.68	1.99	11.19	–	D
FF06	771	Loma Prieta	Golden Gate Bridge	1989	6.9	79.81	1.22	18.11	–	C
FF07	777	Loma Prieta	Hollister City Hall	1989	6.9	27.60	2.42	38.88	–	D
FF08	787	Loma Prieta	Palo Alto—SLAC Lab	1989	6.9	30.86	2.72	31.27	–	C
FF09	836	Landers	Baker Fire Station	1992	7.3	87.94	1.06	9.25	–	D
FF10	1073	Northridge	San Pedro—Palos Verdes	1994	6.7	57.03	0.99	5.52	–	C
FF11	1237	Chi-Chi	CHY090	1999	7.6	58.42	0.75	13.72	–	D
FF12	1295	Chi-Chi	HWA049	1999	7.6	50.76	0.98	19.82	–	C
FF13	1315	Chi-Chi	ILA010	1999	7.6	80.18	0.58	7.56	–	C
FF14	1837	Hector mine	Valyermo Forest Fire Station	1999	7.1	135.77	0.57	4.18	–	C
FF15	1172	Kocaeli	Tekirdag	1999	7.5	165.02	0.33	3.21	–	C
NF01	77	San Fernando	Pacoima Dam (upper left abut)	1971	6.6	1.81	11.96	114.41	1.64	B
NF02	179	Imperial Valley	El Centro Array #4	1979	6.5	7.05	3.63	80.37	4.79	D
NF03	181	Imperial Valley	El Centro Array #6	1979	6.5	1.35	4.41	113.50	3.77	D
NF04	767	Loma Prieta	Gilroy Array #3	1989	6.9	12.82	3.61	45.40	2.64	D
NF05	828	Cape Mendocino	Petrolia	1992	7	8.18	6.49	88.47	3.00	C
NF06	879	Landers	Lucerne	1992	7.3	2.19	7.11	133.33	5.12	B
NF07	1004	Northridge	LA—Sepulveda VA Hospita	1994	6.7	8.44	9.14	76.23	0.93	C
NF08	1045	Northridge	Newhall—W Pico Canyon Rd.	1994	6.7	5.48	4.11	118.12	2.98	D
NF09	1086	Northridge	Sylmar-Olive View Med FF	1994	6.7	5.3	8.27	129.31	2.44	C

(continued)

Table 19.2 (continued)

No	RSN	Earthquake name	Station name	Year	M_w	R_{rup}(km)	PGA(m/s^2)	PGV(cm/s)	T_p(s)	Site class
NF10	1106	Kobe	KJMA	1995	6.9	0.96	8.18	91.06	1.09	D
NF11	1491	Chi-Chi	TCU051	1999	7.6	7.64	1.57	53.81	10.38	D
NF12	1503	Chi-Chi	TCU065	1999	7.6	0.57	7.75	125.28	5.74	D
NF13	1528	Chi-Chi	TCU101	1999	7.6	2.11	2.08	76.77	10.32	C
NF14	1161	Kocaeli	Gebze	1999	7.5	10.92	2.56	44.60	5.99	B
NF15	6975	Darfield	TPLC	2010	7	6.11	2.94	76.29	8.93	D

Note RSN is the record sequence number used in PEER ground motion database value of the remaining ones, the calculated results can be distortive especially when the excluded cases increase. This is because the excluded cases often produce greater C_R and DI than those of the remaining ones, whose average values thus tend to underestimate the spectrum ordinates. Furthermore, an increasing number of excluded cases also indicate an increase in the probability of failure under 15 ground motions, which cannot be reflected in the resulting spectral ordinates. Therefore, it was stipulated in this study that if the probability of failure is larger than 20% under 15 (far-field or near-fault) ground motions, a column devised using that suite of spectrum parameters will be deemed unable to survive under considered earthquakes while there will be no corresponding spectral ordinate.

19.4.4 Calculated Mean C_R and Corresponding DI Spectra

Mean C_R and the corresponding DI spectra for 15 far-field and 15 near-fault ground motions were computed, respectively, by using nine different hysteretic models (including one EPP model and eight SHMs) to investigate the effects of ground excitation, column design parameter, and model type on the spectral ordinates. Only selected results are presented in this paper due to space limitation while completed results can be found in Wang (2017). Among the eight SHMs for various design parameters of columns, the M6 model is considered representative of commonly used design scenario of bridges in practice and is used to demonstrate the analyzed results. Besides, the M1 (EPP) model was introduced for comparing the results from polygonal and smooth hysteretic models given that it was widely used in the literature.

Figure 19.4 shows the computed mean C_R and the corresponding DI spectra for the M6 model together with the mean C_R spectrum for the M1 model subjected to far-field ground motions. It can be obviously seen that in comparison with the conventional C_R spectrum (Fig. 19.4a1), the proposed capacity-based inelastic displacement spectrum (Figs. 19.4b1 and 19.4c1) can provide not only the C_R estimate but also its corresponding damage state (DI). In particular, each spectral curve associated with a given relative strength ratio R possesses a period limit. If the period of vibration is shorter than this limit, there will be no spectral ordinate or no result. In other words, for a given relative strength ratio R, a system with a period of vibration shorter than this period limit would fail or collapse under the considered earthquakes. Furthermore, the period limit increases as the relative strength ratio increases (i.e., as the lateral strength of system decreases). Figure 19.4b1 also indicates that the equal displacement rule approximately holds true for period of vibration larger than about 0.8 s regardless of various R values, while for short period range ($T_n < 0.8$ s) the C_R is evidently larger than one and nearly independent of R when $R \geq 2.0$. Besides, the corresponding DI increases with increasing R for all period range of spectrum as shown in Fig. 19.4c1. On the other hand, the mean C_R spectrum calculated using M1 (EPP) model basically follows the same trend as

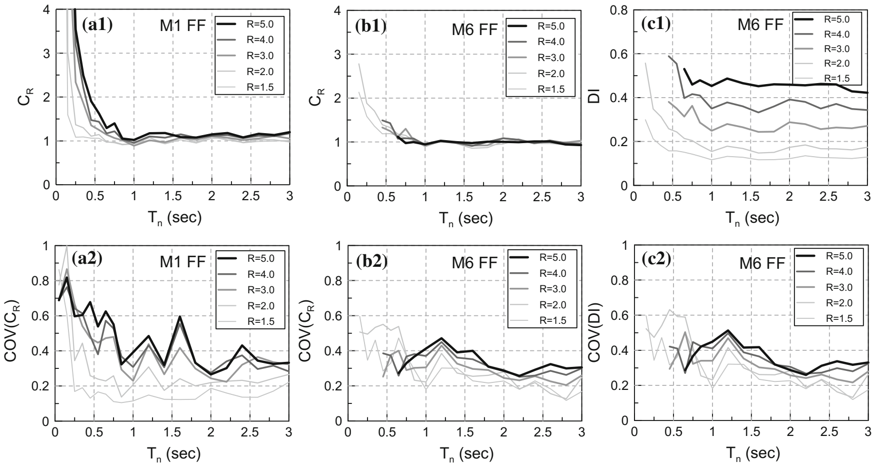

Fig. 19.4 Mean C_R and corresponding *DI* spectra for M6 (SHM) model and mean C_R spectrum for M1 (EPP) model subjected to far-field ground motions

that conducted by Ruiz-Garcia and Miranda (2003) where C_R always increases as R increases even for long period region as shown in Fig. 19.4a1.

Also given in Fig. 19.4 are the coefficient of variations (COVs) corresponding to the mean values of C_R and *DI* to show the level of dispersion, which is defined as the ratio of the standard deviation to the mean. In general, the dispersions in C_R for the M1 model are more susceptible to T_n and R as compared to those for the M6 model. Figure 19.5 further compares the C_R spectra between the M1 and M6 models for different strength ratios under far-field ground motions. It can be observed that the M1 model would result in underestimate C_R for $R \leq 2.0$, overestimate for $R \geq 4.0$, and similar results for $R = 3.0$ compared to the M6 model while no damage information associated with the C_R estimates is available by the M1 model.

Figure 19.6 shows the mean C_R and corresponding *DI* spectra for M6 model as well as the mean C_R spectrum for M1 model under near-fault ground motions, where both models predict C_R practically departing from the equal displacement rule in the whole spectral region. As indicated in Fig. 19.6b1, the C_R from the M6 model increases with increasing R until $R = 3.0$, after which it tends to decrease while the C_R from the M1 model always increases with increasing R in Fig. 19.6a1. And the differences of the estimated C_R between the M1 and M6 models for near-fault ground motions exhibit similar trend to those for far-field ground motions shown in Fig. 19.5. Besides, the dispersions in C_R for the M6 model are more stable and less than those for M1 model, especially in the short period range. Figure 19.7 compares C_R and *DI* differences between far-field and near-fault ground motions for the M6 model. It can be evidently seen that the near-fault ground motions would lead to significantly greater C_R and *DI* than far-field ground motions, and their differences increase with increasing R until $R = 3.0$ and then slightly decrease.

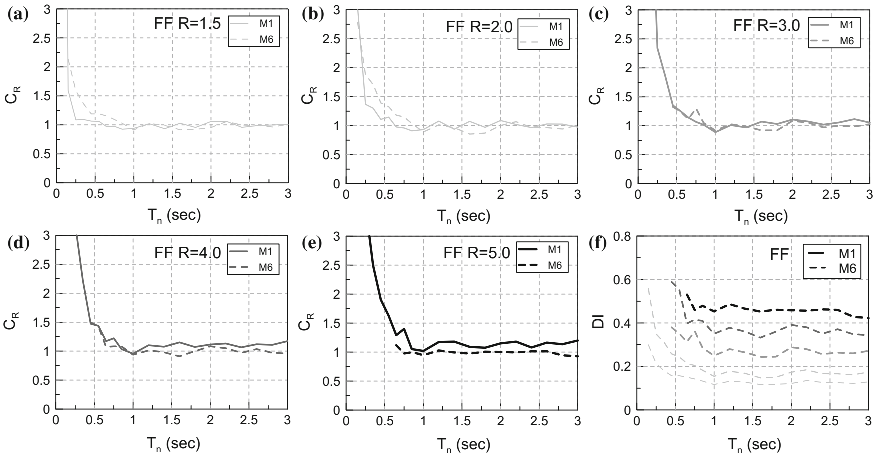

Fig. 19.5 Comparison of C_R between M1 and M6 models for far-field ground motions: **a** $R = 1.5$; **b** $R = 2.0$; **c** $R = 3.0$; **d** $R = 4.0$; **e** $R = 5.0$; **f** comparison of *DI*

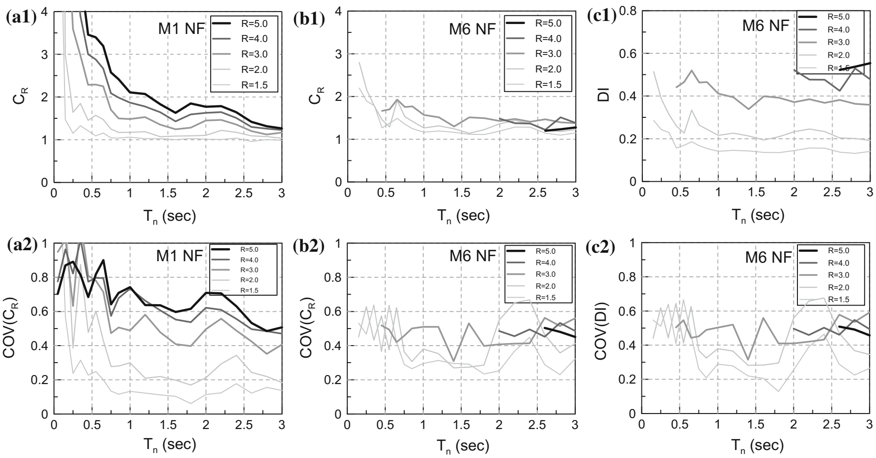

Fig. 19.6 Mean C_R and corresponding *DI* spectra for M6 (SHM) model and mean C_R spectrum for M1 (EPP) model subjected to near-fault ground motions

Moreover, for $R \geq 4.0$ most of systems with the M6 hysteretic behavior could not survive under considered near-fault ground motions except for those with periods of vibration longer than around 2 s.

Regarding the effects of column design parameters on the calculated C_R and *DI* spectra, it can be concluded for far-field ground motions that C_R was approximately independent of column design parameters while *DI* correlated positively with longitudinal reinforcement and axial load ratios but negatively with transverse

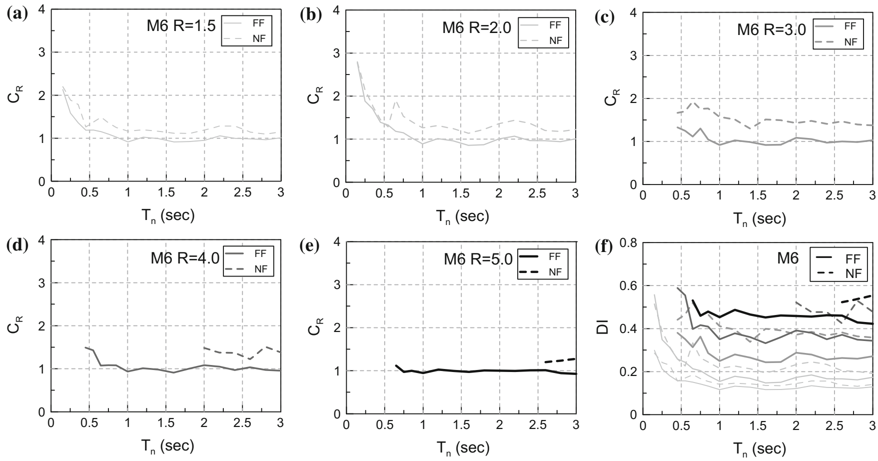

Fig. 19.7 Comparisons of C_R between far-field and near-fault ground motions for M6 model: **a** $R = 1.5$; **b** $R = 2.0$; **c** $R = 3.0$; **d** $R = 4.0$; **e** $R = 5.0$; **f** comparison of *DI*

reinforcement and aspect ratios. For near-fault ground motions, C_R correlated positively with transverse reinforcement and aspect ratios, negatively with longitudinal reinforcement ratios, and was nearly independent of axial load ratios while *DI* followed similar trend to the *DI* of far-field ground motions.

19.5 Evaluation of the Well-Known C_R Formulae

The calculated C_R spectrum using the M6 model is considered satisfactory and accurate to represent the real seismic responses of typical RC bridge columns and is used to evaluate the well-known C_R formulae in the literatures which include those from FEMA 273 (1997), FEMA 440 (2005), and FHWA (2006) based on far-field ground motions. Figure 19.9 shows comparisons of C_R spectra constructed from the well-known C_R formulae and the M6 model for far-field ground motions. In the figures, the C_R for FEMA 273 was computed as a product of coefficients C_1 and C_2 without the contribution of C_3 given that the analyzed spectrum in this research did not consider the P-delta effect. Moreover, value of C_2 was selected for framing type one and the collapse prevention performance level. The characteristic period T_s (or corner period) used to identify the long period spectral region where the equal displacement rule can apply was 0.55 s as suggested by FEMA 440 (2005) for NEHRP site class C considering most of the ground motion records used fell into this category. The C_R for FEMA 440 was also a product of given C_1 and C_2, where the constant a in C_1 was 90 as recommended for site class C. The C_R for FHWA (2006) was identical to the C_1 of FEMA 273 except that the capping on C_1 was excluded and the T_s was magnified by 1.25 to define the long period spectral region.

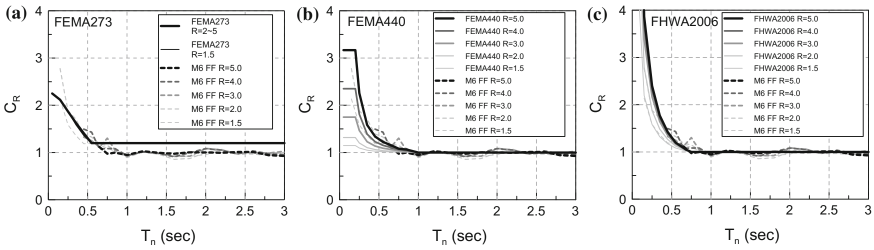

Fig. 19.8 Comparisons of C_R spectra constructed from M6 model for far-field ground motions and from **a** FEMA 273 (1997); **b** FEMA 440 (2000); **c** FHWA (2006)

Figure 19.8a shows that the C_R of FEMA 273 is practically independent of R due to the capping on C_1 and lies between the C_R curves of M6 model corresponding to $R = 1.5$ and 2.0 for $T_n < T_s$, while it apparently leads to overestimation due to C_2 for $T_n > T_s$. Figure 19.8b shows that, in contrast, the FEMA 440 significantly underestimates the C_R for T_n smaller than around 0.8 s compared to that of M6 model but their differences decrease as R increases. Finally, the C_R for FHWA (2006) exhibits surprising agreement with that of M6 model notwithstanding the drawbacks behind its derivation as told by Miranda (2001).

19.6 Proposed C_R and di Formulae

Considering the C_R formula of FHWA (2006) can satisfactorily predict the calculated C_R spectrum for far-field ground motions, the proposed C_R and DI formulae were constructed based on its functional form and were extended for near-fault ground motions. Figure 19.9 illustrated the methodology used to determine the period limits in different design scenarios, where the period of vibrations corresponding to DI = 1.0 on the DI spectrum indicated the period limits that are applicable to the C_R spectrum. Notwithstanding this method would result in overestimation of DI in the vicinity of the period limit where there is only 20% probability of failure, it was thought to be expedient. By using nonlinear regression analysis of the calculated results, the proposed C_R and DI formulae for far-field ground motions were given as follows:

$$C_R = \begin{cases} \left(1 - \frac{1}{R}\right)\frac{T_1^*}{T_n} + \frac{1}{R}, & T_n < T_1^* \\ 1.0, & T_n \geq T_1^* \end{cases} \tag{19.6a}$$

$$T_1^* = C_{T1} T_s \tag{19.6b}$$

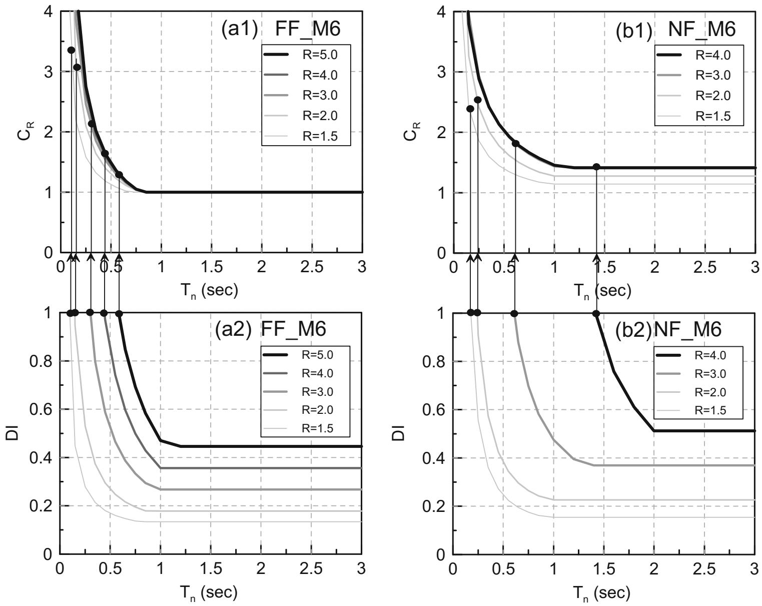

Fig. 19.9 Illustration of proposed C_R and DI spectra for **a** far-field; **b** near-fault ground motions

$$C_{T1} = \begin{cases} 1.25, & R = 1.5 \\ 1.45, & R \geq 2.0 \end{cases} \tag{19.6c}$$

$$DI = \begin{cases} \left(C_{DI} - \frac{C_{DI}}{R}\right)\left(\frac{T_2^*}{T_n}\right)^n + \frac{C_{DI}}{R}, & T_n < T_2^* \\ C_{DI}, & T_n \geq T_2^* \end{cases} \tag{19.7a}$$

$$T_2^* = C_{T2} T_s \tag{19.7b}$$

$$C_{DI} = \{0.065 - 0.01\ln(AD) + 0.017LR - 0.013\ln(TR)\}R \tag{19.7c}$$

$$C_{T2} = 0.37\ln(R) + 1.3 \tag{19.7d}$$

$$n = 0.1R + 1.1 \tag{19.7e}$$

It can be seen that the proposed C_R formula is identical to that of FHWA (2006) except that the coefficient C_{T1} used to define the long period region was magnified to be 1.45 for R $\geq$ 2.0 in order to better fit the computed results. Furthermore, the proposed DI formula was correlated with the design parameters of column (Eq. 19.7c), where AD is the aspect ratio of column, LR is the percentile value of longitudinal reinforcement ratio, and TR is the ratio of transverse reinforcement to that required by the Caltrans bridge seismic design code (Caltrans 2003). The reason to normalize the transverse reinforcement by the code requirement is to allow for different amounts of reinforcing steels needed by circular and rectangular column sections to achieve comparable seismic behaviors. It should be noted that the computed spectra for M8 and M9 models were excluded from the regression analysis since their inclusion would cause unfavorable regression results. This may be attributed to their insufficient transverse reinforcements (around 75% of the code requirement) and the effect of applied axial load on the amount of required transverse reinforcement, which needs further experimental and analytical efforts. Therefore, the proposed formulae are only applicable within the calibrated column design parameters, namely, AD = 3–10, LR = 0.75–3.0, TR = 1.0–1.67, and axial load equal to around 0.1 $f_c' A_g$. For near-fault ground motions, the proposed formulae were given as follows:

$$C_R = \begin{cases} \left(C_{BR} - \frac{C_{BR}}{R}\right)\left(\frac{T_1^*}{T_n}\right)^{n_1} + \frac{C_{BR}}{R}, & T_n < T_1^* \\ C_{BR}, & T_n \geq T_1^* \end{cases} \tag{19.8a}$$

$$T_1^* = C_{T1} T_s \tag{19.8b}$$

$$C_{T1} = 0.095R + 1.565 \tag{19.8c}$$

$$n_1 = -0.08R + 0.92 \tag{19.8d}$$

$$C_{BR} = C_1 R^2 + C_2 R + C_3 \tag{19.8e}$$

$$C_1 = -0.089 - 0.033 ln(AD) + 0.023 LR + 0.008 \ln(TR) \tag{19.8f}$$

$$C_2 = 0.672 + 0.212 ln(AD) - 0.179 LR + 0.036 \ln(TR) \tag{19.8g}$$

$$C_3 = 0.258 - 0.218 ln(AD) + 0.239 LR - 0.127 \ln(TR) \tag{19.8h}$$

$$DI = \begin{cases} \left(C_{DI} - \frac{C_{DI}}{1.5}\right)\left(\frac{T_2^*}{T_n}\right)^{n_2} + \frac{C_{DI}}{1.5}, & T_n < T_2^* \\ C_{DI}, & T_n \geq T_2^* \end{cases} \tag{19.9a}$$

$$T_2^* = C_{T2} T_s \tag{19.9b}$$

$$C_{T2} = n_2 = C_4 \exp[(1 - C_4)R] + C_5 \exp(-R) \tag{19.9c}$$

$$C_{DI} = C_6 R - 0.06 \tag{19.9d}$$

$$C_4 = 0.729 + 0.041 ln(AD) - 0.129 LR + 0.089 \ln(TR) \tag{19.9e}$$

$$C_5 = 1.346 - 0.174 ln(AD) + 0.752 LR - 0.665 \ln(TR) \tag{19.9f}$$

$$C_6 = 0.092 - 0.003 ln(AD) + 0.026 LR - 0.015 \ln(TR) \tag{19.9g}$$

19.7 Application to Performance-Based Seismic Design

The proposed capacity-based inelastic displacement spectra could be applied to the performance-based seismic design of reinforced concrete bridges. Different from the current trend of seismic design codes whose performance objective was based upon displacement or displacement ductility, this research proposed to use the damage index (or damage state) as the performance target for bridge designs. Figure 19.10 shows the flowchart of the proposed seismic design procedure. First of all, the preliminary member and reinforcement sizes can be determined based on the strength and service limit states, where the column longitudinal reinforcement ratio of 1.5% may be a good starting point of design while the amount of transverse reinforcement should meet the code's minimum requirements. By using the preliminary design parameters, the corresponding C_R and DI spectra then can be constructed in accordance with the spectrum formulae given previously. Second, the performance objective of the bridge under design earthquake, which is represented by an anticipated damage index, needs to be defined according to the bridge importance, reparability, or other considerations. Correlation between the actual damage states and the corresponding damage indices for an RC bridge column with a commonly used design scheme can be found in Wang (2017) and Ou et al. (2014).

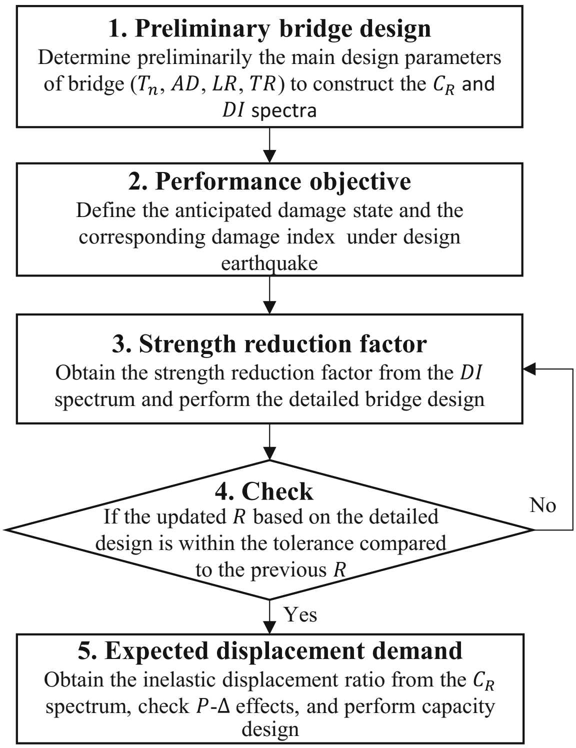

Fig. 19.10 Flowchart of using capacity-based inelastic displacement spectra in performance-based seismic bridge design

Nevertheless, a database regarding the influences of various column design parameters on this correlation remains to be constructed. Third, with the *DI* spectrum, the anticipated damage index, and the bridge fundamental period T_n from preliminary design, the corresponding strength reduction factor R can then be obtained by interpolation. Furthermore, the detailed bridge design can be conducted based on the computed R. Fourth, according to the results of the detailed bridge design, the *DI* spectrum could be updated, and so does the correspondingly computed R to achieve the same anticipated damage index. Then, if the updated R differs significantly from the previous R, redesign of the bridge based on the updated R is needed until the difference between them is within a predefined tolerance. Finally, the inelastic displacement of the bridge can be calculated from the updated C_R spectrum for examining the P-Δ effects and displacement control. In addition, efforts also must be taken on the capacity design of column shear and the force transmission of capacity-protected elements.

19.8 Conclusions

This study aims to propose a capacity-based inelastic displacement spectrum that comprises an inelastic displacement (C_R) spectrum and a corresponding damage state (*DI*) spectrum, using a versatile smooth hysteretic model for seismic evaluation of newly designed or existing reinforced concrete bridges. Important conclusions can be drawn as follows:

1. The computed spectra for far-field ground motions indicate that the equal displacement rule approximately holds true (i.e., $C_R = 1.0$) for periods of vibration larger than about 0.8 s regardless of various R values while for short period range C_R is evidently larger than one and nearly independent of R when $R \geq 2.0$; the corresponding *DI* and period limit increase as R increases or as the lateral strength of system decreases.
2. The computed spectra for near-fault ground motions show that C_R practically departs from the equal displacement rule in the whole spectral region and increases with increasing R until $R = 3.0$, after which it tends to decrease. Moreover, the near-fault ground motions would lead to significantly greater C_R and *DI* than far-field ground motions and most of design scenarios cannot survive the considered near-fault ground motion when $R = 5.0$.
3. Regarding the effects of column design parameters on the calculated spectra, it can be concluded for far-field ground motions that C_R is approximately independent of column design parameters, while *DI* correlates positively with longitudinal reinforcement and axial load ratios but negatively with transverse reinforcement and aspect ratios. For near-fault ground motions, C_R correlates positively with transverse reinforcement and aspect ratios, negatively with longitudinal reinforcement ratios, and is nearly independent of axial load ratios while *DI* follows similar trend to the *DI* of far-field ground motions.

4. Evaluations of the well-known C_R formulae reveal that the C_R formula provided by FHWA (2006) exhibit good agreement with the computed C_R spectrum of the M6 model for far-field ground motions notwithstanding the drawbacks behind its derivation as stated by Miranda (2001).
5. Based on the functional form of FHWA's C_R formula (2006) and by using nonlinear regression analysis of the computed spectra, the proposed C_R and DI formulae were built as a function of period of vibration, relative strength ratio, and various column design parameters for far-field and near-fault ground motions, respectively.

References

Akkar, S., Yazgan, U., Gulkan, P. (2004). Deformation limits for simple non-degrading systems subjected to near-fault ground motions, Paper No. 2276. In *Proceedings 13th World Conference on Earthquake Engineering*, Vancouver, Canada.

American Association of State Highway and Transportation Officials (AASHTO). (2011). *Guide specification for LRFD seismic bridge design*, LRFDSEIS-2, Washington, DC.

Baez, J. I., & Miranda, E. (2000). Amplification factors to estimate inelastic displacement demands for the design of structures in the near field, Paper No. 1561. In Proceedings, 12th *World Conference on Earthquake Engineering*, Auckland, New Zealand.

Baker, J. W. (2007). Quantitative classification of near-fault ground motions using wavelet analysis. *Bulletin of the Seismological Society of America, 97*(5), 1486–1501.

California Department of Transportation (Caltrans). (2003). *Bridge design specifications*. Sacramento, CA.

California Department of Transportation (Caltrans). (2013). *Seismic design criteria (SDC)*, Version 1.7, Sacramento, CA.

California Department of Transportation (Caltrans). (2016). *Seismic design specifications for steel bridges*, Second Version, Sacramento, CA.

Chopra, A. K., & Chintanapakdee, C. (2001). Comparing response of SDF systems to near-fault and far-fault earthquake motions in the context of spectral regions. *Earthquake Engineering and Structural Dynamics, 30,* 1769–1789.

Chopra, A. K., & Goel, R. K. (1999). Capacity-demand-diagram methods based on inelastic design spectrum. *Earthquake Spectra, 15*(4), 637–656.

Fajfar, P. (1999). Capacity spectrum method based on inelastic demand spectra. *Earthquake Engineering and Structural Dynamics, 28,* 979–993.

Federal Emergency Management Agency (FEMA). (1997). *NEHRP guidelines for the seismic rehabilitation of buildings* (Report FEMA 273). Washington, DC.

Federal Emergency Management Agency (FEMA). (2004). *NEHRP recommended provisions for seismic regulations for new buildings and other structures* (Report FEMA 450). Washington, DC.

Federal Emergency Management Agency (FEMA). (2005). *Improvement of inelastic seismic analysis procedures* (Report FEMA 440) Washington, DC.

Federal Highway Administration (FHWA). (2006). *Seismic retrofitting manual for highway structures: Part 1-bridges*, FHWA-HRT-06-032, McLean, VA.

Iervolino, I., & Cornell, C. A. (2008). Prediction of the occurrence of velocity pulses in near-fault ground motions. *Bulletin of the Seismological Society of America, 98*(5), 2262–2277.

Miranda, E. (1993). Evaluation of site-dependent inelastic seismic design spectra. *Journal of Structural Engineering (ASCE), 119*(5), 1319–1338.

Miranda, E. (2000). Inelastic displacement ratios for structures on firm sites. *Journal of Structural Engineering (ASCE), 126*(10), 1150–1159.

Miranda, E. (2001). Estimation of inelastic deformation demands of SDOF systems. *Journal of Structural Engineering (ASCE), 127*(9), 1005–1012.

Ou, Y. C., Song, J., Wang, P. H., Adidharma L., Chang, K. C., & Lee GC. (2014). Ground motion duration effects on hysteretic behavior of reinforcement concrete bridge columns. *Journal of Structural Engineering (ASCE), 140*(3). https://doi.org/10.1061/(asce)st.1943-541x.0000856.

Pacific Earthquake Engineering Research Center (PEER). (2003). *PEER structural performance database*. https://nisee.berkeley.edu/spd/index.html.

Pacific Earthquake Engineering Research Center (PEER). (2013). *PEER ground motion database*. http://ngawest2.berkeley.edu/.

Park, Y. J., & Ang, A. H. S. (1985). Mechanistic seismic damage model for reinforced concrete. *Journal of Structural Engineering (ASCE), 111*(4), 722–739.

Reinhorn, A. M. (1997). Inelastic analysis techniques in seismic evaluations. In Krawinkler and Fajfar (Eds.), *Seismic design methodologies for the next generation of code* (pp. 277–287) Balkema, Rotterdam.

Ruiz-Garcia, J. (2011). Inelastic displacement ratios for seismic assessment of structures subjected to forward-directivity near-fault ground motions. *Journal of Earthquake Engineering, 15,* 449–468.

Ruiz-Garcia, J., & Miranda, E. (2003). Inelastic displacement ratios for evaluation of existing structures. *Earthquake Engineering and Structural Dynamics, 32,* 1237–1258.

Shimazaki, K., & Sozen, M. A. (1984). *Seismic drift of reinforced concrete structures* (pp. 145–165). Tokyo, Japan: Technical Research Reports of Hazama-Gumi Ltd.

The European Standard (British Standard). (2005). Eurocode 8- *Design of structures for earthquake resistance-part 2*: Bridges, EN 1998-2.

Tothong, P., & Cornel, C. A. (2007). *Probabilistic seismic demand analysis using advanced ground motion intensity measures, attenuation relationships, and near-fault effects*, Pacific Earthquake Engineering Research Center, Report PEER 2006/11.

Veletsos, A. S., Newmark N. M., & Chelapati, C. V. (1965). Deformation spectra for elastic and elastoplastic systems subjected to ground shock and earthquake motions. In *Proceedings, 3rd Word Conference on Earthquake Engineering*, Vol. II (pp. 663–682). New Zealand.

Vidic, T., Fajfar, P., & Fischinger, M. (1994). Consistent inelastic design spectra: strength and displacement. *Earthquake Engineering and Structural Dynamics, 23,* 507–521.

Wang, P. H. (2017). *A new smooth hysteretic model and capacity-based displacement spectrum for reinforced concrete bridge columns*. Ph.D. Thesis, National Taiwan University, Taiwan.

Wang, P. H., Ou, Y. C., & Chang, K. C. (2017). A new smooth hysteretic model for ductile flexural-dominated reinforced concrete bridge columns. *Earthquake Engineering and Structural Dynamics, 46,* 2237–2259.

Wen, Y. K. (1976). Method for random vibration of hysteretic systems. *Journal of the Engineering Mechanics Division (ASCE), 102,* 249–263.

Whittaker, A., Constantinou, M., & Tsopelas, P. (1998). Displacement estimates for performance-based seismic design. *Journal of Structural Engineering (ASCE), 124*(8), 905–912.

Chapter 20
Issues Related to the Rapid Seismic Repair of Concrete Bridge Columns

Zachary Krish and Mervyn Kowalsky

Presented in this paper is research aimed at challenging the assumption that severely damaged reinforced concrete bridge columns are not easily repaired. An experimental program was conducted in which six large-scale bridge columns exhibiting buckled and fractured reinforcement were repaired using plastic hinge relocation and conventional materials. Discussion of several repair methods is presented along with the introduction of a simplified analytical approach by which the repair can be designed, and repaired member performance obtained. In addition, the implications of the availability of such a repair method on the limits of residual drift in a damaged system are explored.

20.1 Introduction

The aftermath of large earthquakes is often associated with imagery of collapsed buildings and bridges, such as the I-5 interchange in the 1994 Northridge earthquake and the complete failure of the Hanshin expressway overpass in the 1995 Kobe earthquake, as illustrated in Fig. 20.1a, b respectively. However, modern seismic design implements performance-based earthquake engineering (PBEE) and capacity design principles (Paulay and Priestley 1992; Priestley et al. 1996), allowing structures to sustain much greater deformations prior to collapse than their predecessors. In reinforced concrete (RC) bridges, these designs typically rely on inelastic deformation through the formation of plastic hinges in the columns as the primary means of dissipating seismic forces. Although the intent is that the structure

Z. Krish (✉) · M. Kowalsky
North Carolina State University, 2501 Stinson Dr, Raleigh, NC 27606, USA
e-mail: zfkrish@ncsu.edu

M. Kowalsky
e-mail: kowalsky@ncsu.edu

T. T. C. Hsu (ed.), *Concrete Structures in Earthquake*,
https://doi.org/10.1007/978-981-13-3278-4_20

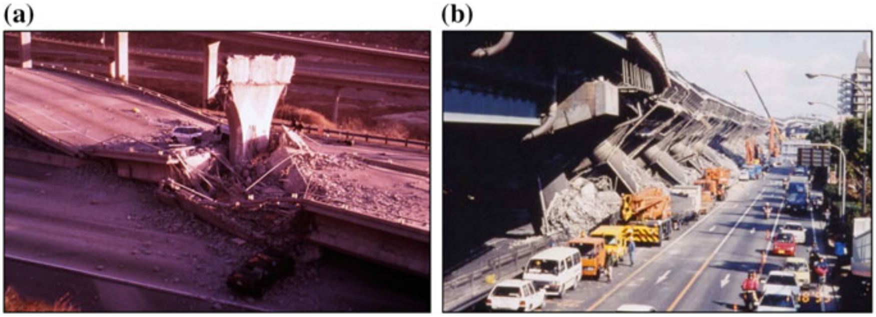

Fig. 20.1 **a** Collapse of I-5 interchange during 1994 Northridge earthquake and **b** collapse of 18 individual bridge piers on the Hanshin expressway during the 1995 Kobe earthquake

as a whole remains intact, the plastic hinge regions can accumulate extensive local damage during large earthquakes including buckling and fracture of longitudinal steel, fracture of transverse steel, and crushing of the concrete core. Once bar buckling occurs, repair of the structure is typically not considered feasible since the strain capacity of the existing hinge has been drastically reduced leaving the column vulnerable to collapse in a future earthquake. Current design guides are limited to solutions for retrofitting existing structures to achieve the performance of modern designs (ACI Committee 341 2007), or to repair those that have undergone lesser damage (ACI Committee 546 2014). Without reliable methods of repairing such damage, these structures are likely to be demolished and reconstructed as the cost to replace portions of the columns can be prohibitive.

Recent research demonstrates the feasibility of a repair technique, called plastic hinge relocation, in which the existing plastic hinge is strengthened such that it remains elastic and future inelastic action is forced to a prescribed, undamaged location in the column (Lehman et al. 2001; Rutledge et al. 2014; Parks et al. 2016). Figure 20.2 illustrates an example of this, where damage in the original column on the left is concentrated at the footing-column interface, whereas a second hinge forms in the repaired specimen above the repair. Previous studies document successful results of this repair method, using a wide variety of materials and configurations, thus establishing plastic hinge relocation as a viable option for the repair of extensively damaged columns. For example, Lehman et al. (2001) uses an enlarged reinforced concrete section with steel spiral to strengthen the damaged region, whereas Parks et al. (2016) uses a CFRP shell as the transverse reinforcement and Rutledge et al. (2014) uses CFRP fan anchors and CFRP confinement wraps. Each approach achieved the desired outcome; however, the mechanisms by which each repair operates vary significantly, particularly that of the CFRP fan anchors. Furthermore, there are but a limited number of tests available in the literature on which to base reliable design recommendations. The research presented in this paper serves to dramatically increase the available data set through experimental testing of six large-scale bridge columns, with repairs focusing on rapid deployment and the use of conventional RC materials. An introduction of an

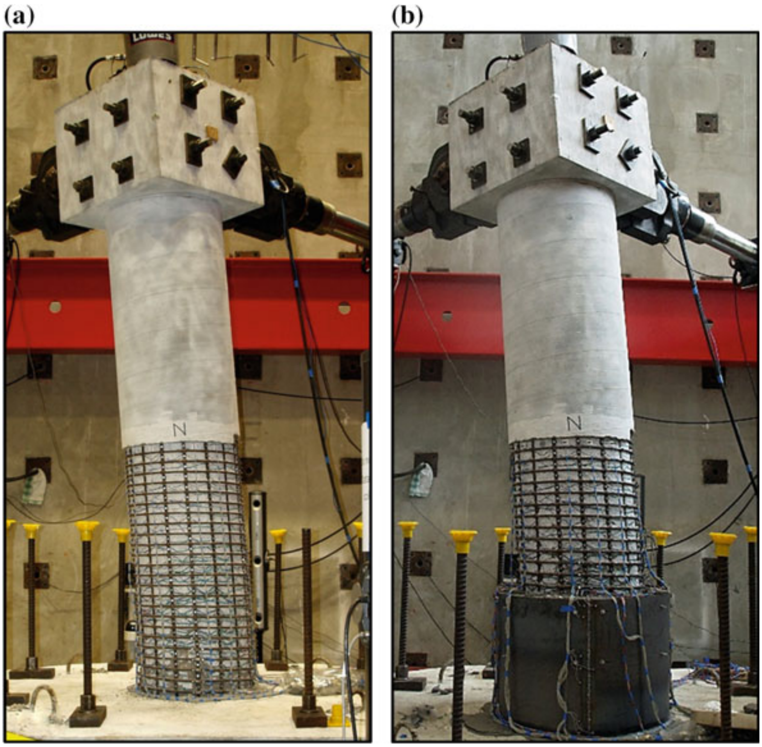

Fig. 20.2 Plastic hinge **a** at column-footing interface of originally tested column; **b** relocated above repair in repaired and retested column

analytical model, which provides the necessary tools to reliably design this repair and obtain accurate global and local response parameters for use in PBEE applications, is also discussed. An application of this model is currently in progress, in which the limits of residual drift are examined when considering this type of repair. A brief discussion of the philosophy and goals of this research is also provided.

20.2 Experimental Program

Each of the six repaired columns were designed, constructed and previously tested as part of a separate research program (Goodnight et al. 2017), under which they were exposed to a bidirectional cyclic loading history through failure. The typical damage state at the conclusion of each initial test included buckling in the majority of the longitudinal bars and some bar fractures. To investigate more severe damage states, additional damage was imposed manually prior to the installation of the repair. Each column specimen is 108 inches tall from the top of footing to the center of loading with an outer diameter of 24 inches $(L/D = 4.56)$ and axial load of 191

Table 20.1 Column repair test matrix

	Repair #:	1	2	3	4	5	6
Original column	Long. steel ρ_l	(16) #7 2.1%	(16) #7 2.1%	(16) #7 2.1%	(16) #6 1.6%	(16) #6 1.6%	(16) #7 2.1%
	σ_y (ksi)	71.2	71.2	71.2	70.3	70.3	69.6
	σ_u (ksi)	97.9	97.9	97.9	98.7	98.7	96.7
	Trans. steel ρ_v	#3 @ 2in. 1.0%	#3 @ 2in. 1.0%	#3 @ 2in. 1.0%	#3 @ 2.75 in. 0.7%	#3 @ 2in. 1.0%	#3 @ 1.5in. 1.3%
	σ_y (ksi)	67.6	67.6	67.6	63.9	63.9	69.6
	σ_u (ksi)	105.6	105.6	105.6	93.6	93.6	96.7
	Column f'_c (ksi)	7.81	7.68	7.60	6.13	6.11	6.13
	Damage state	All long. bars buckled	3 extreme fiber bars on N & S faces fractured, all other bars buckled	All long. bars buckled, spiral fracture, initial torsional deformation	Extreme fiber bar on S face fractured, all other bars buckled	2 bars on E face and 1 on W face fractured, all others buckled, 1.5% residual drift in W direction	3 extreme fiber bars on N & S faces fractured, all other bars buckled
Repair	Long. steel	(12) #10	(12) #10	(16) #7	(12) #7	(16) #7	(12) #10
	σ_y (ksi)	83.6	83.6	90.1	84.3	83.2	83.6
	Trans. steel ρ_v	11ga A36 steel sleeve 1.5%	11ga A36 steel sleeve 1.5%	11ga A36 steel sleeve 1.5%	#3 @ 1.5in 1.0%	11ga A36 steel sleeve 1.5%	11ga A36 steel sleeve 1.5%
	σ_{yv} (ksi)	43.0	43.0	43.0	67.5	48.2	48.2
	Backfill material	Grout	Grout	Grout	Ready-Mix Concrete	Ready-Mix Concrete	Concrete/ Grout
	Repair f'_c (ksi)	8.20	7.20	7.96	4.84	3.84	4.86 11.3

kips $\left(P/f_c'A_g \approx 7.0\%\right)$. The longitudinal and transverse steel content of each column and repair varied between tests, along with the imposed damage state. A summary of these details is provided in Table 20.1.

20.2.1 Repair Design

The intent of plastic hinge relocation as a repair method is to strengthen the damaged region such that it remains elastic under future earthquake loading and force a new plastic hinge to form elsewhere in the member. Assuming that the reinforcement of the original column is uniform over its length, this results in a redistribution of forces with the ultimate moment of the original column, M_o, occurring at the new plastic hinge location as illustrated in Fig. 20.3. For a simple cantilever system, this corresponds to an increased moment demand at the base of the column, M_R, which is calculated from Eq. (20.1), and an increase in the overall shear force in the system, calculated from Eq. (20.2).

$$M_R = \frac{M_o \cdot L_C}{L_C - L_R} \tag{20.1}$$

$$V_R = \frac{M_o}{L_C - L_R} \tag{20.2}$$

Note that the force demand in the system increases with a greater repair length, thus making it desirable to minimize the height of the repair to achieve the most

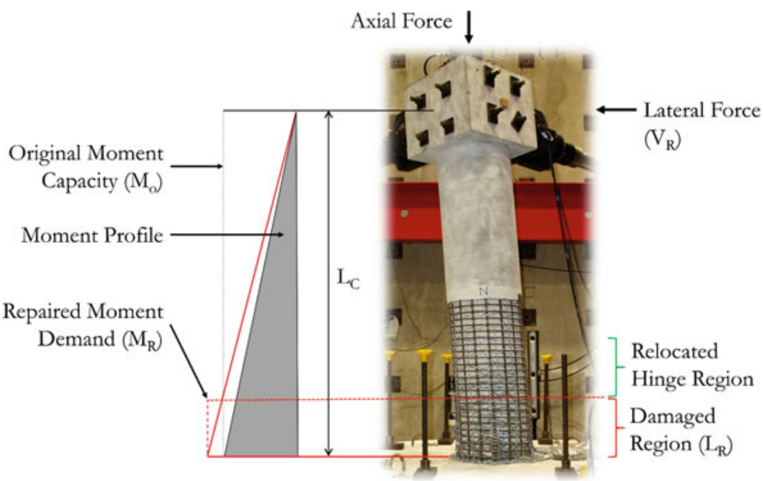

Fig. 20.3 Repaired specimen moment distribution

economical design. The factors which drive the repair height include bond development of the new repair bars and prior damage state of the new hinge location. The development conditions of the repair bars inside of the grouted sleeve are assumed similar to that of reinforcing bars in the grouted pocket connection used in Accelerated Bridge Construction (ABC), for which Eq. (20.3) applies (Matsumoto et al. 2001).

$$l_d = \frac{0.022 d_b f_y}{\sqrt{f_c'}} \geq 18in \,(\text{lbs, in}) \tag{20.3}$$

To ensure that the new hinge is located in a region of sufficiently low damage, the peak prior tension strain was limited to 0.02. This was accomplished for the experimental tests by directly checking the strain distribution in the longitudinal bars to ensure this limit was not exceeded at the new hinge location, as illustrated in Fig. 20.4.

Each repair was designed to resist the base demand moment demand, M_R, elastically assuming composite section behavior between the original column and repair. A moment-curvature analysis was conducted in which the cross section contained both the original column reinforcement and the newly installed repair bars and the moment capacity determined as that which limited the strains in the repair bars to 0.002. The modulus of the original longitudinal bars was reduced to 20% of its original value, as recommended by Vosooghi and Saiidi (2010) for severely damaged reinforcement, whereas that of the repair bars was assumed to be 29,000 ksi. While the resulting repair proved to be sufficient, analysis of the experimental results indicates that the assumption of composite section behavior between the original column and repair was not accurate. Further discussion of these observations, along with a proposed alternative design model, is provided later in this paper.

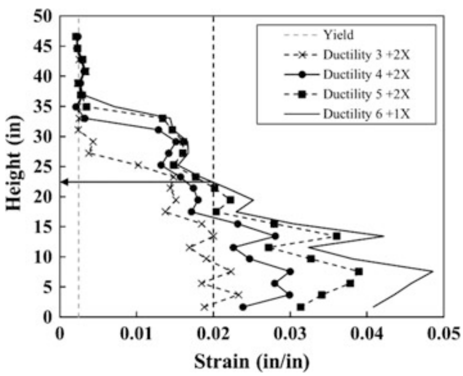

Fig. 20.4 Tension strain distribution of Load Path Test 4. Figure adapted from Goodnight et al. (2017)

20.2.2 Repair Construction

Each repair was constructed using similar methods, except for Repair #4 which uses discrete rebar hoops with welded lap splices in place of a continuous steel sleeve. The installation process is illustrated in Fig. 20.5 and summarized as follows: First, vertical holes are hammer drilled into the footing at locations of the new longitudinal reinforcement. The straight rebar sections are then installed in the footing using a two-part epoxy system and extend above the footing along the height of the repair. Next, two steel sheets, which are rolled to the outer diameter of the repair, are placed around the base of the column. Both seams are then butt-welded over their entire height to create a continuous steel sleeve acting as both a permanent form work and transverse reinforcement. The void space between the steel sleeve and original column is backfilled with either grout or concrete to complete the repair. Depending on the condition of the footing at the location at which the steel sleeve is to be placed, it may be necessary to first patch the footing so that a proper seal can be provided at the sleeve's base. This repair can be completed within a matter of hours with the structure back in service shortly thereafter.

20.2.3 Test Procedure

The original specimens were each tested under different bidirectional loading protocols during a prior study, however, all repaired columns were subjected to the same bidirectional two-cycle set, beginning with single cycles at $1/2\Delta'_y$ and Δ'_y followed by two-cycle sets for displacement ductilities $\mu_{\Delta 1}$, $\mu_{\Delta 1.5}$, $\mu_{\Delta 2}$, $\mu_{\Delta 3}$, $\mu_{\Delta 4}$, $\mu_{\Delta 5}$, and $\mu_{\Delta 6}$.

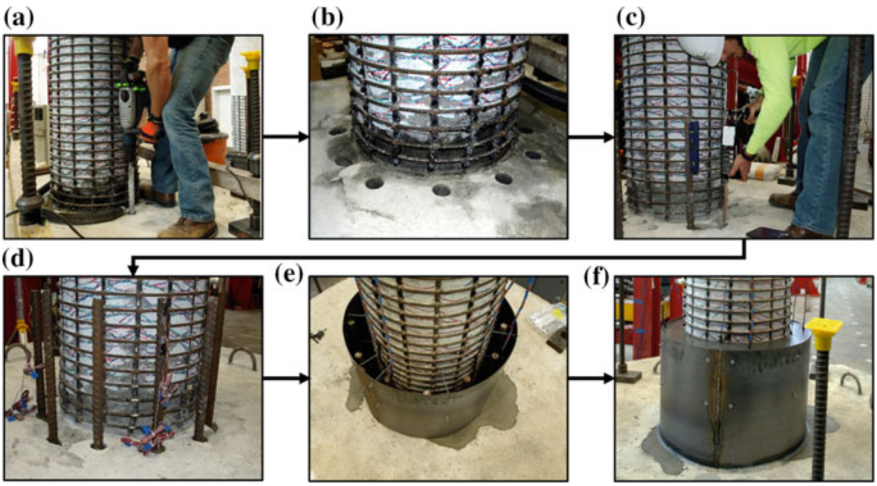

Fig. 20.5 Typical construction sequence of plastic hinge relocation repair

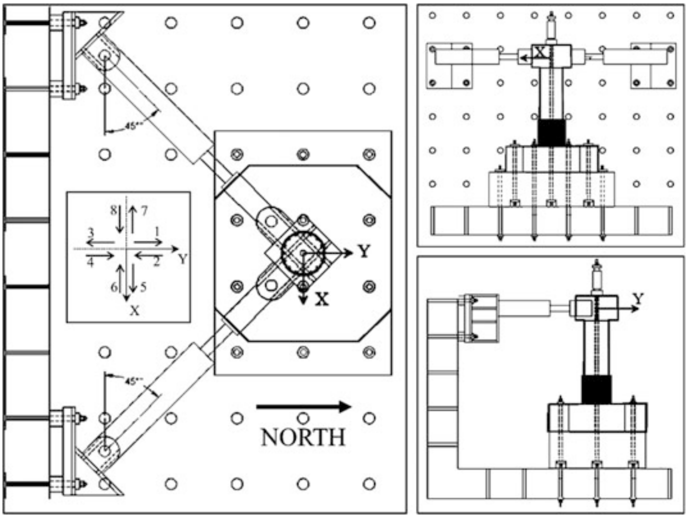

Fig. 20.6 Test specimen orientation and laboratory layout

The orientation of the specimen and defined coordinates are shown in Fig. 20.6 along with the order of loading. For ease of comparison between original column performance and repaired column performance, displacement ductilities are defined based on those calculated for the original columns. Specimens were loaded in the horizontal direction via two 220-kip hydraulic actuators, forming a 45-45-90 triangle with the lab strong wall allowing for top of column movement in any direction within the X-Y plane. Axial load was applied via a single hydraulic jack placed on a spreader plate on top of the column and maintained constant throughout the duration of the test.

20.2.4 Results

The primary goal of each test was to restore the original column's strength and displacement capacity using the plastic hinge relocation method. With regards to this overall goal, each repair performed well and attained at least one of these targets with the majority achieving both. Table 20.2 summarizes the performances of the repaired columns as compared to those of the originals. The discussion below outlines typical trends that arose over the course of the tests and eventually led to the development of the analytical model that is introduced in the following section. A more detailed assessment of each repair is provided in a separate paper titled "Seismic Repair of Circular Reinforced Concrete Bridge Columns by Plastic Hinge Relocation with Grouted Annular Ring" which is currently under peer review (Krish, Kowalsky, and Nau 2018).

Table 20.2 Summary of original and repaired column performance

	Repair #:	1	2	3	4	5	6
Original column	Δ_{max} (in.)	8.24.	8.25	8.24	7.35	8.57	8.83
	F_{max} (kips)	79.9	78.0	77.7	62.4	64.2	79.9
	$\varepsilon_{t,\ max}$	0.044	0.049	0.047	0.034	0.051	0.053
	$\mu_{\Delta,\ max}$	6	6	6	6	7	6.5
Repair	Δ_{max} (in.)	8.31	8.28	6.88	7.51	5.0	8.9
	F_{max} (kips)	95.1	86.2	80.6	75.4	73.2	93.1
	$\mu_{\Delta,\ max}$	6	6	5	6	4	6.5

Each test resulted in a new plastic hinge forming above the repair, except for Repair #5 which failed prematurely through fracture in the steel sleeve due to a faulty weld. Of the remaining tests, damage progressed in the new hinge region at intervals comparable to that of the original column with onset of core crushing during displacement ductility 3 followed by visible bar buckling in either ductility 5 or 6 and concluding with bar fracture. Examples of typical damage are provided in Fig. 20.7.

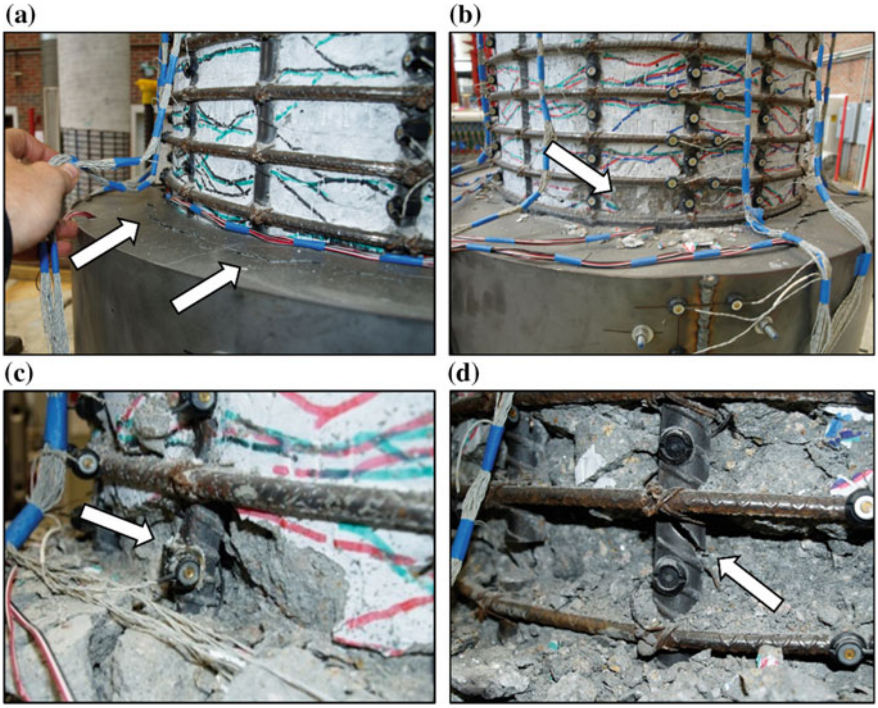

Fig. 20.7 Typical progression of damage: **a** cracking of top repair surface, **b** core crushing, **c** bar buckling and deterioration of top repair surface, and **d** bar fracture

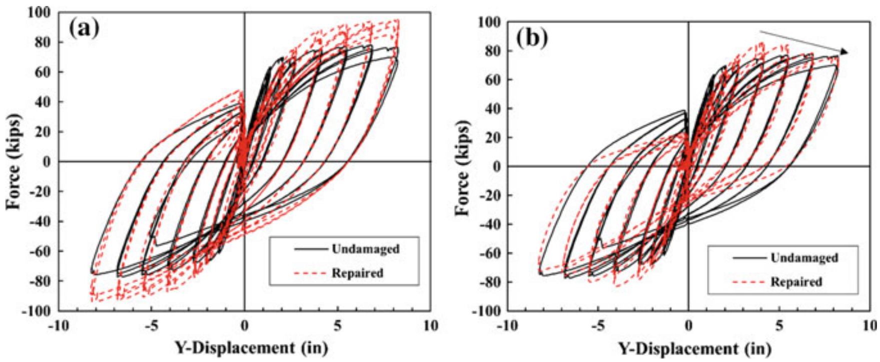

Fig. 20.8 Global force versus displacement response comparison of **a** Repair #1 and **b** Repair #2

The global force response of each repaired column increased as predicted. Figure 20.8 compares the force versus displacement hysteresis in the Y-directions for Repair #1 and #2 to that of an identical column exposed to the same displacement history. Note that Repair #1 considered only buckled bars in the damaged column, whereas Repair #2 had the three extreme fiber bars fractured on the North and South faces. Each specimen was capable of restoring the overall displacement capacity of the original column; however, the softening response of Repair #2 is attributed to the debonding of the fractured bars within the repair as the test progressed beyond displacement ductility three. This behavior is evident in Fig. 20.9b which plots the South longitudinal bar strains in the relocated hinge region (labeled 'S G-2') against the top of column displacement. The tension strains tend to increase with each cycle up to approximately 0.01 through a displacement of about 5 inches, at which point they sharply drop off, indicating that they are no longer carrying any load. This loss of load carrying capacity corresponds directly to the onset of softening response seen in Fig. 20.8b. Compare this to the strains in the same location of Repair #1, shown in Fig. 20.9a, where the tension strains continue to increase through the entire test until buckling eventually occurs.

Figure 20.9a also shows the strains in the original column and repair bars at the footing interface, labeled 'S O-1' and 'S R-4' respectively. Recall that one of the initial design assumptions was that the repair and original column behave as a fully composite cross section at the footing interface, implying that the strains in the original column bars would be lower than those of the repair bars since they are closer to the neutral axis. However, the data shows that the peak strains in the repair bars were approximately 0.001 whereas those in the original column at the same location approached 0.006. Furthermore, the anticipated strains in the repair bars were approximately 0.002, or right at yield for a Grade 60 bar, indicating that the original column is not only deforming more than anticipated, but also carrying more of the load than expected as well. In conclusion, the repair is performing as intended; however, the model by which it was initially designed does not accurately predict the behavior of the repaired system.

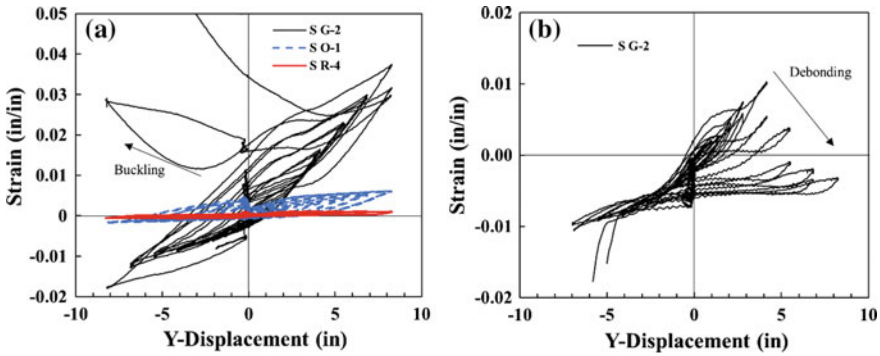

Fig. 20.9 Longitudinal strain versus displacement response on South face of **a** Repair #1 and **b** Repair #2

20.3 Analytical Model

An analytical design model was developed to address the inconsistencies of the original design assumptions described in the previous section. The details provided herein are intended to give a general understanding of the concepts considered. A more complete description will be provided in the previously mentioned publication currently under peer review (Krish et al. 2018) that is currently in progress with plans to be submitted to the *ASCE Journal of Bridge Engineering*.

Performance-based design of RC bridges requires that the designer understands how the structure behaves during an earthquake and can accurately predict key modes of failure. Calculation of the nonlinear force-displacement response of typical RC bridge columns normally follows the well-established plastic hinge method laid out by Priestley et al. (2007). This procedure idealizes the nonlinear curvature profile, as illustrated in Fig. 20.10, and relates the global force and displacement response of the column to the local strains in the plastic hinge region. The model also includes a strain penetration component that accounts for additional rotation at the adjoining member interface; however, this assumes the relative stiffness of the adjoining member is far greater than that of the column resulting in superior bond conditions.

The principles of this method have also been adapted by Hose et al. (1997) for use in columns which are designed such that the plastic hinge forms away from the adjoining member connection, as shown in Fig. 20.11. While this model accounts for increased strain penetration due to lower relative stiffness of the adjoining member, it requires continuous flexural development of the column through the strengthened section which has been shown not to occur in the repair.

The basis of the proposed model recognizes and addresses this through a unique application of the existing plastic hinge method. The key assumption of this method is that the repair does not act to strengthen the damaged column, but instead changes the support boundary conditions resulting in a redistribution of forces and

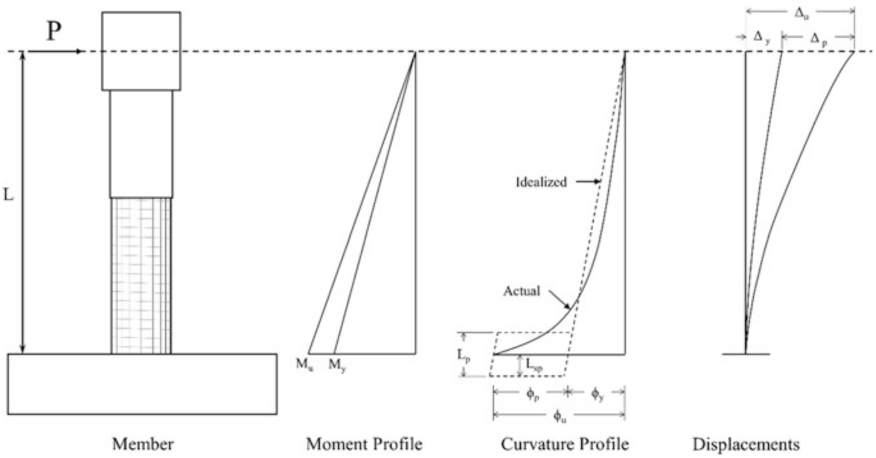

Fig. 20.10 Force and deformation profile for typical single bending column. Adapted from Priestley, Calvi, and Kowalsky (2007)

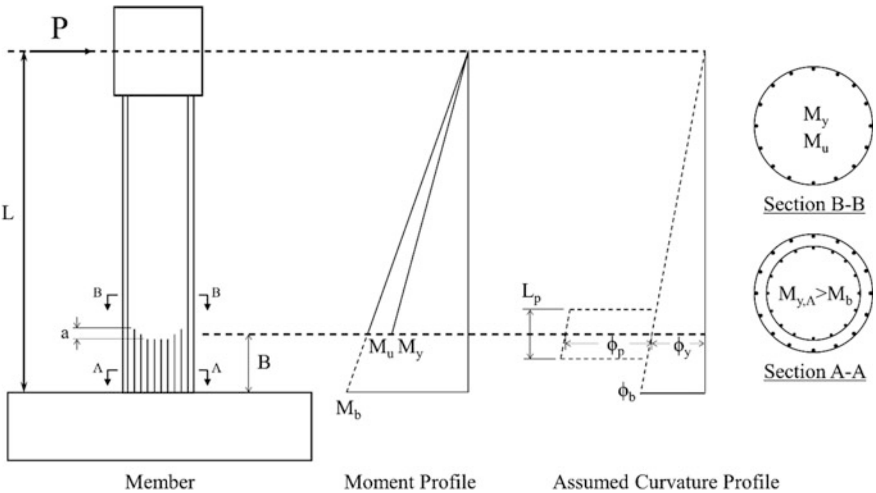

Fig. 20.11 Assumed force and deformation profile in column with plastic hinge located away from footing interface. Adapted from Hose et al. (1997)

deformations within the original member. To illustrate this, consider the series of structural systems depicted in Fig. 20.12.

System (a) is a simply supported column with a single point load applied at the center of the span. The deformation, moment, and elastic curvature profiles are shown along with a plastic curvature profile that develops if the moment exceeds the yield capacity of the member. Recognizing this as a symmetrical system allows for reduction of the model to that shown in system (b), where the mid-span is free to

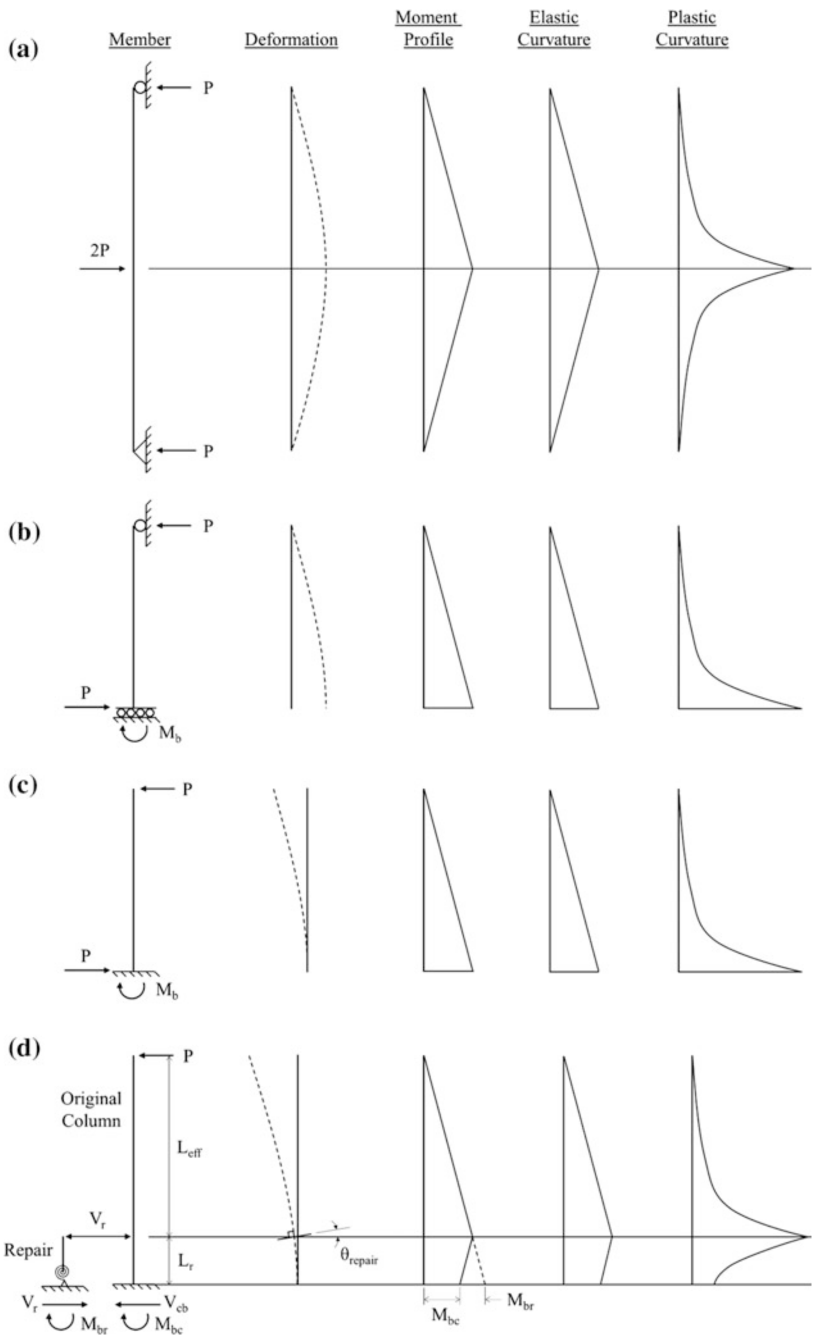

Fig. 20.12 Derivation of mirrored plasticity model through symmetry of simply supported beam system

translate, but rotation is restrained to zero. The force and deformation profiles of system (b) are identical to that of the cantilever column shown in system (c). Finally, system (d) moves the fixed reaction of system (c) down a distance L_r from the mid-span, but provides a flexible reaction at the previous support location with stiffness such that the rotation at this point, θ_{repair}, is equal to that which results at a point L_r from the mid-span of system (a). A rigid link supported by a rotational spring provides the flexible reaction to the member and represents the repair applied to the base of the column. The force transferred at this reaction, V_r, and resulting moment in the rotational spring, M_{br}, represent the design shear force and base moment of the repair respectively. Furthermore, the total rotation at the top of the repair, θ_{repair}, represents the sum of contributions from rotation of the column inside the repair, strain penetration of the column into the footing, and rigid body rotation of the repair, thus accounting for each of the unknown components of deformation. Note also that the sum of the repair moment, M_{br}, and the base column moment, M_{bc}, equal the total extrapolated column moment. Therefore, the necessary quantities for the design of the repair can be directly and easily obtained by describing the repaired system through fundamental principles.

The displacement response of the column is found through application of the moment-area method to the idealized curvature distribution illustrated in Fig. 20.13. The existing plastic hinge method applies to the deformations above the repair. The column rotation within the repair is then taken as the integration of elastic and plastic curvatures between the footing and top of the repair. Strain penetration into the footing is then accounted for by multiplying L_{sp} by the resulting base curvature. Finally, deformation from rigid rotation of the repair is calculated

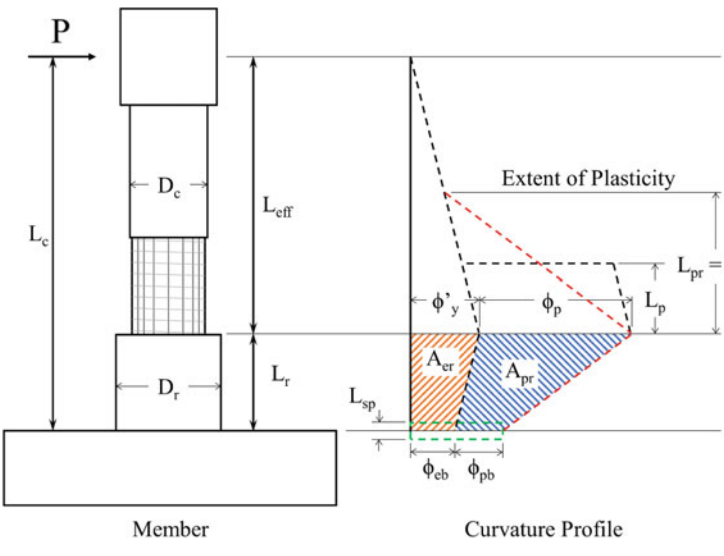

Fig. 20.13 Idealization of repaired column curvature distribution with mirrored plasticity

from the repair moment demand, M_{br}, assuming cracked section properties of the annular ring.

Figure 20.14 illustrates the accuracy of the proposed Mirrored Plasticity Method (MPM), so named for the symmetry of deformation about the top of the repair, in predicting the overall member response of Repairs #1 and #2. The displacement capacity is determined as that at which the tension strain in the longitudinal steel reaches the damage control limit state as defined Goodnight et al. (2015). The predicted buckling strain for each column was 0.041, corresponding to a displacement of Δ_u = 7.60in for Repair #1. This falls directly between $\mu_{\Delta 5}$ and $\mu_{\Delta 6}$ of the experiment, where buckling was observed following the first cycle of $\mu_{\Delta 6}$ = 8.22 in. Note that there are two bounding solutions for Repair #2, with the upper bound assuming all fractured bars remain bonded and the lower bound assuming all fractured bars debond and no longer contribute to the member response. While the model is not capable of predicting the exact behavior of the member as the fractured bars debond, it shows the member response initially following that of the fully bonded system and then softening to approach that of the unbonded system as the test progresses.

Figure 20.15 illustrates the local strains in the relocated plastic hinge as compared to those predicted by the MPM. For Repair #1, the profile of the predicted tension strains match very closely with those measured in the South bar during the test and the predicted peak tension strain prior to bar buckling was in line with that which was observed. Similar results were observed for the East bar in Repair #2, as shown in Fig. 20.15b.

The model is also capable of predicting the strains in the repair bars, as shown in Fig. 20.16. To obtain these values, the calculated proportion of the base moment carried by the repair, M_{br}, is compared to the moment-curvature response of the repair cross section and the resulting strains identified. Thus, the assumed moment

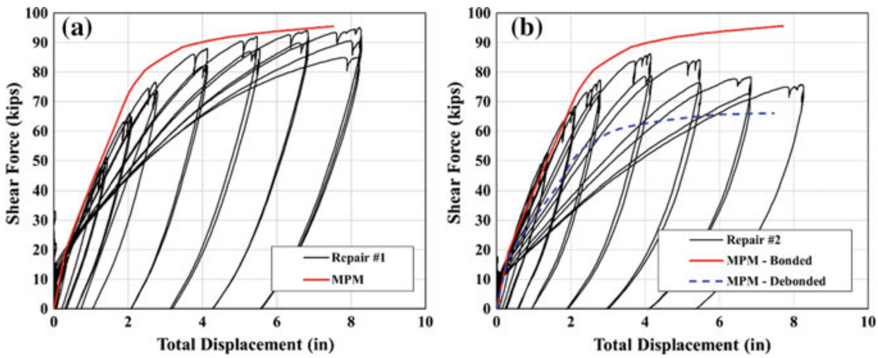

Fig. 20.14 Force versus displacement response with comparison to MPM prediction for **a** Repair #1 and **b** Repair #2

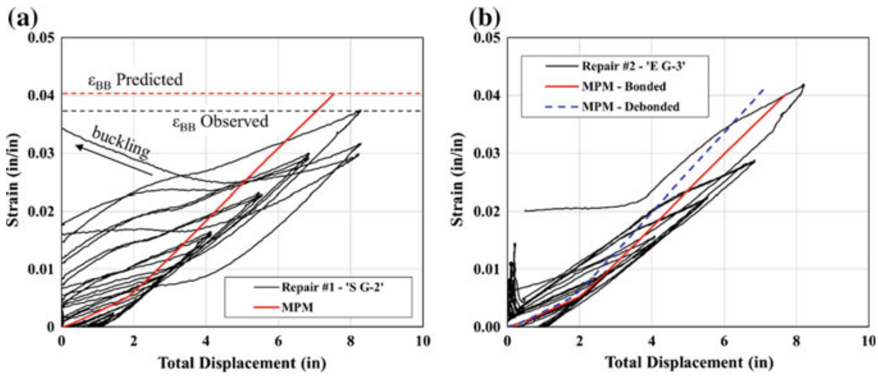

Fig. 20.15 Strain versus displacement response in relocated hinge with comparison to MPM prediction for **a** Repair #1 and **b** Repair #2

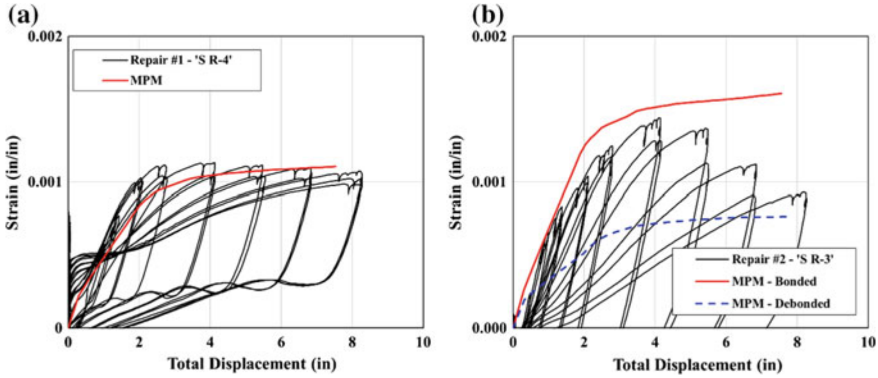

Fig. 20.16 Strain versus displacement response in repair bars with comparison to MPM prediction for **a** Repair #1 and **b** Repair #2

distribution between the original column and repair appears to be validated, whereas the composite cross-sectional assumption grossly over-estimated the demand in the repair bars. Again, for Repair #2, there are two bounding solutions for the demand in the repair bars, with the measured response initially following that of the fully bonded system and then degrading to approach that of the unbonded system as the test progresses.

20.4 Conclusions and Future Work

This paper presents the results of an experimental program in which damaged RC bridge columns with buckled and fractured longitudinal bars are repaired using a plastic hinge relocation method. The repair technique considered is rapidly deployable and utilizes conventional RC materials such as rebar, two-part epoxy, steel sleeves, and concrete or prepackaged grout. It has been shown that this repair method is capable of restoring the original strength and displacement capacity to that of the system; however, underlying assumptions on the mechanics of the repair behavior proved to be incorrect.

As a result, a novel analytical model was developed based upon fundamental engineering principles and existing well-established analytical methods. This model recognizes that the annular repair section does not actually strengthen the damaged column, but instead only provides confinement and acts as a socket against which the original column bears thus modifying the boundary conditions of the system. The distribution of plasticity in the new plastic hinge is then assumed to be mirrored about the axis at the top of the repair with resulting deformations found via the moment-area method. This model was then shown to provide accurate predictions of the global member response and local strains in both the relocated plastic hinge and annular repair cross section.

The next step of this research project, which is currently underway, is to extend the described analytical model to a simple computational model capable of considering dynamic earthquake loading. This model will then be used in a study to investigate the impact of residual drift on a system which has been repaired using the plastic hinge relocation method proposed in this paper. The model will consider increasing levels of residual drift and will be exposed to a suite of unscaled ground motions with a range of hazard parameters. The anticipated result will be a definition of residual drift limits based on specifics of the structure and seismic hazard, as opposed to the prescriptive universal limits that currently exist in practice. These existing limits imply that residual drift is indicative of damage to the structure which is beyond the scope of repair. However, the research presented in this paper has shown that even the most extreme levels of damage can be effectively repaired assuming the structure is otherwise intact. Therefore, it is desirable to provide residual drift limits which are consistent with this definition of repairability. Upon completion, this study is expected to be published in the EERI professional journal *Earthquake Spectra*.

Acknowledgements The authors would like to thank the Alaska Department of Transportation for providing the funding for this research, particularly Mr. Elmer Marx for his engagement throughout the research, as well as the entire technical staff at the Constructed Facilities Laboratory at NC State University. We would also like to thank Edwards, Inc. for providing certified welders and the North Carolina Department of Transportation for providing weld inspections on this project.

References

ACI Committee 341. (2007). *ACI 341.3R-07 seismic evaluation and retrofit techniques for concrete bridges.* Farmington Hills, MI: American Concrete Institute.

ACI Committee 546. (2014). *ACI 546R-14 guide to concrete repair.* Farmington Hills, MI: American Concrete Institutue.

Goodnight, J. C., Kowalsky, M. J., & Nau, J. M. (2015). *The effects of load history and design variables on performance limit stats of circular bridge columns* (AKDOT Report No. 4000 (072)). Raleigh, NC: Department of Civil Engineering, North Carolina State University.

Goodnight, J. C., Kowalsky, M. J., & Nau, J. M. (2017). *Seismic load path effects in reinforced concrete bridge columns and wall piers, Volume 1: Strain limit states for RC bridge columns* (AKDOT Report No. 4000(134)). Raleigh, NC: Department of Civil Engineering, North Carolina State University.

Hose, Y. D., Priestley, M. J. N., Seible, F. (1997). *Strategic relocation of plastic hinges in bridge columns* (Caltrans Report No. SSRP-97/05). San Diego, La Jolla, CA: Division of Structural Engineering, University of California.

Krish, Z. F., Kowalsky, M. J., Nau, J. M. (2018). Seismic repair of circular reinforced concrete bridge columns by plastic hinge relocation: experimental observations. *Submitted to Journal of Earthquake Engineering.*

Lehman, D. E., Gookin, S. E., Nacamull, A. M., & Moehle, J. P. (2001). Repair of earthquake-damaged bridge columns. *ACI Structural Journal, 98*(2), 233–242.

Matsumoto, E. E., Waggoner, M. C., Sumen, G., Kreger, M. E., Wood, S. L., & Breen, J. E. (2001). *Development of a precast bent cap system* (FHWA Report No. TX-0-1748-2). Austin, TX: Center for Transportation Research, The University of Texas.

Parks, J. E., Brown, D. N., Ameli, M. J., & Pantelides, C. P. (2016). Seismic repair of severely damaged precast reinforced concrete bridge columns connected with grouted splice sleeves. *ACI Structural Journal, 113*(3), 615–626.

Paulay, T., & Priestley, M. J. N. (1992). *Seismic design of reinforced concrete and masonry buildings*. New York: Wiley.

Priestley, M. J. N., Calvi, G. M., & Kowalsky, M. J. (2007). *Displacement based seismic design of structures*. Pavia, Italy: IUSS Press.

Priestley, M. J. N., Seible, F., & Calvi, G. M. (1996). *Seismic design and retrofit of bridges*. New York: Wiley.

Rutledge, S. T., Kowalsky, M. J., Seracino, R., & Nau, J. M. (2014). Repair of reinforced concrete bridge columns containing buckled and fractured reinforcement by plastic hinge relocation. *Journal of Bridge Engineering, 19*(8), A4013001.

Vosooghi, A., Saiidi, M. S. (2010). Seismic damage states and response parameters for bridge columns. *American Concrete Institute—Special Publication 271*: 29–46.

Chapter 21
Seismic Performance of Rehabilitated RC Columns Using Material Testing Integrated (MTI) Simulation

Donghyuk Jung and Bassem Andrawes

There is growing interest in the seismic application of shape memory alloys (SMAs) in concrete structures. However, for the seismic performance of such new class of materials with complex thermomechanical behavior to be fully understood, more advanced simulation tools are required. This study focuses on investigating the application of thermally prestressed SMA spirals as a retrofitting measure for RC columns with insufficient flexural ductility. The study adopts a novel simulation framework which incorporates material testing into numerical simulation, hence the name material testing integrated (MTI) simulation. The new MTI simulation is validated using large-scale experimental testing.

21.1 Introduction

During past strong earthquakes, a great number of reinforced concrete (RC) bridges have suffered from major damages. Especially, RC bridges constructed prior to 1971 according to old seismic provisions (AASHO 1969) turned out to be more susceptible to strong seismic events. One of the vulnerabilities of those old bridges was the lack of concrete confinement in RC columns associated with insufficient transverse reinforcement in the form of No. 4 (12.7 mm) steel hoops placed at a spacing of 305 mm. The lack of sufficient confinement resulted in an extremely non-ductile flexural behavior of the bridge columns leading in many cases to their catastrophic collapse.

D. Jung · B. Andrawes (✉)
University of Illinois at Urbana-Champaign, 3122 Newmark Civil Engineering Lab, 205 North Matthews Ave., Urbana, IL 61801, USA
e-mail: andrawes@illinois.edu

D. Jung
e-mail: djung10@illinois.edu

T. T. C. Hsu (ed.), *Concrete Structures in Earthquake*,
https://doi.org/10.1007/978-981-13-3278-4_21

To compensate for the deficient column design, and prevent catastrophic failure of the existing RC bridges, the use of supplementary confinement has been extensively studied as an efficient seismic retrofit method for old RC columns. The confinement strategies developed to date can be divided into two main categories: (1) passive confinement and (2) active confinement. The passive confinement method typically uses steel- or fiber-reinforced polymer (FRP) jackets as the confinement material, and generates the confinement pressure from hoop stresses developed in the external jackets when mobilized by the lateral expansion of concrete (Priestley et al. 1994a, b; Daudey and Filiatrault 2000; Xiao and Wu 2003; Saadatmanesh et al. 1994; Haroun and Elsanadedy 2005 among many others). Active confinement pressure, on the other hand, is applied through prestressing force in the confinement material such as tensioned steel strands even before the dilation of concrete (Gamble et al. 1996; Saatcioglu and Yalcin 2003; Yamakawa et al. 2004; Nesheli and Meguro 2006 among many others). Active confinement shows superior capability in increasing ultimate strain of concrete in compression to its passive confinement counterpart, however, the need for excessive mechanical hardware, labor and time to apply large prestressing force has hindered its widespread use in seismic retrofit.

Recently, active confinement technique using shape memory alloy (SMA) spirals has gained a great potential in seismic retrofitting of RC bridge columns. This retrofit method takes advantage of thermally induced shape memory effect of NiTiNb alloy wires to actively confine concrete without requiring special equipment (Andrawes and Shin 2008; Shin and Andrawes 2010). The efficacy of this new retrofit method has been proven numerically and experimentally (Shin and Andrawes 2011, 2012). For this new SMA-based retrofit method to be widely accepted in the field of earthquake engineering, it is essential to have in-depth investigation of SMA's material behavior and its influence on the overall system response under complicated loading and fast changing loading conditions. However, such performance evaluation can be quite challenging using conventional numerical simulations since complex or unexpected behavior of SMA exhibited under different internal and/or external conditions may not be properly captured by existing numerical models. In order to incorporate more realistic thermos-mechanical characteristics of SMAs under various loading and climate conditions, and to fully exploit them in reinforcing existing RC columns, there is a need for a new simulation framework which carries out accurate, cost-effective structural performance evaluation based on realistic material behavior.

In this paper, a new simulation framework which integrates material testing with numerical simulation, namely material testing integrated (MTI) simulation, is introduced to study the response of a structural bridge columns. The new simulation framework serves as a medium between the two distinctive experimental and analytical domains, and aims to maximize benefits of each domain in evaluating the structural performance. Realistic material behavior under specific conditions can be experimentally drawn from small scale specimens which represent critical regions of a structure, and the obtained material behavior is used in simulating the overall structural response. Herein, the concept of the new simulation technique is applied to an example simulation which studies the seismic performance of RC bridge columns retrofitted with SMA and steel spirals.

21.2 Active Confinement Using Shape Memory Alloy (SMA) Spirals

The fundamental principle of the SMA-based active confinement technique is to utilize large recovery stress of SMA wires which is generated by the shape memory effect (SME) in response to heat application. Typical thermomechanical behavior of SMAs behind the SME is illustrated in Fig. 21.1. In Fig. 21.1a, SMA which initially exist in the full martensite phase at a temperature below the martensite finish temperature (M_f) become partially austenite when the temperature increases to the austenite start temperature (A_s). The full austenite phase will develop in the SMA at a temperature above the austenite finish temperature (A_f). Once the martensite SMA is mechanically loaded then unloaded, it experiences large residual deformation. At a temperature above A_f, the undeformed shape of the SMA is recovered through the SME. If the deformed SMA is constrained from recovering its undeformed shape, large recovery stress is developed in the SMA. Figure 21.2 shows how the prestrained SMA spirals are utilized to actively confine the plastic hinge zone of a RC column. First, martensite SMA wires prestrained by about 6% are wrapped around the plastic hinge zone of the column, forming a spiral shape, and are firmly anchored to the column. Once heated, the constrained SMA spirals develop large recovery stress, and the concrete inside the spiral hoop becomes actively confined.

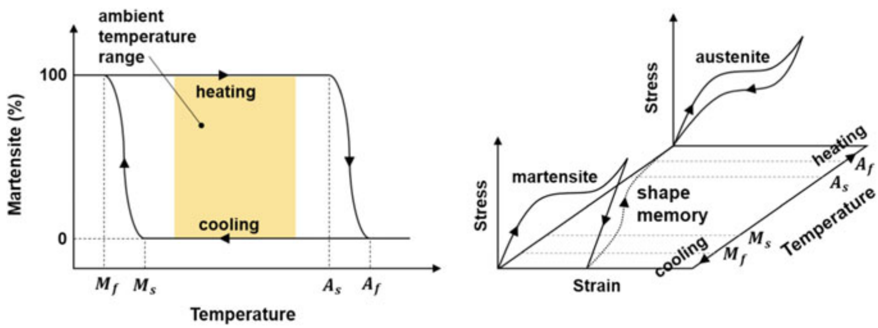

(a) Thermal hysteresis (b) Thermomechanical behavior

Fig. 21.1 Thermal hysteresis and thermomechanical behavior of SMAs

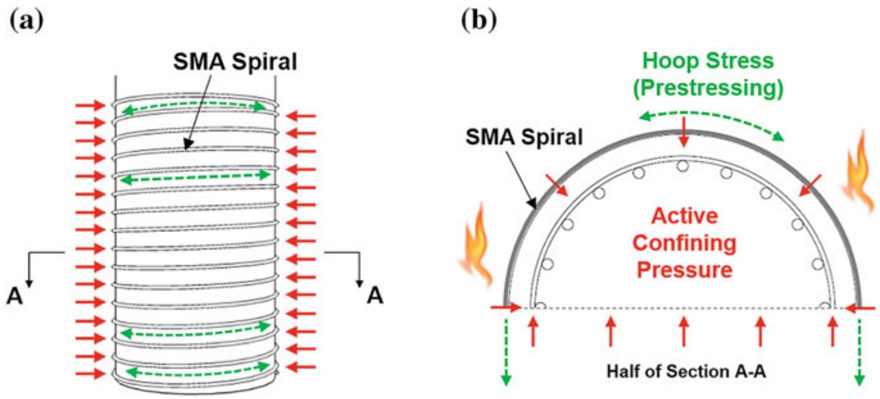

Fig. 21.2 Application of active confinement using SMA spirals: **a** prestrained SMA spirals wrapped around the plastic hinge zone and **b** thermally triggered active confining pressure

21.3 Material Testing Integrated (MTI) Simulation

21.3.1 Conceptual Discussion on MTI Simulation

The main idea of MTI simulation is to derive realistic behavior of materials that have a decisive impact on the structural performance. This is achieved through making full use of experimental test setup, and to use the obtained data to predict its consequences on the basis of numerical simulation techniques. While the overall structural system is numerically represented in an analysis platform by using existing numerical material models, those materials which show complicated or unexpected behaviors can be replaced by physical specimens, and tested in the laboratory under desired conditions. The experimentally obtained data can provide more accurate material behaviors while being integrated into the numerical structural model. The MTI simulation can be considered analogous to pseudo-dynamic hybrid simulation (e.g., Takanashi et al. 1975; Takanashi and Nakashima 1987; Shing et al. 1996) in that the global structural response of a system is constructed through communication and integration of information gained from the two different domains. However, MTI simulation focuses primarily on the material level, and is expected to provide more flexible and cost-effective approaches in cases where a structure has a number of critical regions made of the same material or the impact of varying material-related parameters is of special interest.

MTI simulation can be implemented to study the structural response of a flexural-dominant RC bridge column, assuming that (1) the flexural response of the RC column can be approximated by using a numerical fiber-based beam–column element with uniaxial stress–strain material relationships assigned in each fiber, and that (2) complex response of the RC column which involves high degree of material nonlinearity is concentrated in the limited region of the column (e.g., plastic hinge zone) that can be represented by one or more fiber sections.

Figure 21.3 illustrates the determination of section response within a RC column model based on the experimental concrete behavior. If Sect. 21.1 which describes the plastic hinge response of the RC column is subjected to axial strain (ε_a) and curvature (κ), resultant strain demand (ε_i) of each i th fiber can be computed, according to its location (y_i) in the cross section and the classical beam theory in which the plane section remains plane and perpendicular to the axis of the column (Eq. 21.1). While a physical concrete specimen is loaded under the highest compressive strain (ε_{max}), the obtained stress–strain response of the specimen forms a new uniaxial constitutive relationship of the concrete, and determines concrete stresses. Axial force (N) and bending moment (M) at Sect. 21.1 are calculated by combining concrete fiber stress (σ_i) and area (A_i) as well as numerically modeled steel fiber responses (Eqs. 21.2 and 21.3).

$$\varepsilon_i = \varepsilon_a - y_i \kappa \; i = 1, 2, \ldots, n \tag{21.1}$$

$$\mathrm{N} = \sum_{i=1}^{n} \sigma_i A_i \tag{21.2}$$

$$\mathrm{M} = \sum_{i=1}^{n} -y_i \sigma_i A_i \tag{21.3}$$

21.3.2 Implementation of MTI Simulation Framework

In this study, the MTI simulation strategy was applied to study the seismic behavior of RC column retrofitted with SMA spirals. A simulation framework with three main components was newly established for this study: (1) Main simulation platform which controls overall simulation process, (2) nonlinear analysis tool

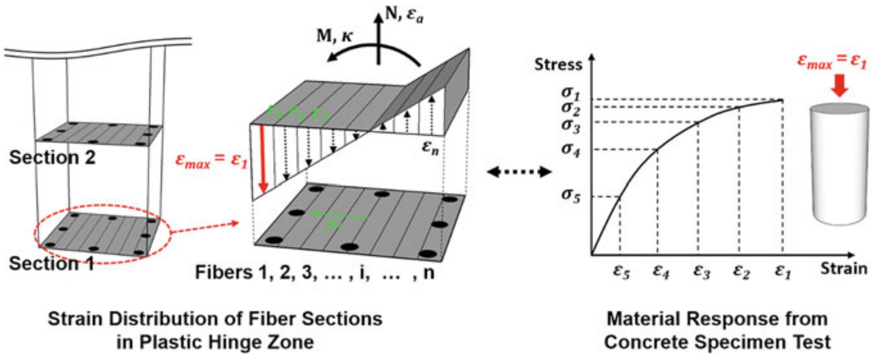

Fig. 21.3 Concept of computing section response using test data of a concrete specimen

predicting the structural response of a RC column model, and (3) experimentally obtained responses of materials of interest.

Figure 21.4 presents schematic diagram and data flow of the MTI simulation framework established in this study. First, UI-SimCor (Kwon et al. 2005) originally developed for pseudo-dynamic hybrid simulation was selected as a main simulation platform of MTI simulation. Through time integration scheme, UI-SimCor computes target displacement (command) of the RC column subjected to earthquake loading at each time step. Once the target displacement is given, the corresponding restoring force (feedback) of the RC column is calculated in a finite element analysis (FEA) software program through nonlinear static analysis, and is returned to UI-SimCor to predict the dynamic response of the column in a step-wise manner. The FEA program which was newly developed in MATLAB for MTI simulation is capable of creating a new hybrid RC column model by incorporating experimental material data into a numerical model constructed based on flexibility-based beam-column element (Spacone et al. 1996a, b). Communication of command and feedback data between UI-SimCor and the FEA program are maintained through Transmission Control Protocol/Internet Protocol (TCP/IP) network.

Experimental data of a material should be able to describe a wide range of material behavior including its limit state. For incorporation into the column model, raw experimental data of concrete are preprocessed to create two main properties: (1) the envelope of the stress–strain curve and (2) the unloading/reloading slopes. Figure 21.4 shows how the uniaxial stress–strain relationship of concrete under

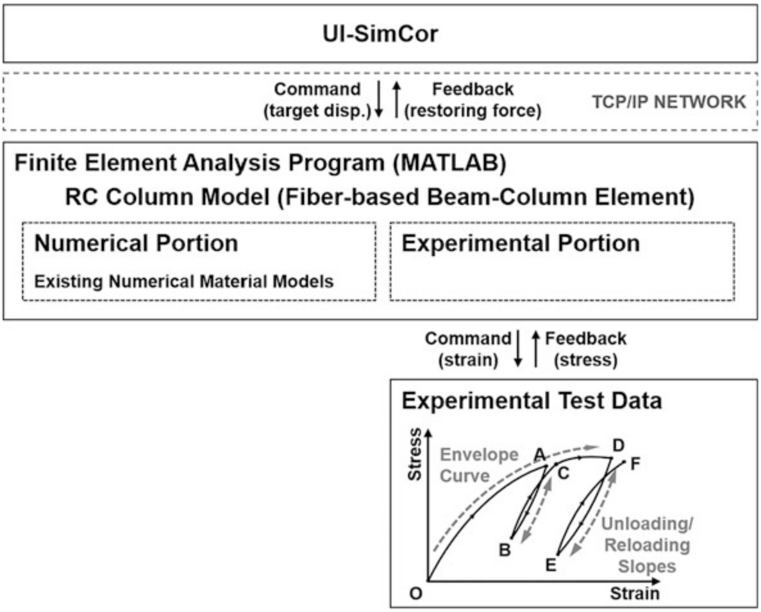

Fig. 21.4 MTI simulation framework and data flow

cyclic loading is converted into the two properties. Data points on the route O-A-C-D constitute the stress–strain envelope, and the data points on the routes A-B-C and D-E-F are used to calculate the unloading/reloading slopes. The tensile behavior of concrete is neglected in this modeling technique. While experimental material data can be provided either through concurrent experimental testing (i.e., real-time mode), or from previous material tests (i.e., non-real-time mode), non-real-time mode was selected in this study.

21.4 Validation of MTI Simulation

In this section, to validate the concept and feasibility of the new simulation approach, MTI simulation was employed to predict response of a RC column specimen obtained from a previous experimental study (Shin and Andrawes 2011). Figure 21.5 shows the configuration of the RC cantilever column tested under quasi-static cyclic loading. The column specimen was retrofitted with SMA spirals at the plastic hinge zone to compensate for the lack of confinement.

According to the geometry and the material properties indicated in Fig. 21.5, a fiber-based numerical model of the tested RC column was first constructed in the FEA program using existing material models, i.e., the Kent–Park–Scott model (Kent and Park 1971; Scott et al. 1982) and the Giuffrè-Menegotto-Pinto model (Giuffrè and Pinto 1970; Menegotto and Pinto 1973) for concrete and longitudinal steel reinforcement, respectively. To mimic the effect of the SMA confinement provided to the tested column, previous test results of concrete cylinders confined

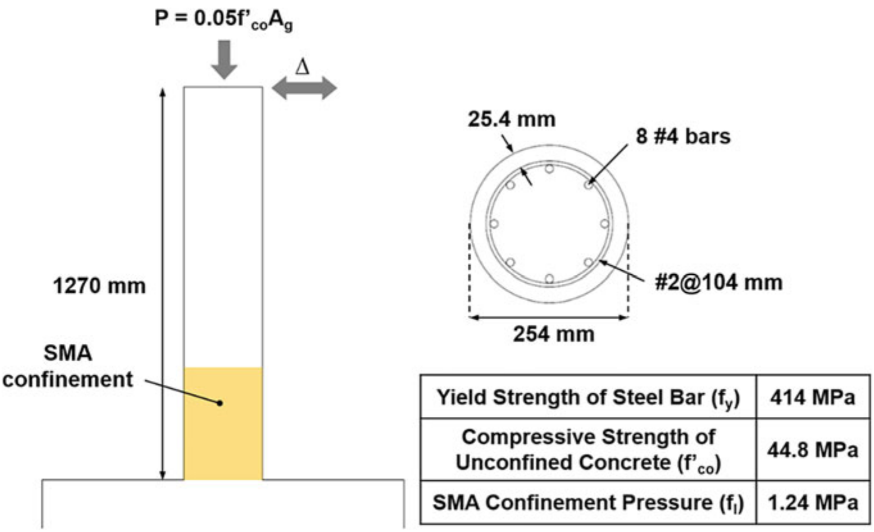

Yield Strength of Steel Bar (f_y)	414 MPa
Compressive Strength of Unconfined Concrete (f'_{co})	44.8 MPa
SMA Confinement Pressure (f_l)	1.24 MPa

Fig. 21.5 Configuration of the tested RC column

with SMA spirals (Chen and Andrawes 2014; Chen 2015) were selected based on the strength of the unconfined concrete ($f'_{co} = 39.6$ MPa) and the confinement pressure ($f_l = 1.23$ MPa). Figure 21.6 shows the uniaxial stress–strain response of SMA confined concrete (SMA-B2S2C) assigned at the first fiber section of the column model which represents the plastic hinge zone. To include the flexibility of the column associated with bond slip behavior of the longitudinal steel bars at the column base, a modified steel bar model (Braga et al. 2012) was implemented at the first fiber section.

MTI simulation was carried out by subjecting the constructed hybrid column model to the constant axial force and lateral cyclic displacements (see Fig. 21.5). Lateral force-displacement responses of the RC column obtained from the experiment and the MTI simulation are compared in Fig. 21.7. While the simulation result showed higher lateral forces at drift ratios around 3% in the positive and negative directions, compared to the experimental result, the overall cyclic responses of the column from the two approaches matched well including the unloading/reloading slopes. The ultimate state of the RC column specimen induced by rupture of the longitudinal steel bar at the drift ratios around 12% was also captured by the MTI simulation without showing crushing of concrete in the SMA confined region.

21.5 Application Example of MTI Simulation

This section presents an application of MTI simulation investigating the seismic performance of RC bridge columns retrofitted with two different confinement schemes. Incremental dynamic analysis (IDA) method proposed by Vamvatsikos and Cornell (2002) was adopted to derive seismic responses of the columns under increasing seismic loading.

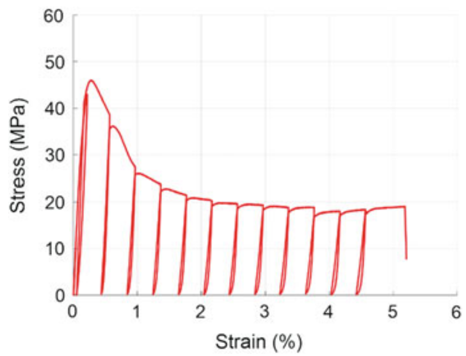

Fig. 21.6 Compressive behavior of the SMA confined concrete cylinder

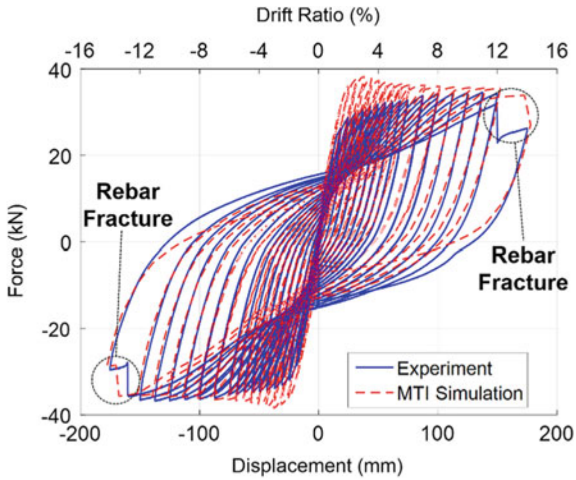

Fig. 21.7 Lateral force-displacement responses of the RC column

21.5.1 Description of RC Bridge Columns

A cantilever RC bridge column was considered in this MTI simulation study. Figure 21.8 shows the geometric configuration of the column which had a diameter of 1.22 m and a height of 4.88 m from the base to the tip. The column was reinforced with 24 No. 10 (32.3 mm diameter) steel bars in the longitudinal direction and with No. 4 (12.7 mm) steel hoops in the transverse direction every 305 mm along the height, respectively. Due to the low volumetric ratio (0.15%) of transverse reinforcement, the expected concrete confinement effect provided by the steel hoops was quite low. To compensate for the lack of flexural ductility, the RC column was equipped with active and passive confinements, using external SMA and steel spirals, respectively at its base along a length (L_c) of 0.8 m where the formation of plastic hinge was expected. To describe the material behaviors of concrete in the confined region, experimental results from a previous concrete cylinder test (Chen and Andrawes 2014; Chen 2015) were utilized. During the test, concrete cylinders with compressive strength of 39.6 MPa were confined with SMA and steel spirals, and tested under uniaxial compression loading. Cyclic stress–strain responses of confined concrete obtained from the test are presented in Fig. 21.9. Comparable confining pressure level was used for both confinement schemes, and confinement properties are summarized in Table 21.1.

The RC column described in Fig. 21.8 was numerically modeled in the FEA program by using a single flexibility-based element with five Gauss-Legendre integration points. While all composite sections were first comprised of existing material models using the Kent-Park-Scott concrete model (Kent and Park 1971; Scott et al. 1982) and the Giuffrè-Menegotto-Pinto steel model (Giuffrè and Pinto 1970; Menegotto and Pinto 1973), only the concrete material at the first section (IP_1) was replaced by the experimental stress–strain responses presented in

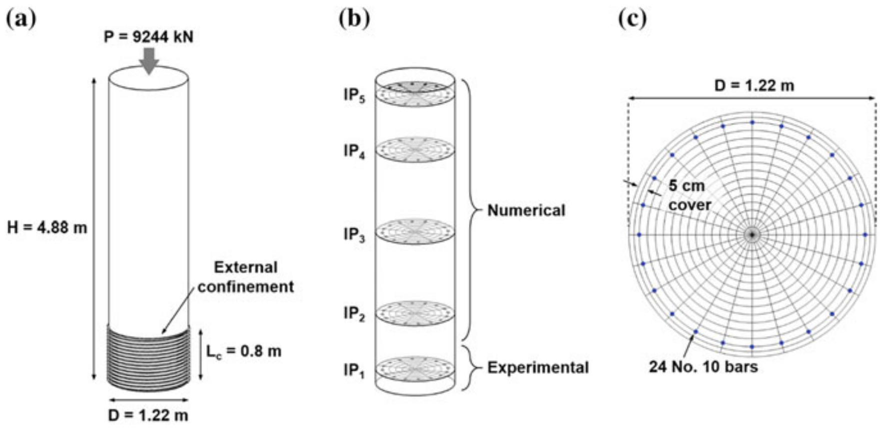

Fig. 21.8 Application of active confinement using SMA spirals: **a** prestrained SMA spirals wrapped around the plastic hinge zone and **b** thermally triggered active confining pressure

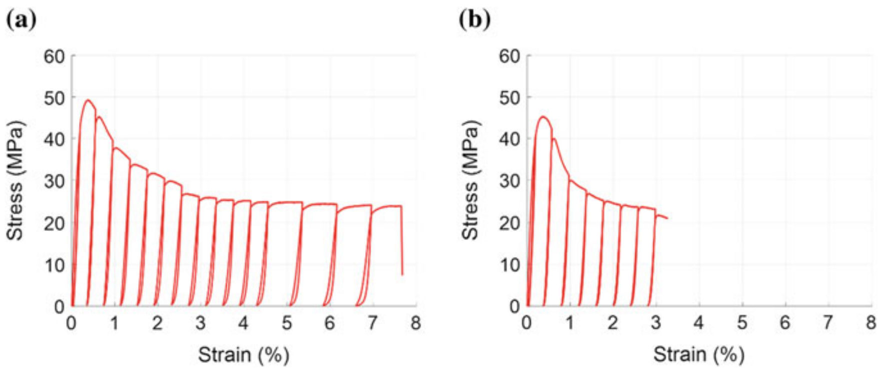

Fig. 21.9 Compressive behaviors of concrete confined by **a** SMA and **b** steel spirals

Table 21.1 Specifications of active (SMA) and passive (steel) confinement schemes used for the concrete cylinders

Confinement properties	SMA spirals	Steel spirals
Wire diameter (mm)	2.0	2.7
Wire spacing (mm)	12.7	12.7
Wire stress (MPa)	607[a]	359[b]
Confining pressure (MPa)	1.92	1.96

[a]Recovery stress of NiTiNb alloy wire
[b]Yield strength of steel wire

Fig. 21.9. Both hybrid column models with the SMA and steel confinements were assumed to have a lumped mass (942280 kg) at the top of the column. The corresponding gravity load (9244 kN) reached about 20% of the column's axial load capacity. P-delta effect (i.e., geometric nonlinearity) of the columns was also considered in the analysis.

21.5.2 Ground Motion Records

Three ground motion records of previous earthquakes were selected from the database of the Pacific Earthquake Engineering Research (PEER) Center to be used as input seismic loading. Table 21.2 shows characteristics of the ground motion records including peak ground acceleration (PGA), predominant period and significant duration.

21.5.3 Simulation Results

During the simulation, the retrofitted RC columns were subjected to the earthquake ground motions with increasing intensities until any of the two limit states was reached, namely, crushing of concrete or fracture of longitudinal steel bars at tensile strain exceeding 12% (Caltrans 2013). The MTI simulation results showed that both columns failed due to the crushing of concrete for all considered ground motion records. The responses of the RC columns were further investigated in terms of PGA (g) of the ground motion records resulting in the failure of the columns, and dynamic pushover curves of the columns exhibited under each ground motion record.

Table 21.2 Characteristics of earthquake ground motion records

Earthquake	Station	PGA (g)	Predominant period (s)	Significant duration[a] (s)
Loma Prieta (1989)	Anderson Dam (Downstream)	0.25	0.20, 0.47	10.5
Imperial Valley (1979)	El Centro Array #13	0.14	0.13	21.6
Northridge (1994)	Hollywood—Willoughby Ave	0.25	0.42, 0.87	12.6

[a]Duration belonging to 5 ~ 95% of Arias intensity

21.5.4 Maximum PGAs

The PGAs of the earthquakes applied to cause the failure of the RC columns are shown in Fig. 21.10. In the figure, the maximum PGAs recorded for the SMA retrofitted column under the three ground motion records ranged from 0.96 to 1.33 g, reaching an average of 1.11 g. On the other hand, the column with the steel confinement recorded an average PGA of 0.65 g at failure. This indicates that the column reinforced with the SMA spirals resisted 71% higher PGA on average under the considered earthquakes, compared to the one with the steel spirals. This result showed that the compressive behavior of concrete enhanced under the active lateral confinement pressure can play a crucial role in increasing the capability of the column to resist higher seismic demand.

21.5.5 Dynamic Pushover Curves

For the purpose of investigating the seismic capacity of the RC columns under specific earthquakes, dynamic pushover curves of the columns were developed from the maximum drift ratio (%) of the columns and the corresponding base shear reported at each simulation run. The maximum drift ratio is equal to the maximum lateral displacement of the column at the center of mass divided by the height from the base. Figure 21.11 compares the dynamic pushover curves of the SMA and steel retrofitted column for each earthquake record. In Fig. 21.11, the responses of the columns which are quite similar in the elastic range start to show deviation after a drift ratio around 1%. After reaching the peak base shear, the steel retrofitted column exhibited a stiffer descending slope, compared to the SMA retrofitted column, and experienced the ultimate state at a drift ratio of 5.2%, on average. The RC column with the SMA confinement showed much gradual softening behavior with an average ultimate drift ratio of 9.8%. The dynamic pushover curves of the columns showed that the experimentally obtained concrete behaviors were well reflected in the post-peak response and the ultimate deformation capacity of the columns reinforced with two different confinement schemes.

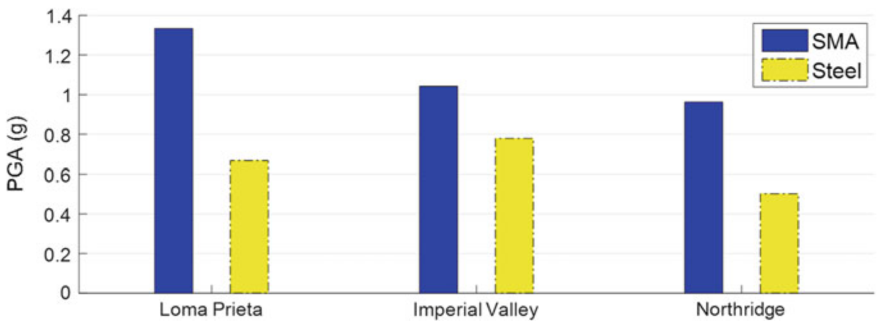

Fig. 21.10 PGAs at the failure of the RC columns

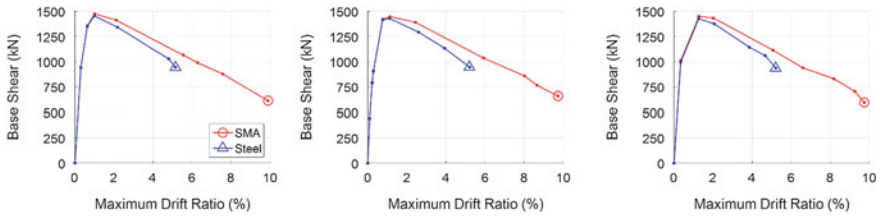

(a) Loma Prieta (b) Imperial Valley (c) Northridge

Fig. 21.11 Dynamic pushover curves of the RC columns

21.6 Conclusions

In this paper, the effectiveness of an SMA-based seismic retrofit method for RC columns was evaluated through a comparative study which adopted a new simulation framework, named material testing integrated (MTI) simulation. The seismic responses of two RC columns retrofitted with SMA and steel spirals were studied based on realistic material behaviors. Important findings of the current study are presented as follows:

- The experimentally obtained concrete behaviors utilized to consider the effect of concrete confinement at the plastic hinge zone greatly affected the overall seismic performance of the RC columns.
- The MTI simulation results demonstrated the superior performance of the SMA confinement in improving the capability of the RC column to resist higher seismic demands to its steel confined counterpart. The SMA retrofitted RC column sustained 71% higher average PGA at failure, compared to the steel retrofitted column.
- The RC column also showed highly ductile response when retrofitted with SMA spirals, achieving an ultimate drift ratio of 88% greater than that of the steel confined column.

It is worth noting that the current MTI simulation study utilized the previous experimental data in the non-real-time mode. More complex SMA related behaviors under various situations such as behavior of SMA confined concrete with severe preexisting damage or significant ambient temperature drop can be concurrently captured by performing MTI simulation in the real-time mode. Furthermore, studies on the active confinement technique using other types of SMAs, e.g., Fe-based SMAs, are required in order to examine the potential of more practical and cost-effective seismic retrofit method.

Acknowledgements This research was funded by the National Science Foundation (NSF) through its Faculty Early Career Development (CAREER) program under Award No. 1055640, and the authors are grateful for the support.

References

American Association of State Highway Officials (AASHO). (1969). *Standard specifications for highway bridges* (10th ed.). Washington DC.

Andrawes, B., & Shin, M. (2008). Seismic retrofit of bridge columns using innovative wrapping technique. In *Proceedings of Structures Congress* (pp. 1–10). Vancouver, Canada.

Braga, F., Gigliotti, R., Laterza, M., D'Amato, M., & Kunnath, S. (2012). Modified steel bar model incorporating bond-slip for seismic assessment of concrete structures. *Journal of Structural Engineering, 138,* 1342–1350.

California Department of Transportation (Caltrans). (2013). *Seismic design criteria, Version 1.7*. Sacramento, CA.

Chen, Q. (2015). *Experimental testing and constitutive modeling of concrete confined with shape memory alloys*. Doctoral dissertation, University of Illinois at Urbana-Champaign.

Chen, Q., & Andrawes, B. (2014). Monotonic and cyclic experimental testing of concrete confined with shape memory alloy spirals. In *Proceedings of 10th US National Conference on Earthquake Engineering*, Anchorage, Alaska.

Daudey, X., & Filiatrault, A. (2000). Seismic evaluation and retrofit with steel jackets of reinforced concrete bridge piers detailed with lap-splices. *Canadian Journal of Civil Engineering, 27,* 1–16.

Gamble, W. L., Hawkins, N. M., & Kaspar, I. I. (1996). Seismic retrofitting experience and experiments in Illinois. In *Proceedings of 5th National Workshop on Bridge Research in Progress*. Buffalo, NY: National Center for Earthquake Engineering Research (NCEER), State University of New York.

Giuffrè, A., & Pinto, P. E. (1970). Reinforced concrete behavior under strong repeated loadings. *Giornale del Genio Civile, 5,* 391–408.

Haroun, M. A., & Elsanadedy, H. M. (2005). Fiber-reinforced plastic jackets for ductility enhancement of reinforced concrete bridge columns with poor lap-splice detailing. *Journal of Bridge Engineering, 10,* 749–757.

Kent, D. C., & Park, R. (1971). Flexural members with confined concrete. *Journal of the Structural Division*.

Kwon, O. S., Nakata, N., Elnashai, A., & Spencer, B. (2005). A framework for multi-site distributed simulation and application to complex structural systems. *Journal of Earthquake Engineering, 9,* 741–753.

Menegotto, M., & Pinto, P. E. (1973). Method of analysis for cyclically loaded reinforced concrete plane frames including changes in geometry and inelastic behavior of elements under combined normal force and bending. In *IABSE Symposium on Resistance and Ultimate Deformability of Structures Acted on by Well-Defined Repeated Loads*, Final report, Lisbon.

Nesheli, K. N., & Meguro, K. (2006). Seismic retrofitting of earthquake-damaged concrete columns by lateral pre-tensioning of FRP belts. In *Proceedings of 8th US National Conference on Earthquake Engineering*. El Cerrito, CA.

Priestley, M. N., Seible, F., Xiao, Y., & Verma, R. (1994a). Steel jacket retrofitting of reinforced concrete bridge columns for enhanced shear strength-part 1: Theoretical considerations and test design. *Structural Journal, 91,* 394–405.

Priestley, M. N., Seible, F., & Xiao, Y. (1994b). Steel jacket retrofitting of reinforced concrete bridge columns for enhanced shear strength-part 2: Test results and comparison with theory. *Structural Journal, 91,* 537–551.

Saadatmanesh, H., Ehsani, M. R., & Li, M. W. (1994). Strength and ductility of concrete columns externally reinforced with fiber composite straps. *Structural Journal, 91,* 434–447.

Saatcioglu, M., & Yalcin, C. (2003). External prestressing concrete columns for improved seismic shear resistance. *Journal of Structural Engineering, 129,* 1057–1070.

Scott, B. D., Park, R., & Priestley, M. J. N. (1982). Stress-strain behavior of concrete confined by overlapping hoops at low and high strain rates. *ACI Journal, 79,* 13–27.

Shin, M., & Andrawes, B. (2010). Experimental investigation of actively confined concrete using shape memory alloys. *Engineering Structures, 32,* 656–664.

Shin, M., & Andrawes, B. (2011). Lateral cyclic behavior of reinforced concrete columns retrofitted with shape memory spirals and FRP wraps. *Journal of Structural Engineering, 137,* 1282–1290.

Shin, M., & Andrawes, B. (2012). Modeling and validation of RC columns seismically retrofitted using shape memory spiral. In *Proceedings of Structures Congress* (pp. 571–580). Chicago, IL.

Shing, P. B., Nakashima, M., & Bursi, O. S. (1996). Application of pseudodynamic test method to structural research. *Earthquake spectra, 12,* 29–56.

Spacone, E., Ciampi, V., & Filippou, F. C. (1996a). Mixed formulation of nonlinear beam finite element. *Computers & Structures, 58,* 71–83.

Spacone, E., Filippou, F. C., & Taucer, F. F. (1996b). Fibre beam-column model for non-linear analysis of R/C frames: Part I Formulation. *Earthquake Engineering and Structural Dynamics, 25,* 711–726.

Takanashi, K., Udagawa, K., Seki, M., Okada, T., & Tanaka, H. (1975). Nonlinear earthquake response analysis of structures by a computer-actuator on-line system. *Bulletin of Earthquake Resistant Structure Research Center, 8,* 1–17.

Takanashi, K., & Nakashima, M. (1987). Japanese activities on on-line testing. *Journal of Engineering Mechanics, 113,* 1014–1032.

Vamvatsikos, D., & Cornell, C. A. (2002). Incremental dynamic analysis. *Earthquake Engineering and Structural Dynamics, 31,* 491–514.

Xiao, Y., & Wu, H. (2003). Retrofit of reinforced concrete columns using partially stiffened steel jackets. *Journal of Structural Engineering, 129,* 725–732.

Yamakawa, T., Banazadeh, M., & Fujikawa, S. (2004). Emergency retrofit of damaged RC columns right after seismic attack using pre-tensioned aramid fiber belts. In *Proceedings of 1st Conference on Applications of FRP Composites in Construction and Rehabilitation of Structures*.

Chapter 22
Test and Analysis of a Self-centering Concrete Frame Under Seismic Action

Chun Jiang, Xilin Lu, Ye Cui and Xu Lu

A new type of self-centering concrete frame was specially designed which consisted of beam–column joint that has limited rotation capacity to release bending moment in the joint, and column foot joint that has uplift and rotation capacity to prevent the joint from damage. Prestressed tendons are used in beams and columns to provide re-centering functions. Shaking table test on this new frame was carried out to investigate the seismic performance and to check the self-centering capacity, and cyclic-static test were conducted to further determine the ultimate capacity of the structure. Test results show that the new type of self-centering concrete frame has excellent seismic performance under strong earthquakes with a little residual deformation. None visible damage is observed in shaking table test. The bearing capacity of the model did not drop under 5% inter-storey drift ratio. Design methodology for this new frame was proposed for future applications to engineering practice.

C. Jiang · Y. Cui · X. Lu
Research Institute of Structural Engineering and Disaster Reduction,
Tongji University, Shanghai 200092, China
e-mail: 2011_Jiang_Chun@tongji.edu.cn

Y. Cui
e-mail: 2010_yecui@tongji.edu.cn

X. Lu
e-mail: b83261835@qq.com

X. Lu (✉)
State Key Laboratory of Disaster Reduction in Civil Engineering,
Tongji University, Shanghai 200092, China
e-mail: lxlst@tongji.edu.cn

T. T. C. Hsu (ed.), *Concrete Structures in Earthquake*,
https://doi.org/10.1007/978-981-13-3278-4_22

22.1 Introduction

Traditional reinforce concrete moment-resisting frames have been proved effective in collapse prevention after several severe earthquakes, such as 2008 Wenchuan earthquake and 2009 Yushu earthquake in China. However, some of the buildings are severely damaged in structural components such as column and beams, which causes great economic lost due to downtime and reconstruction. Higher performance goals have been raised for building structures under seismic excitations in recent decades. Merely collapse prevention is no longer satisfactory, less damage and easier reparation are requested by residents and constructors. Self-centering RC frame is such a new type of frame structure which is characterized by minimal damage under earthquake and immediately rehabilitation after earthquake. Different from traditional monolithic RC frame, precast beam and column components in self-centering frame are connected by clamping force provided by unbonded post-tensioning tendons rather than cast together as a monolithic structure. As severe earthquake arrives, gaps between beams and columns are allowed to open without tensile stress occurred at contact interfaces. Column foot is also allowed to uplift to release excessive axial load. By this opening and uplifting, plastic hinge mechanism is avoided in self-centering frames. Not only the structural damage is limited to some compressive damage at contact interface, the residual deformation will also be minimal since the gaps between components will close due to clamping force provided by post-tensioning tendons. To mitigate this compressive damage and further preserve the integrity of the contact interfaces, various protective measurement has been investigated by researchers, such as inter-locked spiral hoops placed at beam ends (Morgen 2004, Fig. 22.1a), steel angle placed at beam corners (Solberg 2008, Fig. 22.1b), steel plate placed at beam ends (Lu 2015 Fig. 22.1c) or steel jacket armored around the contact region (Song 2015, Fig. 22.1d).

Test results indicates that, depending on the protection measurements adopted, the seismic damage at contact interface could be diminished to some minor crack or even unobservable. For its outstanding seismic performance, as a new type of resilient structure, self-centering RC frame has drawn a lot of research attentions. In order to investigate the over-all structural seismic performance of self-centering frame, a 2/5 scaled tri-axial self-centering RC frame is constructed and tested under both shaking table excitation and cyclic-static load.

22.2 Construction of Tri-Axial Self-centering RC Frame

The difference between self-centering RC frame and monolithic RC frame is focused on the connection region. In this test, all connections between beams columns and slabs are designed to be self-centering to enable the self-centering ability of the structure in both horizontal directions and vertical direction.

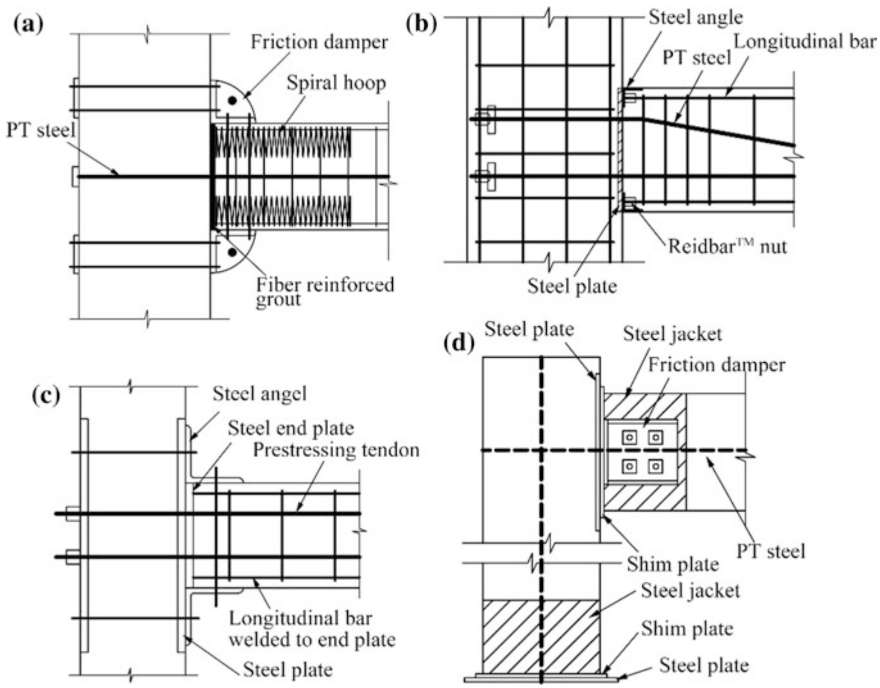

Fig. 22.1 **a** Inter-locked spiral hoops at contact interface. **b** Steel angle at the corner. **c** Steel plate at contact interface. **d** Steel jacket armored at contact interface

Column–base connection of the test model is showed in Fig. 22.2a. Precast column is placed inside the socket foundation. The clearance between column and socket foundation is filled with rubber blocks. The column end is armored with steel jacket which is welded to the longitudinal reinforcement to guarantee the integrity. Steel plate is casted in the bottom of the socket foundation. The column is placed on the steel plate such that the contact between foundation and column foot is steel-to-steel contact, which is expected to be damage-proof. The post-tensioning tendons run through the column, and anchors inside the foundation on one side and on the top of the column on the other side. The PT tendons are designed to remain elastic under severe earthquakes. Hence, as long as no severe damage is occurred at contact interface, PT force together with gravity will always clamp the joint to return to its initial position. In additional, rubber padding could also provide restoring force when the column rotates. This effective is significant especially then the deformation is large (Jiang and Lu 2018).

Self-centering beam–column–slab connection is showed in Fig. 22.2b. Horizontal PT tendons anchored at side columns on both sides of the structure, and run through all components between anchorage points. In order to prevent local compressive damage at contact interface between column and beam ends, steel plates are placed at beam ends and welded to longitudinal reinforcement.

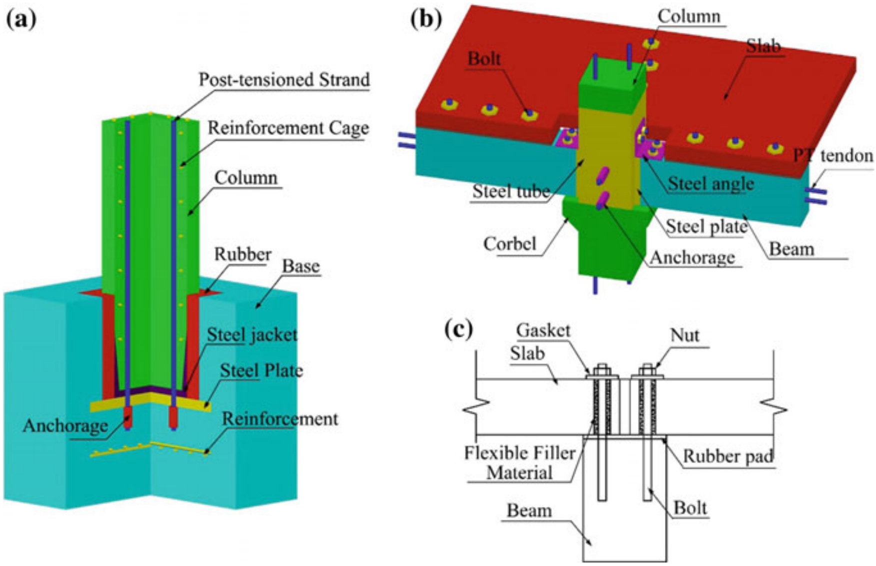

Fig. 22.2 **a** Self-centering column–base connection. **b** Self-centering beam–column connection. **c** Self-centering beam–slab connection

Steel jacket is wrapped around the column near contact region. Beams are placed on the corbel to facilitate the construction on one hand and to avoid collapse in case the PT tendon fails on the other. Steel angles are used to connect the column and beam on the upper side. The steel angles are expected to carry some compressive load at the interface to mitigate the damage, as well as work as energy dissipater.

When the lateral load exceeds the resisting force which initial PT force could provide, the gap will open at the contact interface, the axial distance between columns will increase, and the structure will thus “expand”. If traditional cast-in-place slab is adopted, the monolithic connection between beams and slabs will confine this expansion. Not only slabs will be teared the beam ends also will experience unexpected compressive damage. In order to mitigate this confining effect, special beam–slab connection was adopted as shown in Fig. 22.2c. Precast slab is placed above the beams and connected to the beams by bolts. The diameter of the bolt hole is a little larger than the bolts, hence the sliding between the beams and slabs will not break the bolt connection. In the test, 3 mm of rubber cushions were placed between the slabs and the beams to protect the concrete interface when sliding occurs.

22.3 Shaking Table Test of Self-centering RC Frame

The prototype of the test model is a three-storey concrete frame with seismic fortification intensity of 8(Chinese code), and is 7.0 m in length and 6.0 m in width. The reinforcement of the model satisfies the requirement of Chinese building code. The prototype was scaled to 1:2.5 in length to satisfy the equipment limitations. The similarity relation between the prototype and the model is listed in Table 22.1. The elevation and plan layout of the model is showed in Fig. 22.3a, b. Same section dimension and reinforcement was adopted for all the beams and columns, as shown in Fig. 22.3c, d.

Shaking table test is first conducted to investigate the dynamic response of the structure. Three ground motion record were selected as input excitations, which are Wolong record (Wenchuan, China, 2018), El Centro record (Imperial Valley, US, 1940), Takatori record (Kobe, Japan, 1995). The PGA of seismic records were scaled to 1:0.85 in primary and secondary direction and input to shaking table in X and Y direction respectively. PGA increment between adjacent sequences is 0.1 g or 0.2 g (Table 22.2).

No obvious damage was observed after all test sequences except some minor crack at transition region of concrete to steel plate. However there is still some stiffness degradation according to frequency change during the test as shown in Fig. 22.4. When all test sequence is completed, the frequency of the model

Table 22.1 Main similitude factors of the test model

Parameter	Length	Time	Mass	Stress	Force
Model/ prototype	0.4	0.447	0.08	1	0.16

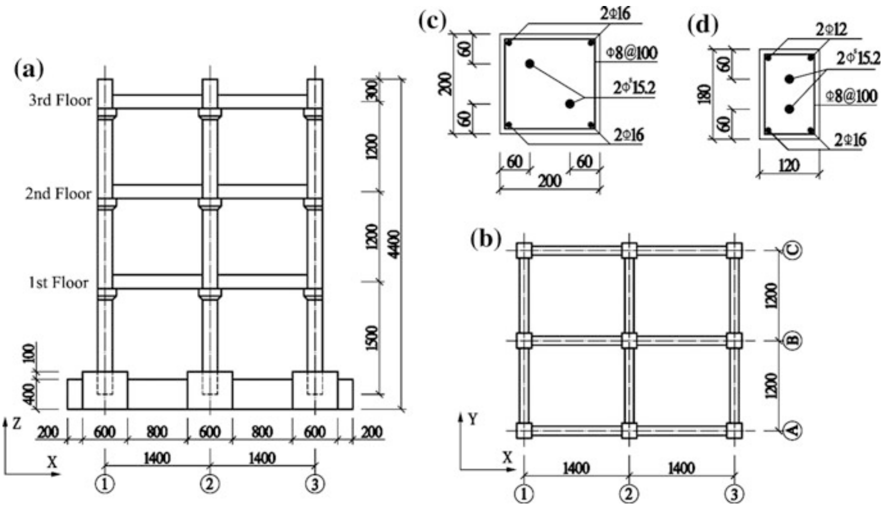

Fig. 22.3 **a** Elevation of the model. **b** Plan layout of the model. **c** Column section. **d** Beam section

Table 22.2 Test sequence in shaking table test

Sequence No.	Input	PGA	Sequence	Input	PGA
1	White noise	0.05	36	White noise	0.05
2–7	Seismic record	0.1	37–39	Seismic record	1
8	White noise	0.05	40	White noise	0.05
9–14	Seismic record	0.2	41–43	Seismic record	1.2
15	White noise	0.05	44	White noise	0.05
16–21	Seismic record	0.4	45–47	Seismic record	1.4
22	White noise	0.05	48	White noise	0.05
23–28	Seismic record	0.6	49–51	Seismic record	1.6
29	White noise	0.05	52	White noise	0.05
30–35	Seismic record	0.8			

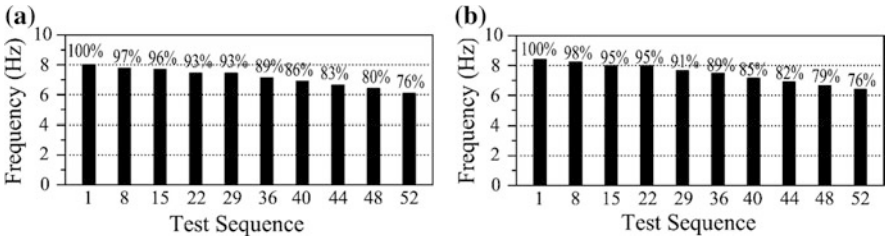

Fig. 22.4 Frequency change in: **a** X direction, **b** Y direction

decreased by 21% in both X and Y direction. The maximum inter-storey drift ratio under 1.6 g excitation is 1/167. The inter-storey drift envelope is showed in Fig. 22.5, this results together with top floor residual displacement is listed in Table 22.3. Which indicate that: first, the inter-storey drift of three floors are very close, the deformation of the structure is dominated by rigid body movement of columns and the gap opening behavior at beam–column connections; second, the residual displacement is negligible compare to maximum displacement.

22.4 Cyclic-Static Test of Tri-Axial Self-centering RC Frame

Considering no obvious damage is observed in shaking table test, and the deformation capacity of the test model is not fully utilized, cyclic-static test is conducted to further investigate the deformation capacity and failure mode of the test model. Cyclic load is applied at three side columns right beneath the third floor corbel by a distributive girder, as shown in Fig. 22.6. To avoid the torsion of the test model, two hydraulic actuators are used in parallel loading. The load scheme is listed in

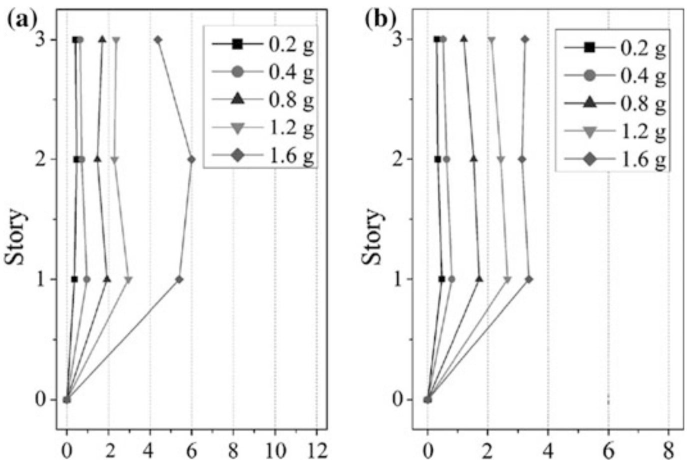

Fig. 22.5 Envelop of Inter-storey drift ratio in: **a** X direction, **b** Y direction

Table 22.3 Summation of model deformation

Test sequence	PGA	Maximum top-floor displacement		Maximum inter-storey drift		Top-floor residual displacement	
		X	Y	X	Y	X	Y
2–7	0.1	1.473	1.726	1/2463	1/2729	0.171	0.132
9–14	0.2	3.199	3.354	1/1577	1/1544	0.203	0.305
16–21	0.4	4.944	5.148	1/1043	1/853	0.082	0.222
23–28	0.6	6.691	7.276	1/628	1/539	0.331	0.28
30–35	0.8	14.752	11.421	1/519	1/583	0.338	0.239
37–39	1	16.093	14.112	1/361	1/462	0.446	0.174
41–43	1.2	18.053	18.136	1/339	1/377	0.15	0.078
45–47	1.4	22.742	21.071	1/279	1/333	0.672	0.151
49–51	1.6	32.506	24.111	1/167	1/291	0.652	0.221

Table 22.3. The load displacement increases step-by-step, and three cycles are applied at each step. Among those load steps, load step 2 with load displacement of 7 mm is 1/550 in loading drift ratio (load displacement/ height of the actuator), which is corresponding to inter-storey drift ratio limitation under minor earthquake according to Chinese code. Load step 7 with load displacement of 71 mm is 1/50 in loading drift ratio, which is corresponding to inter-storey drift ratio limitation under rare earthquake (Table 22.4).

Obvious gap opening behavior at beam–column connection is observed at load step 4. Some minor crack on concrete cover is observed in load step 5, and the crack continues to develop until load step 8. The maximum inter-storey drift ratio exceed the code limitation in load step 7, the structural damage in this step is still limited.

Fig. 22.6 Test setup

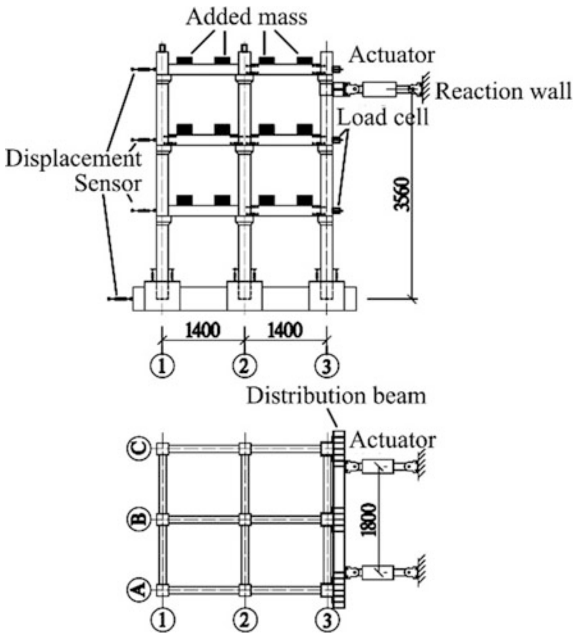

Table 22.4 Loading protocol

Load step	Amplitude (mm)	Cycles	Loading drift ratio
1	3	3	1/1187
2	7	3	1/509
3	14	3	1/254
4	28	3	1/127
5	43	3	1/83
6	57	3	1/62
7	71	3	1/50
8	94	3	1/38
9	118	3	1/30
10	142	3	1/25
11	166	3	1/21
12	190	3	1/19

The most damaged connection in load step 7 is shown in Fig. 22.7a. In load step 9, steel plate separate with beam end at some connections due to rapture of the welding point between longitudinal bars and the steel plate. Rapture occurs at the top side of the beam because of the excessive tensile force applied by steel angle. In load case 10, some cracks on the beam ends (shown as “crack” in Fig. 22.7b) were widely opened while the gaps (shown as “gap” in Fig. 22.7b) between beams and

(a) (b)

Fig. 22.7 Joint damage under: **a** 1/50, **b** 1/25 loading drift ratio

columns are closed. Presumably, the concrete part at beam end was pulled out together with steel plate by the bolt connecting the steel angel at the top of the beam end, due to the bonding failure between reinforcement and the concrete. As the load displacement increases, in load step 12, nearly half of the beams ends experiences this pulling out damage. Some crushing and separation of steel plate also occurred at other beam ends. The lower the storey is the severer the damage is and the damage in middle column is severer than side column. Since this pattern is coincidence with the axial load applied on the beam, there is a positive relation between the axial load and the damage. The lateral load of the model kept increasing in load step 12, however the test could not go further due to the maximum stroke of the actuator. After all load steps were applied, the deformation of the model and the local damage of the connection is shown in Fig. 22.8. As shown by figure, the damage is concentrate in beam ends, the other part of the structure is barely damaged.

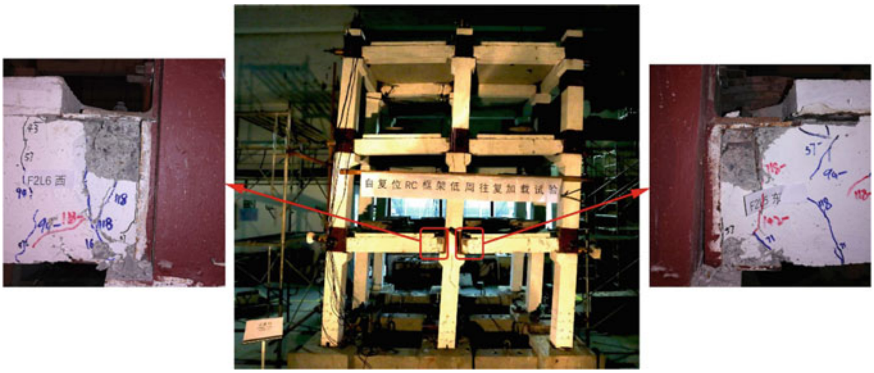

Fig. 22.8 Model deformation and damage after all load steps (1/19 loading drift ratio)

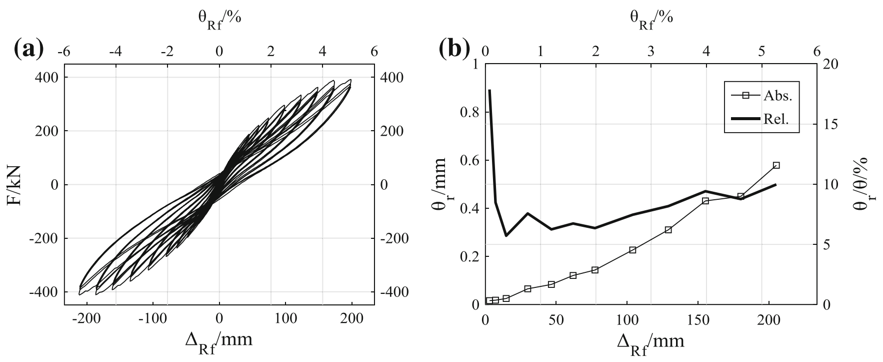

Fig. 22.9 **a** Relationship between lateral load and top-floor displacement. **b** Relationship between load displacement and residual deformation

The relationship between base shear and top displacement is shown in Fig. 22.9a. The hysteretic loop shows some extent of flag-shaped character with low energy dissipating capacity. Which indicate that, although the steel angle is installed in the beam–column connection, the structure is still lack of energy dissipating capacity. The hysteretic loop is plumper when the load displacement in larger, which indicate that some plastic deformation has been developed. Figure 22.9b shows the absolute and relative maximum inter-storey residual drift ratio in each load step. Relative inter-storey residual drift ratio is the ratio of inter-storey residual drift to maximum drift in current load step. The absolute drift increases as the load displacement increases. When all loads were applied, the maximum residual drift ratio is 0.58%, which is only a little exceeds 0.5% residual drift ratio limitation recommended by McCormick (1997). The relative inter-storey residual drift ratio is about 5% before load step 7 (Except for load step 1. As the initial load step, the connection between the actuator and the model is not ideal), and the relative residual drift gradually increases until the last load step to about 10%.

22.5 Conclusion

Seismic performance of proposed tri-axial self-centering frame is investigated by shaking table test and cyclic-static test. The result of shaking table test indicates that the structural damage of self-centering frame is negligible under severe earthquakes. In cyclic-static test, the frame is loaded to over 5% inter-storey drift ratio, the result shows

(1) The test model had excellent deformation capacity, the bearing capacity did not drop within the limitation of test equipment.
(2) The damage under 2% inter-storey drift is limited. The damage under 4% or larger is significant, respiration would be needed before reoccupation.

(3) The damage is concentrated in beam ends at connection region, the damage on other part of the structure is minimal.
(4) The damage is caused by crushing of the concrete cover at the corner of the beam and the rupture of the longitudinal reinforcement due to excessive tensile strength of the steel angle.
(5) The residual deformation is acceptable until maximum inter-storey drift of 5%.

References

Morgen, B., & Kurama, Y. (2004). A friction damper for post-tensioned precast concrete beam-to-column joints. *PCI Journal, 49*(4), 112–133.

Solberg, K., Dhakal, R. P., Bradley, B., Mander, J. B., & Li, L. (2008). Seismic performance of damage-protected beam-column joints. *ACI Structural Journal*, *105*(2), 205–214.

Lu, X., Cui, Y., Liu, J., & Gao, W. (2015). Shaking table test and numerical simulation of a 1/2-scale self-centering reinforced concrete frame. *Earthquake Engineering and Structural Dynamics, 44*(12), 1899–1917.

Song, L. L., Guo, T., Gu, Y., & Cao, Z. L. (2015). Experimental study of a self-centering prestressed concrete frame subassembly. *Engineering Structures, 88,* 176–188.

Jiang, C., & Lu, X. (2018). Simulation of contact surfaces in self-centering reinforced concrete frames with test validation. *Fib symposium 2017*, Maastricht, Netherland.

MacRae, G. A., & Kawashima, K. (1997). Post-earthquake residual displacements of bilinear oscillators. *Earthquake Engineering and Structural Dynamics, 26*(7), 701–716.

Chapter 23
Structural Performance of Slender High-Strength SFRC Columns (Fc300) Under Axial and Lateral Loadings

Yusuke Tanabe, Daisuke Honma and Masaro Kojima

This paper describes an experimental study conducted on slender columns made of Steel Fiber Reinforced Concrete (SFRC). The compressive strength of SFRC ranges from 200 to 300 N/mm^2. The cross section of these slender SFRC columns is reduced to one-fourth that of columns made of ordinary concrete. Lateral loading tests are carried out to investigate the flexural performance of these columns. The test results show that using steel fiber decreases the damage of cover concrete of the columns and increases their flexural strength. In addition, the results show that slender SFRC columns possess high drift capacity.

23.1 Introduction

Along with the increase in constructions of high-rise buildings, the development of high-strength concrete has considerably progressed. In the 1980s, many studies on high-strength concrete of 100 N/mm^2 grade had been made, in Japan. Recently, ultra-high-strength concrete of compressive strength over 150 N/mm^2 has been developed and applied to columns which would bear high level axial forces, such as columns of lower floors in high rise buildings. For example, 150 N/mm^2 concrete was applied in the first floor columns of a 59-storey apartment building and in the CFT columns of a 300 m-high multi-purpose building. Furthermore, because there are more demands for larger spaces, even in low-rise buildings, reduction of the

Y. Tanabe · D. Honma (✉) · M. Kojima (✉)
Takenaka Corporation, 1-5-1 Ohtsuka, Inzai-shi, Chiba 270-1395, Japan
e-mail: daisuke.honma@takenaka.co.jp; honma.daisuke@takenaka.co.jp

M. Kojima
e-mail: kojima.masarou@takenaka.co.jp

Y. Tanabe
e-mail: tanabe.yuusuke@takenaka.co.jp

T. T. C. Hsu (ed.), *Concrete Structures in Earthquake*,
https://doi.org/10.1007/978-981-13-3278-4_23

cross-sectional area of columns is required. Therefore, as Japan is a highly seismic country and for the purpose of examining the structural performance of slender columns using ultra-high-strength concrete, experiments were carried out on two kinds of columns under axial and lateral loads. Steel fibers were added to the concrete in order to prevent a brittle fracture of such high-strength concrete under large compression stresses. In addition, high-strength steel bars were applied in the columns to stand high level axial forces.

23.2 Material Properties of High-Strength SFRC

Table 23.1 shows the composition of the concrete. The water—binder (cement + silica fume) ratio was 9.5%, and silica fume rate was 24%. In order to achieve an Fc300 concrete, two kinds of curing were carried out. Table 23.2 shows the methods of curing. Primary curing was a steam curing and the secondary one was an autoclave curing. The autoclave curing was carried out for more than 4 h.

Steel fibers were added to the concrete in order to prevent a brittle fracture of such high-strength concrete under large compression stresses. Concrete contained steel fibers with a volume ratio V_f = 1.0 vol. %. Figure 23.1 showed mixed steel fibers and flow test of SFRC. Two kinds of steel fibers were used. One kind was of straight type with fine diameter and the other kind was hooked at its ends.

Figure 23.2 shows an example of the compressive test results, and the Young's modulus–compressive strength relationships. In the figure, the calculated Young's modulus based on the Japanese NewRC equation is shown. The coefficients K_1 and K_2 were, respectively, taken as 1.0 and 0.95. Calculated values by the NewRC equation approximately match the experimental results. The Poisson ratio at the time of calculating Young's modulus was about 0.2.

In order to investigate the tensile properties of SFRC, splitting and bending tests were carried out. Figure 23.3 shows an example of the splitting and bending tests' results. For the splitting test specimen, the strain was measured by gauge attached on the specimen in the horizontal radial direction. When the strain exceeded 175 μ, the splitting tensile strength was constant, and split cracking occurred. The average cracking strength was 9.2 N/mm^2.

Bending test was carried out on 100 × 100 × 400 mm prism specimen. The bending stress was obtained by dividing the moment occurring in the specimen by the section modulus and the curvature was calculated from the value of the

Table 23.1 Composition of the concrete

Design compressive strength	W/B (%)	Silica fume ratio (%)	Super plasticizer (%)	Fiber ratio (vol. %)
Fc300	9.5	24%	B × 4.0	1.0

W: Water, B: Binder (Cement + Silica fume)

Table 23.2 Methods of curing

Curing type	Heating rate (°C/h)	Maximum temperature (°C/h)	Cooling rate (°C/h)	Highest temperature retention time (h)
Primary curing	Higher than 20	90 ± 10	Lower than 20	More than 72
Secondary curing	15–40	180 ± 5	Lower than 20	More than 4

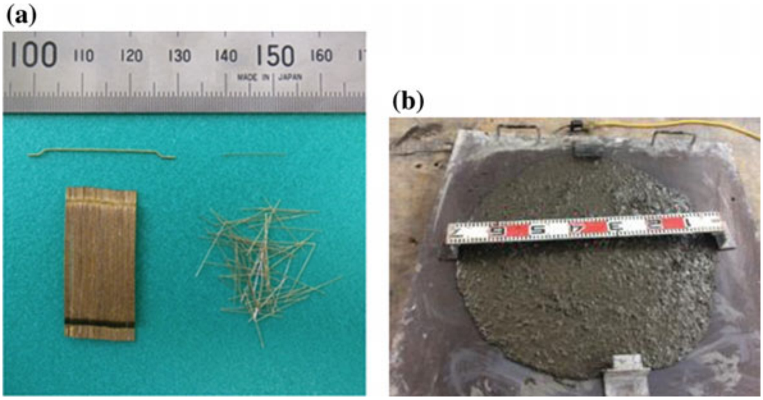

Fig. 23.1 **a** Steel fibers and **b** flow test of SFRC

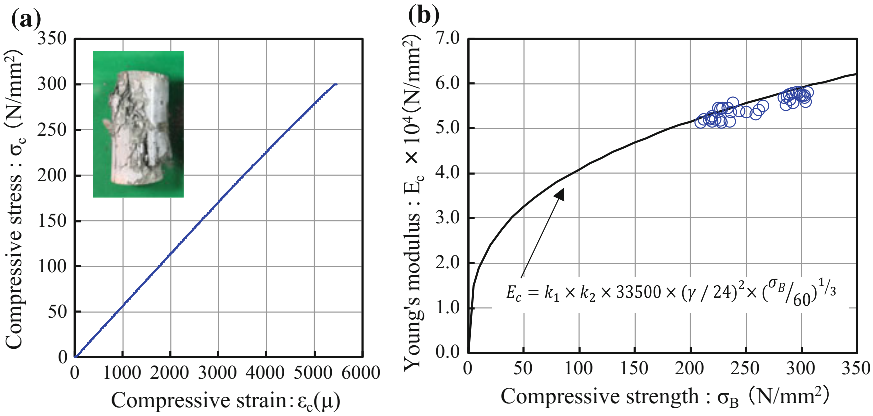

Fig. 23.2 **a** Compressive test result and **b** Young's modulus—Compressive strength relationships

displacement gauge attached to the back of the specimen. Whereas several cracks developed in the specimen after the initial cracking occurred, only one of the cracks expanded gradually, and the load gradually decreased. The average maximum bending stress was 21.1 N/mm^2. The tensile strength and bending strength of concrete were enhanced by steel fibers.

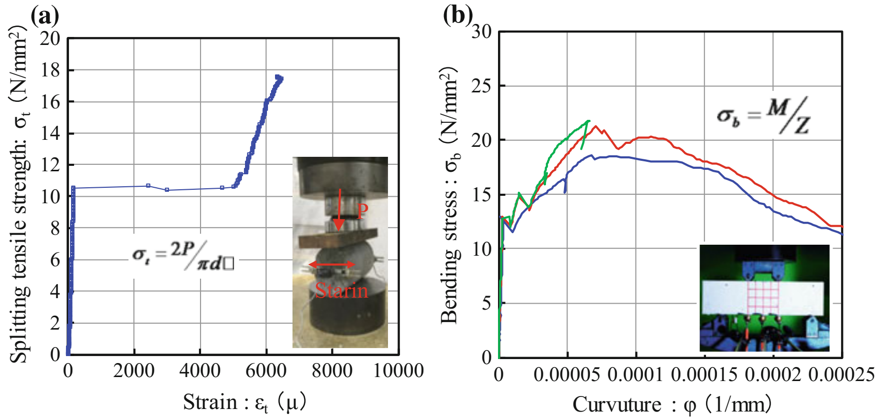

Fig. 23.3 **a** Splitting test and **b** bending test

23.3 Experiments of Super Slender Pin-Joint Columns

23.3.1 Outline of Specimens

Table 23.3 shows the characteristics of the specimens. Figure 23.4 shows their elevation and cross sections, as well as the details at the columns' ends. The constructed specimens were of full size. The specimens' diameter and height were, respectively, 195 mm and 3200 mm. The height-to-diameter ratio (h/D) was 16.4. Each specimen was composed of a column part, two stubs and a gap at each column end. Main bars were inserted in a sheath tube embedded in the stub portion, and then high-strength grout was filled into the gaps. The super slender pin-joint columns were assumed to only sustain axial forces and were required to be able to deform laterally at the time of earthquake. Therefore, in order to reduce the generated moment at the end of the columns, the bond of the main bars was deactivated by wrapping them by rubber tape. At the same time, the cross sections of the joint

Table 23.3 Characteristics of specimens (Pin-joint columns)

Specimen	Main bars	Hoops	Axial force ratio	Bond
S-1	4-D19 SD685	D6@50 SD785	0.1	Unbonded
S-2			0.2	Unbonded
S-3			0.4	Unbonded
S-4			0.2	Bonded

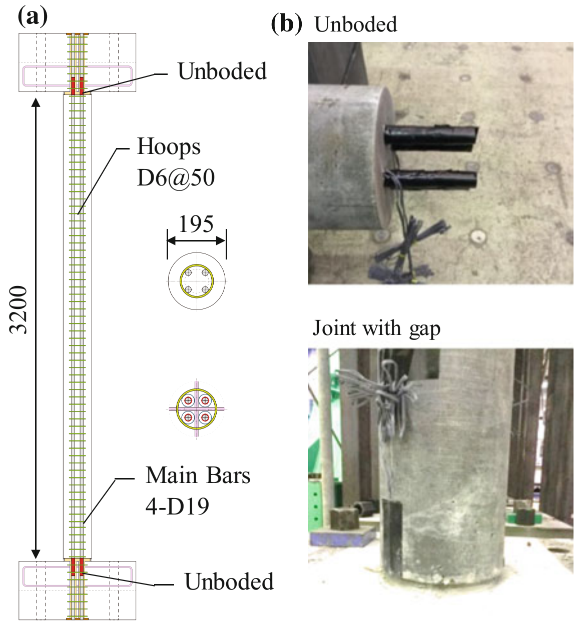

Fig. 23.4 **a** Elevation and cross sections of specimens (Unit: mm), and **b** details at columns' ends

ends of the columns were reduced from 195 mm to 175 mm. By doing so, a rotation margin was provided at the end of the columns, and crushing at the column compression edge was prevented.

For the parameters of the experiment, a total of four elements were set with an axial force ratio η and a state of main bars bonding. The axial force ratio η was set from 0.1 to 0.4. The main bars were of SD685 type, and the hoops were of SD785 type.

23.3.2 Loading Plan

As shown in Fig. 23.5, experiments were carried out using a pantograph system to apply loading. Specimens were subjected, simultaneously, to axial and lateral loads. Figure 23.5 also shows the loading history relative to the lateral load. While the axial load was kept constant when testing each specimen, the axial load ratio varied from a specimen to another and ranged from 0.1 to 0.4. The upper part of the loading setup was provided with linear sliders to let the axial force jacks slide when applying the lateral loading. Reversed cyclic lateral loading was controlled by displacement where the amplitude was gradually increased starting with the drift ratio R = 0.1%. Taking into account the repeated vibrations caused by long-period ground motions, loading cycles of the major drift ratios were repeated 10 times.

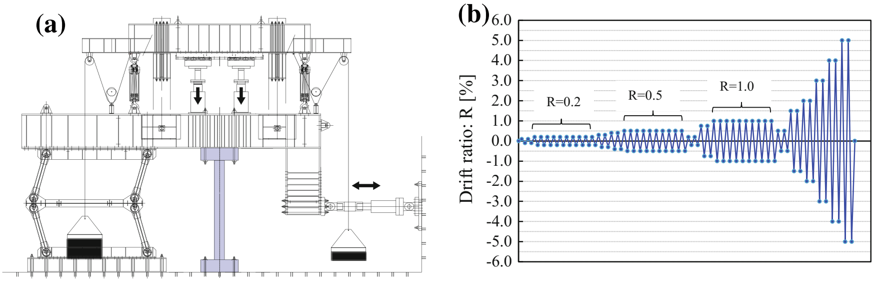

Fig. 23.5 **a** Experimental test setup, and **b** lateral loading history

23.3.3 Experimetal Results

Figure 23.6 shows the lateral load–drift ratio relationships of the specimens by correcting their respective PΔ effect. Figure 23.7 shows the damage undergone by the specimens at the drift ratio R = 1.0% and 3.0%. First, no damage was observed on S-1 (η = 0.1) and S-2 (η = 0.2) specimens between the drift ratio R = 0.1% and 1.0%. Between R = 1.0% and 3.0%, crushing occurred in the grout joints at the base and top ends of the columns, but these two columns could hold the applied axial forces until the end of testing. S-3 (η = 0.4) showed almost the same behavior as S-1 and S-2 until R = 1.0%. But at the ultimate level that corresponded to R = 2.0%, it showed an abrupt failure and lost its capacity to hold the applied axial load.

Figure 23.8a shows the calculated M–N interaction curves of these pin-joint columns based on the bending analysis, assuming the cross section without the main bars. SFRC compressive model was considered linear, and the tensile strength of concrete was ignored. Values by the bending analysis approximately match the experimental results.

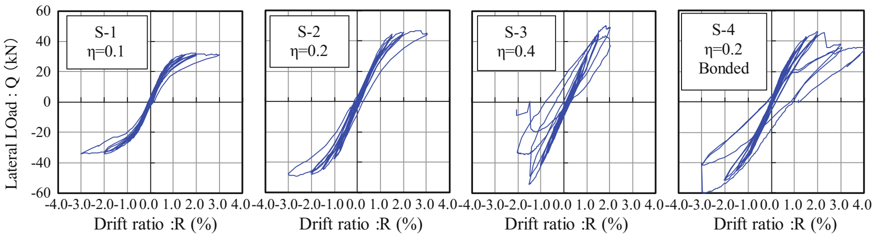

Fig. 23.6 Lateral load—Drift ratio relationships

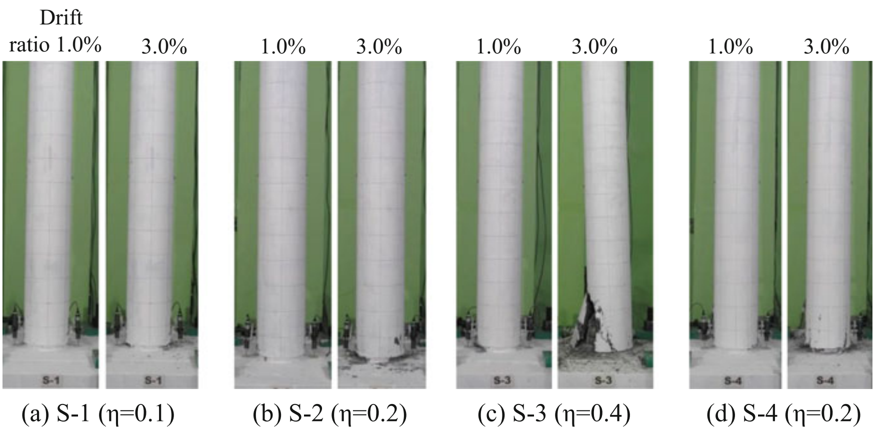

Fig. 23.7 Damage of specimens

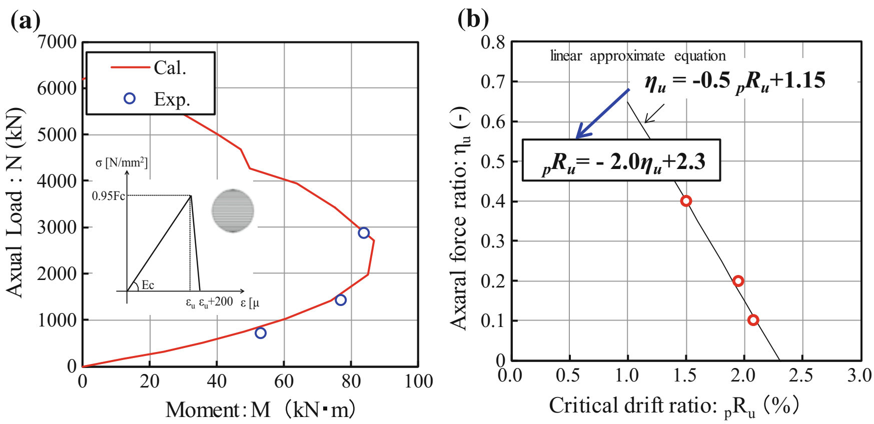

Fig. 23.8 **a** Bending analysis and **b** critical drift ratio

Figure 23.8b shows the critical drift ratios of the pin-joint columns. The critical drift ratio was set as the drift ratio beyond the maximum strength at which the lateral force became 80% of the maximum strength. As the axial force ratio η increased, the critical drift ratio decreased linearly. Therefore the approximate expression of the critical drift ratio was obtained from the experimental result (Eq. 23.1).

$$ {}_{p}R_{u} = -2.0\,\eta_{u} + 2.3\,[\%] \tag{23.1} $$

23.4 Experiment of a Flexural Moment Resistance Column

23.4.1 Outline of Specimen

Table 23.4 shows the characteristics of the full size single specimen. Figure 23.9 shows the elevation and cross sections of the specimens and varying axial load. The column cross section was B × D = 440 × 410 mm, the height was 2500 mm, and the shear span ratio M/QD was 3.0. The main bars were of SD685 type, and the hoops were of SBPD 1275 type. The experiments were carried out using the same pantograph system as before to apply loading. The axial force ratio η was varied between the load 5000 kN (η = 0.09) corresponding to a negative axial load and 10000 kN (η = 0.18) corresponding to a positive axial load. Ultimate flexural strength was calculated using NZS 3101 stress block.

23.4.2 Experimental Results

Figure 23.10 shows the lateral load–drift ratio relationship, and the comparison between the envelope curves corresponding to the axial tension and compression parts. Figure 23.11 shows the damage of specimen from R = 0.5% to the end of loadings. On the positive loading direction, bending cracking occurred at R = 0.5% and damage at the edge splitting cracks at column's end occurred at R = 0.75%. Cover concrete cracks occurred at R = 1.0%, and the specimen reached its maximum strength at R = 1.0%. On the negative loading direction, bending cracking occurred at R = −0.5%, and edge splitting cracks at column's end occurred at R = −1.0%, cover concrete cracks at R = −2.0%. The specimen reached its maximum strength at R = −1.5%. The cracks greatly extended beyond the drift ratio R = 2.0%, but splitting of cover concrete not observed due to the presence of steel fibers. Until the drift ratio R = 0.5%, the hysteresis curve was almost linear. Looking at the influence of the axial force ratio η, the maximum flexural strength on the positive loading direction (compression axial load) was 1.24 times higher than that on the negative loading direction (tension axial load).

Table 23.4 Characteristics of specimen

Specimen	Cross section Height (mm)	Main bars	Hoops	Axial force ratio	Bond
Ro-C1	410 × 440 2500	4-D32 SD685	U12.6@100 SBPD1275	0.09–0.18	Bonded

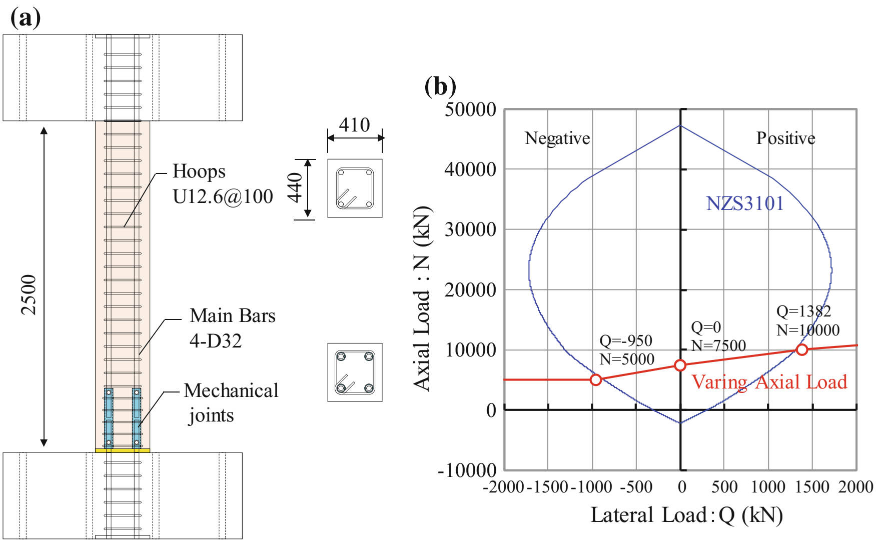

Fig. 23.9 **a** Elevation and cross sections of specimens (Unit: mm) and **b** varying axial load

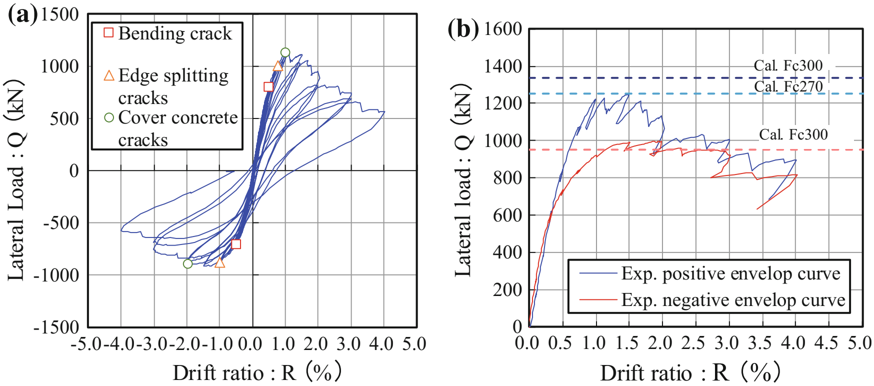

Fig. 23.10 **a** Lateral load—Drift ratio relationship, and **b** comparison between the positive and negative envelope curves

23.4.3 Analytical Simulation

Figure 23.12 shows the model used in the analysis. SFRC was modeled by solid elements, and steel bars by truss elements. Material properties of the model were those obtained by the material tests.

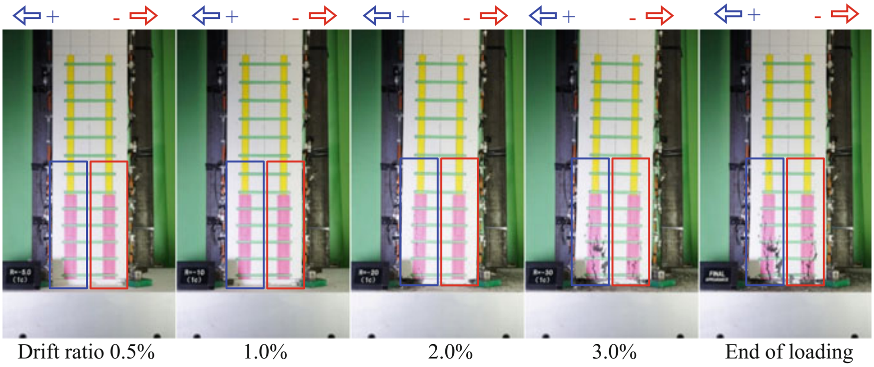

Fig. 23.11 Damage of specimen

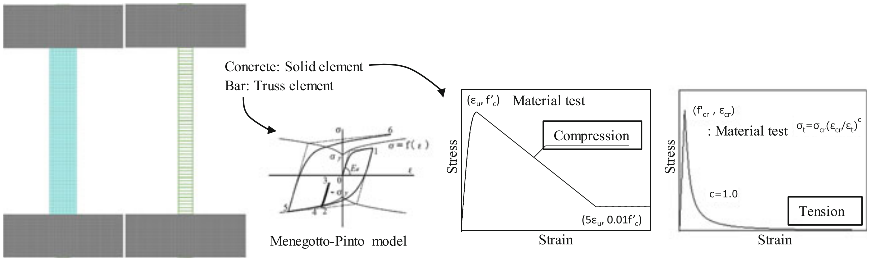

Fig. 23.12 FE model

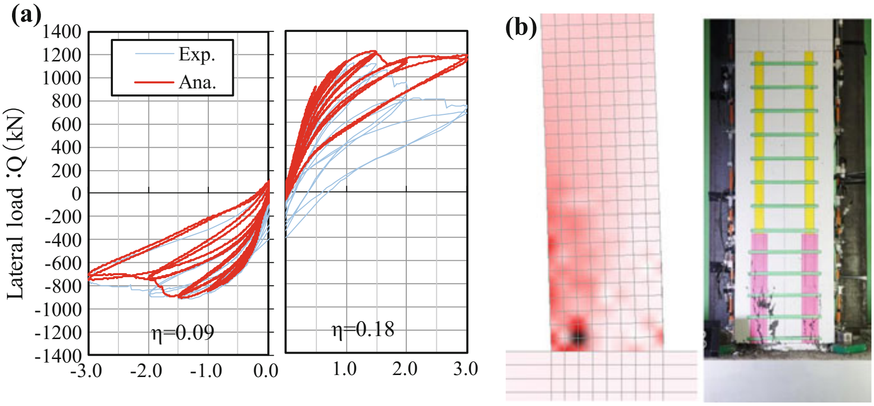

Fig. 23.13 **a** Result of FE analysis and **b** minimum principal stress distribution and damage of specimen at R = 3.0%

Fig. 23.14 View of building and super slender columns using Fc300 concrete

Figure 23.13 shows the result of the FE analysis and minimum principal stress distribution. While the analysis almost reproduced the test results until R = ±1.5% including the maximum strength level, the post peak part was overestimated.

23.5 Application to Building

Figure 23.14 shows an example of applying a high-strength SRFC slender column to a building. It is a four-floor apartment building in Yokohama city. Fc300 slender pin-joint columns were applied for the first time as columns supporting the eaves at the main entrance. By using these slender columns, a good outlook in the main entrance could be achieved. This is because ultra-high-strength SFRC has almost the compressive strength of steel.

23.6 Conclusion

Experimental study was carried out on slender columns made with SFRC of compressive strength about 300 N/mm^2. Two types of fibers were mixed into the concrete of specimens. The tested columns were subjected to combined axial compression and lateral loadings. The following findings were drawn.

(1) Fc300 N/mm^2 was achieved by an appropriate technology of materials and curing.
(2) The tensile strength and flexural strength of concrete were enhanced by steel fibers.
(3) Slender pin-joint columns showed high deformation performance. Critical drift ratio was affected by the axial force ratio and was appropriately estimated by an approximate expression.

(4) A slender moment resistant column was carried out. Using the stress block of NZS3101 resulted in calculated strength values that agreed well with experiment results. Using FE modeling, the flexural response of the tested moment resistant column was simulated analytically and its global behavior was successfully obtained.

References

Fafitis and Shah. (1985). *Lateral reinforcement for high-strength concrete columns, ACI*, No. SP-87, pp. 213–232.

Fintel, M. et al. (1986). *Column shortening in tall structures*, Portland Cement Associations.

The world's highest building is taking shape, Engineers Australia. (2007). 79(2).

Collins, M. P. et al. (1993). *Structural design considerations for high-strength concrete, concrete international*, pp. 27–34, ACI.

Nagashima, T., Sugano, S., Kimura, H., & Ichikawa, A. (1992). Monotonic axial compression test on ultra-high-strength concrete tied columns. In: 10th *World conference on earthquake engineering*, pp. 2983–2988.

Tomosawa, F., & Noguchi, T. (1993). Relationship between compressive strength and modulus of elasticity of high-strength concrete. In *High-strength concrete, third international symposium*, pp. 1247–1254.

Sun, Y., & Sakino, K. (1993). Flexural behavior of reinforced concrete columns confined in square steel tube. In *10th world conference on earthquake engineering*, pp. 4365–4370.

American Concrete Institute: Building Code Requirements for Structural Concrete (ACI318-14) and Commentary. (2014).

Standards Association of New Zealand: Concrete Design Standards, NZS3101 (2011).

Architectural Institute of Japan (AIJ), Ultimate Strength and Deformation Capacity of Buildings in Seismic Design. (1990).

Ozbakkaloglu, T., & Sattcioglu, M. (1996). Rectangular stress block for high-strength concrete. *ACI Structural Journal, 101*(4):475–483, 2004 Applied technology council (ATC). (1996). *Seismic evaluation and retrofit of concrete buildings, 1 and 2*, *Report No. ATC-40,* Redwood City, CA.

Participants from 11 Countries

Book title: Concrete Structures in Earthquake

Originator type (author or editor): Editor

Names, affiliations, email addresses and sequence of the authors/editors
Thomas T. C. Hsu, University of Houston, Department of Civil and Environmental Engineering, 4726 Calhoun Rd, 77204 Houston, TX, USA. Email: thsu@uh.edu

Marketing text
This book gathers 23 papers by top experts from 11 countries, presented at the Houston International Forum: Concrete Structures in Earthquake. The design of infrastructures to resist earthquakes has always been the focus and mission of

T. T. C. Hsu (ed.), *Concrete Structures in Earthquake*,
https://doi.org/10.1007/978-981-13-3278-4

scientists and engineers located in tectonically active regions, especially around the "Pacific Rim of Fire" including China, Japan, and the USA. The pace of research and innovation has accelerated in the past three decades, reflecting the need to mitigate the risk of severe damage to interconnected infrastructures, and to facilitate the utilization of high-speed computers and the internet. The book describes the design and analysis of concrete structures subjected to earthquakes, and the respective papers advance the state of knowledge in disaster mitigation and address the safety of infrastructures in general.

About the Author
Thomas T. C. Hsu is a Moores Professor of Civil Engineering at the Department of Civil and Environmental Engineering, University of Houston (UH). Professor Hsu is a Distinguished Member, American Society of Civil Engineers, and an Honorary Member, American Concrete Institute. The widely recognized Structural Research Laboratory at UH was created and named after him. Professor Hsu authored three books, including "*Unified Theory of Concrete Structures*" (John Wiley and Son.), and edited three books, including "*Infrastructure Systems for Nuclear Energy*" (John Wiley and Son.). The *Thomas T. C. Hsu Symposium on Shear and Torsion in Concrete Structures* at the 2009 New Orlean ACI Convention was pulished as ACI SP-265. He has won seven research awards, including Boase Award, Anderson Award and Wason Medal from American Concrete Institute. His research work has formed the basis for the shear and torsion design provisions in the American Concrete Institute Building Code.

USP
Presents cutting-edge research results from experts in the field of concrete structures
Helps engineers to design concrete structures that are safer and more economical
Enhances the development of codes, specifications and recommendations
Serves as a valuable reference guide for professional engineers working with concrete structures and in earthquake engineering.